Nadia Magnenat-Thalmann
Osman Ratib
Hon Fai Choi *Editors*

3D Multiscale Physiological Human

Springer

3D Multiscale Physiological Human

Nadia Magnenat-Thalmann
Osman Ratib · Hon Fai Choi
Editors

3D Multiscale Physiological Human

Springer

Editors
Nadia Magnenat-Thalmann
MIRALab
University of Geneva
Geneva
Switzerland

and

Institute for Media Innovation
Nanyang Technological University
Singapore
Singapore

Osman Ratib
Division of Nuclear Medicine
and Molecular Imaging
University Hospital of Geneva
Geneva
Switzerland

Hon Fai Choi
MIRALab
University of Geneva
Geneva
Switzerland

ISBN 978-1-4471-6274-2 ISBN 978-1-4471-6275-9 (eBook)
DOI 10.1007/978-1-4471-6275-9
Springer London Heidelberg New York Dordrecht

Library of Congress Control Number: 2013957122

Printed on acid-free paper

Springer is part of Springer Science+Business Media (www.springer.com)

Preface

Recent scientific advancements in the field of 3D physiological human research have enabled the investigation and simulation of human articulations with increasingly more detail. This progress has been made across several research domains, each focusing on separate aspects of the musculoskeletal system with customized modalities tailored for the relevant scale. As a result, knowledge has diversified while being formulated in heterogeneous terminologies specific to each research domain. However, to understand the place of each individual piece, the puzzle must be fit together. Indeed, the physiology of human movement is hierarchically organized in functional units which collaborate over a wide spectrum of spatiotemporal scales, ranging from the molecular to the organ level. Therefore, the need to converge research efforts into a multidisciplinary approach using multi-scale modalities has been formulated. This is especially relevant in the medical field, where the continuous introduction of new technologies has led to an increasing amount of patient data available to the physicians. Therefore, computer-based solutions are needed to assist in obtaining a comprehensive integration and presentation of medical data to improve diagnosis. This is a necessary step to advance the frontiers of personalized healthcare, which is particularly motivated by the rising burden of musculoskeletal disorders, especially in the increasing population of elderly people.

However, integrative solutions can only be successfully achieved through a mutual dialogue between the multiple disciplines involved. This book aims to increase the awareness of the variety in methodologies and knowledge paradigms providing a reference that will help computer scientists, physicians, biomedical engineers, and physiologists in uncovering potential gaps and opportunities for integration.

Overviews and examples of recent scientific and technological advancements are presented for the relevant domains of cell and tissue engineering, imaging and visualization, simulation of articulations, and medical analysis. Chapter 1 introduces the book with an overview of state-of-the-art techniques to create virtual 3D models of patients for diagnosis and treatment. Chapter 2 gives an overview of current tissue engineering approaches in osteochondral regenerative medicine. This is followed by three chapters describing the advancements of multi-modal medical imaging, deformable model image segmentation, and multi-scale visualization of biomedical data. Chapter 6 gives a general overview of current human

musculoskeletal modeling research which is narrowed down to the field of clinical gait analysis in Chap. 7. The advancements in computational approaches is further illustrated by chapters describing examples of joint contact modeling, shoulder joint complex modeling, dynamic hip joint analysis, and coupled biomechanical modeling of the face and oral structures. Finally, the last two chapters present a current state-of-the-art in the development of computer-aided diagnosis tools and an overview of modalities in medical knowledge management.

Nadia Magnenat-Thalmann
Osman Ratib
Hon Fai Choi

Contents

Contributors

Ehsan Arbabi School of Electrical and Computer Engineering, College of Engineering, University of Tehran, Tehran, Iran, e-mail: earbabi@ut.ac.ir

Lazhari Assassi MIRALab, University of Geneva, Battelle, Building A, 7 Route de Drize CH-1227 Carouge, Geneva, Switzerland, e-mail: assassi@miralab.ch

Imon Banerjee CNR IMATI-Genova, Via De Marini 6, 16149 Genova, Italy, e-mail: imon.banerjee@ge.imati.cnr.it

Matthias Becker MIRALab, University of Geneva, Geneva, Switzerland, e-mail: becker@miralab.ch

Chiara Eva Catalano CNR IMATI-Genova, Via De Marini 6, 16149 Genova, Italy, e-mail: chiara.catalano@ge.imati.cnr.it

Ibrahim Fatih Cengiz 3B's Research Group—Biomaterials, Biodegradables and Biomimetics, Headquarters of the European Institute of Excellence on Tissue Engineering and Regenerative Medicine, University of Minho, AvePark, Guimarães, Portugal; ICVS/3B's—PT Government Associate Laboratory, Braga/Guimarães, Portugal, e-mail: fatih.cengiz@dep.uminho.pt

Lorenzo Cesario Softeco Sismat S.r.l, Via De Marini 1, Genova, Italy, e-mail: lorenzo.cesario@softeco.it

Hon Fai Choi MIRALab, University of Geneva, Geneva, Switzerland, e-mail: choi@miralab.ch

Arjan Egges Virtual Human Technology Lab, Utrecht University, Princetonplein 5, 3584, CC, Utrecht, The Netherlands

Sidney Fels Department of Electrical and Computer Engineering, University of British Columbia, Vancouver, Canada

Cormac Flynn School of Engineering, Science and Primary Industries, Wintec, Hamilton, New Zealand

Dr. Karl-Ingo Friese Welfenlab, Division of Computer Graphics, Leibniz Universität Hannover, Welfengarten 1, 30167 Hannover, Germany, e-mail: kif@welfenlab.de

Christoph Hurschler Laboratory for Biomechanics and Biomaterials, Orthopaedic Department, Hannover Medical School, Hannover, Germany

David García Juan Service de Médecine Nucléaire, Hôpitaux Universitaires de Genève, Rue Gabrielle-Perret-Gentil 4, 1205 Genève, Switzerland

Zhiping Luo Virtual Human Technology Lab, Utrecht University, Princetonplein 5, 3584, CC, Utrecht, The Netherlands

Sean Lynch Laboratory for Biomechanics and Biomaterials, Orthopaedic Department, Hannover Medical School, Hannover, Germany

Forough MadehKhaksar Virtual Human Technology Lab, Utrecht University, Princetonplein 5, 3584 CC, Utrecht, The Netherlands

Nadia Magnenat-Thalmann MIRALab, University of Geneva, Battelle, Building A, 7 Route de Drize CH-1227 Carouge, Geneva, Switzerland; Institute for Media Innovation, Nanyang Technological University, 50 Nanyang Drive, Singapore, Singapore, e-mail: thalmann@miralab.ch

Mohammad Ali Nazari Department of Mechanical Engineering, Faculty of Engineering, University of Tehran, Tehran, Iran

Gavin Olender Laboratory for Biomechanics and Biomaterials, Orthopaedic Department, Hannover Medical School, Hannover, Germany

Joaquim Miguel Oliveira 3B's Research Group—Biomaterials, Biodegradables and Biomimetics, University of Minho, Headquarters of the European Institute of Excellence on Tissue Engineering and Regenerative Medicine, AvePark, Guimarães, Portugal; ICVS/3B's—PT Government Associate Laboratory, Braga/Guimarães, Portugal

Patrizia Parascandolo Softeco Sismat S.r.l, Via De Marini 1, Genova, Italy, e-mail: patrizia.parascandolo@softeco.it

Yohan Payan TIMC-IMAG Laboratory, CNRS UMR 5525, University Joseph Fourier, La Tronche, France

Pascal Perrier Grenoble INP, Speech and Cognition Department, Gipsa-lab, UMR CNRS 5216, Stendhal University, Grenoble, France

Nicolas Pronost Virtual Human Technology Lab, Utrecht University, Princetonplein 5, 3584 CC Utrecht, The Netherlands, e-mail: nicolas.pronost@uu.nl

Osman Ratib Hôpitaux Universitaires de Genève, Service de Médecine Nucléaire, Rue Gabrielle-Perret-Gentil 4, 1205 Genève, Switzerland, e-mail: osman.ratib@hcuge.ch

Rui Luís Reis 3B's Research Group—Biomaterials, Biodegradables and Biomimetics, University of Minho, Headquarters of the European Institute of Excellence on Tissue Engineering and Regenerative Medicine, AvePark, Guimarães, Portugal; ICVS/3B's—PT Government Associate Laboratory, Braga/Guimarães, Portugal

Francesco Robbiano CNR IMATI-Genova, Via De Marini 6, 16149 Genova, Italy, e-mail: francesco.robbiano@ge.imati.cnr.it

Jan Rzepecki Welfenlab, Division of Computer Graphics, Leibniz Universität Hannover, Welfengarten 1, 30167 Hannover, Germany, e-mail: jrzepecki@welfenlab.de

Michael Schwarze Laboratory for Biomechanics and Biomaterials, Orthopaedic Department, Hannover Medical School, Hannover, Germany

Frank Seehaus Laboratory for Biomechanics and Biomaterials, Orthopaedic Department, Hannover Medical School, Hannover, Germany

Victor Sholukha Laboratory of Anatomy, Biomechanics and Organogenesis, Université Libre de Bruxelles, Brussels, Belgium, e-mail: vcholouk@ulb.ac.be

Michela Spagnuolo CNR IMATI-Genova, Via De Marini 6, 16149 Genova, Italy, e-mail: michela.spagnuolo@ge.imati.cnr.it

Ian Stavness Department of Computer Science, University of Saskatchewan, 176 Thorvaldson Building, 110 Science Place, Saskatoon, S7N 5C9, SK, Canada

Karelia Tecante Laboratory for Biomechanics and Biomaterials, Orthopaedic Department, Hannover Medical School, Hannover, Germany e-mail: Tecante Gutierrez.Karelia@mh-hannover.de

Daniel Thalmann Institute for Media Innovation, Nanyang Technological University, 50 Nanyang Drive, Singapore, Singapore; EPFL, Lausanne, Switzerland, e-mail: daniel.thalmann@epfl.ch

Sara Trombella Hôpitaux Universitaires de Genève, Service de Médecine Nucléaire, Rue Gabrielle-Perret-Gentil 4, 1205 Genève, Switzerland

Serge Van Sint Jan Laboratory of Anatomy, Biomechanics and Organogenesis, Université Libre de Bruxelles, Brussels, Belgium

Ricardo Manuel Millán Vaquero Welfenlab, Division of Computer Graphics, Leibniz Universität Hannover, Welfengarten 1, 30167 Hannover, Germany, e-mail: rmillan@welfenlab.de

Gianni Viano Softeco Sismat S.r.l, Via De Marini 1, Genova, Italy, e-mail: gianni.viano@softeco.it

Loris Vosilla Softeco Sismat S.r.l, Via De Marini 1, Genova, Italy, e-mail: loris.vosilla@softeco.it

Bastian Welke Laboratory for Biomechanics and Biomaterials, Orthopaedic Department, Hannover Medical School, Hannover, Germany

Franz-Erich Wolter Welfenlab, Division of Computer Graphics, Leibniz Universität Hannover, Welfengarten 1, 30167 Hannover, Germany, e-mail: few@welfenlab.de

Part I
Introduction

Chapter 1
Towards Effective Diagnosis and Prediction via 3D Patient Model: A Complete Research Plan

Nadia Magnenat Thalmann, Hon Fai Choi and Daniel Thalmann

1.1 Introduction

Rapid aging of the society is a global trend. In the aging community, joint diseases are common problems. Major joints (knees, hips, hands and spine) are the most affected sites and typical symptoms are significant functional impairment, inflammation, pain, stiffness and loss of mobility. Magnetic Resonance Imaging (MRI) technique is widely used to capture the cartilage contour morphology and can detect changes in cartilage thickness for the purpose of diagnosis and treatment planning. Effective diagnosis and treatment planning rely heavily on the MRI-based image processing, reconstruction and modeling, analysis, etc. We present in this chapter novel methods and techniques, new algorithms and software to assist the better diagnosis and treatment of joint diseases.

Associated with the aging is the progressive degeneration process of articulation: degenerative chondral lesions typically manifest on MRI as multiple areas of cartilage thinning of varying depth and size, usually seen on opposing surfaces of an articulation. In case of major degenerative lesions, a total knee arthroplasty is practiced. To better treat the disease with long-term outcome, predictive planning is a new concept yet to be explored. Taking into the consideration the progressive

N. Magnenat Thalmann (✉) · H. F. Choi
MIRALab, University of Geneva, Geneva, Switzerland
e-mail: thalmann@miralab.ch

H. F. Choi
e-mail: choi@miralab.ch

N. Magnenat Thalmann · D. Thalmann
Institute for Media Innovation, Nanyang Technological University, 50 Nanyang Drive, Singapore, Singapore

D. Thalmann
EPFL, Lausanne, Switzerland
e-mail: daniel.thalmann@epfl.ch

N. Magnenat-Thalmann et al. (eds.), *3D Multiscale Physiological Human*,
DOI: 10.1007/978-1-4471-6275-9_1,

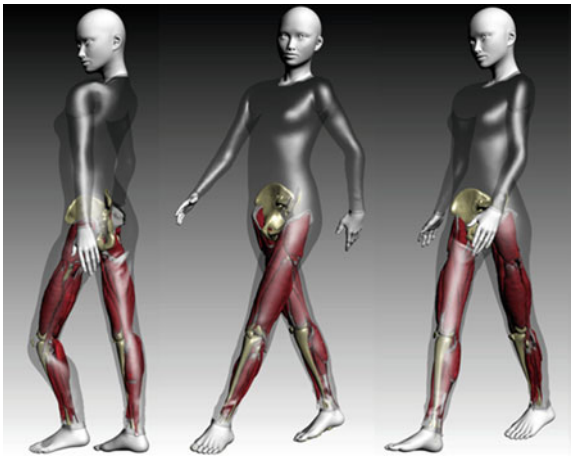

Fig. 1.1 Example of a virtual patient model

degeneration, we explain in this chapter how to develop simulation technology for the optimal planning of joint treatment.

It is essential that multidisciplinary researchers join forces to investigate MRI-based novel segmentation algorithms, multi-scale anatomical modeling techniques, animation-enabled prediction of surgical outcome, and GPU graphics-enhanced optimization. Eventually, these basic research efforts will be applied for simulation-enabled optimal planning of joint treatment.

1.2 Objectives

In the coming twenty years and more, most industrialized countries will bear the burden of an aging population and concurrently grapple with a shortage of healthcare workers. It can be envisioned that in 15–20 years, healthcare could become more convenient as patients could self-diagnose using sensors in tablet computers and the information will be transmitted to a doctor, who will provide online consultation via 3D interactive media systems. A first step towards this vision is to create a time dependent 3D physics-based anatomical and physiological model of a patient (3D patient model) as illustrated in Fig. 1.1. That means, at any time, we can have an instance of the patient model depending on his/her body state. Having this, doctors will have the possibility to compare several different instances of the model in order to decide optimal treatment options. This will also allow patients to be more aware of their state of health at anytime and anywhere. This 3D interactive patient model will help doctors and healthcare professionals improve their diagnosis and treatment as illustrated in Fig. 1.2.

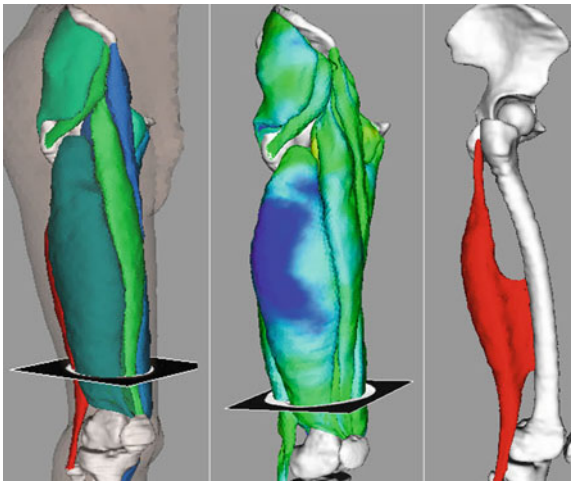

Fig. 1.2 3D interactive patient models

Today, imaging technologies including MRI are becoming more popular in medical diagnosis. However, these imaging technologies are typically limited to patients at rest or over a limited range of motion. They fail to represent the dynamic and physical forces that are critical to understand the mechanical functions of the human body. It is challenging for doctors today to use only images to analyze the patient's motions. To set up the link between the segmented MRI with patient motion behavior, a 3D patient model with kinematic and dynamic functions should be built based on the biomechanics properties of human bones and soft tissues (in health and in disease states). The 3D patient model could assist doctors to diagnose the effect of injured patient, analyze the intervention results and predict the stage of recovery. For example, when seeing a patient with a leg problem, doctors may suggest the following options: a special exercise program, surgery or rest. Traditionally, such diagnosis requires doctors to imagine how human motion with complex movements of dynamic anatomical structures could evolve (Fig. 1.3). Therefore, we believe in a 3D patient model that can be updated with new parameters coming from predictive computing and a database of 3D standardized patients. With comparison of the different possible outcomes, doctors can determine the best treatment plan. This approach could reduce the incidence of inaccurate diagnosis, unnecessary investigation or re-intervention leading to prolonged hospitalization.

Concerns have been expressed that the number of osteoporotic fractures may increase by as much as a factor of four in the next 50 years, due to an increasingly ageing population. Common musculoskeletal diseases/injuries due to old age and misuse may lead to osteoporotic bones and degeneration of intervertebral disc in spine and lower limb articulating joints. These are investigated in three different ways: clinical studies, experimental studies, and computer based modeling studies. The potential to improve clinical outcome is the obvious driving force for all inves-

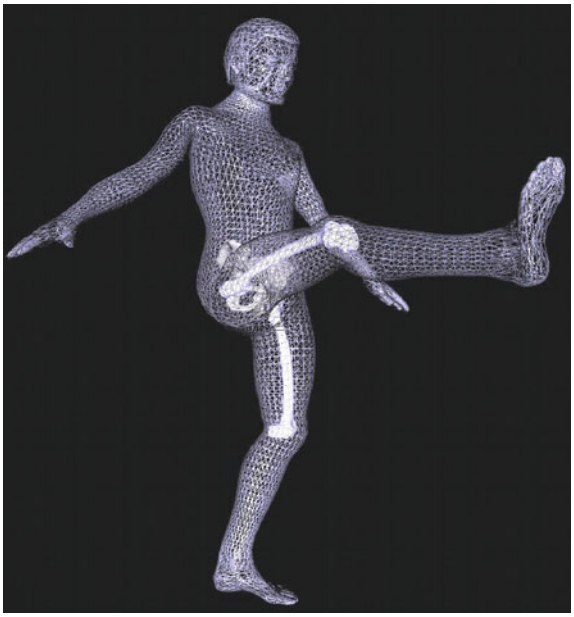

Fig. 1.3 Human motion with complex movements

tigations, with clinical studies themselves having the ability to identify the clinical outcome, but rarely being able to identify "how or why" a certain presentation might occur. Clinical studies are also limited by ethical constraints. Experimental and modeling studies are therefore formulated to further the understanding of why particular outcomes occur in particular circumstances, and to investigate the effect of variables which cannot readily be constrained and/or studied in the clinical situation.

When comparing the capabilities of experimental and validated computer modeling techniques, the latter certainly has the most flexibility to inform experimental investigations and surgical management planning to explore the effect of multiple variables which would be prohibitively expensive or time consuming to explore experimentally.

For the 3D patient model, a detailed 3D musculoskeletal system of spine with lower limb should be incorporated to perform biomechanical investigation into the increased risk of osteoporotic bone, changes in load transfer and kinematical characteristic at different articulating segments following different simulated pre- and post- augmentation procedures and to reduce "post stress shield" effects under various physiological loads/motions interactively. This interactive information is essential for the clinical refinements of the augmentation technique, whether they will be introduced by changes in the mechanical properties of the materials used, in the way the procedure is performed or by a combination of the two. We need to develop breakthrough technologies such as:

(1) Building and visualizing 3D patient model from medical images automatically
(2) Building computational biomechanics models for simulations of deforming hard and soft musculoskeletal tissues
(3) Building prediction and diagnosis models for therapy
(4) Developing integrated patient models for medical education
(5) Validation and evaluation methodologies for 3D patient modeling.

1.3 Building and Visualizing 3D Patient Model from Medical Images Automatically

1.3.1 Multi-Scale Biomechanical Modeling

Intensive studies have been carried out on constitutive modeling of articular cartilage [1–4]. The existing theories of cartilage tissue and the experimental data available in literature [5–7] allow the development of a complex, but accurate, biphasic model of the tissue behavior [8]. We should ideally consider the constitutive modeling of degenerated cartilage [1, 9], and cartilage growth [10, 11], the tissue differentiation models based on biphasic mechano-regulation theory [12] extended to model tissue differentiation during osteochondral defect repair [13], cell migration/proliferation models using random walk modeling [1] as well as developments of earlier diffusion based approaches [10], bone remodeling algorithms based on combined strain/damage-adaptive theory, and single cell combined tensegrity-continuum finite element models. Figure 1.4 shows an example of tissue modeling.

To alleviate the complexity of conducting a simulation involving all levels, we retain to model the musculo-skeletal system at a higher abstraction level with idealized joints. This choice keeps the inverse dynamics computation efficient, hence allowing to exploit it within a decoupled simulation framework where it provides a global view of the individual muscle forces acting at the joint level. This information is then exploited to determine the contact distribution for the patient bone shape in accordance with the tissue level simulation. Conversely, given a modified bone shape the posture will be adjusted by constrained optimization to preserve the equilibrium of the weight bearing experiments. To achieve this task, first the patient-specific muscles action lines will be identified from the medial surfaces of the muscle 3D meshes. Then, given the kinematic and reaction forces data of the weight bearing experiments, Inverse Dynamic computations will be made at the level of the lower limb musculoskeletal system. The resulting muscle activation and force distribution will be used at the joint level simulation where the relative location and movement of joint surfaces is investigated to determine the corresponding contact areas. At that stage, the stress-strain distribution and visco-elastic biphasic behavior is evaluated with the previous task simulation. We will study the joint system at two levels. At the tissue level, the different mechanical properties of each joint component are estimated or retrieved from the data acquisition and a strain/stress analy-

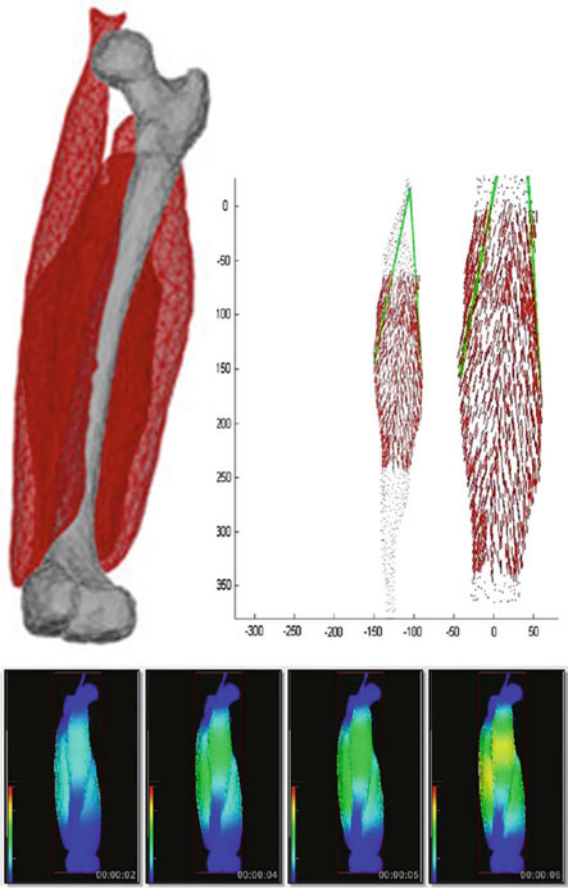

Fig. 1.4 Tissue modeling

sis is conducted. Then the relationship between all the components is studied at a more global functional organ level, where contacts, actuation forces, and dynamics are taken into account. The tissue and joint level simulation components exchange information in cyclic manner: each component will use (partially) as input the output of the other component. This simulation framework can be used for different case scenarios, such as the complex walking simulation. Simulation of deformation and stress distribution calculation with regards to contact forces, velocities, accelerations and actuation (muscles) should be established. Improvements on the models of cartilage could also be proposed to match tissue mechanical behavior more closely to measure non-linear behavior. Non-linear biphasic material models of cartilage should be developed to determine appropriate linear-elastic material properties for a specific range of loading frequencies to adequately match the time-dependent behavior of cartilaginous tissue. To this end, specific models with the accuracy of the contin-

uum physics should be developed which will insure the simulation to be real-time and accurate. In the future, these models will allow at the same time coarse to fine deformation depending on the loading frequencies.

MRI is one of the most widely used medical imaging techniques to visualize the structure and function of the body. Early techniques such as region growing and split-and-merge are mostly heuristic and may not be very robust. Modern techniques use optimization which can be roughly classified into two categories: combinatorial methods [14, 15] and variational methods [16, 17]. Typically, medical image segmentation is done by going through 2D MR slice images. However, even with those advanced 2D methods, the necessity to analyze and edit each slice in every MRI data set is a daunting task. Though the 2D sections convey all the information without any ambiguity, some artifacts can be seen only on 3D views since they do not contribute significantly to each individual 2D slice. Therefore, accurate and precise segmentation of the tissue boundary from 3D MR images is an essential and crucial component for 3D medical computing. When the object of interest is changing, automatic segmentation becomes even harder [18, 19]. We should explore how to integrate various modern techniques, and shape and prior cues to achieve intelligent segmentation [20–22]. After that, the main application will be the creation of 3D mesh models of tissue for finite element modeling (FEM). The surface and volume vector models can be used for further biomechanical processing and analysis. It is thus essential to develop efficient algorithms for automated extraction and reconstruction of patient specific models from medical images.

1.3.2 Segmentation, Deformation and 3D Reconstruction

Medical simulation using patient-specific MRI data requires the design of fast and accurate segmentation techniques to extract, from the images, structures of interest (e.g. muscles, and cartilages). The segmented structures (e.g. bones and ligaments) can be used to reconstruct 3D models from patient-specific MRI data for applications such as stress and other biomechanical analyses. Direct segmentation involves a detection step where regions are identified in images and a classification step where regions are combined to form new regions. For complex problems, direct segmentation is noise-sensitive, not robust and quite inaccurate. The addition of prior knowledge can improve significantly the results, yielding sophisticated classification methods [23–25] using registration algorithms [26–29] or deformable models [30, 31].

Existing deformable models (deformable contours [32], parametric [33], implicit [34] and discrete [28, 35]) are typically controlled by external forces that attract the model towards image features. New methods can extend previous work on deformable models [36, 37], e.g. the simplex mesh framework, in order to improve mathematical definition and internal and external force computation. Complexity will be reduced by using levels of details (LODs), medial axis representations and efficient particle system simulation techniques. Eventually, the variety of acquisi-

tion MRI data will need sophisticated registration techniques to perform data fusion. In the case of elastic registration, deformations are generally constrained to handle the large number of degrees of freedom [38, 39]. For internal forces, we may need physical and statistical parameters [40, 41] for better reconstruction. Such a development should take advantage of existing expertise in deformable models [42–45], to reconstruct 3D models from volumetric MRI image and image segmentation.

Another important component is 3D visualization which can help to validate the result of 3D segmentation [46]. Different approaches to 3D visualization of MRI data segmentations exist. Volumetric methods give a good overall picture of the data set. However, they often appear to be confusing and lacking fine details. Partial occlusion and visual clutter that typically result from the overlay of these traditional 3D scalar-field visualization techniques make it difficult for users to perceive and recognize visual structures. Surface rendering could be a good alternative but some tissue surface is usually not directly available in the original 3D volume MRI data. Hence, an efficient 3D visualization framework suitable for segmentation especially incorporating advanced 3D display technologies is a significant research direction and poses many developmental challenges.

1.4 Building Computational Biomechanics Models for Deforming Hard and Soft Musculoskeletal Tissues

It is important to note that the reliability of computational approaches strongly depends on appropriate 3D mathematical descriptions of the material behavior of soft tissues and their interactions with surrounding structures. Reasonable constitutive models must be designed within the context of associated comprehensive experimental data for tissue, cellular, and molecular structures. Computational models offer, however, the potential to simulate multi-field coupled processes encountered in the micro-heterogeneous soft tissues and to realistically predict physiological functional interactions. Biomechanical simulation has to consider the interaction between the medical device and biological tissue which is deformable and divisible. The large deformation and/or puncture of the tissue can be simulated realistically with a physics-based simulation engine that integrates finite element and multi-body dynamics codes [47]. The simulation engine assumes that the global operating space is divided into many sub-regions. Quantification of tissue biomechanics during deformation is often restricted to excised tissue and using conventional mechanical testing techniques. Despite efforts to recreate in vivo conditions during mechanical testing, the testing environment is far from physiological, with grossly approximated boundary conditions [48]. Image-based quantification will enable deformation analysis to be carried out in the physiological environment and will be entirely non-invasive, preserving tissue-tissue interfaces, providing realistic biomechanical responses. A combination of image processing techniques, together with finite element sim-

ulations [49, 50] can be employed to simulate deforming tissue biomechanics in a non-invasive manner [51].

It is also possible to develop 3D anatomically accurate computer models of whole spine with lower limbs to identify factors influencing the increased fracture risk following augmentation/treatment procedures [52–54].

1.5 Building Prediction and Diagnosis Models for Therapy

We should model the musculoskeletal system at a higher abstraction level with idealized joints. This choice keeps the inverse dynamics computation efficient, hence allowing to exploit it within a decoupled simulation framework which provides a global view of the individual muscle forces acting at the joint level. This information should be exploited to determine the contact distribution for the patient bone shape in accordance with the tissue level simulation. Conversely, given a modified bone shape, the posture should be adjusted by constrained optimization to preserve the equilibrium of the weight bearing experiments. To achieve this task, first the patient-specific muscles action lines should be identified from the medial surfaces of the muscle 3D meshes. Then, given the kinematic and reaction forces data of the weight bearing experiments, inverse dynamic computations should be made at the level of the lower limb musculoskeletal system. The resulting muscle activation and force distribution should be used at the joint level simulation where the relative location and movement of joint surfaces is investigated to determine the corresponding contact areas [55, 56]. At that stage, the stress-strain distribution and viscoelastic biphasic behavior is evaluated with the previous task simulation. Research shows stress and contact analysis can greatly improve the understanding of the pathology and enhance the prediction of the outcomes of surgical procedures [57–59]. Contact analysis should be based on collision techniques which are extremely challenging for musculoskeletal systems [60].

With the fruition of this 3D patient model, we should envision the construction of a huge database of 3D patient case mix describing the major common illnesses which should be a valuable resource for future diagnosis and treatment. Moving forward, a tablet interface with the 3D patient model should be designed to enable convenient patient-doctor interaction. A good solution would be to have a touch interface (IPAD-like) to zoom any area and see the different levels (muscles, skeleton etc.) interactively. It would be also possible to load two models and compare them. Eventually, patients might be aware of their state of health through the help of their own 3D patient model.

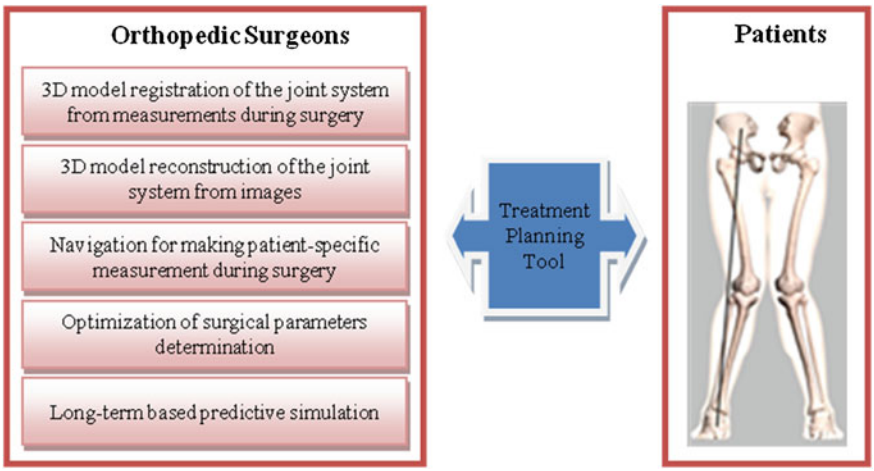

Fig. 1.5 Interactive orthopedic surgical planning

1.6 Simulation-Enabled Prediction and Analysis for Planning of Orthopedic Surgery

The possibility to predict the outcomes of surgery from a pathological and biomechanical point of view will be a tremendous help to clinicians. Abnormal stresses acting on articular joints are believed to be one of the origins of OA. Research shows stress and contact analysis [61] can greatly improve the understanding of the pathology [62–64] and enhance the prediction of the outcomes of surgical procedures [65, 66]. Few collision detection approaches are suitable for anatomical systems in which soft tissues are in quasi permanent contact. Basically, detecting collisions means checking the geometry of the target objects for interpenetration through static interference test methods [67]. In our case, non rigid transformations demand special scene structures [68], space partitioning [69] or space representation [66] that may require costly update phases. The choice of the most appropriate strategy heavily depends on the a priori knowledge on the planned surgery to make the correct simplifying assumptions. With that frame in mind, the a priori knowledge of the hip joint movement characteristics has allowed the exploitation of a spherical sampling of the cartilage surfaces to speed-up the evaluation of the contact distribution [70]. Figure 1.5 shows the principles of an interactive orthopaedic surgical planning.

Because of joint deterioration, the mechanical axis no longer goes through the middle of the knee joint. Instead, the stresses concentrate on the already damaged compartment. Due to this concentration of stresses the cartilage damage continues and increases. This leads to cartilage degeneration in a few years. In case of major degenerative lesions, a total knee arthroplasty is practiced. In certain knee surgery like high tibial osteotomy (HTO), the tibia will be cut close to the knee joint in order to change the limb axis so that the healthy outside of the knee joint will take the load

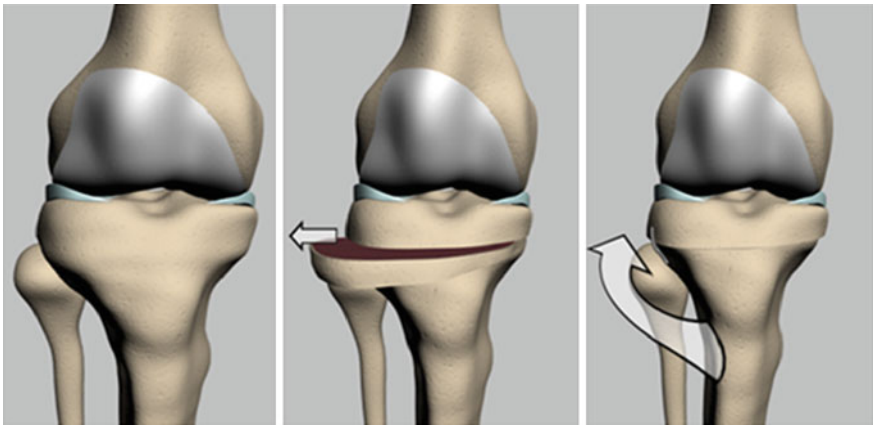

Fig. 1.6 High tibial osteotomy. From *left* to *right*: initial lower leg, removal of a wedge, realignment of lower leg

(Fig. 1.6). The best postoperative angle defined by the three articular centres must stand between 183° and 186° [71–77]. If the correction is not sufficient the degenerative process is not slow done. In case of overcorrection, the controlateral compartment of the knee can be damaged. This 3° target is rather difficult to achieve with conventional techniques, since the procedure is performed extra-articulary, which offers no view on the hip, knee or ankle centres. The right alignment is therefore very difficult to obtain since the surgeon has no control on the location of the real joints centres when he/she is performing the correction.

Moreover, the 3D aspect of the problem is not taken into account. To overcome these issues, we should investigate 3D solutions to assist surgeons' interactive HTO planning. Efforts should be made in 3D navigation and allow surgeons to get morpho-functional parameters to locate the hip centre, the knee centre and the ankle centre in 3D. Based on these parameters, cutting planes should be proposed to the surgeon such that the lower limb is realigned. In the future we will not only consider the morpho-functional aspect of the problem but also integrate the physical constraints induced on cartilages and bones of the knee joints. It will also rely on the experience in modeling contacts and collisions [60, 70, 78]. Figure 1.7 illustrates a misalignment of the lower limb.

1.6.1 Walking Analysis

To determine the impact of HTO on locomotive function of the patient and on autonomy in daily activities, it is essential to extend this simulation framework to the analysis of walking. Additionally, it will allow observational and longitudinal study of patients having undergone HTO surgery. The impact of this study is twofold. First, it

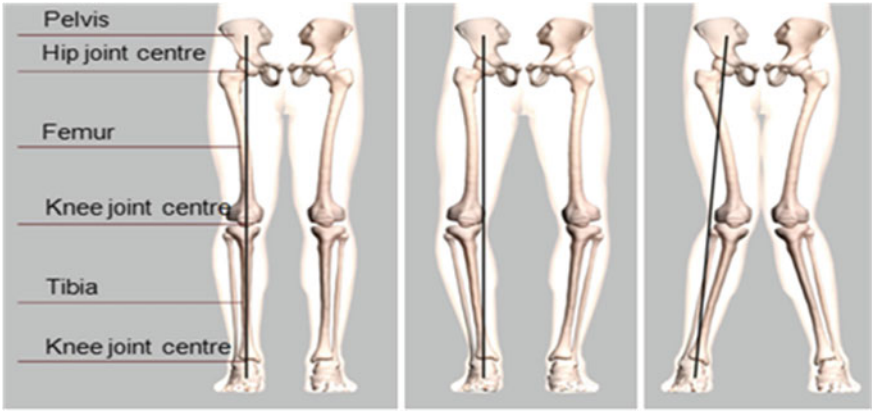

Fig. 1.7 Misalignment of the lower limb

will improve the knowledge regarding the consequences of the surgery for the patient and the repercussions on his/her quality of life. Second, the long term effects of OA at the organ and system levels will be better understood. The results will provide valuable information about how patients may alter their walking after surgery. In computational biomechanics aimed towards gait simulation/walking analysis, there are two separate modeling and simulation domains: multi-body dynamics for body movements and finite element simulation for soft tissue deformations. With increasing computational power and more knowledge on how muscles and bones interact, the next step in biomechanical gait simulation is to create a new simulation domain that would combine both of these fields. Today when muscle simulation is carried out using finite element method no aspects from the anatomy, mass distribution or gait pattern are taken into account, yet these are factors that affect the tissue in the musculoskeletal system. The most common simulation methods for gait movements are the use of muscle action lines along with multi-body dynamics of the skeleton body, which does not include interaction between the movement of bones and the deformation of the muscles [79]. The most common method for the calculation of forces and movement in the skeleton model from muscles are the use of muscle action lines, where the muscle is described as one or multiple lines, without any volume or interaction between muscles due to muscle deformation. During a gait simulation this can alter and invalidate simulations result because no collision detection is used between the muscle action lines and the skeleton. The action lines are designed in such a way that collision should be minimized but this is not guaranteed. If the gait simulation is carried out using a multi-domain model where the skeleton simulation is combined with correct soft tissue simulation, the traditional issues previously mentioned can be resolved. However, current multi-domain modeling/simulations are insufficient, when solving the forward dynamic motion the process uses small time step, in which a new solution is calculated by solving the finite element solutions for the soft tissue resulting in extremely time consuming simulations. These methods

cannot be used to solve large complicated walking pattern, therefore it is interesting to investigate fast multi-domain methods. Since the walking pattern is much more complex than the weight bearing experiments, predicting the consequences of the modification of the joint alignment will require some extra care to handle the alternation of support and swing phases. Compared to the previous task the joint will be submitted to higher frequency of loading/unloading dynamics characterizing this movement. This will have an impact at the tissue simulation level. The constrained optimization framework will be extended to include/enforce the specificities of the walking pattern.

The validation of the methodology should be based on experience in the walking process and gait [80, 81]. We should capture the motion of a patient walking and build the gait model using a data-driven constraint based animation system for interactive human motion editing. The technique should be based on the link between linear motion models such as Principal Component Analysis (PCA) and Prioritized Inverse Kinematics (PIK) [82]. The connection of both techniques could allow us to construct a Low dimensional Prioritized Inverse Kinematics (LPIK) framework. We should then be able to use it to predict the gait of a patient after surgery. Motion capture of the patient after surgery should be compared for validation. In such a view, it is essential that clinicians contribute in the validation process.

If the gait simulation is carried out using a multi-level model where the skeleton simulation is combined with correct soft tissue simulation the traditional issues previously mentioned could be resolved. However, current multi-domain modeling/simulations are insufficient. When solving the forward dynamic motion, the process uses small time step, in which a new candidate solution is calculated by solving the finite element solutions for the soft tissue resulting in extremely time consuming simulations [34]. Previous methods therefore cannot be used to solve large complicated walking patterns, whereas our method leads to faster multi-domain methods.

1.6.2 Simulation of Human Movements

In terms of simulating human movement, very little work has been done on studying a wide range of motion such as specific lateral movements which lead to substantial situations of sports injuries. In the aspect of subject-specific wide range motions simulated through a framework of multi-sensory data, muscle activation and multi-level modeling has not been considered. The use of simulations to elucidate the principle within this framework of multi-sensor and multi-level combination enables better insights in the human locomotion which can be tailored to specific individuals for predictive, preventative and health treatment measures (Fig. 1.8).

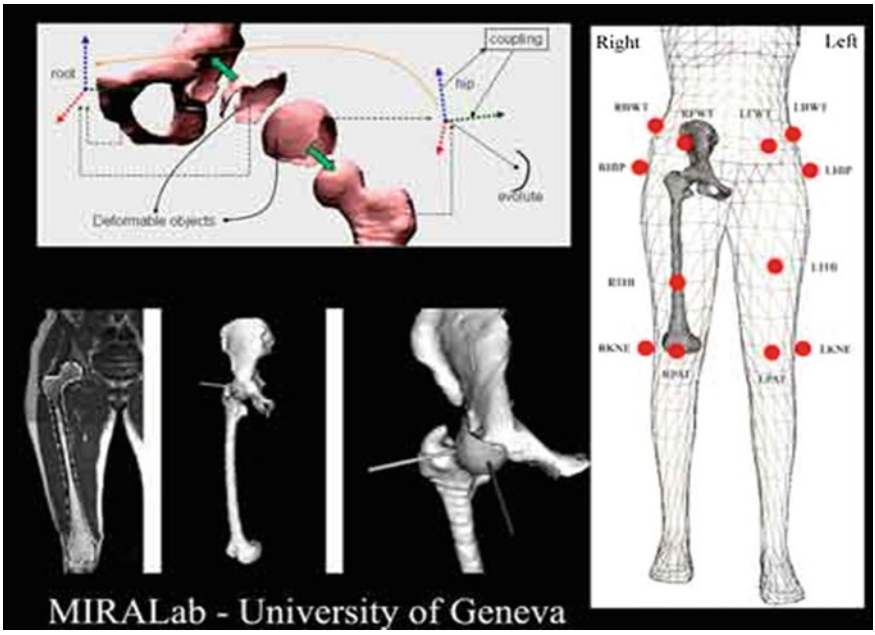

Fig. 1.8 Joint representation

1.6.3 Stress and Contact Analysis

The different tissue mechanical behavior should be modelled especially concerning the biphasic aspect of cartilages. The physical deformation of 3D models could be inspired by cutting-edge cloth simulation research [35–37, 83] where there have been great advances in the efficient and physical simulation of colliding deformable surfaces. To perform stress simulation, tetrahedral meshes are required and current techniques (e.g. [61]) to get such meshes are not well designed for thin structures like cartilages. They tend to produce a too high number of tetrahedral elements so we should apply and improve on recent more effective techniques [84]. In comparison with a recent work [38], we should provide a physical representation that can be used for simulation to yield better insights for analysis.

1.7 Validation and Evaluation Methodology for 3D Patient Modeling

Clinical validation and evaluation will play an important role in the future [85–87]. Firstly, we shall emphasize the use of patient data for modeling and simulation as initial inputs which will substantially increase the realism of the 3D patient model

to be developed [88]. This however will make the research more challenging due to the diversity or individualization of the patient data [89]. Highly adaptive methods should be investigated aiming to deal with both normal and variant anatomy of patients. Secondly, we shall incorporate the clinical knowledge and experience of the medical experts into the tools (such as segmentation) to be designed and developed. These tools shall have optimization functions with simple parameter control based on feedbacks from the end users. The optimization process can be progressive. Thirdly, we should conduct the validation and evaluation as an in-process work during the development cycle of the patient modeling. The in-process validation can help identify and rectify modeling error in the earliest possible time. Feedback from different stake holders including medical professionals, researchers, or even patients at different stages should be used to improve the patient model development. Finally, both experimental and computational validations should be performed taking the advantage of existing biomechanical lab resources and computational expertise. Patient medical images should be used as initial data to reconstruct patient models which will be compared against the initial image data. The prediction function of the patient model should be validated by specially designed experiments with different settings (e.g., material properties) [90, 91].

1.8 Conclusions

The rising incidence of chronic diseases including many musculoskeletal disorders in the ageing population is leading to an untenable societal burden. Therefore, innovative approaches in healthcare are urgently needed to better restore or improve the quality of life in patients. Recent advances in medical technologies have significantly widened the spectrum of patient data available to the physicians, which opens the possibility to tailor diagnosis and treatment planning on the subject-specific level and hence the potential to improve the outcome of medical interventions. This can be realized by means of creating virtual models of patients that allow for an integration of multimodal data, simulations of functional behavior on different levels and 3D interactive visualization. This chapter has presented the challenges that need to be conquered to accomplish this goal as well as a possible strategy for future progress. In order to be successful, research in modeling the 3D physiological human requires an integrative approach that brings together different research domains, combining knowledge on different scales and acquired with multiple modalities. The following chapters provide a sampling of overviews and examples of key domains, illustrating the diversity in scientific paradigms and terminologies that needs to be bridged in the creation of virtual patient models.

Acknowledgments This work was supported by the European Marie Curie Initial Training Network MultiScaleHuman (FP7-PEOPLE-2011-ITN-289897).

References

1. Wilson, W., van Donkelaar, C. C., van Rietbergen, B., & Huiskes, R. (2005). A fibril-reinforced poroviscoelastic swelling model for articular cartilage. *Journal of Biomechanics*, *38*, 1195–1204.
2. Cowin, S. C., & Doty, S. B. (2007). *Tissue Mechanics*. New York: Springer.
3. Mow, V. C., & Guo, X. E. (2002). Mechano-electrochemical properties of articular cartilage. *Annual Review of Biomedical Engineering*, *4*, 175–209.
4. Fung, Y. C. (1993). Biomechanics: Mechanical properties of living tissues (2nd ed.). New York: Springer.
5. Laasanen, M. S., et al. (2003). Biomechanical properties of knee articular cartilage. *Biorheology*, *40*, 133–140.
6. Fortis, A. P., Kostopoulos, V., Panagiotopoulos, E., Tsantzalis, S., & Kokkinos, A. (2004). Viscoelastic properties of cartilage-subchondral bone complex in osteoarthritis. *Journal of Medical Engineering and Technology*, *28*, 223–226.
7. Li, L. P., Korhonen R. K., Iivarinen, J., Jurvelin, J. S., & Herzog, W. (2008). Fluid pressure driven fibril reinforcement in creep and relaxation tests of articular cartilage. *Medical Engineering and Physics*, *22*, 182–189.
8. Huang, C. Y., Mow, V. C., & Ateshian, G. A. (2001). The role of flow-independent viscoelasticity in the biphasic tensile and compressive responses of articular cartilage. *Journal of Biomechanical Engineering*, *123*, 410–417.
9. Wu, J. Z., Herzog, W., & Epstein, M. (2000). Joint contact mechanics in the early stages of osteoarthritis. *Medical Engineering and Physics*, *22*, 1–12.
10. Carter, D. R., & Wong, M. (2003). Modelling cartilage mechanobiology. *Philosophical Transactions of the Royal Society of London Series B*, *358*, 1461–1471.
11. van Donkelaar, C. C., & Huiskes, R. (2006). The PTHrP-Ihh feedback loop in the embryonic growth plate allows PTHrP to control hypertrophy and Ihh to regulate proliferation. *Biomechanics and Modeling in Mechanobiology*, *6*(1–2), 55–62.
12. Lacroix, D., & Prendergast, P. J. (2002). A mechano-regulation model for tissue differentiation during fracture healing: Analysis of gap size and loading. *Journal of Biomechanics*, *35*, 1163–1171.
13. Jelly, K. D., & Prendergast, P. J. (2006). Prediction of the optimal mechanical properties for a scaffold used in osteochondral defect repair. *Tissue Engineering*, *12*, 2509–2529.
14. Boykov, Y., & Funka-Lea, G. (2006). Graph cuts and efficient N-D image segmentation. *International Journal of Computer Vision*, *70*(2), 109–131.
15. Zhang, J., Zheng, J., & Cai, J. (2010). A diffusion approach to seeded image segmentation. In *IEEE Computer Vision and Pattern Recognition (CVPR)*, San Francisco, USA (pp. 2125–2132).
16. Cremers, D., Rousson, M., & Deriche, R. (2007). A Review of statistical approaches to level set segmentation: Integrating color, texture, motion and shape. *International Journal of Computer Vision*, *72*(2), 195–215.
17. Nguyen, A., Cai, J., Zhang, J., & Zheng, J. (2012). Robust interactive image segmentation using convex active contours. *IEEE Transactions on Image Processing*, *21*(8), 3734–3743.
18. Chiang, P., Cai, Y. Y., Mak, K., & Zheng, J. M. (2013). A B-spline approach to phase unwrapping in tagged cardiac MRI for motion tracking. *Magnetic Resonance in Medicine*, *69*, 1297–1309.
19. Sharma, N., & Aggarwal, L. M. (2010). Automated medical image segmentation techniques. *Journal of Medical Physics*, *35*(1), 3–14.
20. Gilles, B., & Magnenat-Thalmann, N. (2010). Musculoskeletal MRI segmentation using multi-resolution simplex meshes with medial representations. *Medical Image Analysis*, *14*(3), 291–302.
21. Schmid, J., Guitián, J., Gobbetti, E., & Magnenat-Thalmann, N. (2011). A GPU framework for parallel segmentation of volumetric images using discrete deformable models. *The Visual Computer*, *27*(2), 85–95.

22. Schmid, J., & Magnenat-Thalmann, N. (2008). MRI bone segmentation using deformable models and shape priors. *Medical Image Computing and Computer-Assisted Intervention*, *1*, 119–126.
23. Fritscher, K. D., Grünerb, A., & Schubert, R. (2007). 3D image segmentation using combined shape-intensity prior models. *International Journal of Computer Assisted Radiology and Surgery*, *1*, 341–350.
24. Pereira, C. S., Alexandre, L. A., Mendonça, A. M., & Campilho, A. C. A. (2006). Multiclassifier approach for lung nodule classification. *International Conference on Image Analysis and Recognition*, *2*, 612–623.
25. Pohl, K. M., Fisher, J., Grimson, W. E. L., Kikinis, R., & Wells, W. M. (2006). A Bayesian model for joint segmentation and registration. *NeuroImage*, *31*, 228–239.
26. Brown, L. G. (1992). A survey of image registration techniques. *ACM Computing Surveys*, *24*(4), 325–376.
27. Johnson, H. J., & Christensen, G. E. (2002). Consistent landmark and intensity-based image registration. *IEEE Transactions on Medical Imaging*, *21*(5), 450–461.
28. Ding, L., Goshtasby, A., & Satter, M. (2001). Volume image registration by template matching. *Image and Vision Computing*, *19*(12), 821–832.
29. Zöllei, L., Grimson, E., Norbash, A., & Wells, W. (2001). 2D–3D Rigid registration of X-ray fluoroscopy and CT images using mutual information and sparsely sampled histogram estimators. In *Proceedings of IEEE Computer Vision and Pattern Recognition* (Vol. 2, pp. II-696–II-703).
30. McInerney, T., & Terzopoulos, D. (1996). Deformable models in biomedical images. *Medical Image Analysis*, *1*(2), 91–108.
31. Montagnat, J., & Delingette, H. (2001). A review of deformable surfaces: Topology, geometry and deformation. *Image and Vision Computing*, *19*(14), 1023–1040.
32. Terzopoulos, D., Witkin, A., & Kass, M. (1988). Constraints on deformable models: Recovering 3D shape and nonrigid motion. *Artificial Intelligence*, *36*(1), 91–123.
33. Staib, L., & Duncan, J. (1992). Deformable fourier models for surface finding in 3D images. *Visualization in Biomedical Computing*, *1808*, 90–104.
34. Malladi, R., Sethian, J. A., & Vemuri, B. C. (1995). Shape modeling with front propagation: A level set approach. *IEEE Transactions on Pattern Analysis and Machine Intelligence*, *17*(2), 158–174.
35. Lötjönen, J., & Mäkelä, T. (2001). Segmentation of MR images using deformable models: Application to cardiac images. *International Journal of Bioelectromagnetism*, *3*(2), 37–45.
36. Delingette, H. (1999). General object reconstruction based on simplex meshes. *International Journal of Computer Vision*, *32*(2), 111–146.
37. Montagnat, J., & Delingette, H. (2005). 4D deformable models with temporal constraints: Application to 4D cardiac image segmentation. *Medical Image Analysis*, *9*(1), 87–100.
38. Gilles, B., Moccozet, L., & Magnenat-Thalmann, N. (2006). Anatomical modelling of the musculoskeletal system from MRI. In *MICCAI'06* (Vol. 4190, pp. 289–296).
39. Gilles, B., Perrin, R., Magnenat-Thalmann, N., & Vallée, J.-P. (2005). Bones motion analysis from dynamic MRI: Acquisition and tracking. *Academic Radiology*, *12*(10), 2385–2392.
40. Montagnat, J., & Delingette, H. (2000). Space and time shape constrained deformable surfaces for 4D medical image segmentation. In *Proceedings of Medical image Computing and Computer-Assisted Intervention (MICCAI '00)*. Lecture Notes on Computer Science (Vol. 1935, pp. 196–205).
41. Wang, Y., & Staib, L. H. (2000). Physical model-based non-rigid registration incorporating statistical shape information. *Medical Image Analysis*, *4*, 7–20.
42. Liu, J., Huang, S., & Nowinski, W. L. (2008). A hybrid approach for segmentation of anatomic structures in medical images. *International Journal of Computer Assisted Radiology and Surgery*, *3*(3/4), 213–219.
43. Ng, H. P., Ong, S. H., Liu, J., Huang, S., Foong, K. W. C., Goh, P. S., et al. (2009). 3D segmentation and quantification of a masticatory muscle from MR data using patient-specific models and matching distributions. *Journal of Digital Imaging*, *22*(5), 449–462.

44. Guan, Y. Q., Cai, Y. Y., Lee, Y. T., & Opas, M. (2006). An Automatic method for identifying appropriate gradient magnitude for 3D boundary detection of confocal image stacks. *Journal of Microscopy*, *223*(1), 66–72.
45. Indhumathi, C., Cai, Y. Y., Guan, Y. Q., & Opas, M. (2009). 3D boundary extraction of confocal cellular images using higher order statistics. *Journal of Microscopy*, *235*(2), 209–220.
46. Friese, K. I., Blanke, P., & Wolter, F.-E. (2011). YaDiV—An open platform for 3D visualization and 3D segmentation of medical data. *The Visual Computer*, *27*(3), 129–139.
47. Chui, C. K., Chng, C. B., & Lau, D. P. C. (2011). Parallel processing for object oriented robotic simulation of tracheal-oesophageal puncture. In *IEEE/SICE International Symposium on System Integration (SI International 2011)*, Kyoto, Japan (pp. 144–149).
48. Revost, P. (2011). Dynamic mechanical response of brain tissue in indentation in vivo, in situ and in vitro. *Acta Biomateriala*, *7*, 4090–4101.
49. Qiu, T. X., Teo, E. C., Yan, Y. B., & Lei, W. (2011). Finite element modelling of 3D coupled foot-boot model. *Medical Engineering and Physics*, *33*(10), 1228–1233.
50. Chui, C. K., et al. (2009). A component oriented software toolkit for patient-specific finite element model generation. *Advances in Engineering Software*, *40*, 184–192.
51. Ahn, B., & Kim, J. (2010). Measurement and characterization of soft tissue behavior with surface deformation and force response under large deformations. *Medical Image Analysis*, *14*, 138–148.
52. Hui, J., Teo, Y. H., Li, L., & Lee, E. H. (2005). A comparative study of efficacy of bone marrow, periosteum and fat as source of MSC (mesenchymal stem cells) transfers in the treatment of partial growth arrest. *Tissue Engineering*, *11*(5–6), 904–912.
53. Thevendran, G., Sarraf, K. M., & Rosenfeld, P. R. (2012). Adult ankle fractures: Acute assessment and management. *British Journal of Hospital Medicine*, *31*(5), 71–74.
54. Sandholm, A., Schwartz, C., Pronost, N., de Zee, M., Voigt, M., & Thalmann, D. (2011). Evaluation of a geometry-based knee joint compared to a planar knee joint. *The Visual Computer*, *27*(2), 161–171.
55. Kong, P. W., & van Haselen, J. (2010). Revisiting the influence of hip and knee angles on quadriceps excitation measured by surface electromyography. *International Sport Medical Journal*, *11*(2), 313–323.
56. King, M. A., Kong, P. W., & Yeadon, M. R. (2009). Determining effective subject-specific strength levels for forward dives using computer simulations of recorded performances. *Journal of Biomechanics*, *42*(16), 2672–2677.
57. Loh, Y. J., Tjan, S. Y., Xu, D., Thia, E., & Kong, K. H. (2010). A feasibility study using interactive commercial off-the-shelf computer gaming in upper limb rehabilitation in patients after stroke. *Journal of Rehabilitation Medicine*, *42*(5), 437–441.
58. Huber, M., Rabin, B., Docan, C., Burdea, G., Abdelbaky, M., & Golomb, M. (2010). Feasibility of modified remotely-monitored in-home gaming technology for improving hand function in adolescents with cerebral palsy. *IEEE Transactions on Information Technology in Biomedical Engineering*, *14*(2), 526–534.
59. Burdea, G., Cioi, D., Martin, J., Fensterheim, D., & Holenski, M. (2010). The Rutgers arm II rehabilitation system—a feasibility study. *IEEE Transactions on Neural Systems and Rehabilitaion Engineering*, *18*(5), 505–514.
60. Arbabi, E., Boulic, R., & Thalmann, D. (2009). Fast collision detection methods for joint surfaces. *Journal of Biomechanics*, *42*(2), 91–99.
61. Teschner, M., et al. (2004). Collision detection for deformable objects. In *Proceedings of Eurographics '04 State-of-the-Art-Reports* (pp. 119–139).
62. Han, S.-K., Federico, S., Epstein, M., & Herzog, W. (2005). An articular cartilage contact model based on real surface geometry. *Journal of Biomechanics*, *38*(1), 179–184.
63. DeFrate, L. E., Sun, H., Gill, T. J., Rubash, H. E., & Li, G. (2004). In vivo tibiofemoral contact analysis using 3D MRI-based knee models. *Journal of Biomechanics*, *37*(10), 1499–1504.
64. Shi, Q., Hashizume, H., Inoue, H., Miyake, T., & Nagayama, N. (1995). Finite element analysis of pathogenesis of osteoarthritis in the first carpometacarpal joint. *Acta Medica Okayama*, *49*(1), 43–51.

65. Armand, M., et al. (2004). Computer-aided orthopaedic surgery with near-real-time biomechanical feedback. *Johns Hopkins APL Technical Digest*, *25*(3), 242–252.
66. Harman, M. K., Banks, S. A., Fregly, B. J., Sawyer, W. G., & Hodge, W. A. (2005). Biomechanical mechanisms for damage: Retrieval analysis and computational wear predictions in total knee replacements. *Journal of Mechanics in Medicine and Biology*, *5*(3), 469–475.
67. Lin, M. C., & Canny, J. F. (1991). A fast algorithm for incremental distance calculation. In *Proceedings of IEEE International Conference on Robotics and Automation* (pp. 1008–1014).
68. Larsson, T., & Akenine-Möller, T. (2001). Collision detection for continuously deforming bodies. In *Proceedings of Eurographics*.
69. Larsson, T., & Akenine-Möller, T. (2003). Efficient collision detection for models deformed by morphing. *The Visual Computer*, *19*(2–3), 164–174.
70. Maciel, A., Boulic, R., & Thalmann, D. (2007). Efficient collision detection within deforming spherical sliding contact. *IEEE Transactions in Visualization and Computer Graphics*, *13*(3), 518–529.
71. Kettelkamp, D. B., Wenger, D. R., Chao, E. Y. S., & Thompson, C. (1976). Results of proximal tibial osteotomy. *The Journal of Bone and Joint Surgery*, *58-A*(7), 952–960.
72. Waugh, W. (1976). Tibial osteotomy in the management of ostéoarthritis of the knee. *Clinical Orthopaedics and Related Research*, *210*, 56–61.
73. Maquet, P. (1976). *Biomécanique du genou* (p. 237). Berlin: Springer.
74. Vainionpaa, S., Laike, E., Kirves, P., & Tiusanen, P. (1981). Tibial osteotomy for osteo-arthritis of the knee (a five to ten year follow-up study). *The Journal of Bone and Joint Surgery*, *63*(A-6), 398–945.
75. Coventry, M. B. (1982). Long term results of upper tibial osteotomy for degenerative arthritis of the knee. *Acta Orthopaedica Belgica*, *48*(1), 139–156.
76. Hernigou, P., Medevielle, D., Debeyre, J., & Goutallier, D. (1987). Proximal tibial osteotomy for osteo-arthritis with varus deformity. *The Journal of Bone and Joint Surgery*, *69A*, 332–354.
77. Thomine, J. M. (1989). Les ostéotomies dans la gonarthrose fémoro-tibiale latéralisée. Théorie et pratique, in Cahier d'enseignement de la SOFCOT *N°* 34 (pp. 99–112). Paris, France.
78. Arbabi, E., Chegini, S., Boulic, R., Tannast, M., Ferguson, S. J., & Thalmann, D. (2010). The penetration depth method—a novel real time strategy for evaluating femoro-acetabular impingement. *Journal of Orthopaedic Research*, *28*(7), 880–886.
79. Maurel, W., & Thalmann, D. (1999). A case study analysis on human upper limb modeling for dynamic simulation. *Computer Methods in Biomechanics and Biomechanical Engineering*, *1*, 65–82.
80. Boulic, R., Magnenat-Thalmann, N., & Thalmann, D. (1990). A global human walking model with real time kinematic personification. *The Visual Computer*, *6*(6), 344–358.
81. Glardon, P., Boulic, R., & Thalmann, D. (2006). Robust on-line adaptive footplant detection and enforcement for locomotion. *The Visual Computer*, *22*(3), 194–209.
82. Carvalho, S. R., Boulic, R., & Thalmann, D. (2007). Interactive low-dimensional human motion synthesis by combining motion models and PIK. *Computer Animation and Virtual*, *18*(4–5), 493–503.
83. Thirion, J. P. (1995). *Fast non-rigid matching of 3D medical images*. Technical Report 2547. Marseilles: INRIA.
84. Charbonnier, C., Gilles, B., & Magnenat-Thalmann, N. (2007). A semantic-driven clinical examination platform. In *Surgetica'2007, Computer-Aided Medical Interventions: Tools and Applications*.
85. Chiang, P., et al. (2012). A VR simulator for intra-cardiac interventional procedure: Concept, design and implementation. *IEEE Computer Graphics and Applications*, *33*(1), 44–57.
86. Pan, J., Chang, J., Yang, X., Zhang, J. J., et al. (2011). A medical VR simulator in laparoscopic rectum surgery. *Cyber Theraphy and Rehabilitation*, *4*(4), 19–20.
87. Cai, Y. Y., Chia, N., Thalmann, D., Kee, N., Zheng, J., & Thalmann, N. Design and development of a virtual dolphinarium for children with autism. *IEEE Transaction on Neural System and Rehabilitation Engineering* (to appear).

88. Chiang, P., Zheng, J. M., Mak, K. H., Thalmann, N., & Cai, Y. Y. (2012). Progressive surface reconstruction for heart mapping procedure. *Computer-Aided Design*, *44*, 289–299.
89. Cai, Y. Y., Zheng, J. M., Chiang, P., Thalmann, N., & Mak, K. H. (2012). *Method of progressive and real-time intra-cardiac surface reconstruction*, US Patent Filed.
90. Chong, W. H., Goh, W., Tang, H. N., Chan, W. P., & Choo, S. (2012). Service practice evaluation of the early intervention programs for infants and young children in Singapore. *Children's Health Care*, *41*(4), 281–301.
91. Chin, P. L., et al. (2011). Intraoperative morphometric study of gender differences in Asian femurs. *Journal of Arthroplasty*, *26*(7), 984–988.

Part II
Cell and Tissue Engineering

Chapter 2
Tissue Engineering and Regenerative Medicine Strategies for the Treatment of Osteochondral Lesions

Ibrahim Fatih Cengiz, Joaquim Miguel Oliveira and Rui Luís Reis

2.1 Introduction

Clinical practice is often challenged by the need for treating lesions of several musculoskeletal tissues, in which osteochondral (OC) tissues have an important share. Figure 2.1a shows an X-ray image of a human OC tissue obtained from a patient diagnosed with knee osteoarthritis (OA); Fig. 2.1b and c show, respectively, the 2D and 3D reconstruction of the images that were obtained by the micro-computed tomography (μ-CT) analysis. OC lesions affect both the articular cartilage and the underlying bone. Figure 2.1d presents an OC lesion in the human knee. Clinical need for repairing OC lesions is not yet fully satisfied. It is difficult to repair the OC tissue by surgical means alone. Lesions in OC tissues may lead to arthritis if not treated correctly in the early stages [1]. However, usually OA develops without a known cause [2]. OA is the most common disease affecting the joints, and it is seen usually in the knee, hips, hands and spine [3]. The majority of the population over 65 years old have evidence of OA [4].

OA is characterized by the imbalance of anabolic and catabolic activities of cartilage cells [5]. It is a progressive degenerative disease with gradual loss of articular cartilage [6] leading to joint deformation and pain [7]. Many tissues can be damaged during OA: articular cartilage, subchondral bone (SB), ligaments, capsule and synovium, and muscles [5, 7]. Degeneration of articular cartilage and remodelling of SB are usually seen in OA [7].

I. F. Cengiz (✉) · J. M. Oliveira · R. L. Reis
3B's Research Group–Biomaterials, Biodegradables and Biomimetics, University of Minho, Headquarters of the European Institute of Excellence on Tissue Engineering and Regenerative Medicine, AvePark, Guimarães, Portugal
e-mail: fatih.cengiz@dep.uminho.pt

I. F. Cengiz · J. M. Oliveira · R. L. Reis
ICVS/3B's–PT Government Associate Laboratory, Braga/Guimarães, Portugal
e-mail: fatih.cengiz@dep.uminho.pt

N. Magnenat-Thalmann et al. (eds.), *3D Multiscale Physiological Human*,
DOI: 10.1007/978-1-4471-6275-9_2, © Springer-Verlag London 2014

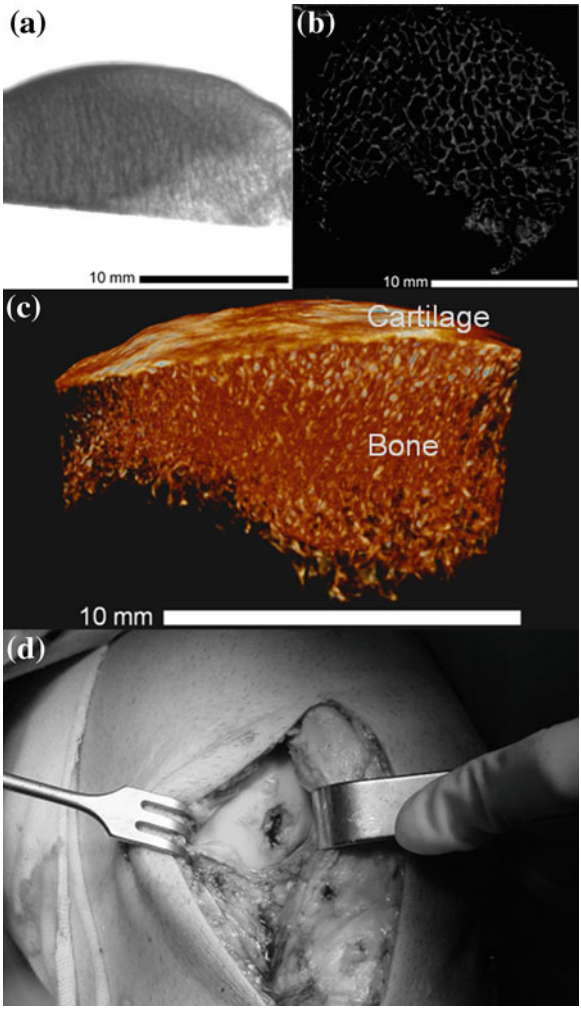

Fig. 2.1 **a** An X-ray image of a freeze-dried human OC tissue (OA knee) acquired with a high-resolution micro-computed tomography equipment, Skyscan 1072 scanner, (SkyScan, Kontich, Belgium). **b** 2D and **c** 3D reconstructions of the images using CT Analyser and CTvox, image-processing softwares from SkyScan. **d** An OC lesion in the human knee

Insufficient self-repair capacity of articular cartilage is well known. The complexity and difficulty of treating articular cartilage lesions are largely agreed [8]. A wide variety of surgical methods has been considered [2, 8–12]. However, none of these applied methods has superiority proven by a controlled clinical study [13]. Articular cartilage tissue cannot function as required or it can function only for a short period of time if it does not have the special biological and mechanical properties that it normally has [9]. Cartilage cells have limited proliferation capacity and cannot migrate

within the matrix. Therefore, strategies for the treatment of cartilage lesions have been developed in which a new cell population are brought to the lesion site [13]. One such strategy is enhancing the cartilage healing by migration of stem cells from the bone marrow to the injury site. Some examples of methods based on this strategy are drilling of SB [14], joint debridement [15] and spongialization [16]. It has been reported that none of these methods is actually helping cartilage to regenerate the original tissue since the new formed tissue is a fibrous tissue. It has been attempted to treat OC lesions with auto- and allografts as well [10, 11]. The eventual fibrous tissue formation caused biomechanical drawbacks, such as instability and reduced mechanical strength and congruency of articular surfaces [12]. In addition, low availability of material and donor site morbidity are also important limitations [17].

The goal of tissue engineering and regenerative medicine (TERM) is to regenerate tissues by preferably using patient's own cells, biodegradable biomaterials, and relevant growth factors, alone or in a combination to increase the effectiveness. Conceptually, in a tissue regeneration process, the cells can be obtained by means of biopsy from the patient, grown in vitro and seeded into a porous scaffold, followed by the cultivation of the scaffold-cell construct for some time in vitro in a cell culture medium. This construct is implanted into the defect, and after the implantation, eventually, cells synthesize their extracellular matrix (ECM) and the scaffold degrades gradually. However, the whole process is challenging. The challenge is bigger when regeneration of more than one type of tissue is required. For example, in the case of OC lesions, both articular cartilage and SB need to be treated.

2.2 Articular Cartilage

Articular cartilage plays important roles in the body. It covers the articulating ends of the bones inside the synovial joints to form a low-friction gliding surface. The cartilage reduces the peak stresses on the SB and also serves as a shock absorber [8]. Articular cartilage is an avascular, aneural and alymphatic tissue with a generally anaerobic metabolism [18]. There are two main components in the cartilage: cells called chondrocytes and the ECM which surrounds the cells [7]. Figure 2.2a presents a histological image of an articular cartilage. The chondrocytes and the ECM are interdependent. The chondrocytes are responsible for the synthesis and the breakdown of the ECM. In return, the ECM surrounds the cells and protects them from mechanical impacts while transmitting signals to the chondrocytes upon loading of the cartilage [19].

Chondrocytes take up only 1–10 % of the cartilage volume [12]. They synthesize many enzymes, cytokines and growth factors that affect the anabolic and catabolic activities [3, 6]. Mechanical loading affects the functions of chondrocytes [20]. Some chondrocytes have short cilia that reach into the matrix, which may have a function in detecting changes in the matrix. Even though individual chondrocytes have active metabolism, the articular cartilage still has slow metabolic activity due to low cellularity [19].

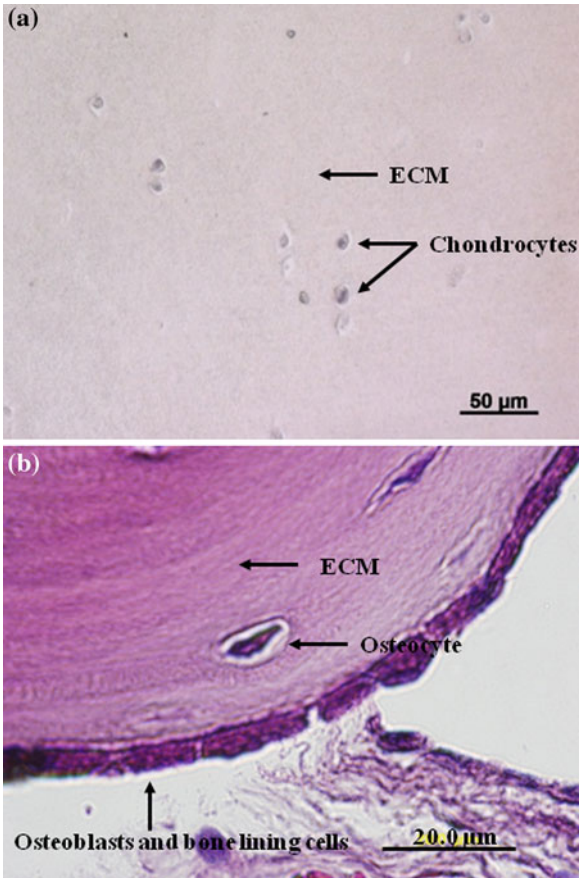

Fig. 2.2 **a** A 5-mm-thick histological sections of fresh healthy human articular cartilage after staining with haematoxylin-eosin showing the chondrocytes in the ECM. **b** A 5-mm-thick histological sections of newly formed bone within a HAp scaffold after staining with haematoxylin-eosin showing the ECM, osteocytes, osteoblasts and bone lining cells

Histological properties and health of cartilage and its mechanical properties are interrelated. For example, the Young's modulus of human cartilage decreases with increasing degrees of degeneration [21]. The ECM provides the tissue's mechanical and biochemical properties and affects cellular function by cell-matrix interactions [22]. The ECM has two phases: a fluid phase and a solid organic matrix that is mainly composed of collagens, non-collagenous proteins, and proteoglycans (PGs). The fluid phase is mainly composed of water, and some of the water is free and can move in and out of the tissue [19]. Water constitutes 65–85 % of the weight of the cartilage. Water is important for processes such as the transport of nutrients and wastes into/from the tissue, and the lubrication of the gap between articulating surfaces. Water content of the cartilage can be affected by pathological conditions, for instance in osteoarthritic

Table 2.1 Mechanical properties of articular cartilage and bone [24]

Tissue	Tensile strength (MPa)	Modulus (MPa)
Articular cartilage	11–35	3.7–400
Trabecular bone	0.1–30	10–2000
Cortical bone	47–133	5500–20000

cartilage the water content is above the normal condition [8]. The increase in the water content causes cartilage to become softer and more permeable [23].

Table 2.1 presents indicative range of values of the mechanical properties of articular cartilage and bone from [24]. The values vary depending on many conditions including loading direction, the anatomical location, age and health of donors [24]. The biomechanical properties of the tissues relate to the structure of and interactions in the collagen network. Collagens are proteins that interact with cells and affect cell functioning such as adhesion, growth and differentiation [22]. Collagens constitute 10–20 % of the weight of the cartilage. Collagen type II is the major component of cartilage that gives tensile strength, and it is the predominant collagen type representing 90–95 % of the collagen content. Other collagen types present in the articular cartilage are VI, IX, X and XI [8]. Collagen type II is a sign for differentiated chondrocytes, while collagen type I, which is not found in articular cartilage, is a sign for fibrocartilage as a result of chondrocyte dedifferentiation to fibroblast [18]. PGs take up 10–20 % of the cartilage weight and give compressive strength [8]. PGs consist of a protein core to which glycosaminoglycans (GAGs) are attached [18]. PGs can help matrix stabilization by binding to other macromolecules and also may affect the cell function by binding to growth factors [19].

Articular cartilage is a four-layered structure: (i) the superficial layer, (ii) the intermediate or transitional layer, (iii) the deep layer, and (iv) the calcified layer that is separated from the deep layer with the 3D border called tidemark. These layers differ in cellularity, cell morphology, concentration of PGs, collagen fibril content and orientation, water content, and thickness [8]. Figure 2.3 illustrates an OC tissue with distinct layers of articular cartilage and subchondral bone. Articular cartilage is a highly organized tissue and possesses a particular cellular and molecular structure [18]. Thus, it is obvious that the properties of the cartilage matrix cannot be achieved just by combining the components of the ECM in right concentrations. Chondrocytes are in charge of the synthesis, organization and maintenance of the ECM in the articular cartilage. Therefore, in response to a damage in the cartilage matrix, the local chondrocytes detect the changes occurring within the matrix and determine the new needs of the matrix. Subsequently, the chondrocytes will give the needed response, synthesizing the required components in right amounts, and assemble and organize them in the matrix [7, 19].

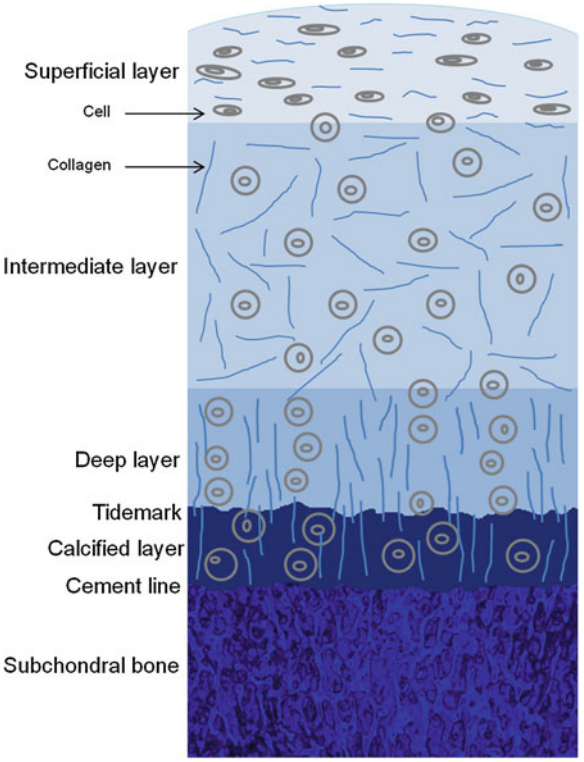

Fig. 2.3 Illustration of the structure of an OC tissue showing the arrangement of the cells and collagen fibres within the articular cartilage. Articular cartilage has four layers: the superficial layer, the intermediate layer, the deep layer, and the calcified layer. The superficial layer is the thinnest layer with flattened chondrocytes and collagen fibres that are parallel to the surface. The intermediate layer represents the thickest layer of the cartilage with spherical chondrocytes and thicker collagen fibrils, which are randomly aligned. The deep layer has spherical chondrocytes that are aligned in columns and collagen fibrils are parallel to each other and perpendicular to the articulating surface. The calcified layer is a thin layer with hypertrophic cells and separated from the deep layer by the tidemark. Subchondral bone is located below the cartilage while the cement line forms the interface between the calcified layer and the subchondral bone

2.3 Bone and Subchondral Bone

Bone is composed of organic and inorganic components. Minerals, principally hydroxyapatite (HAp), comprise 50–70 % of the bone, collagen type I rich organic matrix 20–40 %, water 5–10 %, and lipids less than 3 % [25]. HAp contributes to the rigidity and load-bearing strength, while the organic matrix provides flexibility and elasticity of the tissue. Four cell types are present in bone: osteoblasts, osteoclasts, osteocytes and bone lining cells. Osteoblasts are the mature bone-forming cells found on the bone surface, while osteocytes are embedded in the lacunae encircled with

mineralized matrix (Fig. 2.2b). They support the structure and metabolism of the bone [25]. Osteoclasts are the cells that resorb bone. Bone-lining cells are present in the non-remodelling surface of the bone. They play an important role in mineral homeostasis and can be stimulated to proliferate and differentiate into osteogenic cells [26].

Bones in the body undergo growth, modelling and remodelling throughout life to preserve the strength and mineral balance and adapt to new biomechanical conditions. Mature bones in the body can be classified structurally into cortical bone and trabecular bone. Cortical bone or compact bone covers the outer surface of the bones and has a dense structure with a porosity less than 5 % [25]. Trabecular bone is also known as cancellous or spongy bone, and it is composed of trabeculae that are porous interconnected irregular arrays of lamellar bone plates and rods [24]. Trabecular bone is present near the ends of long bones, inside the small bones as well as between the surfaces of flat bones. Trabecular bone and cortical bone show anisotropic mechanical behaviour due to their structure [27]. Trabecular bone is not as dense as the cortical bone. The metabolic activity of trabecular bone is higher than that of cortical bone [25].

SB lesions are often related with damage in the articular cartilage. SB affects the articular cartilage both biomechanically and biochemically [28]. It absorbs the mechanical stress and maintains the shape of the joint [29]. It forms a transitional layer between the articular cartilage on the surface and the interior bone volume [28]. The calcified layers of the articular cartilage and the SB make contact at a thin interface called the cement line [30]. SB is composed of the SB plate and subarticular spongiosa, which represent cortical and trabecular bone respectively. However, usually the term SB is referred to both regions, regardless of their mechanical and physiological differences [31]. The SB plate is the bony lamella or cortical endplate found under the calcified layer of the articular cartilage, while the subarticular spongiosa refers to the trabeculae under the SB plate [32].

The subchondral region shows large variations in anatomy, for example, in the contour of the tidemark and cement line, and in composition and thickness [33]. SB adapts to the applied stress by altering its density and strength [29]. Long-term mechanical load distribution within a joint surface affects the density, thickness, vascularity and biochemical composition of the SB plate [32]. In patients with OA, the stiffness, the density and the mineral content of SB are lower as compared to normal tissue [34].

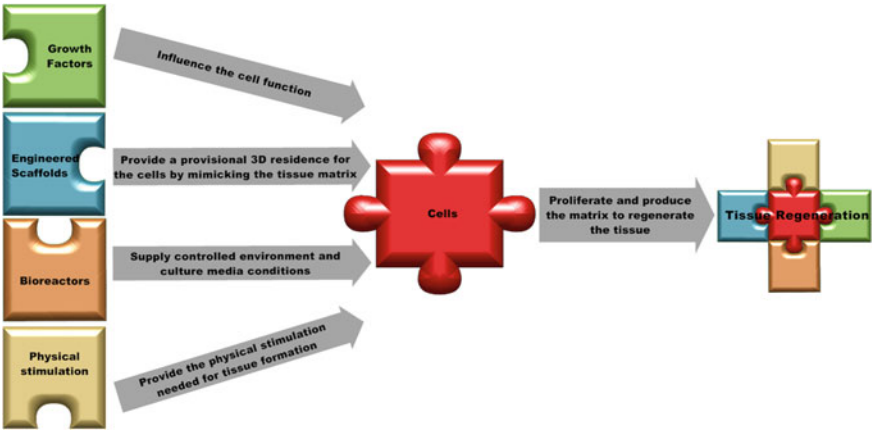

Fig. 2.4 The components of tissue engineering and their role in achieving tissue regeneration. Cells are the basic unit of tissues, they proliferate and generate the tissue matrix; scaffolds are engineered from biomaterials and host the cells provisionally during regeneration process; growth factors and physical stimulation affect the cell function and tissue formation, while bioreactors can mimic the in vivo conditions by supplying controlled environment and conditions for cell culturing

2.4 Tissue Engineering and Regenerative Medicine Strategies

2.4.1 The Components: Cells, Scaffolds, Growth Factors, and Bioreactors

The different components of tissue engineering and their role in achieving tissue regeneration are illustrated in Fig. 2.4. Cells are the basic unit of tissues that generate the tissue matrix, while scaffolds are engineered from biomaterials and host the cells during the regeneration process. Growth factors and physical stimulation contribute to the tissue regeneration with their influence on the cell function, while bioreactors can mimic the in vivo conditions for cell culturing. **Cells** can be categorized as mature differentiated and stem cells. Mature differentiated cells perform highly specialized functions in a specific tissue. Stem cells are in an undifferentiated state having the ability to self-renew and differentiate into specialized cell types to create new tissues. Stem cells can be classified by the tissue type they are isolated from: embryonic [35] and adult stem cells [36]. Embryonic stem cells are isolated during the embryonic stages of development and thus, have a greater natural potential, whereas adult stem cells are relatively more specialized and partially differentiated. Stem cells can also be classified by their potential based on their natural tendency: totipotent, pluripotent, multipotent and unipotent. Totipotent and pluripotent stem cells have an embryonic origin, and totipotent stem cells possess the greatest potential since they have the ability to differentiate into all cell types in the body. Multipotent and unipotent stem

cells are adult stem cells. Multipotent stem cells have the potential of forming a limited subset of cells [37].

Employing autologous cells, i.e. patient's own cells, avoids the risks of immunological responses like rejections. Therefore, it has been considered the gold standard for tissue engineering [38]. There are challenges with the use of autologous differentiated cells, for example with chondrocytes, such as donor site morbidity, low availability of material [17] and dedifferentiation [39]. Chondrocytes in their native tissue are characterised by the macromolecules they synthesize such as collagen type II and aggrecans. When chondrocytes are cultured in a monolayer, they can dedifferentiate to fibroblast-like cells, synthesizing more collagen type I and less collagen type II and aggrecans. For OC tissue regeneration, the mature cells of bone and cartilage can be harvested and grown in vitro. For the cartilage part, Brittberg et al. [40] described a cell-based therapy called autologous chondrocyte implantation (ACI). Patient's own chondrocytes isolated from a small biopsy of a low-weight bearing site of the cartilage were cultured in vitro for 2–3 weeks to obtain a high enough number of cells. Then, the defect surface is covered with a periosteum patch and the cell suspension injected into the area of the lesion. It has been reported that this method had some clinically good results, at 2 years follow-up. However, the predictability and reproducibility of the outcomes of the approach were not high. Moreover, at least two operations are required, one to obtain, and the other to implant cells, risking donor site morbidity and lack of structural support for the cells [41].

The challenges experienced with differentiated cells can be overcome by means of employing stem cells. For example, mesenchymal stem cells (MSCs) [42] (marrow stromal cells) are multipotent stem cells and have high capacity to differentiate into multiple mesenchymal tissue types including bone and cartilage under certain manipulation and culturing conditions. MSCs are often isolated from bone marrow but can be also obtained from muscle, adipose or synovial tissues.

Scaffolds have important functions in the TERM strategies. A scaffold, which is typically a 3D porous structure from biomaterials, carries the cells to the target site and provides a provisional residence for the cells where the cells attach, proliferate, function, and eventually regenerate the tissue. A scaffold should function as more than a simple mechanical structure; it should interact with the cells and the environmental factors by mimicking the ECM of the target tissue as much as possible, so that the process of tissue regeneration is promoted. A scaffold must be biocompatible and biodegradable. The rate of biodegradation should match that of tissue regeneration. The main characteristics of an ideal biodegradable 3D scaffold for tissue engineering applications [10, 43–46] can be summarized as: (i) it should present an adequate structural architecture and surface properties to allow cell adhesion and growth, (ii) it should be highly porous to create a large surface for cell-scaffold interactions and to allow cell migration, (iii) the pores should have an appropriate size, and be interconnected for cell ingrowth, (iv) it must be biocompatible (neither the scaffold nor its degradation products should cause acute inflammation or toxicity), (v) it should provide the needed temporary mechanical support to the site, (vi) the degradation rate of the scaffold should be matched with the regeneration rate of the tissue, and (vii) it should have the appropriate size and shape. Scaffolds can be considered typically

as 3D porous structures into where cells can be seeded, or as hydrogels in which the cells can be encapsulated. The scaffolds can be bioceramic-based, biopolymer-based or based on their composites. Decellularized ECMs [47] are also used as a scaffold in tissue engineering. In general, bioceramics are mechanically strong and show excellent bone integration. Commonly used bioceramics [48, 49] include HAp, calcium phosphates and bioactive glass. There is an extremely wide range of polymeric biomaterials and processing techniques to produce scaffolds with various forms [46, 50, 51]. Polymer-based scaffolds can be produced from: (i) various protein-based polymers such as collagen [52], gelatine [53], fibrin [54] or silk fibroin [55]; or (ii) various carbohydrate-based polymers as, for example, alginate [56], agarose [57], hyaluronan [58], chitosan [59], starch [60] or gellan gum [61]; or (iii) synthetic polymers such as polylactic acid [62], polyglycolic acid [63] and polycaprolactone [64].

Polymers can also be processed into hydrogels [65], which are 3D hydrophilic polymeric networks that have large capacity of absorbing and retaining water. Using hydrogels as a scaffold material is a promising strategy. Cells can be encapsulated in hydrogels [66], which resemble the ECM of tissues and provide homogeneous and efficient cell seeding. They can be prepared in injectable formulations [67]. Injectability allows minimally invasive procedures, which is especially important for defects with an irregular shape. In the case that the hydrogel is photopolymerizable, the cells can be homogenised within the polymer before applying the polymerization process. Using a photopolymerizable hydrogel can be advantageous in TERM strategies [68] such as: (i) scaffold production and cell seeding can become a one-step process, (ii) a homogeneous distribution of cells with high cell viability can be achieved, and (iii) the treatment can be minimally invasive by injecting the system and initiating the polymerization in situ after the injection. Photopolymerizable hydrogels [69] are hydrogels that polymerize in the presence of a photo-initiator upon UV light exposure. Photo-polymerization can be defined as a chain polymerization process initiated by light, where the molecular weight increases and the pre-existing macromolecules are cross-linked. Light in the UV-visible spectral range is absorbed by photo-initiators, and converted into chemical energy as free radicals and reactive cations that initiate polymerization [70].

Gellan gum is a bacterial polysaccharide [71] and was suggested originally by our group [72] as a candidate biomaterial for cartilage tissue engineering. Even though it has been used as drug delivery devices and also in the food industry, it is considered as a new biomaterial for tissue engineering applications [73]. Gellan gum can form thermoreversible gels. Gelation of gellan gum is temperature-dependent, and presence of cations induces the gelling process. The mechanical properties of gellan gum can be tuned by changing the degree of acetylation. One advantage of gellan gum is that it can be processed into hydrogels without using harsh reagents. Gellan gum can be dissolved in water at high temperatures and can form gel upon a decrease in temperature. Another advantageous feature of gellan gum is that it can be also prepared into an injectable system [61]. Silva-Correia et al. [74] developed photo-cross-linkable methacrylated gellan gum hydrogels for tissue engineering applications by the reaction of gellan gum solution with glycidyl methacrylate.

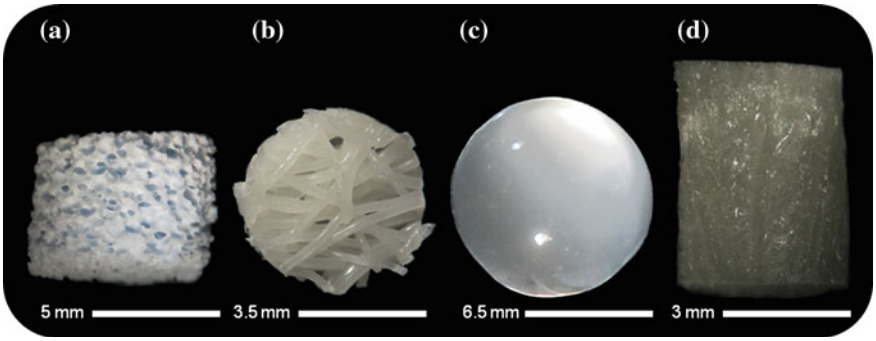

Fig. 2.5 Scaffolds can be processed with different methods into different structures. **a** Sintered HAp. **b** Fibre bonded meshes of starch-polycaprolactone. **c** Methacrylated gellan gum hydrogel. **d** Freeze-dried chitosan

Scaffolds can be manufactured with various methods. Figure 2.5 presents some examples of scaffolds that were processed with different methods into different structures. Figure 2.5a–d present, respectively, a macroporous HAp scaffold produced by sintering [75], a starch-polycaprolactone mesh produced by fibre bonding [76], a methacrylated gellan gum hydrogel obtained by ionic cross-linking [74], and a chitosan sponge obtained by freeze-drying [59].

Rapid prototyping (RP) is an interesting group of non-conventional scaffold manufacturing techniques. With RP, a physical construct can be created layer-by-layer using a computer-aided design data [77–79]. One of the RP techniques is 3D plotting [80], which is a melt-dissolution deposition based technique. In 3D plotting, liquids or hydrogels can be dispensed into a liquid medium through a nozzle that moves on the horizontal plane to build a layer, then the next layers will be created on top of the previous layer by the movement of the nozzle on the vertical plane [77]. For the first time, Landers et al. [81] processed hydrogels into a scaffold with defined pore-size and shape with this technique. RP techniques bring several advantages. It is possible to produce scaffolds with customized structural design based on the computer-aided design data and this will make it possible to produce patient-specific scaffolds [78]. The advantage of customized design is that it gives the opportunity to produce scaffolds with desired porosity and pore size. It is also possible to change the plotting parameters to control the architecture and mechanical properties [82]. These parameters include nozzle size, speed of nozzle arm, speed of extrusion, and distance between the strands [81]. Furthermore, when a computerized manufacturing technique is used, minimum manpower is required and thus, higher throughput manufacturing is possible [78]. Another advantage is the possibility of including the cells and growth factors into the biomaterial before the scaffold is manufactured [81].

Growth factors represent a large number of polypeptides that have a specific effect on the activities of cells by transmitting signals [83, 84]. They can bind to the specific receptors found on the surface or inside the target cells. The effect could be inhibition or stimulation of differentiation, proliferation, adhesion, migration and

gene expression of the cells thereby affecting degradation of the tissue and the ECM synthesis of cells. They can also influence secretion and activation of other growth factors. Effects of growth factors depend on the concentration. New generation strategies incorporate also growth factors into the tissue engineering constructs to promote the regeneration. Frequently employed growth factors for cartilage or bone tissue engineering include bone morphogenetic proteins (BMPs), insulin-like growth factors (IGFs), transforming growth factor-β (TGF-β), fibroblastic growth factors (FGFs), and platelet-derived growth factor (PDGF). For example, insulin-like growth factor-1 is the main anabolic growth factor for cartilage; it has effects on stimulation of synthesis and inhibits the breakdown of PGs and cartilage homeostasis. Also, it may improve the tissue integration and decrease the synovial inflammation in vivo [85]. Fortier et al. [86] showed in a horse model that IGF-1 introduced to chondrocyte-fibrin grafts may facilitate the repair process of the full thickness defects.

Lieberman et al. [84] and Linkhart et al. [87] reviewed the use of growth factors for bone repair. Fortier et al. [88] reviewed the role of growth factors for cartilage tissue regeneration, and their effects on MSCs. Each growth factor affects the cell and the tissue in a specific way; however, the cumulative effects of growth factors are still poorly understood, and should be further investigated since their adequate combination is a must for appropriate tissue regeneration.

Bioreactors are devices that can control the culture media conditions such as the temperature, pH, oxygen ratio, osmolality and nutrients, and thereby can facilitate more advanced tissue regeneration in vitro. They can also promote uniform cell seeding, and facilitate the mass transfer between the culture and the cells. Moreover, with bioreactors it can be possible to have interstitial fluid flow, or mechanical stimulation such as pressure and compression [89]. Various bioreactors have been developed for tissue engineering purposes. For example: (i) spinner flasks [90] are simple bioreactors for cell seeding onto scaffolds where turbulent dynamic flow of medium is generated by a magnetic stirrer; (ii) rotating wall vessels [91] are made of horizontally rotating cylinders filled with culture medium, and provide low-turbulence laminar dynamic flow as well as adequate oxygenation; (iii) flow perfusion bioreactors [92] have a system that can continuously provide direct flow of culture medium through the porous structure of the scaffold and in this way enhance the mass transfer to the interior of the scaffold; and (iv) bioreactors that provide mechanical loading have been developed since it is known that cartilage and bone tissues are affected by mechanical loading. For example, Pei et al. [93] used a bioreactor that can provide a mechanically active environment with efficiently mixed media, low velocity laminar flow and shear stress. They showed that this kind of bioreactor can enhance the structural, functional and molecular properties of in vitro-generated cartilage compared to the use of Petri dishes [93].

2.4.2 Strategies for Tissue Regeneration

One of the two routes [10] that can be followed for tissue regeneration is implanting the cells and scaffolds into the lesion site for enhancing the regeneration process

in vivo. The other route is implanting the entirely in vitro developed construct into the lesion site. When an appropriate bioreactor is used, cell metabolism and ECM production could be controlled better in vitro than in vivo. Mostly, the first route is preferred. It brings also the opportunity of non-destructive characterization of the tissue prior to implantation. The main drawbacks of the second route are mostly associated with tissue integration and mechanical fixation. Also, providing correct mechanical loading is a challenge in vitro. In the first route, the tissue will adapt and integrate better since it is formed in situ under physiological conditions as the result of mechanical loading. However, on the long term, control of cellular activities is more difficult.

Scaffolds may be used with or without cells, but cells are usually incorporated into scaffolds. Various approaches can be used to design scaffolds for OC tissue engineering [17]. These include using different scaffolds for bone and cartilage; using a scaffold only for bone but not for cartilage; or using a single scaffold for both bone and cartilage. Scaffolds can be homogenous or heterogeneous and can consist of a single layer or more layers. In the study of Schaefer et al. [94], different scaffolds were used for bone and cartilage parts. They developed in vitro engineered structures composed of a cell-seeded scaffold and a SB support to be press-fitted into large defects in OC tissue located in the rabbit knee joint. Allogeneic rabbit chondrocytes were dynamically seeded onto a non-woven polyglycolic acid scaffold. SB support was an osteoconductive sponge made of bovine collagen type. As controls, the defects were either treated with cell-free scaffolds or kept empty. Their results showed that the treatments done with composites were structurally superior to the ones done with cell-free scaffolds or kept empty. Composites withstood the physiological loads and showed remodelling into OC tissue with preserved cartilage at the articulating surface and subchondral regeneration. However, the integration of the composites with the host cartilage was not good, whereas a good integration was achieved with the host bone.

In the study of Kandel et al. [95] a scaffold was used only for the bone part. They developed biphasic constructs using cartilaginous tissues grown and fixed on top of porous calcium polyphosphate substrates. Isolated chondrocytes were seeded on top of the substrate and were grown with autologous serum for 8 weeks to generate the cartilaginous tissues. These in vitro-formed constructs were subsequently implanted into OC defects in sheep and maintained up to 9 months. The results supported the suitability of the strategy to treat OC defects. The constructs withstood in vivo loading up to 9 months with good integration to native cartilage and bone ingrowth into the substrate. In another study, Oliveira et al. [59] developed HAp/chitosan bilayered scaffolds through a combination of sintering and freeze-drying methods for OC tissue engineering. Preliminary in vitro tests showed that goat marrow stromal cells grew and differentiated into osteoblasts and chondrocytes, respectively in HAp and chitosan layers. The physicochemical properties and biological performance of the scaffolds revealed their great potential to be employed in the regenerative strategies for treating OC lesions.

As mentioned previously, hydrogels are a group of scaffolding materials for tissue engineering. The conventional hydrogel-based regenerative strategies for cartilage

involve hydrogels with cells to achieve a homogeneous tissue rather than the zonal structure of the cartilage [96]. An approach for regeneration of cartilage in a zonal manner is using chondrocytes that are isolated from different zones of the cartilage. Following this interesting strategy, Kim et al. [97] showed an experimental model where chondrocytes were isolated selectively from different layers of bovine articular cartilage, and multi-layered photo-polymerizable polyethylene glycol diacrylate hydrogel scaffold-cell constructs were developed. That study showed that chondrocytes of different layers present differences in gene expression and proliferation kinetics. Cells survived and stayed in the layer in which they were encapsulated. Histological studies of the layers showed similar results as native articular cartilage. However, several improvements are in great need for further clinical application. For example, gradual transition between the layers, an additional layer in the construct for the regeneration of the calcified layer of the cartilage and using a biodegradable hydrogel.

Another approach could be using hydrogels with different properties for each layer. Ng et al. [98] developed chondrocyte-seeded bilayered agarose constructs to mimic the layer-dependent inhomogeneity of cartilage. As a combination of approaches mentioned above, in a later study, Ng et al. [99] introduced chondrocytes that are isolated from different layers of the bovine calf knee cartilage into the bilayered cartilage construct. In the study, layers with different mechanical properties were obtained for 2 or 3 % agarose hydrogels seeded with chondrocytes from different layers to mimic both the cellular and mechanical inhomogeneity of the native tissue. Although the approach followed in the aforementioned studies is for cartilage regeneration only, it can be also applied in strategies aiming to regenerate OC tissue.

Harley et al. [100] manufactured heterogeneous scaffolds from collagen-glycosaminoglycan and nano-calcium phosphate to mimic the composition, structure and mechanical behaviour of articular cartilage and SB as well as gradual transition between them. Layered scaffolds were mimicking the normal OC tissue with the inter-diffused regions having differential pore microstructure, mechanical properties, and chemical composition, and a gradual transition interface. Also, Jiang et al. [101] developed a multi-phased scaffold from agarose hydrogel, and microspheres of poly(lactic-co-glycolic acid) and bioactive glass. Region-specific co-culture of chondrocytes and osteoblasts were introduced into the scaffolds in a controlled manner. Within the scaffolds, three phases were designed: (i) a hydrogel-chondrocyte phase to mimic the cartilage region, (ii) a hydrogel-polymer-bioactive glass-chondrocyte phase as an interface layer to mimic calcified cartilage, (iii) and a polymer-bioactive glass-osteoblast phase to mimic bone. The in vitro results showed the formation of three distinct yet continuous layers of cartilage, calcified cartilage and bone-like matrices.

An alternative to the direct transplantation of cells as applied in the studies above, is recruiting endogenous cells. A proof of this concept was demonstrated by Lee et al. [102] who showed that the entire articulating surface of a joint can be regenerated in vivo by using endogenous cells. They manufactured anatomically correct composite scaffolds from poly-ε-caprolactone/HAp using a computer-aided design. The scaffolds were infused with TGF-β3-containing or TGF-β3-free collagen hydrogel, and transplanted acellularly into the rabbit condyle. The results showed that inclusion

of TGF-β3 into the scaffolds leads to roughly 130 % more cells in the regenerated cartilage than in the absence of TGF-β3. After 4 months, TGF-β3-infused scaffolds were fully covered with hyaline cartilage in the articular surface with similar mechanical properties as of the native cartilage, whereas TGF-β3-free scaffolds showed inferior results such as only isolated cartilage formation with relatively lower density and thickness [102]. This approach may be useful for the cartilage part of an OC regeneration strategy. In another study, Huang et al. [103] produced calcium phosphate/poly(L-lactic acid) composite scaffolds that were incorporated with basic fibroblast growth factor. The scaffolds were implanted into OC defects of rabbits without in vitro cell seeding. It was reported that the defects were filled with regenerated tissue [103]. The surface was covered with a layer of cartilage tissue with a good integration in the surrounding native tissue. In addition, high levels of collagen type II and aggrecan were reported. With respect to SB regeneration, a continuous layer of trabecular bone was formed below the cartilage [103].

As an alternative to the scaffolding materials used in the studies mentioned above, decellularized tissues can also be used as scaffolds in tissue engineering applications. Yang et al. [104] developed porous decellularized scaffolds from bovine articular cartilage for cartilage regeneration. The scaffolds maintained the collagen and glycosaminoglycan components of cartilage. Rabbit bone marrow MSCs were seeded into the decellularized scaffolds. After implantation of constructs into the knee cartilage defects of rabbits, better histological scores were achieved as compared to control groups. Small intestinal submucosa (SIS) has also been studied experimentally for tissue engineering applications. To repair articular cartilage defects, Peel et al. [105] seeded chondrocytes onto porcine SIS to generate cartilaginous tissue. Full-thickness articular cartilage defects were treated with these constructs. Based on that work, it was suggested that the SIS–cartilaginous tissue constructs might be useful for joint resurfacing. The results of a study with SIS performed by Suckow et al. [106] also suggested that SIS may be a promising biomaterial for bone repair.

2.5 Multiscale Tissue Engineering and Regenerative Medicine Strategies

The current trend in TERM is towards multiscale strategies in which different fields of expertise such as tissue engineering, information technology, and medical imaging collaborate. This part briefly overviews these multiscale approaches. The Laboratory for Multiscale Regenerative Technologies (http://lmrt.mit.edu/) directed by Sangeeta Bhatia, is researching micro- and nanotechnology applications for tissue repair and regeneration. They study how micro-environmental signals influence fate and function of liver cells and use this knowledge to develop robust models of animal and human liver for in vitro [107] and in vivo studies. They use microelectronic circuits [108] to study the role of cell–cell interactions in liver constructs, and to use novel extracellular matrix microarrays [109] to study the role of matrix combinations in liver functions. Moreover, their studies include hydrogels, stem cells, and bioreactors

Fig. 2.6 Step-wise strategy for the patient-specific treatment of an OC defect. The data obtained from medical imaging, such as magnetic resonance imaging (MRI) or computed tomography (CT) is used in the design of a scaffold that is specific for the patient. Autologous cells are isolated and expanded in vitro and encapsulated into the photopolymerizable polymer solution where also growth factors are introduced. Then, the construct (cell/scaffold) is manufactured with a rapid prototyping technique under UV light to obtain the anatomical correct shape and size. The cellular scaffold is dynamically conditioned in vitro with a bioreactor. The tissue engineered OC construct is then implanted into the OC defect of the patient

[110] to provide gradients of soluble stimuli. The systematic approach they developed is oriented towards hepatic tissue engineering. However, it can be taken as a reference point to employ new tools leading to a multiscale approach in TERM for other tissues.

In the studies of Moroni et al. [111] and Ballyns et al. [112] anatomically shaped scaffolds are produced by using the data obtained from medical imaging. In those studies, the meniscus was chosen as a possible application, but the approach might be used for other tissues as well. Moroni et al. [111] combined the computed tomography (CT) and magnetic resonance imaging (MRI) data of menisci with a RP method to manufacture 3D fibre-deposited scaffolds. The scaffolds were in anatomical shape, and the manufacturing technique allowed for tailoring scaffold architecture and mechanical properties to mimic the native meniscus. Ballyns et al. [112] showed the possibility of developing engineered tissues using tissue injection moulding technique combined with computer-aided design based on the anatomic shapes obtained via medical imaging modalities such as CT and MRI. Depending on the size of the lesion, hydrogels could be injected with a minimally invasive operation or could be pre-formed into anatomical shape. A step-wise strategy for the treatment of a patient with OC defect is illustrated in Fig. 2.6, where the data obtained from the medical

images is used in the design of scaffolds having anatomical correct shape and size. Cells are cultured in vitro and encapsulated into the photopolymerizable polymer solution while also growth factors are added into the mixture. With a RP technique, the scaffold is produced under UV light. The cellular scaffold is dynamically conditioned in vitro with a bioreactor. The tissue engineered OC construct is then implanted into the OC defect of the patient.

In another study by Schek et al. [113], a biphasic poly-L-lactic acid/HAp composite scaffolds for OC tissue engineering were developed by means of a RP method with image-based design, which resulted in scaffolds with a matched articular shape and load bearing features. The polymeric phase was seeded with chondrocytes whereas fibroblasts transduced with an adenovirus expressing BMP-7 was introduced into the HAp part. The subcutaneous implantation of the constructs into mice demonstrated the potential of this strategy for OC tissue regeneration.

Lima et al. [114] used finite element modelling to study the biophysical stimuli occurring within the structure under dynamic deformational loading. They developed bilayered OC constructs composed of a cell-seeded agarose gel on the top and a bone part at the bottom where in the middle an interface region of gel/bone was formed. The results showed that relatively more inhomogeneous mechanical signals, such as strain, fluid flow or fluid pressure, occurred within the gel region of the OC composite, compared to the structures only made of gel. That study showed that the cells in the gel may sense these radially and axially varied signals, and it may be beneficial to achieve an inhomogeneity in engineered OC constructs.

2.6 Final Remarks

TERM is a truly multidisciplinary field with the ultimate goal of regenerating damaged/diseased tissues. Several strategies are available for cartilage and bone tissue regeneration. However, the gold standard does not exist. Many factors affect the outcome of the strategies: the type and manufacturing technique of biomaterials, source, type and culturing conditions of cells, employment of growth factors and bioreactors, and their cumulative effect when used in combination. It is also noteworthy that the depth and size of the lesion, and the patient's age and condition affect the repair response. As herein discussed, many options exist for each of the components of tissue engineering. Each strategy has its own advantages and disadvantages. Nevertheless, the new generation strategies of TERM show the trend to be patient-specific and to be built on a multiscale approach, specially benefiting from basic science, engineering, and medical imaging and modelling.

Acknowledgments The authors thank the financial support of the MultiScaleHuman project (Contract number: MRTN-CT-2011-289897) in the Marie Curie Actions—Initial Training Networks.

References

1. Sanders, R. K., & Crim, J. R. (2001). Osteochondral injuries. *Seminars in Ultrasound Ct and Mri*, *22*(4), 352–370.
2. Buckwalter, J. A., & Mankin, H. J. (1997). Articular cartilage. Part II. Degeneration and osteoarthrosis, repair, regeneration, and transplantation. *Journal of Bone and Joint Surgery-American Volume*, *79A*(4), 612–632.
3. Westacott, C. I., & Sharif, M. (1996). Cytokines in osteoarthritis: Mediators or markers of joint destruction? *Seminars in Arthritis and Rheumatism*, *25*(4), 254–272.
4. Goldring, M. B., & Goldring, S. R. (2007). Osteoarthritis. *Journal of Cellular Physiology*, *213*(3), 626–634.
5. Nesic, D., Whiteside, R., Brittberg, M., Wendt, D., Martin, I., & Mainil-Varlet, P. (2006). Cartilage tissue engineering for degenerative joint disease. *Advanced Drug Delivery Reviews*, *58*(2), 300–322.
6. Goldring, M. B. (2000). The role of the chondrocyte in osteoarthritis. *Arthritis and Rheumatism*, *43*(9), 1916–1926.
7. Buckwalter, J. A., Mankin, H. J., & Grodzinsky, A. J. (2005). Articular cartilage and osteoarthritis. *Instructional Course Lectures*, *54*, 465–480.
8. Bhosale, A. M., & Richardson, J. B. (2008). Articular cartilage: Structure, injuries and review of management. *British Medical Bulletin*, *87*(1), 77–95.
9. Buckwalter, J. A., & Mankin, H. J. (1998). Articular cartilage repair and transplantation. *Arthritis and Rheumatism*, *41*(8), 1331–1342.
10. Hunziker, E. B. (2002). Articular cartilage repair: Basic science and clinical progress. A review of the current status and prospects. *Osteoarthritis and Cartilage*, *10*(6), 432–463.
11. Vaquero, J., & Forriol, F. (2012). Knee chondral injuries: Clinical treatment strategies and experimental models. *Injury-International Journal of the Care of the Injured*, *43*(6), 694–705.
12. Wirth, C. J., & Rudert, M. (1996). Techniques of cartilage growth enhancement: A review of the literature. *Arthroscopy*, *12*(3), 300–308.
13. Aigner, T., & Stove, J. (2003). Collagens—major component of the physiological cartilage matrix, major target of cartilage degeneration, major tool in cartilage repair. *Advanced Drug Delivery Reviews*, *55*(12), 1569–1593.
14. Pridie, K. H., & Gordon, G. (1959). A method of resurfacing osteoarthritic knee joints. *Journal of Bone and Joint Surgery-British*, *41*(3), 618–619.
15. Sprague, N. F. (1981). Arthroscopic debriment for degenerative knee-joint disease. *Clinical Orthopaedics and Related Research*, *160*, 118–123.
16. Ficat, R. P., Ficat, C., Gedeon, P., & Toussaint, J. B. (1979). Spongialization—new treatment for diseased patellae. *Clinical Orthopaedics and Related Research*, *144*, 74–83.
17. Martin, I., Miot, S., Barbero, A., Jakob, M., & Wendt, D. (2007). Osteochondral tissue engineering. *Journal of Biomechanics*, *40*(4), 750–765.
18. Heath, C. A., & Magari, S. R. (1996). Mini-review: Mechanical factors affecting cartilage regeneration in vitro. *Biotechnology and Bioengineering*, *50*(4), 430–437.
19. Buckwalter, J. A., & Mankin, H. J. (1997). Articular cartilage. Part I: Tissue design and chondrocyte-matrix interactions. *Journal of Bone and Joint Surgery-American Volume*, *79A*(4), 600–611.
20. Grodzinsky, A. J., Levenston, M. E., Jin, M., & Frank, E. H. (2000). Cartilage tissue remodeling in response to mechanical forces. *Annual Review of Biomedical Engineering*, *2*, 691–713.
21. Kleemann, R. U., Krocker, D., Cedraro, A., Tuischer, J., & Duda, G. N. (2005). Altered cartilage mechanics and histology in knee osteoarthritis: Relation to clinical assessment (ICRS Grade). *Osteoarthritis and Cartilage*, *13*(11), 958–963.
22. Gelse, K., Pöschl, E., & Aigner, T. (2003). Collagens—Structure, function, and biosynthesis. *Advanced Drug Delivery Reviews*, *55*(12), 1531–1546.

23. Armstrong, C. G., & Mow, V. C. (1982). Variations in the intrinsic mechanical properties of human articular-cartilage with age, degeneration and water-content. *Journal of Bone and Joint Surgery-American*, *64*(1), 88–94.
24. Black, J., & Hastings, G. W. (Eds.). (1998). *Handbook of biomaterials properties*. London: Chapman and Hall.
25. Clarke, B. (2008). Normal bone anatomy and physiology. *Clinical Journal of the American Society of Nephrology*, *3*, S131–S139.
26. Miller, S. C., Saintgeorges, L., Bowman, B. M., & Jee, W. S. S. (1989). Bone lining cells—structure and function. *Scanning Microscopy*, *3*(3), 953–961.
27. Yaszemski, M. J., Payne, R. G., Hayes, W. C., Langer, R., & Mikos, A. G. (1996). Evolution of bone transplantation: Molecular, cellular and tissue strategies to engineer human bone. *Biomaterials*, *17*(2), 175–185.
28. Suri, S., & Walsh, D. A. (2012). Osteochondral alterations in osteoarthritis. *Bone*, *51*(2), 204–211.
29. Kawcak, C. E., McIlwraith, C. W., Norrdin, R. W., Park, R. D., & James, S. P. (2001). The role of subchondral bone in joint disease: A review. *Equine Veterinary Journal*, *33*(2), 120–126.
30. Lyons, T. J., McClure, S. F., Stoddart, R. W., & McClure, J. (2006). The normal human chondro-osseous junctional region: Evidence for contact of uncalcified cartilage with subchondral bone and marrow spaces. *Bmc Musculoskeletal Disorders*, *7*, 52.
31. Burr, D. B. (2004). Anatomy and physiology of the mineralized tissues: Role in the pathogenesis of osteoarthrosis. *Osteoarthritis and cartilage / OARS, Osteoarthritis Research Society*, *12 Suppl A*, S20–S30.
32. Madry, H., van Dijk, C. N., & Mueller-Gerbl, M. (2010). The basic science of the subchondral bone. *Knee Surgery Sports Traumatology Arthroscopy*, *18*(4), 419–433.
33. Clark, J. M., & Huber, J. D. (1990). The structure of the human subchondral plate. *Journal of Bone and Joint Surgery-British*, *72*(5), 866–873.
34. Li, B. H., & Aspden, R. M. (1997). Mechanical and material properties of the subchondral bone plate from the femoral head of patients with osteoarthritis or osteoporosis. *Annals of the Rheumatic Diseases*, *56*(4), 247–254.
35. Rippon, H. J., & Bishop, A. E. (2004). Embryonic stem cells. *Cell Proliferation*, *37*(1), 23–34.
36. Young, H. E., & Black, A. C. (2004). Adult stem cells. *Anatomical Record Part a-Discoveries in Molecular Cellular and Evolutionary Biology*, *276A*(1), 75–102.
37. Alison, M. R., Poulsom, R., Forbes, S., & Wright, N. A. (2002). An introduction to stem cells. *Journal of Pathology*, *197*(4), 419–423.
38. Corona, B. T., Ward, C. L., Harrison, B. S., & Christ, G. J. (2010). Regenerative medicine: Basic concepts, current status, and future applications. *Journal of Investigative Medicine*, *58*(7), 849–858.
39. Darling, E. M., & Athanasiou, K. A. (2005). Rapid phenotypic changes in passaged articular chondrocyte subpopulations. *Journal of Orthopaedic Research*, *23*(2), 425–432.
40. Brittberg, M., Lindahl, A., Nilsson, A., Ohlsson, C., Isaksson, O., & Peterson, L. (1994). Treatment of deep cartilage defects in the knee with autologous chondrocyte transplantation. *New England Journal of Medicine*, *331*(14), 889–895.
41. Bedi, A., Feeley, B. T., & Williams, R. J, I. I. I. (2010). Management of articular cartilage defects of the knee. *Journal of Bone and Joint Surgery-American*, *92A*(4), 994–1009.
42. Caplan, A. I. (1991). Mesenchymal stem-cells. *Journal of Orthopaedic Research*, *9*(5), 641–650.
43. Freyman, T. M., Yannas, I. V., & Gibson, L. J. (2001). Cellular materials as porous scaffolds for tissue engineering. *Progress in Materials Science*, *46*(3–4), 273–282.
44. Kinner, B., Capito, R. M., & Spector, M. (2005). Regeneration of articular cartilage. In: Yannas, I. V. (ed.). *Regenerative medicine II: Clinical and preclinical applications*, (Vol. 94). *Advances in Biochemical Engineering-Biotechnology*, (pp. 91–123). New York: Springer.
45. Noeth, U., Rackwitz, L., Steinert, A. F., & Tuan, R. S. (2010). Cell delivery therapeutics for musculoskeletal regeneration. *Advanced Drug Delivery Reviews*, *62*(7–8), 765–783.

46. Puppi, D., Chiellini, F., Piras, A. M., & Chiellini, E. (2010). Polymeric materials for bone and cartilage repair. *Progress in Polymer Science*, *35*(4), 403–440.
47. Gilbert, T. W., Sellaro, T. L., & Badylak, S. F. (2006). Decellularization of tissues and organs. *Biomaterials*, *27*(19), 3675–3683.
48. Hench, L. L. (1991). Bioceramics—from concept to clinic. *Journal of the American Ceramic Society*, *74*(7), 1487–1510.
49. Best, S. M., Porter, A. E., Thian, E. S., & Huang, J. (2008). Bioceramics: Past, present and for the future. *Journal of the European Ceramic Society*, *28*(7), 1319–1327.
50. Mano, J. F., Silva, G. A., Azevedo, H. S., Malafaya, P. B., Sousa, R. A., Silva, S. S., et al. (2007). Natural origin biodegradable systems in tissue engineering and regenerative medicine: Present status and some moving trends. *Journal of the Royal Society Interface*, *4*(17), 999–1030.
51. Hutmacher, D. W. (2000). Scaffolds in tissue engineering bone and cartilage. *Biomaterials*, *21*(24), 2529–2543.
52. Yan, L.-P., Wang, Y.-J., Ren, L., Wu, G., Caridade, S. G., Fan, J.-B., et al. (2010). Genipin-cross-linked collagen/chitosan biomimetic scaffolds for articular cartilage tissue engineering applications. *Journal of Biomedical Materials Research Part A*, *95A*(2), 465–475.
53. Hoshikawa, A., Nakayama, Y., Matsuda, T., Oda, H., Nakamura, K., & Mabuchi, K. (2006). Encapsulation of chondrocytes in photopolymerizable styrenated gelatin for cartilage tissue engineering. *Tissue Engineering*, *12*(8), 2333–2341.
54. Eyrich, D., Brandl, F., Appel, B., Wiese, H., Maier, G., Wenzel, M., et al. (2007). Long-term stable fibrin gels for cartilage engineering. *Biomaterials*, *28*(1), 55–65.
55. Yan, L. P., Oliveira, J. M., Oliveira, A. L., & Reis, R. L. (2012). Development of a bilayered scaffold based on silk fibroin and silk fibroin/nano-calcium phosphate for osteochondral regeneration. *Journal of Tissue Engineering and Regenerative Medicine*, *6*, 24–24.
56. Popa, E. G., Gomes, M. E., & Reis, R. L. (2011). Cell delivery systems using alginate-carrageenan hydrogel beads and fibers for regenerative medicine applications. *Biomacromolecules*, *12*(11), 3952–3961.
57. Pelaez, D., Huang, C.-Y. C., & Cheung, H. S. (2009). Cyclic compression maintains viability and induces chondrogenesis of human mesenchymal stem cells in fibrin gel scaffolds. *Stem Cells and Development*, *18*(1), 93–102.
58. Stillaert, F. B., Di Bartolo, C., Hunt, J. A., Rhodes, N. P., Tognana, E., Monstrey, S., et al. (2008). Human clinical experience with adipose precursor cells seeded on hyaluronic acid-based spongy scaffolds. *Biomaterials*, *29*(29), 3953–3959.
59. Oliveira, J. M., Rodrigues, M. T., Silva, S. S., Malafaya, P. B., Gomes, M. E., Viegas, C. A., et al. (2006). Novel hydroxyapatite/chitosan bilayered scaffold for osteochondral tissue-engineering applications: Scaffold design and its performance when seeded with goat bone marrow stromal cells. *Biomaterials*, *27*(36), 6123–6137.
60. Rodrigues, A. I., Gomes, M. E., Leonor, I. B., & Reis, R. L. (2012). Bioactive starch-based scaffolds and human adipose stem cells are a good combination for bone tissue engineering. *Acta Biomaterialia*, *8*(10), 3765–3776.
61. Oliveira, J. T., Santos, T. C., Martins, L., Picciochi, R., Marques, A. P., Castro, A. G., et al. (2010). Gellan gum injectable hydrogels for cartilage tissue engineering applications: In vitro studies and preliminary in vivo evaluation. *Tissue Engineering Part A*, *16*(1), 343–353.
62. Antunes, J. C., Oliveira, J. M., Reis, R. L., Soria, J. M., Gomez-Ribelles, J. L., & Mano, J. F. (2010). Novel poly(L-lactic acid)/hyaluronic acid macroporous hybrid scaffolds: Characterization and assessment of cytotoxicity. *Journal of Biomedical Materials Research Part A*, *94A*(3), 856–869.
63. Xue, D., Zheng, Q., Zong, C., Li, Q., Li, H., Qian, S., et al. (2010). Osteochondral repair using porous poly(lactide-co-glycolide)/nano-hydroxyapatite hybrid scaffolds with undifferentiated mesenchymal stem cells in a rat model. *Journal of Biomedical Materials Research Part A*, *94A*(1), 259–270.

64. Erisken, C., Kalyon, D. M., Wang, H., Oernek-Ballanco, C., & Xu, J. (2011). Osteochondral tissue formation through adipose-derived stromal cell differentiation on biomimetic polycaprolactone nanofibrous scaffolds with graded insulin and beta-glycerophosphate concentrations. *Tissue Engineering Part A*, *17*(9–10), 1239–1252.
65. Drury, J. L., & Mooney, D. J. (2003). Hydrogels for tissue engineering: Scaffold design variables and applications. *Biomaterials*, *24*(24), 4337–4351.
66. Uludag, H., De Vos, P., & Tresco, P. A. (2000). Technology of mammalian cell encapsulation. *Advanced Drug Delivery Reviews*, *42*(1–2), 29–64.
67. Temenoff, J. S., & Mikos, A. G. (2000). Injectable biodegradable materials for orthopedic tissue engineering. *Biomaterials*, *21*(23), 2405–2412.
68. Chan, B. P., & Leong, K. W. (2008). Scaffolding in tissue engineering: General approaches and tissue-specific considerations. *European Spine Journal: Official Publication of the European Spine Society, the European Spinal Deformity Society, and the European Section of the Cervical Spine Research Society*, *17*(Suppl 4), 467–479.
69. Nguyen, K. T., & West, J. L. (2002). Photopolymerizable hydrogels for tissue engineering applications. *Biomaterials*, *23*(22), 4307–4314.
70. Kaur, M., & Srivastava, A. K. (2002). Photopolymerization: A review. *Journal of Macromolecular Science-Polymer Reviews*, *C42*(4), 481–512.
71. Jansson, P. E., Lindberg, B., & Sandford, P. A. (1983). Structural studies of gellan gum, an extracellular polysaccharide elaborated by Pseudomonas-Elodea. *Carbohydrate Research*, *124*(1), 135–139.
72. Oliveira, J. T., Martins, L., Picciochi, R., Malafaya, I. B., Sousa, R. A., Neves, N. M., et al. (2009). Gellan gum: A new biomaterial for cartilage tissue engineering applications. *Journal of Biomedical Materials Research Part A*, *93A*(3), 852–863.
73. Smith, A. M., Shelton, R. M., Perrie, Y., & Harris, J. J. (2007). An initial evaluation of gellan gum as a material for tissue engineering applications. *Journal of Biomaterials Applications*, *22*(3), 241–254.
74. Silva-Correia, J., Oliveira, J. M., Caridade, S. G., Oliveira, J. T., Sousa, R. A., Mano, J. F., et al. (2011). Gellan gum-based hydrogels for intervertebral disc tissue-engineering applications. *Journal of Tissue Engineering and Regenerative Medicine*, *5*(6), E97–E107.
75. Oliveira, J. M., Silva, S. S., Malafaya, P. B., Rodrigues, M. T., Kotobuki, N., Hirose, M., et al. (2009). Macroporous hydroxyapatite scaffolds for bone tissue engineering applications: Physicochemical characterization and assessment of rat bone marrow stromal cell viability. *Journal of Biomedical Materials Research Part A*, *91A*(1), 175–186.
76. Oliveira, J. M., Sousa, R. A., Kotobuki, N., Tadokoro, M., Hirose, M., Mano, J. F., et al. (2009). The osteogenic differentiation of rat bone marrow stromal cells cultured with dexamethasone-loaded carboxymethylchitosan/poly(amidoamine) dendrimer nanoparticles. *Biomaterials*, *30*(5), 804–813.
77. Landers, R., Pfister, A., Hubner, U., John, H., Schmelzeisen, R., & Mulhaupt, R. (2002). Fabrication of soft tissue engineering scaffolds by means of rapid prototyping techniques. *Journal of Materials Science*, *37*(15), 3107–3116.
78. Leong, K. F., Cheah, C. M., & Chua, C. K. (2003). Solid freeform fabrication of three-dimensional scaffolds for engineering replacement tissues and organs. *Biomaterials*, *24*(13), 2363–2378.
79. Yeong, W. Y., Chua, C. K., Leong, K. F., & Chandrasekaran, M. (2004). Rapid prototyping in tissue engineering: Challenges and potential. *Trends in Biotechnology*, *22*(12), 643–652.
80. Landers, R., & Mulhaupt, R. (2000). Desktop manufacturing of complex objects, prototypes and biomedical scaffolds by means of computer-assisted design combined with computer-guided 3D plotting of polymers and reactive oligomers. *Macromolecular Materials and Engineering*, *282*(9), 17–21.
81. Landers, R., Hubner, U., Schmelzeisen, R., & Mulhaupt, R. (2002). Rapid prototyping of scaffolds derived from thermoreversible hydrogels and tailored for applications in tissue engineering. *Biomaterials*, *23*(23), 4437–4447.

82. Son, J., & Kim, G. (2009). Three-dimensional plotter technology for fabricating polymeric scaffolds with micro-grooved surfaces. *Journal of Biomaterials Science-Polymer Edition*, *20*(14), 2089–2101.
83. Babensee, J. E., McIntire, L. V., & Mikos, A. G. (2000). Growth factor delivery for tissue engineering. *Pharmaceutical Research*, *17*(5), 497–504.
84. Lieberman, J. R., Daluiski, A., & Einhorn, T. A. (2002). The role of growth factors in the repair of bone—Biology and clinical applications. *Journal of Bone and Joint Surgery-American*, *84A*(6), 1032–1044.
85. Schmidt, M. B., Chen, E. H., & Lynch, S. E. (2006). A review of the effects of insulin-like growth factor and platelet derived growth factor on in vivo cartilage healing and repair. *Osteoarthritis and Cartilage*, *14*(5), 403–412.
86. Fortier, L. A., Mohammed, H. O., Lust, G., & Nixon, A. J. (2002). Insulin-like growth factor-I enhances cell-based repair of articular cartilage. *Journal of Bone and Joint Surgery-British*, *84B*(2), 276–288.
87. Linkhart, T. A., Mohan, S., & Baylink, D. J. (1996). Growth factors for bone growth and repair: IGF, TGF beta and BMP. *Bone*, *19*(1), S1–S12.
88. Fortier, L. A., Barker, J. U., Strauss, E. J., McCarrel, T. M., & Cole, B. J. (2011). The role of growth factors in cartilage repair. *Clinical Orthopaedics and Related Research*, *469*(10), 2706–2715.
89. Vunjak-Novakovic, G., Meinel, L., Altman, G., & Kaplan, D. (2005). Bioreactor cultivation of osteochondral grafts. *Orthodontics and Craniofacial Research*, *8*(3), 209–218.
90. Vunjak-Novakovic, G., Obradovic, B., Martin, I., Bursac, P. M., Langer, R., & Freed, L. E. (1998). Dynamic cell seeding of polymer scaffolds for cartilage tissue engineering. *Biotechnology Progress*, *14*(2), 193–202.
91. Schwarz, R. P., Goodwin, T. J., & Wolf, D. A. (1992). Cell culture for three-dimensional modeling in rotating-wall vessels: An application of simulated microgravity. *Journal of Tissue Culture Methods: Tissue Culture Association Manual of Cell, Tissue, and Organ Culture Procedures*, *14*(2), 51–57.
92. Bancroft, G. N., Sikavitsas, V. I., & Mikos, A. G. (2003). Design of a flow perfusion bioreactor system for bone tissue-engineering applications. *Tissue Engineering*, *9*(3), 549–554.
93. Pei, M., Solchaga, L. A., Seidel, J., Zeng, L., Vunjak-Novakovic, G., Caplan, A. I., et al. (2002). Bioreactors mediate the effectiveness of tissue engineering scaffolds. *Faseb Journal*, *16*(10), 1691–1711.
94. Schaefer, D., Martin, I., Jundt, G., Seidel, J., Heberer, M., Grodzinsky, A., et al. (2002). Tissue-engineered composites for the repair of large osteochondral defects. *Arthritis and Rheumatism*, *46*(9), 2524–2534.
95. Kandel, R. A., Grynpas, M., Pilliar, R., Lee, J., Wang, J., Waldman, S., et al. (2006). Repair of osteochondral defects with biphasic cartilage-calcium polyphosphate constructs in a Sheep model. *Biomaterials*, *27*(22), 4120–4131.
96. Klein, T. J., Rizzi, S. C., Reichert, J. C., Georgi, N., Malda, J., Schuurman, W., et al. (2009). Strategies for zonal cartilage repair using hydrogels. *Macromolecular Bioscience*, *9*(11), 1049–1058.
97. Kim, T. K., Sharma, B., Williams, C. G., Ruffner, M. A., Malik, A., McFarland, E. G., et al. (2003). Experimental model for cartilage tissue engineering to regenerate the zonal organization of articular cartilage. *Osteoarthritis and Cartilage*, *11*(9), 653–664.
98. Ng, K. W., Wang, C. C. B., Mauck, R. L., Kelly, T. A. N., Chahine, N. O., Costa, K. D., et al. (2005). A layered agarose approach to fabricate depth-dependent inhomogeneity in chondrocyte-seeded constructs. *Journal of Orthopaedic Research*, *23*(1), 134–141.
99. Ng, K. W., Ateshian, G. A., & Hung, C. T. (2009). Zonal chondrocytes seeded in a layered agarose hydrogel create engineered cartilage with depth-dependent cellular and mechanical inhomogeneity. *Tissue Engineering Part A*, *15*(9), 2315–2324.
100. Harley, B. A., Lynn, A. K., Wissner-Gross, Z., Bonfield, W., Yannas, I. V., & Gibson, L. J. (2010). Design of a multiphase osteochondral scaffold III: Fabrication of layered scaffolds with continuous interfaces. *Journal of Biomedical Materials Research Part A*, *92A*(3), 1078–1093.

101. Jiang, J., Tang, A., Ateshian, G. A., Guo, X. E., Hung, C. T., & Lu, H. H. (2010). Bioactive stratified polymer ceramic-hydrogel scaffold for integrative osteochondral repair. *Annals of Biomedical Engineering*, *38*(6), 2183–2196.
102. Lee, C. H., Cook, J. L., Mendelson, A., Moioli, E. K., Yao, H., & Mao, J. J. (2010). Regeneration of the articular surface of the rabbit synovial joint by cell homing: A proof of concept study. *Lancet*, *376*(9739), 440–448.
103. Huang, X., Yang, D., Yan, W., Shi, Z., Feng, J., Gao, Y., et al. (2007). Osteochondral repair using the combination of fibroblast growth factor and amorphous calcium phosphate/poly(L-lactic acid) hybrid materials. *Biomaterials*, *28*(20), 3091–3100.
104. Yang, Z., Shi, Y., Wei, X., He, J., Yang, S., Dickson, G., et al. (2010). Fabrication and repair of cartilage defects with a novel acellular cartilage matrix scaffold. *Tissue Engineering Part C-Methods*, *16*(5), 865–876.
105. Peel, S. A. F., Chen, H., Renlund, R., Badylak, S. F., & Kandel, R. A. (1998). Formation of a SIS-cartilage composite graft in vitro and its use in the repair of articular cartilage defects. *Tissue Engineering*, *4*(2), 143–155.
106. Suckow, M. A., Voytik-Harbin, S. L., Terril, L. A., & Badylak, S. F. (1999). Enhanced bone regeneration using porcine small intestinal submucosa. *Journal of Investigative Surgery*, *12*(5), 277–287.
107. Khetani, S. R., & Bhatia, S. N. (2008). Microscale culture of human liver cells for drug development. *Nature Biotechnology*, *26*(1), 120–126.
108. Bhatia, S. N., Balis, U. J., Yarmush, M. L., & Toner, M. (1999). Effect of cell-cell interactions in preservation of cellular phenotype: Cocultivation of hepatocytes and nonparenchymal cells. *Faseb Journal*, *13*(14), 1883–1900.
109. Flaim, C. J., Chien, S., & Bhatia, S. N. (2005). An extracellular matrix microarray for probing cellular differentiation. *Nature Methods*, *2*(2), 119–125.
110. Allen, J. W., & Bhatia, S. N. (2003). Formation of steady-state oxygen gradients in vitro—application to liver zonation. *Biotechnology and Bioengineering*, *82*(3), 253–262.
111. Moroni, L., Lambers, F. M., Wilson, W., van Donkelaar, C. C., de Wijn, J. R., Huiskesb, R., et al. (2007). Finite element analysis of meniscal anatomical 3D scaffolds: Implications for tissue engineering. *The Open Biomedical Engineering Journal*, *1*, 23–34.
112. Ballyns, J. J., Gleghorn, J. P., Niebrzydowski, V., Rawlinson, J. J., Potter, H. G., Maher, S. A., et al. (2008). Image-guided tissue engineering of anatomically shaped implants via MRI and micro-CT using injection molding. *Tissue Engineering Part A*, *14*(7), 1195–1202.
113. Schek, R. M., Taboas, J. M., Segvich, S. J., Hollister, S. J., & Krebsbach, P. H. (2004). Engineered osteochondral grafts using biphasic composite solid free-form fabricated scaffolds. *Tissue Engineering*, *10*(9–10), 1376–1385.
114. Lima, E. G., Mauck, R. L., Han, S. H., Park, S., Ng, K. W., Ateshian, G. A., et al. (2004). Functional tissue engineering of chondral and osteochondral constructs. *Biorheology*, *41*(3–4), 577–590.

Part III
Imaging and Visualization

Chapter 3
Hybrid Imaging: From Anatomy to Function

David García Juan, Sara Trombella and Osman Ratib

3.1 The Revolution of Molecular Imaging

Imaging radioactive tracers in the human body is where the origin of Nuclear Medicine applications emerged, allowing for recording the physiological behavior of organs and diseases in vivo and leading to a revolution in medicine, known today as "molecular imaging". While this technique of imaging does not show the molecules themselves, it allows for following infinitesimal traces of some radio-labeled molecules in the body. Different types of radioactive emissions can be observed and used for varied purposes. Electromagnetic radiation exists in a wide range of frequencies or energies starting at the long wave radio band, and arriving at the short ultra-violet (UV), x and gamma (γ) radiation via microwaves, infrared (IR) and visible light.

Positron emission tomography (PET) and single-photon emission computed tomography (SPECT) are nuclear medicine techniques based on the introduction into the human body of a radioactive labeled substance, with the subsequent acquisition of images mapping the distribution of this agent into the whole body or a specific organ of interest. Such substances (radiotracers) are analogues to bio-markers of specific molecules or biological pathways. Therefore, they participate in the physiological processes of the subject, and their bio-distribution quantitatively reflects cellular and molecular behaviors.

The physical process that enables the PET image production is the radioactive beta plus decay (β^+-decay) of the administered radionuclide with the emission of a positron that annihilates with an electron within a short distance into the human body, producing a couple of opposite-sided photons. The two photons are captured using a ring of detectors around the patient and they are revealed *in coincidence*. When two photons are detected within a short time-window they are assigned to a unique

D. García Juan · S. Trombella · O. Ratib (✉)
Hôpitaux Universitaires de Genève, Service de Médecine Nucléaire, 4,
Rue Gabrielle-Perret-Gentil, 1205 Genève, Switzerland
e-mail: osman.ratib@hcuge.ch

N. Magnenat-Thalmann et al. (eds.), *3D Multiscale Physiological Human*,
DOI: 10.1007/978-1-4471-6275-9_3,

annihilation event along the line of response (LOR) connecting the two activated detectors. Raw data from a PET detector are typically stored in a special diagram known as a sinogram. The image reconstruction process starts with such raw data and produces cross-sectional images that represent the radioactivity distribution into the human body.

SPECT is a more conventional technique also based on the use of a radioactive tracer material, but, in contrast with PET, the tracers used in SPECT emits gamma rays (γ-rays) that are measured directly by using gamma-cameras, which acquire two-dimensional images (projections) from multiple angles. Reconstruction algorithms are subsequently used to obtain three-dimensional images from the acquired two-dimensional datasets.

Although SPECT scanners are significantly less expensive than PET devices, a higher resolution can be obtained with PET event detection techniques. Moreover, positron-emitting isotopes used in PET are of much shorter half-life than conventional gamma emitting isotopes used in SPECT and hence expose the patient to much lower dose of radiation.

3.2 Hybrid Imaging: Concepts and Technical Evolution

During the last decades a growing interest arose around hybrid, or multimodal, imaging techniques combining two different imaging devices in one scanner, e.g. a CT and a PET scanner. An increasing amount of studies have demonstrated that multimodal imaging can provide unique and important information in diagnostic and follow-up treatment for different types of pathologies. Such hybrid devices open a whole new scope of diagnostic perspectives and investigative capabilities that goes far beyond the traditional anatomical evaluation of the human body. The ability to obtain functional and metabolic parameters concurrent with anatomical data for the whole human body or for a single organ, has not only opened new perspectives for diagnosis and follow-up of diseases, but also for a better understanding of physiological and biological functions of different parts of the human body.

3.2.1 SPECT/CT

In 1966, David Kuhl demonstrated for the first time the importance of acquiring morphological information together with molecular and functional information derived from scanning a radionuclide distribution within the human body. He experimentally introduced a ^{241}Am radionuclide source in the center hole of a collimated detector and used the opposite detector to simultaneously image the emitted photons from this

same radionuclide source and from a radionuclide distribution of ^{130}I macroaggregated albumin, to obtain a transverse section image through the thorax of a patient [1]. This early SPECT imaging technique can be identified as the first effective evidence for feasibility of hybrid metabolic imaging.

Later, in the 1980s, a significant progress in the development of SPECT devices, image reconstruction and correction techniques was reached. In particular, an iterative algorithm for image reconstruction called maximum likelihood expectation maximization (MLEM) was implemented in 1989 by Tsui and co-workers [2, 3]. However, early tomographic data suffered from low photon flux and poor contrast, facts that coupled with a low convergence speed of the MLEM algorithm finally produced limited anatomical information available from the reconstructed images. In 1994, a new technique was introduced (the ordered subset expectation maximization (OSEM) technique), that led to an efficient image reconstruction when applied to SPECT and CT data [4].

In the same period, the technical feasibility of simultaneous SPECT/CT imaging was demonstrated by Hagesawa et al [5–7], who developed a new imaging system using an array of high-purity germanium (HPGE) detectors to simultaneously acquire emission and transmission data from a low x-ray source. From that moment on, the development of manufactured SPECT/CT systems for clinical use started, giving rise to a series of multimodal SPECT/CT devices. Further attempts were also made to obtain multimodal image visualization by developing automated algorithms to superpose images acquired using different techniques, specifically related to functional and morphological imaging e.g. [8, 9].

3.2.2 PET/CT

In 1992, in an independent manner from the pioneering work of Hasegawa and co-workers on multimodality imaging, and in particular on SPECT/CT, Townsend and co-workers proposed to combine PET and CT. They suggested the use of CT to produce attenuation correction factors for PET, similarly to what was done by Hasegawa et al., who used CT images to correct SPECT images for attenuation. The possibility to acquire bimodal PET/CT images in a single scan session within an integrated multimodal device became available as a prototype in 1998 [10], and clinically only in 2001 [11, 12]. Such a device enabled the acquisition of aligned bimodal images accurately combining, in a single exam session, functional PET information with high-resolution three-dimensional CT information. The integration in a single device of PET and CT scanners showed a greater convenience with respect to using two separate stand-alone machines. The integrated device provided faster and more efficient data acquisition and accurate registration, as this process did not suffer of patient repositioning between subsequent examinations. Technological improvement resulted in a replacement of simple PET by combined PET/CT as a

preferential clinical tool for the detection and identification of lesions or structures in clinical applications requiring detailed anatomical and biological characterization. Currently, vendors no longer offer PET-only scanners, such that all PET scanners now come combined with CT [13]. Nowadays, the acquisition time for a combined PET/CT examination has greatly reduced compared to the first devices. This enabled a more efficient use of short-lived PET tracers while providing better patient comfort and convenience, more timely access to this technology, and, moreover, a greater amortization of costs. At the same time, developments in CT systems and computer processing has resulted in a substantial improvement of image quality and analysis, with a subsequent gain in terms of value and reliability of diagnostic information provided to clinicians [14]. The usual protocol for a PET/CT scan consists of a low-dose CT scan, acquired without contrast medium (CM), followed by the PET scan, and, if needed, followed by a dedicated full-organ or region-focused CM-enhanced CT [15].

3.2.3 PET/MRI

Despite the clinical success of PET/CT, there are some debated points regarding the use of CT as morphological imaging technique within a multimodal imaging device. In particular, CT adds a significant contribution to the final amount of radiation dose that the patient receives during the examination, and moreover, it provides relatively poor soft-tissues discrimination, even when the scan is acquired with contrast media. The desire to overcome these limitations, supported by the great success of hybrid PET/CT imaging in the clinical and medical research environment, encouraged the development of other multimodal imaging techniques, such as PET/MRI.

It is interesting to observe how the idea of combining PET and MRI arose around the same time that PET/CT was conceptualized. PET/MRI was firstly applied to small animal imaging studies in the early 1990s [16, 17], with a major difficulty represented by the interference between the high magnetic field of MRI and the sensitive electronic components of the PET scanners. After this first approach, the first clinical device for human brain PET/MRI imaging was introduced in 2006 using solid state PET detectors that are less sensitive to interference from magnetic field than conventional photomultipliers used in PET scanners [18].

MRI does not show the same limitations as for CT, since it does not involve any ionizing radiation and provides superior soft-tissue imaging compared to CT, in particular if innovative and specific MRI contrast agents are used [19]. This fact, in particular, indicates MRI as a natural and excellent alternative to CT when imaging the brain. Another great advantage of MRI with respect to CT is that it offers a much broader variety of data acquisition techniques than CT that may adapt to a high variety of clinical needs. MRI allows for the use of contrast agents that that have less toxicity than contrast agents used for CT and enables an additional enhancement of soft-tissue contrast. Moreover, MRI allows for advanced functional techniques that

are not feasible by CT, such as diffusion and perfusion imaging, and for other methods using the dynamics of contrast agents to evaluate physiological parameters such as flow, perfusion and diffusion, which may complement and enhance PET functional information. MRI also provides spectroscopy, that allows for better evaluation of tissue composition and allows for detection of organ-specific abnormalities and pathologies by quantifying ratios of concentration of specific molecules.

There are different conceivable options for combining PET and MRI systems. The easiest method as adopted in the earliest devices available for clinical use, is to place the two scanners in series in a manner analogous to PET/CT devices. Nowadays, technical improvements of this configuration, coupled with the excellent results reached by software fusion in many situations (in particular, for brain and heart imaging) brought this sequential multimodal technique approach closer to an ideal simultaneous configuration. In practice, a full integration of the PET system into the MRI gantry is preferred. Such configuration shows many advantages compared to the PET/CT systems adopted in the clinical environment, and to the sequential PET/MRI configuration as well. With a sequential scan, synchronous data acquisition is not feasible. Any temporal separation of the two study components increases the likelihood for image misregistration, and affects attenuation correction, caused by artifacts due to patient movement as well as to the physiological movements occurring internally in the human body, such as gastric emptying or bladder filling. All this can compromise the accuracy of tissue activity quantitation [20–23]. Therefore, fully integrated PET/MRI scanners that may provide accurate temporal correlation of dynamically acquired datasets from the two imaging modalities remain the final goal for the healthcare industry. The main problems in the development of a fully integrated PET/MRI device are:

- The impossibility for the photomultiplier (PMT)-based PET detectors to work within or near the magnetic field generated by the MR scanner. The PET system, and in particular the various hardware components of the PET PMT-based detector, can reduce the MRI performance by degrading the homogeneity of the MR main magnetic field and of the radio-frequency field as well. This interference may cause artifacts in the MR images, i.e. a loss in the MR image quality. Moreover, the variable MR gradients may induce eddy currents in conductive materials of the PET detector, which can distort the effective gradient field. On the other hand, the high magnetic field used in the MRI system excludes the use of PMTs used in traditional PET scanners, since electrons in the vacuum tube of the PMTs are deflected by the interaction with the strong MR magnetic field (Lorentz force). Despite this, a physical integration of PET and MRI devices in a single gantry became possible as innovative solid-state photo-detectors that are insensitive to the external magnetic field, became available (e.g. Geiger-mode avalanche photodiodes or silicon PMTs [24–28]).
- Metallic objects (such as surface coils) used to acquire higher quality MR images interfere with gamma rays from PET, producing attenuation. Surface coil arrangements are needed for better MR image quality, but they contain several metal parts, that may cause artifacts in the PET images, with subsequent need for adequate cor-

rections. Currently, system manufactures are attempting to reduce metallic content both in the detector and in the surface coils, in order to minimize this problem.

- The necessity to adapt the "slow" PET acquisition protocols to the "faster" segmental MRI examination of specific body parts. Traditionally, MRI exams have been limited to portions of the human body, due to long acquisition times. However, recent developments have allowed for faster, high-resolution whole-body MR imaging without the need for patient or surface coil repositioning. The fast acquisition speed reached today by MRI, allows also for acquisition of dynamic data sequences and subsequent visualization of dynamic contrast enhancement [29, 30].
- Finally, space constraints are a major restriction for PET and MRI devices integration, since the bore size of the MR scanner is limited. Therefore, a further challenge was to design PET integration into the MRI system leaving adequate space for patient comfort.

Currently, a number of papers dealing with the potential value of PET/MRI images in the clinical practice have been published, e.g. dealing with neurological diseases [31] and several cancer types evaluation [32–36].

3.3 Quantitative Positron Emission Tomography in Hybrid Imaging

3.3.1 Data Correction

One important characteristic of PET is that it gives an accurate quantification of the radioactivity distribution in the human body or a part of interest, after injection of a metabolic radiotracer. Nevertheless, quantitative use of PET data requires several accurate corrections to be applied. These corrections are typically applied to the sinograms as a series of multiplicative factors prior to image reconstruction.

When both photons coming from an annihilation event are detected, a so-called true coincidence is recorded. Conversely, if some interaction occurs before one or both photons meet the detector surface, then their direction and energy are changed. The most important interactions that photons resulting from the positron annihilation undergo in the human body are Compton scatter and photoelectric absorption. A *scattered coincidence* occurs when at least one of the two photons is diverted by Compton scattering prior to detection. Since the direction of the photon is changed during the Compton scattering process, such events increase the likelihood for the resulting coincidence event to be assigned to the wrong line of response (LOR). When two photons not arising from the same annihilation event are incident on the detectors within the same coincidence time window, they are classified as *random coincidences*. The loss of true coincidence events due to photon absorption within the patient body or any device components (e.g. patient bed, immobilization devices

or radiofrequency coils) or to their scattering out of the detector field of view (FOV) is classified as *attenuation*. Attenuation, scattering and random events are causes of noise and loss of image quality in PET images, with a consequent loss of precision and detail, which means a decrease of clinical and diagnostic utility of the reconstructed images. Therefore, in order to improve image quality, several techniques have been developed to correct for these sources of errors and artifacts.

One possible approach to correct for random events is to add a parallel coincidence circuit to the one measuring the prompt coincidences. Subsequently, the logic pulse from one of the two detectors in coincidence is delayed in time, such that the detector pair cannot produce any true coincidence. Therefore, detected events will be classified as accidental coincidences. It is then possible to extract the number of true coincidences simply by subtracting the number of accidental coincidences from the total number of detected events. This method is virtually free of systematic errors, because the delayed and the prompt coincidences are measured in the same circuitry. However, this subtraction leads to an increase in the statistical uncertainty [37].

The most widely used method for scatter correction is the analytic single scatter simulation (SSS), which has shown a good reliability for whole-body PET [38, 39]. Polycarpou et al. [40] evaluated the accuracy of such a method when applied to cases with high scatter. There are two possible ways to apply attenuation correction (AC) to the acquired data. One way is to compute the so-called attenuation correction factors (ACFs), one for each LOR, store them in an attenuation map and use such information to pre-correct the acquired emission data before image reconstruction. The alternative method is to incorporate the knowledge about the attenuation coefficients directly into the iterative image reconstruction procedure. Earliest AC techniques performed in stand-alone PET machines involved the use of rotating sources placed within the PET gantry. In PET/CT devices, this early attenuation correction technique has been replaced by CT-guided AC, based on the use of CT data to determine the attenuation map containing attenuation coefficients for each voxel. ACFs are then computed by integrating over each LOR. Currently, the challenge is to develop an efficient MRI-guided AC for modern PET/MRI hybrid machines (Fig. 3.1). The major problem when facing MRI-guided AC, i.e. the preparation of an attenuation map, is that MRI images do not provide any direct way of measuring tissue attenuation coefficients. One method adopted to implement MRI-guided AC is to segment MR images into different tissue classes and assign a pre-defined average tissue attenuation coefficient to each class. *Segmentation-based AC* methods have been proposed for brain [41–45] as well as for whole-body PET [46–49]. The idea of segmenting the attenuation map into several classes of tissue was proposed for the first time by Huang et al. in 1981 [50] with the aim to reduce noise propagation from the acquired transmission images [51]. The main problems connected with this technique are:

- The segmentation of bones that appear black in MR images because of the short T2 relaxation times in MR data acquisition, making them difficult to distinguish from air, since both air and bone tissue produce no signal in MR. On the other hand, bone and air have opposite photon attenuation properties: bone is the highly attenuating

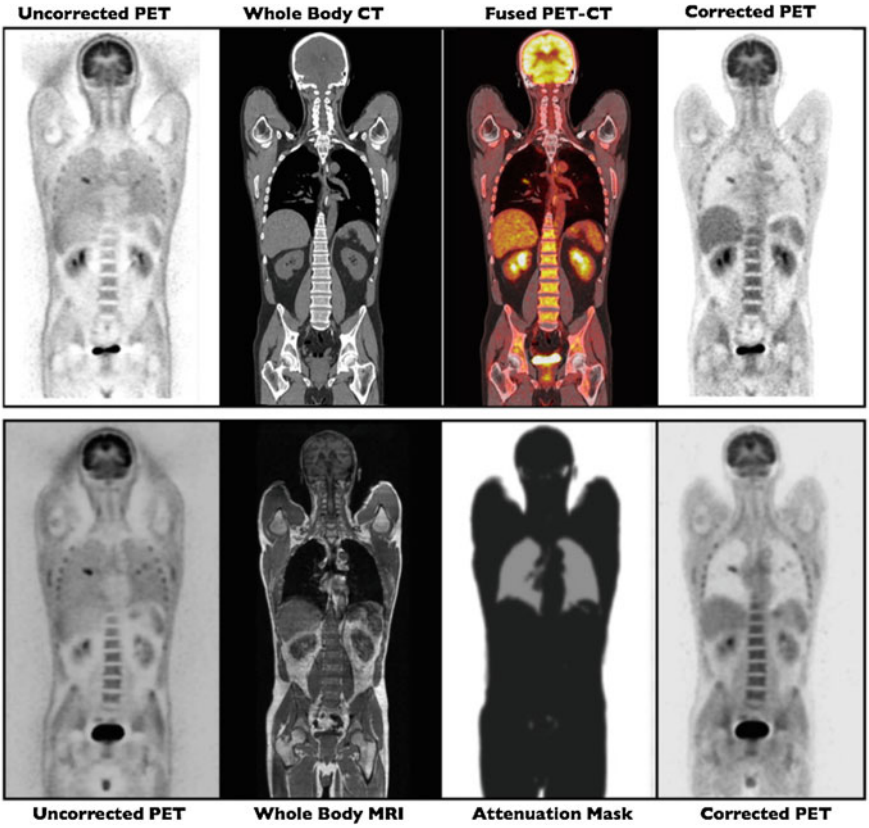

Fig. 3.1 Comparison of CT-guided PET attenuation correction (*upper row*), and MR-guided PET attenuation correction (*lower row*), obtained in the same patient, where the two hybrid studies were acquired sequentially

material within the human body, whereas air does not attenuate PET signal at all. Therefore, MR-based AC mostly uses additional anatomical or spatial information to predict bone in the attenuation map [52]. In the neurological field, it has been suggested also to use ultrashort-echo-time MRI acquisition techniques rather than conventional T1-weighted acquisition in order to facilitate the segmentation of the skull e.g. [42, 45].

- The segmentation of the lungs, since it has been shown that the density of the lung tissue is considerably different from subject to subject. Moreover, it depends on breathing patterns and varies with age that can be up to 30 % in the event of respiratory diseases [53, 54].
- The segmentation of any other unpredictable benign or malign anatomical abnormalities with varying densities [54].

Nevertheless, segmentation-based AC methods are robust, computationally fast and the associated quantification error for bone lesions is repeatable and well understood. This has lead to the use of such AC approach in commercial PET/MRI hybrid scanners: the Siemens Biograph mMR uses an adaptation of the algorithm implemented by Martinez-Möller et al [46], and the Philips Ingenuity TF PET/MR [55] uses an adaptation of the algorithm proposed by Schulz et al. [49, 51].

An alternative method for MRI-guided AC is based on the registration or deformation of an attenuation atlas template to patients' MR images in order to obtain an attenuation map adapted for the specific patient. Machine learning techniques have been used in order to implement such methods and in particular to learn how to convert MR tissue proton density data to CT tissue density Hounsfield unit (HU) values from aligned MR and CT attenuation images. With the advent of hybrid PET/MRI devices, several groups have proposed *template-based AC* approaches for PET images correction [43, 56]. The advantage of such methods is that generally they do not need any additional MR bone imaging in order to predict bone tissue, with a drawback being a time-consuming map calculation. The sensitivity of these methods to anatomical variability has still to be evaluated [52]. In fact, they require an accurate non-rigid registration of the template to the acquired MR image. This is feasible at the level of brain imaging, where template-based methods have shown great potential, but they have been reported to be error-prone when applied for a whole-body analysis [57]. Therefore, Hofmann et al. [47] proposed to complement a template-based AC method with the information available from the segmented MR and pattern recognition, and the feasibility of such method was demonstrated also when applied to whole-body images. Detailed reviews of MR-guided attenuation techniques have been published, e.g. by Bezrukov et al. [52], Wagenknecht et al. [58] Martinez-Möller et al. [51].

Non-uniformities in the efficiencies of the individual detectors, due to variations in detector geometry or electronics, may cause variations in coincidence detection efficiency between different LORs. The *normalization correction* compensates for these non-uniformities. To compute a normalization correction, detector efficiencies, geometrical efficiency variations and variations in plane-to-plane efficiency are measured in order to account for the relative variation in coincidence detection efficiencies between system LORs (e.g. by collecting data from a uniform plane source of activity, positioned at 6–8 equally spaced projection angles). The normalization correction factors can also be computed using the component-based method. In this case, the normalization correction factors [46] are:

$$n_{i,j} = \frac{1}{\epsilon_i \times \epsilon_j \times g_{i,j}}$$

where, the coincidence detection efficiency of a pair of detectors i and j is assumed to be composed of the product of the detector efficiencies, ε_i and ε_j, and geometrical factors, $g_{i,j}$, that include corrections for the angle of incidence of the annihilation photons, systematic variation in crystal efficiency dependent on the position of the crystal in a detector block module, and relative plane efficiency.

Another effect to correct for is the *partial volume effect (PVE)*. Because of the finite spatial resolution in a PET system, decays from an infinite small point source are smeared-out and they finally appear as a finite-size blob that shows a lower activity concentration in the reconstructed image. As a consequence, small objects below a certain size related with detector resolution, appear to have lower activity concentration with respect to larger objects of equivalent activity concentration. The simplest way to recover for PVE is to use objects with simple geometrical shape in order to simulate real targets and to estimate recovery coefficients for PVE [59]. A voxel-based MRI-guided PVE approach had been used by Matsuda et al. [60] in functional FDG-PET of the brain. Recently, the PVE correction problem has been also approached by combining both functional and anatomical knowledge from several sources [61] or by introducing a mathematical model for PVE directly into the reconstruction algorithm [62].

Finally, whereas in an ideal system the net true count rate should increase linearly with increasing activity in the FOV, in a real system the detection unit undergoes some level of *dead time* as the activity within the PET device increases. This is particularly due to the increased data processing in the detector front-end electronics, but also the coincidence event processing, the real-time sorting of data into sinograms, and data transfer give contribution to dead-time. The most common way to correct for dead time is to use a mathematical model to characterize it [37].

3.3.2 Principles of Quantitative Analysis of PET Images

PET imaging is ideally suitable to provide an estimate of the concentration of administered radiolabeled tracers in a given location within the human body as a function of time. It is important to establish the theoretical biological model of tracer uptake in the given tissue and apply it to estimate the true tissue concentration from the images acquired *in vivo*. Such models are important in order to better assess the behavior of different tracers. Commonly, they are developed using semi-quantitative approximations, but in some specific cases full tracer kinetic analysis models can be also carried out.

Semi-Quantitative Analysis of Tissue Concentrations from PET Data

Semi-quantitative measurements include:

- The calculation of the concentration of a tracer on the basis of regional image activity measured from regions of interest (ROIs) of PET data. In such approach, relative tracer concentration is often calculated from ratios of measured activities between different ROIs. A semi-quantitative estimate often used is a relative ratio of *percent injected dose per gram of tissue (%ID/g tissue)*, defined as the percent

of the injected dose of activity that is present in a gram of tissue being analyzed:

$$\%\mathrm{ID}/g = C_T \cdot \frac{V_T}{W_T} \cdot \frac{1}{D_{Inj}} \cdot 100\,\%$$

where, C_T is the radioactivity in the tissue region (unit of mCi/cc tissue), obtained from the PET images by taking the counts/pixel/time from a PET ROI and converting this value to mCi/cc tissue using a cylinder calibration factor; W_T and V_T are the weight and volume of the tissue region, their ratio giving the density of the region, which is typically assumed to be ≈1cc tissue/g tissue; D_{Inj} is the injected dose (unit of mCi).

- The calculation of the *standardized uptake value (SUV)*, which is the most used semi-quantitative estimate of local tracer uptake used in clinical routine. This parameter is related to the %ID/g tissue, but it also normalizes for the mass of the subject (W_S, unit of g):

$$\mathrm{SUV} = C_T \cdot \frac{V_T}{W_T} \cdot \frac{1}{D_{Inj}} \cdot W_S$$

Quantitative Analysis of Tissue Concentrations from PET Data

Tracer kinetic analysis procedures are used to develop more theoretically rigorous models of tracer uptake. Therefore it can be applied to PET images for more objective calculation of tissue tracer concentrations. They can be essentially classified between:

- *Non-compartmental models* or *model-independent approaches* or *statistical moment analysis*: such approaches are independent from an explicit knowledge of the location of the tracer, and they are developed assuming:

  (a) the conservation of matter,
  (b) a steady state for all parameters of interest,
  (c) and linearity with respect to the input.

- *Compartmental models*: the principle that undergoes compartmental models is to describe tracer kinetics by using a system of interconnected pools, each one representing a specific location of the tracer in the blood or an enzyme-mediated reaction to yield metabolites of the tracer. A pool is a mathematical abstraction of a particular behavior or location of the tracer of interest. Pools are interconnected by kinetic pathways that represent how tracer moves between compartments. Linear or nonlinear law may rule the tracer kinetics. Linear connections represent constant values that differ for each tissue but do not depend on time or tracer mass. Linear laws, primarily because of the small amount of tracer that has to be considered, may also usually approximate nonlinear behaviors. The idea is to design and solve a system of differential equations (state equations), in function of mass balance. This means that the quantity of tracer inside a specific region must be equal to

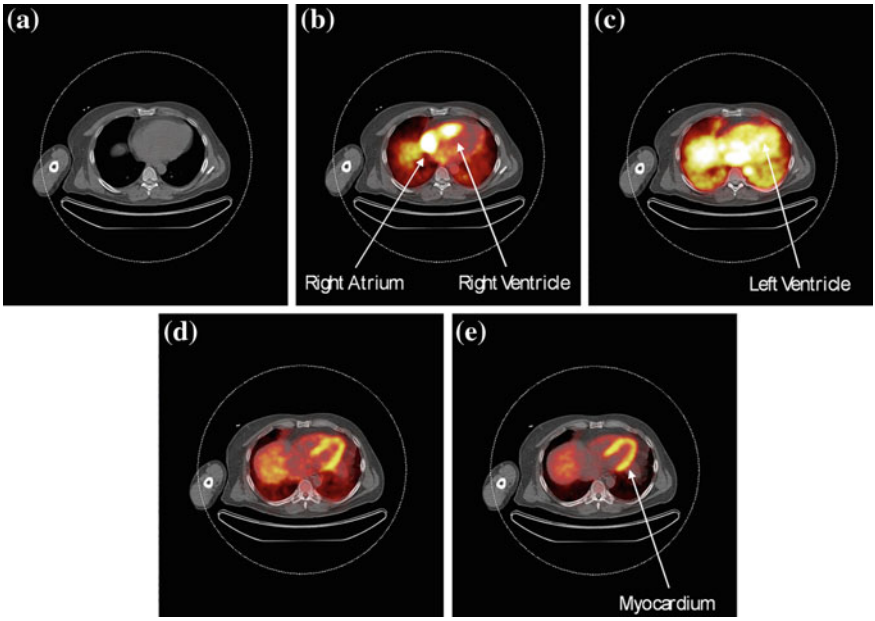

Fig. 3.2 Fused PET and CT images of the heart, showing the dynamic of ^{13}N labeled Ammonia (NH_3), a tissue perfusion tracer: **a** no tracer uptake, **b** transit of the tracer in the blood in the right ventricle, **c** transit in the left ventricle and early uptake in the myocardium, **d** uptake in the myocardium and surrounding tissue, **e** final myocardial uptake

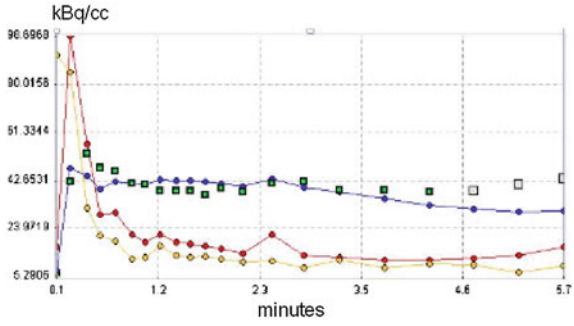

Fig. 3.3 Blood (*red curve* left ventricle, *yellow curve* right ventricle) and tissue (*green curve*) TACs for heart [$^{13}N - NH_3$]PET, and compartmental model fitting curve (*blue curve*)

the difference between the tracer mass entering the pool and the one leaving at a specific time. The convolution between the solutions obtained from the system of state equations and time-activity concentration data, usually referred to as *input function* (or Blood Time-Activity Curve), permits to obtain the tissue response to the tracer in function of time (Fig. 3.2), graphically rendered as the so-called Tissue Time-Activity Curve. Blood and tissue time-activity curves are together referred as TACs (Fig. 3.3).

It is possible to extract the input function directly by sampling arterial blood at regular intervals after tracer injection, or also by dynamic PET heart imaging of the left ventricle, left atrium (Fig. 3.2), or major arterial blood vessels. Historically, Sokoloff and co-workers developed one of the earlier models in this sense in 1977. They implemented a mathematical model for the measurement of local cerebral glucose utilization in albino rat brain [63], which later was adapted to man [64]. The animal study was based on the use of 2-deoxy-D-[^{14}C]glucose ([^{14}C]DG) as a tracer for the exchange of glucose between plasma and brain and its phosphorylation by hexokinase in the tissues. The model was based on an operational parametrical equation derived by assuming a steady state for glucose consumption, a first order equilibration of the free [^{14}C]DG pool in the tissue with the plasma level, and relative rates of phosphorylation of [^{14}C]DG and glucose determined by their relative concentrations in the precursor pools and their respective kinetic constants for the hexokinase reaction [63]. Based on this earlier study, later in 1979, a mathematical model to measure local glucose consumption in human brain structures was developed, and the derived operational equations were applied to two human volunteers. In this case, [^{18}F]-2-deoxy-2-fluoro-D-glucose was used as a tracer for the exchange of glucose between plasma and brain and its phosphorylation by hexokinase in the human brain tissue [64]. Later in 1983, Patlak and co-workers developed a theoretical model of blood-brain exchange, finally deriving a procedure for graphing multiple-time tissue uptake data and determining whether a unidirectional transfer process was dominant during a part of or the whole experimental period. The model assumed linear transfer kinetics, and consisted of a blood-plasma compartment, a reversible tissue region with an arbitrary number of compartments, and one or more irreversible tissue regions. In case of detection of a unidirectionality of uptake, the model enabled to compute an influx constant as the slope of the constructed graph, the intercept being less or equal to the vascular plus steady-state space of the reversible tissue region [65, 66].

3.4 Imaging Devices and Clinical Applications of PET/MRI and PET/CT

3.4.1 Current State-of-the-Art of Available Hybrid Devices

Since the introduction of tomographic imaging devices in nuclear medicine, single-photon emission computed tomography (SPECT) and positron emission tomography (PET) have provided images with three-dimensional physiological information of different parts of the body. The main limitation of the molecular information provided by these devices is its low resolution of anatomic structures. On the other hand, computed tomography (CT) and magnetic resonance imaging (MRI) offer high definition anatomical images (Fig. 3.4). Since the first PET/CT hybrid scanner was introduced as a prototype in 1998 [10], its advantages rapidly led to the replacement of PET-only scanners by the new hybrid ones. Because of this great success,

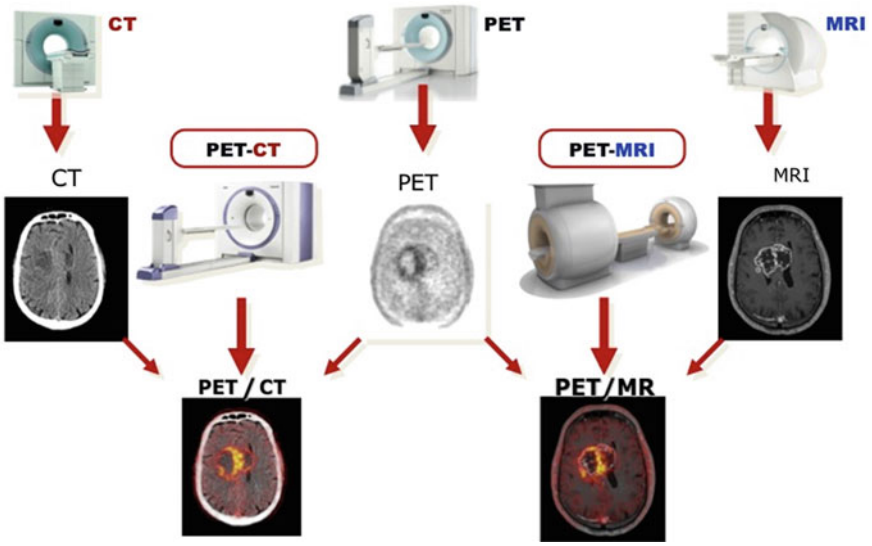

Fig. 3.4 Illustration of the application of hybrid PET/CT and PET/MRI on the same patient (cerebral tumor). The combination of two imaging modalities acquired on the same hybrid device, instead of separate studies acquired at different points in time, is illustrated here. A better identification of tumor morphology can be observed in MRI images due to its better performance in differentiating soft tissues and in better delineating brain anatomy. This makes the combination of PET and MRI images more suitable than the combination of PET and CT images in this particular case

the possibility to replace CT by MRI was explored and discussed [67] with the vision of exploiting the advantages that MRI offers over CT. These advantages are a better soft tissue differentiation and an extended potential for tissue characterization through different imaging techniques, as well as the lack of radiation exposure. Whereas PET/CT devices have been available for over a decade, it is only recent that the first hybrid PET/MRI scanners have become available on the market. Since the appearance of these new hybrid scanners, the question whether PET/MRI will replace PET/CT in the future arose, which still has not a clear answer. Since they are based on different principles and technologies, each of them exploits different advantages and specific values depending on the clinical application where they are used.

In this section, some state-of-the-art devices and their clinical applications will be summarized, without reflecting any particular ranking or judgment of performance.

SPECT/CT scanners. The first SPECT/CT device (1996) [68] was composed of a clinical SPECT gamma camera and a single slice CT scanner. In this design, the patient was firstly imaged with the CT and then with the SPECT after injection of the radiotracer. The data obtained from the CT scan were used for SPECT data attenuation correction, but the low resolution of this first device did not provide adequate CT images for diagnostic purposes. During the last two decades, the SPECT/CT

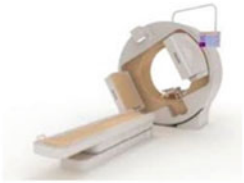

BrightView XCT

CT Scanner
- Tube Voltage : 120kV
- Tube Current: 2,5-20 mA
- Rotation Time: 16-60 s
- Detector: Flat Panel 14 cm FOV

SPECT Detector
- Crystal Type: 3/8 inch. NaI
- Number of Photomultiplier Tubes: 59
- Planar Spatial Resolution: 1 ADC/PMT
- Field of View: 40.6x54 cm

Symbia T16

CT Scanner
- Tube Voltage : 80-130kV
- Tube Current: 20-345 mA
- Rotation Time: 0.5-1.5 s
- Detector: 24 rows (16 slices/ rotation)

SPECT Detector
- Crystal Type: 3/8 inch. NaI
- Number of Photomultiplier Tubes: 59
- Planar Spatial Resolution: 1 ADC/PMT
- Field of View: 38.7x53.3 cm

Fig. 3.5 Key parameters and characteristics of Siemens HealthCare Symbia T16 and Philips Healthcare BrightView XCT

scanners have continuously evolved and currently there are several available options with fully integrated SPECT/CT devices. Two examples of SPECT/CT scanners that are representative for the current state-of-the-art are the BrightView XCT (Philips Healthcare) and the Symbia T series (Siemens Healthcare). These two scanners use similar technologies and show common features in their SPECT component, but the attributes of the CT scanner implemented in each device differ from each other (Fig. 3.5).

PET/CT scanners. The different generations of PET/CT scanners underwent several improvements and technological advancements. Each vendor has progressively introduced higher performance CT scanners and more efficient and better PET scanners. Last technical advances are related with the addition of the time-of-flight (TOF) acquisition mode and the extension of the axial field of view (FOV). TOF acquisition technique improves the image contrast, obtained by better localization of the origin of the annihilation event, by counting the difference in time between the detection of each coincidence photon [69, 70]. Adding PET detectors in the axial direction performs the extension of the axial FOV. With the extension of the axial FOV, the system also gains in detection sensitivity.

Among the most recent devices, three state-of-art PET/CT hybrid scanners have been selected and they are briefly reviewed in the table below (Fig. 3.6): the Biograph mCT (Siemens Healthcare), the Discovery VCT (GE Healthcare) and the Ingenuity TF (Philips Healthcare).

An interesting characteristic of Ingenuity TF is its OpenView gantry design; this design proposes an open space between scanners offering the clinician a better access

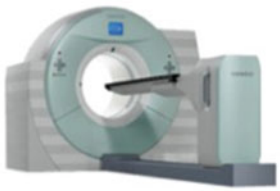

Biograph mCT

- CT: 20 – 128 slices
- Patient Bore: 78 cm
- Weight Limit: 250 kg
- Co-Scan Range: 170 cm
- Number of Rings: 52

- Crystals Type: LSO (Ce)
- Crystals size: 4.0 x 4.0 x 20 mm^3
- Time-of-flight: Yes
- Axial Coverage: 21.6 cm
- Transaxial FOV: 70 cm
- PET Resolution model: Yes

Ingenuity TF

- CT: 16 – 128 slices
- Patient Bore: 70 cm
- Weight Limit: 215 kg
- Co-Scan Range: 190 cm
- Number of Rings: 44

- Crystals Type: LYSO (Ce)
- Crystals size: 4.0 x 4.0 x 22 mm^3
- Time-of-flight: Yes
- Axial Coverage: 18 cm
- Transaxial FOV: 67 cm
- PET Resolution model: Yes

Discovery VCT

- CT: 16 – 128 slices
- Patient Bore: 70 cm
- Weight Limit: 250 kg
- Co-Scan Range: 170 cm
- Number of Rings: 24

- Crystals Type: LYSO (Ce)
- Crystals size: 4.2 x 6.3 x 25 mm^3
- Time-of-flight: Yes
- Axial Coverage: 15.1 cm
- Transaxial FOV: 70 cm
- PET Resolution model: Yes

Fig. 3.6 State-of-the-art PET/CT devices from Siemens Healthcare, Philips Healthcare and GE Healthcare

to the patient and a less traumatic exam experience for claustrophobic or pediatric subjects.

PET/MRI scanners. The wealth of imaging sequences that MRI can provide offering different ways for differentiating soft tissues, combined with a high spatial resolution makes this scanner an invaluable diagnostic tool. Combining this device with a PET scanner represents a major technical challenge attempted by the whole scientific community, from research institutes to universities and industry. Currently, two different design philosophies have been developed for hybrid PET/MRI scanners: placing the PET scanner inside the MRI (Siemens Biograph mMR [71]), or separate the two machines enough in space to avoid the interferences that each scanner could cause on the other (Philips Ingenuity TF PET/MR [55]).

Ingenuity TF PET/MR. Philips Ingenuity TF PET/MRI (Fig. 3.7) is a sequential hybrid scanner with non-integrated PET and MRI devices. It combines the Achieva 3 T MR (Philips) with a TOF PET detector as the GEMINI TF PET/CT (Philips). The two scanners are placed 4.2 m apart and linked by a common turntable bed. The advantage offered by this linking method is that the patient does not move between the two subsequent scans, allowing an easier and more accurate image registration process. Although the two scanners are apart, several shielding strategies

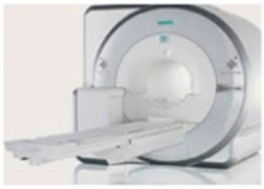

Biograph mMR

MRI Scanner
- Bore Diameter: 60 cm
- Field of View: 50x50x45 cm
- Receive Channels: 18 (32)
- Field Homogeneity: 0.1 ppm

PET Scanner
- Crystals Type: LSO
- Crystals size: 4.0 x 4.0 x 20 mm^3
- Ring Diameter: 66 cm
- Bore Diameter: 60 cm
- Time-of-flight: No
- Axial Coverage: 25.8 cm
- Weight Limit: 200 kg
- Co-Scan Range: 140 cm
- Attenuation: MR-based

Ingenuity TF PET/MR

MRI Scanner
- Bore Diameter: 60 cm
- Field of View: 50x50x45 cm
- Receive Channels: 16 (32)
- Field Homogeneity: 0.5 ppm

PET Scanner
- Crystals Type: LYSO (Ce)
- Crystals size: 4.0 x 4.0 x 22 mm^3
- Ring Diameter: 90 cm
- Bore Diameter: 70 cm
- Time-of-flight: Yes
- Axial Coverage: 18 cm
- Weight Limit: 200 kg
- Co-Scan Range: 190 cm
- Attenuation: MR-based

Fig. 3.7 State-of-the-art PET/MRI devices from Siemens Healthcare and Philips Healthcare

are implemented in the device. In order to avoid the residual magnetic field from the MR, the PET detector is equipped with an annular magnetic soft iron shield and each PMT (photomultiplier) is also covered with a soft iron shield. PMTs are oriented to align their photocathode with the flux lines of the magnetic field produced by the MR. Not only the detectors but also the device electronics can suffer from the mutual interference between the two scanners. The PET RF-generating circuits can affect the MRI system. Thus, these components are placed outside the room where the scanners are installed, and the PMTs power supply is dynamically controlled and dropped during the MRI acquisition [72]. In terms of performance, the ideal goal would be to obtain similar results from the subsystems in the hybrid scanner and the originally independent devices. It has been demonstrated that the performance of PET and MRI subsystems included in the Ingenuity TF PET/MRI scanner fulfills this requirement [55].

Biograph mMR. Siemens Biograph mMR scanner (Fig. 3.7) is a hybrid scanner with the MRI and the PET scanners within the same device. In particular, an APD-based PET detector is inserted in a Verio MRI. The PET detector is inserted between the coils in the MRI bore, which has a diameter of 60 cm (the same as the Philips Ingenuity bore). Crosstalk is avoided in the Ingenuity TF scanner by separating the two scanners in tandem geometry. In the Biograph mMR scanner the two scanners are completely integrated, therefore the PET component works inside an intense electromagnetic field. Due to this, the readout instrumentation of the PET has been re-designed with components capable to work under such conditions. Delso et al. [71] compared PET and MRI performance to other PET/CT and PET/MR scanners. They

concluded favorably about the integration of PET and MRI scanners; regarding PET detector, working inside a magnetic field is not detrimental for its performance. The MRI scanner can also be used as a standalone system for diagnostic MR procedures.

After the explanation of the main challenges that each approach offers and how they were addressed, some key characteristics of both devices are shown in Fig. 3.7:

3.4.2 Most Common Clinical Applications of Hybrid Imaging (PET/CT and PET/MRI).

In the early applications of multimodal imaging in clinical practice, hybrid images were generated by software registration of data obtained separately from different modalities and were mostly used for the brain (its rigid character and its lack of movement made the software registration between images easier and more reproducible). Thus, earlier clinical experiences in multimodal imaging were obtained in the field of neuroscience, being focused on the study of brain disorders and diseases like Alzheimer or Parkinson [73]. With the rapid development of integrated PET/CT and the emergence of new radiolabeled tracers for specific diseases, hybrid imaging has gained wider adoption in a variety of clinical applications in neurodegenerative diseases, in oncology and in cardiovascular diseases. Parallel to the evolution of PET/CT technology, MRI techniques also made significant progress not only in terms of performance, with better resolution and faster acquisition protocols, but also in the development of new imaging algorithms, allowing for a better identification of different body tissues and the extraction of functional parameters. The complementarity of MRI characteristics extending the diagnostic capability of PET/CT has led to the development of combined clinical protocols for patient management where both type of studies are often required for a given clinical situation. In fact, it is very common that in complex situations, such as extended cancer or complex neurological diseases, the patient needs both MRI and PET/CT studies to assert a given diagnosis. The clear added value of better soft tissue contrast that MRI offers over CT makes hybrid PET/MRI systems potentially more attractive than PET/CT for certain conditions such as brain tumors, head and neck tumors, breast cancer and prostate cancers [74, 75]. The advantage of PET/CT remains in its ability to provide whole body scans with much higher spatial resolution than MRI in a very short acquisition time. Today, CT images from PET/CT scanners can be acquired in a few seconds and provide an extended coverage of the whole body with extremely high resolution 3D data, that can be explored in different planes and reconstructed in different ways for better visualization and identification of local anomalies and abnormal focal tracer uptake. Recent technological advances and software algorithms have allowed for a significant reduction of the radiation dose from CT scans to several orders of magnitude lower than the doses delivered by earlier scanners. While PET/MRI may not replace PET/CT in most clinical applications, it still opens a new perspective of a single hybrid imaging technique that can find its place in many protocols of patient workup

and in monitoring of the efficacy of different treatments and therapeutic procedures. Since PET/MRI has only been available in a limited number of centers for a short period of time so far, further clinical validation studies and prospective research programs are needed to assess its clinical applicability and demonstrate its added value in specific clinical scenarios. However, the early reports of its use in clinical diagnosis seem to confirm this hypothesis. New tracers and protocols are constantly becoming available, extending possible applications and benefits of hybrid imaging. Multimodal imaging can potentially be applied in a wide variety of medical fields. Although the main fields where it is currently used are oncology [76, 77], cardiology [78, 79], neurology [80] and psychiatry [81] as well as other applications such as musculoskeletal diseases, infectious and inflammatory diseases, a variety of degenerative disease and aging processes can also benefit from the possibility of combined acquisition of morphological and functional images. In the following paragraph we review some of the most common and widely approved domains of clinical application of hybrid imaging techniques.

Oncology. Determining cancer stage in an oncological patient is the first goal in the diagnosis of this sickness. Staging cancer helps the treating physician in estimating subject prognosis and in planning an appropriate treatment. Staging means to describe the state and the level of expansion of the tumor in the patient's body [82]. Cross-sectional images, and especially hybrid images, play a main role in this purpose. Whole-body imaging is crucial for the evaluation of the state of a cancerous tumor. Moreover, it shows the exact localization and extent of the primary tumor, and the eventual extension of metastases to adjacent lymph nodes or other parts of the body. Accuracy in the detection of tumors and determination of cancer stage are the main criteria for selecting the appropriate imaging technique for clinical examination. PET/CT and PET/MRI scanner performances, with their accurate imaging of the anatomy and morphology of different body organs, combined with the high sensitivity of molecular data for the detection of small focal anomalies, makes them best suitable for cancer staging and follow-up. Even if CT remains the best imaging modality for anatomical localization and follow-up of tumors, the low soft tissue contrast limits its performance in the identification of certain tumors like soft tissue sarcomas or cerebral or liver metastases [83]. Due to the higher soft tissue contrast reached in MRI images, PET/MRI can improve the diagnostic accuracy and tissue discrimination over PET/CT for these specific cancer types. Nevertheless, PET/MRI scanners still show certain limitations. The limited spatial resolution of MRI and the existence of certain tumors not avid with F-FDG radionuclide, typically used in PET scans as a radiotracer, can make PET/MRI scanners fail in the detection of certain very small metastases [84]. Beyond morphologic imaging, MRI can also provide additional molecular and functional information through different imaging techniques. One of these is DWI (Diffusion Weighted Imaging), which measures the apparent cell density in tissues and, therefore, could enable to identify the abnormal cell density that occurs in cancer tissues. In particular, DWI has been shown to have a high sensitivity in detecting abnormal tissue density in small lymph node metastases, however it suffers from lack of specificity since several reasons of augmented tissue

density can also result in abnormal findings [85]. MR spectroscopy can also provide biochemical information about different compounds in a specific tissue. It can be used e.g. for amino acid concentration measurements in certain brain regions, and even as a marker to differentiate tumor brain entities [86]. Nevertheless, MR spectroscopy actually remains a complex imaging technique with limited spatial resolution and long acquisition time that make it unsuitable for clinical applications. Therefore, MR spectroscopy is nowadays mostly used for research purposes. Other MR imaging techniques, such as dynamic contrast-enhanced MRI, provide information about blood perfusion or about the amount of tumor vascularization, and can be helpful e.g. for differentiating benign and malignant breast tumors [87]. PET/CT is widely applied for oncological diagnosis, and its combined metabolic and anatomic imaging has replaced conventional single-modality imaging techniques [84]. PET/MRI, with its better soft tissue contrast and molecular information, is believed to become another major player in the diagnosis and follow-up of tumors. Nevertheless, it is still not clear whether and in which amount this new whole-body hybrid imaging technique will substitute PET/CT for oncological purposes. More clinical studies still have to be carried out in order to assess its real added value and effectiveness in clinical practice. For this purpose, some first experiences evaluating the real value of PET/MRI scanners have been published [88, 89]. An oncological application where PET/MRI outperforms PET/CT is the detection and visualization of focal liver lesions, primary and metastatic, due to the lower soft-tissue contrast of CT with respect to MRI. Contrast media in CT can increase the detection rate but CT still remains at a lower level with respect to MRI. When comparing contrast enhanced (CE) PET/CT and non-CE MRI, and when comparing PET/CT and non-CE PET/MRI, lesion extent in the liver was found to be significantly better on the MRI component of the study with respect to the CT component [90, 91]. Furthermore, CE MRI always evaluates hepato-cellular carcinomas. Therefore, the combination of stand-alone MRI to the functional information derived from PET could improve diagnosis and characterization of liver lesions beyond PET/CT and stand-alone MRI. Another application for which PET/MRI has an advantage over PET/CT is head and neck cancer imaging, in which soft-tissue characterization is essential to isolate tumor lesions from surrounding soft-tissue infiltration, both for local cancer staging and intervention planning [15]. On the other hand, PET/CT proved to be superior in the detection of lymph-node metastases in head and neck cancer [92]. Another potential application of PET/MRI would be primary tumor staging and follow-up, since the use of such technology could dramatically reduce the amount of radiation for the patient, which would be of relevant importance above all for early detection of cancer in children and adolescents. There are also promising results for the use of PET/MRI in bronchial carcinoma detection [93].

Cardiology. Very early in the development of PET imaging, cardiac applications showed a great potential for short-lived PET tracers in quantitative evaluation of coronary perfusion and myocardial viability, which is far superior to existing conventional scintigraphy (Thallium or Tc99-m MIBI scans) and with much higher accuracy than other functional tests such as stress echocardiography. However, the

high cost of PET scans and lack of PET scanners as well as the need for cyclotron proximity for production of short half-life PET tracers limited the wider use of PET imaging for cardiac applications. While these techniques offered the most accurate quantitative measurement of stress induced decrease of myocardial blood flow in coronary artery disease (CAD), they also allowed for accurately measuring the coronary flow reserve and were considered as the reference gold standard for clinical research and evaluation of new therapeutic interventions. However, they were seldom used in routine clinical settings. Furthermore, F18-FDG scans of the heart allow accurate measurement of remaining viable tissue after myocardial infarction [94]. This ability to accurately identify the amount of myocardium that can potentially be salvaged by complex and expensive revascularization interventions is becoming a key parameter for patient management. In a trend toward evidence-based medicine where treatments and therapeutic interventions must be backed up by objective criteria, such information on residual myocardial viability is becoming critical for patient management and clinical decision making. While similar data can be obtained from some specific MRI sequences based on retention of contrast in scar tissue that allows for visually assessment of the extent of damaged tissue through late contrast enhancement on delayed images, PET viability criteria remain the gold standard in this domain. However, even if PET is, nowadays, the most reliable noninvasive technique for the assessment of myocardial viability in the ischemic dysfunctional left ventricle, this technique is currently only modestly applied in the clinical practice, essentially due to the existence of alternative methods that do not imply radiation exposure of the patient (echocardiography and MRI). Driven by oncologic applications, the wider availability of hybrid PET/CT scanners has opened new perspectives in cardiac PET imaging for clinical routine. Furthermore, the evolution of CT scanners in such hybrid machines has allowed for improving the temporal and spatial resolution while considerably reducing the exposure dose. Current scanners also allow getting adequate images of coronary arteries as well as dynamic images of the beating heart for accurate evaluation of myocardial wall motion anomaly and measurement of cardiac function. PET/CT has therefore been more widely adopted in clinical practice for the assessment of myocardial blood flow and myocardial viability, but it is in competition with the new MRI technique that provide similar information with slightly less accuracy but without the additional radiation of CT scans. MRI is currently used to investigate several aspects of cardiovascular disease (cardiac structural disease, myocardial function, thrombus formation, vascular wall evaluation and plaques detection and characterization). Therefore, it is highly anticipated that the combination of PET and MRI in a single hybrid scanner could bring the best of both techniques in a single device. Furthermore, dynamic MRI provides excellent anatomical and functional details of the heart and great vessels that allow a better localization of regional abnormality on PET images, but also to correct PET inaccuracies such as partial volume effect that tends to underestimate tracer concentrations. These valuable features tend to promote PET/MRI scanners as a promising tool for the study of the heart and its different diseases. A combined clinical use of PET and MRI, adding up the specific strengths of these two imaging techniques, may help to better assess and/or investigate several cardiovascular diseases [15]. Several

studies based on the co-registration of MRI and PET images acquired sequentially have anticipated the potential benefits of the use of such technologies in a single device for cardiologic diagnosis [94, 95]. These benefits include the possibility for MRI-based attenuation and partial volume corrections for improved quantification of myocardial blood flow as well as the possibility to combine anatomy and hemodynamic information, to improve stratification of levels of heart failure and to exactly localize anatomical structures [94]. Since PET/MR hybrid scanners recently became available for clinical use, there is still limited bibliography available about their potential applications in cardiology. Currently, some preliminary clinical experiences [96] are starting to be published and are reporting interesting results, confirming the huge potential that this technology could have in the study of cardiac disease. On the other hand, they observe that much work has still to be done in order to make this imaging technique fully available for daily clinical studies.

Neurology. The highest expectations for the use of multimodal PET/MRI systems are in the neurological field, due to the ability of MRI to perform functional imaging of the brain (functional MRI, fMRI) and to study brain connectivity using diffusion-imaging technique, but also because of the wide range of PET applications in neurodegenerative diseases [14, 29, 36, 97–101]. The complementary use of separately acquired MRI and PET images is a widely adopted approach for the assessment of neurological diseases. The images obtained from the two separate studies are then fused with registration software for more convenient analysis and visualization. However, the diagnostic accuracy of such combined studies relies on the assumption that no remarkable changes occur between the two acquisitions, which can be misleading in some neurological diseases such as strokes or migraine, as well as rapidly evolving brain lesions. The use of hybrid scanners, which allows for simultaneous or even sequential acquisitions with both modalities in a single session, opens a new perspective in the assessment of the human brain and neurological diseases. A better understanding of this organ and of its activity is also one of the most encouraging challenges of modern medicine, and hybrid imaging could be a useful tool for this purpose. Stand-alone CT and MRI have been employed in the assessment of morphological alteration of brain structures in degenerative diseases such as dementia and Alzheimer. Recent developments in functional MRI techniques such as perfusion, diffusion, tensor imaging or fMRI may be used for studying resting-state brain activity [102, 103]. The development of new radiolabeled tracers [104, 105] specifically conceived to study some biological alteration in brain diseases, are expected to bring better diagnostic accuracy, prediction and therapy monitoring of dementia at early stages. Hybrid imaging can provide better links between MRI and PET for the observation of multi-parametric changes in the development of such disease and better understanding of its biological process. In acute cerebral diseases, such as cerebral stroke, it is commonly said that “time is brain”. Due to this, although PET methods are considered the gold standard for identifying the regions compromised in an ischemic stroke event [106], CT and MRI are the modalities of choice for such emergencies [107, 108]. PET techniques that would be suitable for this goal are logistically too complicated and they require too much time for tracer preparation

and delivery but also to perform the exam. During an epileptic episode, it is known that hypo-metabolic lesions detected with PET scanning can represent the epileptogenic focus even in absence of detectable structural abnormalities that MRI scanning can show [109]. The possibility of acquiring information from both modalities in a single imaging session would provide a more accurate merging of the available data for better localization of epileptic foci in view of surgical or interventional treatment. Overall, the significant added value of hybrid scanning in neurology may promote hybrid PET/MRI as a key tool for better assessment and management of different neurological diseases. Other important advantages of hybrid devices over separate scanners are improved patient comfort and a decrease in the number of required exam sessions, which could constitute a significant advantage when dealing with neurologic patients.

Musculoskeletal System. Several studies have been carried out showing the utility of stand-alone MRI and PET devices. MRI scanners are commonly used for studies of neuromuscular disorders [110] or the assessment of musculoskeletal function [111]. The high definition anatomical images and the different dynamic acquisition protocols available can also offer very useful information in the field of biomechanics, although these protocols were designed and implemented initially for the assessment of the heart (DENSE MRI, Tagged MRI) [112]. PET devices also offer metabolic information related with the musculoskeletal function, such as the pattern of glucose uptake, which can be used in the analysis of elite athletes [113] or in studies focused on muscular dysfunction in aged or diseased patients [114].

Other clinical applications. Numerous other applications of hybrid imaging have also been introduced in clinical practice. Such as, infectious and inflammatory diseases, and also complex systemic diseases. Hybrid PET/MRI has also a particular advantage in pediatric imaging, where the use of PET/CT is usually restricted by the unnecessary exposure to radiation of the CT scan. A further potential application of PET/MRI hybrid imaging may also be represented by the development of novel individualized computer-based models of the human body or of specific parts of it. Such models, adapted to each individual person, could guide physicians and researchers to a better understanding of the behavior and function of such organs and potentially to predict the effect of some treatments and surgical interventions.

In conclusion, stand-alone MRI and PET scanners provide valuable information that can be applied in different domains. But there is still a lack of evidence proving the added value that simultaneous PET/MRI study can offer in clinical practice over separately acquired studies. The potential added value of these scanners is evident, but further clinical validation studies have to be carried out in the future. It is necessary still more time for exploring all the possibilities that these scanners can offer in the different fields of medicine and medical imaging.

References

1. Kuhl, D. E., Hale, J., & Eaton, W. (1966). Transmission scanning: A useful adjunct to conventional emission scanning for accurately keying isotope deposition to radiographic anatomy. *Radiology*, *87*, 278–284.
2. Bailey, D. L., Hutton, B. F., & Walker, P. J. (1987). Improved SPECT using emission and transmission tomography. *Journal of Nuclear Medicine*, *28*, 844–851.
3. Tsui, B. M., Gullberg, G. T., Edgerton, E. R., et al. (1989). Correction of nonuniform attenuation in cardiac SPECT imaging. *Journal of Nuclear Medicine*, *30*, 497–507.
4. Hudson, H., & Larkin, R. S. (1994). Accelerated image reconstruction using ordered subsets of projection data. *IEEE Transactions on Medical Imaging*, *13*, 100–107.
5. Hasegawa, B. H., Reilly, S. M., Gingold, E. L., et al. (1989). Design considerations for a simultaneous emission-transmission CT scanner. *Radiology*, *173*, 414.
6. Hasegawa, B. H., Gingold, E. L., Reilly, S. M., et al. (1990). Description of a simultaneous emission-transmission CT system. *Proceedings of SPIE*, *1231*, 50–60.
7. Hasegawa, B. H., Stebler, B., Rutt, B. K., et al. (1991). A prototype high-purity germanium detector system with fast photon-counting circuitry for medical imaging. *Medical Physics*, *18*, 900–909.
8. Pietrzyk, U., Herholz, K., & Heiss, W. D. (1990). Three-dimensional alignment of functional and morphological tomograms. *Journal of Computer Assisted Tomography*, *14*, 51–59.
9. Woods, R. P., Cherry, S. R., & Mazziotta, J. C. (1992). Rapid automated algorithm for aligning and reslicing PET images. *Journal of Computer Assisted Tomography*, *16*, 620–633.
10. Beyer, T., Townsend, D. W., Brun, T., et al. (2000). A combined PET/CT scanner for clinical oncology. *Journal of Nuclear Medicine*, *41*, 1369–1379.
11. Townsend, D. W. (2001). A combined PET/CT scanner: The choices. *Journal of Nuclear Medicine*, *42*, 533–534.
12. Kinahan, P. E., Townsend, D. W., Beyer, T., et al. (1998). Attenuation correction for a combined 3D PET/CT scanner. *Medical Physics*, *25*, 2045–2053.
13. Patton, J. A., Townsend, D. W., & Hutton, B. F. (2009). Hybrid imaging technology: From dreams and vision to clinical devices. *Seminars in Nuclear Medicine*, *39*, 247–263.
14. Hicks, R. J., & Lau, E. W. F. (1998). Attenuation correction for a combined 3D PET/CT scanner. *Medical Physics*, *25*, 2045–2053.
15. von Schulthess, G. K., Kuhn, F. P., Kaufmann, P., et al. (2013). Clinical positron emission tomography/magnetic resonance imaging applications. *Seminars in Nuclear Medicine*, *43*, 3–10.
16. Pichler, B. J., Kolb, A., Nagele, T., et al. (2009). PET/MRI: Paving the way for the next generation of clinical multymodality imaging applications. *Journal of Nuclear Medicine*, *51*, 333–336.
17. Shao, I., Cherry, S. R., Farahani, K., et al. (1997). Simultaneous PET and MR imaging. *Physics in Medicine and Biology*, *42*, 1965–1970.
18. Schlemmer, H. P., Pichler, B. J., Shmand, M., et al. (2008). Simultaneous MR/PET imaging of the human brain: Feasibility study. *Radiology*, *248*, 1028–1035.
19. Heesakkers, R. A., Hoevels, A. M., Jager, G. J., van den Bosch, H. C., Witjes, J. A., Raat, H. P., et al. (2008). MRI with a lymph-node-specific contrast agent as an alternative to CT scan limph-node dissection in patients with prostate cancer: A prospective multicohort study. *The Lancet Oncology*, *9*, 850–856.
20. Goerres, G. W., Burger, C., Schwitter, M. R., et al. (2003). PET/CT of the abdomen: Optimizing the patient breathing pattern. *European Radiology*, *13*, 734–739.
21. Goerres, G. W., Kamel, E., Heidelberg, T. N., et al. (2002). PET/CT image co-registration in the thorax: Influence of respiration. *European Journal of Nuclear Medicine and Molecular Imaging*, *29*, 351–360.
22. Brechtel, K., Klein, M., Vogel, M., et al. (2006). Optimized contrast-enhanced CT protocols for diagnostic whole-body 18F-FDG PET/CT: Technical aspects of single- phase versus multiphase CT imaging. *Journal of Nuclear Medicine*, *47*, 470–476.

23. Beyer, T., Antoch, G., Blodgett, T., et al. (2003). Dual-modality PET/CT imaging: The effect of respiratory motion on combined image quality in clinical oncology. *European Journal of Nuclear Medicine and Molecular Imaging*, *30*, 588–596.
24. Hong, S.J., Song, I.C., Ito, N., et al. (2008) An investigation into the use of Geiger/Mode Solid/State Photomultipliers for simultaneous PET and MRI acquisition. *IEEE Transactions on Nuclear Sciences*, *55*, 882–888.
25. Judenhofer, M. S., Wehrl, H. F., Newport, D. F., et al. (2008). Simultaneous PET-MRI: A new approach for functional and morphological imaging. *Nature Medicine*, *14*, 459–465.
26. Yoon, H. S., Ko, G. B., Kwon, S. I., et al. (2012). Initial results of simultaneous PET/MRI experiments with an MRI-compatible silicon photomultiplier PET scanner. *Journal of Nuclear Medicine*, *53*, 608–614.
27. Yamamoto, S., Watabe, T., Watabe, H., et al. (2012). Simultaneous imaging using Si-PM-based PET and MRI for development of an integrated PET/MRI system. *Physics in Medicine and Biology*, *57*, N1–N13.
28. Tatsumi, M., Yamamoto, S., Imaizumi, M., et al. (2012). Simultaneous PET/MR body imaging in rats: Initial experiences with an integrated PET/MRI scanner. *Annals of Nuclear Medicine*, *26*, 444–449.
29. Judenhofer, M. S., & Cherry, S. R. (2013). Applications for preclinical PET/MRI. *Seminars in Nuclear Medicine*, *43*, 19–29.
30. Gallagher, F. A. (2010). An introduction to functional and molecular imaging with MRI. *Clinical Radiology*, *65*, 557–566.
31. Meguro, K., LeMestric, C., Landeau, B., et al. (2001). Relations between hypometabolism in the posterior association neocortex and hippocampal atrophy in Alzheimers disease: A PET/MRI correlative study. *Journal of Neurology, Neurosurgery and Psychiatry*, *71*, 315–321.
32. Borgwardt, L., Hojgaard, L., Carstensen, H., et al. (2005). Increased fluorine-18 2-fluoro-2-deoxy-D-glucose (FDG) uptake in childhood CNS tumors is correlated with malignancy grade: A study with FDG positron emission tomography/magnetic resonance imaging coregistration and image fusion. *Journal of Clinical Oncology*, *23*, 3030–3037.
33. Pauleit, D., Floeth, F., Hamacher, K., et al. (2005). O-(2-[18F]fluoroethyl)-L-tyrosine PET combined with MRI improves the diagnostic assessment of cerebral gliomas. *Brain*, *128*, 678–687.
34. Floeth, F. W., Pauleit, D., Wittsack, H. J., et al. (2005). Multimodal metabolic imaging of cerebral gliomas: Positron emission tomography with [18F]fluoroethyl-L-tyrosine and magnetic resonance spectroscopy. *Physics in Medicine and Biology*, *102*, 318–327.
35. Seemann, M. D., Meisetschlaeger, G., Gaa, J., et al. (2006). Assessment of the extent of metastases of gastrointestinal carcinoid tumors using whole-body PET, CT, MRI, PET/CT and PET/MRI. *European Journal of Medical Research*, *11*, 58–65.
36. Stadlbauer, A., Prante, O., Nimsky, C., et al. (2008). Metabolic imaging of cerebral gliomas: Spatial correlation of changes in O-(218F-fluoroethyl)-L-tyrosine PET and proton magnetic resonance spectroscopic imaging. *Journal of Nuclear Medicine*, *49*, 721–729.
37. Phelps, M. E. (2004). PET—Molecular imaging and its biological applications. NewYork: Springer.
38. Ollinger, J. M. (1996). Model-based scatter correction for fully 3D PET. *Physics in Medicine and Biology*, *41*, 153–176.
39. Watson, C. C., Casey, M. E., Michel, C., et al. (2004). Advances in scatter correction for 3D PET/CT. *IEEE Nuclear Science Symposium Conference Record*, *5*, 3008–3012.
40. Polycarpou, I., Thielemans, K., Manjeshwar, R., et al. (2011). Comparative evaluation of scatter correction in 3D PET using different scatter-level approximations. *Annals of Nuclear Medicine*, *25*, 643–649.
41. Le Goff-Rougetet, R., Frouin, V., Mangin, J. F., et al. (1994). Segmented MR images for brain attenuation correction in PET. *Proceedings of SPIE*, *2167*, 725–736.
42. Keereman, V., Fierens, Y., Broux, T., et al. (2010). MRI-based attenuation correction for PET/MRI using ultrashort eco time sequences. *Journal of Nuclear Medicine*, *51*, 812–818.

43. Malone, I. B., Ansorge, R. E., Williams, G. B., et al. (2011). Attenuation correction methods suitable for brain imaging with a PET/MRI scanner: A comparison of tissue atlas and template attenuation map approaches. *Journal of Nuclear Medicine*, *52*, 1142–1149.
44. Wagenknecht, G., Rota Kops, E., Mantlik, F., et al. (2011). Attenuation correction in MR-BrainPET with segmented T1-weighte MR images of the patient's head—A comparative study with CT. *Proceedings of IEEE Medical Imaging Conference* (pp. 2261–2266).
45. Berker, Y., Franke, J., Salomon, A., et al. (2012). MRI-based attenuation correction for hybrid PET/MRI systems: A 4-class tissue segmentation technique using a combined Ultrashort-Echo-Time/Dixon MRI sequence. *Journal of Nuclear Medicine*, *53*, 796–804.
46. Martinex-Moeller, A., Souvatzoglou, M., & Delso, G. (2009). Tissue classification as a potential approach for attenuation correction in whole-body PET/MRI: Evaluation with PET/CT data. *Journal of Nuclear Medicine*, *50*, 520–526.
47. Hofmann, M., Bezrukov, I., Mantlik, F., et al. (2011). MRI-based attenuation correction for the whole-body PET/MRI: Quantitative evaluation of segmentation- and atlas- based methods. *Journal of Nuclear Medicine*, *52*, 1392–1399.
48. Steinberg, J., Jia, G., Sammet, S., et al. (2010). Three-region MRI-based whole-body attenuation correction for automated PET reconstruction. *Nuclear Medicine and Biology*, *37*, 227–235.
49. Schulz, V., Torres-Espallardo, I., Renisch, S., et al. (2011). Automatic, three-segment, MR-based attenuation correction for whole-body PET/MR data. *European Journal of Nuclear Medicine and Molecular Imaging*, *38*, 138–152.
50. Huang, S. C., Carson, R. E., Phelps, M. E., et al. (1981). A boundary method for attenuation correction in positron emission tomography. *Journal of Nuclear Medicine*, *22*, 627–637.
51. Martinez-Moeller, A., & Nekolla, S. (2012). Attenuation correction for PET/MRI: Problems, novel approaches and practical solutions. *Z Medical Physics*, *22*, 299–310.
52. Bezrukov, I., Mantlik, F., Schmidt, H., et al. (2013). MR-based PET attenuation correction for PET/MRI imaging. *Seminars in Nuclear Medicine*, *43*, 45–59.
53. Robinson, P. J., & Kreel, L. (1979). Pulmonary tissue attenuation with computed tomography: Comparison of inspiration and expiration scans. *Journal of Computer Assisted Tomography*, *3*, 740–748.
54. Zaidi, H., & Del Guerra, A. (2011). An outlook on future design of hybrid PET/MRI systems. *Medical Physics*, *38*, 5667–5689.
55. Zaidi, H., Ojha, N., Morich, M., et al. (2011). Design and performance evaluation of awhole-body ingenuity PET/MRI system. *Physics in Medicine and Biology*, *56*, 3091–3106.
56. Schreibmann, E., Nye, J. A., Schuster, D. M., et al. (2010). MR-based attenuation correction for hybrid PET-MR brain imaging systems using deformable image registration. *Medical Physics*, *37*, 2101–2109.
57. Beyer, T., Weigert, M., Quick, H. H., et al. (2008). MR-based attenuation correction fortorso-PET/MR imaging: Pitfalls in mapping MR to CT data. *European Journal of Nuclear Medicine*, *35*, 1142–1146.
58. Wagenknecht, G., Kaiser, H. J., Mottaghy, F. M., et al. (2012). MRI for attenuation correction in PET: Methods and challenges. *MAGMA*, *26*, 99–113.
59. Kessler, R. M., Ellis, J. R., & Eden, M. (1984). Analysis of emission tomographic scan data: Limitations imposed by resolution and background. *Journal of Computer Assisted Tomography*, *8*, 514–522.
60. Matsuda, H., Ohnishi, T., Asada, T., et al. (2003). Correction for partial-volume effectson brain perfusion SPECT in healthy men. *Journal of Nuclear Medicine*, *44*, 1243–1252.
61. Shidahara, M., Tsoumpas, C., Hammers, A., et al. (2009). Functional and structural synergy for resolution recovery and partial volume correction in brain PET. *Neuroimage*, *44*, 340–348.
62. Baete, K., Nuyts, J., & Laere, K. V. (2004). Evaluation of anatomy based reconstruction for partial volume correction in brain FDG-PET. *Neuroimage*, *23*, 305–317.
63. Sokoloff, L., Reivich, M., Kennedy, C., et al. (1977). The [14c]deoxyglucose method for the measurement of local cerebral glucose utilization: Theory, procedure, and normal values in the conscious and anesthetized albino rat. *Journal of Neurochemistry*, *28*, 897–916.

64. Reivich, M., Kuhl, D., Wolf, A., et al. (1979). The [18F]fluorodeoxyglucose method for the measurement of local cerebral glucose utilization in man. *Circulation Research*, *44*, 127–137.
65. Patlak, C. S., Blasberg, R. G., & Fenstermacher, J. D. (1983). Graphical evaluation of blood-to-brain transfer constant from multiple-time uptake data. *Journal of Cerebral Blood Flow and Metabolism*, *3*, 1–7.
66. Patlak, C. S., & Blasberg, R. G. (1985). Graphical evaluation of blood-to-brain transfer constant from multiple-time uptake data. Generalizations. *Journal of Cerebral Blood Flow and Metabolism*, *5*, 584–590.
67. Zaidi, H., Mawlawi, O., & Orton, C. G. (2007). Simultaneous PET/MR will replace PET/CT as the molecular multimodality imaging platform of choice? *Medical Physics*, *34*, 1525–1528.
68. Blankespor, S. C., Xu, X., Kaiki, K., et al. (1996). Attenuation correction of SPECT using X-ray CT on an emission-transmission CT system; myocardial perfusion assessment. *IEEE Transactions on Nuclear Science*, *43*, 2263–2274.
69. Lewellen, T. K. (1998). Time-of-flight PET. *Seminars in Nuclear Medicine*, *28*, 268–275.
70. Moses, W. W. (2007). Recent advances and future advances in time-of-flight PET. *Methods in Physics Research Section A*, *580*, 919–924.
71. Delso, G., Furst, S., Jakoby, B., et al. (2011). Performance measurements of the siemens mMR integrated whole-body PET/MR scanner. *Journal of Nuclear Medicine*, *52*, 1914–1922.
72. Kalemis, A., Delattre, B., Heinzer, S. (2012) Sequential whole-body PET/MR scanner: concept, clinical use, and optimisation after two years in the clinic. The manufacturer's perspective. *Magnetic Resonance Materials in Physics, Biology and Medicine*, *26*, 5–23.
73. Gilman, S. (1998). Imaging the brain. First of two parts. *New England Journal of Medicine*, *338*, 812–820.
74. Bisdas, S., Nagele, T., Schlemmer, H. P., et al. (2010). Switching on the lights for real-time multimodality tumor neuroimaging: The integrated positron-emission tomography/MR imaging system. *American Journal of Neuroradiology*, *31*, 610–614.
75. Boss, A., Stegger, L., Bisdas, S., et al. (2011). Feasibility of simultaneous PET/MR imaging in the head and upper neck area. *European Radiology*, *21*, 1439–1446.
76. Weissleder, R., & Pittet, M. J. (2008). Imaging in the era of molecular oncology. *Nature*, *452*, 580–589.
77. Czermin, J., Allen-Auerbach, M., & Schelbert, H. R. (2007). Improvements in cancer staging with PET/CT: Literature-based evidence as of september 2006. *Journal of Nuclear Medicine*, *48*, 78–88.
78. Carli, M. F. D., Dorbala, S., Meserve, J., et al. (2007). Clinical myocardial perfusion PET/CT. *Journal of Nuclear Medicine*, *48*, 783–793.
79. Kaufmann, P. A., & Carli, M. F. D. (2009). Hybrid SPECT/CT and PET/CT imaging: The next step in noninvasive cardiac imaging. *Seminars in Nuclear Medicine*, *39*, 341–347.
80. Costa, D. C., Pilowsky, L. S., Ell, P. J. (1999). Nuclear medicine in neurology and psychiatry. *Lancet*, *354*, 1107–1111.
81. Tatsch, K., & Ell, P. J. (2006). PET and SPECT in common neuropsychiatric disease. *Clinical Medicine*, *6*, 259–262.
82. Edge, S.B., Byrd, D.R., Compton, C.C. (2009). *AJCC Cancer staging handbook: From the AJCC cancer staging manual* (7th ed.) New York: Springer.
83. Antoch, G., & Bockisch, A. (2009). Combine PET/MRI: A new dimension in whole-body oncology imaging? *European Journal of Nuclear Medicine and Molecular Imaging*, *36*, 113–1120.
84. Stoeckli, S. J., Steinert, H., Pfaltz, M., et al. (2002). Is there a role for positron emission tomography with 18F-fluorodeoxyglucose in the initial staging of nodal negative oral and oropharyngeal squamous cell carcinoma? *Head Neck*, *24*, 345–349.
85. Punwani, S., Taylor, S. A., Saad, Z. Z., et al. (2013). Diffusion-weighted MRI of lymphoma: prognostic utility and implications for PET/MRI? *European Journal of Nuclear Medicine and Molecular Imaging*, *40*, 373–385.
86. Poptani, H., Gupta, R. K., Roy, R., et al. (1995). Characterization of intracranial mass lesions with in vivo proton MR spectroscopy. *American Journal of Neuroradiology*, *16*, 1593–1603.

87. Gore, J. C., Manning, H. C., Quarles, C. C., et al. (2011). Magnetic resonance in the era of molecular imaging of cancer. *Magnetic Resonance Imaging*, *29*, 587–600.
88. Buchbender, C., Heusner, T. A., Lauenstein, T. C., et al. (2012). Oncologic PET/MRI, part 1: Tumors of the brain, head and neck, chest, abdomen and pelvis. *Journal of Nuclear Medicine*, *53*, 928–937.
89. Buchbender, C., Heusner, T. A., Lauenstein, T. C., et al. (2012). Oncologic PET/MRI, part 2: Bone tumors, soft-tissue tumors, melanoma and lymphoma. *Journal of Nuclear Medicine*, *53*, 1244–1252.
90. Assiri, Y., Schmid, D., Pietsch, C., et al. (2012). Contrast enhanced PET/MRI in abdominal oncological lesions. initial results. *Annual Congress of the European Association of Nuclear Medicine*. (Milan, Italy).
91. Crook, D. W., Mader, C., Kuhn, F. P., et al. (2012). *Diagnostic performance of PET/MRI versus PET/CT in the abdomen*. Vienna: European Congress of Radiology.
92. Hustinx, R., & Lucignani, G. (2010). PET/CT in head and neck cancer: An update. *European Journal of Nuclear Medicine and Molecular Imaging*, *37*, 645–651.
93. Schwenzer, N. F., Schraml, C., Mueller, M., et al. (2012). Pulmonary lesion assessment: comparison of whole-body hybrid MR/PET and PET/CT imaging. Pilot study. *Radiology*, *264*, 551–558.
94. Nekolla, S., & Martinex-Möller, A. (2009). A, S.: PET and MRI in cardiac imaging: From validation studies to integrated applications. *European Journal of Nuclear Medicine and Molecular Imaging*, *36*, 121–130.
95. Buescher, K., Martin, S. J., Kuhlmann, M. T., et al. (2010). Isochronous assessment of cardiac metabolism and function in mice using hybrid PET/MRI. *Journal of Nuclear Medicine*, *51*, 1277–1284.
96. Vargas, M.I., Becker, M., Garibotto, V., et al. (2012). Approaches for the optimization of MR protocols in clinical hybrid PET/MRI studies. *MAGMA*, *26*, 57–69.
97. Prvulovic, D., Bokde, A. L., Faltraco, F., et al. (2011). Functional magnetic resonance imaging as a dynamic candidate biomarker for Alzheimers disease. *Progress in Neurobiology*, *95*, 557–569.
98. Barnes, J., Ourselin, S., & Fox, N. C. (2009). Clinical application of measurement of hippocampal atrophy in degenerative dementias. *Hippocampus*, *19*, 510–516.
99. Wattjes, M. P. (2011). Structural MRI. *International Psychogeriatrics*, *23*, S13–S24.
100. Utriainen, M., Komu, M., Vuorinen, V., et al. (2003). Evaluation of brain tumor metabolism with [11C] choline PET and 1H-MRS. *Journal of Neuro Oncology*, *62*, 329–338.
101. Floeth, F. W., Pauleit, D., Wittsack, H. J., et al. (2005). Multimodal metabolic imaging of cerebral gliomas: positron emission tomography with [18F]fluoroethyl-L-tyrosine and magnetic resonance spectroscopy. *Journal of Neurosurgery*, *102*, 318–327.
102. Chua, T. C., Wen, W., Slaving, M. J., et al. (2008). Diffusion tensor imaging in mild cognitive impairment and Alzheimers disease: A review. *Current Opinion in Neurology*, *21*, 83–92.
103. Dickerson, B. C., & Sperling, R. A. (2004). Functional abnormalities of the medial temporal lobe memory system in mild cognitive impairment and Alzheimers disease: insights from functional MRI studies. *Neuropsychologia*, *55*, 1624–1635.
104. Klunk, W. E., Engler, H., Nordberg, A., et al. (2004). Imaging brain amyloid in Alzheimers-disease with Pittsburgh compound-B. *Annals of Neurology*, *55*, 306–319.
105. Rowe, C. C., & Villemagne, V. L. (2011). Brain amyloid imaging. *Journal of Nuclear Medicine*, *52*, 1733–1740.
106. Heiss, W. D. (2000). Ischemic penumbra: Evidence from functional imaging in men. *Journal of Cerebral Blood Flow and Metabolism*, *20*, 1276–1293.
107. Loevblad, K. O., Laubach, H. J., Baird, A. E., et al. (1998). Clinical experience with diffusion-weighted MR in patients with acute stroke. *American Journal of Neuroradiology*, *19*, 1061–1066.
108. Sorensen, A. G., Copen, W. A., Ostergaard, L., et al. (1999). Hyperacute stroke: Simultaneous measurement of relative cerebral blood volume, relative cerebral blood flow, and mean tissue transit time. *Radiology*, *210*, 519–527.

109. LoPinto-Khoury, C., Sperling, M. R., Skidmore, C., et al. (2012). Surgical outcome in PET-positive, MRI-negative patients with temporal lobe epilepsy. *Epilepsia*, *53*, 342–348.
110. Mercuri, E., Pichiecchio, A., Allsop, J., Messina, S., Pane, M., & Muntoni, F. (2007). Muscle MRI in inherited neuromuscular disorders: Past, present and future. *Journal of Magnetic Resonance Imaging*, *25*, 433–440.
111. Segal, R. L. (2007). Use of imaging to assess normal and adaptive muscle function. *Physical Therapy*, *87*, 704–718.
112. Prompers, J. J., Jeneson, J. A. L., Drost, M. R., Oomens, C. C., Strijkers, G. J., & Nicolay, K. (2006). Dynamic MRS and MRI of skeletal muscle function and biomechanics. *NMR in Biomedicine*, *19*, 927–953.
113. Tai, S., Liu, R., Kuo, Y., Hsu, C., & Chen, C. (2010). Glucose uptake patterns in exercised skeletal muscles of elite male long-distance and short-distance runners. *Chinese Journal of Physics*, *53*(2), 91–98.
114. Heinonen, I., Nesterov, S. V., Kemppainen, J., Fujimoto, T., Knuuti, J., & Kalliokoski, K. K. (2012). Increasing exercise intensity reduces heterogeneity of glucose uptake in human skeletal muscles. *PLoS ONE*, *7*(12), e52191.

Chapter 4
Deformable Models in Medical Image Segmentation

Matthias Becker and Nadia Magnenat-Thalmann

4.1 Introduction

Medical imaging nowadays is part of the routine in hospitals. The acquired images get better in quality and improvements are made to reduce the exposure of patients to radiation. Modern techniques allow to capture small details and to differentiate between kinds of soft tissue. But with the increased number of images and their higher resolution, interpretation has become a more complex task. Nonetheless, medical image segmentation is required for applications like radiotherapy, preoperative planning and postoperative evaluation. Medical image segmentation, as described by Elnakib et al. [1] in a survey, is the process of identifying regions of interest in images. Approaches range from simple ones that only exploit intensity values or region information to model-based ones that include a priori knowledge. The images often suffer from noise, aliasing and anomalies or may contain gaps in boundaries, providing challenges that are hard to handle with non model-based approaches.

Deformable models have been first proposed by Terzopoulos et al. in 1987 [2]. They provide a robust segmentation approach that uses bottom-up image-based constraints and top-down constraints from prior knowledge. Deformable models can be curves or surfaces (or of higher dimension, e.g. for temporal segmentation). They evolve under the influence of internal and external energies. The internal energy controls the curves smoothness and the external energy aims to attract the model towards boundaries in the image domain. Deformable models are an interesting approach as they combine geometry (to describe the shape), physics (to simulate the behavior) and approximation theory (for model fitting).

M. Becker (✉) · N. Magnenat-Thalmann
MIRALab, University of Geneva, Geneva, Switzerland
e-mail: becker@miralab.ch; thalmann@miralab.ch

N. Magnenat-Thalmann
Institute for Media Innovation, Nanyang Technological University,
50 Nanyang Drive, Singapore, Singapore

N. Magnenat-Thalmann et al. (eds.), *3D Multiscale Physiological Human*,
DOI: 10.1007/978-1-4471-6275-9_4,

Deformable models have a broad range of possible applications. They have been used in computer graphics [3], to calculate the deformation of clothes [4] and in image composition [5]. Other uses include optical flow analysis for facial animation [6] and the determination of vehicle types [7].

Due to their power and robustness, deformable models are often used in medical applications. For example, Deserno et al. [8] presented an application for segmenting the bony orbit while Heimann et al. [9] proposed a grand challenge for knee segmentation. Schmid [10] presented the segmentation of the hip bone, Snel et al. [11] used a deformable model for wrist segmentation and Rafai et al. [12] proposed a method for skull segmentation. Another medical use is surgery simulation which has been reviewed by Meyer et al. [13]. Medical simulation approaches that use deformable models to describe the mechanical behavior need proper evaluation. Marchal et al. [14] proposed a new and open framework to combine several metrics and models to compare different algorithms.

Several surveys on deformable models have been published, e.g. by McInerney et al. [15] in 1996, Montagnat et al. [16] in 2001 and Hegadi et al. [17] in 2010. Moore et al. [18] provided a general survey on deformable models while Jain et al. [19] have reviewed deformable template models, which are used for segmentation, image retrieval and video tracking.

Deformable models can be divided into discrete and continuous representations [16]. The discrete models can be split into particle systems and meshes. Continuous representations can have either an explicit (snakes) or implicit (level sets) description of their surface. These different classes of deformable models will be surveyed in this overview. First we will introduce active contour models, also known as snakes (Sect. 4.2). Next, several approaches to the level sets method will be discussed (Sect. 4.3), followed by a description of discrete deformable models (Sect. 4.4). We take a look at knowledge-based deformable models (Sect. 4.5) that are a specialization and at some alternative approaches (Sect. 4.6). An overview of external forces (Sect. 4.7) and approaches for segmentation initialization will also be given (Sect. 4.8). In the conclusion, the most important aspects are summarized and future prospects are briefly discussed.

4.2 Snakes

Active contour models, usually called snakes, are a class of deformable models with a continuous representation based on an explicit surface description. They have been originally proposed by Kass et al. [20] in 1988 and have been applied as a method for edge detection [21], motion tracking [22], stereo matching [23] and interactive image interpretation [20]. Other applications are shape modeling [24, 25] and segmentation [21, 26].

The main concept is to use an energy-minimizing parametric curve or a spline, reducing the problem to a minimization problem. Snakes need to be initialized closely to the final shape to ensure that they are attracted to the correct features.

The energy of a snake $\alpha(s)$ can be written as

$$E_{\text{snake}}(\alpha(s)) = E_{\text{ext}}(\alpha(s)) + E_{\text{int}}(\alpha(s)). \tag{4.1}$$

The external energy E_{ext} represents external constraints and image influence to get the contour pulled towards desired image features.

$$E_{\text{ext}}(\alpha(s)) = \int -\omega_1 |\nabla \alpha(s)| ds \tag{4.2}$$

The internal energy expresses smoothness and tension constraints:

$$E_{\text{int}}(\alpha(s)) = \frac{1}{2}\left(\int \omega_2 \left|\frac{\partial \alpha(s)}{\partial s}\right|^2 + \int \omega_3 \left|\frac{\partial^2 \alpha(s)}{\partial s^2}\right|^2\right) \tag{4.3}$$

where ω_2 is the weight for the influence of stretching on the contour and ω_3 weighs the bending.

Xu et al. [27] have proposed the gradient vector flow (GVF, see Sect. 4.7.2.5) as a new external image force to improve segmentation results. This concept has been extended by Cheng et al. [28] to a directional GVF. In 1993 Ivbins and Porril [29] have shown a region growing segmentation that exploits a snake with pressure force and statistical characteristics of the image. Mitrea et al. [30] have reviewed snakes and proposed an iterative method for snake calculation. Wang et al. [31] showed a method for muscle extraction from the leg using snakes. Kauffmann et al. [32] proposed a snake-based method to quantify cartilage thickness and volume in MR images.

Ip and Shen [33] proposed affine invariant active contour models (AI snakes) in 1998. AI snakes are an efficient method of establishing correspondence between model and data. The basis for their energy function is formed by local and global affine-invariant features.

In 1999, Vemuri and Guo [34] presented hybrid geometric active models. They introduced a hybrid geometric snake to allow for topology changes. Their model allows for the representation of global shapes with local details.

Another approach to topology adaptive snakes has been proposed by McInerney and Terzepoulos in 2000 [35]. Their T-Snakes offer topological flexibility and significantly extend conventional snakes. This approach has been extended further by others [36, 37].

4.3 Level Sets

Level sets have been introduced in 1988 by Osher and Sethian [38] to overcome the difficulties that snakes have with changes in topologies. Their work has proven to be a

powerful tool in segmentation. The ability of level sets to perform automatic topology changes can be useful in many cases, especially for the segmentation of objects with high shape variations. Implementations can be found in tools like ITK-SNAP [39] and YaDiV [40] or libraries like LSMLib.[1]

Like snakes, level sets can be regarded as continuous deformable models. To overcome the drawbacks of snakes and to allow topology changes, level sets make use of an implicit representation. A deformable surface S is implicitly represented as an iso-surface of a time-varying scalar function, embedded in 3D.

Let $\Phi{:}\Omega \times \mathbb{R} \rightarrow \mathbb{R}$, $\Omega \in \mathbb{R}^3$. A level set S can be defined as an iso-hypersurface on Φ as follows:

$$S = \{x \in \Omega | \Phi(x) = 0\} \tag{4.4}$$

We assume Φ to be a distance map that is negative inside the level set and positive outside. To integrate a temporal evolution we iteratively modify Φ and get

$$\frac{\partial \Phi}{\partial t} + F\,|\nabla_{\Phi}| = 0 \tag{4.5}$$

with F as speed function. The speed function controls the image influence on the evolution of the level set surface. This formulation leads to the need to solve partial differential equations (PDE). To define the speed function we use the surfaces normal N and curvature k, defined as:

$$N = \frac{\nabla \Phi}{|\nabla \Phi|}, \quad k = div\left(\frac{\nabla \Phi}{|\nabla \Phi|}\right). \tag{4.6}$$

Common approaches for speed functions are edge stopping and energy minimization, which we will present in the following sections.

4.3.1 Edge Stopping Level Sets

Osher and Sethian [38] proposed a level set approach that exploits edges. To slow down the expansion of the model, image gradients are used. The speed function is defined as the sum of a curvature force and an expansion force. This force is scaled by a stopping function that makes use of the image gradient at this point. The following equation is an example of a stopping function:

$$g(x) = \frac{1}{\left(1 + \sqrt{|\nabla x|}\right)^p}$$

[1] http://ktchu.serendipityresearch.org/software/lsmlib/index.html

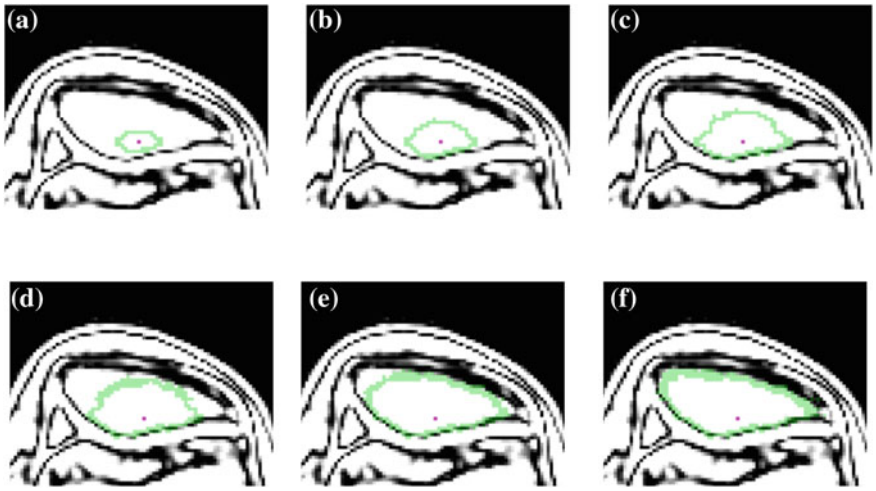

Fig. 4.1 Example of an edge stopping level set for segmentation of the patella after **a** 10, **b** 20, **c** 30, **d** 40, **e** 60 and **f** 80 steps

Using these speed values, the new distance map can be updated. The resulting contour is the input for the next iteration step. This approach does not stop the contour at high gradient completely but only slows it down. Therefore it is possible that after a large number of steps, the contour could overcome high gradients. This is a behavior that should always be considered. Figure 4.1 shows an example of patella segmentation using an edge stopping level set approach.

4.3.2 Energy Minimizing Level Sets

Instead of a gradient stopping function, an alternative approach defines an energy potential that is consequently minimized. The foundational work on this approach has been done by Mumford and Shah in 1989 [41]. The area and volume covered by the level set S are important in this approach and can be determined using the Heaviside function, which needs to be smoothed as described by Zhao et al. in [42]. The calculation is performed in three steps. First the average image intensity for voxels inside and outside the segment is calculated. The next step is to compute the energy of each voxel using the weighted area, volume and image intensities inside and outside the region of interest. Finally the distances are being updated using these energies.

4.3.3 Extensions

Over the years several extensions to level sets have been proposed. Sethian [43] developed an extension for fast marching, allowing the contour to move more than one voxel per iteration step. This was previously prevented by numerical instabilities. In 2001 Chan and Vese [44] have presented an approach to level sets that is not based on an edge-function and can operate on very noise, unsmoothed images. Zhang et al. [45] showed a hybrid approach that uses both boundary and region information to get accurate results by reducing leaking problems. Yeo et al. [46] have proposed a new external force in 2009. Their geometric potential force is based on hypothesized interaction between relative geometry and image gradients. Caselles et al. [47] have proposed geodesic active contours as a connection between snakes and geometric curves. Unger et al. [48] have extended this approach with GPU usage to improve performance.

Other extensions focus on performance optimizations. In 1999, Adalsteinsson and Sethian [49] have proposed to only calculate the speed function for a narrow band around the current contour. Whitaker [50] showed a computational method (sparse-field algorithm) that combines the level sets approach with the efficiency and accuracy of parametric representation. A solution to use level sets without the need of solving PDEs has been proposed by Shi and Karl in 2005 [51]. Meziou et al. [52] have presented an approach that uses fractional entropy applicable for cell nuclei segmentation.

4.4 Discrete Deformable Models

Unlike snakes and level sets, discrete deformable models do not use a continuous representation of their surface. Instead, they are modeled using particles or meshes (see Sect. 4.4.2). In a discrete deformable model, forces are calculated in an iterative process and applied to the particles or vertices in the mesh. Several physical and numerical schemes can be used for this purpose, while an abort criterion terminates the segmentation. When dealing with meshes, special attention has to be paid to local resampling, topology adaptation and the avoidance of (self-) intersections and collisions. Kainmueller et al. [53] proposed coupled deformable models. They exploited redundant structures that appear when segmenting multiple connected objects in parallel. They demonstrated a model for femur and ilium that reduces the need for expensive self-intersection testing. In their approach, the logical relationship can be retained using combined intensity profiles.

Bredno et al. [54] gave a description of the components needed for a discrete deformable model. It consists of a surface, forces, a surface resolution adjustment approach and an abort criterion. In an iterative process, forces are calculated and applied. Afterwards the surface is adjusted. The iteration end is defined by the abort criterion. This process is illustrated in Fig. 4.2. The calculation of forces, e.g. the

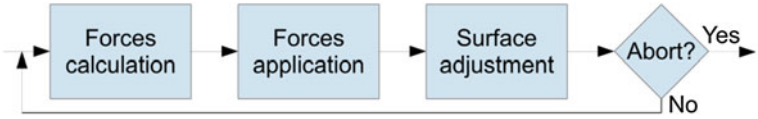

Fig. 4.2 Process of the iterative deformation of a surface using forces

ones described in Sect. 4.7, is the first step. If a force is calculated for an edge or a triangle, it has to be distributed to the corresponding vertices. The next step is the movement of the vertices. The translation of each vertex is determined according to the selected numerical implementation. If the volume or shape of the models changes significantly, resampling processes are often needed. They adjust the mesh to ensure the geometrical quality of the triangles and modify the mesh in a way that triangles are small enough to fit through the desired structures. For example, the segmentation of a small vein needs a constant refinement as the model grows along the tubular structure. In a final step, a check is performed to see if the iteration process should be terminated. This can be triggered for example after a certain number of steps or once the vertices have reached equilibrium.

4.4.1 Implementation

There are several possibilities to implement the physical properties of a discrete deformable model. The forces may be modeled directly or as hookean spring forces, as presented by Gilles and Magnenat-Thalmann [55] and Schmid [10]. In their formulation, a translation from the point x_i to x_j is weighted by a factor α_h:

$$F_{\mathrm{h}} = \alpha_{\mathrm{h}}(x_j - x_i) \tag{4.7}$$

A common approach to describe the forces is by applying Newtonian physics, but a popular alternative is to use Lagrangian dynamics [11]. Other approaches include the Finite Difference Methods (FDM) [2] and Finite Element Methods (FEM) [25, 56–58].

4.4.2 Mesh Types

Simple segmentation algorithms often create point clouds as a result. To initialize a deformable model, an initial shape has to be provided, which can be derived from point clouds. The conversion from a point cloud can be done using the marching cube algorithm as proposed by Lorensen and Cline [59] in 1987. The resulting mesh will be closed but also will contain a high number of faces, higher than needed in

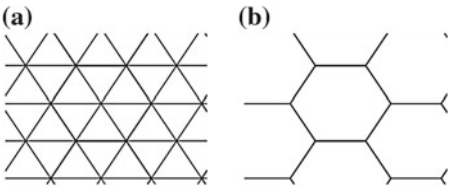

Fig. 4.3 Triangle (**a**) and simplex (**b**) meshes

most cases. In this case, reduction techniques can be applied, but they will have an impact on the mesh quality. Miller et al. [60] have proposed another approach, the Geometrically Deformable Model (GDM) in which the mesh of a deformable model is grown into the point cloud. This results in a lower number of triangles while preserving the topology and details. Most discrete deformable models use traditional triangle meshes. Delingette [61, 62] proposed to use a simplex representation to store the model geometry. A n-simplex mesh contains vertices that all have n+1 distinct neighbors. Using 2-simplex meshes (each vertex has exactly 3 neighbors), arbitrary topologies can be represented. Faces can have an arbitrary number of vertices and can be non-planar. A comparison between simplex and triangle meshes is shown in Fig. 4.3. Simplex meshes have been used for example in the segmentation of cardiac structures by Montagnat et al. [63] and for musculoskeletal structures in the lower limb by Gilles [64].

To improve iteration performance, Lachaud and Montanvert [65] proposed a coarse to fine model while Snel et al. [11] have demonstrated a multi-resolution scheme. Pons et al. [66] demonstrated an implicit triangular mesh that performs a delauney triangulation on-the-fly when needed. A permanent connection through tessellation has been presented by Gilles et al. [67].

4.4.3 Particle Systems

A different approach to discrete deformable models are particle systems which operate mesh-less. A collection of independent particles get assigned physical properties, such as mass, position, speed and acceleration and evolve according to classical Newtonian mechanics.

Particle system can represent arbitrary topologies but pose a great challenge when it comes to visualization and the definition of surfaces. Szeliski and Tonnensen [68] have proposed to use oriented particles to represent surfaces. They use several techniques to derive a surface from the particles. This approach has been extended by Lombardo [69] to define curvature and to get an implicit surface description.

4.5 Knowledge-Based Deformable Models

Deformable models require initial shape information to achieve better results. Knowledge-based deformable models are a group of approaches that aim to invoke more prior knowledge through additional features. This increases the flexibility in poor images and the robustness against inaccurate initializations. A comprehensive overview of knowledge-based deformable models has been given by Schmid [10] in 2011. A simple approach would be assigning labels with an associated behavior to the model. Other models use the statistical or probabilistic variation of selected features. In this section, possibilities for feature selection are discussed, followed by the alignment process and construction of the statistical model. We conclude with the description of the two main approaches: active shape models and active appearance models.

4.5.1 Feature Selection

Features select the property of the models that will be exploited. They can be summed up in three categories: shape-, appearance- and transformation-based features.

4.5.1.1 Shape-Based Features

Cootes et al. [70, 71] have proposed shape-based features in 1994. They use prior shape information to improve results and limit shape variability to the shape variations from training data. A set of points, called landmarks, represents image features. They have to be (usually manually) selected from a large number of training data. Another approach for these point distribution models (PDM) can be used to replace landmarks with parameters of a medial axis [72].

4.5.1.2 Appearance-Based Features

To exploit image properties, appearance-based features can be intensity, gradient, texture, momentum, etc. Intensity profiles (IP, see Sect. 4.7.2.1) are very important and commonly used. In 3D, appearance-based features suffer from an increased complexity (highly increased memory consumption and computational effort).

4.5.1.3 Transformation-Based Features

A third group of not very common approaches are transformation-based features. They exploit transformation parameters that can be used for the statistical deformation model. They have been extended to also support non-rigid transformations.

4.5.2 Construction

The creation process of statistical or probabilistic models of feature variation can be divided into two parts. Initially, the training models have to be aligned before the construction can be performed.

The alignment process aims at eliminating pose changes that are not feature related. To do this, commonly the iterative generalized Procrustes approach [73] is applied.

$$T^* = \underset{T}{\operatorname{argmin}} \sum_i ||y_i - T(x)||^2 \tag{4.8}$$

The transformation T^* is obtained by finding a transformation that minimizes the distance between a model x and all other models y_i. The resulting transformation T^* is combination of a translation, a rotation and scaling. Once this transformation is applied, all models are in a common coordinate frame: the model space of the point distribution model. Although aligned, these models still have a substantial amount of shape variability.

The actual construction process uses the corresponding and aligned features and performs a principal component analysis (PCA). PCA has been introduced by Pearson [74] in 1901. This technique has been used for the point distribution model (PDM) by Cootes and Taylor [70]. Given n shapes $Y_1, Y_2, \ldots, Y_n$, the mean shape can be defined as

$$\overline{Y} = \frac{1}{n} \sum_{i=1}^{n} Y_i. \tag{4.9}$$

The covariance matrix is defined as

$$S = \frac{1}{n-1} \sum_{i=1}^{n} (Y_i - Y)(Y_i - Y)^T \tag{4.10}$$

and its eigenvectors correspond to the largest eigenvalues of S. The eigenvectors describe the most significant variation modes from which a subset (much smaller than the number of points) is used.

This approach needs a sufficiently high number of training models. Otherwise a poor generality is given, leading to poor adaptation to new data and enforcement of

an over-constrained behavior. Approaches to solve this problem include Bayesian inference [75], synthetic shape variations [76] or the derivation of new artificial shapes from existing training shapes [77].

4.5.3 Active Shape Models (ASM) and Active Appearance Models (AAM)

Active Shape Models use a statistical model of shape feature variations. To implement them, a model fitting process constrains movement to the modes defined by the trained models. In each iteration step of this process, the closest parametric model to the model X with the deformation dX is searched for and forces are applied to deform the model towards this shape. Given the model shape Y, the model X can be represented as follows:

$$X = MY + X_c \tag{4.11}$$

with M being the matrix for scaling and rotation and X_c the translation vector of the center of X. The estimation of the pose adjustment can be done efficiently using a standard least-squares approach as described in [71]. An example for the segmentation of lung and cerebellum using ASMs is given by Ginneken et al. [78]. Lamecker et al. [79] presented an approach to use ASMs for the segmentation of the bony orbit.

Active Appearance Models have been proposed by Cootes et al. [80] in 1998. They combine a statistical model of the shape and the gray-level appearance. This extends the models for shape X_s with another one for the image texture X_t, assuming that all textures have been warped to the mean shape. Olabarriaga et al. [81] have presented the use of AAMs for thrombus segmentation; Shen et al. [82] have extended the approach to active volume models.

4.6 Other Deformable Models

In this section we will give a short overview of other types of deformable models that fall outside the classification described so far. We will discuss deformable Fourier models, the modal analysis, deformable superquadrics and graph-cut approaches.

4.6.1 Deformable Fourier Models

In 1992 Staib and Duncan [83] have proposed to use a Fourier representation for deformable contours and surfaces. In the following we will take a look at a closed

Fourier contour, described as:

$$X(s) = \begin{bmatrix} X(s) \\ Y(s) \end{bmatrix} = \begin{bmatrix} a_0 \\ c_0 \end{bmatrix} + \sum_{k=1}^{\infty} \begin{bmatrix} a_k & b_k \\ c_k & d_k \end{bmatrix} \begin{bmatrix} \cos 2\pi ks \\ \sin 2\pi ks \end{bmatrix} \tag{4.12}$$

with the Fourier coefficients $a_0, c_0, a_k, b_k, c_k, d_k$. They are defined as

$$a_0 = \frac{1}{2\pi} \int_0^1 X(s)\, ds, \quad a_k = \tfrac{1}{\pi} \int_0^1 X(s) \cos 2\pi ks\, ds,$$
$$b_k = \tfrac{1}{\pi} \int_0^1 X(s) \sin 2\pi ks\, ds \tag{4.13}$$

A smooth representation can be obtained by truncating the series. The shape translation is defined by the coefficients a_0 and c_0. The subsequent terms follow the parametric form of an ellipse and can be mapped to the standard properties of an ellipse [84]. The parameters follow scale ordering, with low indices for global properties and high indices describing local deformations.

To incorporate prior knowledge, Staib and Duncan [83] use a Bayesian approach. A prior probability approach is defined by manual delineation and the consequent parameterization of Fourier coefficients using a converted ellipse parameter set. In this way, a mean and variance can be calculated for each parameter.

4.6.2 Deformable Models Using Modal Analysis

Modal analysis has been introduced by Pentland and Horowitz [85]. Deformable models using it are similar to deformable Fourier models but their basis functions and nominal values are derived from templates. The objects consist of finite elements, stacked in the vector X. Displacements are stored in U, so that the new state after a deformation step is given by $X + U$. They are constrained using the following differential equation

$$M \frac{d^2U}{dt^2} + C \frac{dU}{dt} + KU = f \tag{4.14}$$

with M as mass, C as damping and K as stiffness matrix. The vector f contains the external forces and f and U are defined as functions of time.

4.6.3 Deformable Superquadrics

To incorporate local and global shape features, Terzopoulos and Metaxas [58] have proposed deformable superquadrics. These deformable models use a superquadric surface. While global deformations have a large influence on the global shape characteristics, local deformations capture the details. Local and global deformations are being performed in parallel. The closed surface $x(u)$ in parametric coordinates $u = [v, w]$ is expressed as:

$$x(u) = c + Rp(u) \tag{4.15}$$

with c a translation vector and R a rotation matrix. The model shape is expressed by $p(u)$ and is the sum of the reference shape $s(u)$ and the local deformations $d(u)$. Superquadrics are a popular extension to quadrics and can model many shapes with few parameters. Examples for superquadrics are superellipsoids, which are described in Ref. [86].

4.6.4 Graph-Cut-Based Approaches

Graph cuts are used to efficiently solve computer vision problems through global optimization. A formulation as energy minimizing approach (e.g. in level sets) can be reduced to the maximum-flow problem. Ababneh et al. [87] have presented an application of this approach for the segmentation of the knee bones in MR images. Zhou et al. [88] have presented a graph-cut-based method for industrial image segmentation. Zhu-Jacquot et al. [89] have proposed a method to combine graph-cuts with statistical shape priors. A similar approach has been presented by El-Zehiry et al. [90]. Chen et al. [91] have demonstrated a combination of graph-cuts and active appearance models to get more accurate segmentation results.

Vineet and Narayanan [92] demonstrated how to calculate graph cuts on the GPU. Their approach achieves a better performance as it exploits the highly parallel structure of GPUs for concurrent calculation. Another optimization has been proposed by Delong and Boykov in 2008 [93]. Their approach reduces the memory requirements for large data sets and achieves a near linear increase in computational speed with respect to number of processors in multi-core systems. Lee et al. [94] have proposed Branch-and-MinCut in 2010. This approach combines graph cuts and other techniques like branch-and-bound to allow a global optimization for a wide class of energies. This can be used to include shape- or color-distribution priors.

4.7 External Forces

The deformation of the model is determined by forces. They bridge the gap between the model with its internal forces and the image domain. Over the years these external forces have evolved from intensity or gradient based image forces to complex approaches using statistics or vector flow techniques. In this section we will present some basic forces that are commonly used in deformable models. Advanced forces follow as an extension. We conclude with the description of interactive forces. All following forces will be calculated for a vertex x with the normal n_x and will be scaled by a factor α.

4.7.1 Basic Forces

4.7.1.1 Pressure Force

In areas with low image information, the model tends to stay at its current position as there are no image features to attract it. To overcome this issue and to reduce the need for very close initialization, Cohen et al. [95] have proposed a balloon or pressure force.

$$F_{\text{pressure}}(x) = \alpha_{\text{p}} n_x \tag{4.16}$$

It evolves the model along its surface normals and depending on the sign of α_{p} the model can either shrink or expand.

4.7.1.2 Laplacian Smoothing Force

Image noise or artifacts may stop small parts of the model. To prevent this from happening, model smoothing can be applied. An example for a common approach is the Laplacian smoothing:

$$F_{\text{smooth}}(x) = \alpha_{\text{s}} \frac{1}{|U_x(\Delta)|} \sum_{y \in U_x(\Delta)} y - x \tag{4.17}$$

It calculates the centroid of the neighboring vertices and defines a force towards that point. Improvements have been proposed by Shen et al. [96]. Figure 4.4 shows an example for smoothing (transformation from cube to sphere) and pressure force (growing).

Fig. 4.4 The combination of pressure force and smoothing transforms a cube into a sphere

4.7.1.3 Simple Image Force

A simple approach to include image features is the use of normalized intensity gradients that, for example, can be calculated using central differences. Along the vertex normal, several gradients are being calculated and the force will be directed towards the higher gradients:

$$F_{\text{image}}(x) = -\alpha_{\text{i}} n_x \sum_{\delta_{min}}^{\delta_{max}} k(\delta) * \Phi(x + \delta \cdot n_x) \tag{4.18}$$

where $k(\delta)$ is a weighting factor with respect to the distance δ and $*$ is the convolution operator. An image interpretation factor Φ can be calculated, in this case the gradient.

4.7.2 Advanced Forces

The basic forces can be extended by more advanced approaches to improve results and runtime.

4.7.2.1 Image Intensity Profiles

Instead of simply using the image gradient, intensity profiles can be used to compare the intensity curve along the normals. By doing so, the desired structure can be described more powerful and it allows a distinction between noise-induced gradients and targeted edges. This approach is commonly used [70, 97, 98]. To reduce the complexity of the high number of intensity profiles, clustering has been proposed. For instance, Chung and Delingette [99] have proposed an Expectation-Maximization-based algorithm for clustering and classification. An example of image intensity profiles in a magnetic resonance (MR) image of the femur is shown in Fig. 4.5.

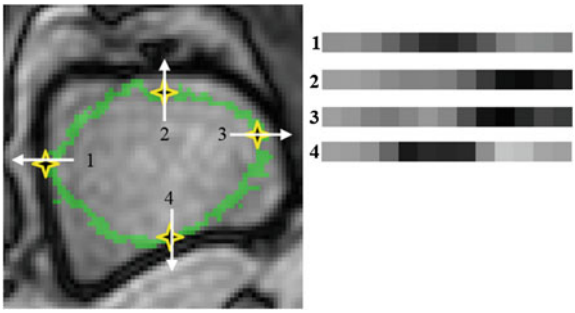

Fig. 4.5 Example of intensity profiles sampled in an MR image of the femur

4.7.2.2 Multiscale Gaussian Potential Force

The Gaussian Potential Force is designed to attract a model towards image features and is defined as

$$F_{\mathrm{g}}(x) = \alpha_{\mathrm{g}} |\nabla [G_{\sigma}(x) * I(x)]|^2 \tag{4.19}$$

with I(x) the intensity image, $G_{\sigma}(x)$ a Gaussian function, α_g a weight and $*$ the convolution operator. This force has been extended by Terzopoulos et al. [100] to a multi-scale scheme. To overcome the need of an initialization close to the final contour, they propose to use a large initial value of s to broaden the search space. Once equilibrium has been reached, σ could be decreased to maintain the accuracy of the original approach. Until now, no criterion has been established to determine when to reduce σ, limiting the utility of the multi-scale gaussian potential force.

4.7.2.3 Distance Potential Force

To extend the attraction range, Cohen and Cohen [57] have proposed to use a distance map in 1993. The values in this map are obtained by using either the Euclidian distance [101] or Chamfer distance [102] to calculate the distance between a voxel and the closest boundary point.

4.7.2.4 Dynamic Distance Force

This force extends the distance potential force to include a larger spatial area around the surface [103, 104]. The dynamic distance has improved handling of boundary concavities. It is calculated by examining the image for features or gradients along the surfaces normal. The maximal search distance is limited by a threshold $D_{\max}$.

$$F_{\mathrm{dynamic}}(x) = \alpha_{\mathrm{d}} \frac{D(x)}{D_{max}} n(x) \tag{4.20}$$

The resulting force can pull the model towards distant image features. Nonetheless, the search is very time consuming and has to be repeated in every step. Lowering the threshold can shorten the runtime but also reduces the attraction range for image features.

4.7.2.5 Gradient Vector Flow

In 1998, Xu and Prince [27] have proposed a new external force model. Their Gradient Vector Flow (GVF) field is calculated as the diffusion of an intensity image. It allows a more flexible initialization and supports a more efficient convergence to concavities.

Ng et al. [105] present a medical image segmentation that uses a feature-based GVF snake. The iteration is stopped once the accuracy is sufficient by exploiting image features. Zhao et al. [106] have improved the dynamic GVF force field and introduced a strategy of deformable contour knots for a B-spline based model.

4.7.2.6 Omnidirectional Displacements

When working with deformable surfaces, forces are commonly directed along a line, usually the surfaces local normal. Kainmueller et al. [107] have proposed omnidirectional displacements for deformable surfaces (ODDS) that consider a sphere around each vertex. By doing so, a global optimization can be performed. This technique has been proven to be useful in regions of high curvature, e.g. tips. They have also proposed a hybrid approach, fast ODDS to overcome the high memory and runtime requirements.

4.7.3 Interactive Forces

Image artifacts, different protocols and implants can cause problems in automated segmentation of medical images. In a clinical environment, operators can provide guidance to the deformable model to overcome these problems. The so called interactive forces provide a link between real-time user input and model iteration.

Kass et al. [20] have proposed two interactive forces. Spring forces are designed to pull the model in the direction of a point p. Their strength is proportional to the distance from p:

$$F_{\text{spring}}(x) = \alpha_{\text{s}}(p - x) \tag{4.21}$$

The opposite effect can be achieved using volcano forces. They push a model away from a point p:

$$F_{\text{volcano}}(x) = \alpha_{\text{v}} \frac{r}{|r|^3} \tag{4.22}$$

with $r = x - p$. Interaction forces often are only computed for a small neighborhood to reduce computational costs. When using all points the complexity is of order $O(n^2)$, while a small neighborhood m with $m \ll n$ can reduce the complexity to order $O(n \cdot m)$.

4.8 Initialization

All the previously presented approaches for segmentation require the placement of an initial model in the proximity of the desired boundaries. In this section we will present several possible approaches: manual and landmark-based initialization as well as automatic methods using the general Hough transform and atlas registration.

4.8.1 Manual Initialization

A simple approach to initialization is to ask the user to place the model manually. This can be done by using several interaction tools such as the mouse, keyboard or haptic devices. The manual placement is a time-consuming process and requires an experienced user, depending on the quality of the images. Nonetheless, this approach is not usable for large-scale applications. It also reduces the reproducibility, as the results often depend on the initial model and expertise of the user.

4.8.2 Landmarks

The use of landmarks is an extension of the manual approach. Instead of translating and scaling the whole model, the user selects a set of strong landmarks in the image and the initial model is automatically adjusted to obtain the best fit. In this way, the user input and hence the margin of error can be significantly reduced. Landmarks should be positioned at significant areas that can be easily detected in the image. Examples would be areas of high curvature, e.g. a fissure in a bone, or a measurable location, e.g. the middle of the femural shaft. An initialization of a model using seeds has been proposed by Neuenschwander et al. [108]. The correct scaling and positioning of the model has to be determined from the seeds. This warping can be done using the Thin Plate Spine (TPS) transform. If the number of landmarks is very small and not sufficient for a confident pose estimation, different positions can be evaluated using a cost function that incorporates a penalty based on image properties. An example for that can be found in Ref. [10].

Using landmarks at key anatomical positions allows the invocation of prior knowledge. Other approaches extend landmarks with inclusion of spatial knowledge. For

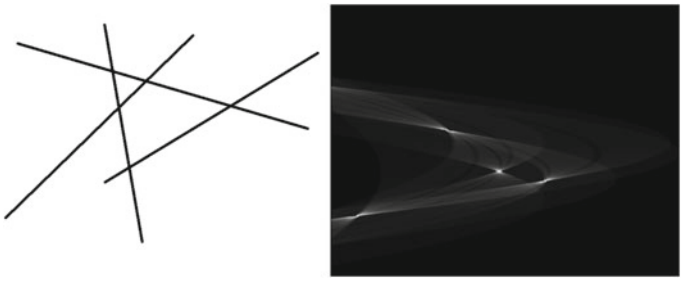

Fig. 4.6 Example of the Hough Transform for lines. Original image (*left*) and voting space (*right*)

example, Fripp et al. [109] proposed a cartilage initialization system that exploits prior knowledge of the bone location.

4.8.3 General Hough Transform

In 1962, Hough [110] was granted a patent for *Method and Means for Recognizing Complex Patterns*. His approach uses templates and a voting space. For each identified image feature all templates create votes for possible poses. The highest vote represents a set of parameters of the best corresponding template. An example with original image and voting space is shown in Fig. 4.6. Illingworth and Kittler [111] have presented a review of the Hough transform and Khoshelham [112] has demonstrated an extension to 3D object detection.

The general Hough transform can be used for the initialization of deformable models. Van der Glas et al. [113] have demonstrated a method to detect ball joints. Seim et al. have proposed approaches for the hip [114] and the knee [115]. In 2010, Ruppertshofen et al. [116] have proposed a discriminative approach for lower extremities, which has been extended to a multi-level scheme [117].

4.8.4 Atlas Registration

Rather than using a reference model, a reference image (called atlas) can be used. The atlas contains a specific initialization. A registration step tries to find the transform T, that matches the reference image to the actual image. T can then be used to transform the initialization to the actual image.

Atlas-based initialization requires a registration process, e.g. using ElastiX [118]. Another requirement is the subjects pose, which has to be same in each image to get satisfactory results. Examples for atlas registration based initialization have been proposed by Fripp et al. [119, 120].

4.9 Conclusion

We have presented an overview of the current state of deformable models in medical image segmentation. They are a powerful tool for the given image conditions and therefore play an important role. We have surveyed current snakes and level sets methods that are examples for continues shape representation. These usually two-dimensionally used approaches achieve good results with high computational costs. However, they are highly dependent on a good initialization. Contrary to snakes, level sets are able to adapt to different topology automatically. Discrete deformable models are three-dimensional approaches, which can be represented as particle systems or through different mesh types. They can also be based on several physical foundations. They provide great flexibility and haven proven useful in many cases. Depending on the structure of interest, deformable models have to be carefully configured and parameterized. An extension to deformable models is the incorporation of prior knowledge to make them more robust in complex image conditions. These knowledge-based deformable models exploit prior knowledge on shape and appearance. They need a large training base and complex training but are very robust. We have presented several forces that cover the tools needed for creating deformable models. We have also extended the view by presenting other deformable model approaches. Lastly we have presented the main approaches to the important initialization problem.

A challenge for future research is the development of more general approaches. Although very sophisticated and robust, deformable model applications are tuned to specific organs and well-defined image conditions. Knowledge-based models for example have to be trained with a large database of examples and image forces like the intensity profiles have to be recreated if imaging sequences are modified. Depending on the chosen approach, the initialization can be a critical task. Speed and robustness still can be improved.

Acknowledgments This work has been funded by the EU FP7 Marie Curie Initial Training Network project MultiScaleHuman (http://multiscalehuman.miralab.ch) under Grant No. 289897.

References

1. Elnakib, A., Gimel, G., Suri, J. J., El-baz, A., & Gimel'farb, G. (2011). Medical image segmentation: A brief survey. In A. S. El-Baz, U. R. Acharya, A. F. Laine, & J. S. Suri (Eds.), *Medical image segmentation* (pp. 1–39). New York: Springer.
2. Terzopoulos, D., Platt, J., Barr, A., Fleischer, K., Terzopoulost, D., & Fleischert, K. (1987). Elastically deformable models. *SIGGRAPH Computer Graphics*, *21*(4), 205–214.
3. Nealen, A., Müller, M., Keiser, R., Boxerman, E., & Carlson, M. (2006). Physically based deformable models in computer graphics. *Computer Graphics Forum*, *25*(4), 809–836.
4. Baraff, D., & Witkin, A. (1998). Large steps in cloth simulation. In *Proceedings of the 25th Annual Conference on Computer Graphics and Interactive Techniques—SIGGRAPH '98*, New York, USA, 1998 (pp. 43–54). New York: ACM Press.

5. Mortensen, E. N., & Barrett, W. A. (1995). Intelligent scissors for image composition. *Proceedings of the 22nd Annual Conference on Computer Graphics and Interactive Techniques SIGGRAPH 95*, *84602*(801), 191–198.
6. DeCarlo, D., & Metaxas, D. (2000). Optical flow constraints on deformable models with applications to face tracking. *International Journal of Computer Vision*, *38*(2), 99–127.
7. Zhang, Z., Tan, T., Huang, K., & Wang, Y. (2012). Three-dimensional deformable-model-based localization and recognition of road vehicles. *IEEE Transactions on Image Processing*, *21*(1), 1–13.
8. Deserno, T. M., Liao, W., Metzger, M. C., Kleiner, M. E. H., & Schulze, D. (2009). Ein routine-integrierbares Planungswerkzeug zur operativen Rekonstruktion der Orbita. *GMS Medizinische Informatik, Biometrie und Epidemiologie*, *5*(3), 1–9.
9. Heimann, T., Morrison, B., Styner, M., Niethammer, M., & Warfield, S. (2010). Segmentation of knee images: A grand challenge. In *Proceedings of MICCAI Workshop on Medical Image Analysis for the Clinic*, 2010, pp. 207–214.
10. Schmid, J. (2011). Knowledge-based deformable models for medical image analysis, Ph.D. Thesis, University of Geneva, Switerzerland.
11. Snel, J. G., Venema, H. W., & Grimbergen, C. A. (2002). Deformable triangular surfaces using fast 1-D radial Lagrangian dynamics-segmentation of 3-D MR and CT images of the wrist. *IEEE Transactions on Medical Imaging*, *21*(8), 888–903.
12. Rifai, H., Bloch, I., Hutchinson, S., Wiart, J., & Garnero, L. (2000). Segmentation of the skull in MRI volumes using deformable model and taking the partial volume effect into account. *Medical Image Analysis*, *4*(3), 219–233.
13. Meier, U., López, O., Monserrat, C., Juan, M. C., & Alcañiz, M. (2005). Real-time deformable models for surgery simulation: A survey. *Computer Methods and Programs in Biomedicine*, *77*(3), 183–197.
14. Marchal, M., Allard, J., Duriez, C., & Cotin, S. (2008). Towards a framework for assessing deformable models in medical simulation. In F. Bello & P. Edwards (Eds.), *Biomedical simulation, lecture notes in computer science* (pp. 176–184). Berlin/Heidelberg: Springer.
15. McInerney, T., & Terzopoulos, D. (1996). Deformable models in medical image analysis: A survey. In *Proceedings of the Workshop on Mathematical Methods in Biomedical Image Analysis 1996* (vol. 1, pp. 171–180). New York: Elsevier.
16. Montagnat, J., Delingette, H., & Ayache, N. (2001). A review of deformable surfaces: Topology, geometry and deformation. *Image and Vision Computing*, *19*(14), 1023–1040.
17. Hegadi, R., Kop, A., & Hangarge, M. (2010). A survey on deformable model and its applications to medical imaging. *IJCA*. Special Issue on RTIPPR, *2*, 64–75.
18. Moore, P., & Molloy, D. (2007). A survey of computer-based deformable models. *International Machine Vision and Image Processing Conference IMVIP 2007*, pp. 55–66.
19. Jain, A. K., Zhong, Y., & Dubuisson-Jolly, M. P. (1998). Deformable template models: A review. *Signal Processing*, *71*(2), 109–129.
20. Kass, M., Witkin, A., & Terzopoulos, D. (1988). Snakes : Active contour models. *International Journal of Computer Vision*, *331*(4), 321–331.
21. Leymarie, F., & Levine, M. D. (1993). Tracking deformable objects in the plane using an active contour model. In *Proceedings of IEEE International Conference on Multimedia Computing and Systems* (vol. 15, pp. 617–634).
22. Peterfreund, N. (1999). Robust tracking of position and velocity with Kalman snakes. *IEEE Transactions on Pattern Analysis and Machine Intelligence*, *21*(6), 564–569.
23. Bascle, B., & Deriche, R. (1993). Stereo matching, reconstruction and refinement of 3D curves using deformable contours. In *Proceedings of 4th International Conference on Computer Vision 1993*, Berlin, pp. 421–430.
24. Terzopoulos, D., & Fleischer, K. (1988). Deformable models. *The Visual Computer*, *4*(6), 306–331.
25. McInerney, T., & Terzopoulos, D. (1995). A dynamic finite element surface model for segmentation and tracking in multidimensional medical images with application to cardiac 4D image analysis. *Computerized Medical Imaging and Graphics*, *19*(1), 69–83.

26. Durikovic, R., Kaneda, K., & Yamashita, H. (1995). Dynamic contour : A texture approach and contour operations. *The Visual Computer*, *11*(6), 277–289.
27. Xu, C., & Prince, J. L. (1998). Snakes, shapes, and gradient vector flow. *IEEE Transactions on Image Processing*, *7*(3), 359–369.
28. Cheng, J., Foo, S. W., & Krishnan, S. M. (2004). Directional gradient vector flow for snakes. In *Proceedings of the 4th IEEE International Symposium on Signal Processing and Information Technology 2004* (pp. 318–321). IEEE.
29. Ivins, J., & Porrill, J. (1994). Statistical snakes : Active region models. *Proceedings of the British Machine Vision Conference*, pp. 377–386.
30. Mitrea, A. I., Badea, R., Mitrea, D., Nedevschi, S., Mitrea, P., Ivan, D. M., et al. (2012). Iterative methods for obtaining energy-minimizing parametric snakes with applications to medical imaging. *Computational and Mathematical Methods in Medicine*, *2012*, 918510.
31. Wang, C., Guo, X., Yao, L., Li, K., & Jin, Z. (2007). A practical method for muscles extraction and automatic segmentation of leg magnetic resonance images. In *IEEE/ICME International Conference on Complex Medical Engineering 2007 (CME 2007)*, May 2007, pp. 885–890.
32. Kauffmann, C., Gravel, P., Godbout, B., Gravel, A., Beaudoin, G., Raynauld, J. P., et al. (2003). Computer-aided method for quantification of cartilage thickness and volume changes using MRI: Validation study using a synthetic model. *IEEE Transactions on Biomedical Engineering*, *50*(8), 978–988.
33. Ip, H. H. S., & Shen, D. (1998). An affine-invariant active contour model (AI-snake) for model-based segmentation. *Image and Vision Computing*, *16*, 135–146.
34. Vemuri, B. B., & Guo, Y. (1999). Hybrid geometric active models for shape recovery in medical image. In *Proceedings of Information Processing in Medical Imaging (IPMI '99)*, pp. 112–125.
35. McInerney, T., & Terzopoulos, D. (2000). T-snakes: Topology adaptive snakes. *Medical Image Analysis*, *4*(2), 73–91.
36. Dias, A. V., & Furuie, S. S. (2001). Refinement of T-snakes using adaptive parameters. In *Proceedings 14th Brazilian Symposium on Computer Graphics and Image Processing* (p. 387). Los Alamitos: IEEE Computer Society.
37. Oliveira, A., Ribeiro, S., Esperanca, C., & Giraldi, G. (2005). Loop snakes: The generalized model. *In Ninth International Conference on Information Visualisation IV05,* pp. 975–980.
38. Osher, S., & Sethian, J. A. (1988). Fronts propagating with curvature-dependent speed: Algorithms based on Hamilton–Jacobi formulations. *Journal of Computational Physics*, *79*(1), 12–49.
39. Yushkevich, P. A., Piven, J., Hazlett, H. C., Smith, R. G., Ho, S., Gee, J. C., et al. (2006). User-guided 3D active contour segmentation of anatomical structures: Significantly improved efficiency and reliability. *NeuroImage*, *31*(3), 1116–1128.
40. Friese, K. I., Blanke, P., & Wolter, F. E. (2011). YaDiVan open platform for 3D visualization and 3D segmentation of medical data. *The Visual Computer*, *27*(2), 129–139.
41. Mumford, D. H. U., & Shah, J. N. U. (1989). Optimal approximations by piecewise smooth functions and associated variational problems. *Communications on Pure and Applied Mathematics*, *XLII*, 577–685.
42. Zhao, H. K., Chan, T., Merriman, B., & Osher, S. (1996). A variational level set approach to multiphase motion. *Journal of Computational Physics*, *127*(1), 179–195.
43. Ciarlet, P. G., Iserles, A., Kohn, R. V., & Wright, M. H. (Eds.). (1999). *Level set methods and fast marching methods: Evolving interfaces in computational geometry, fluid mechanics, computer vision, and materials science*. Cambridge monograph on applied and computational Mathematics. Cambridge: Cambridge University Press.
44. Chan, T. F., & Vese, L. A. (2001). Active contours without edges. *IEEE Transactions on Image Processing*, *10*(2), 77–266.
45. Zhang, Y., Matuszewski, B. J., Shark, L. K., & Moore, C. J. (2008). Medical image segmentation using new hybrid level-set method. In *5th International Conference BioMedical Visualization Information Visualization in Medical and Biomedical Informatics 2008* (vol. 26, pp. 71–76). IEEE.

46. Yeo, S.Y., Xie, X., Sazonov, I., & Nithiarasu, P. (2009). Geometric potential force for the deformable model. In *Proceedings of the British Machine Vision Conference* (pp. 99.1–99.11). BMVA Press.
47. Caselles, V., Kimmel, R., & Sapiro, G. (1995). Geodesic active contours. In *Proceedings of IEEE International Conference on Computer Vision* (vol. 22, pp. 61–79). IEEE Computer Society Press.
48. Unger, M., Pock, T., & Bischof, H. (2008). Continuous globally optimal image segmentation with local constraints. In J. Pers (Ed.), *Proceedings of the Computer Vision Winter Workshop 2008*.
49. Adalsteinsson, D., & Sethian, J. A. (1995). A fast level set method for propagating interfaces. *Journal of Computational Physics*, *118*(2), 269–277.
50. Whitaker, R. T. (1998). A level-set approach to 3D reconstruction from range data. *International Journal of Computer Vision*, *29*(3), 203–231.
51. Shi, Y., & Karl, W. C. (2005). A fast level set method without solving PDEs. In *Proceedings of IEEE International Conference on Acoustics, Speech, and Signal Processing (ICASSP '05)*, 2005 (vol. 2, pp. 97–100).
52. Meziou, L., Histace, A., Precioso, F., Matuszewski, B., & Carreiras, F. (2012). Fractional entropy based active contour segmentation of cell nuclei in actin-tagged confocal microscopy images. In *Proceedings of the 16th MIUA Conference*, p. accepted. Swansea, Royaume-Uni, Jul 2012.
53. Kainmueller, D., Lamecker, H., Zachowa, S., Heller, M., & Hege, H. C. (2008). Multi-object segmentation with coupled deformable models. In *Proceedings of the 12th Annual Conference on Medical Image Understanding and Analysis 2008*.
54. Bredno, J., Lehmann, T. M. T., & Spitzer, K. (2003). A general discrete contour model in two, three, and four dimensions for topology-adaptive multichannel segmentation. *IEEE Transactions on Pattern Analysis and Machine Intelligence*, *25*(5), 550–563.
55. Gilles, B., & Magnenat-Thalmann, N. (2010). Musculoskeletal MRI segmentation using multi-resolution simplex meshes with medial representations. *Medical Image Analysis*, *14*(3), 291–302.
56. Cohen, I., Cohen, L. D., & Ayache, N. (1992). Using deformable surfaces to segment 3-D images and infer differential structures. *Comp Vision Graphics and Image Understanding*, *56*(2), 242–263.
57. Cohen, L., & Cohen, I. (1993). Finite-element methods for active contour models and balloons for 2-D and 3-D images. *IEEE Transactions on Pattern Analysis and Machine Intelligence*, *15*(11), 1131–1147.
58. Terzopoulos, D., & Metaxas, D. (1991). Dynamic 3D models with local and global deformations: deformable superquadrics. *IEEE Transactions on Pattern Analysis and Machine Intelligence*, *13*(7), 703–714.
59. Lorensen, W. E., & Cline, H. E. (1987). Marching cubes: A high resolution 3D surface construction algorithm. *Computer*, *21*(4), 163–169.
60. Miller, J. V., Breen, D. E., Lorensen, W. E., O'Bara, R. M., & Wozny, M. J. (1991). Geometrically deformed models: A method for extracting closed geometric models form volume data. *SIGGRAPH Computer Graphics*, *25*(4), 217–226.
61. Delingette, H. (1994). Simplex meshes: A general representation for 3D shape reconstruction. In *Computer Vision and Pattern Recognition 1994* (vol. 2214, pp. 856–857). IEEE Computer Society Press.
62. Delingette, H. (1999). General object reconstruction based on simplex meshes. *International Journal of Computer Vision*, *32*(2), 111–146.
63. Montagnat, J., & Delingette, H. (2005). 4D deformable models with temporal constraints: Application to 4D cardiac image segmentation. *Medical Image Analysis*, *9*(1), 87–100.
64. Gilles, B., Moccozet, L., & Magnenat-Thalmann, N. (2006). Anatomical modelling of the musculoskeletal system from MRI. In *Proceeings of International Conference on Medical Image Computing and Computer Assisted Intervention (MICCAI06)*, Oct 2006 (vol. 4190, pp. 289–296).

65. Lachaud, J. O., & Montanvert, A. (1999). Deformable meshes with automated topology changes for coarse-to-fine three-dimensional surface extraction. *Medical Image Analysis*, *3*(2), 187–207.
66. Pons, J. P., & Boissonnat, J. D. (2007). Delaunay deformable models: Topology-adaptive meshes based on the restricted delaunay triangulation. In *2007 IEEE Conference on Computer Vision and Pattern Recognition* (vol. 13, pp. 384–394). IEEE.
67. Gilles, B. (2007). Anatomical and kinematical modelling of the musculoskeletal system from MRI. Phd Thesis, University of Geneva, Aug 2007.
68. Szeliski, R., & Tonnesen, D. (1992). Surface modeling with oriented particle systems. *ACM SIGGRAPH Computer Graphics*, *26*(2), 185–194.
69. Lombardo, J. C. (2004). *Modélisation dobjets déformables avec un système de particules orientées*. Phd, Université Joseph Fourier, Grenoble.
70. Cootes, T. F., Hill, A., Taylor, C. J., & Haslam, J. (1994). The use of active shape models for locating structures in medical images. *Image and Vision Computing*, *12*(6), 355–366.
71. Cootes, T. F., Taylor, C. J., Cooper, D. H., & Graham, J. (1995). Active shape models—Their training and application. *Computer Vision and Image Understanding*, *61*(1), 38–59.
72. Yushkevich, P. A., Zhang, H., & Gee, J. C. (2005). Statistical modeling of shape and appearance using the continuous medial representation. *Medical Image Computing and Computer-Assisted Intervention*, *8*(Pt 2), 725–732.
73. Gower, J. C. (1975). Generalized procrustes analysis. *Psychometrika*, *40*(1), 33–51.
74. Pearson, K. (1901). On lines and planes of closest fit to systems of points in space. *Philosophical Magazine*, *2*(6), 559–572.
75. Everson, R., & Roberts, S. (2000). Inferring the eigenvalues of covariance matrices from limited, noisy data. *IEEE Transactions on Signal Processing*, *48*(7), 2083–2091.
76. Cootes, T. F., & Taylor, C. J. (1995). Combining point distribution models with shape models based on finite element analysis. *Image and Vision Computing*, *13*(5), 403–409.
77. Tölli, T., Koikkalainen, J., Lauerma, K., & Lötjönen, J. (2006). Artificially enlarged training set in image segmentation. *Medical Image Computing and Computer-Assisted Intervention*, *9*(Pt 1), 75–82.
78. Ginneken, B. V., Frangi, A. F., Staal, J. J., Bart, M., Romeny, H., Viergever, M. A., van Ginneken, B., & ter Haar Romeny, B. M. (2002). Active shape model segmentation with optimal features. *IEEE Transactions on Medical Imaging*, *21*(8), 924–933.
79. Lamecker, H., Kamer, L., Wittmers, A., Zachow, S., Schramm, A., Noser, H., & Hammer, B. (2007). A method for the three-dimensional statistical shape analysis of the bony orbit. *Proceedings of Computer Aided Surgery around the Head (CAS-H)*, pp. 2–5.
80. Cootes, T., Edwards, G., & Taylor, C. (1998). Active appearance models. In H. Burkhardt & B. Neumann (Eds.), *Computer Vision ECCV98, Lecture Notes in Computer Science* (vol. 1407, pp. 484–498). Berlin/Heidelberg: Springer.
81. Olabarriaga, S. D., Breeuwer, M., & Niessen, W. J. (2004). Multi-scale statistical grey value modelling for thrombus segmentation from CTA. In *Proceedings of MICCAI* (vol. 3216, pp. 467–474). Springer.
82. Shen, T., Li, H., & Huang, X. (2011). Active volume models for medical image segmentation. *IEEE Transactions on Medical Imaging*, *30*(3), 774–791.
83. Staib, L. H., & Duncan, J. S. (1992). Boundary finding with parametrically deformable models. *IEEE Transactions on Pattern Analysis and Machine Intelligence*, *14*(11), 1061–1075.
84. Székely, G., Kelemen, A., Brechbühler, C., & Gerig, G. (1996). Segmentation of 2-D and 3-D objects from MRI volume data using constrained elastic deformations of flexible Fourier contour and surface models. *Medical Image Analysis*, *1*(1), 19–34.
85. Horowitz, B., & Pentland, A. (1991). Recovery of non-rigid motion and structure. *Proceedings of IEEE Computer Society Conference on Computer Vision and Pattern Recognition*, 1991, pp. 325–330.
86. Bardinet, E., Cohen, L. D., & Ayache, N. (1998). A parametric deformable model to fit unstructured 3D data. *Computer Vision and Image Understanding*, *71*(1), 39–54.

87. Ababneh, S. Y., Prescott, J. W., & Gurcan, M. N. (2011). Automatic graph-cut based segmentation of bones from knee magnetic resonance images for osteoarthritis research. *Medical Image Analysis*, *15*(4), 438–448.
88. Zhou, J., Ye, M., & Zhang, X. (2010). Graph cut segmentation with automatic editing for Industrial images. In *2010 International Conference on Intelligent Control and Information Processing*, Aug 2010 (pp. 633–637). IEEE.
89. Zhu-Jacquot, J. Z. J. J., & Zabih, R. (2007). Graph cuts segmentation with statistical shape priors for medical images. In *3rd International IEEE Conference on Signal Image Technologies and Internet Based System 2007* (pp. 631–635). IEEE.
90. El-Zehiry, N., & Elmaghraby, A. (2008). Graph cut based deformable model with statistical shape priors. In *19th International Conference on Pattern Recognition 2008* (pp. 1–4). IEEE.
91. Chen, X., Udupa, J. K., Bagci, U., Zhuge, Y., & Yao, J. (2012). Medical image segmentation by combining graph cuts and oriented active appearance models. *IEEE Transactions on Image Processing*, *21*(4), 2035–2046.
92. Vineet, V., & Narayanan, P. J. (2008). CUDA cuts: Fast graph cuts on the GPU. In *IEEE Computer Society Conference on Computer Vision and Pattern Recognition Workshops 2008 (CVPRW '08)*, Jun 2008, pp. 1–8.
93. Delong, A., & Boykov, Y. (2008). A scalable graph-cut algorithm for N-D grids. In *IEEE Conference on Computer Vision and Pattern Recognition 2008 (CVPR 2008)*, Jun 2008, pp. 1–8.
94. Lee, S., Shim, H., Park, S. H., Yun, I. D., & Lee, S. U. (2010). Learning local shape and appearance for segmentation of knee cartilage in 3D MRI. In *Proceedings of the 4th Medical Image Analysis for the Clinic—A Grand Challenge workshop (MICCAI 2010)*.
95. Cohen, L. D. L. (1991). On active contour models and balloons. *CVGIP: Image understanding*, *53*(2), 211–218.
96. Shen, T., Huang, X., Li, H., Kim, E., Zhang, S., & Huang, J. (2011). A 3D Laplacian-driven parametric deformable model. In *IEEE International Conference on Computer Vision (ICCV) 2011*, pp. 279–286.
97. Behiels, G., Maes, F., Vandermeulen, D., & Suetens, P. (2002). Evaluation of image features and search strategies for segmentation of bone structures in radiographs using Active Shape Models. *Medical Image Analysis*, *6*(1), 47–62.
98. Cootes, T. F., & Taylor, C. J. (2001). *Statistical models of appearance for computer vision*. World Wide Web Publication February.
99. Chung, F., & Delingette, H. (2009). Multimodal prior appearance models based on regional clustering of intensity profiles. *Medical Image Computing and Computer-Assisted Intervention*, *12*(Pt 2), 1051–1058.
100. Terzopoulos, D., Witkin, A., & Kass, M. (1987). Symmetry-seeking models and 3D object reconstruction. *International Journal of Computer Vision*, *221*, 211–221.
101. Danielsson, P. (1980). Euclidean distance mapping. *Computer Graphics and Image Processing*, *14*(3), 227–248.
102. Borgefors, G. (1984). Distance transformations in arbitrary dimensions. *Computer Vision Graphics and Image Processing*, *27*(2), 321–345.
103. Sapiro, G. (1995). Geometric partial differential equations in image analysis: Past, present, and future. In *Proceedings of International Conference on Image Processing* (vol. 3, pp. 1–4). IEEE Computer Society Press.
104. Adalsteinsson, D., & Sethian, J. A. (1999). The fast construction of extension velocities in level set methods. *Journal of Computational Physics*, *148*(1), 2–22.
105. Ng, H. P., Foong, K. W. C., Ong, S. H., Goh, P. S., & Nowinski, W. L. (2007). Medical image segmentation using feature-based GVF snake. In *Engineering in Medicine and Biology Society, 2007. EMBS 2007. 29th Annual International Conference of the IEEE*, Jan 2007 (vol. 2007, pp. 800–803).
106. Zhao, B., Cheng, S., & Zhang, X. (2011). A new adaptive deformable model using gradient vector flow. *Integration The Vlsi Journal*, *134*, 472–482.

107. Kainmueller, D., Lamecker, H., Heller, M. O., Weber, B., Hege, H. C., & Zachow, S. (2013). Omnidirectional displacements for deformable surfaces. *Medical Image Analysis*, *17*(4), 429–441.
108. Neuenschwander, W., Fua, P., Székely, G., & Kübler, O. (1997). Velcro surfaces: Fast initialization of deformable models. *Computer Vision and Image Understanding*, *65*(2), 237–245.
109. Fripp, J., Crozier, S., Warfield, S., & Ourselin, S. (2005) Automatic initialization of 3D deformable models for cartilage segmentation. In *Digital Image Computing Techniques and Applications DICTA05*, 2005 (pp. 513–518). IEEE Computer Society.
110. Hough, P. V. C. (1962). Method and means for recognizing complex patterns. US Patent US3069654 A.
111. Illingworth, J., & Kittler, J. (1988). A survey of the Hough transform. *Computer Vision, Graphics, and Image Processing*, *44*, 87–116.
112. Khoshelham, K. (2007). Extending generalized Hough transform to detect 3D objects in laser range data. *ISPRS Workshop on Laser Scanning and SilviLaser 2007*, 12–14 September 2007, Espoo, Finland, pp. 206–210.
113. van der Glas, M., Vos, F. M., Botha, C. P., & Vossepoel, A. M. (2002). Determination of position and radius of ball joints. In *Proceedings of SPIE 4684, Medical Imaging 2002: Image Processing* (vol. 157. pp. 1–7).
114. Seim, H., Kainmueller, D., Heller, M., Lamecker, H., Zachow, S., & Hege, H. C. (2008). Automatic segmentation of the pelvic bones from CT data based on a statistical shape model. In *Eurographics Workshop on Visual Computing for Biomedicine (VCBM)*, 2008, pp. 93–100.
115. Seim, H., Kainmueller, D., Lamecker, H., Bindernagel, M., Malinowski, J., & Zachow, S. (2010). Model-based auto-segmentation of knee bones and cartilage in MRI data. In *Proceedings of the 4th Medical Image Analysis for the Clinic—A Grand Challenge workshop (MICCAI 2010)*.
116. Ruppertshofen, H., Lorenz, C., Schmidt, S., Beyerlein, P., Salah, Z., Rose, G., et al. (2010). Discriminative generalized Hough transform for localization of joints in the lower extremities. *Computer Science—Research and Development*, *26*(1), 97–105.
117. Ruppertshofen, H., Künne, D., Lorenz, C., Schmidt, S., Beyerlein, P., Rose, G., & Schramm, H. (2011). Multi-level approach for the discriminative generalized Hough transform. In *CURAC 2011: 10. Jahrestagung der Deutschen Gesellschaft für Computer-und Roboterassistierte Chirurgie*, Magdeburg, Germany, 15–16 September 2011.
118. Klein, S., Staring, M., & Pluim, J. P. W. (2007). Evaluation of optimization methods for nonrigid medical image registration using mutual information and B-splines. *IEEE Transactions on Image Processing*, *16*(12), 2879–2890.
119. Fripp, J., Warfield, S. K., Crozier, S., & Ourselin, S. (2006). Automatic segmentation of the knee bones using 3D active shape models. In *18th International Conference on Pattern Recognition 2006 (ICPR 2006)*, pp. 167–170.
120. Fripp, J., Bourgeat, P., Crozier, S., & Ourselin, S. (2007). Segmentation of the bones in MRIs of the knee using phase, magnitude, and shape information. *Academic Radiology*, *14*(10), 1201–1208.

Chapter 5
Visualization and User Interaction Methods for Multiscale Biomedical Data

Ricardo Manuel Millán Vaquero, Jan Rzepecki, Karl-Ingo Friese and Franz-Erich Wolter

5.1 Introduction

Biological processes in the human body interact continuously in order to sustain physiological function. A complete study of a phenomenon in human physiology requires merging data from several measurements, not only from different domains of knowledge (chemistry, biology, physics, and medicine) but also across different spatiotemporal scales. As an example, a musculoskeletal disease of the human knee affecting the motion (behavior scale), can be seen on a CT or MRI scan (organic scale) and has its cause on cellular or even molecular level. To simulate the related processes, different temporal scales have to be taken into account as well. Those time scales range from seconds on the behavioral level to microseconds on the cellular scale.

However, merging of data alone is not enough to obtain valuable knowledge. Visualization that generates images from these measurements is necessary to help scientists understanding complex relations between modalities and spatiotemporal scales. Multiscale visualization deals with the question: "How can visualization help in extracting information from several scales that cannot be attained or understood by traditional techniques?" More specifically, multiscale visualization will also support extracting information that cannot be obtained or understood from evaluating data from a single scale alone or even from different scales without having the flexibility

R. M. Millán Vaquero (✉) · J. Rzepecki · K.-I. Friese · F.-E. Wolter
Welfenlab, Division of Computer Graphics, Leibniz Universität Hannover,
Welfengarten 1, 30167 Hanover, Germany
e-mail: rmillan@welfenlab.de

J. Rzepecki
e-mail: jrzepecki@welfenlab.de

K.-I. Friese
e-mail: kif@welfenlab.de

F.-E. Wolter
e-mail: few@welfenlab.de

N. Magnenat-Thalmann et al. (eds.), *3D Multiscale Physiological Human*,
DOI: 10.1007/978-1-4471-6275-9_5,

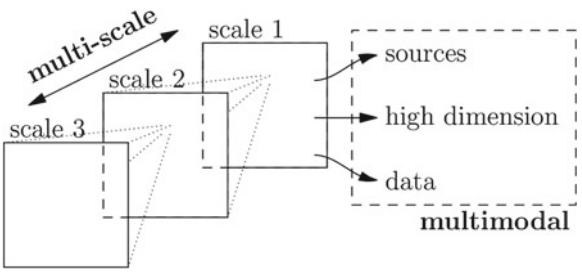

Fig. 5.1 Multimodal and multiscalar requirements in the visualization of biomedical data

to match and compare the data according to criteria defined by the scientist using the system.

Visualization is the primary channel through which biomedical data is communicated. In this work, interaction is a way to control the flow of this channel. It allows the user to decide in real-time on visualization contents that are to be presented. The user queries for data through interaction methods, and receives semantic meaningful results through visualization. Thus, visualization combined with and controlled by user interaction constitutes in the given context the complete tool for biomedical data exploration.

The next section discusses the complexity of biomedical data and the requirements of a multiscale environment. The third section proposes current lines of work to design an efficient scientist-centric visualization tool. Current multiscale visualization techniques and the foundation of the Human Computer Interaction (HCI) field are described in the fourth section. Finally, an overview of strategies and lines of work on multiscale visualization and interaction with biomedical data is given in the last section.

5.2 Visualization of Biomedical Data

The presentation of image data has become more challenging due to the increasing complexity of biomedical datasets. Here it is necessary to integrate all data from different modalities in the same reference system for a specific domain of knowledge (multimodal requirement). Furthermore, it is also necessary to consider the merging of several domains across scales (multiscalar requirement). Both of the aforementioned requirements are crucial in the biomedical environment as illustrated in Fig. 5.1.

The complexity of data is due to the following factors:

- **Variety of sources:** Biomedical data can be acquired by a broad range of modalities, e.g. CT, MRI, motion capturing or microscopy. Even sources of the same modality might not share a common standard. Currently, no standardization of formats in microscopy imaging exists. This leads to a loss of metadata during format conversion, or problems by organizing images from time-lapse experiments [1].

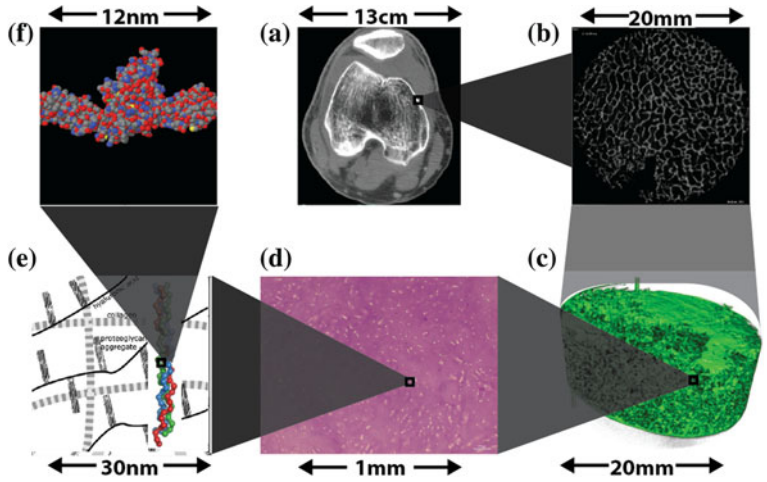

Fig. 5.2 Example of a knee joint multiscale dataset: (**a**) Cross-section of knee CT scan, (**b**) micro-CT slice of cartilage tissue, (**c**) 3D reconstruction of micro-CT scan of cartilage tissue, (**d**) histological image of cartilage, (**e**) schematic of extracellular components of cartilage tissue, (**f**) JMol visualization of aggrecan particle [7]. Images (**b**, **d**) and dataset (**c**) courtesy of 3B's Research Group. Dataset (**a**) courtesy of OsiriX Project [8]

- **High-dimensional image data:** Images carry more information in the form of additional dimensions (beside x- and y-resolution): e.g. time, space and channels. For instance, multispectral imaging (acquisition of spectrally resolved information at each pixel of an imaged scene) has become widely offered by microscopy manufacturers [2].
- **Amount of data:** Massive datasets from large scale experiments are difficult to manage due to the memory limitations. Even though the amount of available memory is increasing and out-of-core techniques have been developed [3], data memory requirements increase due to a more detailed data collection. This creates another challenge: representing datasets in a user intuitive manner is more difficult in relation to the increasing amount of data.

3D reconstruction and projection techniques are important when dealing with high-dimensional image data. This is illustrated in an example of tomographic mineralogical data analysis [4]. The software used (YaDiV [5]) allowed the experts from mineralogy to understand the geometric spatial structure intuitively, which was not observed in the respective 2D slice images used before. This investigation method can also be applied in the context of biomedical multiscale visualization, where reconstruction of micro-CT data of cartilage clearly exhibits complicated spatial tissue structures (Fig. 5.2c).

The *multimodal requirement* is born by this variety of data properties: multiple imaging sources provide vast amounts of data with heterogeneous dimensionality that should be merged. This requirement is needed to help physicians and scientists of the same domain to interpret this wide range of collected data [6].

For example, the extraction of information from both the hard and the soft tissues, acquired with different imaging modalities (CT and MRI), is essential in an anatomical study. It can be used to obtain information in many musculoskeletal clinical applications [9].

On the other hand, the *multiscalar requirement*, i.e. mixing information between scales, is needed because systems and pathologies in the human body are often hierarchical. Events on the cellular scale propagate upwards to the tissue or organ levels (Fig. 5.3). In some cases, a complete evaluation of medical risks can only be obtained if data from different scales is available [10].

For example, musculoskeletal diseases depend on several factors from multiple scales. For a complete study, information sources from different scales have to be considered. Specifically, studies of cartilage [11] have shown the impact of extracellular matrix (molecular) components on macroscale elements. The degradation of their nanoscale structure greatly influences the behavior of the tissue. This causes degeneration with age, injury, or diseases such as osteoarthritis. Sources of information range from cross-sectional histology at the cellular level, to body motion captures at the behavior scale, with additional data on the tissue and organ level in between (Fig. 5.2). Research projects as of [12–14] prove that the integration of multiscale data can lead to deeper understanding with practical consequences.

Another example is the study of the cardiovascular system. In [17], it is shown that the multiscale conception of the human blood circulation system, from molecular to organ level, can enhance the understanding of diseases, such as vascular atherogenesis.

Until today no major advances have been made in multiscale biomedical visualization, except in the domains of genomics and proteomics [18]. Hence, many authors called for efforts to create a multidisciplinary work in an integrated visualization [19, 20] of biological data: “the revolution in biological data visualization hasn’t started yet” [21].

5.3 Visualization Helps Understanding Science

Scientific visualization [22] presents numerous types of data that are inherently spatial in a visual form. It typically aims to represent data based on physical measurements e.g. obtained via acoustic waves (sonography) or often via electromagnetic waves including e.g. digital X-ray - and CT-imaging as well as light microscopy. Electronic microscopy uses electron beams to illuminate a specimen producing a magnified image. Most of the aforementioned imaging techniques already use sophisticated mathematical computations evaluating the respective physical measurements in an initial processing step needed (to prepare further steps) for presenting an appropriate visualization of the respective spatial data. Those computations may include methods from signal processing such as Hilbert transform for sonography imaging or Radon transform for CT-imaging [23, 24]. Further processing steps may use more mathematical methods e.g. for segmentation of CT-volume data separating

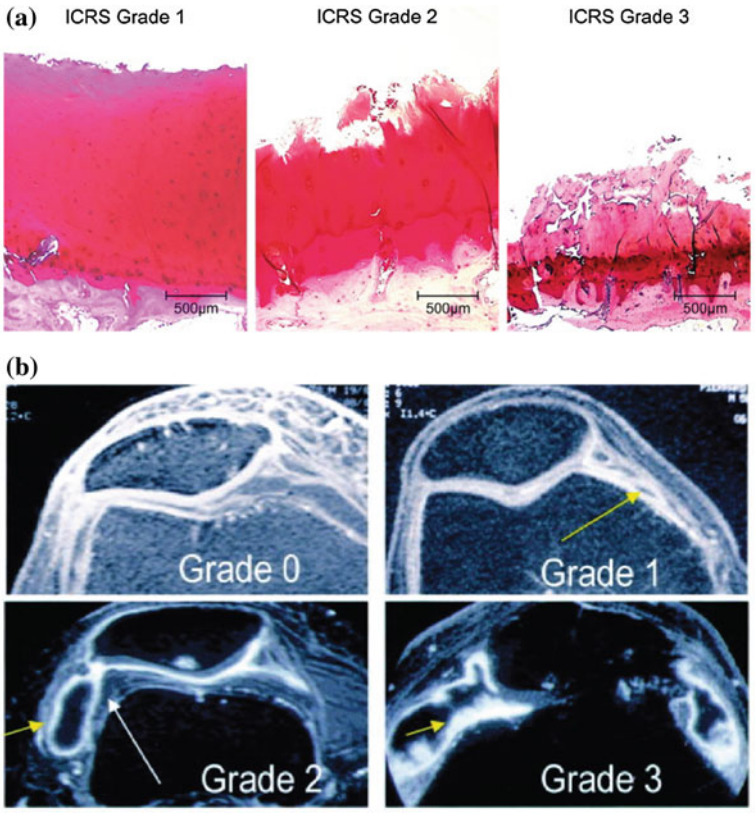

Fig. 5.3 Different grades of osteoarthritis disease obtained using (**a**) microscopic imaging [15] (**b**) MRI imaging [16], (Fig. 5.3a reprinted from *Osteoarthritis and cartilage*, vol. 13, no. 11, Kleemann, R. U. et al., Altered cartilage mechanics and histology in knee osteoarthritis: relation to clinical assessment (ICRS Grade), pp. 958–963, 2005, Copyright © 2005 OsteoArthritis Research Society International, with permission from Elsevier.) (Fig. 5.3b reprinted from *Arthritis & Rheumatism*, vol. 52, no. 11, Loeuille, D. et al. Macroscopic and microscopic features of synovial membrane inflammation in the osteoarthritic knee: correlating magnetic resonance imaging findings with disease severity, pp. 3492–3501, Copyright © 2005, American College of Rheumatology, with permission from Wiley Online Library.)

and indicating different biological structures. The initial computational evaluation of physical measurements for visualization of small scale molecular data [25] as well as the theoretical concepts and subsequent additional computations needed for processing the respective data may be even more complicated than they were in case of the preceding large scale visualization problems. The molecular visualization will result in visualizing certain structural aspects of molecules being consistent with our current scientific physico-chemical model of the respective molecular and atomic structures. One might still claim that the latter small scale visualization is

still attempting to present inherently spatial physico-chemical data in visual form. However the visualization obtained in this context reflects quite abstract model based information supposed to (indirectly) present some data and some properties of the respective molecules. One particular example of this is the visualization in Fig. 5.2f showing an artificial 3D-illustration of molecules illustrating e.g. the different atoms involved and their bondings.

One might go one step further, and could consider information visualization presenting (abstract semantic) data that is purposely *not* inherently of spatial origin, but is rather using a spatial representation of information (e.g. via trees or graphs) taking advantage of human's visual perception capable to see and understand a lot of information at once. Indeed the field named *information visualization* [26] is referring to this aforementioned type of visualization. The abstract nature of the latter information data requires the selection of an appropriate spatial representation and also the transformation of the information data into that spatial representation. Only after that transformation into a spatial presentation being graphically intuitively accessible it is possible to get benefit from this data as a means to amplify cognition.

Research in visualization is complex by itself, because it can be approached from different points of view. Many algorithms, techniques, and interactions have been explored and improved, but fundamental theories are insufficient [27, 28]. Many innovative biomedical tools provide visualization that integrates data from multiple sources, and even can interoperate with other tools or be embedded into web pages. An overview of examples has been presented in [29].

Although huge developments in visualization research have been done, only limited attention has been given to methodologies that provide understanding to users, because current approaches are not user-centric. Visualization depends on several aspects, such as the properties of the data, human physiological factors or physical characteristics of the display device. Furthermore, the use of visualization for understanding science should not make a distinction between scientific and information visualization [30, 31]. Figure 5.2f is a clear example where visualization is based both on physical measurements and abstract structure of molecule. Effective visual abstractions based on information visualization can help the representation of complex data in large-scale biomedical systems.

Thus, certain current lines of work have paid more attention to all these aspects than creating new techniques or algorithms. The design of a biomedical visualization tool should take into account the user experience (see Sect. 5.3.1) and the scientific meaning (see Sect. 5.3.2) as required. The features summarized in this section eliminate the gap between the visualization research community and the scientist as a user of a visualization system.

5.3.1 Improving the User Experience

Taking User Experience (UX) into account is an established procedure in the design of any man-machine-interface. These interfaces are not designed by the will of the

programmer (or company), but based on user feedback, e.g. if the user calls a certain feature of the software very frequently, it will get a hotkey.

Although UX could be applied universally to every visualization system, these features are gaining more importance in the scientific visualization context [27]. They consist of the following aspects:

Perception Factors

Users are part of the visualization process. Thus, human factors should be strongly considered in order to improve the visualization design. A faithful representation is not the only goal. Visualization can go beyond incorporating different features that human perception can decode; it might take advantages of the mechanisms in the human visual system.

- **Use of color:** Considerations of color theory (distance, linear separation, categories) can help choosing colors that facilitate understanding [32, 33]. As an example, red color can help to bring the user attention to an important feature, e.g. abnormalities in a biomedical scan.
- **Texture:** The use of perceptual texture elements also known as pexels, characterized by color, density, height, orientation or randomness can help users in shape perception [33].
- **Pre-attentive processing:** A limited group of visual features can be processed unconsciously by obtaining information from the visualization without the need for focused attention, independent of the number of data elements and the display size [32].

Other relevant aspects are shape, size, contour, sharpness and the use of 3D primitives [34]. However, these features together are not always favorable: a combination in a specific application should be evaluated.

Innovative and Standardized Representations

Visualizing new types of data or supporting new analysis tasks accelerates the appearance of innovative representations. The problem for the users is the lack of standards in representations. Walter et al. proposed both innovative and standardized representations [1]. Perception of information not only depends on how the visualization is designed, but also on the viewer's understanding of the given symbol system, e.g. hard tissues are represented with white color, soft tissues black. This results in two aspects:

- educating viewers may improve their data understanding (helping them to gain new insights) [35] and
- the usability could be enhanced by the adoption of standards in representation.

Frequent Evaluation During the Design Process

An important instrument for UX is user study [33]. These studies require a good experimental design, which is often difficult to achieve. A flawed experimental design (or wrong execution) may lead to results that are not helpful or—even worse—lead to wrong conclusions.

Working closely with users is the best way to develop a visualization tool. Thus, it is important that experts from the field (here: biomedical science) should participate in the studies. Is the visualization really giving the user the information he needs, e.g. at a certain simulation step? Or is it distracting him with too many aspects? In order to provide concrete usability to the visualization, a frequent evaluation has to be done during the design cycle, e.g. by testing isolated and specific usability hypotheses [34].

5.3.2 Bringing Scientific Meaning to Visualization

Visualization can be a powerful tool in the understanding of data and its context. In this chapter we will distinguish between *scientists* in general ("users"), who work on a specific topic and *visual researchers*, who research data visualization and closely work together with the general scientists. Scientists and visualization researchers try to give meaning to visual data and to gain systematic insights into many domains [1]. For this purpose, researchers of scientific visualization need to create field-centric tools focused on the scientific process of data analysis [27, 36].

Visualization Suitability for Data Analysis

Scientists make connections between the quantitative image description and its (biomedical) meaning. For this purpose, they need to focus on identifying meaningful features and on exploring potential relationships [1]. Visualization systems are suitable tools for exploratory data analysis. The visualization must be highly linked to the type of information, and show relevant image-based data in an intuitive manner, satisfying the scientists' inquiries.

Visualization software tools for analyzing data can be difficult to learn due to the complexity of data and task. To simplify the learning process visualization tools should focus on the following features:

- **Integration:** Merging of tools in the same program as long as it is useful. Elimination of unnecessary navigation reduces manual interaction times, however increasing application complexity too much can lead to user confusion.
- **Interoperability:** Complete integration in the same software is almost impossible. If a data format is not supported, it should at least be possible to process or convert

it with an external program, as described in [13]. Thus, interoperability requires clear software protocols and the support of common data formats.

- **Navigation aids:** In a complex (multiscale) visualization, it is easy to lose track of the current (spatiotemporal) position and context. Navigation aids like an overview map, colored floating labels or a zone tracker can help to keep track of the zone (or scale) the user is currently exploring [37]. The starting screen of such a system should enable the navigation across all the structures.

Most progress has been made in the field thanks to the incorporation of software usability principles. However, the achievement of these improvements has been a slow process; working on usability enhancements is less rewarding in science than inventing new ideas and approaches [21].

Challenges in Representing Small Structures

Biological data gathered on nanoscale level is often large in size and resolution. Additionally, it usually does not have a naturally understandable representation. Visualization of these structures creates interpretations of the measurements, which are not comparable with the physical object, as in the case with larger scale images. A set of different techniques involving volume rendering, isocontouring and dynamic mesh reduction should be used as a guide for visualizing and navigating these data-intensive structures [38]. In some cases images acquired on small scale level are blurred or have low-contrast. Representing this data requires a computationally sophisticated post-processing step to enhance image quality and extract structures in the segmentation process.

Realistic Representations

Additional data that improves the image quality in terms of visual experience can drastically increase understanding. Enhancing the quality of images is an ongoing research subject [1, 39]. For the purpose of prediction, customization of models should be available in order to be patient-specific [40]. Medical images should be visualized together with the representation of different structures by using specific techniques. For instance, texture based volume rendering can be used to give the user an overall impression of the measured data. Surface rendering as a method of providing extra-information for structures of interest (see also [41]) can support the spatial scene understanding (Fig. 5.4).

Use of the Scientific Method During the Design Process

In the real world, tool designers have limited sources of information about the application being designed. User opinions are rarely taken into consideration and technique

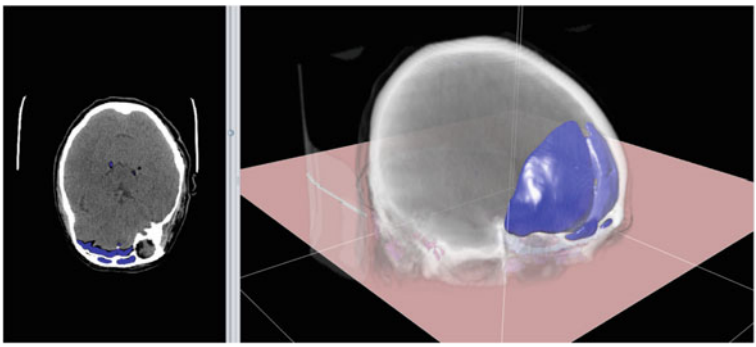

Fig. 5.4 Segment visualization in YaDiV [5], showing intracranial air after brain surgery

improvements are often not evaluated. During the design process, visualization researchers should use the scientific method (phenomena observation, hypothesis formulation, results prediction and evaluation) to prevent creating a toolset that is detached from the biomedical meaning [27].

Evaluation of Visualization Tool Design

Considering visualization as a technology, evaluation and validation are vital in order to provide effectiveness and efficiency. Wijk explains in [28] an economic model of visualization. The cost associated with using a visualization system depends on the user and the initial development. The user cost is related to the learning time required to use the new tool, to convert the user data to the system's format and to interpret the presented results. The high price of the initial development costs (i.e. to have a novel idea and to develop it) is the major factor. The researcher's process that tries to provide a visualization tool to a scientist in order to help him in the understanding of complex data is described in [28]. The state of the art review and the development of a new idea is not enough to achieve success. Thus, it is crucial to prepare a study on advantages and limitations before starting to work on a new visualization method. Wijk also states that "visualization is not good by definition" [28]. Designers should avoid visualizing information that could be extracted by automated analysis of data, and do not require direct human interpretation. Reusing existing visualization software can also be a viable solution.

5.4 Multiscale Visualization and Interaction

Multiscale visualization is necessary due to the division of science into domains, each investigating the nature on a specific spatiotemporal scale and working with its own type of data. This specialization can even prevent scientific progress if phenomena

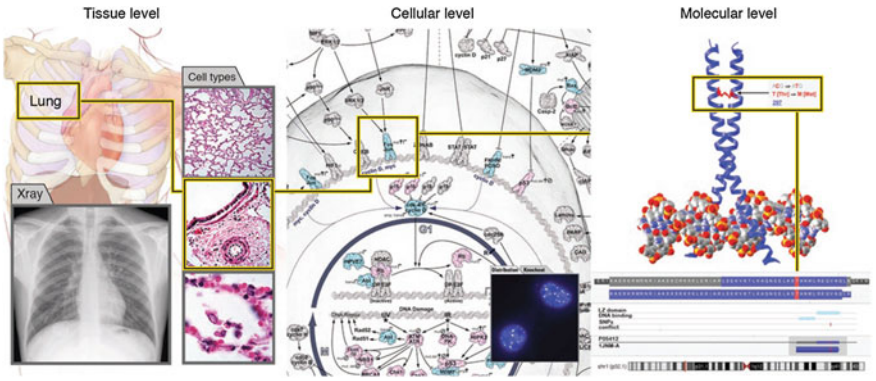

Fig. 5.5 Integrated visualization environment proposed by [21] (Reprinted by permission from Macmillan Publishers Ltd: *Nature Methods,* vol. 7, O'Donoghue, S. I. et al.: Visualizing biological data—now and in the future, S2–S4, Copyright © 2010 Nature America, Inc. Images courtesy of ClearScience (drawing), iStockPhoto (lung X-ray), University of Kansas Medical Center, Department of Anatomy and Cell Biology (lung histology), Digizyme and Cell Signaling Technology (pathway). Protein structure and sequence alignment made using SRS 3D [43]. Chromosome image from UCSC Genome Browser [44], *Nucleic Acids Res.*, vol. 38, Rhead, B. et al.: The UCSC Genome Browser database: update 2010, D613–D619, 2010, by permission of Oxford University Press

are analyzed in strongly separated scales. This fact is considered the "tyranny of the scales" [8]. The observation and quantification of natural processes occurring at multiple scales is not possible without a multi-scalar framework, resulting from a multi-disciplinary conception among scientists and visualization researchers [42].

The main challenge for multiscale visualization of biomedical data is: *how to display simultaneously multiple visual features that map to very different space-time regions?* [27]. Detailed and global content information are usually distributed at different scale levels, and also small scales should have visibility in large scales (Fig. 5.5).

Requests for biomedical multiscale modeling and visualization have been made during the last decade. Additionally, the level of integration of multi-disciplinary and multiscale research has been increasing in the last years, as discussed later in this section. However, according to Gehlenborg, "Truly integrated visualization of systems biology data across the entire range of possible data types is still very much in its infancy" [45].

Lorensen [20] emphasized the need to form alliances with the fields of application of visualization. An understanding of each scale is required, but the importance lies in coupling scales in a multiscale user interface. This interplay will provide a more complete meaningful analysis and lead to solutions that will provide scientists with new knowledge that would have not been understood without a proper multiscale visualization.

In this context, different interaction strategies can solve problems normally associated with visualization in a more efficient manner. Prominent examples are VR interaction strategies, e.g. augmented reality, navigation devices or haptic interfaces.

5.4.1 Multiscale Visualization

This section discusses multiscale visualization. It presents the design process, important techniques and recent realizations.

Multiscale Design Process

The current multiscale design process consists of choosing the appropriate techniques to create a multiscale system, depending on the following factors [18, 46]:

- Type of data and their features: formats, dimensionality and amount.
- Visualization style: e.g. isosurfaces, volume rendering, vector field, tensor field visualization, … [47].
- Nature of multiscale: Considerations to be taken into account are based on the relations between the different types of data, as the order of magnitude or the relation between space and time scale. If the data does not have time-space continuity, a smooth transition is required. The presence of these gaps between different scales is one of the major challenges in the design process.
- Style of interaction: navigation, augmented reality, haptic and gesture interaction (see Sect. 5.5.2).

Multiscale Techniques

Current multiscale techniques can be categorized by their function [18]. The most relevant of these techniques are:

- **Out-of-core visualization:** This collection of techniques handles datasets that are larger than the available memory [3]. General external-memory techniques can be divided in two groups: *batched computations* and *on-line techniques*. The first group involves data streaming into internal memory. Later the data is processed in multiple passes. In the second group, also based on batched computations, the data is pre-processed according to possible queries and results are stored in a specific structure that facilitates the access.
- **Level of detail (LoD):** The representation complexity of an object in the scene depends on its relevance (e.g. position, camera speed or user focus). As datasets grow in size and complexity, the importance of LoD techniques is increasing [48].
- **Call-outs and lensing:** These two techniques allow simultaneous view of detailed and global content. Call-outs (Fig. 5.6a) are enlarged sub-regions that link to a

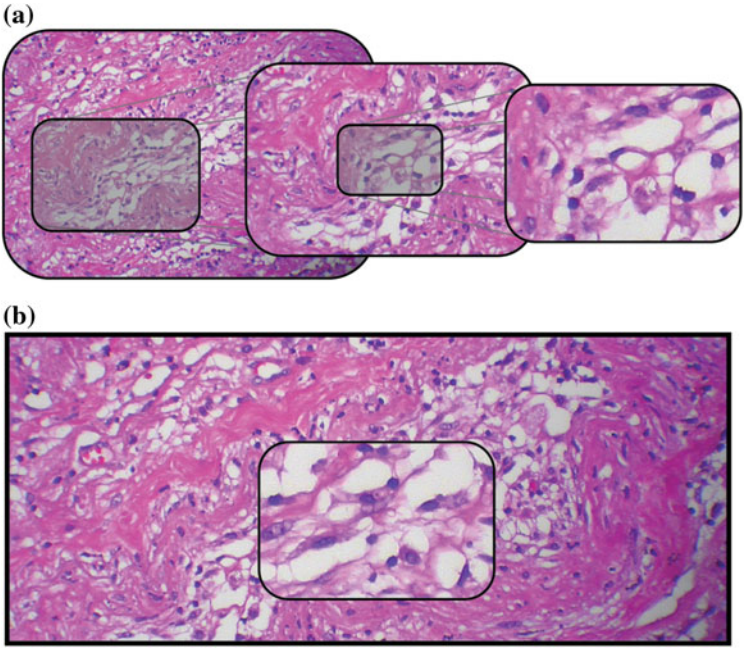

Fig. 5.6 Example of multiscale visualization techniques applied to a histological image of fibrocartilaginous tissue (**a**) call-out technique, (**b**) lensing technique. Images courtesy of 3B's Research Group

point of the parent image. Movable lenses can magnify small-scale objects or show different features from other scales (Fig. 5.6b).

- **Methods for large-scale:** When objects are very small compared to their distance from the origin of the reference system, the resolution of the object geometry can be lower than the numerical precision of the computer. This problem is often called ill-conditioning. In medical datasets, registering the positions of small objects with respect to their local parents can solve this issue. Another alternative, used in astrophysics, is the use of power scaled coordinates, which can represent positions of distant objects in a uniform mode [18].
- **Time-varying data visualization:** When using time-varying data, the insertion of the time dimension introduces new requirements, e.g. the correlation between temporal sampling frequency and spatial scales [46].

Examples of Multiscale Visualization

Among the biomedical visualization tools that currently exist (examples can be found in [45, 49]), fully interactive and multimodal visualizations were rarely achieved in concrete practical research. Genomics, proteomics and information visualization

domains have dealt more with the multiscale problem in depth. *Biodigital Human* [50] and *Zygote Body* [51] are clear examples of how web-visualization for a general audience has improved.

Recent projects enable collaborative investigation of the human body as a single complex system. Some of them are being developed under the framework of the *Virtual Physiological Human (VPH)* [52], including the *Multiscale Spatiotemporal Visualisation (MSV) Project* [53]. The *MSV Project* aims to cover the lack of specific interactive visualization paradigms for biomedical multiscale data. By using the LoD approach with placeholders [12], it allows for example navigation across CT scans at different scales. This project and others use open-source systems and libraries for image processing and visualization for rapid development of medical imaging applications, such as the *Visualization Tool Kit (VTK)* [54]. They constitute the basis of many advanced tools [55] and are suitable in a multi-scalar environment. Another example is the *Multimod Application Framework (MAF)* [13], which supports the combination of biomedical time-varying data from several sources, allowing for instance an effective analysis of human motion [56].

In short, development of data fusion and multimodal visualization demonstrates how these approaches can solve concrete multidisciplinary biomedical problems. Thus, research groups and current projects highlight this need in order to solve their challenges (e.g. [14]), and try to explore new approaches [42].

5.4.2 Human Computer Interaction (HCI)

HCI is a known concept that has its roots in the pre-computer era, when it was better known as Man-Machine Interaction (MMI). Recent development of different technologies has blurred the border between HCI reality and fiction [57]. This section briefly discusses the basics of the field of HCI, its definitions and terminology and categorizes different approaches.

Definitions and Terminology

Two different aspects of HCI need to be named. *Functionality* defines all abilities of a system that HCI should provide access to. Different realizations of user interfaces can result in different ranges of functionality. This variation is referred to as *usability*. Every designer should keep the fragile balance between functionality and usability at equilibrium [58].

Categories

A first approach to categorize HCI is based on activities performed by the user:

- **Physical:** It constitutes all interactions involving direct use of senses and muscle actions [57].
- **Cognitive**: It includes all mental capabilities of the user connected with understanding, learning and reasoning [59]. The cognitive aspect is also emphasized in a more direct manner in Brain Computer Interfaces (BCIs) where the interface senses the user's cognitive state of the brain (via EEG) [60].
- **Affective**: The second class of mental capabilities focuses on the emotional state, e.g. if the user is tired or angry. Sensing this allows the system to react on emotions and to create emotional feedback [61].

Cognitive and affective activity approaches are still relatively new fields in HCI. This overview focuses more on the physical interaction, which can be divided in three subcategories, related to human senses [62]:

- **Vision:** Many input devices rely on human vision, as for example, pointing devices: mice, trackballs, graphic tablets and touch screens. Also commonly used visual output devices are screens and printers.
- **Audition:** This category includes all means that involve hearing, human speech and audio signalization.
- **Touch:** Although keyboards and buttons could be classified here, this category focuses more on all force passing interfaces. This includes sending sensations to human skin and muscles and receiving force feedback from the user.

It is important to note that even for the simplest interfaces, this categorization can be vague. Since humans process information from the environment using different senses in parallel, it is difficult to distinguish between meaningful and meaningless stimuli. For example, keyboard keys have glyphs, which allow selecting keys visually, but they have also a force threshold that permits to sense the state by touching.

Recent Trends in HCI

Although HCI and MMI have a long research tradition, only recent technological advancements allowed the implementation of techniques that were already proposed in the 1960s, like Augmented Reality (AR) [63]. This advancement enabled testing of new ideas in practical trials, giving rise to further investigation. New research trends that have become prominent in the past years are: Intelligent HCI, Adaptive HCI, Ubiquitous Computing and Ambient Intelligence [64, 65].

Intelligent HCI refers to all techniques that are intelligent in the sense of preprocessing data received from the user. Hence, simple interfaces become complex systems, enhancing the received data into a complete stream of information.

Adaptive HCI refers to the adaptiveness of interfaces to become better suited to a certain user. An example of this is the T9 system [66] used in cell phones, allowing input of alphanumeric text with just a single press of the digit keys for each alphanumerical sign. It uses a form of intelligence, i.e. algorithms that process key sequences, comparing them with statistical models of languages and providing missing information. The T9 example is also useful to explain the concept of adaptiveness, because

the T9 interface can adapt to the user's behavior by means of a custom dictionary where all exceptions are stored.

The principle behind *ubiquitous computing* and *ambient intelligence* is to form a network of computers and interfaces that surround the user, sharing input and output of individual machines and creating a synergy of interactions [64].

In the HCI context, each channel of communication between human and machine is called a *modality*. This concept allows separating interfaces as unimodal and multimodal ones. Multimodal interfaces are becoming an increasingly prominent field of research [67]. However, multimodal realizations are only a combination of multiple unimodal systems. For the purpose of this overview it is enough to describe in detail only the building blocks, i.e. unimodal systems. More insight into multimodal systems is given in the context of multiscale interaction in the following sections.

Examples of Unimodal Systems in HCI

Prominent examples for *visual systems* are algorithms that detect human faces on digitized images [68]. Starting with the simple detection, these methods soon evolved to analyze facial expressions. Improvements in computational power and resolution of images enabled full body movement tracking with markers [69] and without markers [70]. This progress allowed implementing gesture recognition systems [71]. Another interesting technique is gaze detection and eye tracking, which is commonly used as a form of communication for disabled people [72].

Audio systems have been growing in popularity since robust cloud based voice recognition systems have been introduced [73]. However, traditional desktop voice recognition systems are also starting to offer ways to recognize the speaker, based on a pre-learned database of voices [74]. Another approach to audio systems is the extraction of the emotional state of the speaker (laugh, cry, sigh) from audio signals in addition to the word content [75].

Sensor systems are commonly used. Keyboard, mouse, joystick are most prominent examples of sensor systems [62]. Pen based input grew popular for some time, as a highly natural means of communication, but because the implementation was unreliable and expensive, the idea of Tablet PC computing never became mainstream. With the renaissance of tablets, manufactured as light and mobile devices, it is expected that the pen-based input will become as important as touch-based interaction like keyboard and mouse [76]. Haptic and pressure interactions are valuable for robotics and medicine. These sensors allow robots to sense the environment as humans do, to enable telepresence application [77]. Biomedical approaches consider the utilization of sensor systems during microsurgeries. The use of the robotic interface could help translating senses of surgeon from a small movement scale to familiar macro surgery scale [78].

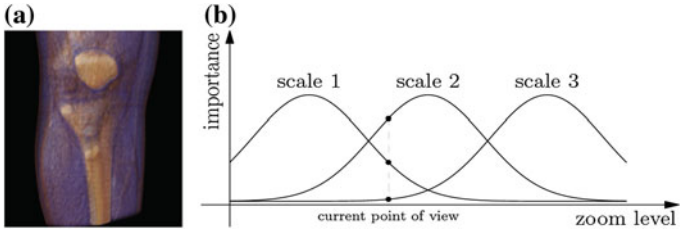

Fig. 5.7 Superimposing of knee joint multiscale dataset (**a**). Features from diverse scales have a specific importance at the current point of view (**b**)

5.5 Potential Solutions for Biomedical Multiscale Visualization and Interaction

In this section we present an overview of strategies on multiscale visualization and interaction for biomedical data. Especially the multiscale aspect requires novel approaches for graphical user interfaces (GUIs).

5.5.1 Multiscale Visualization

The introduction of the *strategies* described below and the use of concepts coming from *other disciplines* are meant to improve the quality of current visualization systems, such as the tools presented in the Sect. 5.4.1 (Examples of Multiscale Visualization).

Strategies for Biomedical Multiscale Navigation

The multiscale techniques described in Sect. 5.4.1 (Multiscale Techniques) have to be combined with several considerations in order to provide the scientist with a suitable multiscale environment. For this aim, we propose several system requirements for supporting multiscale navigation.

Need for representing complex biological systems with interacting scales

The development of new visualization models for data representation is required in order to provide an integrated framework that can be used to navigate across several scales. This framework should create spatial correlations in 3D structures to visualize multiple properties at the same time and in a compact way, facilitating the alignment of features from different scales (Fig. 5.7).

The presentation of data must be adequate for the working environment, which is strongly related to the professionals using the tool (medical doctors, biologists, bioengineers, etc.). Selecting the optimal point of view and providing habitual software

tools can help them to focus on extracting valuable knowledge from the measurements.

Consistent interaction

The multi-scalar environment should lead to a modification of standard visualization navigation tools [79], for example, by reusing them at different navigation levels. Possible features are:

- **Incorporation of GUI into the visualization scene**
  A standard GUI, composed of the 3D model and an interface based on (classic) windows and dialog boxes to configure the viewport, does not facilitate the transition between scales.
  The interface can be **immersive** or **hybrid**.
  - In the *immersive* case, the 3D model is the interface, where all actions and commands used to locate datasets (and metadata) require the user only to navigate to the right position in the virtual model.
  - *Hybrid* GUI provides features known from immersive 3D visualization such as a high degree of interactivity with the 3D model. However, it still provides access to standard desktop-based GUI widgets.
- **Automatic modification of navigation parameters**
  Navigation and viewing parameters should be optimized to provide a seamless transition between two scales and reduce manual user inputs.

Perception considerations

Facilitating the perception of multiscale visualization is very relevant. Attentiveness should be aided by avoiding occlusions and through visual cues on the objects of interest (e.g. highlighted, always visible, conservation of focal point, …). 3D location awareness can be solved by navigation facilities (e.g. "here-you-are", navigation mediator maps, landmarks, flexible viewpoint lists, and destination lists [80]). For instance, when click-and-zoom interaction is implemented, the involved movement should be slow enough in order to ensure that the user keeps the information of spatial position [81], but without any unnecessary delay ("as fast as suitable"). An initial virtual tour (e.g. from macroscale to microscale) presenting all these navigation facilities can rapidly improve the viewer's perception.

Influence of Other Disciplines

The adoption of concepts coming from other disciplines and fields is necessary in order to increase the scientific meaning (see Sect. 5.3.2) and to create new ways to understand (multiscale) biomedical data.

Knowledge Formalization

Visualization researchers should consider the use of knowledge formalization principles to store meta-information efficiently along the data [19]. Ontology can be used to

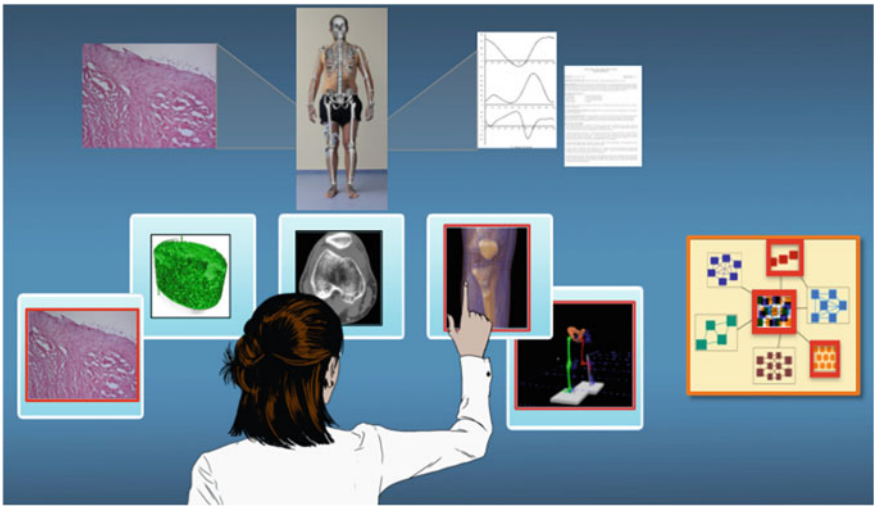

Fig. 5.8 Proposal of semantic visualization with ontology integration, represented with an information visualization view. This can be considered as another scale because information is presented in a different kind of abstraction. Images courtesy of 3B's Research Group (histological images of meniscus and cartilage micro-CT dataset), OsiriX Project (knee CT dataset) [10], and LBB-MHH (gait motion analysis)

organize biomedical data into semantically connected pieces of information. Clear examples of that are tools for visually exploring biological networks as VisANT [82], which works with Gene Ontology [83]. The annotation of knowledge associated to the data, either ontology-driven or keyword-based, can provide a semantically meaningful visualization and interaction (see Fig. 5.8).

The use of ontology concepts and relations could provide means for a rapid retrieval of interesting relations during the interaction with the system [84], for instance, allowing direct transition between parts that have similar meaning or have been stored in the same dataset, but their spatial position is different. In addition, the presentation of the content could be enhanced by view setup according to the stored user profile. This user profile knowledge would be based on analysis of ontology user queries and usage patterns [85].

Representation of uncertainty

The representation of uncertainty and errors in 3D diagrams should have the same importance as in normal 2D scientific diagrams [41] because it is crucial for understanding the correctness of the visualization. There are several sources of uncertainty during the representation process: acquisition, model, transformation (i.e. rescaling, rotating) and visualization. Among others, the following methods can be used to present uncertainty: use of displacement glyphs, arrows or patterns, blurring (note the use of human psycho-physical abilities), and the combination of isosurfaces and

volume rendering methods. The representation of uncertainty can be an opportunity for the integration of scientific and information visualization [27].
Visual analytics

The environments proposed should also provide tools to assist scientists to assimilate the resulting knowledge. Although data management and data mining are not covered in this chapter, they are also important in visual analytics, a multidisciplinary field that includes also visualization, HCI and perception concepts [85].

5.5.2 Multiscale Interaction

This section describes different software and hardware techniques that could be applied in the multiscale context.

Navigation

Since the dawn of the graphical interface era, the computer mouse has been the most popular pointing device. Pointing and clicking are common interaction patterns. They form a ground base for other interactions that can be used in a multiscale context [46]:

- *Click-and-zoom* is used when sub-scale data is too small to be resolved on the display screen and it is marked by a token (labels, landmarks, etc.). The aim of the click is to magnify the target. The occlusion of tokens inside larger objects is a common problem.
- The technique *push-out* avoids occlusion when the camera is inside an object and a path zooming out to the larger scale is constructed: a system can search the nearest open hole, generating a curved path that the camera will follow [79].
- *Click-and-fly* interactions move the visualization through the scene and do not necessarily imply a change of scale.
- *Look-and-fly* allows the user to freely change the direction of zooming if the mouse cursor is moved during this process from the screen center to another position [79].

Traditional navigation, however, can be inefficient in environments of massive three-dimensional data. The introduction of 3D Computer Aided Design (CAD) required the development of 3D navigator devices that offer 6-DOF (degree of freedom) view control inside a virtual space. Using 6-DOF devices together with a standard pointing device could satisfy the input requirements.

In this scenario, the 3D navigator would provide a position in space and a heading direction, giving an intersection plane of the screen where the view is cast on. The mouse pointer would then navigate through the simplified 2D content of the screen plane.

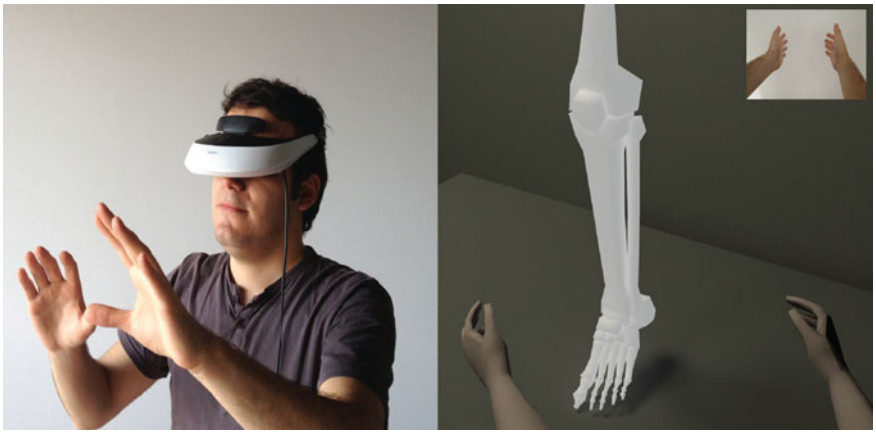

Fig. 5.9 Example of augmented reality interaction. The user is wearing a VR helmet and is interacting with VR content with a reference image of reality

As humans tend to solve two dimensional problems more quickly than three dimensional ones [86], it is worth simplifying the model of navigation by limiting the number of dimensions where it is applicable. A good example of dimension reduction is a geographic coordinate system. Every position on a three dimensional planet is limited to a point on a surface, described by two angles [87]. While considering this, it should be kept in mind that temporal data introduce time as another dimension.

Augmented Reality

Generating a convincing reconstruction of the world is difficult to achieve. Another approach tries to enhance live video images with abstract data visualization, the so called augmented reality [88].

In the multiscale context, the augmented reality approach could improve understanding of visualization and solve 3D navigation issues. Humans have natural awareness of their position and are able to navigate in space. The user can freely approach objects and examine them from different angles. Therefore, viewing multiscale content overlaid on real objects could be most natural in terms of navigation and interaction. Of course, the realization of such interaction is non-trivial. Benefits, however, outweigh potential problems, e.g. transformation of pre-registered datasets to fit the current pose of the subject.

Augmented reality can be realized with different tools like:

- using a tablet device to compute a virtual "image frame", showing the live recorded background combined with visualization,
- using a wearable head mounted translucent display, e.g. Google Glass [89] or

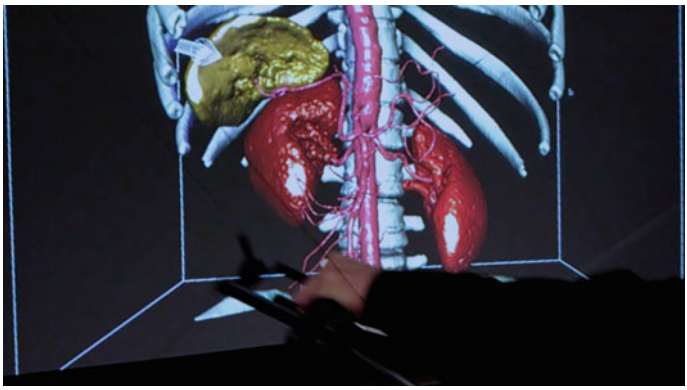

Fig. 5.10 Welfenlab virtual reality room with a Haption INCA^{TM} 6D device

- a VR helmet (Fig. 5.9) with an additional camera source for the reference image of reality [63].

Different interfaces allow different scenarios of interaction. However, a common use scenario for all of the described technologies is e.g. a *slate perspective*. In this scenario the augmented reality display is a "window" to view data overlaid on a real-time image of a subject.

Haptic Interaction

As noted in Sect. 5.4.2, touch and haptic interfaces play significant roles in medical applications. An example of a haptic environment is presented in Fig. 5.10. The ability to give haptic feedback, while preparing pre-operational planning, is crucial for achieving success in medical procedures e.g. assembling fragments of fractured bones. Vlasov et al. describe different approaches for haptic rendering [90–92]. As many diagnostic procedures involve touch examination, creating a synergy between touch and access to digitally recreated multiscale content can be invaluable as a new diagnostic modality.

Gesture Interaction

As it has already been mentioned, much of multiscale medical content has rich diagnostic meaning and can be used for pre-operational planning. Therefore, creating a strategy for utilizing gesture interaction for a sterile surgery room should be considered as important.

This kind of interaction should not only be limited to navigation but could also allow interactive modification and processing of data. Beside hand gestures, facial expressions can play an important role in multiscale environments. As an example, visual systems detecting an eye wink can help in reducing user tasks [93].

5.6 Conclusions

The creation of an integrated multiscale visualization framework is only possible when the conception is changed: the system should be user- and field-centric. Human perception considerations and tight cooperation between study domains and visualization researchers should become the gold standard. In addition, new concepts in this field, e.g. statistical parameters and the utilization of ontologies, can consolidate experimental data. All these efforts should serve a single purpose: to improve understanding.

In the recent years, interaction strategies underwent a revolution. Technologies that were previously considered too expensive have become widely available. This allows interaction with biomedical data with new (low cost) interfaces, ameliorating the user experience.

Multiscale visualization and interaction are challenging disciplines of research. These areas are constantly evolving and expanding to other fields. Due to a multitude of expertise required, creating a good multiscale design is a demanding task. Future progress in this field will depend on the utilization of current trends and further expansion in user experience and ontological/semantic directions.

Acknowledgments This work was supported by the framework of the EU Marie Curie Project MultiScaleHuman (FP7-PEOPLE-2011-ITN, Grant agreement no.: 289897).

References

1. Walter, T., et al. (2010). Visualization of image data from cells to organisms. *Nature Methods*, *7*, S26–S41.
2. Levenson, R. M., & Mansfield, J. R. (2006). Multispectral imaging in biology and medicine: Slices of life. *Cytometry Part A*, *69A*(8), 748–758.
3. Chiang, Y. J., et al. (2003). Out-of-core algorithms for scientific visualization and computer graphics. *IEEE Visualization*, *22*(1), 35–48.
4. Friese, K.-I., et al. (2013). Analysis of tomographic mineralogical data using YaDiV–Overview and practical case study. *Computers and Geosciences*, *56*, 92–103.
5. Friese, K. I., et al. (2011). YaDiV–an open platform for 3D visualization and 3D segmentation of medical data. *The Visual Computer*, *27*(2), 129–139.
6. Auer, M., et al. (2007). Development of multiscale biological image data analysis: Review of 2006 international workshop on multiscale biological imaging, data mining and informatics, Santa Barbara, USA (BII06). *BMC Cell Biology*, *8*(1), S1.
7. Jmol: an open-source Java viewer for chemical structures in 3D, http://www.jmol.org/
8. OsiriX Imaging Software, DICOM sample image sets, http://www.osirix-viewer.com/datasets/
9. Fishman, E. K., & Kuszyk, B. (2001). 3D imaging: Musculoskeletal applications. *Critical Reviews in Diagnostic Imaging*, *42*(1), 59–100.
10. Oden, J. T. et al. (2006). Simulation-based engineering science: Revolutionizing engineering science through simulation, http://www.nsf.gov/pubs/reports/sbes_final_report.pdf
11. Han, L., et al. (2011). Nanomechanics of the cartilage extracellular matrix. *Annual Review of Materials Research*, *41*, 133.
12. Testi, D. et al. (2012). New interactive visualisation of multiscale biomedical data. ACM SIGGRAPH 2012 Posters, (pp. 76:1–76:1), ACM, New York.

13. Viceconti, M., et al. (2007). Multimod Data Manager: A tool for data fusion. *Computer Methods and Programs in Biomedicine*, *87*(2), 148–159.
14. MultiScaleHuman Project (2012). MultiScaleHuman Project, http://multiscalehuman.miralab.ch/
15. Kleemann, R. U., et al. (2005). Altered cartilage mechanics and histology in knee osteoarthritis: Relation to clinical assessment (ICRS Grade). *Osteoarthritis Cartilage*, *13*(11), 958–963.
16. Loeuille, D., et al. (2005). Macroscopic and microscopic features of synovial membrane inflammation in the osteoarthritic knee: Correlating magnetic resonance imaging findings with disease severity. *Arthritis and Rheumatism*, *52*(11), 3492–3501.
17. Liu, W. K., et al. (2006). Immersed finite element method and its applications to biological systems. *Computer Methods in Applied Mechanics and Engineering*, *195*(13–16), 1722–1749.
18. Mcfarlane, N. J. B. et al. (2012). A survey and classification of visualisation in multiscale biomedical applications. Information Visualisation (IV), 2012 16th International Conference on. pp. 561–566.
19. Chen, J., et al. (2005). Grand challenges for multimodal bio-medical systems. *IEEE Circuits and Systems Magazine*, *5*(2), 46–52.
20. Lorensen, B. (2004). On the death of visualization. Proceedings of the NIH/NSF Fall 2004 Workshop on Visualization Research Challenges.
21. O'Donoghue, S. I., et al. (2010). Visualizing biological data–now and in the future. *Nature Methods*, *7*, S2–S4.
22. Nielson, G. M., et al. (Eds.). (1997). *Scientific visualization, overviews, methodologies, and techniques*. Washington: IEEE Computer Society.
23. Huang, N. E., & Shen, S. S. P. (2005). Hilbert-Huang Transform and Its Applications. *World Scientific*, *5*, 1–15.
24. Helgason, S. (1999). The Radon transform, Springer.
25. Leach, A. R. (2001). *Molecular modelling: Principles and applications*. Harlow: Pearson Education.
26. Card, S. K., et al. (1999). *Readings in information visualization: Using vision to think*. San Francisco, CA: Morgan Kaufmann.
27. Johnson, C. (2004). Top scientific visualization research problems. *IEEE Computer Graphics and Applications*, *24*(4), 13–17.
28. Van Wijk, J. J. (2005). The value of visualization. Proceedings of the 16th Conference IEEE Visualization (VIS 05), pp. 79–86.
29. Evanko, D. (2010). Supplement on visualizing biological data. *Nature Methods*, *7*, S1–S1.
30. Rhyne, T.-M. (2003). Does the difference between information and scientific visualization really matter? *IEEE Computer Graphics and Applications*, *23*(3), 6–8.
31. Rhyne, T. M. et al. (2003). Information and scientific visualization: Separate but equal or happy together at last. Proceedings of the 14th IEEE Visualization, p. 115.
32. Healey, C. G., & Enns, J. T. (1998). On the use of perceptual cues & Data mining for effective visualization of scientific datasets. In Proceedings Graphics, Interface, pp. 177–184.
33. Kosara, R., et al. (2003). Thoughts on user studies: Why, how, and when. *IEEE Computer Graphics and Applications*, *23*(4), 20–25.
34. Tory, M., & Moller, T. (2004). Human factors in visualization research. *IEEE Transactions on Visualization and Computer Graphics*, *10*(1), 72–84.
35. Damle, A. (2002). Explain me visually: Exploring information design through multimedia. Information visualisation, 2002. Proceedings of the Sixth International Conference on, pp. 265–267.
36. Springmeyer, R. R., et al. (1992). A characterization of the scientific data analysis process. Proceedings of the 3rd Conference on Visualization'92, pp. 235–242.
37. Ibrahim, N., & Noor, N. F. M. (2004). Navigation technique in 3D information visualisation. Proceedings IEEE Region 10 Conference TENCON 2004, pp. 379–382.
38. Bajaj, C., et al. (2003). Volumetric feature extraction and visualization of tomographic molecular imaging. *Journal of Structural Biology*, *144*(1–2), 132–143.

39. Yu, Z., & Bajaj, C. (2004). A fast and adaptive method for image contrast enhancement. Proceedings of 2004 IEEE International Conference on Image Processing (ICIP'04). *Vol.*, *2*, 1001–1004.
40. Bajaj, C., & Goswami, S. (2009). Modeling cardiovascular anatomy from patient-specific imaging. In J. M. R. S. Tavares & R. M. N. Jorge (Eds.), *Advances in computational vision and medical image processing* (pp. 1–28). Netherlands: Springer.
41. Johnson, C. R., & Sanderson, A. R. (2003). A next step: Visualizing errors and uncertainty. *IEEE Computer Graphics and Applications*, *23*(5), 6–10.
42. Westerhoff, H. (2012). White paper: VPH, Molecular Systems Biology (MSB), and their ITFoM, http://www.itfom.eu/images/article_PDFs/white_paper_vph_msb_itfom_2012.pdf
43. O'Donoghue, S. I., et al. (2004). The SRS 3D module: Integrating structures, sequences and features. *Bioinformatics*, *20*(15), 2476–2478.
44. Rhead, B., et al. (2010). The UCSC Genome Browser database: Update 2010. *Nucleic Acids Research*, *38*(1), D613–D619.
45. Gehlenborg, N., et al. (2010). Visualization of omics data for systems biology. *Nature Methods*, *7*, S56–S68.
46. McFarlane, N., et al. (2012). Report on best practice, Multiscale Spatio-temporal Visualisation Project.
47. Hansen, C. D., & Johnson, C. R. (2005). *Visualization handbook*. San Diego: Academic Press.
48. Luebke, D., et al. (2002). *Level of detail for 3D graphics*. San Francisco: Morgan Kaufmann.
49. Staadt, O. G., et al. (2007). Interactive processing and visualization of image data for biomedical and life science applications. *BMC Cell Biology*, *8*(1), S10.
50. Biodigital Human (2012). Biodigital Human, https://www.biodigitalhuman.com/
51. Zygote Body (2012). Zygote Body http://www.zygotebody.com/
52. Hunter, P., et al. (2010). A vision and strategy for the virtual physiological human in 2010 and beyond. *Philosophical Transactions of The Royal Society: A Mathematical Physical and Engineering Sciences*, *368*(1920), 2595–2614.
53. Testi, D., et al. (2011). Interactive visualization of multiscale biomedical data: An integrated approach. Proceedings of the 1st IEEE Symposium on Biological Data Visualization (BioVis), pp. 3–4.
54. Visualization Toolkit (2012). Visualization Toolkit, http://www.vtk.org/
55. Caban, J. J., et al. (2007). Rapid development of medical imaging tools with open-source libraries. *Journal of Digital Imaging*, *20*(Suppl 1), 83–93.
56. Leardini, A., et al. (2005). Advanced multimodal visualisation of clinical gait and fluoroscopy analyses in the assessment of total knee replacement. *Computer Methods and Programs in Biomedicine*, *79*(3), 227–240.
57. Karray, F., et al. (2008). Human-Computer Interaction: Overview on state of the art. *International Journal on Smart Sensing and Intelligent Systems*, *1*(1), 137–159.
58. McNamara, N., & Kirakowski, J. (2006). Functionality, usability, and user experience: Three areas of concern. *Interactions.*, *13*(6), 26–28.
59. St Amant, R., & Riedl, M. O. (2001). A perception/action substrate for cognitive modeling in HCI. *International Journal of Human-Computer Studies*, *55*(1), 15–39.
60. Cutrell, E., & Tan, D. (2008). BCI for passive input in HCI. Proceedings of CHI.
61. Picard, R. W. (1999). Affective computing for HCI. Proceedings of HCI International (8th International Conference on Human-Computer Interaction): Ergonomics and User Interfaces, pp. 829–833.
62. Myers, B. A. (1998). A brief history of human-computer interaction technology. *Interactions*, *5*(2), 44–54.
63. Sutherland, I. E. (1968). A head-mounted three dimensional display. Proceedings of Fall Joint Computer Conf., pp. 757–764, Washington: Thompson Books.
64. Friedewald, M., & Raabe, O. (2011). Ubiquitous computing: An overview of technology impacts. *Telematics Informatics*, *28*(2), 55–65.
65. Maybury, M. (1998). Intelligent user interfaces: an introduction. Proceedings of the 4th International Conference on Intelligent User interfaces, pp. 3–4.

66. How, Y., & Kan. M. Y. (2005). Optimizing predictive text entry for short message service on mobile phones. Proceedings of HCII.
67. Jaimes, A., & Sebe, N. (2007). Multimodal human-computer interaction: A survey. *Computer Vision and Image Understanding*, *108*(1–2), 116–134.
68. Hjelmås, E., & Low, B. K. (2001). Face detection: A survey. *Computer Vision and Image Understanding*, *83*(3), 236–274.
69. Herda, L., et al. (2000). Skeleton-based motion capture for robust reconstruction of human motion. *In Proceedings of Computer Animation*, *2000*, 77–83.
70. Lange, B., et al. (2011). *Markerless full body tracking: Depth-sensing technology within virtual environments*. Simulation and Education Conference (I/ITSEC) : The Interservice/Industry Training.
71. Mitra, S., & Acharya, T. (2007). Gesture recognition: A survey. *IEEE Transactions on Systems, Man and Cybernetics, Part C: Applications and Reviews*, *37*(3), 311–324.
72. Jacob, R. J. K., & Karn, K. S. (2003). Eye tracking in human-computer interaction and usability research: Ready to deliver the promises. *Mind*, *2*(3), 4.
73. Bennett, I. M., et al. (2003). Distributed realtime speech recognition system.
74. Zwyssig, E., et al. (2012). Determining the number of speakers in a meeting using microphone array features. *2012 IEEE International Conference on Acoustics Speech and, Signal Processing (ICASSP)*, (pp. 4765–4768).
75. Vogt, T., et al. (2008). EmoVoice–a framework for online recognition of emotions from voice. In E. André (Ed.), *Perception in multimodal dialogue systems* (pp. 188–199). Berlin Heidelberg: Springer.
76. Hume, S. (2001). Pen-based computing. *Applied Clinical Trials*, *10*(7), 32.
77. Ueberle, M., et al. (2009). Haptic feedback systems for virtual reality and telepresence applications. *Feedback*, *56*, 97.
78. Okamura, A. M. (2009). Haptic feedback in robot-assisted minimally invasive surgery. *Current Opinion in Urology*, *19*(1), 102.
79. McCrae, J., et al. (2009). Multiscale 3D navigation. Proceedings of the 2009 Symposium on Interactive 3D Graphics and Games, p. 714.
80. Darken, R. P., & Peterson, B. (2002). *Spatial orientation, wayfinding, and representation* (pp. 493–518). Handbook of Virtual Environments, Mahwah NJ : Lawrence Erlbaum Associates.
81. McFarlane, N. J. B., et al. (2008). 3D Multiscale visualisation for medical datasets. BioMedical Visualization, 2008. MEDIVIS'08. Fifth International Conference. pp. 47–52.
82. Hu, Z., et al. (2009). VisANT 3.5: multi-scale network visualization, analysis and inference based on the gene ontology. *Nucleic Acids Research*, *37*(suppl 2), W115–W121.
83. Gene Ontology Project (2012). Gene Ontology Project, http://www.geneontology.org
84. Catalano, C. E., et al. (2011). Semantics and 3D media: Current issues and perspectives. *Computers and Graphics*, *35*(4), 869–877.
85. Keim, D., et al. (2008). Visual analytics: Definition, process, and challenges. In A. Kerren (Ed.), *Information Visualization* (pp. 154–175). Berlin Heidelberg: Springer.
86. Bowman, D. A., et al. (2008). 3D user interfaces: New directions and perspectives. *IEEE Computer Graphics and Applications*, *28*(6), 20–36.
87. Hanson, A. J., & Wernert, E. A. (1997). Constrained 3D navigation with 2D controllers. Proceedings of Visualization '97, pp. 175–182.
88. Azuma, R. T. (1997). A survey of augmented reality. *Presence: Teleoperators and Virtual Environments*, *6*(4), 355–385.
89. Hodson, H. (2012). Wearable gadgets enhance symbiosis of man and machine. *New Scientist*, *216*(2886), 22.
90. Vlasov, R., et al. (2013). Haptic rendering of volume data with collision detection guarantee using path finding. In *Transactions on Computational Science XVIII* (pp. 212–231). Berlin Heidelberg: Springer.
91. Vlasov, R., et al. (2012). Haptic rendering of volume data with collision determination guarantee using ray casting and implicit surface representation. 2012 International Conference on Cyberworlds (CW), pp. 91–98.

92. Vlasov, R., et al. (2012). Ray casting for collision detection in haptic rendering of volume data. Proceedings of the ACM SIGGRAPH Symposium on Interactive 3D Graphics and Games. (pp. 215–215), New York: ACM.
93. Abásolo, M. J., & Della, J. M. (2007). Magallanes: 3d navigation for everybody. Proceedings of the 5th international conference on Computer graphics and interactive techniques in Australia and Southeast, Asia. pp. 135–142.

Part IV
Simulation of Articulations

Chapter 6
Modeling and Simulating Virtual Anatomical Humans

Forough MadehKhaksar, Zhiping Luo, Nicolas Pronost and Arjan Egges

6.1 Introduction

This chapter presents human musculoskeletal modeling and simulation as a challenging field that lies between biomechanics and computer animation. One of the main goals of computer animation research is to develop algorithms and systems that produce plausible motion. On the other hand, the main challenge of biomechanics is investigating the influence of internal and external forces and stimulators on the biological behavior of different tissues. By combining the two approaches, it is possible to produce real-time animation of a user's avatar under different activities and to simulate the related biological effects of that activity. In this chapter we review the challenges and issues of modeling, simulating, and animating virtual anatomical humans, as well as an overview of the benefits and limitations of such systems.

The main advantage of using virtual anatomical models is the capability to study the biomechanical effects of a variety of different activities that real humans perform. The virtual world allows us to visualize these activities. Because of the use of virtual models and simulations, these studies can be done without spending a lot of money on measuring equipment, and without presenting any hazard to human subjects. The biggest challenge in achieving this lies in the conflict between the real-time nature of computer animation and the time-consuming computations required in biomechanics. This chapter serves as a starting point for research into addressing this conflict, by providing an overview of the differences and similarities between the two fields.

Modeling and simulating the human body has been extensively researched in the last decades. For example, recently, large consortia investigated new technologies around virtual representations of the human body [1] and the multi-scale biological data visualization of physiological human articulation [2]. Individual labs also take

F. MadehKhaksar · Z. Luo · N. Pronost (✉) · A. Egges
Virtual Human Technology Lab, Utrecht University, Princetonplein 5,
3584 CC Utrecht, The Netherlands
e-mail: nicolas.pronost@uu.nl; url:http://www.vhtlab.nl

N. Magnenat-Thalmann et al. (eds.), *3D Multiscale Physiological Human*,
DOI: 10.1007/978-1-4471-6275-9_6,

part in that research such as the Riverside Graphics Lab of University of California developing an anatomically inspired torso simulator for breathing and laughing [3, 4]. The Center of Computer Graphics and Visualization of the University of West Bohemia developed a musculoskeletal model, where bones and muscles are represented by their triangulated surfaces obtained from MRI data, and adopted the action-lines muscle description and FEM musculoskeletal models for the simulation to provide clinicians with a tool fast enough to be suitable for the clinical practice but with enhanced accuracy. The Computer Graphics and Vision Laboratory at UCLA also participated by developing a comprehensive biomechanical model of the human upper body with modeling and controlling nearly all relevant articular bones and muscles, as well as simulating the physics-based deformations of the soft tissues [5].

This chapter is structured as follows. First, we will discuss how to create an accurate virtual anatomical *model* of a human, based on real-world information from animation and biomechanics. Then, we discuss the various techniques that allow us to *simulate* the various aspects of this model such as muscular actuation and deformable objects. Finally, we will discuss a number of practical issues that are of use to anyone who wants to *implement* such a simulation.

6.2 Modeling Virtual Anatomical Humans

The ultimate goal of modeling virtual humans is to develop a generation of digital humans that comprise of realistic human models including anatomy, biomechanics, physiology, and intelligence. In this section we present the state-of-the-art approaches regarding the modeling of physical humans in the fields of animation and biomechanics. First the human biomechanics is introduced, then we present how the different anatomical entities are usually modeled, and finally we indicate how acquisition and processing techniques are used to generate such models.

6.2.1 The Human Biomechanics

Human motion is a complex process driven by various biological triggers. These triggers lead to the exertion of mechanical forces that in the end are visualized as movements by the human body. The role of human biomechanics is to study the structure as well as function of humans through the lens of mechanics. In his classic book, David Winter states that human biomechanics is an interdisciplinary field that describes, analyses, and assesses human movement [6]. Human biomechanics is also intertwined with other fields of movement science such as neurophysiology, exercise physiology, and anatomy.

6.2.1.1 Statics, Dynamics and Deformation

The Newton's first law of motion is used in a branch of mechanics known as *statics*. In mechanics, statics refers to the analysis of rigid bodies (solids) that are in a state of equilibrium, i.e. in a state where a rigid body's acceleration is zero which also means that both net forces (for translational movement) and net moments (for rotational movement) are also zero. Studying systems in states of equilibrium are useful to understand what forces are in play or should be taken into consideration. According to Nordin and Frankel [7], statics is generally used in biomechanics to investigate the unknowns in problems that involve the magnitudes of joint reaction forces and muscle tensions.

Dynamics, also commonly referred to as *physics*, takes the simulation one step further in that it studies how forces and torques causes the state of motion of an object to change, i.e. how a physical system changes over time with respect to applied loads. When forces are exerted on an object, three things can happen, either the object exhibits a change in linear and/or rotational motion, or in the case of equilibrium, the object experiences a localized shape change over time, a *deformation*. Forces that can be ascribed when an object gets deformed are:

1. *Normal* or *axial*:
   - *Tensile* forces (when an object elongates)
   - *Compressive* forces (when an object shrinks)
2. *Tangential*:
   - *Shear* forces (which in some cases result in bending or twisting of an object)

Because deformation of an object depends also on its material properties, having a quantity that defines the average force per unit area is helpful in approximating solutions for the analysis of intrinsic properties of the object under load. This concept known as *stress* is the amount of applied force divided by the area it is applied on. Similarly, two forms of stress are used, namely the *normal* stress σ and *shear* stress τ. Normal or axial stress can be calculated when the exerted force lies orthogonal to the cross-affected area under consideration. In cases where the exerted force lies tangent or parallel to the affected area, shear stress can be calculated. Under the assumption that the forces are uniformly distributed along the area and therefore consist of a simple stress pattern, the stress equation can be formally written as:

$$\tau, \sigma = \frac{\mathbf{F}}{A}$$

where $\mathbf{F}$ is the force and A the cross-sectional area.

Besides stress, there is also the concept of *strain*, denoted ϵ, that quantifies the normalized amount of deformation after an initial configuration, i.e. the amount of displacement of the intrinsic properties of an object from its original length to its current length. Similarly to stress it has also two basic forms, which are *normal* and

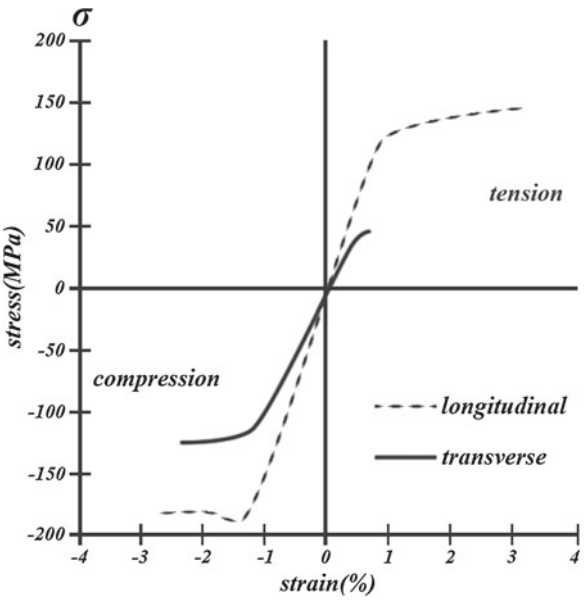

Fig. 6.1 Stress–strain diagram of a typical human cortical bone with strain percentage along the horizontal axis and stress in Mega Pascal along the vertical axis. When forces are exerted in the longitudinal direction instead of the transverse, the material can withstand more stress before it reaches the point of failure, characterized by the longer dotted graph. Also apparent is the toughness of the cortical bone material during compression when compared to tension. Inspired by Ref. [8]

shear strain. Normal strain occurs when the displacement happens along the material fibers and is formally written as:

$$\epsilon = \frac{l_1 - l_0}{l_0} = \frac{\Delta l}{l_0}$$

where Δl is the displacement in length and l_0 is the initial length before any deformation occurred. A negative outcome represents a compressive strain, while a positive outcome represents a tensile strain. For shear strains, denoted γ, deformations made by shear forces are measured. γ represents the tangent between relative displacements of shear forces.

Studying the relationship between stress and strain provides insight into the intrinsic behavior of an object under different load conditions. Figure 6.1 shows a typical stress–strain diagram of the human cortical bone.

When an object experiences tensile or compressive forces in one direction it can contract or expand in other directions that lie orthogonal to the direction of the applied forces. This characteristic is known as the *Poisson effect*. This effect can be measured by taking the ratio between the change in normal strain with the change in shear strain and is referred to as *Poisson's ratio*, denoted ν. Formally it is written as:

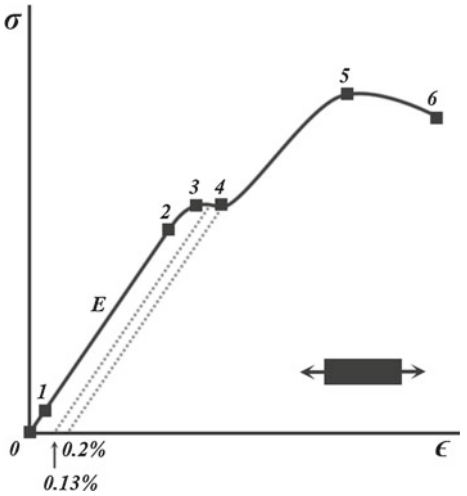

Fig. 6.2 Engineering stress–strain diagram for illustration purposes, showing key characteristics of a hypothetical object that experienced different tensile forces

$$\nu = -\frac{d\epsilon_n}{d\epsilon_s}$$

where ϵ_n and ϵ_s denote respectively the normal and shear strains.

6.2.1.2 Elasticity and Plasticity

A deformed object is considered *elastic* when it deforms back to its original configuration after the applied load is removed and *plastic* when at least parts of the deformation are permanent. The graph in Fig. 6.2 illustrates a stress–strain curve of a hypothetical object that experienced different tensile forces. The numbers along the curve represent several known characteristics that play a key role in the analysis of the material.

Point 0 represents the initial configuration, when no forces are exerted on the object. Point 1 represents the *true elastic limit*. Between point 0 and 1 no dislocations are visible on the atomic level or molecular scale. Point 2 represents the *proportionality limit*, after this point the elasticity of the material does not behave linearly. The segment of the curve between point 0 and 2 is said to be linear-elastic or Hookean implying a conformance to *Hooke's law*. The principle of Hooke's law, which in mechanics is used for models such as springs, can be described in terms of material functions of stress and strain for both normal and tangential forces:

$$\sigma = E\epsilon$$

$$\tau = G\gamma$$

where E denotes the elastic modulus or *Young's modulus* for normal forces and G denotes the shear modulus or *modulus of rigidity* for tangential forces.

Table 6.1 Mechanical properties of three biological materials: compact bone, trabecular bone, and tendon-ligament. Adapted from Ref. [9]

Material	Ultimate strength (MPa)	Modulus (GPa)	Elongation (%)
Compact bone	100–150	10–15	1–3
Trabecular bone	8–50	–	2–4
Tendon, ligament	20–35	2–4	10–25

Young's modulus is representative for the stiffness of a material, the higher the elastic slope, the stiffer the material. Point 3 represents the *elastic limit*, also known as the yield strength or yield point. The segment between point 2 and 3 defines the complete elastic behavior of the material, removing any load that falls within this segment would allow the material to deform back to its original configuration. After this point, the material behaves plastic and any further deformation is considered permanent. In this example, the load that is applied on the object is removed at the point on the curve between 3 and 4. The dotted line represents the linear regression of the elastic deformation with the same Young's or rigidity modulus that eventually intersects the strain axis. The intersection point on this axis is called the *plastic strain* that quantifies the amount of permanent strain, in this example 0.13 %. Point 4 represents the *offset yield point* that can be derived using the offset method. The offset method is used for cases where it is difficult to measure the exact point when the material yields. Similarly to the previous derivation of plastic strain, the method works by drawing a line, which starts generally with a strain offset of 0.1–0.2 %, and progresses in parallel with the linear-elastic segment of the curve. The intersecting point 4 between this line and the original curve is considered the offset yield point. Point 5 on the curve represents the ultimate tensile strength of the material followed by point 6 that represents the rupture point of the material; when the object finally fractures. An overview of mechanical properties for three biological materials is shown in Table 6.1.

6.2.2 The Musculoskeletal System

6.2.2.1 The Bones and Joints

The human body is a complex structure composed of a variety of interacting anatomical entities. Among them, the skeletal system includes the bones, cartilages, ligaments, and tendons. The average adult skeleton has 206 bones although actual number of bones slightly varies from person to person. The skeleton is usually divided into the axial and appendicular skeletons. The axial skeleton forms the upright axis of the body. It is divided into the skull, auditory ossicles, hyoid bone, vertebral column, and thoracic cage, or rib cage. The axial skeleton protects the brain, the spinal cord, and the vital organs housed within the thorax. The appendicular skeleton consists of the bones of the upper and lower limbs and the girdles by which they are attached to

the body. The term girdle means a belt or a zone and refers to the two zones, pectoral and pelvic, where the limbs are attached to the body.

Bones are connected to each other by *articulations*, also referred to as *joint*. A joint is then the union between two or more bones. The joints are located at the bones extremities, where the participant bones are in contact with each other and relative motion may occur. Many joints allow only limited relative movement, and some even allow no apparent movement. The structure of a given joint is directly correlated with its *degrees of movement*, or *degrees of freedom* (DOF). To model a human joint, a perfect model should consider the mechanics of the joint structure and its biomechanical interactions. It should not only visually react as the real joint but also include the real biomechanical behavior and biological properties. Biomechanical systems share many properties with mechanically engineered systems, and it is possible to employ mechanical engineering simulation software to investigate the mechanical behavior of diverse biological mechanisms. But as a challenge in biomechanical modeling of human articulation, unlike their man-made counterparts, biomechanisms rarely exhibit the simple, uncoupled, pure-axial motion that is engineered into mechanical joints such as sliders, pins, and ball-and-socket joints [10]. To ensure valid biological simulation and modeling, models must be accurate and subjected to sensitivity and design optimization analyses, demanding vast amounts of computation [10]. Most of existing models in computer graphics are far from being perfect in that sense. In the other hand, they do not need to be as little focus is given to biomedical application. Moreover, they should be simple enough to work in real-time. Most of the existing models in biomechanics focus on biomechanical accuracy and computationally expensive calculations. Accuracy, efficiency and visualization are generally competing and compromising tasks in biomechanics and computer graphics.

In addition, joint modeling in computer graphics is accompanied with a trade-off between generic but simplified models and specific but accurate models. It is possible to find works that consider a large range of fundamental types of the human articulation system [11], but they still behave differently from real joints. Joints are typically modeled as rotational constraints around one or more fixed axes and/or translational constraints along one or more of the three Cartesian directions. While in real joints the motion axes can change position by rotation [12]. Wilhelms [13] introduced a general method that simplifies the skeleton and where the geometry of bones is composed of three ellipses. A tree hierarchy is then utilized in which every group of bones is considered a segment of the body. The root segment is connected to the world reference frame by a free (six DOF) joint and the other segments connected to each other by constrained joints. Each segment has a parent segment and zero or more child segments. In addition, each segment is described in its own local reference frame, and the geometric relations between all the segments are known and used to calculate the global position of each body part. This structure is still nowadays used in almost every modeling and simulation frameworks.

In cases where more complexity is necessary, specific models, e.g. of individual joints and specific regions, have been proposed. As an example, Maurel and Thalmann [14] presented a model based on restrictions for the displacement of the scapula over the thorax. In this work a shoulder model is developed and each of the

clavicular, scapular and arm joints has three DOFs for rotation, and the scapula is bound to the thorax by means of a five DOFs joint (three rotations and two translations constrained to the surface of the thorax).

6.2.2.2 The Muscles, Tendons and Ligaments

Muscles are the active tissues that generate forces and cause motion. There are three different types of muscle in the body: cardiac, smooth and skeletal muscles. *Skeletal muscles* play a major role in motion. Their contraction is controlled through the somatic nervous system and this contraction produces active muscle forces that lead to postural stability and human body movement. Skeletal muscles are also major body components in size and mass, and partly characterize the body shape. Hence they constitute a critical part of biomechanics analysis and animation modeling. Skeletal muscles are attached to the bones by *tendons* while *ligaments* connect bones to bones. Tendons transmit the contractile force produced by muscle contraction to the bones and improve stability.

Skeletal muscles are composed of *muscle fiber bundles* called fascicles which themselves consist of internal fibers. Different internal arrangements of the muscle fascicles make different *muscle architectures*. In the simplest architecture, fascicles are all parallel to the length of the muscle. But in most of human muscles there is an angle between the fascicle's tendinous attachment direction and the longitudinal axis of the muscle. This angle is called *pennation angle*.

The earliest musculoskeletal mathematical model of skeletal muscle was suggested by Gasser and Hill [15]. That model was a one-dimensional representation of the muscle, called *action line*, and captured the global muscle mechanical properties. This model allowed later to describe the macroscopic relationships between muscle actuation, force-length and velocity along a muscle path, known as the *Hill's type model* [16]. In this model, the muscle is modeled by three components including the series element (SE), the parallel element (PE), and the contractile element (CE). A skeletal muscle is considered as a large sarcomere that is the contractile element and accounts for producing active muscle force which is dependent on the muscle length and time-varying neural signal. The series element represents the additional passive viscoelastic properties contributing for the tendon and aponeuroses. And the parallel element represents the behavior of the connective tissues epimysium, perimysium and endomysium. This model describes the contraction force of a muscle as the sum of the three elements.

The Hill's type model was improved by Zajac [17] to a dimensionless aggregate model which can be scaled to represent subject specific musculo-tendon units (MTUs). The force components are modeled from the measurement of isolated muscle fibers, which directly reflect the non-linear properties due to the sliding filaments. The series elastic elements can then be grouped with the tendon and removed from the model. Pennation effects are directly included into the model. For an extended view on skeletal muscle modeling we refer the reader to Lee et al.s' survey [18].

One-dimensional representation of muscles is sufficient in many applications, but many cases also require three-dimensional modeling. Three-dimensional modeling of muscle not only allows studying more complex structures but also leads to more realistic simulations. Three-dimensional muscle simulations can be obtained by using *finite element methods* (FEM) by subdividing muscles (and other anatomical entities) into small elements and applying continuum mechanics (see Sect. 6.2.1). As one of the earliest work, Chen and Zeltzer [19] modeled individual muscles as coarse linear elastic finite elements and used a Hill's type model to approximate the constitutive behavior. Active muscle forces were approximated as parametric functions and embedded into selected edges between vertices of a FEM-based solid.

Blemker and Delp [20] developed and evaluated a new formulation for creating three-dimensional finite element models that represent complex muscle geometry and the variation in moment arms of fibers within a muscle. This 3D muscle model has the advantage to represent complex muscle path motion but it is computationally expensive and impractical to use in real-time applications. At the same time, Teran et al. [21] used a finite volume method (FVM) with quasi-incompressible, transversely isotropic, hyper-elastic constitutive model to simulate soft tissue contraction and deformation. B-spline solids were used to model fiber directions, and the muscle activation levels were derived from key-frame animations. They claimed that FVM inherently requires less computation and memory usage in comparison with FEM. Later, Lee et al. [22] introduced one of the most detailed biomechanical model of the human upper body composed of a dynamic articulated skeleton, Hill's type muscle actuators including the force–velocity relation, and realistic finite element simulation of soft tissues and skin deformation. They used inverse dynamic with target poses and co-activation as input to compute muscle activation. The activation is then used to simulate skeleton dynamics and soft tissue deformation. The skin and underlying soft tissues were also simulated using FEM.

By using these detailed three-dimensional representations, accurate musculoskeletal simulation is achievable. In addition to be more accurate in comparison to one-dimensional representations, three-dimensional representations lead to more realistic visualization which is usually one goal in computer animation. But the computation cost and time consuming procedures of these methods make them impractical in many real world applications. Moreover, making three-dimensional representations of anatomical entities require generic or subject-specific data, as discussed in Sect. 6.2.3.

6.2.2.3 The Connective Tissue and Skin

The human skin has experimentally been approximated as a layered, nonlinear, thin, elastic and incompressible material. In computer animation and graphics, many models of physical skin have been proposed, notably for anatomy-based character rigging, and especially for body parts where skin deformation is clearly visible. It is sometimes important that a model can exhibit dynamics effects (e.g. jigging and bulging) and not only pure kinematics effects from geometric rigging techniques, as it thus

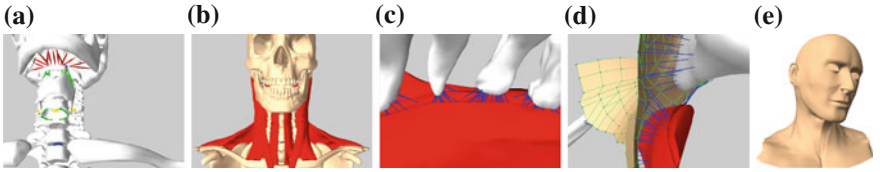

Fig. 6.3 Example of physical simulation of layered anatomical human neck. **a** Skeleton, **b** Underlying musculature, **c** Muscle to bone attachments, **d** Elastic skin and connective tissue **e** Result of a dynamic skinning

produces much more convincing character animation. In general, such models are broken down into several well-defined layers that contribute to the overall visual appearance and behavior. The fat and connective tissue layers both separate and attach the skin to the underlying muscle and bone layers. For instance, the fat layer can be specified simply as a thickness between the skin and muscle layers, and the connective tissue modeled as rubber bands strung between points on the skin surface and on the muscle layer surface [23].

The discretization of the numerical modeling of the physical skin is widely employed in deformable character with a geometric- or physically-based rigger. When a character skeleton is rigged, the influence of a joint can be calculated. That influence gives the transformations of the skin surface vertices to apply according to the character pose. These transformations can either be propagated by inverse and forward kinematic forces to the skin directly or through attached soft tissues (see Fig. 6.3). Two popular surface modeling approaches exist. The first one accounts for the elasticity only from the consideration of the thin feature. In the second, volumetric models with volume conservation can take the incompressible factor into account.

Focusing on the elastic surface is one possible approach to a fast solution for physically-based deformation of anatomical humans. Turner and Thalmann [23] discretized the skin surface using the finite difference method (FDM), i.e. used a rectangular mesh of three-dimensional points as representation together with the physical characteristics (e.g. mass, elasticity) and current state information (e.g. position, velocity). Spring is also a popular approximation to the elasticity of a material and the mass-spring system is widely used for skin modeling, especially facial deformation, which can date back to the layered elastic model used by Terzopoulos and Waters for facial animation [24]. In this model, a 3D mass-spring lattice is attached to a human skull model and deformed by muscles which take the form of force constraints between the skin surface and the underlying bone. The springs are biphasic to emulate the non-linear behavior of real skin. Galoppo et al. [25] presented a fast method to capture dynamic deformations on the surface of a soft body including a rigid core, and they extended their method later to apply to soft body characters with multiple rigid bones [26]. Shi et al. [27] developed a surface-based deformable model to enrich the skeleton-driven character skinning in real-time, with physically-based secondary deformation. They learned the material parameters, mainly the stiffness, of the surface model from a surface mesh and a few sample sequences of its physical behavior. However, these simulations only consider the elastic energy from skin-layer

deformation and do not include the deformation inside the volume, so it does not capture pose-dependent deformations correctly.

The incompressibility of the human skin is realized in mathematical models by simulating the volume conservation of the deformable bodies. Terzopoulos and Waters [24] used a multi-layered mass-spring structure to yield the volume preserving constraints to simulate the effects of incompressible fatty tissue. However, the difficulty in handling the volume preservation in a mass-spring system makes the finite element methods widely used as an alternative approach. The nonlinear Green-Lagrangian strain tensor can express large deformations correctly whereas expensive computation is required. However, using a quasi-static approximation, it is still possible to have a practical character skinning. Teran et al. [28] presented a quasi-static solution for flesh deformation driven by a skeleton. Lee et al. [5] used a similar method to compute the deformation of the soft tissue in their biomechanical model of the human upper body. Though such quasi-static solutions are much faster than a fully dynamics simulation with the same model size, they do not capture the dynamic behaviors of the soft body such as jiggling. Fast simulation also can be pursued by simplifying the computation using a linearized strain, or infinitesimal strain under the assumption of small deformation [29]. Nonetheless, it causes serious problems such as inflation of the body especially when the deformation contains rotational part. To alleviate this shortcoming, many corotational methods (e.g. [30, 31]) are proposed to remove as much of the rigid rotation as possible by using local coordinate frames following the global motion of the body. Though corotated linearized strain has been widely used in interactive graphics applications, it is still valid only when the deformation is very small.

In deformable character animation, the size of the skin model can be large, and often requires a lifelike skin deformation, especially in animation film and interactive graphics application. A high resolution finite element model has to be built with a large amount of elements, which can eventually be million-scale [5]. This makes the simulation totally impractical by current common computing power.

Methods using modal reduction to reduce the complexity of a finite element system have been investigated, whereas they are not sufficient to capture the nonlinear deformations. Alternatively, many current techniques called *mesh embedding* use the concept of spatial embedding, where a relatively low-dimensional coarse volumetric mesh enclosing the entire deformable body is generated, and it expresses the behavior of the body and embeds a fine geometry which is also for the visualization of the skin deformation. One of these techniques relies on a free-form deformation lattice attached to the skeleton [32].

Mesh embedding has been widely used to simulate soft bodies as it reduces the DOF of the deformable bodies without losing the fine geometry of the characters and the internal skeleton can be handled more easily in the embedding mesh system compared to the modal reduction [33]. For that reason, Lee et al. [5] embed a high-resolution skin surface as the visualization geometry into the simulation mesh in their comprehensive upper human body model.

Since in skinning, the realism delivered to observers lies in the visualization of skin deformation, some frameworks prefer to replace the skin simulation by

a post-processing shape deformation component. Zordan et al. [3], in their breathing simulation model, recorded the trajectories of pre-selected points attached to the model used as control vertices of a NURBS surface. The surface shape is then updated to show skin deformation. However, the surface shape is implicitly defined by how the control vertices are selected and limited to the captured data. High-quality rendering of the skin can be considered to be done offline using advanced skin rendering engines like Pixar's RenderMan [34] or NVIDIA's Mental Ray [35], to enrich the visualization referenced to real human skin.

6.2.3 Acquisition and Processing of the Human Anatomy

In this section we present the typical pipelines for automatic generation of volumetric meshes of anatomical structures. We introduce techniques to acquire anatomical structures from the real-world and to process these structures into a musculoskeletal model that can be simulated.

6.2.3.1 Artistic Anatomy

In computer animation and graphics applications, most human figure models use a simplified articulated skeleton consisting of relatively few connected segments. The bones are constrained by joints which allow them to move relative to one another within limits. Since the focus is on the capability of articulation, it is usually not necessary for the skeleton geometry to conform to the real world, even when movable joints are modeled with sets of curves [36, 37]. Nonetheless, subject-specific and accurate geometries are generally required in biomedical research like surgery simulation.

In an anatomical human (see Fig. 6.4), the musculature system is typically more complex than the skeletal system. Indeed in the human anatomy, muscles are arranged side-by-side and in layers on top of bones and other muscles. They often span multiple joints and typically consist of different types of tissue, allowing some portions to be contractile and others not. Depending on their state of contraction, muscles have different shapes and influence their surface form in different ways.

In an effort to achieve real-time performances, muscles are usually constructed from NURBS or spline patch (see Fig. 6.5). Scheepers et al. [11] developed anatomy-based models of skeletal muscles used to flesh-out a skeleton. They use ellipsoids to represent muscle bellies and deformation is achieved by updating the volume when the lengths of the principal axes are adjusted. As a general muscle model, they construct a bicubic patch mesh by sweeping a varying ellipse along a cubic Bezier curve, and reach the deformation by manipulating the control points sampled along the curves. Pratscher et al. [39] use elliptical muscle models and a procedural deformation for the muscle simulation in their anatomy-based character rigging system.

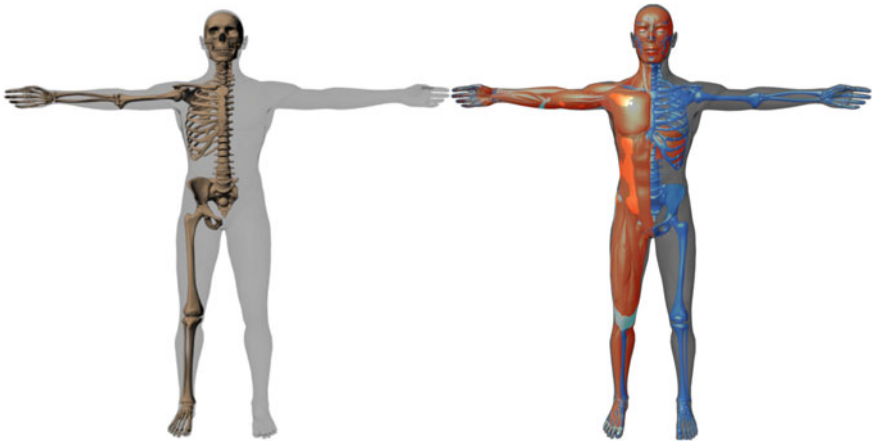

Fig. 6.4 The Ultimate Human Model data set by cg Character, an artistic and anatomically accurate human model [38]

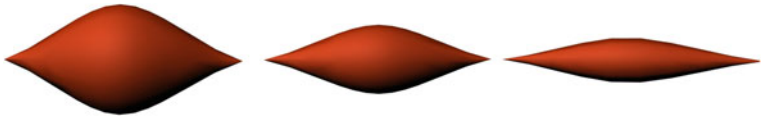

Fig. 6.5 Muscle deformation by manipulating the control points of a NURBS surface

These geometrical skinning techniques consider the anatomy such that they can reproduce muscle bulging, yet the deformation cannot be considered as realistic.

6.2.3.2 Segmented MRI and CT scans

3D representation of musculoskeletal models have been used extensively in animation to make better visualization and in biomechanics to study musculoskeletal function in different clinical cases [40]. These representations can be generic or subject-specific. Generic musculoskeletal models have some limitations. Most of the software packages for biomechanical analysis of muscle function are based on biomechanical studies of cadaveric specimens and use the musculoskeletal geometry of a healthy, average-sized adult male with normal musculoskeletal geometry [41–43]. These models are useful for studying general trends in large populations. However, if modeling results are to be used to plan surgical procedures, guide treatment decisions and trial implant designs, they must take into account a subject's individual musculoskeletal anatomy. The musculoskeletal system is very intricate and large anatomical variations exist among individuals. The different musculoskeletal geometry due to size or pathology can also affect the accuracy of results derived from generic models. Neuromuscular diseases, such as cerebral palsy, are often responsible for producing

differences in bony geometry and muscle attachment sites. To understand the effects of joint disease, a subject's unique articulation shape and cartilage thickness must be known, both of which contribute to the contact pressure distribution. The need to customize musculoskeletal anatomy is an essential step in the modeling process, if the predictions of computer models are to be useful to clinicians [44].

Scheys et al. [45] have demonstrated the inaccuracy of gait kinematics calculated from scaled generic models in subjects with increased femoral anteversion. Since the results of simulations are often sensitive to the accuracy of the functional musculoskeletal model, individualized musculoskeletal models may be a better alternative. Hence, for an accurate representation of subject-specific anatomical structures, segmentation of medical images are extensively used. Medical imaging techniques such as Magnetic Resonance Imaging (MRI), Computed Tomography (CT) and also Positron Emission Tomography (PET) are used in order to generate 3D volumetric data sets of the human body and to study in vivo the complex geometric relationships among the muscles, bones, and other structures [46, 47]. However, it is time consuming and requires extensive imaging protocols to capture the muscle and joint geometries at different limb positions. Subject-specific musculoskeletal modeling also addresses the problem of image segmentation, which consists of extracting anatomical structures from medical image data such as MRI. Semi-automatic or fully automatic segmentation methods are fast but inaccurate since muscle distinction is often difficult or impossible to assess with currently used methods. Thus, soft tissue volumetric representations are most often and most accurately acquired by defining contours manually. Blemker et al. [20] built for example volumetric finite element representations of muscles from manually segmented MRIs.

6.2.3.3 Preparing Anatomical Data for Simulation

The anatomical data resulting from artist models or segmented scans usually need to be processed to produce a model that can be simulated. In this section we consider two case studies.

In our first case study, we want to focus on the production of FEM-ready volumetric meshes from raw segmented surface models of medical images [48]. At first, it comes handy to store areas such as attachment sites and tendon vertices in an index-invariant structure by defining them by geometry as some tasks may change the amount and ordering of the vertices. Then smoothing out the surface geometries is usually performed by a three-parameter low-pass filter [49] to remove acquisition artifacts. Missing entities can be generated semi-automatically such as tendon extremities but the most important step is the resolution of self-intersections and overlaps. While using Boolean operators for solving overlaps, Peeters and Pronost [48] proposed an algorithm to remove self-intersections in anatomical entities. The final steps consist in generating the volume meshes with the relevant materials and designing the FEM constraints from the index-invariant structure of the first step.

In our second case study, we want to create a realistic and comprehensive model for the human neck, starting from the surface models of an anatomical artistic human data

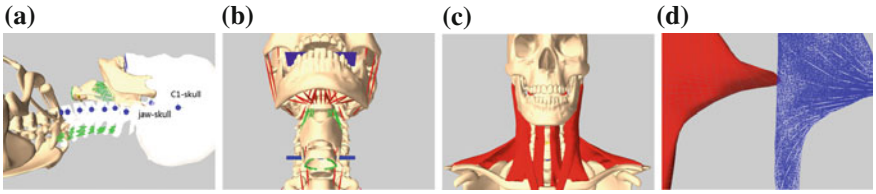

Fig. 6.6 **a** Skeleton (*green lines* represent damped springs), **b** Deep muscles (*red lines*), **c** Superficial muscles and **d** Muscle fibers

set (see Fig. 6.6). Our skeletal structure contains the skull, jaw, C1–C7 cervical bones. First, one to three DOF rotational joints are inserted between adjacent vertebrae, and the jaw-skull system by carefully locating the pivot points (blue dots in Fig. 6.6a). Joints are also limited to a certain range from a study on the human neck [50]. Bones that are involved in the neck mechanics are modeled as fixed rigid bodies. Notice that two extra unilateral planar constraints can be added between the upper and lower teeth (blue planes in Fig. 6.6b), hence to resist penetration between jaw and skull. For stabilization, damped springs can be attached between certain adjacent vertebrae (green lines in Fig. 6.6a). At that point, the stiffness of the ligaments can be included [51]. In order to simulate the aspects of the throat, the hyoid, thyroid, and cricoid bones can be incorporated. A revolute joint (blue cylinder in Fig. 6.6b) is created between thyroid and cricoid, and damped springs (green lines in Fig. 6.6b) are attached between hyoid–sternum, thyroid–cricoid and cricoid–sternum. The skeleton structure is then simulated using a multi-body approach.

Then we have to generate the volumetric (e.g. tetrahedral) meshes of our deformable bodies using a mesher such as TETGEN [52] or CGAL [53]. Applying some standard geometrical operations beforehand may be useful, such as *edge bridge* followed by *fill hole* to fill the holes, and/or employ self-intersection removal algorithms [48, 54]. In order to obtain more accurate simulations, a maximum tetrahedron volume constraint may be needed to ensure that the size of the finite elements is reasonably small.

Next, muscle fibers can be modeled as polygon curves with a small number of segments along the direction of muscle contraction. To achieve it, we can select points at each attachment area to the bone and additional points on the surface of the polygon mesh. According to the principle that each pair of points should lie on a line in the direction of muscle contraction, we can pair the points up. Linear interpolation between two points can then be performed to generate the segments. Next, Hill's type muscle models (see Sect. 6.2.2.2) are defined at the segmental scale. The method proposed by Tan et al. [55] can be used to calculate the force on nearby elements induced by muscle contraction. Figure 6.6c–d shows an example of muscles and muscle fibers generated for the trapezius. Finally, the FE models are coupled to the skeletal system by attaching nodes to the bones.

6.2.4 Acquisition of the Function of Human Anatomy

Once a 3D model of the human body is built, motion and force can be captured and used to derive simulations in order to add realism to computer animation and allow for accurate results in biomechanical simulation. Capturing data related to kinematics variables that describe movement can be two-dimensional or three-dimensional. Kinematics data describe the motion of a system without consideration to its mass or the acting forces and usually consist of coordinates of tracked markers or joint articular trajectories. This data can be applied to a biomechanical model in order to analyze the movement of a subject, but also to an animation to drive the motion of a user's avatar. Kinetic data describes the forces that produce or result from movement. The most commonly used equipment to collect motion and force data are video cameras, optoelectronic systems, electromyography, force plates, and inertial systems.

6.2.4.1 Video Cameras and Optoelectronic Systems

Video recording and optoelectronic systems are used in motion capturing to track poses over time of an actor or a patient being tested. While video capture can be solely based on the subject's shape, in practice often markers are placed on the body as well. Markers are either solid shapes covered with retro-reflective tape in *passive* marker systems, usually sensitive to infrared light (IR), or they are emitting diodes (LEDs) in *active* marker systems.

These latter LED markers are pulsed sequentially, so the system automatically knows the identification of each marker. The system can then maintain the identification of each marker, if it is occluded by other body parts, or if it temporarily moves outside of the viewport. Mixing up markers cannot occur in such a system and therefore markers can be placed very close together. However, these systems have the disadvantage that it requires much more equipment to be placed and held by the user. Also for long duration trials, the heat generated by the LEDs might be a problem.

On the other hand, passive markers reflect light which is emitted by LEDs (usually IR and near IR) placed around cameras. IR filters are used on the camera lenses and thresholds are set to distinguish between bright light from markers and dim light considered as background noise. Each marker trajectory must be identified with a label and tracked throughout the trial. When markers are lost from view or their trajectories cross, this may cause loss of their proper identification. There is also a limitation on how close markers can be placed together. These systems have the advantage of using lightweight reflective markers without the need for electrical cables or batteries on the user [56].

Two-dimensional analysis requires only one camera positioned perpendicular to the plane of movement. Any marker movement outside this plane will be distorted. Three-dimensional analysis looks at movement in all directions and requires more than one camera. To achieve 3D analysis, a computer software calculates the 3D

coordinates for each marker based on the 2D data from two or more cameras and the known location and orientation of the cameras. In practice, the points of interest on the subject must be visible by at least three cameras at all times in order to reconstruct their positions [56, 57]. If markers are used, skin movement artifacts caused by the skin moving over the musculoskeletal structure must be removed from the data before reconstruction of movement can be performed.

6.2.4.2 Electromyography

Electromyography (EMG) is used to detect and measure the small electric signal produced by muscles during contraction. Electrodes (sensors) are used to detect electric signals and there are two types: *surface* electrodes and *wire* electrodes. Surface electrodes are placed on the skin and wire electrodes inserted into the muscle. Surface electrodes have gained widespread use due to their ease of application and because skin penetration is not required. However, placing the sensors on the skin can give erroneous readings for a specific muscle as other muscles lying around or on top can cause cross-talk in the signal. Deep muscle signals can be reliably obtained only with intramuscular wire electrodes. Inserting electrodes into the muscle itself gives more accurate readings for the muscle activation but is invasive. Surface electrodes come in two basic types: *passive* and *active*. Active electrodes have become quite popular, as they provide signal amplification at the electrode site [56, 58].

6.2.4.3 Force Plates

A force plate is used to measure ground reaction forces exerted by a person and consists of a steel plate and transducers at each corner. When a load is applied to the plate, transducers detect it and the load is converted into an electrical signal. The magnitude and direction of the force (vertical and shear forces) are measured and the instantaneous center of pressure can be calculated. Two types of force plates are available: *piezoelectric* and *strain gauge*. Piezoelectric force plates use quartz transducers which generate an electric charge when stressed. They do not require a power supply to excite the transducers. However, special charge amplifiers and low noise coaxial cables are required to convert the charge to a voltage proportional to the applied load. In general, piezoelectric force plates are more sensitive and have a greater force range than strain gauge types. Strain gauge force plates use strain gauges to measure the stress in specially constructed load cells when a load is applied. They do not require the special cabling and charge amplifiers of the piezoelectric type. However, they require excitation of the strain gauge bridge circuit. The size of force plate and the range of readings depend on the application. Force plates can be combined with kinematics data and inverse dynamic systems to work out parameters such as the net moment about each joint, muscle forces and joint contact forces [59].

6.2.4.4 Inertial Systems

Inertial systems include *accelerometers* and *gyroscopes* and are based on the principle of measurement of inertia. Accelerometers operate on a mass-spring principle. Two charged plates are separated and a capacitance or resistance between them is given as a function of their separation. One plate is suspended over the other on flexible mounting and acceleration causes this mounting to flex giving a change in plate separation. The change in capacitance or resistance is measured and the change in separation calculated. The second derivative of the change in separation with respect to time gives the acceleration at the attachment point [57].

Gyroscopes are devices used for measuring orientation and can be used in gait analysis to give segment orientation. In order to obtain the limb orientation the angular acceleration must be integrated twice with respect to time and this will amplify any initial errors. The sensors themselves are small and lightweight, and can detect a large range of angular velocities. If gyroscopes are combined with accelerometers then the data can be used to easily obtain the kinematics of the subject's movement [57, 60].

6.3 Simulating Virtual Anatomical Humans

6.3.1 Rigid Body Physics and Muscular Actuation

Physical simulation offers the possibility of truly responsive and realistic animation. We have observed in the last decade a renewed interest in the use of physical simulation for interactive character animation and simulation, and many recent publications demonstrate tremendous improvements in robustness, visual quality and usability. For a detailed review about physics-based character animation, we refer the reader to the survey paper [61]. In a physics-based system, virtual humans need forces and torques to actively move around. In order for such forces or torques to be realistic, they must originate from within the character. We use the term *actuators* to describe the mechanisms that generate the forces and torques that make a character move. Common frameworks make use of a combination of joint torques (straightforward DOF actuation model), external forces (e.g. to control the global translation and rotation) and virtual forces (joint torque emulation of external force effect). In addition to these actuation schemes, a fair amount of recent works are dedicated to actively actuate virtual anatomical humans through simple muscle actuators.

Biological systems are actuated through contraction of muscles, which are attached to bones through tendons. When muscles contract, they generate torques at the joint(s) over which they operate, causing the attached limbs to rotate in opposite directions. In addition to contracting when activated, muscles (and tendons, in a lesser degree) have the ability to stretch. This makes them behave like unilateral springs and allows for an efficient mechanism for energy storage and release. Since muscles can only pull, at least two muscles are required to control a single DOF

(so-called antagonistic muscles). In physics-based character animation, use of muscle-based actuation models is uncommon, because of the increased number of DOFs that require control and decreased simulation performance [62]. However, examples of muscle based actuation do exist, and we witness an increased interest in using more advanced muscle-based actuation models for controlling physics-based characters [63–65]. This reflects the need for more accurate anatomical virtual humans.

In one of the latest work to date, Wang et al. [66] propose a biologically-motivated locomotion controller. Their lower-body model is actuated by sixteen Hill's type MTUs (see Sect. 6.2.2.2). To determine muscle excitation patterns, biologically-motivated laws are used for muscle control, and stance and swing phases. The parameters of these control laws are set by an optimization procedure that satisfies a number of locomotion task terms while minimizing a biological model of metabolic energy expenditure. This work demonstrates the importance of modeling constraints on torque generation due to muscle physiology, both in restricting the space of possible torque trajectories and in providing a realistic model of effort.

6.3.2 Deformable Body Simulation

The human body consists of intricate deformable tissues. To achieve realistic animation and to study biomechanics of deformation in medical applications, the realistic deformation of the human body system is required. Several approaches have been proposed to model human body deformations. As the emphasis of this chapter is on challenges in biomechanics and animation, we classified modeling approaches into non-physically based methods and physically based methods.

6.3.2.1 Non-Physically Based Methods

Non-physically based methods are useful methods in many applications especially when a high level of geometric control is needed. They usually use simplified physical principles to achieve visually appealing results. The most important non-physically based methods described here are based on surface data (parametric and polygonal surface and implicit surface) and free-form deformation.

3D Surface

Parametric and polygonal surfaces can be used to model deformable bodies. One method to model deformation is using *splines*. Splines are used as a tool to create and interpolate curves and surfaces mainly in the field of computer aided geometric design. This technique is based on the representation of both planar and 3D curves and surfaces by a set of control points or landmarks. Bezier curves are widely used to model smooth curves. The curve is completely contained in the convex hull of its control points which can be graphically displayed and used to manipulate the curve

intuitively. Transformations such as translation, scaling and rotation can be applied on the curve by applying the respective transform on the control points. Bezier splines are sets of low-order Bezier curves patched together to represent more complex shapes. Another type of spline is Basis spline (B-spline) which is a generalization of Bezier curves. They depend on the k-nearest control points at any point on the curve. Combining B-splines allows creating B-spline surfaces. Another generalization of Bezier splines is non-uniform rational basis spline (NURBS). The primary difference of this type is the weighting of the control points which makes them rational.

Another method to model deformation of bodies is using *implicit surfaces*. Implicit surfaces are introduced as an extra layer coating any kind of structure that moves and deforms over time. They can provide an efficient collision detection mechanism by offering a compact definition of a smooth surface around an object [67]. An implicit surface [18] generated by a set of skeletons s_i $(i = 1, 2, \ldots, n)$, with associated field functions f_i, is defined at the isovalue c by:

$$\left\{ P \in \Re^3 | f\,(P) = c \right\}$$

where

$$f\,(P) = \sum_{i=1}^{n} f_i\,(P)$$

The field function is generally a decreasing function of the distance from a given point P to the associated skeleton. Based on the type of field function, various implicit surfaces have been developed such as blobs, metaballs, soft objects, and convolution surfaces [18].

Free Form Deformation

Free Form Deformation (FFD) consists in deforming the space embedding objects. FFDs provide simple and fast control, but they do not permit direct manipulation. Also, the regular lattice spacing used by FFDs prevents the detailed control needed to produce more complex shapes [18]. As one of the early works, Chadwick et al. [68] employed FFDs to represent muscle deformation. Articulated skeletons, located inside muscles, transform a surrounding lattice and cause changes in the shape of the muscles. As another example, Moccozet and Thalmann [69] presented a generalized method for FFDs that combines the traditional model with techniques of scattered data interpolation based on Delaunay and Drichlet–Voronoi diagrams. They applied the method to model deformations around a human hand model.

6.3.2.2 Physically Based Methods

While non-physical based methods are useful methods in many applications, physically based methods are a better choice for biomechanical human modeling with

medical application. Physically based methods lead to more realistic simulation and also provide the capability to study a case as a mechanical simulation and to find the real behavior of tissues during deformation. In this method, *partial differential equations* (PDEs) which govern the evolving shape of the deformable objects and their motion through space should be solved. The major difficulty in these methods lies in the complexity of the physical phenomena that should be simulated and computationally solved from the PDEs. To overcome this difficulty, one should simplify the model and apply numerical techniques to solve the PDEs. We describe hereafter two relevant methods based on mass-spring systems and finite elements.

Mass-spring systems

A mass-spring system is a physically based technique that has been widely and effectively used for modeling deformable objects. An object is modeled as a collection of point masses connected by massless springs in a lattice structure. Springs connecting point masses exert forces on neighboring points when a mass is displaced from its rest position. The elastic force acting on mass i connected by a spring to mass j is given by:

$$f_{ij} = k\left(|x_{ij}| - l_{ij}\right)\frac{x_{ij}}{|x_{ij}|}$$

where $x_{ij} = x_j - x_i$ and x_i, x_j are the locations of point masses i and j, respectively, l_{ij} is the rest length between them and k is the spring's stiffness. Applying this equation on all the points leads to a differential system of ordinary equations that can be solved explicitly using various algorithms [18]. Mass-spring systems are easy to construct, and both interactive and real-time simulations of mass-spring systems are possible. Also it has the ability to handle large deformations. As a disadvantage, usually spring constants are approximated from measured material property and allocating suitable constants that express all tissue properties in a natural way is difficult.

Mass-spring systems have been widely used in facial animation. As an example in biomechanical modeling, mass-spring systems were used by Nedel and Thalmann [70] to simulate muscle deformation. Muscles were represented at two levels, action lines and muscle shapes. The muscle shapes were deformed using a mass-spring mesh. They used angular spring to control the volume of muscles during deformation and smooth out mesh discontinuities.

Finite element method

Finite element method (FEM) is another physically-based technique that has been widely used in soft tissue modeling. Contrary to mass-spring systems that treat the mechanics as a discrete process, FEM views it as a continuum (see sect. 6.2.1.1). For that reason, FEM usually leads to more accurate physical models compared to

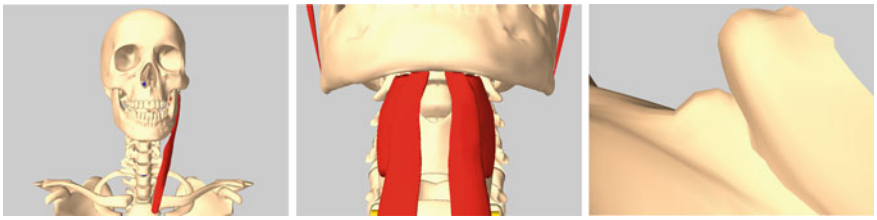

Fig. 6.7 Illustrations of an anatomical simulation of the neck, including skeletal muscles actuation and Adam's apple simulation

mass-spring systems. Each finite element model of a 3D object consists of a solid body with mass and energies throughout. In FEM, an object is divided into small elements (e.g. hexahedra or tetrahedra in 3D, quadrilaterals or triangles in 2D) joined at discrete nodes. Displacements and positions in an element are approximated from discrete nodal values using interpolation functions:

$$\Phi(x) \approx \sum_i h_i(x)\, \Phi_i$$

where h_i is the interpolation function for the element containing x and Φ_i is the scalar weight associated with h_i.

Choosing the appropriate element type and the interpolation functions depends on the object geometry, accuracy requirements, and computational budget. Higher order interpolation functions and more complex elements lead to more accurate solutions however it needs more computation. To sum up, finite element methods provide more realistic simulations than mass-spring methods but they are more computationally expensive. To achieve real-time deformation, reducing the computation time is necessary. Unfortunately, it is not always possible to use large timesteps to achieve this reduction, due to the large deformations that occur with the soft tissues present in the human body, in particular muscles. Some examples of usage of this technique to simulate muscle deformation have been mentioned in Sect. 6.2.2.2.

6.4 Implementing Virtual Anatomical Humans

Several open simulation architectures have been presented to the biomedical community in recent years. In this section, we introduce four well-known subsystems and provide this information as a reference to whom would like to quickly start researching and developing in anatomical modeling and simulation of humans. Comparisons are implicitly given by presenting some of our research in the simulation of neck muscles and the Adam's apple.

We researched the simulation of neck muscles and the Adam's apple based on anatomical modeling and simulation (see Fig. 6.7). The muscles are modeled as

deformable bodies and the skeletal mechanism as a dynamic multibody system. Besides the simulation of the underlying structures, we also simulate skin deformation with the ultimate goal of achieving realistic real-time facial animation (see Sects. 6.2.2.3 and 6.2.3.3). To reach the desired simulation, we leverage features from ArtiSynth [71]. ArtiSynth is an open source, Java-based biomechanical simulation environment for modeling complex anatomical systems composed of both rigid and deformable structures. It provides fully coupled FEM/multibody capabilities.

Nonetheless, we still design the musculoskeletal dynamics using OpenSim's neck model [50]. OpenSim [41, 43] is a multibody simulator with inverse modeling capabilities designed for musculoskeletal studies. In such simulator, it is impossible to directly obtain deformation of muscle shape conforming to real world. The muscles in OpenSim are 1D action lines using the Hill's type model, and therefore the system does not support deformation of anatomical structures. It hinders the skinning of the musculoskeletal structure, nonetheless critical for animation purposes.

As nonlinear FEM produces more accurate muscle deformation, we use the FEBio solver [72] to simulate the muscles. FEBio is a non-linear finite element toolkit with special support for tissue modeling and some support for rigid-bodies, contact and constraints. Our FE models are generated by a meshing algorithm on the polygon meshes of an artistic anatomical data set. Because FEBio only support the skeleton modeling weakly, especially the integration with the muscles, we have to give much manual efforts to model the skeleton, and attach the finite nodes to the relevant bones by the selection functions it provides.

Nonlinear FEM simulation is usually too computationally expensive to be used in interactive graphics application. As aforementioned, the mesh embedding is a useful solution to speed up the performance while it still can keep high-fidelity emulation. Sofa [73] is such an environment which implements several schema of mesh embedding such as barycentric interpolation and mesh topology mapping. There is one highlight of its architecture, the modularization, where each simulation component (e.g. mechanical state, FEM simulation, collision, mesh embedding and visualization) is an individual module. Through its GUI, we can drag modules into the scene graph to form a simulator. Moreover, the modules can be customized by modifying a set of parameters. To simulate a deformable body in real-time, Sofa is highly recommended while it is not a comprehensive biomechanical modeling and simulation environment.

In order to study the biomechanics of a system for simulation in character animation, we advise to use ArtiSynth. It provides several material implementations including nonlinear, linear and corotational linear materials, and explicit and implicit time integrators. Automatic coupling of the skeleton–muscle systems can be implemented by spatial search using various bounding volume hierarchies. However, in practice, we have experienced an easier and more accurate manual selection of attachment nodes in the FEBio environment.

To sum up, each open simulation environment has its unique advantages and supports for different tasks. We can make extensive use of one or multiple of such environments to start a research or development project. We believe that it

is a promising solution to adopt results from biomechanical modeling for the production of believable character animations.

6.5 Conclusion

In order to realistically animate the human body, it is necessary to take into account the biomechanical aspects of modeling. Although this makes procedures more complicated and thus computationally expensive, it will result in more meaningful medical simulations. Below, we describe possible steps to undertake in order to model and simulate the complex human musculoskeletal structure.

- Defining tissue material properties and mechanical principles that should be applied to simulate the human body.
- Studying the anatomy of the tissues which contribute to the modeling of the bones, muscles, joints and skin.
- Making anatomical geometry of the tissues either generic or subject-specific based on study case. Patient specific models can be made by using medical images for specific users.
- Preparing the anatomical geometries to be used in the modeling procedure.
- Defining a method that models each tissue given a realism criterion and that contains the biological behavior of the tissues. The method may also take into account interactions of different tissues.
- Defining different techniques to control the function of the anatomical structures, producing human movement and simulating clinical cases. These techniques may make use of resulting forces and motion capture data to derive the simulations.
- Defining a suitable method to show deformations of soft tissues making the simulations as close to reality as desired.

Achieving realistic animation that includes plausible biomechanics leads to more visually appealing visualization of virtual humans and may allow medical application as well. However, as mentioned in this chapter, the modeling and simulation procedures are time consuming and typically result in low frame rates. One of the reasons for such performance lies on the nonlinear mechanical properties of anatomical structures. In addition, the detailed geometries that are necessary for the continuum simulation of deformable bodies relate directly to the computation time. In an effort to reduce computation time, we observe a trade-off between simplification of mechanical relations and tissue properties, and accuracy. Considering bones as rigid bodies is one example. Another possibility consists in using methods that combine offline and online computations. And hopefully, the computer graphics community has in the last decade proposed many efficient techniques in that regard.

Moreover, we have to notice that virtual anatomical human modeling and simulation often induce a large number of parameters to be tuned to reach a desired result. In practice this task may reveal itself as difficult and time consuming. A good starting point is to initially adopt parameter values from the experimental works and then

tune them until converging to a satisfactory solution according to measurements. In a virtual scene where the deformation of human body is simulated, graphical visualization can be incorporated into the system. For example, in the simulation of the human skin, high-end rendering could be used to make the visualization more intuitive to observers. The better the visualization, the more realistic the simulation can become.

Acknowledgments This work has been supported by the Dutch research project COMMIT—Virtual Worlds for Well-Being [74].

References

1. 3D anatomical human. EU Research Project. http://3dah.miralab.ch/, 2010.
2. Multi scale biological modalities for physiological human articulation. EU Research Project. http://multiscalehuman.miralab.ch/, 2013.
3. Zordan, V. B., Celly, B., Chiu, B., & DiLorenzo, P. C. (2006). Breathe easy: Model and control of human respiration for computer animation. *Graphical Models*, *68*(2), 113–132.
4. DiLorenzo, P. C., Zordan, V. B., & Sanders, B. L. (2008). Laughing out loud: Control for modeling anatomically inspired laughter using audio. *ACM Transactions on Graphics*, *27*(5), 125:1–125:8.
5. Lee, S.-H., Sifakis, E., & Terzopoulos, D. (2009). Comprehensive biomechanical modeling and simulation of the upper body. *ACM Transactions on Graphics*, *28*(4), 99:1–99:17.
6. Winter, D. A. (2005). *Biomechanics and motor control of human movement* (3rd ed.). Hoboken: Wiley.
7. Nordin, M., & Frankel, V. H. (2012). *Basic biomechanics of the musculoskeletal system* (4th ed.). USA: Wolters Kluwer Health.
8. Gibson, L. J., & Ashby, M. F. (1999). *Cellular solids: Structure and properties*. Cambridge Solid State Science Series. Cambridge: Cambridge University Press.
9. Spivak, J. M., DiCesare, P., Feldman, D., Koval, K., Rokito, A., & Zuckerman, J. D. (1999). *Orthopaedics: A study guide*. New York: McGraw-Hill.
10. Seth, A., Sherman, M., Eastman, P., & Delp, S. (2010). Minimal formulation of joint motion for biomechanisms. *Nonlinear Dynamics*, *62*(1–2), 291–303.
11. Scheepers, F., Parent, R. E., Carlson, W. E., & May, S. F. (1997). Anatomy-based modeling of the human musculature. In *Proceedings of the 24th annual conference on Computer Graphics and Interactive Techniques*, 1997, pp. 163–172.
12. Yamaguchi, G. T., & Zajac, F. E. (1989). A planar model of the knee joint to characterize the knee extensor mechanism. *Journal of Biomechanics*, *22*(1), 1–10.
13. Wilhelms, J. (1997). Animals with anatomy. *IEEE Computer Graphics and Applications*, *17*(3), 22–30.
14. Maurel, W., & Thalmann, D. (2000). Human shoulder modeling including scapulo-thoracic constraint and joint sinus cones. *Computers and Graphics*, *24*(2), 203–218.
15. Gasser, H. S., & Hill, A. V. (1924). The dynamics of muscular contraction. *Proceedings of the Royal Society of London. Series B, containing papers of a biological character*, *96*(678), 398–437.
16. Hill, A. V. (1938). The heat of shortening and the dynamic constants of muscle. *Proceedings of the Royal Society of London. Series B, Biological Sciences*, *126*(843), 136–195.
17. Zajac, F. E. (1988). Muscle and tendon: Properties, models, scaling, and application to biomechanics and motor control. *Critical Reviews in Biomedical Engineering*, *17*(4), 359–411.
18. Lee, D., Glueck, M., Khan, A., Fiume, E., & Jackson, K. (2010). A survey of modeling and simulation of skeletal muscle. *ACM Transactions on Graphics*, *28*(4).

19. Chen, D. T., & Zeltzer, D. (1992). Pump it up: Computer animation of a biomechanically based model of muscle using the finite element method. *SIGGRAPH Computer Graphics*, *26*(2), 89–98.
20. Blemker, S. S., & Delp, S. L. (2005). Three-dimensional representation of complex muscle architectures and geometries. *Annals of Biomedical Engineering*, *33*(5), 661–673.
21. Teran, J., Sifakis, E., Blemker, S. S., Ng-Thow-Hing, V., Lau, C., & Fedkiw, R. (2005). Creating and simulating skeletal muscle from the visible human data set. *IEEE Transactions on Visualization and Computer Graphics*, *11*(3), 317–328.
22. Lee, S.-H., Sifakis, E., & Terzopoulos, D. (2009). Comprehensive biomechanical modeling and simulation of the upper body. *ACM Transactions on Graphics (TOG)*, *28*(4), 99.
23. Turner, R., & Thalmann, D. (1993). The elastic surface layer model for animated character construction. *Communicating with virtual worlds*. Tokyo: Springer Verlag.
24. Terzopoulos, D., & Waters, K. (1991). Techniques for realistic facial modeling and animation. *Computer animation*. Tokyo: Springer-Verlag.
25. Galoppo, N., Otaduy, M. A., Mecklenburg, P., Gross, M., & Lin, M. C. (2006). Fast simulation of deformable models in contact using dynamic deformation textures. In *Proceedings of the 2006 ACM SIGGRAPH/Eurographics Symposium on Computer Animation*, 2006, pp. 73–82.
26. Galoppo, N., Otaduy, M. A., Tekin, S., Gross, M., & Lin, M. C. (2007). Soft articulated characters with fast contact handling. *Computer Graphics Forum*, *26*, 243–253.
27. Shi, X., Zhou, K., Tong, Y., Desbrun, M., Bao, H., & Guo, B. (2008). Example-based dynamic skinning in real time. *ACM Transactions on Graphics*, *27*(3), 29:1–29:8.
28. Teran, J., Sifakis, E., Irving, G., & Fedkiw, R. (2005). Robust quasistatic finite elements and flesh simulation. In *Proceedings of the 2005 ACM SIGGRAPH/Eurographics Symposium on Computer Animation*, 2005, pp. 181–190.
29. Kim, J., & Pollard, N. S. (2011). Fast simulation of skeleton-driven deformable body characters. *ACM Transactions on Graphics*, *30*(5):121:1–121:19.
30. Müller, M., Dorsey, J., McMillan, L., Jagnow, R., & Cutler, B. (2002). Stable real-time deformations. In *Proceedings of the 2002 ACM SIGGRAPH/Eurographics Symposium on Computer Animation*, 2002, pp. 49–54.
31. Müller, M., & Gross, M. (2004). Interactive virtual materials. In *Proceedings of Graphics Interface*, 2004, pp. 239–246.
32. Sederberg, T. W., & Parry, S. W. (1986). Free-form deformation of solid geometric models. In *Proceedings of the 13th Annual Conference on Computer Graphics and Interactive Techniques*, 1986, pp. 151–160.
33. Nesme, M., Kry, P. G., Jeřábková, L., & Faure, F. (2009). Preserving topology and elasticity for embedded deformable models. *ACM Transactions on Graphics*, *28*(3).
34. Pixar. RenderMan, http://renderman.pixar.com/
35. NVidia. Mental Ray, http://www.nvidia-arc.com/mentalray.html
36. Lee, S. -H., & Terzopoulos, D. (2008). Spline joints for multibody dynamics. *ACM Transactions on Graphics*, *27*(3):22:1–22:8, 2008.
37. Pronost, N. Sandholm, A. & Thalmann, D. (2010). Correlative joint definition for motion analysis and animation. *Computer Animation and Virtual Worlds*, CASA 2010 Special Issue, *21*, 183–192.
38. The ultimate human model data set. cgCharacter. http://www.cgcharacter.com/ultimatehuman.html
39. Pratscher, M., Coleman, P., Laszlo, J., & Singh, K. (2005). Outside-in anatomy based character rigging. In *Proceedings of the 2005 ACM SIGGRAPH/Eurographics Symposium on Computer Animation*, 2005, pp. 329–338.
40. Pronost, N., Sandholm, A., & Thalmann, D. (2011). A visualization framework for the analysis of neuromuscular simulations. *The Visual Computer*, *27*(2), 109–119.
41. Delp, S. L., & Loan, J. P. (1995). A graphics-based software system to develop and analyze models of musculoskeletal structures. *Computers in Biology and Medicine*, *25*(1), 21–34.
42. Damsgaard, M., Rasmussen, J., Christensen, S. T., Surma, E., & de Zee, M. (2006). Analysis of musculoskeletal systems in the anybody modeling system. *Simulation Modelling Practice and Theory*, *14*(8), 1100–1111.

43. Delp, S. L., Anderson, F. C., Arnold, A. S., Loan, P., Habib, A., John, C. T., et al. (2007). OpenSim: Open-source software to create and analyze dynamic simulations of movement. *IEEE Transactions on Biomedical Engineering*, *54*(11), 1940–1950.
44. Fernandez, J. W., & Pandy, M. G. (2006). Integrating modelling and experiments to assess dynamic musculoskeletal function in humans. *Experimental Physiology*, *91*(2), 371–382.
45. Scheys, L., Desloovere, K., Spaepen, A., Suetens, P., & Jonkers, I. (2011). Calculating gait kinematics using MR-based kinematic models. *Gait and Posture*, *33*(2), 158–164.
46. Assassi, L., Charbonnier, C., Schmid, J., Volino, P., & Magnenat-Thalmann, N. (2009). From MRI to anatomical simulation of the hip joint. *Computer Animation and Virtual Worlds*, *20*(1), 53–66.
47. Gilles, B., Moccozet, L., & Magnenat-Thalmann, N. (2006). Anatomical modelling of the musculoskeletal system from MRI. In *Medical Image Computing and Computer-Assisted Intervention (MICCAI)*, 2006, pp. 289–296.
48. Peeters, P., & Pronost, N. (2013). A practical framework for generating volumetric meshes of subject-specific soft tissue. *The visual computer*, pp. 1–11.
49. Taubin, G. (1995). Curve and surface smoothing without shrinkage. In *5th International Conference on Computer Vision*, 1995, pp. 852–857.
50. Vasavada, A. N., Li, S., & Delp, S. L. (1998). Influence of muscle morphometry and moment arms on the moment-generating capacity of human neck muscles. *Spine*, *23*(4), 412–422.
51. Lee, S.-H., & Terzopoulos, D. (2006). Heads up!: Biomechanical modeling and neuromuscular control of the neck. *ACM Transactions on Graphics*, *25*(3), 1188–1198.
52. Si, H. (2013). TetGen: A quality tetrahedral mesh generator and a 3D delaunay triangulator. http://tetgen.berlios.de
53. Oudot, S., Rineau, L., & Yvinec, M. (2005). Meshing volumes bounded by smooth surfaces. In *Proceedings of 14th International Meshing Roundtable*, 2005, pp. 203–219.
54. Zaharescu, A., Boyer, E., & Horaud, R. P. (2007). Transformesh: A topology-adaptive mesh-based approach to surface evolution, vol. II. In *Proceedings of the 8th Asian Conference on Computer Vision*. LNCS, *4844*, 166–175.
55. Tan, J., Turk, G., & Liu. C. K. (2012). Soft body locomotion. *ACM Transactions on Graphics*, *31*(4), 26:1–26:11.
56. Clayton, H. M., & Schamhardt, H. C. (2001). Measurement techniques for gait analysis. *Equine locomotion*, pp. 55–76. London: W.B. Saunders.
57. Nigg, B. M., Herzog, W., & Wiley, J. (1999). *Biomechanics of the musculo-skeletal system*, vol. 2. New York: Wiley.
58. Stokes, I. A. F., Henry, S. M., & Single, R. M. (2003). Surface EMG electrodes do not accurately record from lumbar multifidus muscles. *Clinical Biomechanics*, *18*(1), 9–13.
59. Allard, P., Stokes, I. A. F., & Blanchi, J. -P. (1995). *Three-dimensional analysis of human movement*. IL: Human Kinetics Champaign.
60. Mayagoitia, R. E., Nene, A. V., & Veltink, P. H. (2002). Accelerometer and rate gyroscope measurement of kinematics: An inexpensive alternative to optical motion analysis systems. *Journal of Biomechanics*, *35*(4), 537–542.
61. Geijtenbeek, T., & Pronost, N. (2012). Interactive character animation using simulated physics: A state-of-the-art review. *Computer Graphics Forum*, *31*(8), 2492–2515.
62. Weinstein, R., Guendelman, E., & Fedkiw, R. (2008). Impulse-based control of joints and muscles. *IEEE Transactions on Visualization and Computer Graphics*, *14*(1), 37–46.
63. Grzeszczuk, R., & Terzopoulos, D. (1995). Automated learning of muscle-actuated locomotion through control abstraction. In *ACM SIGGRAPH Papers Conference Proceedings*, Los Angeles, CA, USA, 1995, pp. 63–70.
64. Hase, K., Miyashita, K., Ok, S., & Arakawa, Y. (2003). Human gait simulation with a neuromusculoskeletal model and evolutionary computation. *The Journal of Visualization and Computer Animation*, *14*(2), 73–92.
65. Murai, A., & Yamane, K. (2011). A neuromuscular locomotion controller that realizes human-like responses to unexpected disturbances. *International Conference on Robotics and Automation (ICRA) 1*, *2–3*, 1997–2002.

66. Wang, J. M., Hamner, S. R., Delp, S., & Koltun, V. (2012). Optimizing locomotion controllers using biologically-based actuators and objectives. *ACM Transactions on Graphics*, *31*(4), 25:1–25:11.
67. Cani-Gascuel, M.-P., & Desbrun, M. (1997). Animation of deformable models using implicit surfaces. *IEEE Transactions on Visualization and Computer Graphics*, *3*(1), 39–50.
68. Chadwick, J. E., Haumann, D. R., & Parent, R. E. (1989). Layered construction for deformable animated characters. *SIGGRAPH Computer Graphics*, *23*(3), 243–252.
69. Moccozet, L., & Magnenat-Thalmann, N. (1997). Dirichlet free-form deformations and their application to hand simulation. In *Computer Animation'97*, 1997, pp. 93–102.
70. Nedel, L. P., & Thalmann, D. (1998). Modeling and deformation of the human body using an anatomically-based approach. In *Proceedings of Computer Animation '98*, 1998, pp. 34–40.
71. ArtiSynth. A 3D biomechanical modeling toolkit for physical simulation of anatomical structures. www.artisynth.org
72. Maas, S. A., Ellis, B. J., Ateshian, G. A., & Weiss, J. A. (2012). FEBio: Finite elements for biomechanics. *Journal of Biomechanical Engineering*, *134*(1), 011005.
73. Allard, J., Cotin, S., Faure, F., Bensoussan, P. J., Poyer, F., Duriez, C., Delingette, H., & Grisoni, L. (2007). SOFA: An open source framework for medical simulation. In *Medicine Meets Virtual Reality (MMVR) 15*.
74. COMMIT. (2013). Virtual worlds for well-being, Dutch Research Project. http://www.commit-nl.nl/

Chapter 7
Clinical Gait Analysis and Musculoskeletal Modeling

Karelia Tecante, Frank Seehaus, Bastian Welke, Gavin Olender, Michael Schwarze, Sean Lynch and Christoph Hurschler

7.1 Introduction

This chapter intends to provide an overview of important concepts of human gait analysis and dynamic simulation of multi-body (MBS) systems for clinical applications. Basic gait concepts are introduced just enough to understand that walking and running involves a large series of musculoskeletal adjustments with specific functions to achieve motion and thus, is a complex process. In recent years, engineering and computer science tools developed with a primary focus on specific engineering problems have expanded into the study of complex dynamic biological structures.

A specific area of interest is human locomotion, specifically walking and/or running (gait). These movements are achieved by the interaction and coordination of many elements of the musculoskeletal system in conjunction with other systems such as the neurological system. Research has been done to better understand gait and thus, researchers investigate the mechanics of the muscle, the relationships between muscles and bones and the motions of joints. In the clinical area, gait analysis is used to plan surgery, for therapy treatments, recovery assessment and for the development of tools for diagnosis. However, gait analysis has its limits since it can only reveal the external forces in the joint and not the surrounding muscle forces or their point of application [1, 2]. As a result, in the last decade, research has focused on multi-body simulation (also referred as musculoskeletal modeling) with the aim to integrate the elements of the musculoskeletal system and the joint mechanics in order to better understand what has been learned through in vivo and in vitro experiments.

The chapter is divided as follows: Sect. 7.2 presents an introduction of basic concepts of gait and motion capture which are crucial to gait analysis and musculoskeletal modeling. Section 7.3 gives a short description of the necessary steps to build a musculoskeletal model for dynamic simulation, which involves a series of long

K. Tecante (✉) · F. Seehaus · B. Welke · G. Olender · M. Schwarze · S. Lynch · C. Hurschler
Laboratory for Biomechanics and Biomaterials (LBB) Orthopaedic Department, Hannover Medical School (MHH), Hannover, Germany
e-mail: TecanteGutierrez.Karelia@mh-hannover.de

N. Magnenat-Thalmann et al. (eds.), *3D Multiscale Physiological Human*,
DOI: 10.1007/978-1-4471-6275-9_7,

and complex processes. This section does not intend to elaborate in detail on each one of these processes but merely to illustrate and explain in general the pipeline and concepts required to construct a model. Section 7.4 describes the importance of in-vitro studies for musculoskeletal validation. Section 7.5 briefly overviews widely used simulation softwares, while Sect. 7.6 provides a short overview describing some of the most recent work on multi-body simulation with a focus on clinical applications. This section groups the research according to the modeling software used. Section 7.7 presents an Illustrative case study of a state of the art multi-body simulation study with focus on clinical application [3, 4] performed at the Laboratory of Biomechanics and Biomaterial of the Hannover School of Medicine (LBB-MHH, Germany). Finally a brief conclusion is formulated in Sect. 7.8.

7.2 Clinical Gait Analysis and 3D Motion Capture

Gait analysis is the study of human motion, more precisely the mechanical quantification and assessment of walking and/or running. The knowledge obtained from gait analyses provide the foundation to study a wide range of movements from hand grasping to swallowing. In the case of clinical gait analysis, the aim is not only to understand movement patterns but also to discern gait abnormalities and to assist in treatment decision making and rehabilitation. Some of the more prevalent applications of clinical gait analysis is in studies related to cerebral palsy, orthopaedics, physiotherapy, prosthetics, orthotics, motor control [5] and gait variability in neurological disorders [6–8].

Gait is cyclic and thus, divided into phases for better understanding and analysis (Fig. 7.1). A complete gait cycle is from heel strike (when the heel touches the ground) to the next heel strike of the same foot. This cycle is divided into phases known as the stance phase and the swing phase. Stance phase starts with heel strike and ends with toe off of the same foot (foot is in contact with the ground) and swing phase starts with toe off and ends with heel strike (foot is in the air). Stance phase has been divided into the following sub-phases: contact phase (heel strike until the first sign of forefoot loading), mid-stance phase (first sign of forefoot loading until heel lift) and propulsive phase (heel lift until toe off). Several muscles of the leg are responsible for creating the gait cycle and maintaining balance during walking. Moreover, it is presently known that foot, ankle and knee interactions, lateral pelvic tilt in the front plane, pelvic rotation in the transverse plane and knee flexion at mid-stance interact dynamically to obtain higher walking efficiency by displacing the center of mass vertically and/or horizontally [9]. Consequently, the acquisition of kinematic and kinetic data is fundamental to analyze walking. Kinematics describe the pattern and temporal aspects of motion such as positions, angles, velocities, and accelerations of body segments and joints during motion while kinetics refer to the study of forces causing the motion of the body.

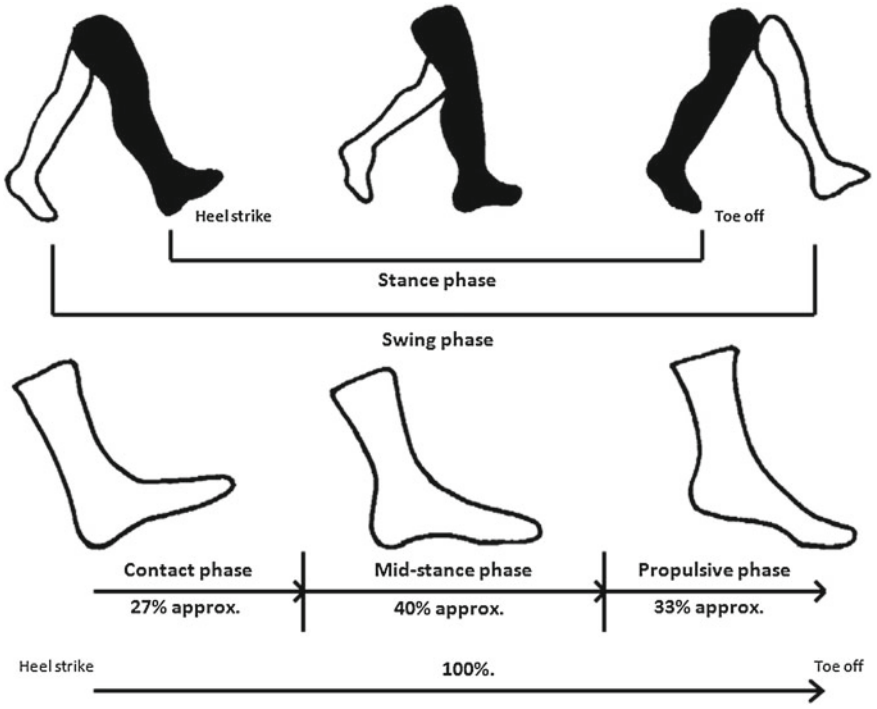

Fig. 7.1 Phases of the gait cycle

This data is most often measured with optical motion capture techniques. For this purpose, retro-reflecting markers are placed on the skin of an individual in relation to specific bone landmarks. The markers are tracked using eight or more infrared high speed cameras arranged so that they surround the entire volume in which the measurements are taking place. The markers positions are known as the individual performs a movement inside the measurement volume such that joint kinematic and kinetic data can be derived with dedicated analysis software. It is important to mention that motion capture recordings are commonly accompanied by other measurements such as electromyography (muscle activation), foot pressure and oxygen consumption measurements among many others.

7.3 Musculoskeletal Modeling and Dynamic Simulation

Musculoskeletal modeling is a predictive computational approach that consists of detailed representations of the bones, muscles, tendons and ligament anatomy, driven in simulation by measurements of subject specific mechanics.

Same as in clinical gait analysis, research on musculoskeletal models in the clinical context is used not only to better understand a musculoskeletal pathology but also to help clinicians to improve procedures, treatment and rehabilitation techniques. For example, musculoskeletal models have been used to study stroke, spinal cord injury, osteoarthritis and neurological deficits such as cerebral palsy [10, 11].

At present, musculoskeletal simulation can be performed based on a generic or on a subject specific model. In the first most commonly applied case, an anthropometric model of the bones, muscles and tendons is created based on biomechanical studies of cadaveric specimens [12, 13] and the musculoskeletal geometries of any average adult healthy subject [12–14]. Subsequently, this generic model is scaled to approximate the anatomy of a particular subject. To determine the scaling factor motion capture is used. Kinematic and kinetic parameters are obtained for each joint during a specific motion (e.g. walking, running or jumping). The length and position of each body segment is known and used to estimate the scaling factor needed for a specific individual. In the case of subject specific musculoskeletal modeling, the model is created based on imaging-data which allows the use of actual subject's bone and muscle geometries [15, 16]. However, this modeling approach still requires assumptions and data from cadaveric specimens. In addition, it is still extremely time consuming despite interpolation techniques used to reduce effort and time required for the creation of this type of models.

In both cases, the inputs required to build a musculoskeletal model are (1) three-dimensional bone surface geometry, (2) the equations of motion of the body (mathematical descriptions of joint kinematics, (3) parameters describing each muscle's path geometry (defined for a range of joint motions) and (4) muscle architecture (which defines the force-generating capacity of each muscle).

Bone and muscle surface geometries can be obtained by reconstructing muscle and bone surfaces from multiple series of MRI images. This is achieved by a process known as segmentation which consists of identifying and outlining the anatomical structures of interest in each MRI image. Typically, images from multiple imaging series are combined to create a full limb model. At present, much research is dedicated to speed up this process by developing novel algorithms to make segmentation automatic or semi-automatic [17–19]. However, these algorithms are more successful for bone than for muscle segmentation, since the boundaries between muscles do not appear sharply in MRI images. Thus a great amount of manual segmentation is still necessary to delineate the muscles boundaries. Depending on the purpose of the model being created, tendons can also be traced from MRI images.

Once the muscle, tendon and bone geometries have been created, joint centers need to be calculated and used as the center point for the moment force generated by the muscles [20]. Subsequently, the kinematic structure of each joint must be created to drive skeletal motion and finally, boundary conditions are specified to attach muscle and tendon to bone [21]. In other words, a mathematical method (most commonly the Newton-Euler method; [22]) is used to obtain a series of equations that describe the translational and rotational movements of the body segments. Once the

equations of motion are derived, they must be solved to yield the motion of the skeletal system (movement is influenced by the constraints imposed by its articulations, by the external muscle forces, by gravity and by the environment). Thus, external forces are required for the solution of the skeletal equations of motion. These forces are quantified by their magnitude, direction, and their point of application on the skeletal system. The calculation of a given muscle force is needed (also referred to as muscle tendon actuator) but its correct application to the skeletal system requires accurate knowledge of the musculotendon path running from the origin to the insertion of the muscle (also known as musculotendon geometry). In the past, the musculotendon path has been modeled as a straight-line path [23, 24], as a centroid line method [25] or by finite element modeling of the path of individual muscle fibers [26]. Moreover, to accurately represent the musculotendon geometry, it is often required to simulate how muscles wrap around adjacent structures and different techniques employing cylinders, spheres, and ellipsoids have been used as wrapping surfaces [27–29].

Finally, muscle force has a crucial role in musculoskeletal modeling. The function of individual muscles is influenced by the architecture of each muscle, which must thus be considered. Muscle architecture refers to the arrangement of fascicles within the muscle and has been defined as "the arrangement of muscle fibers within a muscle relative to the axis of force generation" [30]. Scientists typically categorize muscle fiber arrangements in three general conceptual classes: muscle fibers that run (1) parallel, (2) at a fixed angle (unipennate architecture) and (3) at several angles (multipennate architecture) relative to the muscle force generating axis. These architectural differences between muscles are important predictors of force generation. The force-length relationship of the muscle is well established and thus, it is known that once the muscle begins to develop force the tendon begins to carry load and transfers force from the muscle to the bone. Therefore, much of the muscle-tendon length change does not occur in the fibers themselves but in the associated tendon and muscle (muscle-tendon mechanics) aponeurosis [30].

In musculoskeletal modeling, the muscle force generation is generally represented by a Hill-type muscle model in which the muscle-tendon unit acts as the spring in a spring-mass system [31, 32]. This model typically requires four parameters to scale generic curves for active and passive force generation of the muscle–tendon unit: optimal fiber length, maximum isometric force, pennation angle (angle from the muscle fibers with respect to the tendon), and tendon slack length [13].

These parameters are obtained from cadaveric measurements. As pointed out by Blemker et al. [33], one main disadvantage is that fascicle length measurements from each muscle are averaged in most cadaveric studies, giving a single length estimate; therefore, models of muscle generally assume that all fascicles within each muscle have the same length. Furthermore, Hill-type muscle models also assume that the pennation angle is constant across all fibers.

In summary, development of an adequate musculoskeletal model is not an easy task and has been achieved through several years of research. Some of the limitations or difficulties are that (1) musculoskeletal models are constructed on the basis of assumptions on the geometrical relationships within the musculoskeletal system [34], (2) muscle models tend to be parameterized by the limited data available from

cadaveric specimens, with the results heavily dependent on the small number of individuals measured and the techniques used and (3) scaling of a generic model versus a model build upon individually collected parameter sets such as MRI and/or CT. Scaling muscle fiber length by stature or limb length may not be entirely adequate, a more subject specific model might be more representative [35]. However, this second option is extremely time consuming which makes modeling and simulation not entirely suitable for clinical applications.

Despite these limitations and obstacles the use of musculoskeletal models is now successfully entering the clinical field, although further research is undoubtedly needed. At the moment, once a suitable musculoskeletal model is created, the model is loaded into simulation software and matched with the acquired motion capture data. This model is then used in the second phase, along with the experimental motion capture data to simulate and analyze a specific motion.

7.4 Musculoskeletal Model Validation

Computer based modeling and simulation, used to calculate and estimate stresses and strains for specific areas of interest, has seen a rapid growth in use and development. Modeling has benefited from further advancements in medical imaging and motion-capturing techniques, supporting continued efforts in development of patient specific models. Before scientists and clinicians can use models extensively, credibility must be established through a process of verification and validation. The process of verification and validation in its simplest form involves comparing an output generated by a mathematical model to the data captured using motion capture [36]. In other words, validation is the process of determining that the model accurately reflects reality to the degree necessary to answer the study questions.

Motion capture is most commonly based on optical reflective skin markers, and is widely used as a standard procedure in clinical diagnosis. There are known limiting factors, such as soft tissue artifacts, that determine the outcome of gait analysis. Soft tissue artifacts can be defined as the motion differences between the actual joint (bone) motions in comparison to the motion observed at the skin level. It is common to notice excess skin motion around the knee joint during bending [37, 38]. Roentgen stereophotogrammetric analysis, ball pins surgically implanted, fluoroscopy and cadaveric studies are a select few methods that are currently available for an accurate reconstruction of bone motion [39–41].

Two known methods for motion capture and simulation modeling verification of anatomical structures include usage of bone-pin markers and in vitro measurements, both of which have known advantages and disadvantages. In vitro studies are known to be restrictive in their motion capture area and are restricted to manipulated motions induced by an external force to replicate in-vivo motion on cadaveric specimens. Methods based on bone-pin markers involve pin insertions of markers in subjects'

bones that are effective to counter soft tissue artifacts, in motion capturing of actual motion. However, bone-pin marker placement may affect an individual's gait as the pin insertion is invasive and requires surgery. Hence, obtaining ethical clearance poses the largest constraint for most countries [42]. Because of this, in vitro studies, to this date, are the preferred method to gain reliable data as the advantages of in vitro studies, in certain contexts, outweigh the limitations [43].

With the advancements of hydraulic motor-controlled test rigs and robotic technologies that allow six degrees of freedom, in vitro studies are advancing in parallel to these technologies. Cadaveric studies using robotic technologies allow for the investigation of kinematics bearing a simulated bodyweight or zero loading. Weight bearing simulators are more commonly used for clinical research due to the influence of tendons and muscles in vivo. Simulation of the quadriceps and hamstrings has shown to influence kinematic output such as flexion-extension of the tibia in relation to the femur about the knee joint, in addition patella kinematics, contact area and forces [44, 45]. Additional advantages of in vitro studies include the possibility to obtain data concerning contact forces and areas as well as investigate the role of muscles and tendons around joint, where this is normally in conjunction with clinical studies comparing pre and post operative surgeries [46, 47].

7.5 Software for Human Gait Analysis and Simulation

In the last decade, musculoskeletal modeling software design and development have flourished. Commercial software packages able to perform kinematic and dynamic analysis of human musculoskeletal systems have been introduced and made available to researchers. Some of the first commercial software packages used for musculoskeletal modeling are ADAMS (Mechanical Dynamics Inc., MI, USA), SDFAST (Symbolic Dynamics Inc., CA, USA), DADS (LMS International, Leuven, Belgium) and Working Model (MSC Software Corp., CA, USA) among others. These software packages are still maintained and frequently used, but were known to have limitations regarding musculotendinous force production, musculoskeletal moment arms and the ability to generate realistic animations of the motion in musculoskeletal systems [48]. Delp and coworkers [49] indicated that musculoskeletal models created by different research groups were generally done with different programming language and software platforms which constituted an obstacle to facilitate sharing among the research community. Thus, the article suggested the need for more specialized computer software packages able to shorten the time and simplify the pipeline to build a musculoskeletal model and run simulations. This situation propelled the development of commercial software packages with the sole purpose of musculoskeletal simulation such as SIMM (Software for Interactive Musculoskeletal Modeling, MusculoGraphics, Inc., CA, USA), Visual3-D (C-Motion, Inc., TN, USA), AnyBody (AnyBody Technology, Aalborg, Denmark), VIMS (Virtual Interactive Musculoskeletal system, Engineering Animation Inc., IA, USA), LifeMOD (LifeModeler, Inc., CA, USA) among others.

However, these commercially available packages do not provide source code access to users, which severely limits sharing of models, data exchange and the possibility to extend the software capabilities [50]. In order to overcome these restrictions, an open-source modeling and simulation platform called OpenSim was developed as an extension of the musculoskeletal software package SIMM. The main aim of this platform is to promote sharing and faster development of biomedical simulations [49]. OpenSim not only provides modeling and analysis tools or the ability to generate dynamic simulations but also makes the source code available. As a result, the researcher is able to modify and adapt existing models created by other research groups to fulfill his own research interests.

As a conclusion, it is important to mention that add-on implementations are continuously developed to complement and get around limitations of commercial and/or non–commercial musculoskeletal modeling software packages. The aim is to achieve an affordable and easy to use musculoskeletal modeling pipeline to advance research on human locomotion and its clinical applications.

7.6 Musculoskeletal Simulations in Clinical Gait Analysis in the Last Decade

SIMM, Anybody and OpenSim are currently the most widely used musculoskeletal modeling software for dynamic simulations of movement in clinical gait research. The next paragraphs present a brief overview of recent studies conducted with these softwares. SIMM was developed in the early 1990's by Delp and Loan with the goal of enabling scientists to develop, alter and evaluate different musculoskeletal models with varying bone geometries and muscle-tendon parameters [12]. The following paragraphs present examples of studies using SIMM.

Higginson and coworkers [51] studied the muscle coordination patterns of an individual with post-stroke hemiparesis in comparison with healthy individuals during walking. In this case, a muscle-actuated forward dynamic simulation was generated of the patient and the healthy individuals. Subsequently, muscle forces were perturbed to determine the muscles contributing most to body weight support during walking. The main conclusion of this study was that contributions of individual muscles to body support during mid-stance are altered for an individual with post-stroke hemiparesis compared to a healthy one. In this case musculoskeletal simulation is advantageous in the sense that it may improve the understanding of muscle coordination in a special group suffering from hemiparesis. This, in the future, can influence the rationale for therapeutic interventions.

In the study of cerebral palsy, musculoskeletal modeling has been used to calculate the rectus femoris length and lengthening velocity in stiff knee gait in a children population [52]. Although no statistically significant relation between different spasticity levels and muscle-tendon length changes was detected, this study provided new data on rectus femoris length and lengthening velocity changes during the phases of gait.

Joint loading is an important factor for the development of arthritis. Thus, researchers are interested in how joint geometry and joint center location affects joint and muscles moments and joint contact forces. For this purpose, Lenaerts and coworkers [15] quantified hip joint and muscle moments using three different models which varied in the amount of subject specific details. Their results show that variations in joint geometry incorporated in musculoskeletal models can significantly alter results of dynamic simulations. Based on these results, they proposed that musculoskeletal models should include subject-specific bone geometry and joint center location for surgery decision making.

The usage of the SIMM software also contributed to the understanding of how muscles adapt to ankle foot orthoses. Crabtree and Higginson [53] added fifteen muscles to an existing musculoskeletal model in SIMM to predict ankle torque and identify changes in muscle excitation during a walking simulation. In another study, the influence of an orthosis on ankle, knee and hip joint kinematics and kinetics during the phases of walking was investigated [54]. It is common to use foot orthotics to stabilize, facilitate and restore normal gait pattern during locomotor training in patients with post incomplete spinal cord injury. However, this study showed that ankle foot orthoses need to be evaluated more accurately in neurological populations based on goals of the intervention and desired outcomes.

Simulations using SIMM also allowed the detection of five specific muscles that played a role in a simple neural strategy that enables the basic tasks of walking defines as body support, forward propulsion and leg swing [55].

In lower limb amputation cases, musculoskeletal modeling has been used not only to understand how amputees compensate for the loss of ankle plantar flexors but also to determine individual muscle contributions to body support and forward propulsion [56]. Recently, Fey et al. [57] looked at the influence of different stiffness levels on muscle function in a prosthetic foot using forward dynamics simulations, and found that prosthetic stiffness has a clear impact during the different phases of gait.

An alternative software is Anybody, which is well accepted in the biomechanics community despite being more recently developed compared to other softwares. The advantages brought by this software are useful in areas like the automotive field, ergonomics, sports, orthopaedics, rehabilitation, spine biomechanics and others. For example, Worsley and coworkers [58] evaluated tibiofemoral joint (TFJ) kinematics and kinetics during gait, sit–stand–sit, and step–descent in healthy older subjects using motion capture data and inverse dynamic musculoskeletal models. Another study focused on creating a more detailed foot model scalable with the option to be integrated into an existing AnyBody whole musculoskeletal model [59]. Asfour and Eltoukhy [1] presented a case study where the goal was the development of a model to evaluate the quadriceps behavior in patients with total knee replacement. In a recent study, a new model with special focus on cartilage, menisci and ligaments was investigated in order to better understand the influence of hard and soft tissue on the knee joint [60].

Anybody has found wide application in the mechanical function of the anterior and posterior cruciate ligament injuries. For example, the force equilibrium of the tibia and loading pattern of the cruciate ligaments was studied during a forward lunge

in order to better understand strain of these ligaments [61]. More recently, a study created and validated a musculoskeletal model for some particular movements to explain why more females injured their ACL compared to men [62]. Also, AnyBody has been used to introduce a new method to estimate muscle forces in a rehabilitation system designed to assist patients during sit and stand [63].

Moreover, a vast research using AnyBody has been done on the shoulder [63–65] and spine as well [66–68]. In both cases, musculoskeletal modeling and simulation has proved its usefulness for determining the influence of prosthetic geometries on muscle force, estimation of optimal post-operative immobilization body postures to minimize stress on repaired tendons, to predict loads on the lower back when wearing a lift assist device which support the reduction of back muscle activity by such devices, back muscle fatigue, and spinal loading during lifting.

Finally, the OpenSim platform has greatly increased in popularity in recent years because of its open source implementation [49]. As an example, a recent study looked into the validation of a parametric model for predicting knee joint contact forces against measurements in four subjects with instrumented total knee replacement (TKR) during the stance phase of gait [69]. One of the mathematical model inputs was the maximum physiological lower limb muscle forces obtained from an OpenSim musculoskeletal model. The results were very similar for three of the subjects but the fourth one had a different outcome, attributed to a quadriceps avoidance pattern. When the model input was more specific to this particular subject the model predictions improved.

Taddei and coworkers [70] investigated the minimization of fracture risk through long rehabilitation protocols in biological massive skeletal reconstructions (limb reconstruction using intercalary massive bone allograft after tumor removal usually caused by osteosarcoma). They developed a subject-specific musculoskeletal model of a patient with a massive biological skeletal reconstruction in order to investigate the loads acting on the femur during gait after long term rehabilitation. Their findings showed that the patterns of joint rotations and moments were coherent between the two legs at each joint as well as with data from healthy subjects. The only relevant difference was the variability on the femoral forces on the hip. The study concluded that small asymmetries in kinematic patterns might be associated to significant difference in the skeletal loads.

A different research focused on the association of externally increased valgus knee moment and anterior cruciate ligament (ACL) injury [71]. In this case, OpenSim was used to create nine subject-specific full body torque-driven simulations of athletic males performing unplanned sidestep. In addition, an algorithm was used to produce an optimized kinematic solution to not only reduce peak valgus knee moment but also the associated subsequent ACL injury. The simulations showed that the resultant strategy was to redirect the whole-body center of mass medially towards the desired direction of travel.

Osteoarthritis (OA) has also been investigated using OpenSim [72]. A three-dimensional musculoskeletal model was used in conjunction with optimization theory to calculate lower-limb muscle forces during walking. The aim was to determine if hip and knee muscle forces were lower in people with patellofemoral joint (PFJ)

OA compared to those without. The results demonstrated that individuals with PFJ OA walk with lower peak hip abductor muscle forces than the healthy group.

Because OpenSim allows for the implementation of neuromotoric control patterns, it has proven to be a useful research tool in the study of neurological conditions like cerebral palsy. This software has been used to perform forward dynamic simulations to investigate the influence of pre-operative unilateral and bilateral rectus femoris transferred models on balance recovery [73]. The outcome of the study was that rectus femoris tendon transfer changes balance recovery illustrating the biomechanical difference that biarticular muscles have in motor control.

In the past, models were mostly applicable on a general mechanical level such as simulations of tendon transfer options or in prosthesis placement [34]. However, musculoskeletal modeling and simulation has since then progressed into many more clinical applications. The last paragraphs only illustrate a small part of this progress using well known softwares. This shows that musculoskeletal modeling and simulation are not only used to simply better understand how tendons, ligaments and muscle work to achieve a motion or another specific function in healthy cases or pathological cases, but also to improve or assess implant designs, surgical techniques and rehabilitation procedures. The ultimate goal for clinical applications is to aid decision making for specific pathologies and individual cases. In that sense, a great deal of research is still required to achieve more accurate models and easier implementation.

7.7 State of the Art Illustrated Through the Analysis of Subject Simulated Falls with a Transcutaneous Osseointegrated Prosthesis for Transfemoral Amputees

This section describes one of the most common situations of fitting a shaft prosthesis on above knee amputees patients and how the use of multi-body simulation brings insight into relevant differences between prosthetic attachment designs during specific daily life situations. The next paragraphs present the methodology and findings from a study performed at the LBB-MHH recently published by Schwarze et al. [3] and Welke et al. [4].

Prosthetic design is very important, especially the socket design as it is the portion of the prosthetic device that interfaces with the patient's residual limb. The socket most important function is to distribute pressure and weight bearing over specific areas. If the socket fits well and is comfortable it helps prevent the skin, bones and nerves from being damaged. At present, a prosthetist custom designs the interface (socket and frame). This custom design is usually based on the prosthetist experience on predicting the shape of the loaded residual limb. The goal is for the amputated limb to experience a loading pattern that relieves areas sensitive to pressure. Therefore, socket shaping is almost an art that requires time and experience. In addition, another critical factor is the mechanism or system that keeps the prosthetic limb attached to the body which can be a harness system, straps, belts, sleeves or simply suction (all depending on the type of amputation).

Over the years, extensive research on socket design and interaction between biological tissue and synthetic components has been conducted [74]. This partly originated when Brånemark [75] showed that living bone could become so fused with the titanium oxide layer of an implant that the two could not be separated without fracture, which is basically known as "oseointegration". Nowadays, this principle has been used for the design of prosthetic limbs commonly referred as osseointegrated prosthesis. These devices are anchored in the residual femur and protrude through the skin and soft tissue which allows the prosthesis attachment to an abutment. Clinical results show an improvement in the quality of life of patients with this type of prosthesis [76].

Recent studies illustrated the danger of skeletal and implant fractures of osseointegrated prosthetic interfaces [77]. The main risk of such fractures not only arises from torsional loads but also in the mechanical loosening by bending moments. Thus, it is important to define thresholds of forces and bending moments during activities of daily living and during highrisk situations such as falling, since approximately half of the population with a lower extremity amputation experiences a fall at least once a year.

The TExoPro cooperative was funded by the Bundesministerium für Bildung and Forshung (BMBF AZ: 01EZ0775, Federal German Ministry of Education and Research) in order to deal with the persistent issues of microbiological infection in the percutaneous passage and possible bone-implant interface overloading. In this context, it was important to investigate the loads in the region of the prosthesis in activities of daily living and risk situations, more specifically during falling.

However, as direct measurement is not possible for obvious practical and ethical reasons, the loads acting on the interface of osseointegrated fixation and attached prosthesis were investigated in the present study with a multi-body simulation in different cases of falling. As mentioned at the beginning of this chapter, multi-body simulations (MBS) offer the possibility to determine loads of the musculoskeletal system in a non-invasive manner allowing the investigation of cases like falling scenarios.

Due to the highly accessible situation of above-knee amputees it is feasible to measure forces and moments directly at the prosthesis interface with a six degrees of freedom strain-gauge based transducer. Therefore, a comparison of calculated and measured data was also conducted to validate the numerical model prior to the evaluation of falling scenarios. The aim of the study was to provide upper bounding of loading conditions to serve as design parameters for a safety element in order to prevent skeletal fractures and implant failure.

Validation of the multi-body simulation

Six subjects with one-sided above-knee amputation were fitted with a C-Leg (Otto Bock Healthcare Gmb, Göttingen, Germany) exoprosthesis and a conventional socket. Level walking was performed in the gait laboratory of the LBB-MHH. Kinetic and kinematic data was recorded with a VICON motion capturing system (8 cameras

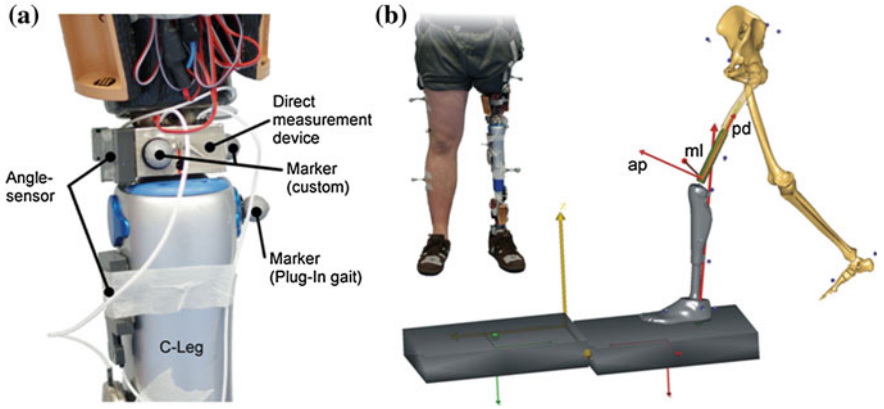

Fig. 7.2 **a** Detailed view of the transducer location and its integration between socket and exoprosthesis. **b** Lower extremity of one of the subjects and corresponding multi-body model during gait with the transducer location marked by the coordinate system, where loads are determined. Position and orientation of the DOF joint above the implant, determining loads

Vicon MX-20/MX-40, PlugIn-Gait marker set lower extremity) and two force plates (AMTI, USA).

Forces and moments at the socket–prosthesis interface (Fig. 7.2a) were synchronously measured with motion capture data during all trials using a six-axis force-moment sensor (FMS). A minimum of six valid walking trials at self-selected speed was collected per subject.

A lower extremity MBS model was generated using the AnyBody environment (Version 4.2, AnyBodyTech A/S, Aalborg-Denmark). Individual models were generated by scaling according to the parameters height, body mass and leg length of each participating subject. The socket worn by the subjects was regarded as being rigidly connected to the remaining stump. In order to calculate forces and moments at the location of the FMS, a zero degree of freedom joint located above the knee joint of the amputated thigh segment was introduced. The contribution of muscle-force was neglected, as there are no muscles present which span the knee-prosthesis or the interface of the socket to the prosthesis.

Comparison of measured and simulation data were performed using the following characteristic gait cycles parameters: anteroposterior force (FAP), mediolateral force (FML), proximal-distal force (FPD), anteroposterior moment (MAP), mediolateral moment (MML) and proximal-distal moment (MPD). Calculated and measured forces in all six subjects revealed very closely matched time dependent values in the best, and good agreement in the worst case observed (Fig. 7.3). The amount of difference varied from subject to subject, but showed good coherence within the set of trials of a single subject. Differences in force reach a maximum of 8 %BW at only few time-steps in the best (subject DR, Fig. 7.3a) and more than 20 %BW over around 20 % of the gait cycle in the worst case (subject MS, Fig. 7.3b).

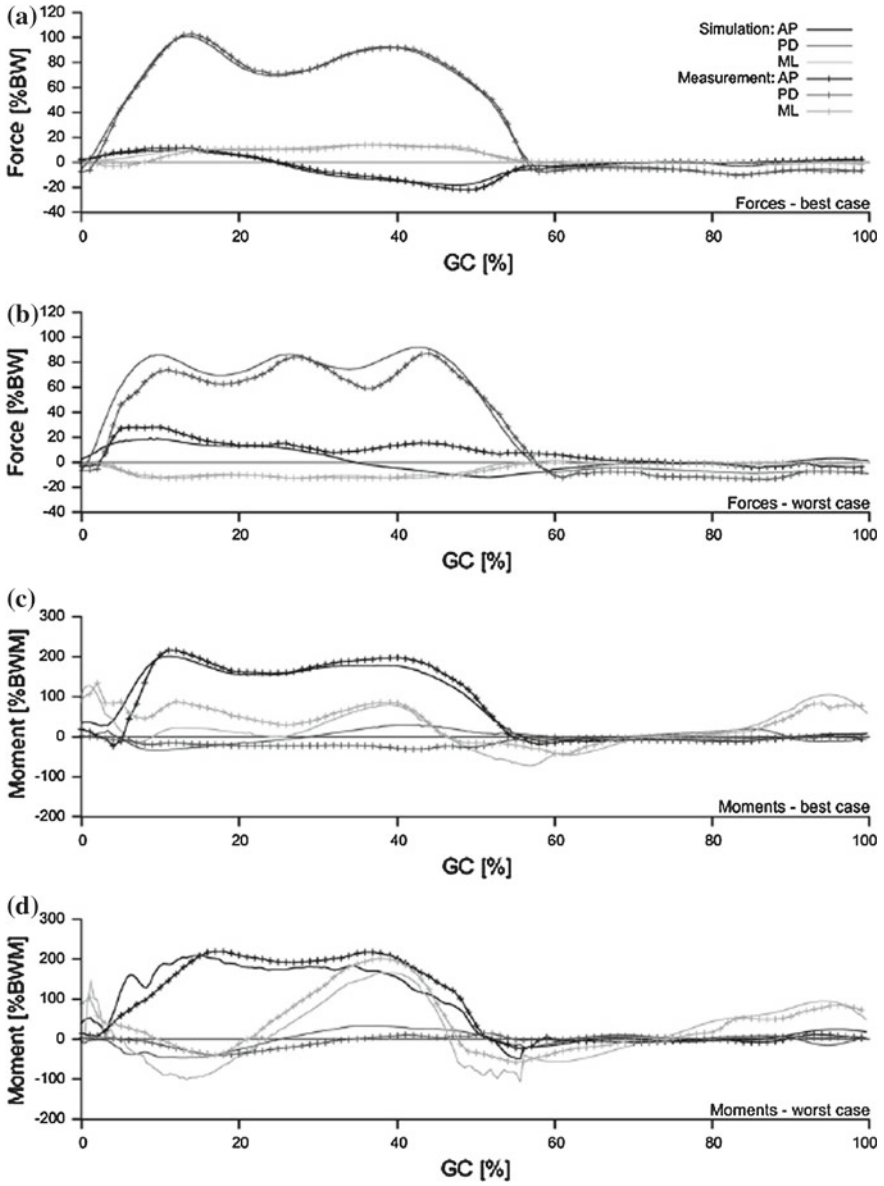

Fig. 7.3 Best and worst case scenario of forces and moments based on lowest and highest RMSD: simulation-data is represented by plain lines, measurement data by lines with asterisks. AP-direction is represented by black, PD-direction by gray and ML-direction by light gray shade. **a** best case of forces (trial DR05, RMSD = 1.6 %BW), **b** worst case of forces (trial MS20, RMSD = 12.2 %BW), **c** best case of moments (trial SK07, RMSD = 18.9 %BWM) and **d** worst case of moments (trial VE13, RMSD = 35.6 %BWM). Reproduced with permission from Fig. 7.1 in Schwarze et al. [3]

Table 7.1 Overview of falling scenarios for maximum stress in the femur No. 4 has additional ground contact with the second foot to balance the fall. No. 5 induces stress via maximum knee flexion.

No.	Direction	Stance/Gait	Ground contact
1	Forwards	Stance	Both knees
2	Forwards	Stance	One knee
3	Forwards	Gait	One knee
4	Forwards	Gait	One knee and foot
5	Backwards	Gait	Hands

Calculated and measured time-dependent moments revealed good agreement in the best case, and only general agreement in the worst case observed (Fig. 7.3). Patterns and magnitudes of moments show good agreement within the trials of individual subjects; whereas as a group, the subjects show only general agreement. Absolute differences in moments range from a maximum of 30 %BWM for about 10 % of the gait cycle in the best (subject SK, Fig. 7.3c), to a maximum of more than 50 %BWM over around 40 % of the gait cycle in the worst case (subject VE, Fig. 7.3d). The RMSD observed for the resultant moment was 27 %BWM.

As presented, forces obtained in the simulation showed a good agreement with the measured loads despite the moments showing a somewhat lower accuracy which is still accurate enough for most clinical applications. Therefore, the model was considered to be fully validated for calculations of resultant forces and moments.

7.7.1 Biomechanical Application of the MBS—Stress Resultants in Different Cases of Falling

Once the model was validated, it was driven by kinematic and kinetic data from a healthy subject who mimicked the five documented falling scenarios of amputees as listed in Table 7.1 and illustrated by an example in Fig. 7.5.

The essential motion data as well as ground reaction forces for driving and loading the model are acquired with the same motion capturing set-up as for the validation study [78, 79]. The PlugInGait marker set and model for the lower extremity (kinematic model V 2.3) was used to generate the kinematic data [79]. It consists of 16 reflective markers with a 14 mm diameter attached to anatomical landmarks: superior/anterior spina illiaca, thigh, lateral epicondyle, shank, lateral malleolus, and second metatarsal head and on the calcaneous for left and right leg (Fig. 7.2b). No knee alignment device was used. Captured marker data were processed (VICON-Nexus 1.5.1, VICON Motion Systems Ltd., Oxford, UK) and trajectories were labeled using the PlugInGait model. Kinematic data were post-processed with a Woltring-filter with a mean squared error (MSE) setting of 10.

Different cases of falling of transfemoral amputees with a conventional shaft prosthetic were developed and analyzed. Based on the analysis of video sequences, five particular scenarios of falling (Table 7.1) were selected for the study. These scenarios were repeated by a healthy subject (185 cm, 75 kg) without the harness. The subject was protected with hockey pads to prevent injury and the study design was approved by the local ethics committee.

Forces and moments as determined per multi-body simulation about the antero-posterior (ap), mediolateral (ml) and proximodistal (pd) axes are reported in the left rigid femur segment 240 mm superior to the knee joint axis (Fig. 7.1b). This location was chosen in consultation with experienced orthopaedic surgeons as representative of the height of above-knee amputations.

All trials for each scenario were averaged with the force peaks aligned at time ~ 0.1 s. The duration of the load peak was defined as the time interval in which the load was $>50\,\%$ of the peak load to enable comparisons between scenarios.

The results showed that all forward falling scenarios displayed a distinct force peak, but not the backward falling scenario. For S1, falling from a stationary standing position with ground contact on both knees, a mean peak force of 2014 ± 528 N over 11 ± 2 ms was observed. For S2, from the same position but with ground contact on one knee, the mean peak force was higher (2614 ± 346 N) and the mean duration was longer (35 ± 21 ms). The largest internal force in all five scenarios were observed in G1, falling on one knee from normal gait (Fig. 7.4). The mean peak force was 3274 ± 519 N over a loading period of 35 ± 21 ms with a resulting moment of 176 ± 55 Nm over a loading period of 267 ± 150 ms. The largest component of the resultant force was directed axially along the bone. The mean peak force for G2 was 2234 ± 659 N with a mean peak moment of 109 ± 37 Nm. The reduced force compared with G1 was due to the support of the contralateral leg. The lowest peak force of 1099 ± 269 N was observed for the only backwards-falling scenario, G3. Conversely, the largest peak moment, 187 ± 177 Nm, was observed for this scenario (Fig. 7.4).

According to the load limits reported to be 190 Nm in a related study of bone failure of osseointegrated prosthesis fixation [80], the findings of this study suggest the possibility of fracture of the affected leg in every investigated scenario. Further work is warranted to determine the load magnitudes that will cause damage to the bone-implant interface.

For the first time, the bending moments for cases of unsupported falling that could be relevant for the design of multi-axial safety elements has been reported. These findings will be of interest in combination with finite element (FE) analysis to determine real stresses in the osseointegrated bone to allow conclusions about location and risk of fracture under high loading situations.

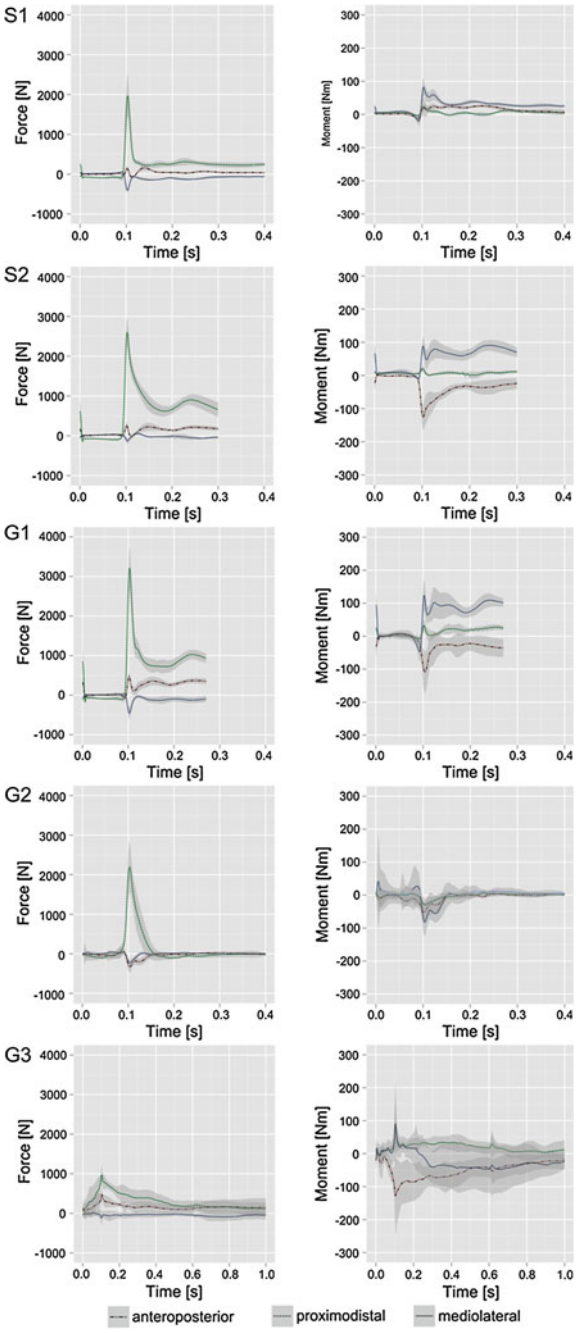

Fig. 7.4 Means and SD of forces (*left*) and moments (*right*) 240 mm superior to the knee joint axis in falling scenarios. Loads in the anteroposterior (Mx), proximodistal (My and mediolateral (Mz) directions are indicated by the solid red, green and blue lines. Reproduced and adapted with permission from Figs. 7.3 and 7.4 in Welke et al. [4]

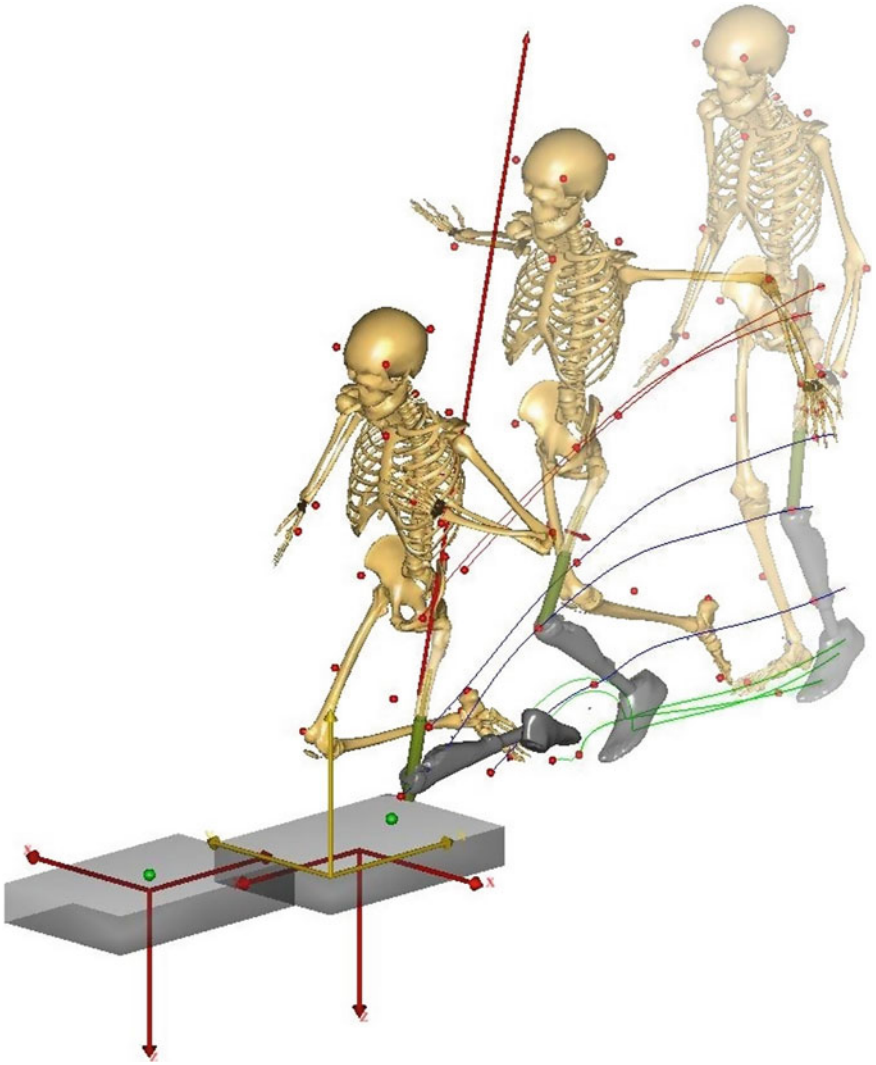

Fig. 7.5 Single sided, self-induced fall from gait with impact on the left knee: the falling scenario with the highest loading conditions

7.8 Conclusion and Future Work

This chapter focused in the clinical area and presented a short introduction on (1) general concepts of gait analysis and motion capture, (2) a fundamental explanation of the pipeline used at present in musculoskeletal modeling, (3) the current available

software and research done in musculoskeletal modeling and simulation and (4) a specific study using multi-body simulation with a clinical application purpose.

Musculoskeletal modeling and simulation is not yet a simple task despite research advances and efforts to decrease its complexity over the years. Currently, modeling processes require time, resources and expertise and must be carefully validated. Thus, this topic is far from being completely explored. A great deal of research is still needed to accurately represent the human system. At this time and in the next years, research is and will be channeled to the development of subject-specific models with higher accuracy. Advances in imaging techniques, re-assessment of basic modeling assumptions and better modeling approaches will provide more accurate and improved simulations as well as greater insight into the clinical area.

Acknowledgments This study was funded by the German Federal Ministry of Education and Research (BMBF AZ: 01EZ0775).
The authors like to thank TU Berlin and Otto Bock Healthcare GmbH, Duderstadt, Germany for cooperation in TExoPro and EU Marie Curie Actions-Marie Curie Research Training Networks/ Multi-scale Biological Modalities for Physiological Human articulation 289897 (FP7-PEOPLE-2011-ITN) for their funding

References

1. Shihab, A., & Moataz, E. (2011). Development and validation of a three-dimensional biomechanical model of the lower extremity. In V. Klika (Ed.), *Theoretical biomechanics*. ISBN: 978-953-307-851-9, InTech, DOI:10.5772/24156.
2. Erdemir, A., Scott M., Walter H., van den Bogert, A. J., et al. (2007). Model-based estimation of muscle forces exerted during movements. *Clinical Biomechanics (Bristol, Avon)*, *22*(2), 131–154.
3. Schwarze, M., Hurschler, C., Seehaus, F., Oehler, S., & Welke, B. (2013). Loads on the prosthesis-socket interface of above-knee amputees during normal gait: Validation of a multi-body simulation. *Journal of Biomechanics*, *46*(6), 1201–1206.
4. Welke, B., Schwarze, M., Hurschler, C., Calliess, T., & Seehaus, F. (2013). Multi-body simulation of various falling scenarios for determining resulting loads at the prosthesis interface of transfemoral amputees with osseointegrated fixation. *Journal of Orthopaedic Research*, *31*(7), 1123–1129.
5. Simon, S. R. (2004). Quantification of human motion: Gait analysis-benefits and limitations to its application to clinical problems. *Journal of Biomechanics*, *37*(12), 1869–1880.
6. Hausdorff, J. M., Merit, E. C., Renée F., Jeanne Y. W., & Ary L. G. (1998). Gait variability and basal ganglia disorders: Stride-to-stride variations of gait cycle timing in parkinson's disease and Huntington's disease. *Movement Disorders*, *13*(3), 428–437.
7. Hausdorff, J. M., Apinya, L., Merit, E. C., Amie, L. P., David, K., Ary, L. G., et al. (2000). Dynamic markers of altered gait rhythm in amyotrophic lateral sclerosis. *Journal of Applied Physiology*, *88*(6), 2045–2053.
8. Hausdorff, J. M., Schaafsma, J. D., Balash, Y., Bartels, A. L., Gurevich, T., & Giladi, N. (2003). Impaired regulation of stride variability in Parkinson's disease subjects with freezing of gait. *Experimental Brain Research*, *149*(2), 187–194.
9. Bowen, J. D., & Gerry S. M. B. A. (2010). Gait Assessment. In *The hip and pelvis in sports medicine and primary care* (pp. 71–86). New York: Springer.

10. Klets, O., Riad, J. & Gutierrez-Farewik, E. M. (2010). Personalized musculoskeletal modeling of lower extremities based on magnetic resonance imaging data of 15 patients with hemiplegic cerebral palsy, IUTAM Symposium on human movement analysis and simulation, 2010 September 13th–15th, Belgium: Leuven.
11. Klets, O. (2011). Subject-specific musculoskeletal modeling of the lower extremities in persons with unilateral cerebral palsy. Licentiate dissertation. Stockholm: KTH Royal Institute of Technology.
12. Delp, S. L., & Loan, J. P. (1995). A graphics-based software system to develop and analyze models of musculoskeletal structures. *Computers in Biology and Medicine*, *25*(1), 21–34.
13. Arnold, E. M., Samuel, R. W., Richard L. L., & Scott L. D, (2010). A model of the lower limb for analysis of human movement. *Annals of Biomedical Engineering*, *38*(2), 269–279.
14. Delp, S. L., Loan, J. P., Melissa, G. H., Felix E. Z., Eric L. T., & Joseph M. R. (1990). An interactive graphics-based model of the lower extremity to study orthopaedic surgical procedures. *IEEE Transactions on Biomedical Engineering*, *37*(8), 757–767.
15. Lenaerts, G., Ward, B., Frederik, G., Michiel, M., Arthur, S., Van der Perre, G., et al. (2009). Subject-specific hip geometry and hip joint centre location affects calculated contact forces at the hip during gait. *Journal of Biomechanics*, *42*(9), 1246–1251.
16. Correa, T. A., Baker, R., & Pandy, M. G. (2011). Accuracy of generic musculoskeletal models in predicting the functional roles of muscles in human gait. *Journal of Biomechanics*, *44*(11), 2096–2105.
17. Cuypers, R., Tang, Z., Luther, W., & Pauli, J. (2008). Efficient and accurate femur reconstruction using model-based segmentation and superquadric shapes. *Proceedings of the Fourth IASTED International Conference*, *619*(007), 99.
18. Brunner, G., Nambi, V., Yang, E., Kumar, A., Virani, S. S., Kougias, P., et al. (2011). Automatic quantification of muscle volumes in magnetic resonance imaging scans of the lower extremities. *Magnetic Resonance Imaging*, *29*(8), 1065–1075.
19. Schmid, J., Kim, J., & Magnenat-Thalmann, N. (2011). Extreme leg motion analysis of professional ballet dancers via MRI segmentation of multiple leg postures. *International Journal of Computer Assisted Radiology and Surgery*, *6*(1), 47–57.
20. Schmid, J., Sandholm, A., Chung, F., Thalmann, D., Delingette, H., & Magnenat-Thalmann, N. (2009). Musculoskeletal simulation model generation from MRI data sets and motion capture data. In *Recent advances in the 3D physiological human* (pp. 3–19). Berlin: Springer.
21. Teran, J., Sifakis, E., Blemker, S. S., Ng-Thow-Hing, V., Lau, C., & Fedkiw, R. (2005). Creating and simulating skeletal muscle from the visible human data set. *IEEE Transactions on Visualization and Computer Graphics*, *11*(3), 317–328.
22. Nikravesh, PE. (1998). Computer-aided analysis of mechanical systems, Prentice-Hall Inc, NJ: Englewood Cliff.
23. Seireg, A., & Arvikar, R. J. (1973). A mathematical model for evaluation of forces in lower extremeties of the musculo-skeletal system. *Journal of Biomechanics*, *6*(3), 313–326.
24. Raikova, R. (1992). A general approach for modelling and mathematical investigation of the human upper limb. *Journal of Biomechanics*, *25*(8), 857–867.
25. Jensen, R. H., & Davy, D. T. (1975). An investigation of muscle lines of action about the hip: a centroid line approach vs the straight line approach. *Journal of Biomechanics*, *8*(2), 103–110.
26. Blemker, S. S., & Delp, S. L. (2005). Three-dimensional representation of complex muscle architectures and geometries. *Annals of Biomedical Engineering*, *33*(5), 661–673.
27. Van der Helm, F. C., Veeger, H. E., Pronk, G. M., Van der Woude, L. H., & Rozendal, R. H. (1992). Geometry parameters for musculoskeletal modelling of the shoulder system. *Journal of Biomechanics*, *25*(2), 129–144.
28. Arnold, A. S., Salinas, S., Asakawa, D. J., & Delp, S. L. (2000). Accuracy of muscle moment arms estimated from MRI-based musculoskeletal models of the lower extremity. *Computer Aided Surgery*, *5*(2), 108–119.
29. Garner, B. A., & Pandy, M. G. (2000). The Obstacle-set method for representing muscle paths in musculoskeletal models. *Computer Methods in Biomechanics and Biomedical Engineering*, *3*(1), 1–30. doi:10.1080/10255840008915251.

30. Lieber, R. L., & Fridén, J. (2000). Functional and clinical significance of skeletal muscle architecture. *Muscle and Nerve*, *23*(11), 1647–1666.
31. Hill, A. V. (1938). The heat of shortening and the dynamic constants of muscle. *Proceedings of the Royal Society*, *B126*, 136–195.
32. Zajac, F. E. (1989). Muscle and tendon: Properties, models, scaling, and application to biomechanics and motor control. *Critical Reviews in Biomedical Engineering*, *17*(4), 359.
33. Blemker, S. S., Asakawa, D. S., Gold, G. E., & Delp, S. L. (2007). Image-based musculoskeletal modeling: Applications, advances, and future opportunities. *Journal of Magnetic Resonance Imaging*, *25*(2), 441–451.
34. Veeger, D. H. (2011). "What if": The use of biomechanical models for understanding and treating upper extremity musculoskeletal disorders. *Manual Therapy*, *16*(1), 48–50.
35. Stewart, C., & Shortland, A. P. (2010). The biomechanics of pathological gait-from muscle to movement. *Acta of Bioengineering and Biomechanics*, *12*(3), 3–12.
36. Anderson, A. E., Ellis, B. J., & Weiss, J. A. (2007). Verification, validation and sensitivity studies in computational biomechanics. *Computer Methods in Biomechanics and Biomedical Engineering*, *10*(3), 171–184.
37. Leardini, A., Chiari, L., Croce, U. D., Cappozzo, A., et al. (2005). Human movement analysis using stereophotogrammetry. Part 3. Soft tissue artifact assessment and compensation. *Gait and Posture*, *21*(2), 212.
38. Lu, T. W., & O'connor, J. J. (1999). Bone position estimation from skin marker coordinates using global optimisation with joint constraints. *Journal of biomechanics*, *32*(2), 129–134.
39. Högfors, C., Peterson, B., Sigholm, G., & Herberts, P. (1991). Biomechanical model of the human shoulder joint–II. The shoulder rhythm. *Journal of Biomechanics*, *24*(8), 699–709.
40. Komistek, R. D., Kane, T. R., Mahfouz, M., Ochoa, J. A., & Dennis, D. A. (2005). Knee mechanics: A review of past and present techniques to determine in vivo loads. *Journal of Biomechanics*, *38*, 215–228.
41. Anderst, W., Zauel, R., Bishop, J., Demps, E., & Tashman, S. (2009). Validation of three-dimensional model-based tiobio-femoral tracking during running. *Medical Engineering and Physics*, *31*, 10–16.
42. Nester, C. J., et al. (2009). Lessons from dynamic cadaver and invasive bone pin studies: Do we know how the foot really moves during gait. *Journal of Foot and Ankle Research*, *2*, 18.
43. Hurschler, C., Wülker, N., Windhagen, H., Hellmers, N., & Plumhoff, P. (2004). Evaluation of the lag sign tests for external rotator function of the shoulder. *Journal of Shoulder and Elbow Surgery*, *13*(3), 298–304.
44. Elias, J. J., Kirkpatrick, M. S., Saranathan, A., Mani, S., Smith, L. G., & Tanaka, M. J. (2011). Hamstrings loading contributes to lateral patellofemoral malalignment and elevated cartilage pressures: An in vitro study. *Clinical Biomechanics*, *26*(8), 841–846.
45. Wünschel, M., Leichtle, U., Obloh, C., Wülker, N., & Müller, O. (2011). The effect of different quadriceps loading patterns on tibiofemoral joint kinematics and patellofemoral contact pressure during simulated partial weight-bearing knee flexion. *Knee Surgery, Sports Traumatology, Arthroscopy*, *19*(7), 1099–1106.
46. Wülker, N., Hurschler, C., & Emmerich, J. (2003). In vitro simulation of stance phase gait part II: Simulated anterior tibial tendon dysfunction and potential compensation. *Foot and Ankle International*, *24*, 623–629.
47. Wünschel, M., Leichtle, U., Lo, J., Wülker, N., & Müller, O. (2012). Differences in tibiofemoral kinematics between the unloaded robotic passive path and a weightbearing knee simulator. *Orthopedic Reviews*, *4*(1), e2. doi:10.4081/or.2012.e2.
48. Davoodi, Rahman, & Gerald, E. (2002). A software tool for faster development of complex models of musculoskeletal systems and sensorimotor controllers in simulinkTM. *Journal of Applied Biomechanics*, *18*(4), 357–365.
49. Delp, S. L., Frank, C., Chand, T., & Darryl, G. (2007). OpenSim: Open-source software to create and analyze dynamic simulations of movement. *IEEE Transactions on Biomedical Engineering*, *54*(11), 1940–1950.

50. Mansouri, M., & Reinbolt, J. A. (2012). A platform for dynamic simulation and control of movement based on OpenSim and MATLAB. *Journal of Biomechanics*, *45*(8), 1517–1521.
51. Higginson, J. S., Zajac, F. E., Neptune, R. R., Kautz, S. A., & Delp, S. L. (2006). Muscle contributions to support during gait in an individual with post-stroke hemiparesis. *Journal of Biomechanics*, *39*(10), 1769–1777.
52. Jonkers, I., Stewart, C., Desloovere, K., Molenaers, G., & Spaepen, A. (2006). Musculo-tendon length and lengthening velocity of rectus femoris in stiff knee gait. *Gait and Posture*, *23*(2), 222–229.
53. Crabtree, C. A., & Jill, S. (2009). Modeling neuromuscular effects of ankle foot orthoses (AFOs) in computer simulations of gait. *Gait and Posture*, *29*(1), 65–70.
54. Nair, P. M., Rooney, K. L. Kautz, S. A. Behrman, A. L. et al. (2010). Stepping with an ankle foot orthosis re-examined: A mechanical perspective for clinical decision making. *Clinical Biomechanics (Bristol, Avon)*, *25*(6), 618.
55. Sherman, M. A., & Seth, A. (2011). Simbody: Multibody dynamics for biomedical research. *Procedia IUTAM*, *2*, 241–261.
56. Silverman, A. K., & Neptune, R. R. (2010). Individual muscle function in below Knee amputee walking. In *Conference Proceedings of the Annual Meeting of the American Society*, p. 166.
57. Fey, N. P., Klute, G. K., & Neptune, R. R. (2013). Altering prosthetic foot stiffness influences foot and muscle function during below-knee amputee walking: A modeling and simulation analysis. *Journal of Biomechanics*, *46*(4), 637–644.
58. Worsley, P., Stokes, M., & Taylor, M. (2011). Predicted knee kinematics and kinetics during functional activities using motion capture and musculoskeletal modelling in healthy older people. *Gait and Posture*, *33*(2), 268–273.
59. Michiel, O., Telfezr, S., Tørholm, S., Carbes, S., van Rhijn, L., Ross, M. et al. (2011). Generation of subject-specific, dynamic, multisegment ankle and foot models to improve orthotic design: A feasibility study. *BMC Musculoskeletal Disorders*, *12*(1), 256.
60. Nolte, D., Andersen, M. S., Rasmussen, J., & Al-Munajjed, A. (2013). Development of a patient-specific musculoskeletal model of a healthy knee to analyze hard and soft tissue loading. In *21th Annual Symposium on Computational Methods in Orthoopeadic Biomechanics*.
61. Alkjær, T., Wieland, M. R., Andersen, M. S., Simonsen, E. B., & John, R. (2012). Computational modeling of a forward lunge: Towards a better understanding of the function of the cruciate ligaments. *Journal of Anatomy*, *221*(6), 590–597.
62. Ali, Nicholas, Michael Skipper Andersen, John Rasmussen, D Gordon E Robertson, and Gholamreza Rouhi. 2013. "The application of musculoskeletal modeling to investigate gender bias in non-contact ACL injury rate during single-leg landings". Computer methods in biomechanics and biomedical engineering (ahead-of-print): 1–15.
63. Cao, E., Inoue, Y. Liu, T. & Shibata, K. (2012). Estimation of lower limb muscle forces during human sit-to-stand process with a rehabilitation training system. In *2012 IEEE-EMBS International Conference on Biomedical and Health Informatics (BHI)*, pp. 1016–1019.
64. Lemieux, P. O., Tétreault, P. Hagemeister, N. & Nuño, N. (2012). Influence of prosthetic humeral head size and medial offset on the mechanics of the shoulder with cuff tear arthropathy: A numerical study. *Journal of Biomechanics*, *46*(3), 806–812.
65. Jackson, M., Sylvestre, É. Bleau, J. Allard, P & Begon, M. (2012). Estimating optimal shoulder immobilization postures following surgical repair of massive rotator cuff tears. *Journal of Biomechanics*, *46*(1), 179–182.
66. Galibarov, P. E., Dendorfer, S., & Rasmussen, J. (2011). *Two computational models of the lumbar spine: Comparison and validation*. Long Beach, CA: ORS—Orthopaedic Research Society.
67. Han, K. S., Zander, T., Taylor, W. R., & Rohlmann, A. (2012). An enhanced and validated generic thoraco-lumbar spine model for prediction of muscle forces. *Medical Engineering and Physics*, *34*(6), 709–716.
68. Ulrey, B. L., & Fathallah, F. A. (2012). Subject-specific, whole-body models of the stooped posture with a personal weight transfer device. *Journal of Electromyography and Kinesiology*.

69. Lundberg, H. J., Foucher, K. C., Andriacchi, T. P., & Wimmer, M. A. (2012). Direct comparison of measured and calculated total knee replacement force envelopes during walking in the presence of normal and abnormal gait patterns. *Journal of Biomechanics*, *45*(6), 990–996.
70. Taddei, F., Martelli, S., Valente, G., Leardini, A., Benedetti, M, G., Manfrini, M., et al. (2012). Femoral loads during gait in a patient with massive skeletal reconstruction. *Clinical Biomechanics*, *27*(3), 273–280.
71. Donnelly, C. J., & Lloyd, D. G. (2012). Optimizing whole-body kinematics to minimize valgus knee loading during sidestepping: Implications for ACL injury risk. *Journal of Biomechanics*, *45*(8), 1491–1497.
72. Crossley, K. M, Dorn, T. W. Ozturk, H., van den Noort, J., Schache, A. G., & Pandy, M. G. (2012). Altered hip muscle forces during gait in people with patellofemoral osteoarthritis. *steoarthritis and Cartilage*.
73. Mansouri, M., Clark, A. E., & Reinbolt, J. A. (2012). The use of a platform for dynamic simulation of movement: Application to balance recovery. *Proceedings of the American Society of Biomechanics*, Gainesville, FL. Aug. 2012 (Available at: http://works.bepress.com/jeffrey_reinbolt/57).
74. Branemark, R., Branemark, P. I., Rydevik, B., & Myers, R. R. (2001). Osseointegration in skeletal reconstruction and rehabilitation: A review. *Journal of rehabilitation research and development*, *38*(2), 175–182.
75. Brånemark, P. I. (1983). Osseointegration and its experimental background. *The Journal of prosthetic dentistry*, *50*(3), 399–410.
76. Hagberg, K., Branemark, R., Guntorberg, B., et al. (2008). Osseointegrated trans-femoral amputation prostheses: Pro-spective results of general and condition-specific quality of life in 18 patients at 2-year follow-up. *Prosthetics and Orthotics International*, *32*, 29–41.
77. Grundei, H., Von Stein, T., Schulte-Bockhof, D., Kausch, C., Gollwitzer, H., & Gradinger, R. (2009). Die Endo-Exo-Femurprothese—Update eines Versorgungskonzeptes zur Rehabilitation von Oberschenkelamputierten. *Orthopädie-Technik*, *12*, 143–149.
78. Kadaba, M. P., Ramakrishnan, H. K., & Wootten, M. E. (1990). Measurement of lower extremity kinematics during level walking. *Journal of Orthopaedic Research?: official publication of the Orthopaedic Research Society*, *8*(3), 383–92. doi:10.1002/jor.1100080310.
79. Vicon Plug-in Gait Product Guide–Foundation Notes Revision 2.0 March 2010 For use with Plug-in Gait Version 2.0 in Vicon Nexus, 2010.
80. Tomaszewski, P. K., Verdonschot, N., Bulstra, S. K., & Verkerke, G. J. (2010). A comparative finite-element analysis of bone failure and load transfer of osseointegrated prostheses fixations. *Annals of Biomedical Engineering*, *38*(7), 2418–2427.

Chapter 8
Contact Modeling and Collision Detection in Human Joints

Ehsan Arbabi and Daniel Thalmann

8.1 Introduction

Using computer aided simulations for investigating the joints behavior in normal and pathological cases [1] could be proven to assist physicians to diagnose the illness faster and more accurately, and also to achieve a more precise surgical plan, [2–9]. Human joint simulations usually starts by reconstructing three dimensional meshes of the joint tissues (bones, cartilages, etc) from CT or MR Images [10] and estimating the center of rotation such as for the hip [7, 11]. Once the three-dimensional model is constructed, the critical task to handle can be the precise detection of collisions between virtual tissues so that the stresses in the colliding areas are faithfully evaluated [4, 8, 9, 12] or the range of motion in a specific orientation is correctly estimated [3, 6, 7].

Most of the methods for collision detection are for general/semi-general purposes and therefore they may not be considered as an optimum method in specific applications. This generality can be problematic in case we need higher speed and still accurate results, especially when the other time consuming computations may be done in parallel to the collision detection.

In Sect. 8.2, two recent accurate and fast collision detection methods for rotating or sliding objects will be explained. In addition to detecting the collisions faster than general methods, they also return penetration depths in either radial or cylindrical direction. In general, the methods are capable of detecting the collisions and returning the penetration depths in the applications that the movement is modeled as either rotation or sliding [13, 14].

E. Arbabi (✉)
School of Electrical and Computer Engineering, College of Engineering,
University of Tehran, North Kargar Ave., Tehran, Iran
e-mail: earbabi@ut.ac.ir

D. Thalmann
Institute for Media Innovation, Nanyang Technological University, 50 Nanyang Drive, Singapore
e-mail: daniel.thalmann@epfl.ch

N. Magnenat-Thalmann et al. (eds.), *3D Multiscale Physiological Human*,
DOI: 10.1007/978-1-4471-6275-9_8, © Springer-Verlag London 2014

By applying these collision detection methods for hip 3D models, recently a fast strategy for evaluating hip pathologies has been proposed. This method will be covered in Sect. 8.3. The strategy is suitable for real time medical hip simulations, and allows differentiation between the subtypes of hip impingement. The method can give some diagnostic information, especially in cases with combined impingement where the major component has to be defined and treated [13, 15].

For diagnosing some of the human joint diseases, it is important to obtain the joint's range of motion. For example, loss of internal rotation in the hip is one of the first signs of internal hip pathology and can be related to diagnoses, such as arthritis. Also, increase in femoral or acetabular anteversion usually demonstrates an increase in the internal rotation [1]. In Sect. 8.4, a fast and accurate method for finding maximum range of motion in joints will be explained. This joint range finder method works based on the pre-processing stage of the cylindrical segmenting collision detection method explained in Sect. 8.2.2. However, the method is calculating the range of motion without applying successive collision detection algorithms (vs. traditional methods). In addition, it needs to be performed only once per simulation to find both anti-clockwise and clockwise range of motion [3, 13].

The orthopedic simulations are usually based on rotation and may need to have an estimation of the joint center of rotation. Therefore, it is very important to know how the results of a simulation depend on the joint center estimating method. In Sect. 8.5 an investigation on the sensitivity of the penetration depths of hip tissues to the methods applied for estimating hip joint center of rotation (HJC) will be discussed. Different centers of rotation calculated by five methods were applied during hip movement of 10 patients. The virtual penetration depths were calculated by using the collision detection methods explained in Sect. 8.2. The results of this investigation highlight the importance of the HJC estimation methods because of their influence on computer-aided medical research and diagnosis [13, 16].

8.2 Collision Detection for Rotating or Sliding Objects

8.2.1 Overview

In computer graphics, many methods have been proposed to speed up the processing time for collision detection among virtual objects. Usually the methods developed for collision detection are for either very general cases or very specific applications. Arbabi et al. have proposed two new methods for collision detection based on finding the penetrating vertices (not edges) when the objects are rotating or sliding, which can be used for a wide range of applications [14]. The methods take advantage of the constraints imposed on the rotating/sliding objects in order to ignore unnecessary calculations of the general methods and speed up the processing. The main strategy applied in these methods is spatial segmentation in the angular or radial orientations. These kinds of segmentation help the methods to be more adjusted to

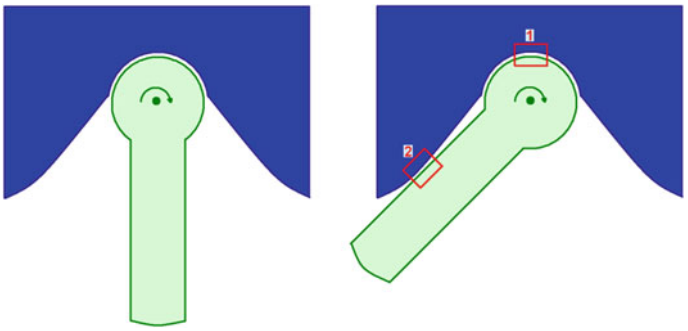

Fig. 8.1 Sliding and striking collision during rotation. The *light green object* is rotating about its center and can collide with the *dark blue object* in two different ways: 1-sliding, 2-striking [13, 14] (Reprinted from Journal of Biomechanics, Vol. 42, Arbabi E, Boulic R, Thalmann D, Fast collision detection methods for joint surfaces, pp. 91–99, Copyright (2009), with permission from Elsevier)

the style of movement (rotation or sliding), and consequently improve the efficiency of the collision detection for the rotational cases. The methods are tested in different scenarios and compared with some of the previous methods (including general and specific ones), where the comparisons show the efficiency of the proposed ones.

When an object is rotating, two kinds of collision may happen: 1-sliding or 2-striking. In the sliding case the colliding area is almost parallel to the rotational trajectory and the penetration is usually considered in the radial direction. On the other hand, in the striking case, the objects' colliding area is almost perpendicular to the rotational trajectory and the penetration is usually considered in the angular direction (Fig. 8.1).

8.2.2 Cylindrical Segmenting Collision Detection

Arbabi et al. proposed a novel fast method suitable for rotational strike, based on discretizing the space in the cylindrical orientation [14]. This kind of segmentation helps the method to be more adjusted to the style of movement (rotation), and consequently improve the efficiency of the collision detection for the rotational cases. The cylindrical segmentations are done in the same orientation of rotation which does not only increase the speed of rigid collision detection but also increases the speed of updating for deformable collision detection (in angular direction). The corresponding ring-shaped segments (see Fig. 8.2) are optimal for conducting collision detection for the associated axis of rotation vs. cube shaped cells (e.g. [17]).

After the cylindrical segmentation of the space (around the fixed object) is done, a table for the fixed object, based on the cylindrical segmentation, is created. Then, the list of the fixed polygons is stored in the corresponding table cells. By comparing the position of each mobile vertex with the fixed polygons stored in the corresponding

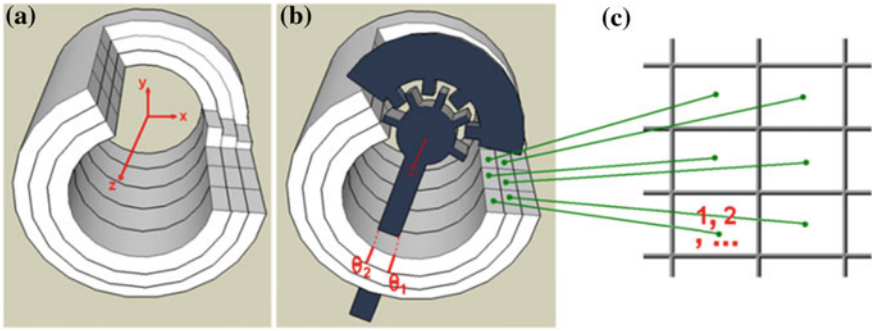

Fig. 8.2 **a** Cylindrical segmentation of the space without objects, **b** with *rotating objects*, **c** the corresponding table cells for storing list of the *fixed polygons* in each ring segment [3, 13, 14] (Reprinted from Journal of Biomechanics, Vol. 42, Arbabi E, Boulic R, Thalmann D, Fast collision detection methods for joint surfaces, pp. 91–99, Copyright (2009), with permission from Elsevier)

cell of the table, the polygons which have a chance to collide with the mobile vertex (during rotation) are found. Among the found polygons the one with the smallest angular distance to the mobile vertex is saved. The mobile vertex is checked to see whether it is penetrating the saved polygon or not. If yes, the mobile vertex and the saved polygon are returned as a penetrating pair.

This method does not only return the penetrating mobile vertices, but it also returns the corresponding penetrating fixed triangles in the angular direction, which consequently provides the curvilinear penetration depth of the vertices without applying any additional computations.

8.2.3 Radial Segmenting Collision Detection

Maciel et al. proposed a ray-based sampling method for detecting collision among rotating or sliding objects [18]. This method returns the pairs of penetrated mobile vertices and their corresponding penetrated fixed triangles. The method could be shown to be faster than many other general methods and also to be suitable for evaluating human joints. However, it also suffers from some weaknesses in accuracy and in processing stages.

Later, Arbabi et al. proposed another method working by radial segmentation of the object's spatial occupancy [14]. The collision is found by comparing the position of the vertices and the polygons occupying the same radial segment (see Fig. 8.3) [14]. Generally, the method is inspired by the work done by Maciel et al. [18]. However, an important part of the method, i.e. the strategy used for creating and filling the table, is different from this work. The proposed new strategy not only makes the method return accurate collision answers (vs. the approximated answer of [18]), but also increases the speed of table updating significantly. Arbabi et al. also

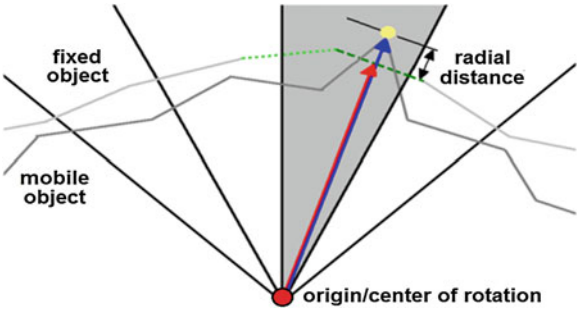

Fig. 8.3 Checking whether the mobile vertex (*yellow dot* on the *dark gray* rough 2D mesh) is penetrating the fixed polygon (*green dashed line* on the *light gray* 2D mesh). Both of the *green fixed triangles* (*dark dashed line* and *light dotted line*) are inside the *gray* spatial cell (segmented by *black radial lines*). However, only the *dark green triangle* (*dashed line*) is intersected by the vector connecting the origin (*red dot*) to the mobile vertex. The signed radial distance between the *dark green triangle* and the vertex is calculated by subtracting the *red vector* (*short vector*) from the *blue* one (*long vector*) [13, 14] (Reprinted from Journal of Biomechanics, Vol. 42, Arbabi E, Boulic R, Thalmann D, Fast collision detection methods for joint surfaces, pp. 91–99, Copyright (2009), with permission from Elsevier)

investigated the effect of the mapping function (to map from Cartesian coordinates to radial segments) on the processing time to check the importance of simplicity of the function versus uniformity of its output's distribution [14]. The main steps of the algorithm are listed as follows:

1. Radial segmentation of the space around the fixed object;
2. Creating one table for the fixed object based on the radial segmentation;
3. Storing a list of all the fixed polygons in the corresponding table cells;
4. Comparing the position of each mobile vertex with all the fixed polygons stored in the corresponding cell of the table;
5. Finding the polygon which has a chance to collide with the mobile vertex;
6. Checking the radial distance between the vertex and the found polygon;
7. If the mobile vertex is penetrating the fixed polygon, return them as a penetrating pair [13, 14].

8.2.4 Testing and Comparison

To evaluate the proposed methods for collision detection during rotation (striking and sliding), Arbabi et al. compared the performance of the proposed methods with the performance of the previous methods in different scenarios [13, 14]. Based on the results, it could be seen that the total processing time of the proposed cylindrical and radial segmenting methods can be respectively up to about one and two orders of magnitude faster than the other methods. Both of these methods are able to be used

accurately for different kinds of joints whose movement can be modeled as rotation (ball-and-socket joints such as hip joint and shoulder). In case the joint movement contains some non-negligible translations (e.g. knee), the radial segmenting collision detection method can still be used to return accurately the radial penetration depths [13, 14].

8.3 Using Virtual Penetration Depth for Hip Medical Diagnosis

8.3.1 Overview

In the past few years, femoroacetabular impingement (FAI) was recognized as the leading pathomechanism leading to a significant number of so-called 'primary' hip osteoarthritis [19, 20]. It is defined by an early pathological contact between primary osseous prominences of the acetabulum and/or the femoral head-neck junction. Depending on the underlying pathomorphology and its related pathomechanism, two different types of FAI are distinguished: 'pincer' and 'cam' impingement. The pincer type of FAI describes a linear contact between the acetabular rim and the femoral head-neck junction. A cam impingement occurs when the femoral head-neck junction has an abnormally large radius. Diagnosis of FAI can prove to be difficult, particularly in cases with subtle pathomorphologies and/or combined hip dysplasia and FAI occurring in the same hip [21]. Several computer aided simulations for three-dimensional analysis of hip pathologies have been presented before [2, 3, 7, 22–25]. Most of these methods imply substantial drawbacks for use in daily clinical practice or for research purposes. These limitations include mainly the neglect of soft tissue structures (labrum, cartilage) or the inability to achieve a real-time simulation. Approaches based on finite element (FE) analysis can provide an excellent evaluation of static hip problems such as developmental dysplasia of the hip [23–26]. However, having a better estimation of stresses for a dynamic pathomechanism such as FAI is very time-consuming and not applicable for real time medical hip simulations [23]. Finally, there is a lack of a fast method evaluating penetration depth of the colliding soft and bony tissues in FAI, and which has been correlated with available biomechanical simulation data [13, 15].

Arbabi et al. introduced a computer-assisted method for real-time evaluation of FAI based on virtual penetration depth for the colliding tissues including soft tissue structures [15]. Analogous to the pincer type of FAI, the 'curvilinear' penetration occurs in the angular direction, which is tangential to the rotational trajectory. By applying cylindrical segmenting collision detection method proposed Arbabi et al. [14] (see Sect. 8.2.2),the curvilinear penetration depth during hip movement can be calculated. Also, analogous to the cam type of FAI, the 'radial' penetration takes place in the radial direction. By using the radial partitioning collision detection method proposed by Arbabi et al. (see Sect. 8.2.3), the radial penetration depth during hip movement can be calculated too [14].

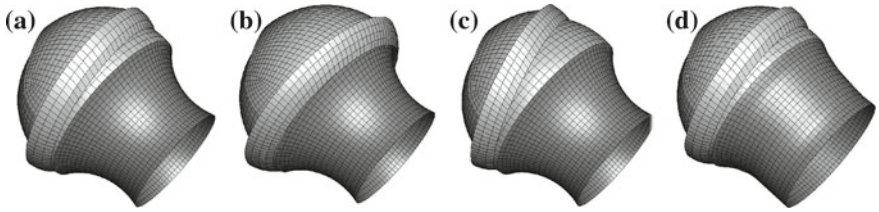

Fig. 8.4 **a** Normal joint, **b** pincer joint, **c** dysplastic joint, **d** cam type joint [13, 15, 23]; (Image courtesy of Salman Chegini, ARTORG, University of Bern) (With kind permission from Wiley: Journal of Orthopaedic Research, Penetration depth method—novel real-time strategy for evaluating femoroacetabular impingement, Vol. 28, 2010, pp. 880–886, Arbabi E, Chegini S, Boulic R, Tannast M, Ferguson S J, Thalmann D, Figs. 3 and 6)

8.3.2 Hip Models

The morphology of the human hip can be described by various selected anatomical and radiographical parameters [27]. For simplicity and comparability, only two important parameters were chosen to quantify acetabular and femoral pathomorphologies: the lateral center-edge (CE) angle of Wiberg [28], and the α angle of Nötzli [29], respectively. The hip models were prepared by Salman Chegini at ARTORG, University of Bern, by using CAD software.[1] These models included acetabular and femoral bone, articular cartilage, the labrum and the chondrolabral transition zone. In order to create a wide range of hip geometries, a consecutive series of α and CE angles were chosen for evaluation, covering normal and pathological joint morphologies. The CE angle values ranged from 0° to 40°, α angles ranged from 40° to 80°. Increments of 10° were selected for both parameters, resulting in a total of 25 different joints for evaluation, e.g. normal (CE $= 20°, \alpha = 40°$), cam (CE $= 20°, \alpha = 80°$), pincer (CE $= 40°, \alpha = 40°$), combined FAI (CE $= 40°, \alpha = 80°$), dysplastic (CE $= 0°, \alpha = 40°$), or combined dysplastic and impinging morphologies (CE $= 0°, \alpha = 80°$) (Fig. 8.4) [23].

8.3.3 Simulation

The hip models were simulated during standing-to-sitting movement. Known average in-vivo load and motion data for standing-to-sitting were used for evaluation [30]. The total motion for standing-to-sitting was divided into 30 equal and consecutive sub-motions. All of the penetrating vertices were found, and both curvilinear and radial penetration depths as well as the von Mises stresses were calculated in each sub-motion.

[1] Solidworks 2005, Solidworks Corp., Boston, MA, USA.

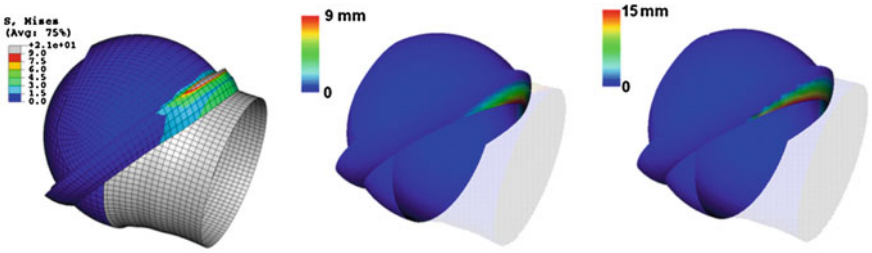

Fig. 8.5 *Left* Von Mises stress in a deformed FEM model (α=60°, CE=40°). *Center* and *Right* Labrum is colored based on its radial and curvilinear penetration depths in the same model, respectively (femur bone is semi-transparent) [13, 15]; (*Left image* courtesy of Salman Chegini, ARTORG, University of Bern) (With kind permission from Wiley: Journal of Orthopaedic Research, Penetration depth method—novel real-time strategy for evaluating femoroacetabular impingement, Vol. 28, 2010, pp. 880–886, Arbabi E, Chegini S, Boulic R, Tannast M, Ferguson S J, Thalmann D, Figs. 3 and 6)

For each hip model, a curve describing the maximum curvilinear and radial penetration depths for different motion angles was created. For quantitative evaluation, the maximum of the curve values (peak) was extracted from each curve. In order to detect patterns for the curvilinear and the radial penetration for specific hip pathomorphologies, the difference of the normalized maximum penetration depths was calculated. The calculated differences could show which type of penetration is stronger for the corresponding hip pathologies (if the difference is positive (negative), the curvilinear (radial) penetration depth is stronger).

8.3.4 Evaluation

Although the maximum penetration depth and maximum stress are not occurring in the same zone (Fig. 8.5.), there is a cause and effect relationship between them that can be well quantified. Hence, the quantitative values resulting from the proposed method were shown to be correlated strongly with the von Mises stresses of the FE analysis [15, 23]. The maximum curvilinear penetration depth was found for a combined cam-pincer pathomorphology. The maximum radial penetration depth was found for pure cam deformities. The maximum normalized difference between curvilinear and radial penetration depths was found for combined cam-pincer hips. The minimum normalized distance was seen for pure cam impingement. Finally it could be concluded that the penetration depth method allows a differentiation between characteristic pathomorphotypes related to femoroacetabular impingement, and it can be used for real time medical applications, which are desired by physicians.

8.4 Joint Range Finder

8.4.1 Overview

Clinical hip examinations are usually based on rotating the hip in special orientations. For instance, the flexion-adduction-internal rotation test is used to aid in the diagnosis of femoroacetabular impingement [1]. Such methods are usually based on the patient's feedback during the examinations and therefore the diagnosis may not be easy and accurate. After diagnosing the hip disease, the treatment may be based on surgery. For example, options for treatment of femoroacetabular impingement include trimming of the anterior aspect of the acetabular rim [31]. Since the operation can be highly invasive, it is essential that the surgeon has a good knowledge of the joint's range of motion before the operation to know exactly the surgery strategy and reduce the risk of miss-operation [3, 31].

Not many studies have been performed on finding the joint's range of motion. The current methods used for finding range of motion in human joints are usually based on performing successive rotation increments as long as no collision occurs between the 3D meshes of the fixed part and the mobile part along the selected anatomical axis of rotation [7]. This can be highly time-consuming due to the fact that we cannot know the number of rotation steps in advance. For increasing the simulation speed sometimes the collision detection is restricted to certain area of the tissues. Imposing such restrictions needs defining different areas of the tissues for the simulation program [7], which is not easy to be done automatically. These traditional methods can take a large amount of computing time. Arbabi et al. [3] proposed a method for finding the maximum range of motion for human joints with rotating movements, based on classifying the fixed part of the joint in a cylindrically segmented space (similar to the pre-processing step of cylindrical segmenting collision detection method, explained in Sect. 8.2.2), without using any collision detection algorithm. It proved to be much faster than traditional ones, and needs to be performed only once per axis of orientation [3, 31].

8.4.2 Method

Similar to the pre-processing step of cylindrical segmenting collision detection method, the algorithm starts by discretizing the space in the cylindrical orientation, in the same orientation of rotation [3, 14, 31]. Then one table is prepared, with a size that is function of the search interval and of the resolution. Each cell of the table corresponds to one ring of the space and the indices of the fixed polygons occupying that ring are stored in the corresponding table cell. For every vertex of the mobile object, the corresponding ring-segment which contains the vertex is found. Finally, the angular distance between the mobile vertex and the fixed polygons are calculated in the corresponding table cell of the ring segment. By evaluating all ring segments,

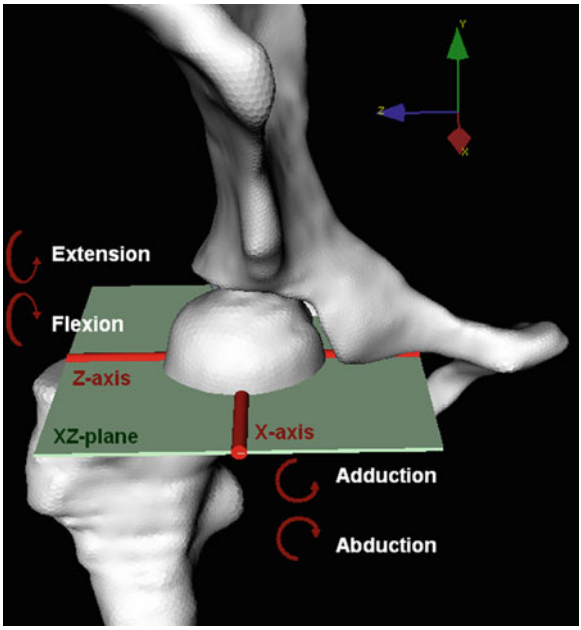

Fig. 8.6 Finding the range of motion in the human hip joint based on a hip graphical model [3, 13] (2007 IEEE. Reprinted, with permission, from Arbabi E, Boulic R, Thalmann D (2007) A fast method for finding range of motion in the human joints. Paper presented at the 29th Annual international conference of the IEEE engineering in medicine and biology society, Lyon, France)

the minimum angular distance is returned as the maximum range of motion. In addition to calculating the maximum range of motion, parts of the objects which would collide first (when meeting the maximum range of motion) are also found [3, 31].

8.4.3 Testing and Comparison

The proposed method was evaluated for finding the range of motion in the human hip joint. The tests were based on finding the bone to bone range of motion; where the femoral bone was considered as a mobile part constraint by the pelvis (see Fig. 8.6). For evaluating their method, Arbabi et al. [3] used 3D triangular meshes obtained by segmenting MR Images taken from a patient by the method described in [10]. Center of rotation was also found based on the scanned 3D models [7].[2] The method was tested for four different mesh resolutions.

The experiments showed that the proposed algorithm is significantly faster than the previous methods (10–66 times faster) and can be used for the biomedical

[2] The 3D Meshes were prepared by Benjamin Gilles at MIRALab, University of Geneva.

applications such as musculo-skeletal simulation as it is difficult to infer precisely the relative range of motion from scanned or reconstructed 3D models. The estimated range of motion was also an accurate value, which is another advantage comparing to the collision detection based methods, where we have to define rotation steps as a resolution. The results were also validated by confirming that the found range of motion is never less than the full capsule's range of motion, and it is even almost the same of full hip capsule's range of motion for flexion/extension [3, 13].

8.5 Importance of Joint Center of Rotation in Medical Simulations

In orthopedic simulations the behavior of bones and related tissues such as cartilages are investigated during their movements. For this reason, it is usually needed to have an estimation of the joint center of rotation in advance. There are several methods for estimating joint center of rotation, and different simulations may apply different methods for obtaining the joint center. Therefore, it is very important to know how the results of simulation may vary based on the methods used for estimating the joint center of rotation. Arbabi et al. have evaluated this issue for hip joints by calculating the virtual penetration depth during hip movement [13, 16].

8.5.1 Hip Joint Center of Rotation

Many different methods of estimating hip joint center of rotation (HJC) have been proposed that can be classified in predictive and functional approaches. The predictive (static) approach relies upon the location of anatomical landmarks [32–35]. The functional (dynamic) approach estimates the HJC from recorded [11, 36–39] or simulated [7, 40, 41] motion. Gilles depicted three predictive and two functional approaches [40]. They are described here briefly.

8.5.1.1 Predictive Approaches

The HJC is estimated as the center of the sphere that approximates the best the femoral head or the acetabulum. The approximation is thus a least square fitting, which aims to find the center (and radius) of the fitted sphere to the reconstructed data. These two methods are denoted as *femoral head sphere* and *acetabulum sphere* methods. The *double sphere* approach considers the joint as a perfect ball- and socket-joint in which inter-articular distance is constant. It aims at finding the common center of the femoral and acetabulum spheres [13, 16, 40].

8.5.1.2 Functional Approaches

The main idea in the functional approach is to enforce a certain inter-articular distance: given each vertex P_i of the acetabulum, the difference $|d_i - d_i^{ref}|$ is minimized, where d_i (d_i^{ref}) denotes the (reference) distance between the vertex P_i and the femoral head. For a given joint transform, a minimization process is used to minimize the differences $|d_i - d_i^{ref}|$ through hip bone infinitesimal translations. Two different approaches are thus explored: (i) the *dconst* approach that uses a *constant* reference distance for *all* the vertices equal to the radii difference between the fitted femoral and acetabulum spheres, (ii) the *dref* approach that uses the initial distances acquired in the reconstructed position. In a simulated motion, each joint transform can be hence optimized in terms of shifts to seek reference inter-articular distances. The HJC is then considered as the point of the femur which moves the less in the hip bone frame during the optimized motion [13, 16, 40].

8.5.2 Simulation

In many computer-based hip simulations, it is the contact among hip tissues that should be investigated. Therefore, three dimensional virtual models of real tissues are created based on CT or MR images, and we simulate the virtual tissues that penetrate one another during the movement. In reality stresses corresponding to the amount of virtual penetration occur to avoid such inter-penetration of real tissues. Therefore having an estimation of virtual penetration depth can give an appropriate measure for investigating hip contacts during the simulation [13, 16].

Arbabi et al. investigated the sensitivity of hip simulation to the estimated center of rotation [16]. The HJCs were estimated by five different methods for ten patients, using 3D meshes.[3] For each patient and each estimated HJC they rotated hip about different medical axes and estimated changes in the penetration depth of hip tissues during the rotation [16]. The penetration depths have been calculated by using the collision detection methods explained in Sect. 8.2. Therefore, two kinds of penetration are investigated. By using the cylindrical segmenting method proposed by Arbabi et al. [14], the penetration depth of a labrum vertex is estimated by calculating the smallest distance that the femur bone needs to be moved away in its rotational trajectory in order to leave the penetrated vertex of labrum out (Fig. 8.7). The penetration among femur and acetabular soft tissues are evaluated by using radial segmenting method proposed by Arbabi et al. [14]. In this method, the returning penetration depths are calculated by finding the radial distance between each femur cartilage vertex and the acetabular polygons occupying the same radial segment of the vertex (Fig. 8.8) [13, 14, 16].

[3] The 3D meshes and HJCs were prepared by Jerome Schmid at MIRALab, University of Geneva.

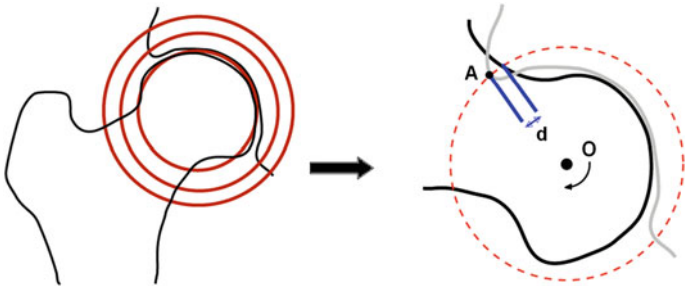

Fig. 8.7 *Left* Cylindrical segmentation of the space around the hip joint. *Right* Curvilinear penetration depth obtained by cylindrical segmenting method ('*d*' represents the amount of curvilinear penetration depth of vertex '*A*' located on the labrum (*light colored*) inside femur bone (*dark colored*), when the bone is rotating about '*O*') [13, 14, 16] (With kind permission from Springer Science+Business Media: Journal of Medical and Biological Engineering and Computing, Sensitivity of hip tissues contact evaluation to the methods used for estimating the hip joint center of rotation, Vol. 50, 2012, pp. 595–604, Arbabi E, Schmid J, Boulic R, Thalmann D, Magnenat-Thalmann N, Fig. 8.2)

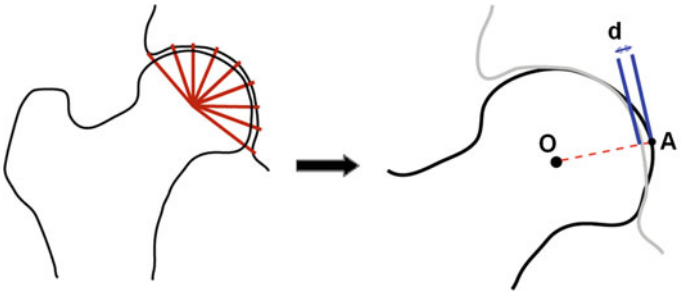

Fig. 8.8 *Left* Radial segmentation of the space around the hip joint. *Right* Radial penetration depth obtained by radial segmenting method. '*d*' represents the amount of radial penetration depth of vertex '*A*' located on the femur cartilage (*dark colored*) inside acetabular cartilage (*light colored*), when the bone is rotating about '*O*') [13, 14, 16] (With kind permission from Springer Science+Business Media: Journal of Medical and Biological Engineering and Computing, Sensitivity of hip tissues contact evaluation to the methods used for estimating the hip joint center of rotation, Vol. 50, 2012, pp. 595–604, Arbabi E, Schmid J, Boulic R, Thalmann D, Magnenat-Thalmann N, Fig. 8.2)

8.5.3 Evaluation

Ten healthy female subjects (average age: 24) were selected by MIRALab, University of Geneva for the study. A subject's hip meshes have been simulated by rotating the hip about five different HJCs, and calculating tissues contact penetration depths (curvilinear and radial). These rotations and calculations have been done for all the subjects (totally 50 simulations).

When the penetration depth for different subjects are investigated separately, it could be seen that for almost all of the estimated HJCs, radial penetration depth differs

considerably (about 30 % in average) compared to when HJC is estimated based on *dref*. Such amount of differences highlights the fact that the hip simulations can give different results and conclusions when the HJC estimation method shifts to one another, (especially from *dref* to *dconst*). The results also show that the difference in penetration depth is subject dependent. In addition, the *dconst* and acetabulum sphere present the highest variability with respect to the femoral head sphere and double sphere methods. With regard to the different axes of rotation, the radial and curvilinear penetration depths during adduction and external rotation show to be less sensitive to the methods used for estimating HJC. On the other hand, flexion is among the most sensitive types of rotation to the HJC estimation methods. As a brief summary, the results indicate that hip medical investigations are not robust when the HJC estimation method changes. In fact, researchers should be careful in choosing the methods of HJC estimation, before providing any conclusion from their medical research.

8.6 Summary and Conclusion

In this chapter a brief review of two different collisions detection methods, suitable for evaluating rotating/sliding objects such as human joints, has been presented. These methods can provide a basis for further studies of contact evaluation in human joints. These studies can vary from medical investigation to medical applications. Two different medical applications, inspired by these collision detection methods, have been covered in this chapter. In one of these applications, maximum range of motion of human joint could be calculated accurately and fast. In the other medical application, penetration depths calculated in different directions could be used as an indicator for diagnosing and also classifying different kinds of joint diseases (i.e. FAI). In addition to these applications, again by exploiting the mentioned collision detection strategy, sensitivity of the joint simulations to the estimated joint center of rotation has been investigated. The experiments and validations were done in 3D hip models. However, due to the generality of the explained collision detection methods for joint evaluation, the investigations and the applications can be used or extended for other human joints.

References

1. Martin, H. D. (2005). Clinical examination of the hip. *Operative Techniques in Orthopaedics*, *15*, 177–181.
2. Tannast, M., Kubiak-Langer, M., Langlotz, F., Puls, M., Murphy, S. B., & Siebenrock, K. A. (2007). Noninvasive three-dimensional assessment of femoroacetabular impingement. *Journal of Orthopaedic Research*, *25*(1), 122–131.
3. Arbabi, E., Boulic, R., & Thalmann, D. (2007). *A fast method for finding range of motion in the human joints*. Paper presented at the 29th Annual International Conference of the IEEE

Engineering in Medicine and Biology Society, Lyon, France, 2007.
4. Chegini, S., Beck, M., & Ferguson, S. J. (2006). *Femoro acetabular impingement as a possible initiator of cartilage degeneration*. Paper presented at the 7th International Symposium on Computer Methods in Biomechanics and Biomedical Engineering, Antibes, France, 2006.
5. Teran, J., Sifakis, E., Blemker, S. S., Ng-Thow-Hing, V., Lau, C., & Fedkiw, R. (2005). Creating and simulating skeletal muscle from the visible human data set. *IEEE Transaction on Visualization and Computer Graphics*, *11*(3), 317–328.
6. Armand, M., Lepistö, J. V. S., Merkle, A. C., Tallroth, K., Liu, X., Taylor, R. H., et al. (2004). Computer-aided orthopedic surgery with near-real-time biomechanical feedback. *Johns Hopkins Apl Technical Digest*, *25*, 242–252.
7. Kang, M., Sadri, H., Moccozet, L., & Magnenat-Thalmann, N. (2003). *Hip joint modeling for the control of the joint center and the range of motions*. Paper presented at the 5th IFAC Symposium on Modeling and Control in Biomedical Systems, 2003.
8. Scifert, C. F., Brown, T. D., Pedersen, D. R., & Callaghan, J. J. (1998). A finite element analysis of factors influencing total hip dislocation. *Clinical Orthopaedics and Related Research*, *355*, 152–162.
9. Genda, E., Konishi, N., Hasegawa, Y., & Miura, T. (1995). A computer simulation study of normal and abnormal hip joint contact pressure. *Archives of Orthopaedic and Trauma Surgery*, *114*, 202–206.
10. Gilles, B., Moccozet, L., & Magnenat-Thalmann, N. (2006). *Anatomical modelling of the musculoskeletal system from MRI*. Paper presented at the International Conference on Medical Image Computing and Computer Assisted Intervention (MICCAI), 2006.
11. Camomilla, V., Cereatti, A., Vannozzi, G., & Cappozzo, A. (2006). An optimized protocol for hip joint centre determination using the functional method. *Journal of Biomechanics*, *39*, 1096–1106.
12. Rapperport, D. J., Carter, D. R., & Schurman, D. J. (1985). Contact finite element stress analysis of the hip joint. *Journal of Orthopaedic Research*, *3*, 435–446.
13. Arbabi, E. (2009). *Contact modeling and collision detection in human joints*. PhD Thesis, École Polytechnique Fédérale de Lausanne, Switzerland.
14. Arbabi, E., Boulic, R., & Thalmann, D. (2009). Fast collision detection methods for joint surfaces. *Journal of Biomechanics*, *42*(2), 91–99.
15. Arbabi, E., Chegini, S., Boulic, R., Tannast, M., Ferguson, S. J., & Thalmann, D. (2010). The penetration depth method—a novel real time strategy for evaluating femoro-acetabular impingement. *Journal of Orthopaedic Research*, *28*(7), 880–886.
16. Arbabi, E., Schmid, J., Boulic, R., Thalmann, D., & Magnenat-Thalmann, N. (2012). Sensitivity of hip tissues contact evaluation to the methods used for estimating the hip joint center of rotation. *Journal of Medical and Biological Engineering and Computing*, *50*(6), 595–604.
17. Teschner, M., Heidelberger, B., Mueller, M., Pomeranets, D., & Gross, M. (2003). *Optimized spatial hashing for collision detection of deformable objects*. Paper presented at the Vision, Modeling, Visualization, 2003.
18. Maciel, A., Boulic, R., & Thalmann, D. (2007). Efficient collision detection within deforming spherical sliding contact. *IEEE Transaction on Visualization and Computer Graphics*, *13*(3), 518–529.
19. Murphy, S., Tannast, M., Kim, Y. J., Buly, R., & Millis, M. B. (2004). Debridement of the adult hip for femoroacetabular impingement indications and preliminary clinical results. *Clinical Orthopaedics and Related Research*, *429*, 178–181.
20. Ganz, R., Parvizi, J., Beck, M., Leunig, M., Nötzli, H., & Siebenrock, K. A. (2003). Femoroacetabular impingement: A cause for osteoarthritis of the hip. *Clinical Orthopaedics and Related Research*, *407*, 112–120.
21. Günther, K. P., Thielemann, F., Hartmann, A., & Bernstein, P. (2008). Combined hip-dysplasia and femoroacetabular impingement: Diagnosis and simultaneous surgical treatment. *Orthopäde*, *37*, 577–586.
22. Kubiak-Langer, M., Tannast, M., Murphy, S. B., Siebenrock, K. A., & Langlotz, F. (2007). Range of motion in anterior femoroacetabular impingement. *Clinical Orthopaedics and Related Research*, *458*, 117–124.

23. Chegini, S., Beck, M., & Ferguson, S. J. (2008). The effects of impingement and dysplasia on stress distributions in the hip joint during sitting and walking: A finite element analysis. *Journal of Orthopaedic Research*, *27*(2), 195–201.
24. Russell, M. E., Shivanna, K. H., Grosland, N. M., & Pedersen, D. R. (2006). Cartilage contact pressure elevations in dysplastic hips: A chronic overload model. *Journal of Orthopaedic Surgery*, *3*, 1–6.
25. Michaeli, D. A., Murphy, S. B., & Hipp, J. A. (1997). Comparison of predicted and measured contact pressures in normal and dysplastic hips. *Medical Engineering & Physics*, *19*(2), 180–186.
26. Hipp, J. A., Sugano, N., Millis, M. B., & Murphy, S. B. (1999). Planning aetabular redirection osteotomies based on joint contact pressures. *Clinical Orthopaedics and Related Research*, *364*, 134–143.
27. Tannast, M., Siebenrock, K. A., & Anderson, S. E. (2007). Femoroacetabular impingement: Radiographic diagnosis-what the radiologist should know. *American Journal of Roentgenology*, *188*(6), 1540–1552.
28. Wiberg, G. (1939). Studies on dysplastic acetabular and congenital subluxation of the hip joint: With special reference to the complication of osteo-arthritis. *Acta Chirurgica Scandinavica*, *58*, 7–38.
29. Nötzli, H. P., Wyss, T. F., Stoecklin, C. H., Schmid, M. R., Treiber, K., & Hodler, J. (2002). The contour of the femoral head-neck junction as a predictor for the risk of anterior impingement. *The Journal of Bone and Joint Surgery*, *84*, 556–560.
30. Bergmann, G., Deuretzbacher, G., Heller, M., Graichen, F., Rohlmann, A., Strauss, J., et al. (2001). Hip contact forces and gait patterns from routine activities. *Journal of Biomechanics*, *34*, 859–871.
31. Mardones, R. M., Gonzalez, C., Chen, Q., Zobitz, M., Kaufman, K. R., & Trousdale, R. T. (2005). Surgical treatment of femoroacetabular impingement: Evaluation of the effect of the size of the resection. *Journal of Bone & Joint Surgery*, *87-A*, 273–279.
32. Bell, A., Petersen, D., & Brand, R. (1990). A comparison of the accuracy of several hip center location prediction methods. *Journal of Biomechanics*, *23*, 617–621.
33. Boudriot, U., Hilgert, J., & Hinrichs, F. (2006). Determination of the rotational center of the hip. *Archives of Orthopaedic and Trauma Surgery*, *126*, 417–420.
34. Kirkwood, R., Culham, E., & Costigan, P. (1999). Radiographic and non-invasive determination of the hip joint center location: Effect on hip joint moments. *Clinical Biomechanics*, *14*, 227–235.
35. Seidel, G. K., Marchinda, D. M., Dijkers, M., & Soutas-Little, R. W. (1995). Hip joint center location from palpable bony landmarks: A cadaver study. *Journal of Biomechanics*, *28*(8), 995–998.
36. Cappozzo, A. (1984). Gait analysis methodology. *Human Movemenent Science*, *3*, 27–54.
37. Chang, L., & Pollard, N. (2007). Constrained least-squares optimization for robust estimation of center of rotation. *Journal of Biomechanics*, *40*(6), 1392–1400.
38. Piazza, S., Okita, N., & Cavanagh, P. (2001). Accuracy of the functional method of hip joint center location: Effects of limited motion and varied implementation. *Journal of Biomechanics*, *34*(7), 967–973.
39. Siston, R., & Delp, S. (2006). Evaluation of a new algorithm to determine the hip joint center. *Journal of Biomechanics*, *39*, 125–130.
40. Gilles, B. (2007). *Anatomical and kinematical modelling of themusculoskeletal system from MRI*. PhD Thesis, University of Geneva, Switzerland.
41. Kang, M. (2004). *Hip joint center location by fitting conchoid shape to the acetabular rim region of MR images*. Paper presented at the 26th Annual International Conference of the IEEE Engineering in Medicine and Biology Society, San Francisco, USA, 2004.

Chapter 9
Combined Motions of the Shoulder Joint Complex for Model-Based Simulation: Modeling of the Shoulder Rhythm (ShRm)

Victor Sholukha and Serge Van Sint Jan

9.1 Anatomical and Articular Components of the Shoulder Girdle Complex

The shoulder joint complex includes 4 bony segments showing articular relationships with each other: the humerus (Hum) (1 in Fig. 9.1), the scapula (Scap) (2), the clavicle (Clav) (3) and the thorax (Thor) (4). For modeling purposes as presented in this chapter, the thorax segment includes all ribs, sternum and thoracic vertebrae. These bony components articulate with each other through several joints to define the shoulder joint complex including: the scapulohumeral (or glenohumeral) joint (A), the acromioclavicular joint (B), the sternoclavicular (or sternocostoclavicular) joint (C) and the scapulothoracic joint (D). Each individual joint allows the related bony components to move independently. However, the combined action of the shoulder joint ligament organization and the shoulder muscle control create a functional synergy between these joints. This functional joint synergy is widely acknowledged to follow a given pattern called the "*shoulder rhythm*" or ShRm mechanism as called further in this chapter. Modeling activities should take this synergy into account in order to reproduce the real shoulder behavior. Note that the literature sometimes refers to the motions of the humerus relative to the thorax as taking place in a so-called "*thoracohumeral joint*". Anatomically, the latter joint does not exist. We will use this term as synonym to the joint mechanism describing the entire ShRm behavior that involves a synergy between all previously-mentioned anatomical joints.

V. Sholukha (✉) · S.Van Sint Jan
Laboratory of Anatomy, Biomechanics and Organogenesis (LABO), Université Libre de Bruxelles, Brussels, Belgium
e-mail: vcholouk@ulb.ac.be
url:http://www.homepages.ulb.ac.be/∼labo

S.Van Sint Jan
e-mail: sintjans@ulb.ac.be

N. Magnenat-Thalmann et al. (eds.), *3D Multiscale Physiological Human*,
DOI: 10.1007/978-1-4471-6275-9_9,

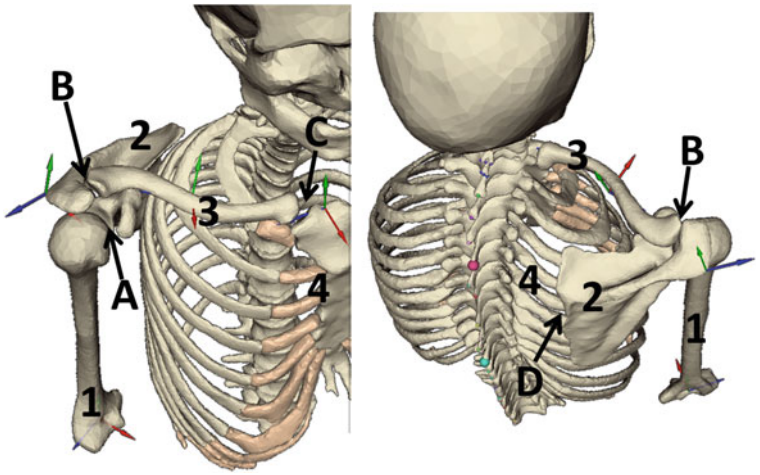

Fig. 9.1 Anatomy of the shoulder joint complex. *Left*: antero-superior view. *Right*: postero-superior view. See text for explanations. *1*: humerus (Hum); *2*: scapula (Scap); *3*: clavicle (Clav); *4*: thorax (Thor)

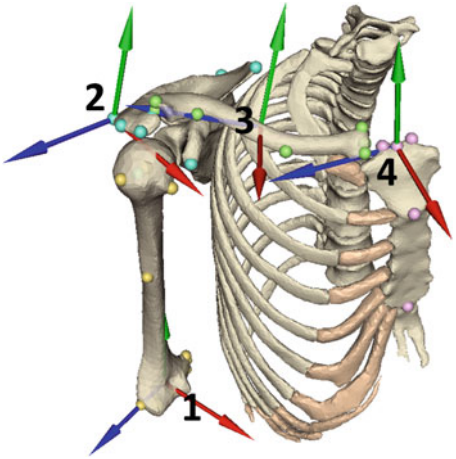

Fig. 9.2 Shoulder bony segments and related anatomical frames (right shoulder, anterosuperior view). *1*: humerus. *2*: scapula. *3*: clavicle. *4*: sternum/thorax. Conventionally, *Red*/*Green*/*Blue* (RGB) color-coding has been adopted to label the frame axes: *red* = X-axis, *green* = Y-axis; *blue* = Z-axis. See text for more explanations. Spheres attached to the bones indicate the locations of key ALs that are used for modeling purposes (see later sections). These ALs are located using so-called "virtual palpation". Note that the displayed local frames are according the recommendations of the International Society of Biomechanics [1]. The local frames used in this study to represent motions were slightly different (see section "Construction of anatomical frames", later in this chapter)

Each segment displacement is conventionally characterized along 3 anatomical planes, defined from anatomical landmarks (ALs) [1] as following. The scapulo-humeral joint allows the humerus to move relative to the scapula: flexion/extension along the sagittal plane (around the Z-axis, Fig. 9.2); abduction/adduction along the frontal plane (X-axis); and internal/external rotation along the horizontal plane (Y-axis).

The acromioclavicular joint and scapulothoracic joint conjointly allow the scapula to move relative to the clavicle and thorax, respectively: anterior/posterior tilt (around the Z-axis running parallel to the scapular spine); protraction/retraction (around the Y-axis vertical axis) and lateral/medial rotation (around the X-axis perpendicular to the two previous ones). Note that scapula motions simultaneously occur in these two joints.

The sternoclavicular joint allows the clavicle to move relative to the thorax: protraction/retraction (around the vertical axis Y-axis); elevation/descend (X-axis); and axial rotation (Z-axis running through the clavicle longitudinal axis).

9.1.1 Literature Review on Shoulder-Related Studies

The human shoulder joint is one of the most mobile joint complexes due to the sequence of the 4 above-mentioned intermediate joints connecting the humerus to the thorax. Theoretically, each of these joints shows 6 degrees-of-freedom (6DoF), but for practical reason it is usually simplified as a ball-and-socket mechanism. Most of the overall thoracohumeral motion takes place in the glenohumeral joint, which shows a humeral elevation and axial rotation up to 120 and 135°, respectively [2, 3]. The sternoclavicular joint allows clavicle elevation of between 11 and 15°, retraction between 15 and 29° during arm elevation, and a large axial rotation of up to 40°. Since the longitudinal axis of the clavicle is almost perpendicular to the scapular plane, the axial rotation of the clavicle and the lateral rotation of the scapula (in the scapular plane) are equivalent and require minor displacements (about 15°) in the acromioclavicular joint.

It must be stressed that normal motions of the scapula are constrained by the medial border of the scapula, which is maintained against the thorax by the combined action of the Serratus Anterior muscle and Rhomboideus muscle. Scapular motions are also constrained by the clavicle, which allows the acromion to move more or less along a spherical pathway around the sternoclavicular joint. The contribution of scapular and clavicle motions to arm elevation follows a general pattern in which scapular motion is responsible for approximately one third of the total arm elevation.

During the last twenty years, detailed reviews were published about data collection procedures related to the ShRm mechanism and the shoulder joint complex organization [1, 4–16]. These procedures, and their conclusions, are briefly presented here according to the nature of the data collection.

The use of pins that are drilled into the bony joint segments allows collecting accurate data. In such study, each pin is equipped with a technical frame (TF) that allows displacement tracking of the bone-of-interest. Several research groups previ-

ously reported their results as "gold standard" by collecting data in-vivo with TFs rigidly inserted into the sternum, clavicle, scapula and humerus [17–23]. Comparison of these past results with of our own results will be given later. We can already anticipate that our modeling results are in agreement with the literature although it must be stressed that quantitative comparison is strongly dependent on the joint motion representation used for result presentation. Despite the scientific value of the data, organizing such experiments is difficult for obvious ethical reasons, i.e., related to the very invasive nature of the underlying research protocols (such protocols are not accepted by ethical committees in Belgium). Such data were therefore difficult to obtain on a large population of healthy volunteers in the framework of this chapter.

Other research reports found in the literature are related to in-vitro measurements (i.e., performed on cadaveric specimens). Collected data usually include motion data, soft tissue properties and accurate joint morphology [6, 11, 13, 15, 16, 24–33]. In-vitro experiments allow being more invasive than during in-vivo protocol. However, one must be careful when interpreting motion patterns, especially for shoulder data. In essence, in-vitro kinematics cannot include physiological muscle recruitment and muscle control on the joints. Nevertheless, such muscle control on the shoulder joint complex is recognized in the literature as one of the main stability factors especially during large motion ranges, for example to maintain the scapula against the thorax during physiological shoulder movements. Models based on in-vitro motion data alone will therefore show limitations for in-vivo applications due to the unrealistic bone displacement patterns modeled from the intrinsic passive conditions obtained from cadavers; the lack of muscle activity will lead to bone instability, and disturb the physiological shoulder motion pattern and ShRm. Our own experimental data obtained from two cadavers (i.e., 4 shoulders) confirmed the observation of non-physiological ShRm due to artefacts produced from the in-vitro nature of the experimental protocol. In summary, one can conclude that in-vitro protocols usually show accurate reproducibility for the ShRm during movements requesting a limited range-of-motion. For larger range, the absence of muscle stability during in-vitro data collection introduces non-physiological ShRm, and alternatives must be found in order to build a ShRm model. Note that the importance of muscle activity for joint stability is usually less important for most other major joints (e.g., elbow, wrist, hip, knee, ankles, etc) for which stability is guaranteed by more congruent joint surfaces and by a more developed ligamentous apparatus than within the shoulder complex.

These observations show that neither invasive in-vivo protocols nor in-vitro experiments lead to satisfactory results (i.e., the former because of the small population that can be analyzed due to ethical limitations, the latter because of the lack of muscle control). Alternatives can be found in in-vivo data collection using specially-designed skin mounted cluster including reflective markers (such marker clusters will be described later in this chapter). Most publications devoted to in-vivo data collection aim to derive the thoracohumeral mechanism from TFs build from the reflective markers used within standard motion analysis settings [15, 17, 18, 22, 23, 30, 34–40]. The protocol presented in this work also includes such skin mounted TFs, but supplementary 3D bone models were fused to the motion data. Such fusion between the subjects' morphology and the underlying segment kinematics allows performing

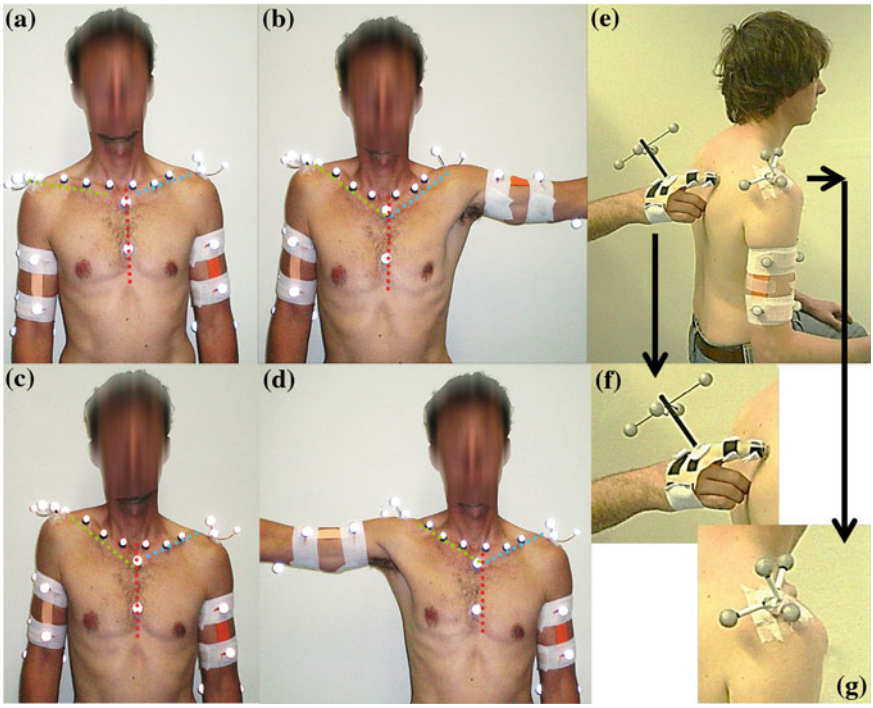

Fig. 9.3 ShRm data collection. **a**–**d** gross shoulder behavior observed in-vivo. **e**, **f** use of reflective markers for TF building and AL calibration. The images showing the shoulder behavior (**a**–**d**) illustrate the non-unique spatial relationships between humerus and the other shoulder girdle components, i.e. clavicle and scapula (**a** neutral position. **b** subject's right shoulder performing a vertical translation, while the left shoulder is performing abduction. **c** right shoulder elevation with vertical translation. **d** right shoulder elevation with abduction). Note that the entire shoulder girdle shows a similar elevation during vertical translation (**c**) and abduction (**d**). This is due to the fact that the humerus intimately follows clavicle displacements due to joint ligament tension. *Red line*: vertical through the sternum; *green line*: runs through right clavicle longitudinal axis; *blue line*: runs through left clavicle longitudinal axis. **e** calibration of shoulder ALs using the A-palp palpation protocol [50]. **f** finger gauntlet that allows natural AL calibration using finger palpation instead of an artificial pointer, such as in the CAST protocol [60]. **g** specially designed marker cluster glued on the scapula acromion; the AL calibrated using the A-palp protocol is defined in the local TF built from these clusters

a quality check of the results through visual feedback obtained in a tailored 3D visualization application (called lhpFusionBox). This control allows improving the final results of the ShRm reconstruction substantially by comparing the motion obtained from proper data collection with predicted motions from modeling activities.

To improve in-vivo data obtained from skin mounted TFs, several groups proposed the use of a so-called "scapula locator" used for AL location and calibration [6, 34, 36–38, 41–49]. The reported results show that such procedure can be useful especially when the subject's range-of-motion is close to the physiological limit. We did not adopt such locator in our protocol because measurements relied on the use

of a specially developed calibration device, called "A-palp", allowing the observer to use the finger tip directly as digitizing tool without requiring the interposition of cumbersome locating device [50] (Fig. 9.3e–g).

Once collected, motion data must be represented using some conventions. The ShRm is frequently reported following the Euler–Cardan convention [10, 12, 18, 20, 35, 45, 51–59]. Results in the present chapter will also be represented using the Cardan ZXY convention, next to attitude vector (orientation vector, following Cappozzo [60]) projections. The use of attitude vectors and related helical axis representation for rotational degrees of freedom (DoFs) is justified because such procedures have been intensively reported as the most robust methods for general joint motion representation [13, 40, 47, 48, 60–71]. Following Woltring [71], such approach of motion data storing seems robust for segment motion evaluation in global coordinate system: "*The attitude vector dispenses with the 'gimbal-lock' and non-orthogonality disadvantages of Cardanic/Eulerian conventions; therefore, its components have better metrical properties, and they are less sensitive to measurement errors and to coordinate system uncertainties than Cardanic/Eulerian angles.*"

9.2 Data Collection for Scaling Methods

This section describes the specificities of the data collection performed to determine the ShRm, keeping in mind the modeling context of the model-based approach to be developed. The main aim is to find a good compromise between anatomical reality and the constraints of in-vivo modeling (e.g., within an ergonomic context or for musculoskeletal analysis).

The main challenge of the underlying research is to find on the one hand the relationships between the humerus position and orientation and on the other hand the related attitude of the scapula and clavicle at the same moment of time. This answers a practical problem in in-vivo motion analysis. Indeed, although data related to the humerus instantaneous spatial position is relatively easy to obtain (for example, using stereophotogrammetry based on reflective markers), the same information is more difficult to collect for the clavicle (which is a small elongated bone offering limited space to attach markers) and the scapula (of which the real motion is largely hidden beneath the shoulder soft tissue). Furthermore, a unique and straightforward one degree-of-freedom mechanism like in the knee joint or the ankle joint [72] is physiologically not observable (this is depicted in Fig. 9.3a–d).

This is due to the fact that motions within the sternoclavicular joint will be similar during shoulder translation (that does not require displacement within the scapulohumeral joint) and scapulohumeral abduction. Consequently, it is not directly possible to estimate clavicle instantaneous orientation from one unique humerus pose. This is clearly visible in Fig. 9.3b: both clavicles show similar angles with the thorax line, while the humerus orientation is very different. The scapula shows similar relationships with the clavicle through the acromioclavicular joint and with the thorax through the scapulothoracic joint. The above example demonstrates that an algorithm

Table 9.1 ALs used in this research for ShRm analysis. Most ALs in the list are readily palpable through the subject's skin

Segments	Anatomical landmarks	
	Acronyms	Names
Spine	MTV3, MTV8	Thoracic spinous processes
Sternum	MSJN	Jugular notch
	MSXS	XiphiSternal joint
Clavicle	LCAJ, RCAJ	Acromioclavicular joint
	LCSJ, RCSJ	Sternoclavicular joint
	LCAS, RCAS	Anterior sternoclavicular joint
Scapula	LSIA, RSIA	Inferior angle
	LSRS, RSRS	Root of spine
	LSAJ, RSAJ	Acromioclavicular joint
Humerus	LHCH, RHCH	Humeral head center
	LHME, RHME	Medial epicondyle
	LHLE, RHLE	Lateral epicondyle
Ulna	LUSP, RUSP	Styloid process

Not palpable ALs (such as joint centres like the humeral head centre in the list) are approximated using the coordinates of palpable ALs within regression procedures [74]. These ALs are visible in Fig. 9.2

that aims to estimate clavicle and scapula displacements from humerus instantaneous postures, must first deal with the primary nature of the observed shoulder girdle displacements, i.e. simultaneous clavicle elevation within the sternoclavicular joint with scapula gliding on the thorax via the scapulothoracic joint, combined or not with a humerus displacement within the scapulohumeral joint. This is the purpose of this research.

The next section describes the anatomical landmarks required for shoulder motion characterization first. Then, the entire data collection protocol, including in-vivo validation activities, is given. Finally, the newly-developed method to estimate the various components of the shoulder rhythm is explained.

9.2.1 Anatomical Landmarks for the Upper Limb

The palpation protocol is fully described in Van Sint Jan [73]. The list of ALs used in this work for the upper limbs and thorax is given in Table 9.1. These ALs are used for several tasks related to modeling anthropometric measurements, anatomical features approximation using regression procedures, data registration and data fusion, joint reference frame construction and motion representation. Accurate and reproducible AL palpation and AL spatial location is therefore important to increase result validation, and strict and standardized definitions facilitate result comparison [73]. This must be kept in mind when using modeling algorithms integrating 3D locations of

palpated ALs. Without careful palpation during data collection, simulation results may lead to poor visualization.

9.2.2 Joint Kinematics Data for Shoulder Rhythm Determination

This section describes the experimental protocol used to collect joint kinematics related to the shoulder complex in order to perform ShRm estimation through a newly-developed approximation method. The aim of the method is to allow the following pipeline:

- Numerical data on the orientation and position of the humerus related to the thorax is first collected.
- Then, the collected data are processed by the new method to estimate the orientation and position of the scapula and clavicle.

ShRm and Shoulder Motion Datasets

Data must be collected in order to determine the relationships between on the one hand the humerus behavior and, on the other hand the related displacements of the clavicle and scapula. These relationships will be used for defining the "shoulder rhythm mechanism". It has been already stressed that it is recognized that muscle tension play an important role to explain the scapula displacements along the thorax [75, 76], even more than for any other joints in which joint stability is less dependent on muscle control. This explains why differences are observed between ex-vivo measurements performed on cadaveric specimens and during active in-vivo shoulder data. It is therefore of importance that modeling activities concentrate on both kind of data.

For this reason, data collection related to the work presented in this chapter first concentrates on ex-vivo measurements because it allows, thanks to the nature of the experiment, accurate kinematic data collection through the use of pins, including reflective markers, drilled directly into the specimen skeleton. These first datasets allowed performing a first ShRm estimation. However, the analyzed ex-vivo joint movements were passive. Supplementary data were required to assess the precision of the determined shoulder rhythm during in-vivo activities (similar to the displacements visible at Fig. 9.3). These supplementary data were used in order to improve the initial model prototype towards a final model usable for both in-vivo and ex-vivo applications.

In summary, several datasets obtained from various specimens and subjects were collected. Shoulder kinematic data were acquired from various specimens and volunteering subjects (Table 9.2). Thirty different datasets were collected from 2 fresh-frozen specimens: these datasets included passive shoulder displacements in all conventional anatomical planes (i.e., sagittal, frontal and horizontal planes) and along intermediary planes. Three volunteers were asked to perform actively sim-

Table 9.2 Information on specimens and subjects analyzed to determine ShRm and to perform validation activities

	Gender	Weight (kg)	Height (cm)
Specimen 1	Male	84	176
Specimen 2	Male	70	170
Subject 1	Male	71	182
Subject 2	Male	57	170
Subject 3	Female	80	168

None of the specimens or volunteers showed external signs of musculoskeletal disorders prior to the motion analysis. This was confirmed for the specimens by joint dissection after data collection

ilar shoulder movements (25 active datasets were collected for each volunteer). The volunteers' shoulders were also passively mobilized along each anatomical plane (12 passive datasets were collected for each volunteer). The collected ex-vivo and in-vivo raw data were then combined (as explained in further sections) to perform accurate modeling of the human shoulder joint complex behavior or ShRm.

Data Collection

This section describes the experimental protocol used to collect the above-mentioned datasets.

Ex-vivo Data Collection

The following protocol was adopted for each specimen. Technical clusters with four infra-red reflective markers were drilled into each of the bony segment of interest (i.e., thorax, scapula, clavicle and humerus) (Fig. 9.4). Careful and minimal dissections of the soft tissue were realized to minimize the effects of the skin traction on the wand of the cluster. Incisions in muscles were kept as small as possible. Each cluster allowed defining a local technical frame.

Next, the specimen was processed by computed tomography (CT) using conventional sequences [77, 78]. Medical imaging datasets were segmented using commercial software (Amira®, Dev. 4.0, Konrad-Zuse-Zentrum Berlin, http://www.vsg3d.com/amira) to obtain 3D models of all bones and joints of interest through semi-automated and manual operations. The following models were obtained for each processed individual (specimens or volunteers): thorax (including the relevant section of the spine), two clavicles, two scapulae and two humeral bones. The same reconstruction procedure was applied for ex-vivo and in-vivo data. Location of the TFs was also obtained from the available CT datasets by processing the 3D coordinates of the centroid of each reflective marker. Marker locations and bone models were naturally defined in the same global CT reference frame.

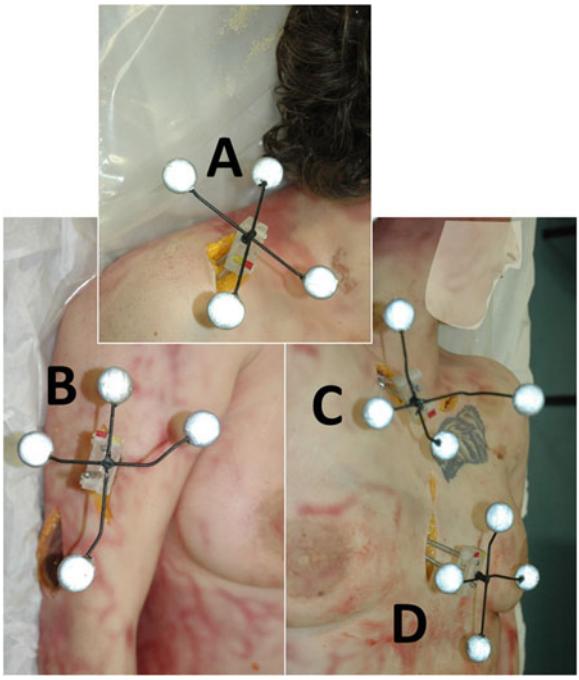

Fig. 9.4 Drilling of TF with reflective markers in the bony segments of a fresh-frozen specimen (this illustration is made of 3 snapshots, right anterolateral view). *A* scapula TF inserted in the acromion. *B* humerus TF drilled in the bone shaft. *C* clavicle TF. *D* thorax TF inserted in the sternal body. Each TF was secured to the underlying bones using two small surgical pins to increase the TF fixation. Skin and muscle incisions were kept as minimal as possible to reduce possible motion artefacts due to soft tissue dissection

Once the 3D models were available, virtual palpation was performed to determine spatial locations of all palpable ALs on the 3D models [50]. Such ALs serve three purposes:

(1) to allow approximation of geometrical joint centre (for example, for the humerus head);
(2) to allow registration of bone to motion during motion analysis; and
(3) to allow creation of anatomical frames.

Spatial coordinates of all palpated landmarks were also given in the original global frame of the medical imaging system. The same palpation procedure was applied for ex-vivo and in-vivo data.

After CT imaging, the specimen was secured within a special jig in a sitting position in order to align gravity along the conventional anatomical planes (i.e., the gravity vector ran perpendicular to the shoulder horizontal plane). Before movement data capture, the joint was manually set in neutral position (arm along the thorax,

Table 9.3 Motion in the shoulder complex tested during ex-vivo experiments

Primary movement	Humeral orientation	Plane
Abduction	Internal rotation	Frontal ($\cong 0°$)
	Neutral	
	External rotation	
Flexion-Extension	Internal rotation	Sagittal ($\cong 90°$)
	Neutral	
	External rotation	
Elevation	Internal rotation	2 intermediate plane of elevation ($\cong 30$ and $60°$)
	Neutral	
	External rotation	
Hand-to-back	Neutral	Quasi frontal plane
Hand-to-head	Neutral	Quasi frontal plane
Humeral translation	Shoulder elevation and pro-/retro-traction	

elbow flexed at 90°, forearm in neutral position with the thumb up). Planar and out-of-plane passive motions were performed by an experienced physiotherapist who moved the specimen's upper limbs along the required motion planes (as described in Table 9.3) and controlled the humerus longitudinal orientation (internal or external rotations, or neutral). Motions covering a wide range of the reaching volume of the shoulder complex were recorded.

All movements were recorded using a stereophotogrammetry system including, eight cameras (VICON 612, Oxford Metrics Ltd, Oxford, UK, frequency: 120 Hz, resolution: 1000×1000 pixels). All movement data sets include spatial information, i.e. 3D coordinates, related to the trajectory of the reflective markers fixed on the subject. Data was stored in the standard C3D format. Technical cluster trajectories were then solidified and smoothed.

In-vivo Data Collection

Preparation of the volunteers was similar then during ex-vivo experiments. The only difference was the placement of the reflective markers. The technical clusters including the markers were strapped around the volunteers' segments-of-interest (Fig. 9.3). Special care was taken that the strapping did not disturb the volunteers when performing shoulder displacements. The remaining of the in-vivo protocol was similar to the ex-vivo one (see above).

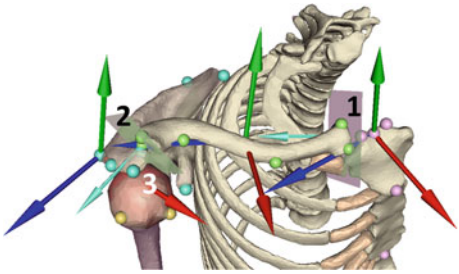

Fig. 9.5 Approximation of supplementary joint information using multiple regression equations. Joint plane location (semi-transparent magenta planes) and perpendicular vectors (*in cyan*) displayed for sternoclavicular joint (*1*), acromioclavicular joint (*2*) and glenohumeral joint (*3*)

Data Pre-processing

This section describes how the collected data have been pre-processed in order to generate results required for the development of the ShRm estimation algorithm and related validation.

Joint Center Coordinates and Dimensions

Supplementary morphological information had to be extracted from the bone models in order to fully comply with the recommendations of the International Society of Biomechanics [1] which request the spatial coordinates of joint centres, such as the scapulohumeral joint center) for the creation of specific anatomical frames. Therefore, joint centres required for further joint motion representation was estimated using regression equations [74] applied on the described ALs.

After joint estimation the following information were available (Fig. 9.5):

Sterno-Clavicular Joint:

- Joint center spatial location.
- Joint main plane and normal orientation to this plane.

Acromio-Clavicular Joint:

- Joint center spatial location.
- Joint main plane and normal orientation to this plane.

Gleno-Humeral Joint:

- Joint center spatial location (HCH: RHCH for right, LHCH for left).
- Head humerus (modeled as a sphere).

Table 9.4 Segment local coordinate system definitions

	G_1	G_2	G_3	G_4	LCS AFs
Thorax	MSJN	MSXS	MTV3	MTV8	$G_C = G_1$; $V = (G_1 + G_3)/2 - (G_2 + G_4)/2$
					$Y = [\|V\|]$, $Z = [\|(G_1 - (G_2 + G_4)/2) \otimes Y\|]$
					$X = [\|Y \otimes Z\|]$
Right clavicle	RCAJ	RCSJ	RCAS		$G_C = G_2$; $Z = [\|(G_1 - G_2)\|]$, $Y_t = [\|(G_2 - G_3)\|]$
					$X_t = [\|Yt \otimes Z\|]$, $Y = [\|Z \otimes X_t\|]$, $X = [\|Y \otimes Z\|]$
Right scapula	RSRS	RSAJ	RSIA	RHCH	$G_C = G_2$; $X_t = [\|(G_1 - G_3) \otimes (G_2 - G_3)\|]$
					$Y = [\|G_2 - G_4\|]$, $Z = [\|X_t \otimes Y\|]$, $X = [\|Y \otimes Z\|]$
Right humerus	RHLE	RHME	RHCH	RUSP	$G_C = G_3$; $Y = [\|G_3 - (G_1 + G_2)/2\|]$
					$Z = [\|(G_4 - (G_1 + G_2)/2) \otimes Y\|]$, $X = [\|Y \otimes Z\|]$

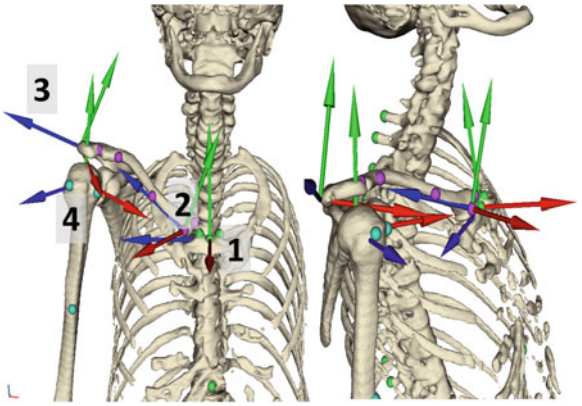

Fig. 9.6 Anatomical frames built in this study. *Left* anterior view. *Right* lateral view. 1-thorax, 2-clavicle 3-scapula and 4-humerus anatomical frames. The same color convention as in Fig. 9.2 has been used for the axes orientation

Construction of Anatomical Frames

In order to represent motions, the following anatomical frames were built (Table 9.4, Fig. 9.6).

Let's assume $G_i, i = \overline{1,4}$ as vector columns $G_i = (G_{ix}, G_{iy}, G_{iz})^T$ corresponding to the digitized segment AL locations defined in the global coordinate system (GCS). The origin of the segment local coordinate system (LCS) are defined as G_C. Let's define $\otimes$ as the matrix cross product sign, $[|P|] = P/\|P\|$, $P = (P_x, P_y, P_z)^T$ and $\|P\|$ is the norm of the vector column of point P. Table 9.4 contains segment anatomical frames (AFs) or local coordinate system definitions.

In order to define the ALs in the LCS, let us define the rotation matrix $R = (X, Y, Z)$. Then, we obtained the vector columns $L_i = RT(G_i - G_C), i = \overline{1,4}$, where L_i are the ALs in the LCS.

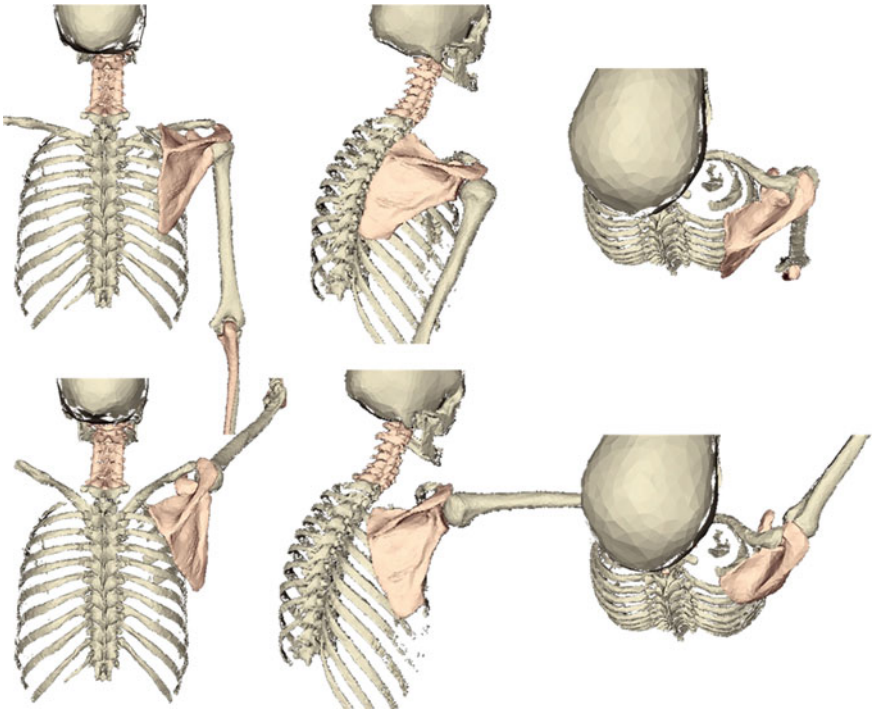

Fig. 9.7 Motion data collection visualization after least square registration between morphological data (medical imaging) and functional data (stereophotogrammetry). *Top row* neutral position. *Bottom row* shoulder performing a flexion/abduction of the right shoulder. *Left* posterior view. *Middle* posterolateral view. *Right* superior view. Note the natural gliding of the scapula along the thorax and the clavicle elevation determined from the data fusion described in this section. This physiological behavior must be represented within the modeling mechanism to allow natural representation of the shoulder rhythm

Registration of morphological models to motion data—ShRm visualization

The previous sub-section described the construction of a so-called morphological model relative to the shoulder complex made of 3D bone models, anatomical landmarks, reflective markers, joint information and anatomical frames. This model must now be registered with the available motion data. Model registration, or data fusion, was performed using least-square algorithms to determine the relationships of the landmark position between the medical imaging datasets and the motion datasets [79]. Results of this registration allow representing the collected motion data according to the estimated anatomical frames.

Registration results were then visualized to allow controlling of the anatomical realism of the obtained model and its adequacy with the above-mentioned literature. This was important to ensure that collected data was sufficient for modeling purposes. Figure 9.7 represents visualization snapshots of a so-called upright pose and range of

motion for a right shoulder abduction/adduction and flexion/extension. As previously mentioned, the estimation aimed to find the relationships between on the one hand the humerus poses relative to the thorax, and on the other hand the scapula and clavicle poses.

9.3 ShRm Mathematical Modeling

This section describes several multiple regression approaches for ShRm modeling and evaluation based on the fused data as described above. The method analyzes the ShRm as a six degrees-of-freedom (6 DoFs) mechanism including translation of the humeral head and attitude vectors for rotation. Humerus, scapula and clavicle displacements are defined relative to the thorax. The results of the motion reconstruction and ShRm prediction were visualized within a home-made software (called lhpFusionBox) build from the open-source MAF library [80]. Prediction accuracy has been estimated by processing the discrepancy of ALs trajectories for selected motions before and after data fusion between the real motions (collected for control) and the estimated motion (obtained from the mathematical description, see below). Analysis of 15 different motions shows mean accuracies of the clavicle and scapula rhythm reconstruction of 8.5 ($SD = 6.1$) mm and 19.8 ($SD = 5.2$) mm, respectively.

The last section of this chapter introduces a supplementary correction method in order to reduce the artefacts that could be observable after applying the described model-based approach.

9.3.1 Motion Representation: Mathematical Background

The motion representation used local body coordinate systems definition for thorax, clavicle, scapula and humerus based on Tables 9.1 and 9.4. Subsequently, the motion representation was processed for the clavicle and humerus relative to the thorax, and additionally for the scapula relative to the clavicle.

Orientation Matrix and Cardan Angle Convention

A model-based approach for shoulder motion reconstruction supposes predefined sequences of rotational joint DoFs. In this study, we implemented a shoulder model based on Cardan angle conventions. Fixed (world) axes and column vectors, with intrinsic composition (composition of rotations about body axes) of active rotations and the right-handed rule for the positive sign of the angles are assumed. This means for example that a convention named (ZXY) is the result of performing first an intrinsic Z rotation, followed by an X and a Y rotation in the moving axes. Its matrix is the product of Rot($\mathbf{Z}$, θ_3) Rot($\mathbf{X}$, θ_1) Rot($\mathbf{Y}$, θ_2) as following:

$$R = \begin{bmatrix} (c_2c_3 - s_1s_2s_3) & -s_3c_1 & (s_2c_3 + s_1s_3c_2) \\ (s_3c_2 + s_1s_2c_3) & c_1c_3 & (s_2s_3 - s_1c_2c_3) \\ -c_1s_2 & s_1 & c_1c_2 \end{bmatrix} = \begin{bmatrix} c_3 & -s_3 & 0 \\ s_3 & c_3 & 0 \\ 0 & 0 & 1 \end{bmatrix} \begin{bmatrix} 1 & 0 & 0 \\ 0 & c_1 & -s_1 \\ 0 & s_1 & c_1 \end{bmatrix} \begin{bmatrix} c_2 & 0 & s_2 \\ 0 & 1 & 0 \\ -s_2 & 0 & c_2 \end{bmatrix},$$

where $s_i = \sin(\theta_i), c_i = \cos(\theta_i), i = 1, 2, 3$.

From the known joint rotation matrix R, angles of rotation can be derived as:

$$c_1 = \sqrt{R_{12}^2 + R_{22}^2}, \theta_1 = \arctan(R_{22}/c_1),$$
$$\theta_2 = \arctan(-R_{31}/R_{33}), \theta_3 = \arctan(-R_{12}/R_{22}).$$

Finite Helical Axis Representation

In the finite helical axis (FHA) or screw approach, joint motion is represented at each instant by a translation s along a line of space and a rotation θ about the same line, determined by a unit direction attitude vector $\mathbf{u} = (u_x, u_y, u_z)^T$ and the position $\mathbf{T}$ of one of its points [71]. The relation between $\mathbf{u}$ and the rotation matrix R is given by: $R = C_\theta E + S_\theta A(\mathbf{u}) + V_\theta \mathbf{u}\mathbf{u}^T$, where: $S_\theta = \sin(\theta)$, $C_\theta = \cos(\theta)$, $V_\theta = 1 - C_\theta$, E-(3,3) is the identity matrix and $A(\mathbf{u})$ is the screw symmetric matrix, defined as:

$$A(\mathbf{u}) = \begin{bmatrix} 0 & -u_z & u_y \\ u_z & 0 & -u_x \\ -u_y & u_x & 0 \end{bmatrix}$$

When the joint rotation matrix R is known, the sine of the rotation angle can be found from $2S_\theta = \pm\sqrt{(R_{32} - R_{23})^2 + (R_{13} - R_{31})^2 + (R_{21} - R_{12})^2}$, while the angle of rotation θ about the axis $\mathbf{u}$ is given by the relation $\theta = Arc\tan(S_\theta/C_\theta)$.

The orientation of the FHA, i.e. the components of the unit vector u, is given by:

$$2u_x = (R_{32} - R_{23})/S_\theta, 2u_y = (R_{13} - R_{31})/S_\theta, 2u_z = (R_{21} - R_{12})/S_\theta.$$

Note that for very small rotation angles(θ), the axis of rotation $\mathbf{u}$ is not well-defined due to the small magnitude of both numerator and denominator.

Following a previously-advised joint rotational motion representation [60], orientation vector $\theta = \theta \cdot \mathbf{u}$ projections (also called OVP convention) was adopted because of its robustness [71]. The distal bone frame has been projected in this work on the proximal bone frame to represent the distal joint segment displacements.

Linear Multiple Regression

To analyze the available motions, the dependent DoFs, i.e. clavicle and scapula motions, were plotted using the humerus displacement as the independent DoF. Raw

Table 9.5 Clavicle linear and parabolic ($\mathbf{a}_3\mathbf{x}^2+\mathbf{a}_2\mathbf{x}+\mathbf{a}_1$) fitting coefficients for rotational DoFs versus thoracohumeral elevation in sagittal (range $[-50, 100]^\circ$) and frontal (range $[-100, 0]^\circ$) planes and center of humeral head vertical translation (range [0, 80] mm)

	Linear			Parabolic			
	a_2	a_1	mean(SD)	a_3	a_2	a_1	mean(SD)
Three DoFs rotations versus thoracohumeral flexion/extension (ZXY convention)							
X	−0.11159	−23.2327	3.2(2.2)	−0.00098513	−0.061326	−21.4709	2.8(1.6)
Y	0.16736	−7.0886	2.1(1.8)	0.0001033	0.16209	−7.2734	2.1(1.8)
Z	0.23586	14.7331	1.7(1.4)	0.00052921	0.20886	13.7866	1.5(1.1)
Three DoFs rotations versus thoracohumeral flexion/extension (OVP convention)							
X	−0.1466	−22.5823	3.5(2.4)	−0.0013939	−0.080827	−20.5679	3.0(1.6)
Y	0.095759	−10.2201	2.4(1.8)	−0.00045932	0.11743	−9.5563	2.2(1.8)
Z	0.20731	15.8171	1.6(1.1)	0.0005262	0.18248	15.0566	1.5(0.8)
Three DoFs rotations versus thoracohumeral abduction/adduction (ZXY convention)							
X	0.41363	−10.6629	2.6(2.0)	−0.0034611	0.1206	−14.5356	2.1(2.1)
Y	−0.19048	−14.1894	3.3(2.3)	0.0046046	0.19937	−9.0372	2.5(2.4)
Z	−0.21968	10.1708	4.0(2.4)	0.0059972	0.28807	16.8813	2.8(2.6)
Three DoFs rotations versus thoracohumeral abduction/adduction (OVP convention)							
X	0.32993	−11.4658	1.5(1.1)	−0.00093541	0.24472	−12.4539	1.4(1.1)
Y	−0.01723	−12.3698	1.3(1.0)	0.0010837	0.081494	−11.2251	1.2(0.9)
Z	−0.13985	12.6652	1.9(0.9)	0.0011174	−0.038051	13.8456	1.8(0.8)
Three DoFs rotations versus humeral head vertical translation (ZXY convention)							
X	−0.32202	−15.225	1.6(0.9)	−0.00035388	−0.29515	−15.4762	1.5(1.0)
Y	0.19283	−12.1147	3.7(3.2)	0.002303	0.017935	−10.4796	3.5(3.2)
Z	0.2721	9.144	4.7(4.3)	0.0049868	−0.10661	12.6846	4.3(3.6)
Three DoFs rotations versus humeral head vertical translation (OVP convention)							
X	−0.34035	−13.8726	2.0(0.6)	−0.00042286	−0.30824	−14.1729	1.1(0.9)
Y	0.062493	−12.4087	2.8(2.3)	0.00039623	0.032402	−12.1274	2.7(2.3)
Z	0.22085	11.304	3.9(3.3)	0.0037506	−0.063977	13.9668	3.7(2.8)

data were fitted by polynomial regressions. These non-linear functional relationships were then used to construct multiple regression functions for ShRm evaluations covering the full humerus reach. A linear multiple regression approach is presented in this section to estimate possible solutions.

This approach allows predicting 6 DoFs dependent motions (relative clavicle and scapula displacements) from the combination of up to 6 DoFs that characterizes humerus displacements relative to the thorax anatomical frame.

Let's define for the current frame of motion $Q_i = c_i q_i, i = 1, \ldots, 6$, where c_i, q_i are predefined weight coefficient and value of humerus i-th DoF. A set of normalized weight coefficients is defined as $w_i = c_i \left|q_i\right| / S, i = 1, \ldots, 6$, where $S = \sum_{i=1}^{6} c_i \left|q_i\right|$. Using these weights one can predict the current values of the dependent DoFs as:

Table 9.6 Scapula linear and parabolic fitting coefficients for rotational DoFs versus thoracohumeral elevation in sagittal (range [−50, 100]°) and frontal (range [−100, 0]°) planes and center of humeral head vertical translation (range [0, 80] mm)

	Linear			Parabolic			
	a_2	a_1	mean(SD)	a_3	a_2	a_1	mean(SD)
Three DoFs rotations versus thoracohumeral flexion/extension (ZXY convention)							
X	0.020119	6.0054	2.0(1.5)	−0.00046513	0.043852	6.8373	1.9(1.4)
Y	0.09294	50.8051	2.9(2.2)	−0.0009794	0.14292	52.5566	2.4(1.8)
Z	0.12492	−14.7824	1.4(0.9)	0.00043213	0.10288	−15.5552	1.1(0.9)
Three DoFs rotations versus thoracohumeral flexion/extension (OVP convention)							
X	−0.02953	11.9511	2.5(1.9)	−0.0010389	0.019496	13.4524	2.1(1.5)
Y	0.10499	49.88	2.7(1.9)	−0.00099679	0.15203	51.3205	2.3(1.6)
Z	0.1491	−11.0295	1.0(0.8)	$8.15E-05$	0.14526	−11.1472	1.0(0.7)
Three DoFs rotations versus thoracohumeral abduction/adduction (ZXY convention)							
X	0.077288	7.4494	1.2(1.2)	−0.0015569	−0.054526	5.7073	1.1(1.1)
Y	0.07309	54.7748	2.3(1.6)	−0.00053144	0.028096	54.1801	2.3(1.6)
Z	−0.16818	−19.6822	1.7(1.3)	0.0023177	0.028045	−17.0889	1.3(1.3)
Three DoFs rotations versus thoracohumeral abduction/adduction (OVP convention)							
X	0.10553	14.1098	1.7(1.1)	−0.0015217	−0.033093	12.5436	1.5(0.8)
Y	0.015219	51.2514	2.6(1.1)	−0.00079354	−0.057072	50.4131	2.6(1.0)
Z	−0.08861	−14.3055	0.9(0.9)	0.00026744	−0.064244	−14.023	0.9(0.7)
Three DoFs rotations versus humeral head vertical translation (ZXY convention)							
X	−0.02934	6.0313	2.2(2.0)	−0.0015105	0.085367	4.9588	2.1(1.8)
Y	0.028533	50.9272	3.9(2.6)	0.0011468	−0.058561	51.7414	3.9(2.6)
Z	0.17281	−18.7816	2.2(1.7)	0.00177	0.038394	−17.5249	2.0(1.7)
Three DoFs rotations versus humeral head vertical translation (OVP convention)							
X	−0.10428	13.9165	2.2(1.9)	−0.0019829	0.046308	12.5087	2.1(1.6)
Y	0.043608	49.519	3.8(2.6)	0.0013712	−0.060522	50.4926	3.7(2.6)
Z	0.14933	−14.7645	2.7(2.1)	0.0010673	0.068281	−14.0067	2.6(2.1)

$\Psi_i^k = \sum_{j=1}^{6} w_j P_{ij}^k(q_j), i = 1, \ldots, 6$, where k represents either the clavicle or scapula, and $P_{ij}^k(q_j)$ are the regression polynomials. Note, by specifying $c_i = 0$ one can "manually" neglect any independent DoF. By only including linear and parabolic fitting, the total amount of analyzed polynomials was 144 ($2 \times 2 \times 6 \times 6$). Based on the residual of the fitting estimation, polynomials were restricted to parabolic representation, while linear fitting was discarded (examples of both representation are described in the next section including Tables 9.5 and 9.6). Furthermore, only two humerus DoFs (flexion/extension and abduction/adduction) were selected by comparison a fitting residual for thoracohumeral six DoF motions.

9.3.2 Motion Representations: Comparison of Basic Motions

In this section we present the comparison of the ShRm evaluation using Cardan (ZXY) and OVP (Orientation Vector Projected on proximal LCS as explained above) conventions. Then, the evaluated ShRm will be illustrated by the model-based shoulder motion simulation in near scapula and frontal plane humerus elevations.

9.4 ShRm Regression Equations

This section contains results related to the estimation of the position and orientation of the clavicle and scapula from the humerus attitude.

Figure 9.8 shows typical raw source data and results from regression as obtained for all DoFs processed in this work. Raw source data (plotted by colored dots) together with results of fitting (full curves, equations are given in the legend box) are given for one DoF (flexion-extension). This figure shows displacements for the right clavicle (longitudinal rotation) and right scapula (tilt motion). The definitions of the DoFs are as explained in the first section of this chapter. This figure shows linear and parabolic polynomial fitting of the right sternoclavicular (Clav, $[0.00052921x^2 + 0.20886x + 13.7866$; mean error $= 1.5(SD = 1.1)]$) and acromioclavicular (Scap, $[0.00043213x^2 + 0.10288x - 15.5552$; mean error $= 1.1(SD = 0.9)]$) motions compared to the humerus sagittal displacement in the thoracohumeral joint (flexion/extension) using the ZXY conventions. Precision of fitting is also indicated in the figure caption behind each fitting equation (with mean and standard deviation).

Results for the other DoFs are given in Tables 9.5 and 9.6 for the clavicle and scapula, respectively.

Figure 9.9 shows the results of the comparison between Cardan (ZXY, on the left) and OVP (on the right) conventions for data representation. It is illustrated by the fitting of clavicle (elevation) and scapula (upward rotation) motion around the X-axis of the proximal body versus the humerus thoracohumeral abduction/adduction. Comparison of the fitting residual (e.g., for the clavicle data: Cardan representation $= 2.1(2.1)$ and OVP $= 1.4(1.1)$) shows that OVP conventions seem more appropriate to approximate the scapula and clavicle behavior.

Tables 9.5 and 9.6 contain values of linear and parabolic fitting coefficients of three rotational DoFs for clavicle and scapula respectively. Residual of fitting analysis shows that both ZXY cardan and OVP conventions show similar mean(SD) values, but comparison of clavicle motion for humeral abduction/adduction motion shows lower residuals for the OVP approach (i.e., compare fitting residual in the mean(SD) columns of Table 9.5 for XYZ lines from 7 to 12). Therefore, OVP convention was used in this work for shoulder rhythm prediction and model-based simulation. Transformation to ZXY cardan convention was then performed using a rotation matrix.

The analysis of the results presented above suggests that linear multiple regressions must be applied for final clavicle and scapular orientation prediction (e.g.

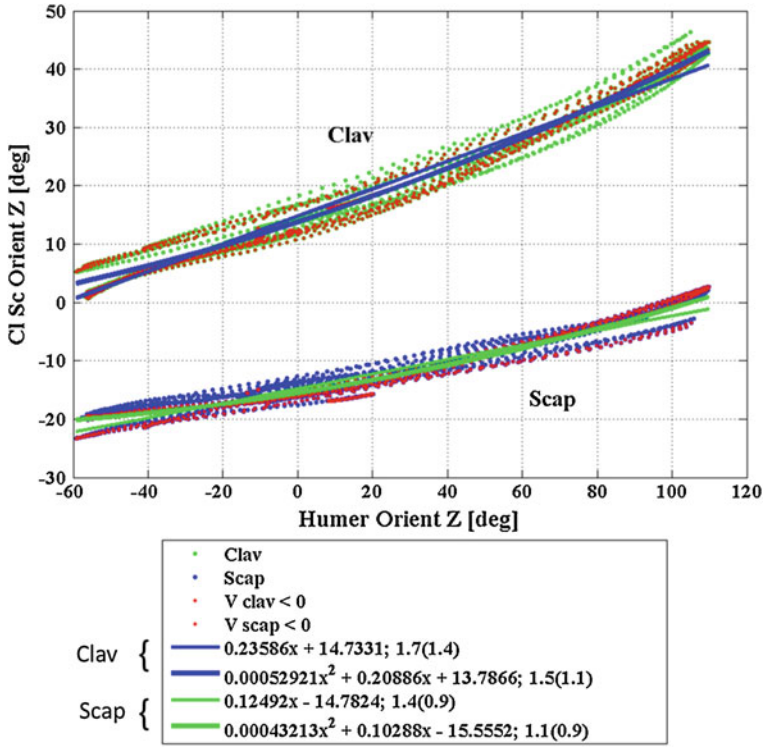

Fig. 9.8 Fitting results for the right clavicle (Clav) rotation and scapula (Scap) tilt versus the humerus sagittal elevation in the thoracohumeral joint (flexion/extension around thorax AF Z-axis). Raw data depicted by colored dots as indicated in the legend box. The displacements orientations are defined as (V stands for velocity): posterior (Clav) and anterior (V clav < 0) longitudinal Clav rotations in green and red dots, respectively; posterior (Scap) and anterior (V scap < 0) Scap tilt in blue and red dots, respectively. Coefficients of linear and parabolic fitting are given in the legend box together with mean(SD) fitting residual estimation (behind the ';' sign). Linear and parabolic fitting are also displayed in full lines. Several motion cycles are represented. All regression equations determined in this study can be found in Tables 9.5 (clavicle) and 9.6 (scapula)

using approach presented in the section "Linear multiple regression"). To simplify this approach to one independent parameter, a humeral head vertical translation could be suggested as this is presented by fitting coefficients in the two last sections of the Tables 9.5 and 9.6.

Supplementary Correction for Results of ShRm

The above regression methods lead to relative small residual errors (on average less than 5° for all processed DoFs). Such error is dependent on the quality of the raw data obtained to quantify the humeral displacement used in the underlying model to feed the fitting equations; poor data collection will lead to low motion analysis precision and therefore lead to worse regression results. The most frequent artifact one can be observed is the penetration of the Scap segment within the Thor volume,

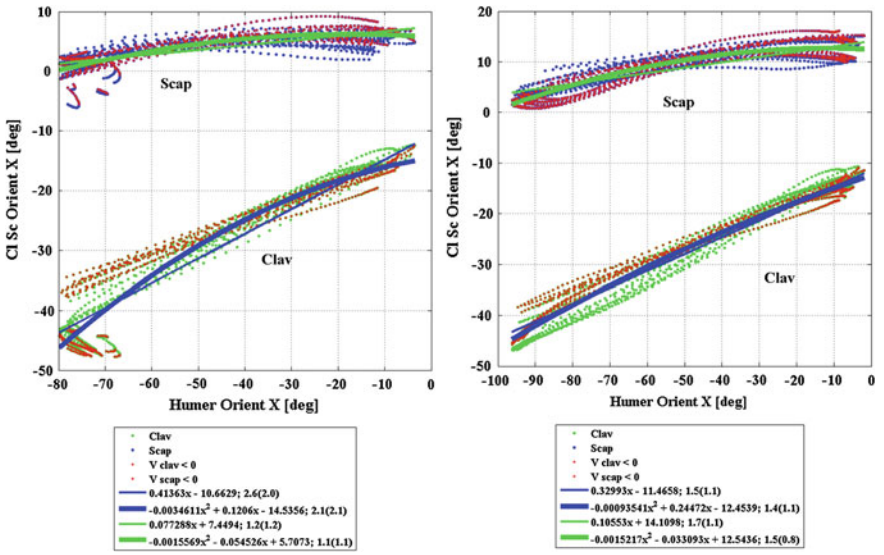

Fig. 9.9 Comparison between ZXY Cardan (*on the left side*) and OVP (*on the right*) conventions for humerus abduction/adduction (humerus rotation around X axis of the thorax LCS). Note that the raw input data show different values between both graphs because they are represented according different conventions

or a pseudo-dislocation of Scap (i.e., a so-called "winged Scap"). This is obviously not physiological and should be avoided.

This last section present the implementation of a supplementary method do avoid this kind of artifact provoked by the appearance of non-physiological relationships between the anterior aspect of Scap and the posterior aspect of Thor. The correction used the model described above including all shoulder joint related segments (Thor, Clav, Scap, Hum). Sternoclavicular and acromioclavicular joints were modeled as ball-and-socket structures while the glenohumeral joint included six DoFs. At first, the ShRm prediction model allows frame-by-frame estimation of the attitude of Clav and Scap. If Scap artefacts occur, then the following scapulothoracic gliding constraints can be implemented as a correction step to Scap behavior. We advised to constraint Scap using ellipsoidal surfaces derived from the outer aspects of the rib surface. The constraint equation supposes that the distance [81] between the Scap inferior angle (RSIA, see Table 9.1) anatomical landmark and its projection on the ellipsoidal surface remains constant.

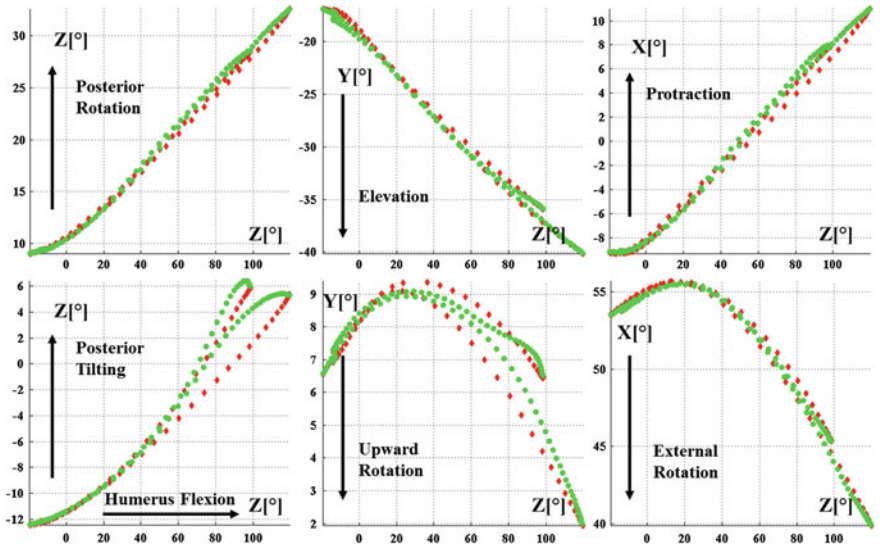

Fig. 9.10 ShRm modeling results during humeral displacement in the sagittal plane. *Top row* Clav results. *Bottom row* Scap results. All results are given according to Hum Z-axis rotation (flexion/extension) in the thoracohumeral frame. *Green* and *red dots* correspond to humerus flexion and extension, respectively. Two motion cycles are given

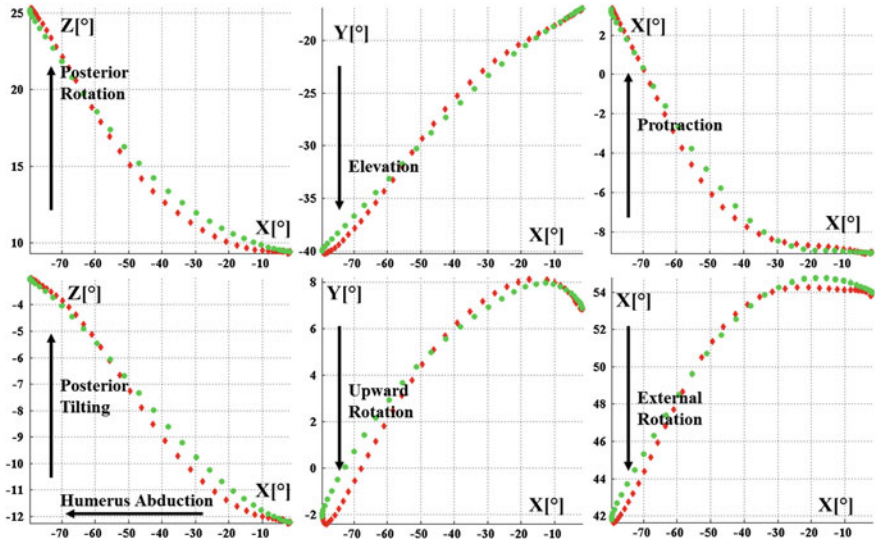

Fig. 9.11 ShRm modeling results during humeral displacement in the frontal plane. *Top row* Clav results. *Bottom row* Scap results. All results are given according to Hum X-axis rotation (adduction/abduction in the thoracohumeral frame. *Green* and *red dots* correspond to humerus abduction and adduction, respectively. Two motion cycles are given

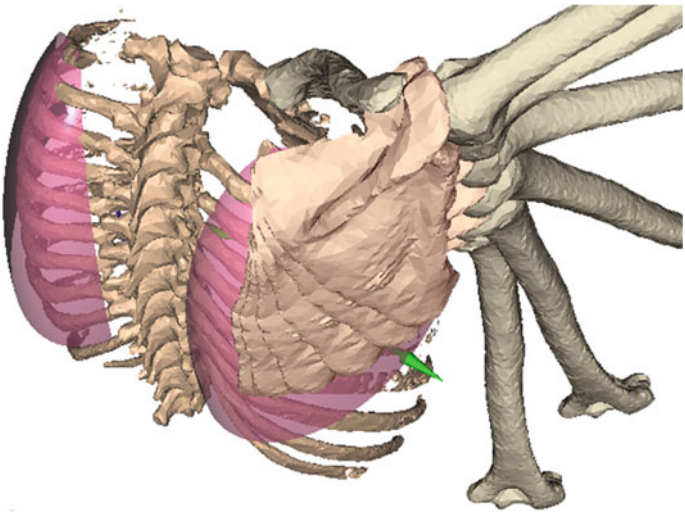

Fig. 9.12 ShRm visualization (right shoulder, posterosuperior view). These results were obtained after optimization from humeral poses (6 key snapshots are displayed here) to predict the position and orientation of the scapula and clavicle using the presented method

9.4.1 Final Results: Motion Representation and Visualization After ShRm Estimation

The following section shows results obtained from the above regression equations to estimate the instantaneous poses of the ShRm Scap and Clav components during Hum displacements in the thoracohumeral joint. Hum and Thor motion data were collected using the same stereophotogrammetry system as described in section "Data collection for scaling method". A supplementary correction (see previous section) was applied to avoid scapula gliding artefacts along the thorax surface.

Figures 9.10 and 9.11 show the estimation results for Scap and Clav during Hum extension/flexion and adduction/abduction.

Graphical visualization of the 3D segments and estimated Scap and Clav displacements are shown in Fig. 9.12 (see also [82] supplementary material movies). Results are similar to qualitative and quantitative description found in the literature [3, 9, 13–15, 20].

9.5 Conclusion

The presented approach for ShRm estimation was entirely obtained from data collected from validated experiments to gather as much physiological information as possible. Anatomical realism of the results allows applying the developed method

in various fields requiring computational anatomy modeling (e.g., biomechanics, ergonomics, computer graphics, etc). Results were validated for normal shoulder physiology. Mean pose accuracy of the clavicle and scapula rhythm reconstruction were 8.5(6.1) mm, 19.8(5.2) mm, respectively. Prior to clinical applications the presented approach request supplementary development to integrate pathological behavior into the model.

Acknowledgments This work was funded by the European Commission through the LHDL (IST-2004-026932) and DHErgo (SCP7-GA-2008-218525) projects, and by the Brussels Government through the ICT4Rehab project (2010/PFS-ICT03). Our gratitude also goes to Dr. P.-M. Dugailly, Dr. P. Salvia, Mr. H. Bajou et Mr. J-L. Sterckx for their assistance in the data collection related to this work.

References

1. Wu, G., van der Helm, F. C. T., Veeger, H. E. J., Makhsous, M., Van Roy, P., Anglin, C., et al. (2005). ISB recommendation on definitions of joint coordinate systems of various joints for the reporting of human joint motion-Part II: shoulder, elbow, wrist and hand. *Journal of Biomechanics*, *38*, 981–992.
2. van der Helm, F. C. T., & Pronk, G. M. (1995). Three-dimensional recording and description of motions of the shoulder mechanism. *Journal of Biomechanical Engineering*, *117*, 27–40.
3. Veeger, H. E. J., & van der Helm, F. C. T. (2007). Shoulder function: The perfect compromise between mobility and stability. *Journal of Biomechanics*, *40*, 2119–2129.
4. Altmann, S. (1989). Hamilton, Rodrigues, and the Quaternion scandal. *Mathematics Magazine*, *62*, 291–308.
5. Anglin, C., & Wyss, U. (2000). Review of arm motion analyses. Proceedings of the Institution of Mechanical Engineers, Part H. *Journal of Engineering in Medicine*, *214*, 541–555.
6. Bey, M. J., Zauel, R., Brock, S. K., & Tashman, S. (2006). Validation of a new model-based tracking technique for measuring three-dimensional, In vivo Glenohumeral joint kinematics. *Journal of Biomechanical Engineering*, *128*, 604–609.
7. Buckley, M. A., Yardley, A., Johnson, G. R., & Carus, D. A. (1996). Dynamics of the upper limb during performance of the tasks of everyday living AOa review of the current knowledge base. ARCHIVE: Proceedings of the Institution of Mechanical Engineers, Part H. *Journal of Engineering in Medicine 1989–1996*, *203—-210*(210), 241–247.
8. Cappozzo, A., & Della Croce, U. (2005). Human movement analysis using stereophotogrammetry: Part 1: Theoretical background. *Gait & Posture*, *21*, 186–196.
9. Cutti, A., & Veeger, H. (2009). Shoulder biomechanics: Today's consensus and tomorrow's perspectives. *Medical and Biological Engineering and Computing*, *47*, 463–466.
10. de Groot, J. H. (1999). The scapulo-humeral rhythm: Effects of 2-D roentgen projection. *Clinical Biomechanics*, *14*, 63–68.
11. Hill, A., Bull, A., Dallalana, R., Wallace, A., & Johnson, G. (2007). Glenohumeral motion: Review of measurement techniques. *Knee Surgery, Sports Traumatology, Arthroscopy*, *15*, 1137–1143.
12. Hill, A. M., Bull, A. M. J., Richardson, J., McGregor, A. H., Smith, C. D., Barrett, C. J., et al. (2008). The clinical assessment and classification of shoulder instability. *Current Orthopaedics*, *22*, 208–225.
13. Hill, A. M., Bull, A. M. J., Wallace, A. L., & Johnson, G. R. (2008). Qualitative and quantitative descriptions of glenohumeral motion. *Gait & Posture*, *27*, 177–188.
14. Lugo, R., Kung, P., & Ma, C. B. (2008). Shoulder biomechanics. *European Journal of Radiology*, *68*, 16–24.

15. Massimini, D. F., Warner, J. J. P., & Li, G. (2011). Non-invasive determination of coupled motion of the scapula and humerus-An in-vitro validation. *Journal of Biomechanics*, *44*, 408–412.
16. Veeger, H. E. J., van der Helm, F. C. T., Van der Woude, L. H. V., Pronk, G. M., & Rozendal, R. H. (1991). Inertia and muscle contraction parameters for musculoskeletal modelling of the shoulder mechanism. *Journal of Biomechanics*, *24*, 615–629.
17. Bourne, D. A., Choo, A. M. T., Regan, W. D., MacIntyre, D. L., & Oxland, T. R. (2007). Three-dimensional rotation of the scapula during functional movements: An in vivo study in healthy volunteers. *Journal of Shoulder and Elbow Surgery*, *16*, 150–162.
18. Braman, J. P., Engel, S. C., LaPrade, R. F., & Ludewig, P. M. (2011). In vivo assessment of scapulohumeral rhythm during unconstrained overhead reaching in asymptomatic subjects. *Journal of Shoulder and Elbow Surgery*, *18*, 960–967.
19. Karduna, A. R., McClure, P. W., Michener, L. A., & Sennett, B. (2001). Dynamic measurements of three-dimensional scapular kinematics: A validation study. *Journal of Biomechanical Engineering*, *123*, 184–190.
20. Ludewig, P. M., Phadke, V., Braman, J. P., Hassett, D. R., Cieminski, C. J., & LaPrade, R. F. (2009). Motion of the shoulder complex during multiplanar humeral elevation. *Journal of Bone and Joint Surgery*, *91*, 378–389.
21. Ludewig, P. M., Hassett, D. R., LaPrade, R. F., Camargo, P. R., & Braman, J. P. (2010). Comparison of scapular local coordinate systems. *Clinical Biomechanics*, *25*, 415–421.
22. Lunden, J. B., Braman, J. P., LaPrade, R. F., & Ludewig, P. M. (2010). Shoulder kinematics during the wall push-up plus exercise. *Journal of Shoulder and Elbow Surgery*, *19*, 216–223.
23. McClure, P. W., Michener, L. A., Sennett, B. J., & Karduna, A. R. (2001). Direct 3-dimensional measurement of scapular kinematics during dynamic movements in vivo. *Journal of Shoulder and Elbow Surgery*, *10*, 269–277.
24. Fung, M., Kato, S., Barrance, P. J., Elias, J. J., McFarland, E. G., Nobuhara, K., et al. (2001). Scapular and clavicular kinematics during humeral elevation: A study with cadavers. *Journal of Shoulder and Elbow Surgery*, *10*, 278–285.
25. Gerber, C., Werner, C. M. L., Macy, J. C., Jacob, H. A. C., & Nyffeler, R. W. (2003). Effect of selective capsulorrhaphy on the passive range of motion of the glenohumeral joint. *Journal of Bone and Joint Surgery*, *85*, 48–55.
26. Graichen, H., Stammberger, T., Bonel, H., Karl-Hans, E., Reiser, M., & Eckstein, F. (2000). Glenohumeral translation during active and passive elevation of the shoulder—a 3D open-MRI study. *Journal of Biomechanics*, *33*, 609–613.
27. Harryman, D. T., Sidles, J. A., Clark, J. M., McQuade, K. J., Gibb, T. D., & Matsen, F. A. (1990). Translation of the humeral head on the glenoid with passive glenohumeral motion. *Journal of Bone and Joint Surgery*, *72*, 1334–1343.
28. Holzbaur, K. R. S., Murray, W. M., & Delp, S. L. (2005). A model of the upper extremity for simulating musculoskeletal surgery and analyzing neuromuscular control. *Annals of Biomedical Engineering*, *33*, 829–840.
29. Karduna, A. R., Kerner, P. J., & Lazarus, M. D. (2007). Contact forces in the subacromial space: Effects of scapular orientation. *Journal of Shoulder and Elbow Surgery*, *14*, 393–399.
30. Meskers, C. G. M., van der Helm, F. C. T., Rozendaal, L. A., & Rozing, P. M. (1997). In vivo estimation of the glenohumeral joint rotation center from scapular bony landmarks by linear regression. *Journal of Biomechanics*, *31*, 93–96.
31. van der Helm, F. C. T., Veeger, H. E. J., Pronk, G. M., Van der Woude, L. H. V., & Rozendal, R. H. (1992). Geometry parameters for musculoskeletal modelling of the shoulder system. *Journal of Biomechanics*, *25*, 129–144.
32. van der Helm, F. C. T. (1994). A finite element musculoskeletal model of the shoulder mechanism. *Journal of Biomechanics*, *27*, 551–569.
33. van der Helm, F. C. T. (1994). Analysis of the kinematic and dynamic behavior of the shoulder mechanism. *Journal of Biomechanics*, *27*, 527–550.
34. Bey, M. J., Kline, S. K., Zauel, R., Lock, T. R., & Kolowich, P. A. (2008). Measuring dynamic in-vivo glenohumeral joint kinematics: Technique and preliminary results. *Journal of Biomechanics*, *41*, 711–714.

35. Matsuki, K., Matsuki, K. O., Mu, S., Yamaguchi, S., Ochiai, N., Sasho, et al. (2011). In vivo 3-dimensional analysis of scapular kinematics: Comparison of dominant and nondominant shoulders. *Journal of Shoulder and Elbow Surgery*, *20*(4), 659–665.
36. Meskers, C. G. M., Fraterman, H., van der Helm, F. C. T., Vermeulen, H. M., & Rozing, P. M. (1999). Calibration of the Flock of Birds electromagnetic tracking device and its application in shoulder motion studies. *Journal of Biomechanics*, *32*, 629–633.
37. Meskers, C. G. M., van de Sande, M. A. J., & de Groot, J. H. (2007). Comparison between tripod and skin-fixed recording of scapular motion. *Journal of Biomechanics*, *40*, 941–946.
38. Nikooyan, A. A., Veeger, H. E. J., Westerhoff, P., Graichen, F., Bergmann, G., & van der Helm, F. C. T. (2010). Validation of the delft shoulder and elbow model using in-vivo glenohumeral joint contact forces. *Journal of Biomechanics*, *43*, 3007–3014.
39. Nishinaka, N., Tsutsui, H., Mihara, K., Suzuki, K., Makiuchi, D., Kon, Y., et al. (2003). Determination of in vivo glenohumeral translation using fluoroscopy and shape-matching techniques. *Journal of Shoulder and Elbow Surgery*, *17*, 319–322.
40. Phadke, V., Braman, J. P., LaPrade, R. F., & Ludewig, P. M. (2011). Comparison of glenohumeral motion using different rotation sequences. *Journal of Biomechanics*, *44*(4), 700–705.
41. Barnett, N. D., Duncan, R. D. D., & Johnson, G. R. (1999). The measurement of three dimensional scapulohumeral kinematics—a study of reliability. *Clinical Biomechanics*, *14*, 287–290.
42. Brochard, S., Lempereur, M., & Remy-Neris, O. (2011). Accuracy and reliability of three methods of recording scapular motion using reflective skin markers. Proceedings of the Institution of Mechanical Engineers, Part H. *Journal of Engineering in Medicine*, *225*, 100–105.
43. Brochard, S., Lempereur, M., & Remy-Neris, O. (2011). Double calibration: An accurate, reliable and easy-to-use method for 3D scapular motion analysis. *Journal of Biomechanics*, *44*(4), 751–754.
44. Meskers, C. G. M., Vermeulen, H. M., de Groot, J. H., van der Helm, F. C. T., & Rozing, P. M. (1998). 3D shoulder position measurements using a six-degree-of-freedom electromagnetic tracking device. *Clinical Biomechanics*, *13*, 280–292.
45. Pascoal, A. G., van der Helm, F. F. C. T., Pezarat Correia, P., & Carita, I. (2000). Effects of different arm external loads on the scapulo-humeral rhythm. *Clinical Biomechanics*, *15*, S21–S24.
46. Price, C. I. M., Franklin, P., Rodgers, H., Curless, R. H., & Johnson, G. R. (2000). Active and passive scapulohumeral movement in healthy persons: A comparison. *Archives of Physical Medicine and Rehabilitation*, *81*, 28–31.
47. Stokdijk, M., Nagels, J., & Rozing, P. M. (2000). The glenohumeral joint rotation centre in vivo. *Journal of Biomechanics*, *33*, 1629–1636.
48. van Andel, C. J., Wolterbeek, N., Doorenbosch, C. A. M., Veeger, D., & Harlaar, J. (2008). Complete 3D kinematics of upper extremity functional tasks. *Gait & Posture*, *27*, 120–127.
49. van Andel, C., van Hutten, K., Eversdijk, M., Veeger, D., & Harlaar, J. (2009). Recording scapular motion using an acromion marker cluster. *Gait & Posture*, *29*, 123–128.
50. Salvia, P., Jan, S. V. S., Crouan, A., Vanderkerken, L., Moiseev, F., Sholukha, V., et al. (2009). Precision of shoulder anatomical landmark calibration by two approaches: A CAST-like protocol and a new anatomical palpator method. *Gait & Posture*, *29*, 587–591.
51. Braman, J., Thomas, B., LaPrade, R., Phadke, V., & Ludewig, P. (2010). Three-dimensional in vivo kinematics of an osteoarthritic shoulder before and after total shoulder arthroplasty. *Knee Surgery, Sports Traumatology, Arthroscopy*, *18*, 1774–1778.
52. Crosbie, J., Kilbreath, S. L., Hollmann, L., & York, S. (2008). Scapulohumeral rhythm and associated spinal motion. *Clinical Biomechanics*, *23*, 184–192.
53. de Groot, J. H. (1997). The variability of shoulder motions recorded by means of palpation. *Clinical Biomechanics*, *12*, 461–472.
54. de Groot, J. H., Valstar, E. R., & Arwert, H. J. (1998). Velocity effects on the scapulo-humeral rhythm. *Clinical Biomechanics*, *13*, 593–602.
55. Fayad, F., Hoffmann, G., Hanneton, S., Yazbeck, C., Lefevre-colau, M. M., Poiraudeau, S., et al. (2006). 3-D scapular kinematics during arm elevation: Effect of motion velocity. *Clinical Biomechanics*, *21*, 932–941.

56. Forte, F. C., Peduzzi de Castro, M., & Mahnic de Toledo, J. (2009). Scapular kinematics and scapulohumeral rhythm during resisted shoulder abduction—Implications for clinical practice. *Physical Therapy in Sport*, *10*, 105–111.
57. Garofalo, P., Cutti, A., Filippi, M., Cavazza, S., Ferrari, A., Cappello, A., et al. (2009). Inter-operator reliability and prediction bands of a novel protocol to measure the coordinated movements of shoulder-girdle and humerus in clinical settings. *Medical and Biological Engineering and Computing*, *47*, 475–486.
58. Hogfors, C., Peterson, B., Sigholm, G., & Herberts, P. (1991). Biomechanical model of the human shoulder joint-II. The shoulder rhythm. *Journal of Biomechanics*, *24*, 699–709.
59. Kon, Y., Nishinaka, N., Gamada, K., Tsutsui, H., & Banks, S. A. (2011). The influence of handheld weight on the scapulohumeral rhythm. *Journal of Shoulder and Elbow Surgery*, *17*, 943–946.
60. Cappozzo, A., Catani, F., & Leardini, A. (1995). Position and orientation in space of bones during movement: Anatomical frame definition and determination. *Clinical Biomechanics*, *10*, 171–178.
61. Blankevoort, L., Huiskes, R., & de Lange, A. (1990). Helical axes of passive knee joint motions. *Journal of Biomechanics*, *23*, 1219–1229.
62. Challis, J. H. (1995). A procedure for determining rigid body transformation parameters. *Journal of Biomechanics*, *28*, 733–737.
63. Cheze, L., Fregly, B. J., & Dimnet, J. (1998). Determination of joint functional axes from noisy marker data using the finite helical axis. *Human Movement Science*, *17*, 1–15.
64. Cheze, L. (2000). Comparison of different calculations of three-dimensional joint kinematics from video-based system data. *Journal of Biomechanics*, *33*, 1695–1699.
65. Koh, T. J., Grabiner, M. D., & Brems, J. J. (1998). Three-dimensional in-vivo kinematics of the shoulder during humeral elevation. *Journal of Applied Biomechanics*, *14*, 312–326.
66. Spoor, C. W., & Veldpaus, F. E. (1980). Rigid body motion calculated from spatial co-ordinates of markers. *Journal of Biomechanics*, *13*, 391–393.
67. van den Bogert, A. J., Reinschmidt, C., & Lundberg, A. (2008). Helical axes of skeletal knee joint motion during running. *Journal of Biomechanics*, *41*, 1632–1638.
68. Veldpaus, F. E., Woltring, H. J., & Dortmans, L. J. (1988). A least-squares algorithm for the equiform transformation from spatial marker co-ordinates. *Journal of Biomechanics*, *21*, 45–54.
69. Woltring, H. J., Huiskes, R., de, L. A., & Veldpaus, F. E. (1985). Finite centroid and helical axis estimation from noisy landmark measurements in the study of human joint kinematics. *Journal of Biomechanics*, *18*, 379–389.
70. Woltring, H. J. (1991). Representation and calculation of 3-D joint movement. *Human Movement Science*, *10*, 603–616.
71. Woltring, H. J. (1994). 3-D attitude representation of human joints: A standardization proposal. *Journal of Biomechanics*, *27*, 1399–1414.
72. Sholukha, V., Leardini, A., Salvia, P., Rooze, M., & Van Sint Jan, S. (2006). Double-step registration of in vivo stereophotogrammetry with both in vitro 6-DOFs electrogoniometry and CT medical imaging. *Journal of Biomechanics*, *39*, 2087–2095.
73. Van Sint Jan, S. (2007). *Color atlas of skeletal landmark definitions. Guidelines for reproducible manual and virtual palpations*. Edinburg: Churchill Livingstone–Elsevier.
74. Sholukha, V., Van Sint Jan, S., Snoeck, O., Salvia, P., Moiseev, F., & Rooze, M. (2009). Prediction of joint center location by customizable multiple regressions: Application to clavicle, scapula and humerus. *Journal of Biomechanics*, *42*, 319–324.
75. Escamilla, R., Yamashiro, K., Paulos, L., & Andrews, J. (2009). Shoulder muscle activity and function in common shoulder rehabilitation exercises. *Sports Medicine*, *39*, 663–685.
76. Konrad, G. G., Jolly, J. T., Labriola, J. E., McMahon, P. J., & Debski, R. E. (2006). Thoracohumeral muscle activity alters glenohumeral joint biomechanics during active abduction. *Journal of Orthopaedic Research*, *24*, 748–756.
77. Van Sint Jan, S., Salvia, P., Sholukha, V., & Rooze, M. (2006). Strict palpation guidelines of skeletal landmarks for more accurate data registration, data representation and data comparison. *Journal of Biomechanics*, *39*, S77–S78.

78. Van Sint Jan, S., Sobzack, S., Dugailly, P. M., Feipel, V., Lef vre, P., Lufimpadio, J. L., et al. (2006). Low-dose computed tomography: A solution for in vivo medical imaging and accurate patient-specific 3D bone modeling? *Clinical Biomechanics*, *21*, 992–998.
79. Van Sint Jan, S., Salvia, P., Hilal, I., Sholukha, V., Rooze, M., & Clapworthy, G. (2002). Registration of 6-DOFs electrogoniometry and CT medical imaging for 3D joint modeling. *Journal of Biomechanics*, *35*, 1475–1484.
80. Viceconti, M., Zannoni, C., Testi, D., Petrone, M., Perticoni, S., Quadrani, P., et al. (2007). The multimod application framework: A rapid application development tool for computer aided medicine. *Computer Methods and Programs in Biomedicine*, *85*(2), 138–151.
81. Sholukha, V., Chapman, T., Salvia, P., Moiseev, F., Euran, F., & Rooze, M. (2011). Femur shape prediction by multiple regression based on quadric surface fitting. *Journal of Biomechanics*, *44*, 712–718.
82. Sholukha, V., Bonnechere, B., Salvia, P., Moiseev, F., Rooze, M., & Van Sint Jan, S. (2013). Model-based approach for human kinematics reconstruction from markerless and marker-based motion analysis systems. *Journal of Biomechanics*, *46*(14), 2363–2371.

Chapter 10
A Biomechanical Approach for Dynamic Hip Joint Analysis

Lazhari Assassi and Nadia Magnenat-Thalmann

10.1 Introduction

The musculoskeletal system (MS) is composed of various and heterogeneous elements with complex geometries, mechanical behaviors and interactions. This system provides form, support, stability, protection and locomotion to the human body. Because of these important functions, research into the MS and in related pathologies is of great interest. Indeed, musculoskeletal disorders (MSDs) are common causes of different pathologies and physical disability, affecting many people across the world [1]. With the aging population, the social impact and economic burden (e.g., medical institutions and health insurance companies) of MSDs are becoming more and more important to the society [2]. Therefore, a significant amount of effort has to be put into maintaining the functional capabilities of the aging population to allow them to have a better quality-of-life. For young people, the focus is on prevention in order to reduce the impact of MSDs and on the development of new tools which can provide useful information for medical experts to improve medical procedures (e.g., diagnosis, surgery planning and rehabilitation).

Among these pathologies, osteoarthritis (OA), also known as a degenerative joint disease, is the most common form of arthritis (articular disease). OA is characterized by the breakdown or the degeneration of the articular cartilage which becomes brittle and splits. Consequently, bones are uncovered and rub against each other, causing symptoms such as pain, muscle weakness and limitation of movement in the joint. The most common sites of OA include the hands, spine, hips and knees.

L. Assassi (✉) · N. Magnenat-Thalmann
MIRALab, University of Geneva, Battelle,
Building A 7 Route de Drize, CH-1227 Carouge Geneva, Switzerland
e-mail: assassi@miralab.ch

N. Magnenat-Thalmann
Institute for Media Innovation, Nanyang Technological University,
50 Nanyang Drive, Singapore, Singapore
e-mail: thalmann@miralab.ch

N. Magnenat-Thalmann et al. (eds.), *3D Multiscale Physiological Human*,
DOI: 10.1007/978-1-4471-6275-9_10, © Springer-Verlag London 2014

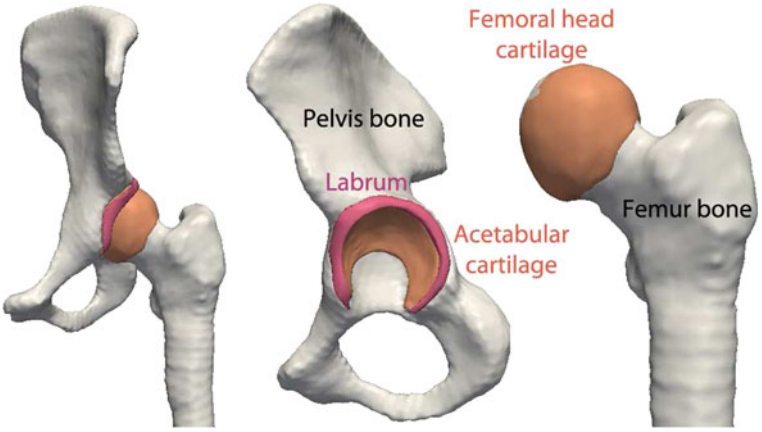

Fig. 10.1 Hip joint anatomy: bones and cartilage layers

To understand the human joints mechanism and thoroughly investigate the development of OA, several studies were conducted. Different disciplines (e.g., medicine, biology, biomechanics and applied sciences) are involved in the exchange and combination of knowledge from different expertise domains. Despite the growing advancements, limitations still exist and much work remains to be done to better respond to the complexity of both the human anatomy and medical procedures.

10.1.1 Medical Context

This study focuses on the hip joint, which is crucially important in the musculoskeletal system. The hip joint supports the weight of the body in both static and dynamic postures. It allows for a large range of movement and for the transfer of high forces between the femur and the pelvis during daily activities [3]. The hip joint is classified as a ball and socket joint, with the acetabulum acting as the socket in which the spherical femur head articulates (see Fig. 10.1). Both bone surfaces are covered with an articular cartilage which prevents direct bone-to-bone contact and allows a pressure distribution inside the joint. Connected to the acetabulum rim, the acetabular labrum is a fibrocartilaginous structure that increases the acetabulum depth, grips the femoral head and provides stability to the hip joint. The hip joint is further reinforced by ligaments [4]. Given its role in the MS, the hip joint is especially vulnerable to different pathologies and mostly OA. Although the frequency of hip OA increases with age, OA is not exclusively an aging process as it is also seen in younger patients [5]. In fact, the damage of the labrum or labral tear was associated with the development of hip OA. Studies have shown that a labral tear is frequently found in younger patients, while for older patients the labral tear is more often associated with chondral

damage [6]. Therefore, it is hypothesized that the degeneration process starts by a labral tear and may lead to articular damages. However, different factors can be at the origin of hip joint damage.

Although genetics, obesity, injury and infections have been identified as marginal factors, the abnormal joint morphologies including femoroacetabular impingement (FAI) and dysplasia are considered as the most common reasons of the cartilage and the labrum degeneration [7–9]. Nevertheless, the exact mechanisms of degeneration are still unknown because the development process of this pathology generally takes a significant amount of time [6, 10]. Therefore, different hypotheses were suggested as potential factors. Some studies highlighted the physical activities that produce high forces or stresses on the hip joint [11], while others focused on repetitive microtrauma (e.g., hip dislocation) and extreme movements [12, 13]. Indeed, athletes may practice sports which are stressful for joints (e.g., golf, hockey, football), as well as ballet dancers who perform some excessive motions such as twisting, pivoting and hyper-abduction/extension. Therefore, they are considered as a population at a higher risk for developing hip labral tears or cartilage damage [14, 15]. This risk can be more important for athletes in the presence of other factors such as structural abnormalities [16, 17].

Thus, various hypotheses related to dynamics and kinematics were proposed to explain the mechanisms of degeneration. The difficulty of establishing a link between the causes and the degeneration of the labrum or cartilage is because they often remain undiagnosed for a period of time [18]. Nevertheless, these hypotheses need to be investigated by analyzing the hip mechanics such as the labrum and cartilages stresses during activities [10].

10.1.2 Biomechanical Background

Several biomechanical studies were conducted to assess the intra-articular contacts of the hip joint. These studies are classified in two categories: experimental and computational methods. Experimental methods based on *in vitro* and *in vivo* measurements have been performed on cadaver hips by using different techniques (e.g., miniature pressure transducers [19], pre-scaled sensitive films [10] and stereo-photogrammetry [20]) or by using pressure transducers implanted into patients' hip prostheses [21]. Direct measurements presented valuable results but unfortunately these methods present some limitations. Indeed, it is evident that the mechanical behavior of cadaveric and living hip tissue will be different. Moreover, the direct measurement is highly invasive and not feasible in non-operated hips.

Nowadays, there is no direct and noninvasive method to directly assess the hip contact. Consequently, computational methods based on analytical and numerical models were proposed as non-invasive alternatives. Analytical models are based on mathematical functions [22, 23], while the numerical models are based on Mass-Springs systems [24] or Finite Element methods [8, 25]. Compared to numerical models, analytical models are less accurate because they neglect different aspects of

biomechanics such material properties and cartilages layers. Numerical models are widely used in numerous domains and were thus adopted for medical applications. Moreover, the evolution of computing power, the accessibility of high resolution data images and segmentation techniques reconstructing accurate 3D subject-specific models have contributed to the growing use of computational models. These models were successfully used in different applications, such as the analysis of symptomatic and asymptomatic hips during daily activities [16, 17, 26]. Nevertheless, the models used in these studies are not fully subject-specific. In fact, studies exploit generic [17] or subject-specific anatomical models [16, 26] but combine them with generic kinematical and physical data resulting from other experimental studies [3]. Moreover, the studied movements are often artificial (e.g., variation of anatomical angles) or limited to routine activities (e.g., walking, climbing stairs) which are characterized by low motion amplitude [17, 22]. Finally, the results of these computational models are often presented without clinical validation [16, 27].

Therefore, there is a lack of studies combining subject-models (anatomical, kinematical and physical data) to analyze the hip joint during excessive movements. Nevertheless, the biomechanical modeling of a subject-specific hip joint is a difficult task and requires an adapted pipeline.

To address this issue, this paper presents a functional approach based on subject-specific models to simulate the mechanical behavior of the hip joint under excessive movement. The analysis of the deformation location and the assessment of the stress on the articular layers (cartilage and labrum) during such movements will be helpful to determine whether such activities can be a factor of hip joint degeneration.

10.2 Functional Approach

The proposed functional approach is based on non invasive acquisition modalities. Magnetic Resonance Imaging (MRI) is used for anatomical modeling, a motion capture system (Mocap) for kinematical modeling and simulation models for physical modeling. Techniques which have their origin in computer graphics are used to reconstruct subject anatomical, kinematical and physical models. These models are used to set up the simulation model to achieve accurate physically-based simulation of the hip joint.

10.2.1 Anatomical Modeling

Given the numerous differences that exist between individuals, the use of subject-specific anatomical models is of paramount importance to clinical diagnosis. To reconstruct the subject models, the first step is to select medical modalities that allow the best imaging of the structures to model. Compared to other modalities (e.g., Computed Tomography (CT)), MRI is a good choice for musculoskeletal imaging,

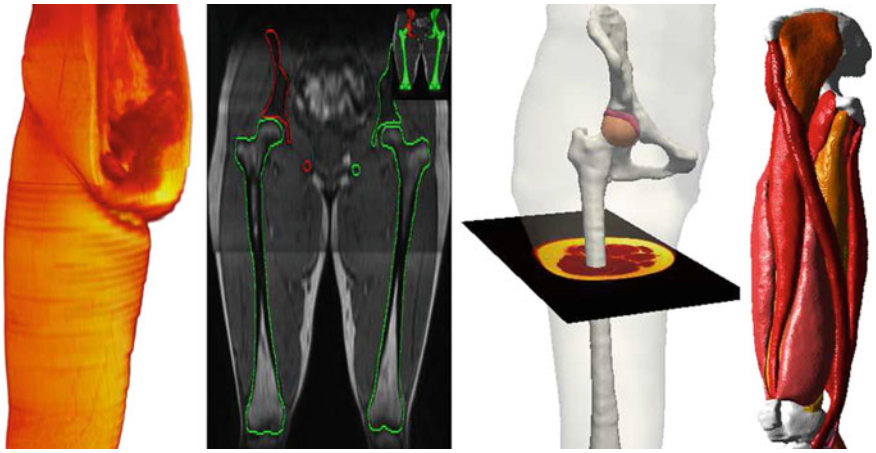

Fig. 10.2 MRI dataset volume used to segment hip joint anatomical structures (*bones* and *cartilage*) and leg muscles

because it offers the simultaneous examination of soft and bony tissue. The next step consists of devising the best imaging protocol to satisfy imaging and clinical constraints. This is achieved by an adapted MRI protocol based on an adequate trade-off between the image quality and acquisition time [28]. From the acquired medical images, a segmentation approach needs to be used to identify the anatomical structures of interest. Despite the numerous studies, a universal segmentation approach has not yet been proposed, due to noise and artifacts inherently present in medical images. To overcome this problem, the segmentation needs to be regulated by the introduction of constraints and prior-knowledge.

A segmentation approach based on robust deformable models is devised to accurately segment bones and soft tissue of the hip [29–31]. In this approach, each model's vertex is considered as a particle that is subjected to various internal and external forces. Internal forces constrain the shape evolution, while the external forces attract the shape toward the anatomical boundaries. The segmentation evolution is then performed by the integration of a system of discrete differential equations. A stable implicit integration scheme [32] based on a conjugate gradient technique is used. To avoid the inter-penetration of the different evolving shapes, collisions methods are implemented as well as post-processing techniques [33]. Figure 10.2 shows various results (bone, cartilage and muscles) of the segmentation approach.

Once segmented, models need to be converted to volumetric meshes in order to be used in physically-based simulations. Various methods are proposed to generate volumetric meshes based on tetrahedral/hexahedral (Tet/Hex) elements. Tet elements are more suitable than Hex elements for meshing complex geometry. Three main approaches are commonly used: an octree-based method [34], advancing front method [35] and a method based on a Delaunay criterion [36]. Despite the performance of classical approaches, the quality of the resulting meshes is not totally

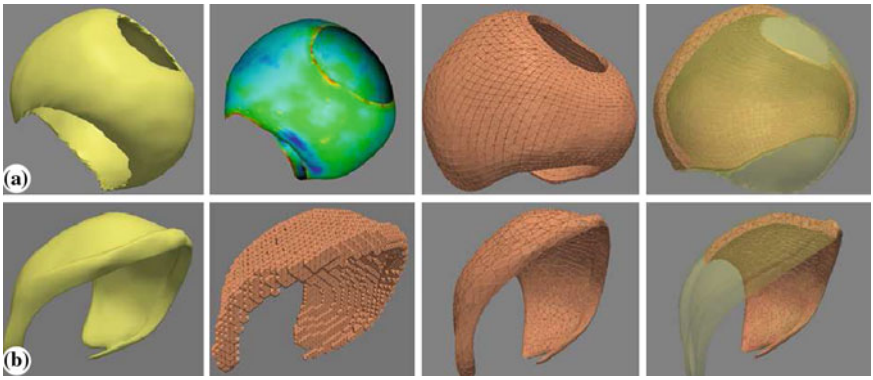

Fig. 10.3 **a** Tet meshing of the femoral cartilage based on the use of the 2D deformable medial surface approach where color present the thickness of the model. **b** Tet mesh of acetabulum cartilage and labrum generated by the 3D deformable models approach

guaranteed, especially for complex geometries. In fact, a large number of Tet elements (potentially with a low quality such as slivers) is often generated.

To generate Tet meshes, meshing approaches based on 2D and 3D deformable models are proposed in this work. For models which can be approximated by their medial surface, a 2D deformable medial-axis based approach [37, 38] is used. This approach exploits the thickness information included into the medial surface to generate Tet meshes. For more complex shapes, where the medial surface is not easily computed, a 3D deformable models approach [39] based on octree subdivision with a body centered cubic lattice [40] of the surface mesh is used. These approaches produce Tet meshes of satisfactory quality (with respect to the dihedral angle and aspect ratio) and complexity (low number of Tet) which ensure the simulation accuracy and stability (see Fig. 10.3).

To set up the mechanical model, appropriate mechanical properties and boundary conditions are assigned to mesh elements. These parameters are defined according to the tissue properties and their attachments.

10.2.2 Kinematical Modeling

The description of the skeletal system movement involves the definition of specific sets of axes for each bone segment [41]. This is achieved by setting a geometric rule that constructs the axes by using selected anatomical landmarks defined on the reconstructed 3D surface of the subject's hip and femur bones. The same bone models are used to compute the hip joint center (HJC) position [42].

The subject's movements are then recorded with an optical motion capture system (Vicon MX 13i, Oxford Metrics, UK) using eight infrared cameras, sampling at 120

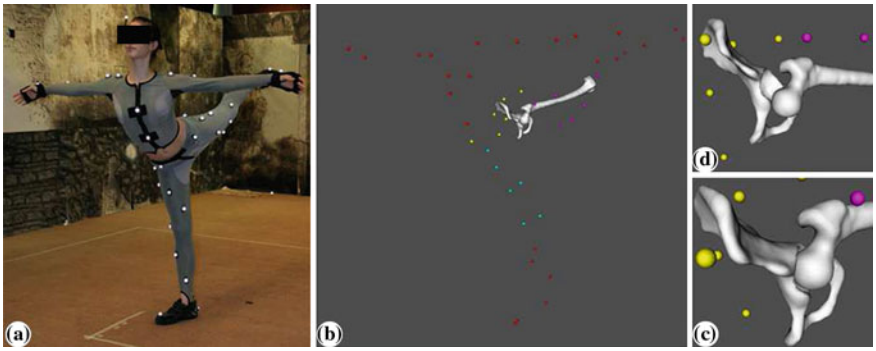

Fig. 10.4 **a** Movement recording with the Mocap system and **b** Computed subject posture. **c** A corrected position by applying the optimization and constraint approach and **d** An error position (dislocation) due to the STA

Hz and tracking markers in a 45.3 m3 measurement volume ($3.6 \times 4.2 \times 3$ m) (see Fig. 10.4). The set of spherical markers (7 mm) are placed according to an appropriate protocol to ensure their visibility to the cameras [18]. Unlike other motion acquisition devices (e.g., intra-cortical pins [43], external fixators [44], fluoroscopy [45]), the optical system is not invasive and allows the recording of larger ranges of motion. However, due to muscle activities and inertial movements, the skin markers move over the underlying structures. This relative movement represents an artifact, typically referred to as soft tissue artifact (STA) [46]. Consequently, rigid motion of the bone segment cannot be robustly estimated from the markers trajectories. Correcting these errors is thus necessary for clinical relevance.

To minimize STA, a nonlinear optimization algorithm [47] is used to find, for each segment and for each frame of movement, the best rigid transformation that minimizes the error made globally on all the markers. Since it was observed that joint dislocation may occur due to STA, kinematic constraints allowing some shifts at the joint are also applied (see Fig. 10.4c and d). The proposed approach [48, 49] ensures an accurate kinematical modeling for the hip joint [28].

10.2.3 Physical Modeling

In addition to anatomical and kinematical models, the forces acting on the hip joint as well as a simulation model are needed to achieve physically-based simulation of the hip joint.

10.2.3.1 Hip Loads Estimation

Hip forces or loads were measured in the literature experimentally by using telemetric implants [3, 50]. Unfortunately this *in vivo* method cannot be used in a non operated hip. Moreover, the resulting data cannot be considered as subject-specific. In fact, measured forces concern aged persons who underwent hip replacement surgery (cartilage and labrum removed). Finally, the studied movements are limited to routine activities which are not useful in our case study.

To overcome this problem, a neuromuscular simulation [51–53] is exploited as an alternative. This kind of simulation offers the possibility to estimate internal parameters (e.g., muscle activations, forces) by analyzing the subject kinematics and kinetics during the performance of activities. Such simulations were used in different applications like gait analysis [54], simulation of neuromuscular abnormalities [55], or design of ergonomic furniture [56]. In neuromuscular simulations, several sets of data measured experimentally (e.g., motion capture, force plates and Electromyography (EMG)) are exploited into a specific process [57].

In this study, a neuromuscular model is adopted [58] to analyze the dynamic simulations of movements. A specific pipeline is required to estimate forces acting on the hip joint. The first step consists of scaling the generic model to match the anthropometry of the subject-specific anatomical model. The achieved scaling is based on a hybrid method using measured data resulting from different approaches (3D body scan model [48], 3D anatomical models, MRI data and initial marker positions). These sets of data are combined and processed to realize an anisotropic scaling by calculating the scaling factors for each part of the body. From the resulting model and motion capture data, the joint coordinate values (e.g., joint angles) that reproduce the subject movement (markers positions) are calculated by using an inverse kinematic (IK) approach (see Fig. 10.5).

To complete the process, the ground reaction force (GRF) is required. In our case, a computational method based on Newtonian analysis is used to replace the unavailability of the force plate's data. A dynamic 3D model using the motion capture data and the scaling model data (body segment weights) is used to estimate GRF. This approach is conceivable due the nature of studied movements. Indeed, the studied movements are characterized by the static foot position of one leg and the air position of the other leg (e.g., arabesque movement), or static position of both feet (e.g., bending movement). Estimated GRF $\mathbf{F_{LG}}$ of the leg acting on the ground is expressed as:

$$\sum_i \mathbf{F_i} = \mathbf{F_{LG}} + m.\mathbf{g} = \sum_i m_i.\mathbf{a_i} \tag{10.1}$$

where m is the subject mass, $\mathbf{g}$ denotes the gravity vector, m_i and $\mathbf{a_i}$ are the masses and the accelerations of the body segments, respectively.

Based on kinematical data, the body segments' velocity $\mathbf{v_i}$ and acceleration $\mathbf{a_i}$ are computed from their mass center positions $\mathbf{p_i}$:

$$\mathbf{v_i} = (\mathbf{p_{i+1}} - \mathbf{p_i})/t \tag{10.2}$$

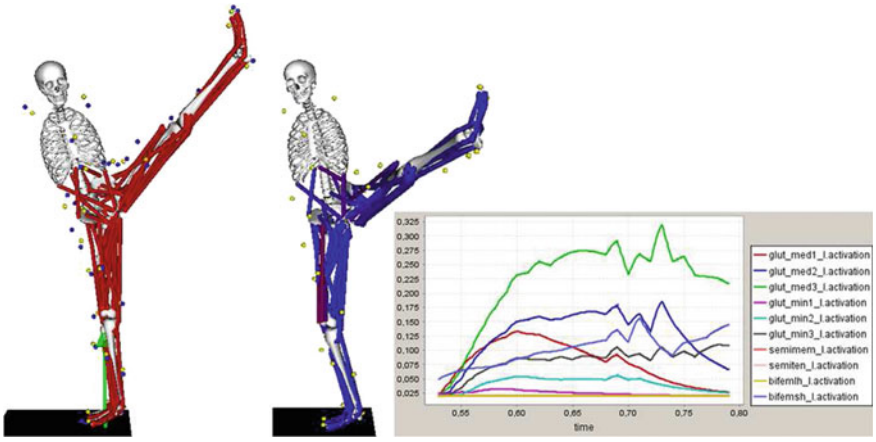

Fig. 10.5 IK and ID steps of the neuromuscular simulation: Computation of the movement with estimated GRF and muscles activation presented by curves

$$\mathbf{a_i} = (\mathbf{v_{i+1}} - \mathbf{v_i})/t \tag{10.3}$$

where t denotes the time step.

The force contact point $\mathbf{p_{LG}}$ is finally computed by using the moment equation:

$$\sum_i \mathbf{M_i} = \mathbf{F_{LG}} \wedge \mathbf{p_{LG}} + m.\mathbf{g} \wedge \mathbf{p_{mc}} = \sum_i m_i.\mathbf{a_i} \wedge \mathbf{p_i} \tag{10.4}$$

where $\mathbf{p_{mc}} = \sum_i m_i.\mathbf{p_i}/m$ is the body center of mass.

The output of IK and the computed GRF are used as input in an inverse dynamic (ID) procedure to compute muscle activation, which are involved in the produced movement. Finally, the results of the ID step are used in the analysis procedure step to compute forces acting upon joints. The resulting forces are exported from the neuromuscular coordinate system to the hip joint coordinate system which is used in the physically-based simulation.

10.2.3.2 Simulation Model

A physical simulation model is required to compute the deformation of the mechanical objects. However, different criteria should be taken into account to achieve an accurate simulation, which faithfully reflects the mechanical behavior of biological tissues. Indeed, biomechanical constraints such as the nonlinearity, large displacements and deformations of soft tissue have to be considered. Different models based on mass-spring systems [24], the Finite Element Method [17] and Finite Volume Method [59] have been proposed to simulate the deformations of soft tissue.

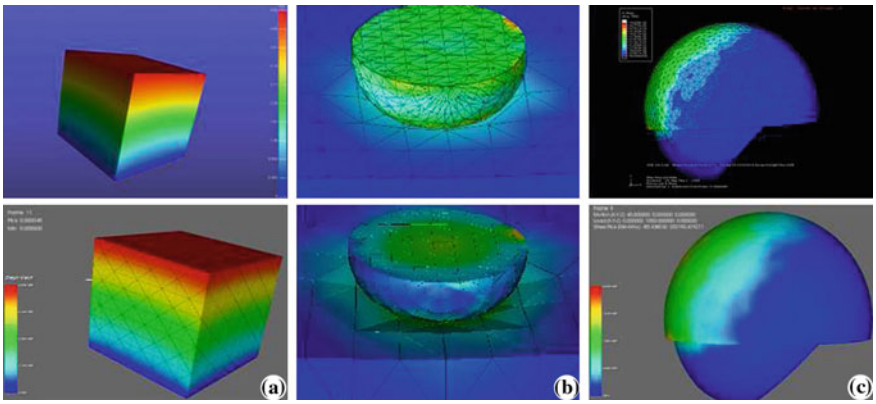

Fig. 10.6 Accuracy comparison between the developed model and available FEM models. Computation of deformation by applying loads on a simple object (**a**), 2 objects (**b**) and a generic hip joint (**c**)

To simulate the mechanical behavior of deformable objects, our simulation model [37, 39] is based on a fast 1st-order Finite Element system implementation, which offers a good trade-off between accuracy and computation speed. This model based on a particle-system representation allows for the accurate representation of anisotropic nonlinear viscoelastic deformation models and is particularly well suited for modeling the behavior of highly deformable materials. Thanks to its lumped mass approximation, such models can be integrated with high-efficiency numerical integration methods typically used in particle systems, as well as with efficient integration of collision effects and geometrical constraints. Moreover, an efficient numerical integration technique is used to provide good performance in the computation of these mechanical models, both in the context of dynamic animation and quasi-static relaxation. Concretely speaking, the different techniques considered to build an efficient simulation model are [32, 60, 61]:

- A fast 1st-order Finite Element implementation system for non linear behavior.
- 3D specific improvements of the co-rotational element transformation which is appropriate to simulate anisotropic and isotropic materials and allow accurate computation of the large deformations.
- Pseudo-Dynamic Stop-and-Go relaxation for fast convergence for large displacements.
- Modeling elasticity strain-stress relationships with polynomial formulations for simple and efficient modeling of the non-linear material behavior.
- Efficient collision processing techniques based on incremental computation method.

The developed simulation model is implemented in a framework offering an adequate compromise between efficiency and versatility. The accuracy of the mechanical model has been validated through simulation comparisons with publicly available

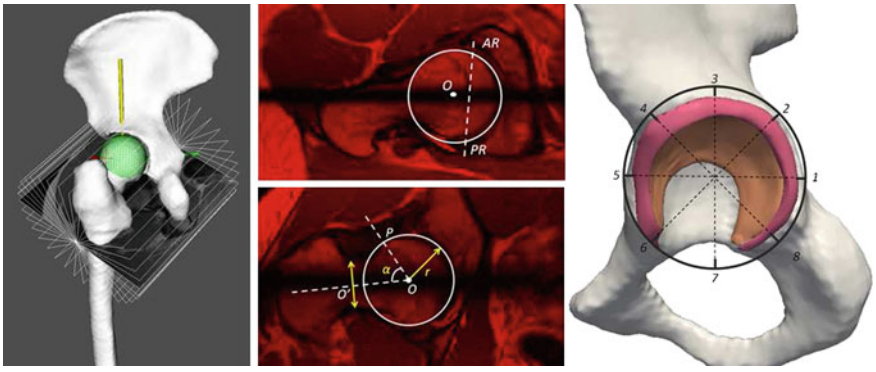

Fig. 10.7 Standard morphological measurement based on subject-specific 3D models and MRI data. Devision of the acetabulum in eight sectors for radiological analysis

Finite Element packages (FEBio [62], SOFA [63] and Code-Aster [64], and has shown to offer similar accuracy (see Fig. 10.6). Meanwhile, computation times are kept very low (a few seconds per frame) thanks to ad-hoc tuning of the numerical integration parameters, as well as to a specific handling of collisions which ensures high simulation stability.

Finally, the resulting aforementioned models (meshes, kinematics, loads, etc.) are used as input for the simulation model to analyze the mechanical behavior of the subject's hip joint.

10.3 Clinical Analysis

To validate the simulation results, a clinical study based on morphological and radiological analysis was performed by medical experts. To eliminate the typical abnormalities of the hip joint that could lead to hip joint degeneration, a morphological analysis was performed to evaluate the prevalence of the subjects' hip joint. To this end, standard morphological measurements were performed [7, 65] (see Fig. 10.7). The first measurement consists of computing the depth of the acetabulum. If the acetabulum is too deep, the excessive over-coverage of the femoral head by the acetabulum causes abutment against the acetabular rim. The depth is defined as the distance in mm between the center of the femoral head (O and the line $AR - PR$ connecting the anterior (AR) and posterior (PR) acetabular rim. The value is considered as positive and normal if O is lateral to the line $AR - PR$. The second measure related to the femur geometry is the femoral alpha (α) neck angle. A non-spherical head damages the articular cartilages by abutting the acetabulum rim. The angle is defined by the angle formed by the line $O - O'$ connecting the center of the femoral head (O) and the center of the femoral neck (O') at its narrowest point; and the line $O - P$ connecting O and the point P where the distance between the bony contour of

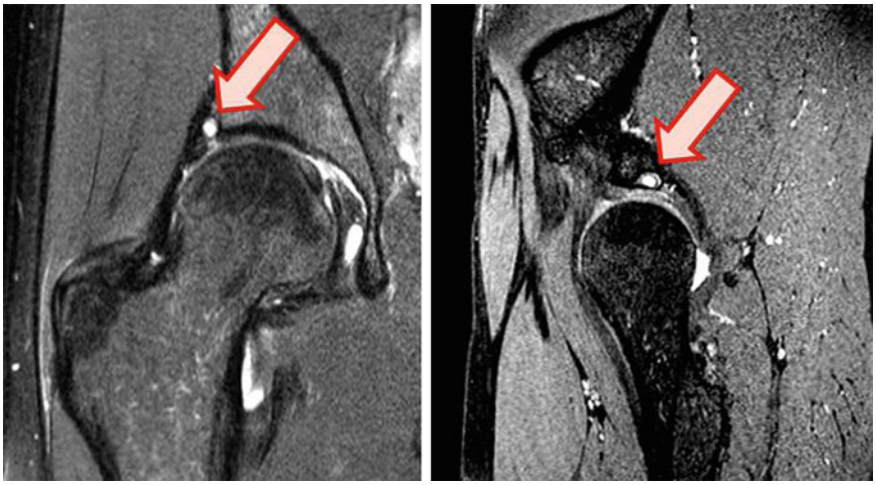

Fig. 10.8 Radiological analysis: Diagnosis of acetabular and labral lesions (*arrow*) in the posterior part of the acetabular rim

the femoral head and O starts to exceed the radius (r) of the femoral head. Deviation from the normal geometry is usually associated with larger α angles (>60°).

Based on subject-specific data (MRI and 3D bones reconstruction), these standard measurement methods were numerically implemented, improving the (subjective) reading of medical images. The dancer hip was thus analyzed, according to those two anatomical parameters. No morphological abnormalities were detected and it was concluded that the measured hips have an average positive depth (left hip: 8.16 mm, right hip: 7.89 mm) and an average α angle in the normal range ($36.15° < \alpha < 54.43°$). The results were validated by radiological experts.

The same radiological experts performed consensus readings of the subjects' MR images [5]. The acetabular cartilage and labral abnormalities were assessed qualitatively. For this subject, acetabular and labral lesions were diagnosed in the posterior part of the acetabular rim (see Fig. 10.8). To describe the exact location of the lesions, the acetabulum was divided into eight sectors (1: anterior, 2: anterosuperior, 3: superior, 4: posterosuperior, 5: posterior, 6: inferoposterior, 7: inferior, 8: anteroinferior), as depicted in Fig. 10.7.

10.4 Biomechanical Analysis of Professional Ballet Dancer Hip Joint

This study was conducted in collaboration with doctors from the department of Radiology and department of Orthopedic Surgery of the University Hospital of Geneva and female professional ballet dancer from the ballet of the Great Theater of Geneva.

The developed approach is used to analyze the mechanical behavior of articular layers of a dancer's hip joint. The choice of subject is justified by the nature

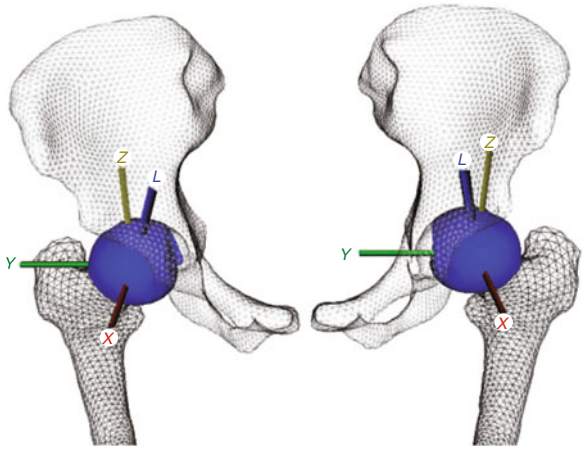

Fig. 10.9 Loads (*L axis*) and movement (Flexion/Extension (*Y axis*), Adduction/Abduction (*X axis*) and Internal/External rotation (*Z axis*)) are expressed in hip joint anatomical axes

of practiced movements. Indeed, several dance movements such as Grand-Plié (bending), Circumduction, Arabesque, Developpé-Latéral (lateral leg bench) and Developpé-Avant (forward leg bench) require intensive hip flexion and/or abduction with rotation. Given the subject feedback, such movements are recognized as excessive. Therefore, the daily practice of these exercises is assumed to be a potential cause which can contribute to an early hip osteoarthritis for the subject.

Subject-specific kinematics and kinetics of the simulated movements are discretized into several frames. Femoral kinematics and joint contact forces are expressed according to standard hip joint anatomical axes (6 degrees of freedom) with origin located at the center of the femoral head [41]. The three rotation angles and load components are defined along these three anatomical axes (see Fig. 10.9).

The range of motion in the subject hip joint of the simulated dancing movements and the estimated GRF magnitude $\left(GRF = \sqrt{GRF_x^2 + GRF_y^2 + GRF_z^2}\right)$ are presented in Table 10.1. Movements concern the leg in elevated position (except Grand-Plié) and are expressed with anatomical angles (Flexion/Extension, Adduction/Abduction and Internal/external rotation) according to the hip joint axes. Each movement is presented with an average and a standard deviation (SD) angle. To compare the amplitude of dancing and normal movements, walking angles during stance phase are presented. The GRF concerns the second leg (foot on the ground). The forces are presented with average and SD values and expressed as a percentage of the subject's body weight (% BW).

As shown in Table 10.1, dancing involves intensive hip flexion and abduction (except the arabesque in which the hip is in extension). Globally, estimated loads depend on movements (angles). Figure 10.10 shows the evolution of loads according to the angles of bending movement.

Table 10.1 Range of motion of the left hip joint and estimated GRF magnitude on the right foot. Angles are reported in deg and force in newton (N)

Movement	Flex/Ext (°)	Abd/Add (°)	Int/Ext rot (°)	GRF = % BW (N)
Arabe.	0/36.1 ± 9.8	0/32.1 ± 6.6	0/79.5 ± 6.4	97.4 ± 2.0
Circum.	52.4 ± 26.1/0	0/37.9 ± 24.8	0/22.5 ± 9.1	95.9 ± 7.8
Dev.Av.	71.3 ± 17.1/0	0/22.2 ± 7.9	0/34.8 ± 8.1	95.4 ± 10.4
Dev.Lat	72.9 ± 35.8/0	0/54.5 ± 15.3	0/11.3 ± 28.5	96.0 ± 4.6
Gra.Pl.	70.9 ± 49.4/0	0/8.7 ± 1.7	0/1.5 ± 7.1	48.0 ± 3.1
Walk.S-P	30.6 ± 10.9/0	0/12.2 ± 3.6	0/10.4 ± 6.1	95.7 ± 8.3

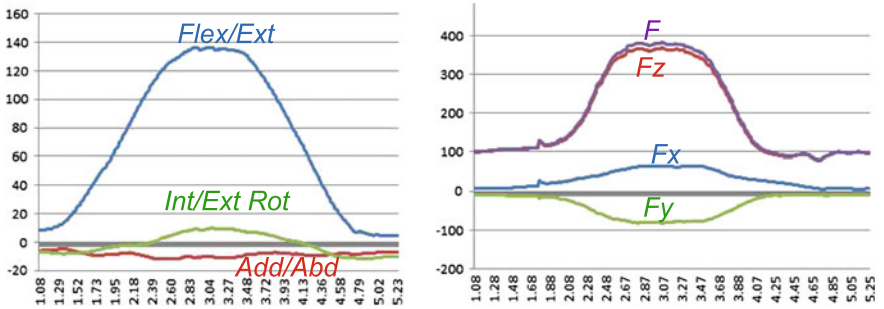

Fig. 10.10 *Curves* of angles and loads for bending movement. Angles are expressed in degree and loads in % BW

To build the biomechanical model, the mechanical properties of soft tissue are considered. Given (i) the significant difference of the Young modulus between the labrum (20 MPa), articular cartilage (12 MPa) and cortical bone (17 GPa) [8] and (ii) the small mechanical role of trabecular bone [16], bone deformation will be minimal (0.01–0.1%) compared to cartilage deformation [66]. Therefore, it is more convenient to consider bones as rigid surface structures to reasonably simplify the model and considerably reduce computation times [17].

Then, the subject-specific deformable models of the soft tissue consist of two tetrahedral meshes (see Fig. 10.3). The first mesh (18k Tet) is composed of both the labrum and acetabulum cartilage, for which the tetrahedral elements of each cartilage are defined with mechanical properties specific to the tissue type. The second mesh (7k Tet) exclusively represents the femoral cartilage. Such modeling (2 meshes instead of 3) reduces the computation of collision detection. External surfaces of tetrahedral meshes are extracted to define the boundary conditions in the simulation model: vertices of the first mesh attached to the hip bone are considered as fixed, while those of the second mesh attached to the femur will transfer loads. Since soft tissues are characterized by large deformations, which are tackled by the used simulation model, mesh elements of the labrum, acetabulum and femoral cartilages are parameterized with appropriate mechanical behavior [67, 68].

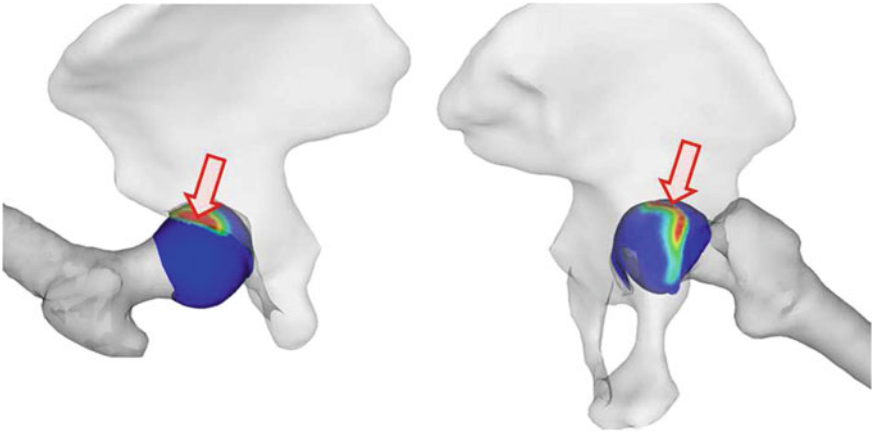

Fig. 10.11 Distribution of the stress on actebular and femoral cartilage (the labrum is not shown for clarity). Peak stress (*red color*, *arrow*) on position 3 and 4 of the acetabular rim

The physically based simulation exploits this model to analyze articular layers (labrum, acetabular and femoral cartilage) deformations. For each frame of simulated movements, the contact and the peak stress are computed. The stress refers to the stress along the direction of the maximal compression. To analyze the intra-articular contacts and especially the labrum deformation, peak stresses on each layer are reported. Individual analysis of stresses makes it possible to quantify the load absorbed by the labrum to characterize its role in the hip joint structure [69].

On the other hand, the simulation calculates the peak stress locations, which are also of paramount importance in the analysis. Indeed, such examination provides insight into which region of labrum or cartilage is subjected to high stress during movement in order to investigate regions susceptible to damage.

The simulated movements showed that the peak stresses were usually located in the superior and postero-superior (respectively positions 3 and 4 in Fig. 10.7) parts of the labrum and actebuar cartilage (see Figs. 10.11 and 10.12). Some other parts exhibited high stress but not in the same significant way.

10.5 Discussion and Conclusion

The morphological measurements were analyzed by a radiological expert. The results of morphological analysis showed that no values indicating potential morphological problems were reported. FAI (Cam or pincer) morphology was not observed, nor was possible hip dysplasia. However, radiological analysis indicated that lesions were observed in the superior part of the labrum and acetabular cartilage. By putting in correspondence the location of the lesions with the stress analysis of the simulation, high stresses were located in the superior area of the acetabular rim (see Fig. 10.12),

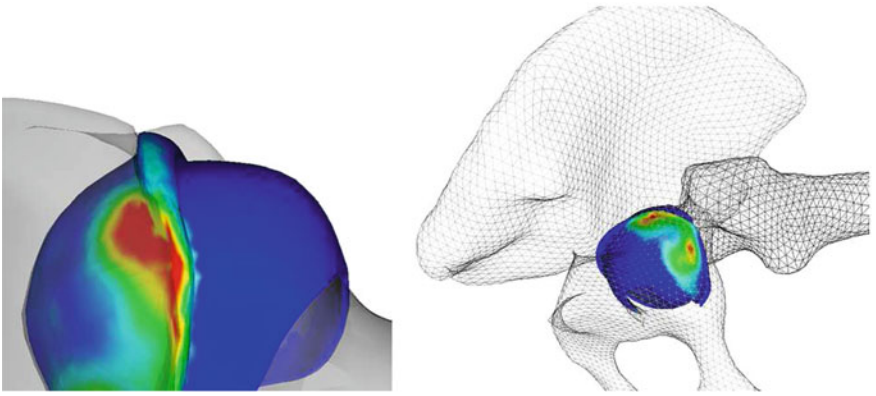

Fig. 10.12 Location of the stress peak (*red color*) observed during simulation in the superior and postero-superior parts of the labrum and actebuar cartilage

which corresponds to the localization of diagnosed lesions (see Fig. 10.8). Based on these results, it is hypothesized that excessive movements may explain these lesions of idiopathic OA. This hypothesis is supported by the nature of the dancer's movements.

Nevertheless, additional work is required to assess some simulation components in order to fully accept the results. In fact, the accuracy of the different stages involving anatomy, kinematics and dynamics can have some impact on the quality of the simulation. To improve the significance of the results, analysis of more subjects is planned.

Acknowledgments We are grateful to the University Hospital of Geneva and the ballet dancers of the great theater of Geneva for their collaboration.

References

1. Arthritis foundation, http://www.arthritis.org
2. Bevan, S., McGee, R., & Quadrello, T. (2009). Key findings of the fit for work europe report on musculoskeletal disorders and work. *Occupational Health at Work 2009* (Vol. 6, pp. 30–30). The At Work Partnership.
3. Bergmann, S. G., Deuretzbacher, G., Heller, M., Graichen, F., Rohlmann, A., Strauss, J., et al. (2001). Hip contact forces and gait patterns from routine activities. *Journal of Biomechanics*, *34*, 859–871.
4. Standring, S. (2005). *Gray's anatomy: The anatomical basis of clinical practice* (39th ed.). Edinburgh: Elsevier.
5. Duthon, V., Menetrey, J., Kolo-Christophe, F., Charbonnier, C., Duc, S., Pfirrmann, C. et al. (2009). Professional dancers hip: Correlation of clinical and mri findings. In *Swiss Medical Weekly* (Vol. 139, pp. 23–24). Switzerland: EMH.

6. McCarthy, J. C., Noble, P. C., Schuck, M. R., Wright, J., Lee, J., & Waterman, M. S. (2009). The Otto E Aufranc Award the role of labral lesions to development of early degenerative hip disease. *Clinical Orthopaedics*, *393*, 25–37.
7. Tannast, M., Goricki, D., Beck, M., Murphy, S., & Siebenrock, K. (2008). Hip damage occurs at the zone of femoroacetabular impingement. *Journal of Clinical Orthopaedics Related Research*, *466*, 273–280.
8. Russell, M., Shivanna, K., Grosland, N., & Pedersen, D. (2006). Cartilage contact pressure elevations in dysplastic hips: A chronic overload model. *Journal of Orthopaedic Surgery and Research*, *1*, 169–177.
9. Kelly, B. T., Weiland, D. E., Schenker, M. L., & Philippon, M. J. (2005). Arthroscopic labral repair in the hip: surgical technique and review of the literature. *Arthroscopy*, *21*, 496–504.
10. Macirowski, T., Tepic, S., & Mann, R. W. (1994). Cartilage stresses in the human hip joint. *Journal of Biomechanical Engineering*, *116*, 10–18.
11. Pool, A. R. (1995). Imbalances of anabolism and catabolism of cartilage matrix components in osteoarthritis. In V. M. Goldberg & K. E. Kuettner (Eds.), *Osteoarthritic Disorder* (pp. 247–260). Rosemont: American Association of Orthopaedic Surgeons.
12. Narvani, A. A., Tsiridis, E., Tai, C. C., & Thomas, P. (2003). Acetabular labrum and its tears. *British Journal of Sports Medicine*, *37*, 207–211.
13. Narvani A. A., Tsiridis, E., Kendall. S., Chaudhuri, R., & Thomas, P. (2003). A preliminary report on prevalence of acetabular labrum tears in sports patients with groin pain. *Knee Surgery, Arthroscopy and Sports Traumatology*, *11*, 403–408.
14. Bharam, S. (2006). Labral tears, extra-articular injuries, and hip arthroscopy in the athlete. *Clinic Sports Medicine*, *25*, 279–292.
15. Binningsley, D. (2003). Tear of the acetabular labrum in an elite athlete. *British Journal of Sports Medicine*, *37*, 84–88.
16. Anderson, A. E., Ellis, B. J., Maas, S. A., Peters, C. L., & Weiss, J. A. (2008). Validation of finite element predictions of cartilage contact pressure in the human hip joint. *Journal of Biomechanical Engineering*, *130*, 1–10.
17. Chegini, S., Beck, M., & Ferguson, S. (2008). The effects of impingement and dysplasia on stress distributions in the hip joint during sitting and walking: A finite element analysis. *Journal of Orthopaedic Research*, *27*, 195–201.
18. Byrd, J. W., Jones, K. S., Smith, T. F., & Waterman, M. S. (2000). Prospective analysis of hip arthroscopy with 2-year follow-up. *Arthroscopy*, *16*, 578–587.
19. Brown, T. (1983). *in vitro* contact stress distributions in the natural human hip. *Journal of Biomechanics*, *16*, 373–384.
20. Ahmad, M. C., Cohen, Z., Levine, W., Ateshian, G., & Mow, V. (2001). Biomechanical and topographic considerations for autologous osteochondral grafting in the knee. *American Journal of Sports Medicine*, *29*, 201–206.
21. Hodge, W., Carlson, K., Fijan, R., Burgess, R., Riley, P., Harris, W., et al. (1989). Contact pressures from an instrumented hip endoprostheses. *Journal of Bone and Joint Surgery*, *71*, 1378–1386.
22. Xishi, W., Tianying, W., Fuchuan, J., & Yixiang, D. (2005). The hip stress level analysis for human routine activities. *Biomedical Engineering: Applications, Basis and Communications*, *17*, 43–48.
23. Mavcic, B., Pompe, B., Antolic, V., Daniel, M., Iglic, A., & Kralj-Iglic, V. (2002). Mathematical estimation of stress distribution in normal and dysplastic human hips. *Journal of Orthopaedic Research*, *20*, 1025–1030.
24. Maciel, A., Sarni, S., Boulic, R., & Thalmann, D. (2005). Stress distribution visualization on pre- and post-operative virtual hip joint. In: *Proceedings of Computer Assisted Orthopaedic Surgery* (CAOS05) (pp. 298–301).
25. Ahmet, C., Vahdet, U., & Recep, K. (2007). Three-dimensional anatomic finite element modelling of hemi-arthroplasty of human hip joint. *Trends in Biomaterials and Artificial Organs*, *21*, 63–72.

26. Harris, M. D., Anderson, A. E., Henak, C. R., Ellis, B. J., Peters, C. L., & Weiss, J. A. (2012). Finite element prediction of cartilage contact stresses in normal human hips. *Journal of Orthopaedic Research*, *30*(7), 1133–1139.
27. Henak, C. R., Anderson, A. E., & Weiss, J. A. (2013). Subject-specific analysis of joint contact mechanics: Application to the study of osteoarthritis and surgical planning. *Journal of Biomechanical Engineering*, *135*(2), in press.
28. Magnenat-Thalmann, N., Charbonnier, C., & Schmid, J. (2008). Multimedia application to the simulation of human musculoskeletal system: A visual lower limb model from multimodal captured data. In: *Proceedings of IEEE International Workshop in Signal Processing* (pp. 520–525).
29. Schmid, J., Kim, J., & Magnenat-Thalmann, N. (2011). Robust statistical shape models for mri bone segmentation in presence of small field of view. *Medical Image Analysis*, *15*, 155–168.
30. Gilles, B., & Magnenat-Thalmann, N. (2010). Musculoskeletal mri segmentation using multiresolution simplex meshes with medial representations. *Medical Image Analysis*, *14*, 291–302.
31. Schmid, J., & Magnenat-Thalmann, N. (2008). Mri bone segmentation using deformable models and shape priors. In: *Proceedings of International Conference Medical image Computing and Computer Assisted Intervention (MICCAI)* (Vol. 5241, pp. 119–126). Heidelberg: Springer.
32. Volino, P., & Magnenat-Thalmann, N. (2005). Implicit midpoint integration and adaptive damping for efficient cloth simulation. *Computer Animation and Virtual Worlds*, *16*, 163–175.
33. Schmid, J., Sandholm, S., Chung, F., Thalmann, D., Delingette, H., & Magnenat-Thalmann, N. (2009) Musculoskeletal simulation model generation from mri datasets and motion capture data. In: *Recent advances in the 3D Physiological Human* (pp. 3–20). Heidelberg: Springer.
34. Shephard, M., & Georges, M. (1991). Three-dimensional mesh generation by finite octree technique. *International Journal for Numerical Methods in Engineering*, *32*, 709–749.
35. Lohner, R. (1996). Progress in grid generation via the advancing front technique. *Engineering with Computers*, *39*, 501–511.
36. Alliez, P., Cohen-Steiner, D., Yvinec, M., & Desbrun, M. (2005). Variational tetrahedral meshing. In: *SIGGRAPH05* (pp. 193–204).
37. Assassi, L., Charbonnier, C., Schmid, J., Volino, P., & Magnenat-Thalmann, N. (2009). From mri to anatomical simulation of the hip joint. *Computer Animation Virtual World*, *20*, 53–66.
38. Assassi, L., Guillard., G., Gilles., B., & Magnenat-Thalmann, N. (2007). Volumetric meshes based on medial representation for medical applications. In: *Proceedings of Computer Assisted Orthopaedic Surgery (CAOS07)* (pp. 259–262).
39. Magnenat-Thalmann, N., Schmid, J., Assassi, L., & Volino, P. (2010). A comprehensive methodology to visualize articulations for the physiological human. In: *Cyberworlds. IEEE Computer Society* (pp. 1–8).
40. Molino, N., Bridson, R., Teran, J., & Fedkiw, R. (2003). A crystalline red green strategy for meshing highly deformable object with tetrahedral. In: *Proceedings of the 12th International Meshing Roundtable* (pp. 103–114).
41. Wu, G., Siegler, S., Allard, P., Kirtley, C., Leardini, A., Rosenbaum, D., et al. (2002). ISB recommendation on definitions of joint coordinate system of various joints for the reporting of human joint motion- part I: Ankle, hip and spine. *Journal of Biomechanics*, *35*, 543–548.
42. Gilles, B., Kolo-Christophe, F., Magnenat-Thalmann, N., Becker, C., Duc, S., Menetrey, J., et al. (2009). Mri-based assessment of hip joint translations. *Journal of Biomechanics*, *12*, 1201–1205.
43. Benoit, D., Ramsey, D., Lamontagne, M., Xu, L., Wretenberg, P., & Renstroem, P. (2006). Effect of skin movement artifact on knee kinematics during gait and cutting motions measured *in vivo*. *Gait and Posture*, *24*, 152–164.
44. Cappozzo, A., Catani, F., Leardini, A., Benedetti, M., & Croce, U. D. (1996). Position and orientation in space of bones during movement: experimental artefacts. *Clinical Biomechanics*, *11*, 90–100.
45. Garling, E., Kaptein, B., Mertens, B., Barendregt, W., Veeger, H., Nelissen, R., et al. (2007). Soft-tissue artefact assessment during step-up using fluoroscopy and skin-mounted markers. *Journal of Biomechanics*, *40*, 18–24.

46. Kepple, T., Arnold, A., Stanhope, S., & Siegel, K. (1994). Assessment of a method to estimate muscle attachments from surface landmarks: A 3d computer graphics approach. *Journal of Biomechanics*, *27*, 365–371.
47. Lawrence, C., & Tits, A. (2001). A computationally efficient feasible sequential quadratic programming algorithm. *SIAM Journal on Optimization*, *11*, 1092–1118.
48. Charbonnier, C., Assassi, L., Volino, P., & Magnenat-Thalmann, N. (2009). Motion study of the hip joint in extreme postures. *The Visual Computer*, *25*, 873–882.
49. Charbonnier, C., Lyard, E., & Magnenat-Thalmann, N. (2008). Analysis of extreme hip motion in professional ballet dancers. In: *Proceedings of 10th International Symposium of 3D Analysis of Human Movement*. Amsterdam.
50. Park, S., Krebs, D., & Mann, R. (1999). Hip muscle co-contraction: evidence from concurrent *in vivo* pressure measurement and force estimation. *Gait and Posture*, *10*, 311–322.
51. Erdemir, A., McLean, S., Herzog, W., & van den Bogert, A. (2007). Model based estimation of muscle forces exerted during movements. *Clinical Biomechanics*, *22*, 131–154.
52. Damsgaard, M., Rasmussen, J., Christensen, S., Surma, E., & de Zee, M. (2006). Analysis of musculoskeletal systems in the anybody modeling system. *Simulation Modelling Practice and Theory*, *14*, 1100–1111.
53. Delp, S., Loan, J., Hoy, M., Zajac, F., Topp, E., & Rosen, J. (1990). An interactive graphics-based model of the lower extremity to study orthopaedic surgical procedures. *IEEE Transactions on Biomedical Engineering*, *37*, 757–767.
54. Piazza, S., & Delp, S. (1996). The influence of muscles on knee flexion during the swing phase of gait. *Journal of Biomechanics*, *29*, 723–733.
55. Fox, M., Reinbolt, J., Unpuu, S., & Delp, S. (2009). Mechanisms of improved knee flexion after rectus femoris transfer surgery. *Journal of Biomechanics*, *42*, 614–619.
56. Rasmussen, J., & de Zee, M. (2008). Design optimization of airline seats. *SAE International Journal of Passenger Cars—Electronic and Electrical Systems*, *1*, 580–584.
57. Sandholm, A., Pronost, N., & Thalmann, D. (2009). Motionlab: A matlab toolbox for extracting and processing experimental motion capture data for neuromuscular simulations. In: *Proceedings of the Second 3D Physiological Human, Workshop (3DPH)* (Vol. 5903).
58. Delp, S., Anderson, F., Arnold, A., Loan, P., Habib, A., John, C., et al. (2007). Opensim: Open-source software to create and analyze dynamic simulations of movement. *IEEE Transactions on Biomedical Engineering*, *54*, 1940–1950.
59. Irving, G., Teran, J., & Fedkiw, R. (2004). Invertible finite elements for robust simulation of large deformation. In: *ACM SIGGRAPH'04* (Vol. 131, pp. 131–140). ACM Press.
60. Volino P., Magnenat-Thalmann, N., & Faure, F. (2009). A Simple Approach to nonlinear tensile stiffness for accurate cloth simulation. In: *ACM Transactions on Graphics* (Vol. 28, pp. 105–116). ACM Press.
61. Volino, P., & Magnenat-Thalmann, N. (2007). Stop-and-go cloth draping. *Visual Computer*, *23*, 669–677.
62. Finite Element Software: FEBio, http://mrl.sci.utah.edu/software.php
63. SOFA:Simulation Open-Framework Architecture, http://www.sofa-framework.org
64. Finite Element Software:Code-Aster, http://www.code-aster.org
65. Pfirrmann, C., Mengiardi, B., Dora, C., Kalberer, F., Zanetti, M., & Hodler, J. (2006). Cam and pincer femoroacetabular impingement: Characteristic mr arthrographic findings in 50 patients. *Journal of Radiology*, *240*, 778–785.
66. Dalstra, M., Huiskes, R., & Van-Erning, L. (1995). Development and validation of a three-dimensional finite element model of the pelvic bone. *Journal of Biomechanical Engineering*, *117*, 272–278.
67. Park, S., Hung, C., & Ateshian, G. (2004). Mechanical response of bovine articular cartilage under dynamic unconfined compression loading at physiological stress levels. *Osteoarthritis Cartilage*, *12*, 65–73.

68. Ferguson, S., Bryant, J., & Ito, K. (2001). The material properties of the bovine acetabular labrum. *Journal of Orthopaedic Research*, *19*, 887–896.
69. Henak, C. R., Ellis, B. J., Harris, M. D., Anderson, A. E., Peters, C. L., & Weiss, J. A. (2011). Role of the acetabular labrum in load support across the hip joint. *Journal of Biomechanics*, *44*, 2201–2206.

Chapter 11
Coupled Biomechanical Modeling of the Face, Jaw, Skull, Tongue, and Hyoid Bone

Ian Stavness, Mohammad Ali Nazari, Cormac Flynn, Pascal Perrier, Yohan Payan, John E. Lloyd and Sidney Fels

11.1 Introduction

Over the past three decades, modeling and simulation of musculoskeletal systems has greatly enhanced our understanding of the biomechanics and neural control of human and animal movement. Musculoskeletal simulations have been used to analyze human posture, gait, reaching, and other motor tasks (for review, see Delp et al. [1]). Musculoskeletal simulations have been reported across multiple spatial scales; however, macro-scale anatomical models have been most prevalent. Such models represent the human body as a series of rigid skeletal components connected by 1D lumped-parameter springs for muscles and tendons. There is increasing interest in modeling human biomechanics at smaller spatial scales and in particular at the tissue-level scale in 3D. These directions are motivated in part by a desire for more

I. Stavness (✉)
Department of Computer Science, University of Saskatchewan,176 Thorvaldson Building, 110 Science Place, Saskatoon, SK S7N 5C9, Canada
e-mail: stavness@gmail.com

M. A. Nazari
Department of Mechanical Engineering, Faculty of Engineering, University of Tehran, Tehran, Iran

C. Flynn
School of Engineering, Science and Primary Industries,Wintec, New Zealand

P. Perrier
Speech & Cognition Department, Gipsa-lab, UMR CNRS 5216, Grenoble INP & Grenoble University, Grenoble, France

Y. Payan
TIMC-IMAG Laboratory, CNRS UMR 5525, University Joseph Fourier, La Tronche, France

J. E. Lloyd · S. Fels
Department of Electrical and Computer Engineering, University of British Columbia, Vancouver, Canada

N. Magnenat-Thalmann et al. (eds.), *3D Multiscale Physiological Human*,
DOI: 10.1007/978-1-4471-6275-9_11,

predictive power in musculoskeletal models, as well as by a desire to simulate more complex anatomical structures.

Tissue-scale muscle models, based on the Finite-Element (FE) method, can capture details regarding internal tissue strain, the wrapping of muscles around bones and other structures, and the transmission of force by muscles with internal connective tissue and broad attachments [2]. The FE modeling paradigm can also be used to represent highly deformable muscular structures such as the face, lips, tongue, and pharyngeal tract, where changes in shape of the structures have functional significance. The face and vocal tract have received less attention by computational biomechanists than the limbs and whole-body. This is likely due to the additional biomechanical complexity of the head and neck anatomy. However, it is this very complexity that makes face and vocal tract systems excellent candidates for simulation in order to elucidate the unique biomechanics of these structures in breathing, feeding, and speaking.

Biomechanical face models have a long history. The earliest physically-based face model was reported by Terzopoulos and Waters [3]. The model was composed of a linear spring-mass mesh and was used to generate compelling animations of facial expression for its time. More recent models have used FE methods to improve the representation of facial tissue and muscle mechanics. Sifakis et al. [4] developed a detailed FE model and simulated speech movements using a kinematically driven jaw. Hung et al. [5] have recently developed a FE face model targeted for visual effects in film. Few previous models have integrated the craniofacial and vocal tract components into a unified simulation. For this reason, much of our modeling efforts have targeted the integration of face and vocal tract anatomy in dynamic simulations [6–11].

Tissue-scale simulations of face and vocal tract biomechanics can be applied in a wide range of domains, including computer animation, medicine, and biology. Much of the previous face modeling work has come out of the computer graphics community in an attempt to create realistic simulations of facial appearance for visual effects in films [3, 4, 12]. Robotic and computer generated faces suffer from the so-called "uncanny valley" phenomenon [13]. This phenomenon, first postulated by Mori in the 70s based on his work building humanlike robots, suggests that as artificial faces become closer to reality they become more eerie and repulsive to a perceiver. Biomechanics-based face simulations have the potential to surpass the uncanny valley, as the facial movements would theoretically mimic the real physical system perfectly. Motion-capture techniques for face animation have improved dramatically for use in computer generated films [14]; however, biomechanics-based face animations have not yet achieved the same level of realism. Synthesizing face animations through simulation without an actor remains an attractive research direction with the potential to reduce the production costs and constraints of motion-capture driven animation.

Biomedical applications of face and vocal tract modeling are also numerous. Dysfunctions in breathing (e.g. obstructive sleep apnea) and feeding (e.g. dysphagia) are thought to involve combined deficits to both the tissue mechanics and neural control of patients. Also, maxillofacial surgeries can benefit from tissue-level cranio-

facial simulations [15]. For example, simulations can be used to predict the soft-tissue deformations following surgical alteration of the underlying jaw and skull shape [16–18]. Similarly, computer-assisted planning of complex maxillofacial reconstructive surgery has improved outcomes and reduced patient recovery time [19].

Basic questions pertaining to orofacial physiology, such as speech production, can also be investigated with tissue-level simulations. Speech production involves highly coordinated movements of the lips, jaw, and tongue. While speech movements can be analyzed with experimental measurement techniques such as ultrasound, MRI, electromagnetic articulography, electropalatography, and (to a limited extend) electromyography, the principal anatomical structures of the vocal tract are all mechanically coupled. Therefore, in order to understand the neural control of speech articulations, one must account for the role of the intrinsic, coupled mechanics of the articulators.

For simulations to impact the above stated applications, two particular considerations must be addressed. First, many biomedical applications require models that are representative of individual patients. Patient-specific modeling is commonly done to only match the size, shape, and kinematics of a model to a particular patient. For tissue-scale models, the tissue properties should also be matched to the particular patient. Second, face-tissue simulations require integration with the underlying skull and jaw as well as the vocal tract articulators. This is particularly important for modeling speech production because the interactions between the lips and teeth, tongue and teeth, and tongue and jaw position are critical issues. Many applications also require that simulations capture the dynamics of the face and vocal tract structures, because breathing, mastication, swallowing, and speech production are all dynamic acts. The effect of tissue dynamics is more pronounced on fast speed movements, such as speech production, however these effects can also have an impact on slower speed movements.

In order to address these varied modeling requirements and to apply simulations to scientific and clinical questions, we have been developing a set of biomechanical modeling tools as well as a 3D dynamic model of the jaw, skull, tongue, and face. These models were originally developed in the commercial software package ANSYS (www.ansys.com, ANSYS, Inc., Canonsburg, PA) and were more recently re-implemented in the in-house developed software package ArtiSynth (www.artisynth.org, University of British Columbia, Vancouver, Canada). ArtiSynth provides us with flexibility to incorporate state-of-the-art algorithms for very efficient simulations, while ANSYS provides us with a reliable engineering package against which we can corroborate our ArtiSynth simulation results. In this chapter, we provide a description of our tissue-scale modeling approach developed in the ArtiSynth platform. We will focus on aspects of our approach that pertain to the dynamic coupling between the face and the jaw at the tissue scale. We will also review our results for muscle-driven simulations of speech movements and facial expressions.

11.2 Subject Specific Orofacial Modeling

One of the basic design decisions that we employed in our approach to orofacial modeling was to create a workflow for generating subject-specific face, jaw tongue, skull and hyoid bone models. Subject specificity is important for a number of reasons. Validation of orofacial simulations can be made directly with experimental data from the same subject to which the model is matched. Also, a number of biomedical applications require patient-specific models. Our approach to subject specific modeling involves adapting a set of reference models to a specific subject based on medical imaging data and other clinical measurements. Our subject-specific workflow involves two main components: morphology and material properties.

11.2.1 Subject Specific Morphology

Subject specific morphology involves creating a model with anatomical size and proportions matched to a subject. For whole-body musculoskeletal modeling this typically involves an overall scaling of a generic model to a specific subject [1]. For our purposes with a face and vocal tract model, we require a more detailed type of subject-specific morphology, whereby the shapes of individual bones, muscles, ligaments, and other structures are matched to a subject. This is achieved by adapting the shape of the model's anatomical structures to medical imaging data of a specific subject.

Our workflow for a heterogeneous model, such as the face-jaw-tongue system, involves creating reference models for each model sub-component, adapting the morphology of each sub-component to fit medical imaging data for a single subject and then dynamically attaching the sub-components. In this section, we discuss the reference models for the face, skull, jaw, tongue, and hyoid bone as well as the adaptation process for morphing the reference models into an integrated subject-specific model.

11.2.1.1 Reference Face Model

The reference face model was manually built from a CT dataset of a male subject and has been described in detail elsewhere [20]. This FE model is based on a hexahedral mesh that was carefully constructed to control element quality (such as Jacobian ratio), midsagittal symmetry, and the density of elements such that more elements exist in regions of the face that are known to deform to a greater extent (Fig. 11.1). The mesh includes three layers of elements from superficial to deep. In total, the model includes 6342 hexahedral elements. In this reference model, all layers use an isotropic material, however in the revised model we have implemented an anisotropic passive material in the most superficial layer representing the epidermis and dermis (as described below in the *Anisotropic in-vivo measurements* section).

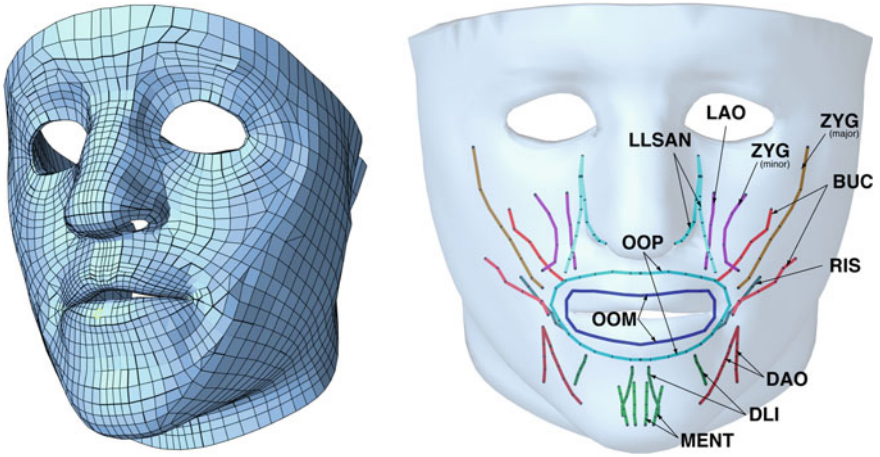

Fig. 11.1 The reference finite-element face model. Muscles include the levator labii superioris alaeque nasi (LLSAN), levator anguli oris (LAO), zygomaticus (ZYG), buccinator (BUC), risorius (RIS), depressor anguli oris (DAO), depressor labii inferioris (DLI), mentalis (MENT), orbicularis oris peripheralis/marginalis (OOP/M)

The muscles of the face are represented in the reference model with line-based muscles called "cable-elements" embedded within the model that apply muscle forces onto the FE mesh. Importantly, these cable elements include stress-stiffening effects of muscle contraction [9, 20]. Our revised face model uses transversely-isotropic muscle materials with muscle elements chosen within a volume surrounding the original cable elements and fiber directions consistent with the cable directions.

11.2.1.2 Reference Jaw-Skull-Hyoid Model

The reference jaw-skull-hyoid model was developed to simulate muscle-driven masticatory movements in ArtiSynth. The model is pictured in Fig. 11.2 and has been described in detail elsewhere [21]. It includes rigid-bodies for the skull, jaw, and hyoid bone derived from cone-beam CT data. The inertia of the jaw and hyoid were computed from the bone shapes, assuming uniform density of 3600 and 2000 kg/m^3 for the jaw and hyoid respectively. Curvilinear constraint surfaces are included to represent the articular surfaces of the temporomandibular joints. Planar contact surfaces are used to represent teeth contact.

The model includes 30 Hill-type line muscles to represent the main compartments of the mandibular muscles. Muscle properties, including maximum cross-sectional area and fiber lengths, are based on previous anatomical and modeling studies [22]. The origin and insertion points for each muscle are specified according to anatomical landmarks. The hyoid bone is attached to a fixed larynx with a linear translational/rotational spring representing the hyothyroid membrane and ligament.

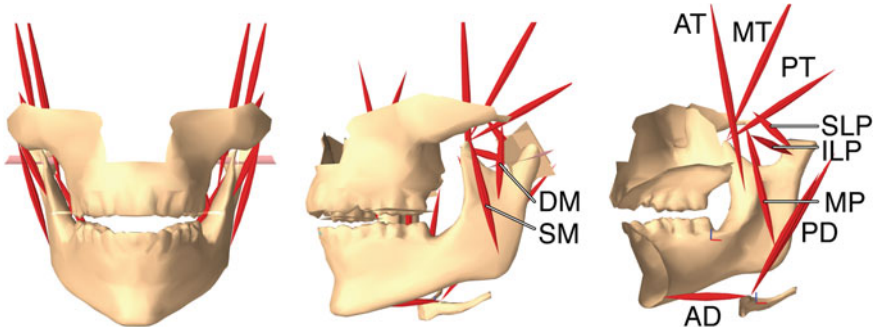

Fig. 11.2 The subject-specific rigid-body jaw-maxilla-hyoid model. Muscles include the deep/superficial masseter (D/SM), anterior/middle/posterior temporalis (A/M/PT), superior/inferior lateral pterygoid (S/ILP), medial pterygoid (MP) and posterior/anterior belly of the digastric (P/AD). From Ref. [8]. Copyright 2011 by John Wiley & Sons, Ltd. Reproduced with permission

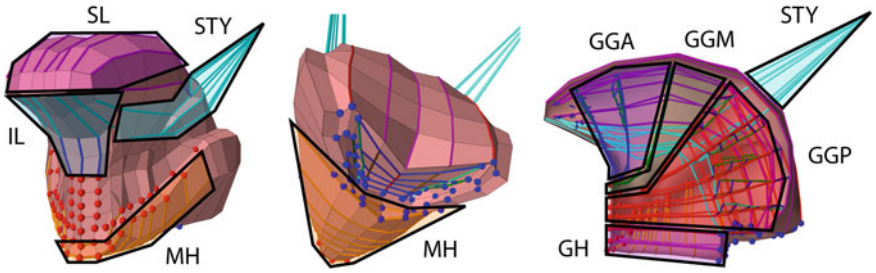

Fig. 11.3 The subject-specific finite-element tongue model. Muscles include the superior/inferior longitudinal (S/IL), mylohyoid (MH), styloglossus (STY), geniohyoid (GH), anterior/middle/posterior genioglossus (GGA/M/P), as well as the transverse, vertical, and hyoglossus muscles (not shown). From Ref. [8]. Copyright 2011 by John Wiley & Sons, Ltd. Reproduced with permission

11.2.1.3 Reference Tongue Model

The reference FE tongue model was originally developed by Gerard et al. [6] and Buchaillard et al. [7] in ANSYS and subsequently re-implemented by Stavness et al. [8] in ArtiSynth. It is pictured in Fig. 11.3. The shape of the reference tongue model is based on CT and MRI data for a single male subject. The model's FE mesh includes 740 hexahedral elements with a density of 1040 kg/m^3 for a total tongue mass of 106 g.

The FE mesh was constructed to approximate the shape of the lingual muscles. Therefore, in the reference model, muscle fiber directions are specified along the edges of the FE mesh. Our revised model uses transversely-isotropic muscle materials with fiber directions consistent with the original reference model.

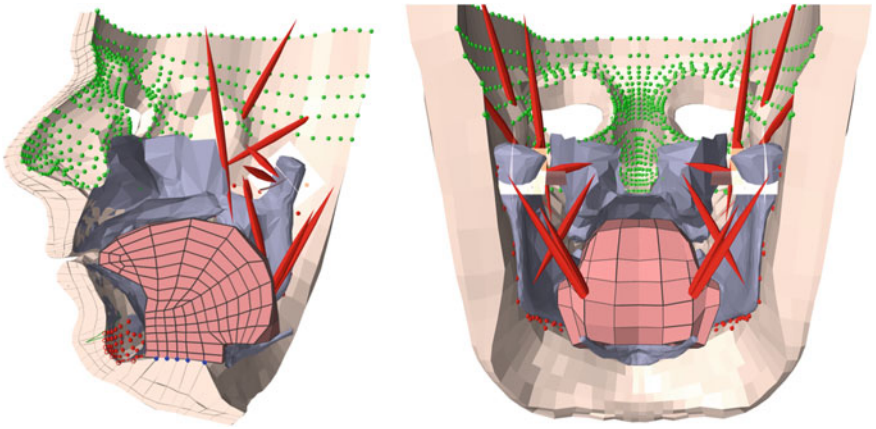

Fig. 11.4 The registered and coupled face-jaw-tongue-hyoid model. From Ref. [10]. Copyright 2013 by American Speech-Language-Hearing Association. Adapted with permission

11.2.1.4 Adaptation to Subject Morphology

In order to create a unified model of the face, skull, jaw, tongue, and hyoid bone with the morphology of a single subject, we used an adaptation procedure to morph the skeletal and muscle geometries of reference models to fit a CT dataset. The 3D jaw, skull, and hyoid surface meshes were adapted to a 3D skull surface segmented from CT data. Symmetry was attained by mirroring the left-side of the registered meshes. The reference face model was adapted based on the boundary conditions of the skull surface and the outer air-skin surface segmented from the CT data. The reference tongue model was originally constructed based on the CT data and therefore adaptation was not required.

The adaptation process used a non-elastic mesh-based registration algorithm called MMRep [23, 24], which is automatically driven in order to conform the surface mesh of the model to the segmented surface of the CT scan. Additional control points were used to enforce particular correspondences between the model and the CT scan. Importantly, for FE models, the MMRep algorithm attempts to maintain element regularity during the adaptation process, and thus the adapted FE face mesh maintained sufficient element quality for use in FE analysis.

The automatic adaptation to CT data achieved satisfactory results for the main features of the model (Fig. 11.4). However, the lip region of the model was found not to conform well. Discretization artifacts of the CT voxel data caused the lip region to become unrealistically flat. Manual node-by-node registration was performed in the region of the lip with guidance from the original CT dataset [10]. This fine-tuning was important only for detailed simulations of lip protrusion.

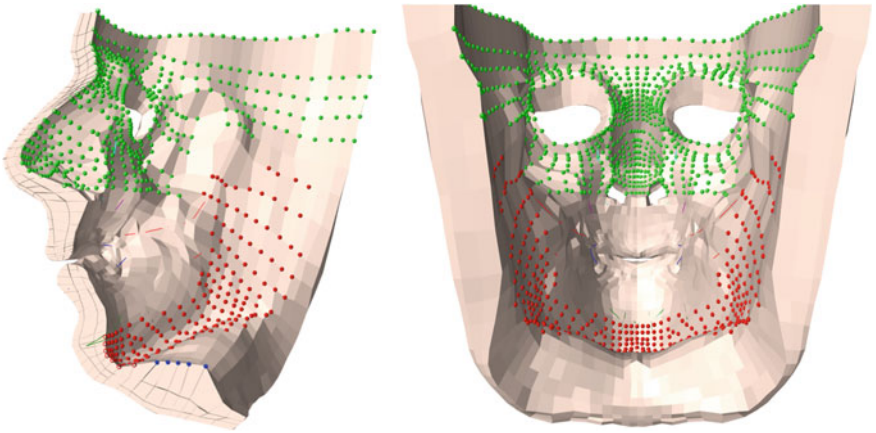

Fig. 11.5 Attachment points between the face and underlying bony structures. From Ref. [10]. Copyright 2013 by American Speech-Language-Hearing Association. Adapted with permission

11.2.1.5 Face-Jaw-Tongue Attachments

The insertion sites of the facial and lingual muscles define the primary attachments between the face, jaw, and tongue models. Line-based mandibular muscles couple the hyoid bone to the jaw and skull. These include the digastrics, stylohyoid, and geniohyoid muscles. The tongue is coupled to the jaw and hyoid bone by node attachments and by the end-points of the genioglossus and mylohyoid muscles. These attachments are implemented with the nodes of the muscle elements in the FE model.

The face muscles are attached to the underlying jaw and skull with node attachments. In addition, a number of inner-surface nodes of the face are attached to the jaw and maxilla to represent the zygomatic and mandibular ligaments. The nodes in the region of the lips and cheeks are unattached. Adjacent surfaces of the tongue and face models are attached near the region of the floor of the mouth. The attachment points are illustrated in Fig. 11.5.

Contact between the upper and lower lip, the lips and the teeth, the tongue and jaw, and the tongue and hard-palate are also implemented in the model. Unlike attachment constraints, which are always coupling the tissues together, contact constraints are only active when the meshes of the structures are in contact. Contact handling is described below.

11.2.2 Subject Specific Material Properties

In addition to subject specific morphology, material properties are also required for a biomechanical model. Subject specific material properties are much more challenging to acquire than morphology because experimental techniques for measur-

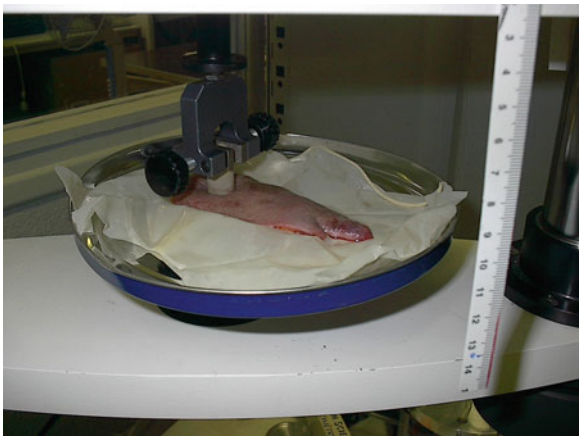

Fig. 11.6 Experimental setup for indentation-based mechanical testing of cheek and tongue tissue

ing tissue mechanics are much less routine than medical imaging for morphology. Our reference models incorporate average material properties from cadaver studies and previously published literature. Recently, we have worked with collaborators to develop new experimental protocols to measure subject-specific material properties in vivo [25, 26]. Our general approach for representing soft-tissue mechanics is to combine a passive matrix for tissue elasticity together with along-fiber muscle mechanics using an uncoupled strain energy formulation [27, 28].

11.2.2.1 Isotropic Indentation Measurements

The initial material properties for our FE models were taken from literature data in combination with mechanical testing with fresh cadaveric cheek and tongue tissues [29]. The mechanical testing involved uniaxial indentation tests using an EnduraTEC indentation device (Bose Corporation, Framingham, MA). The experimental setup is pictured in Fig. 11.6. Indentation measurements characterized the relationship between the local force applied to the external surface of the tissue and the resulting displacement. These measurements were used to fit parameters in a isotropic, nonlinear, hyperelastic material—a fifth-order Mooney-Rivlin material [30, 31],

$$W = C_{10}\,(I_1 - 3) + C_{20}\,(I_1 - 3)^2 + \frac{\kappa}{2}\,(\ln J)^2\,,$$

where the $\kappa/2\,(\ln J)^2$ term enforces tissue incompressibility. Other terms in the Mooney-Rivlin material were omitted, i.e. $c_{01} = c_{11} = c_{02} = 0$. For the face tissue, material coefficients were found of $c_{10} = 2500\,\text{Pa}$, $c_{20} = 1175\,\text{Pa}$ [20]. For the tongue tissue, material coefficients were found of $c_{10} = 1037\,\text{Pa}$, $c_{20} = 486$ Pa

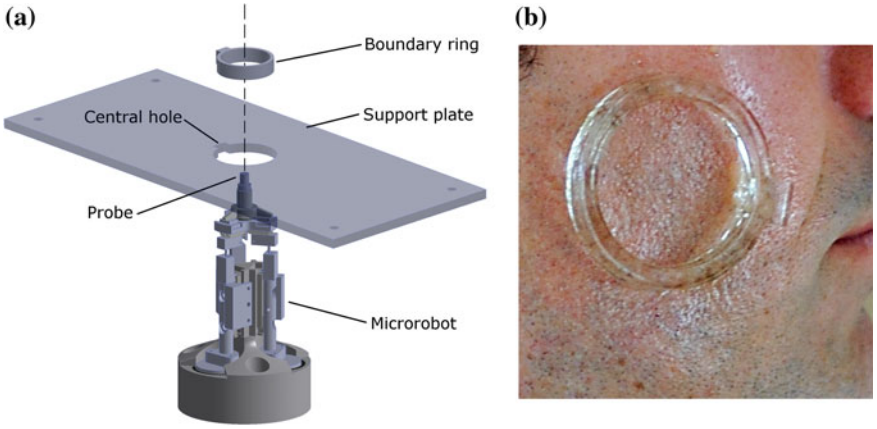

Fig. 11.7 **a** Robotic probe for in vivo mechanical testing, **b** boundary ring attached to volunteer's central cheek area. From Ref. [25]. Copyright 2013 by Elsevier. Adapted with permission

[7]. Both models had a density of $1040\,\mathrm{kg/m^3}$ and used Rayleigh damping, which is a viscous damping proportional to both tissue stiffness (β coefficient) and tissue mass (α coefficient). Rayleigh damping coefficients were set to achieve critically damped response for each model ($\beta = 0.055\,\mathrm{s}$ and $\alpha = 19\,\mathrm{s^{-1}}$ for the face model, and $\beta = 0.03\,\mathrm{s}$ and $\alpha = 40\,\mathrm{s^{-1}}$ for the tongue model).

11.2.2.2 Anisotropic In-vivo Measurements

Recently, we have characterized the mechanical behavior of in vivo facial skin using a combined experimental and numerical approach [25]. The facial skin of the central cheek area of five subjects was characterized. Five additional locations on the face were also characterized for one of the subjects. To the best of our knowledge, these are the first reported values of in vivo facial pre-stresses in the literature.

For the experiment, a region of interest on the subject's face was isolated with a boundary ring with inside diameter of 37.5 mm. A micro-robot applied a rich set of deformation cycles at 0.1 Hz to the skin surface via a 4 mm cylindrical probe (Fig. 11.7). The probe was attached using liquid cyanoacrylate adhesive to the surface of the skin. A series of in-plane deformations was applied followed by a series of out-of-plane deformations. The probe position and reaction force were measured and recorded along with a time-stamp for each data point.

For the numerical simulation, an FE simulation of the experiment was used in an optimization framework to find material parameters and pre-stresses that best-fit the model data to the experimental data from each subject and each facial region. The FE model was developed in ANSYS using an Ogden strain energy function to represent the skin and a quasi-linear viscoelastic law [32] to model the dissipative characteristics of skin. During the first load-step of the analysis an orthogonal pre-

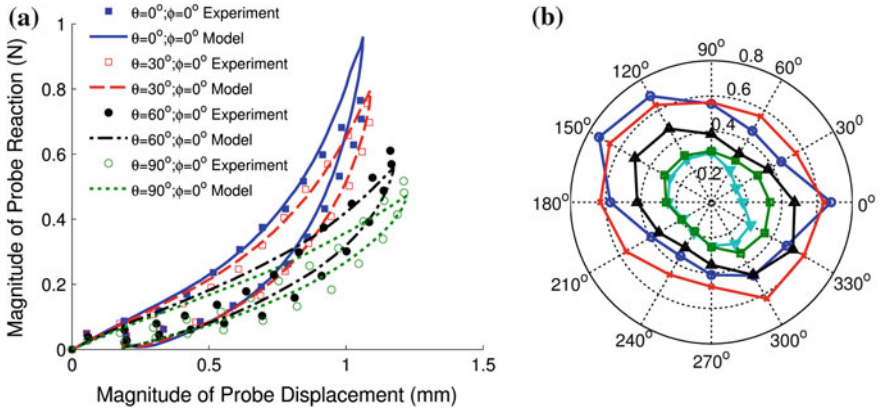

Fig. 11.8 **a** Comparison of experimental and model force-displacement response of forehead region of one volunteer, **b** force at 1.1 mm displacement in different in-plane directions for all central cheek area of all volunteers. From Ref. [25]. Copyright 2013 by Elsevier. Adapted with permission

stress was applied representing the in vivo tension inherent in human skin. After the pre-stress was applied the domain was remeshed such that the diameters of the large and small partitions were 37.5 and 4 mm, respectively. For the second step of the analysis, all nodes outside the 37.5 mm diameter partition were fixed. The nodes inside the probe area were moved according to the protocol in the experiment. The total sum of the nodal reaction forces in the probe region was calculated.

The measured force-displacement response for all tests was non-linear, anisotropic, and viscoelastic (Fig. 11.8). There was a large inter-subject variation in the skin stiffness of the central cheek area and also a large intra-subject variation in the skin stiffness at different facial locations. The direction in which the force-displacement response was stiffest at each location corresponded to the reported direction of Relaxed Skin Tension Lines (RSTL) [33] at that location. The one exception to this was the forehead region, where the direction of stiffest response was orthogonal to the RSTL direction.

The finite element model simulated the non-linear, anisotropic, and viscoelastic behaviour of the skin observed in the experiments (Fig. 11.8). The error-of-fit between the model and experiments ranged from 12 to 23 %. The in vivo stresses ranged from 15.9 to 89.4 kPa.

11.2.2.3 Muscle Materials

To represent muscle mechanics in the FE face and tongue models we used a transverse-isotropic muscle material based on the constitutive equation proposed by Blemker et al. [27]. This type of material has stiffness properties in the direction along the muscle fiber that differ from properties in the directions orthogonal to

it. Passive stress along the fiber direction was made to increase exponentially with increasing fiber stretch (see Weiss et al. [28], Eq. 7.2, p. 123). Parameters for the constitutive model were taken to be consistent with Blemker et al. [27]: $\lambda^* = 1.4$ (the along fiber stretch at which collagen fibers are straightened), $C_3 = 0.05$ (scales the exponential stresses) and $C_4 = 6.6$ (rate of uncrimping of the collagen fibers). The maximum active fiber stress was 100 kPa.

11.3 Coupled Rigid-Body/FE Modeling

Simulating orofacial biomechanics is particularly challenging because of the mechanical coupling between relatively hard structures (such as the jaw, skull, and teeth) and relatively soft structures (the face, tongue, soft-palate, and pharyngeal tract). Previous models of the face, jaw, and tongue have largely neglected these coupling effects, but we have shown these effects to be significant [8]. In this section, we discuss the simulation methods that we have developed in ArtiSynth for coupled simulation of our face-jaw-tongue model. The main components of the simulator necessary for face and vocal tract simulations are: (1) FE simulation, (2) coupling and (3) contact handling.

11.3.1 Finite-Element Simulation

ArtiSynth is an interactive simulation platform that combines multibody models, composed of rigid bodies connected by joints, with FE models composed of nodes and elements. The physics solver is described in detail in Sect. 11.4 of Lloyd et al. [34].

The positions, velocities, and forces for all rigid bodies (6 DOF) and FE nodes (3 DOF) are described respectively by the composite vectors **q, u**, and **f**. Likewise, we have a composite mass matrix **M**. The forces **f** are the sum of external forces and internal forces due to damping and elastic deformation. Simulation consists of advancing **q** and **u** through a sequence of time steps k with step size h. The velocity update is determined from Newton's Law, which leads to update rules such as the first order Euler step $\mathbf{M}\mathbf{u}^{k+1} = \mathbf{M}\mathbf{u}^k + h\mathbf{f}^k$. In addition, we enforce both bilateral constraints (such as joints or incompressibility) and unilateral constraints (such as contact and joint limits), which respectively lead to constraints on the velocities given by $\mathbf{G}\mathbf{u}^{k+1} = 0$ and $\mathbf{N}\mathbf{u}^{k+1} \geq 0$, where **G** and **N** are the (sparse) bilateral and unilateral constraint matrices. These constraints are enforced over each time step by impulses $\boldsymbol{\lambda}$ and **z** acting on $\mathbf{G}^T$ and $\mathbf{N}^T$, so that the velocity update becomes

$$\mathbf{M}\mathbf{u}^{k+1} = \mathbf{M}\mathbf{u}^k + h\mathbf{f}^k + \mathbf{G}^T\boldsymbol{\lambda} + \mathbf{N}^T\mathbf{z}. \tag{11.1}$$

The presence of FE models means that the system is often stiff, requiring the use of an implicit integration step where an approximation of $\mathbf{f}^{k+1}$ is used in place of $\mathbf{f}^k$. This can be achieved by replacing $\mathbf{M}$ and $\mathbf{f}^k$ in (11.1) with $\hat{\mathbf{M}}$ and $\hat{\mathbf{f}}^k$, which contain additional terms derived from the force Jacobians $\partial\mathbf{f}/\partial\mathbf{q}$ and $\partial\mathbf{f}/\partial\mathbf{u}$ [34]. Combining all this into a matrix form with the constraint conditions leads to a mixed linear complementarity problem (MLCP), which we solve at each time step:

$$\begin{pmatrix} \hat{\mathbf{M}} & -\mathbf{G}^{\mathbf{T}} & -\mathbf{N}^T \\ \mathbf{G} & 0 & 0 \\ \mathbf{N} & 0 & 0 \end{pmatrix} = \begin{pmatrix} \mathbf{u}^{k+1} \\ \boldsymbol{\lambda} \\ \mathbf{z} \end{pmatrix} + \begin{pmatrix} \mathbf{M}\mathbf{u}^k + h\hat{\mathbf{f}}^k \\ \mathbf{g} \\ \mathbf{n} \end{pmatrix} = \begin{pmatrix} 0 \\ 0 \\ \mathbf{w} \end{pmatrix}$$
$$0 \leq \mathbf{z} \perp \mathbf{w} \geq 0. \tag{11.2}$$

Here $\mathbf{g}$ and $\mathbf{n}$ arise from the time derivatives of $\mathbf{G}$ and $\mathbf{N}$, $\mathbf{w} \equiv \mathbf{N}\mathbf{u}^{k+1}$, and the complementarity condition $0 \leq \mathbf{z} \perp \mathbf{w} \geq 0$ arises from the fact that for unilateral constraints, $\mathbf{z} > 0$ and $\mathbf{N}\mathbf{u}^{k+1} > 0$ must be mutually exclusive. The system (11.2) is also applicable to higher order integrators such as the trapezoidal rule [34], and is also used to compute position corrections $\delta\,\mathbf{q}$ that remove errors due to constraint drift and contact interpenetration.

11.3.2 Coupling FE Models and Rigid Bodies

In models such as our orofacial model, it is necessary to connect FE models to other FE models and rigid bodies. In ArtiSynth, connecting FE and rigid-body is done using point-based attachments, whereby an FE node is attached either to another FE node, an FE element, or a rigid body. In all cases, this results in the state (position and velocity) of the attached node becoming an explicit function of the states of several other nodes or bodies. If we let β denote the set of all attached nodes, and α denote all unattached (or *master*) nodes and bodies, and denote these sets' respective velocities by $\mathbf{u}_\beta$ and $\mathbf{u}_\alpha$, then at any time $\mathbf{u}_\beta$ can be determined by the velocity constraint

$$\mathbf{u}_\beta + \mathbf{G}_{\beta\alpha}\mathbf{u}_\alpha = \mathbf{0}$$

where $\mathbf{G}_{\beta\alpha}$ is time varying and sparse. In other words, attachments can be implemented as a special kind of bilateral constraint. If we partition system (11.2) into the sets β and α, let $\mathbf{b} \equiv \mathbf{M}\mathbf{u}^k + h\hat{\mathbf{f}}$, and ignore unilateral constraints for simplicity, we obtain

$$\begin{pmatrix} \hat{\mathbf{M}}_{\alpha\alpha} & \hat{\mathbf{M}}_{\alpha\beta} & -\mathbf{G}_{\alpha\alpha}^T & -\mathbf{G}_{\beta\alpha}^T \\ \hat{\mathbf{M}}_{\beta\alpha} & \hat{\mathbf{M}}_{\beta\beta} & -\mathbf{G}_{\alpha\beta}^{\mathbf{T}} & -\mathbf{I} \\ \mathbf{G}_{\alpha\alpha} & \mathbf{G}_{\alpha\beta} & 0 & 0 \\ \mathbf{G}_{\beta\alpha} & \mathbf{I} & 0 & 0 \end{pmatrix} \begin{pmatrix} \mathbf{u}_\alpha^{k+1} \\ \mathbf{u}_\beta^{k+1} \\ \boldsymbol{\lambda}_\alpha \\ \boldsymbol{\lambda}_\beta \end{pmatrix} = \begin{pmatrix} \mathbf{b}_\alpha \\ \mathbf{b}_\beta \\ \mathbf{g}_\alpha \\ \mathbf{g}_\beta \end{pmatrix}. \tag{11.3}$$

The presence of the identity matrices in this system makes it easy to solve for $\mathbf{u}_\beta^{k+1}$ and $\boldsymbol{\lambda}_\beta$ as

$$\mathbf{u}_\beta^{k+1} = \mathbf{g}_\beta - \mathbf{G}_{\beta\,\alpha}\mathbf{u}_\alpha^{k+1},$$

$$\boldsymbol{\lambda}_\beta = -\mathbf{b}_\beta + (\hat{\mathbf{M}}_{\beta\,\alpha} - \hat{\mathbf{M}}_{\beta\,\beta}\mathbf{G}_{\beta\,\alpha})\mathbf{u}_\alpha^{k+1} + \hat{\mathbf{M}}_{\beta\,\beta}\mathbf{g}_\beta - \mathbf{G}_{\alpha\,\beta}^T\boldsymbol{\lambda}_\alpha$$

and therefore condense (11.3) into a reduced system

$$\begin{pmatrix} \hat{\mathbf{M}}' & -\mathbf{G}'^T \\ \mathbf{G}' & 0 \end{pmatrix} \begin{pmatrix} \mathbf{u}_\alpha^{k+1} \\ \boldsymbol{\lambda}_\alpha \end{pmatrix} = \begin{pmatrix} \mathbf{b}' \\ \mathbf{g}'_\alpha \end{pmatrix}.$$

11.3.3 Contact Handling

Contact handling is another important feature of our face model, in particular the ability to handle contact between FE models and other FE models (e.g. tongue/lips contacts) or rigid bodies (e.g. tongue/teeth contacts). In ArtiSynth, contact involving FE models is based on interpenetration of the surface nodes. First, the surface meshes of the respective bodies are intersected to determine which FE surface nodes are interpenetrating. A constraining direction is then determined for each interpenetrating node, based on the normal of the opposing face closest to that node (see Fig. 11.9). These directions are then used to form velocity constraints between the interpenetrating nodes and the opposing faces. These constraints are then added to system (11.2) for the subsequent time step to prevent the resulting velocity from increasing the interpenetration, and they are also used to solve for the nodal displacements required to correct the initial interpenetration.

In principle, these nodal constraints should be unilateral constraints. However, because they are relatively decoupled, it is usually possible to implement them as temporary bilateral constraints for the duration of the next time step, with the constraints being removed after the time step if the computed impulse indicates that the contact is trying to separate. This significantly improves computation time, since bilateral constraints in (11.2) are much faster to solve than unilateral constraints.

11.4 Applications of Biomechanical Face Modeling

Biomechanical face modeling permits a wide range of applications, as discussed in the introduction to this chapter. Thus far, we have focused our simulation studies on coupled face-jaw actions. In particular, we have used simulations to analyze the biomechanics of lip rounding and protrusion, lip closure, and facial expressions.

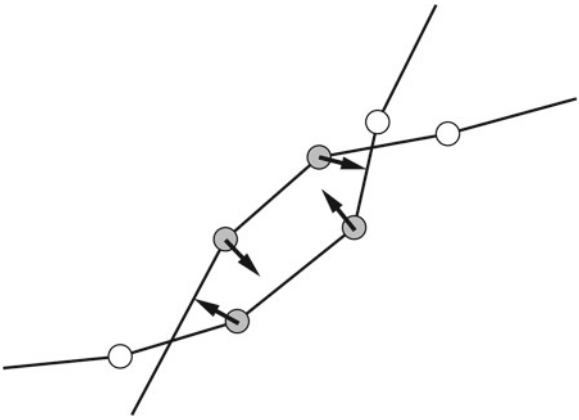

Fig. 11.9 Contact handling between two deformable models, shown schematically in 2D, with inter-penetrating nodes shown in *grey* and the associated constraint directions shown using *arrows*

11.4.1 Lip Stiffness Enables Protrusion and Rounding

One motivation for our face modeling efforts was to better understand the biomechanics underlying speech articulations with the lips. The production of rounded vowels in speech, such as /u/, /o/, or /y/ in French, requires a small area of opening between the upper and lower lip. Although a small lip opening could be generated in a number of different ways, many speakers achieve it by protruding the lips. The regularity of this speech articulation across speakers suggests that protrusion is an efficient way to achieve small lip opening areas. We were interested in using biomechanics simulation to analyze how the intrinsic properties of lip muscles could enable small lip aperture through lip protrusion during rounded vowel production [9].

Stiffness is an intrinsic property of muscle tissue. It increases with muscle activation, which is known as the "stress-stiffening" effect. In order to assess the role of intrinsic muscle stiffness, we simulated lip-rounding movements with and without stress-stiffening effects. Simulations were performed by activating the orbicularis oris (OO) muscle in the model and results are shown in Fig. 11.10. Simulations showed that a proper protrusion and rounding lip gesture was achieved by including stress-stiffening in the OO muscle. A saturation effect was also observed such that for a sufficient level of stiffness, lip protrusion and rounding was maintained as the OO activation level increased. Likewise, with a sufficient amount of OO activation, the lip gesture was maintained as the magnitude of stiffness increased. The differences in resulting lip shapes for simulations with and without stiffening were sufficient to affect the spectral characteristics of the speech signal obtained for the French vowel /u/. This result suggests that a simple strategy to generate protruded and rounded lips could be to activate the OO muscle while stiffening the tissues [9].

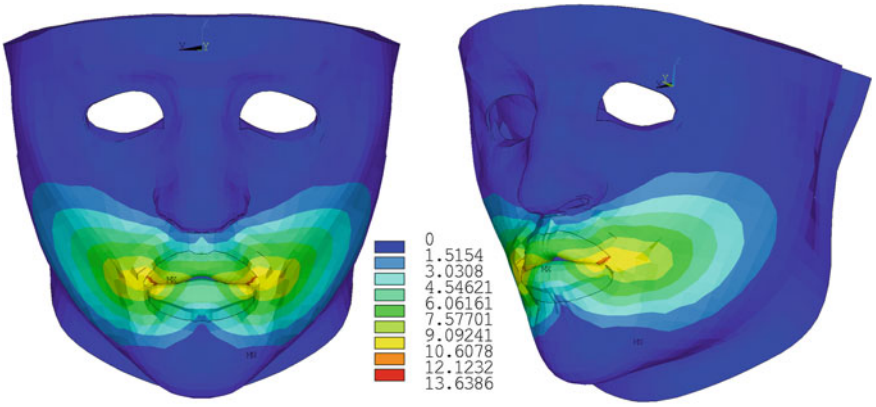

Fig. 11.10 Stress stiffening of the orbicular oris muscles enables a protrusive rounding gesture of the lips. *Color plot* shows tissue displacement from rest (mm)

11.4.2 Lip Muscles Morphology Affects Protrusion and Rounding

Having shown that the stiffness of the OO muscle is an important factor in lip rounding and protrusion, we also expected that the morphology of the muscle would be an important factor. Face morphology, including face muscle size and structure, is known to vary between individuals and across different populations. These differences could potentially account for variations in face shapes and speech sounds that are found in different languages across the world. We evaluated our hypothesis by simulating lip protrusion and rounding with various configurations of the OO muscle [10].

The OO muscle was modeled as a continuous loop of muscle elements around the lips. We varied the deepness and peripheralness of this ring of muscles, simulated lip rounding and protrusion, and observed differences in resulting lip shapes. In general, we found that activating the more peripheral region of the OO muscle resulted in greater lip protrusion.

Simulation results of lip protrusion for different configurations of OO muscle geometry are shown in Fig. 11.11 for the same level of activation of the muscle elements. General trends in the simulation results showed that more peripheral OO implementations were associated with larger protrusion, independent of deepness. The degree of deepness seemed to influence the covariation of protrusion and lip area. For a deep OO implementation, peripheralness and protrusion were systematically associated with larger lip width and lip height, and therefore with larger lip area. For a superficial implementation, peripheralness was also associated with larger lip area, mainly due to an increase in lip width. Also, a superficial implementation seemed to be inappropriate for generating protrusion and rounding and instead facilitated lip-closing gestures.

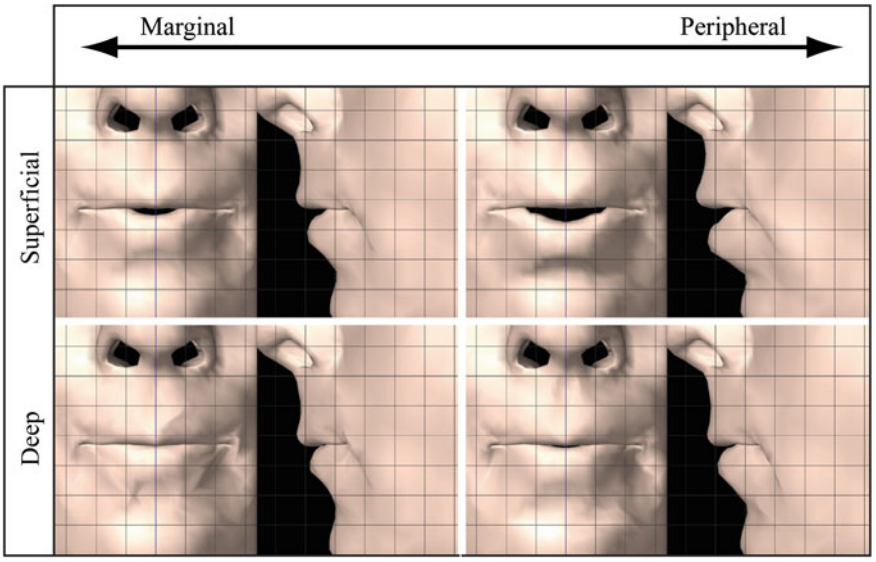

Fig. 11.11 Regional activation of the orbicularis oris muscle (deep vs. superficial and marginal vs. peripheral) changes the shape of the lips, the degree of opening, and the magnitude of protrusion for the same level of muscle activation. From Ref. [10]. Copyright 2013 by American Speech-Language-Hearing Association. Adapted with permission

11.4.3 Teeth Support Lip Protrusion

In addition to intrinsic properties and morphology of the lip muscles, we also expected that mechanical coupling with the underlying rigid structures of the jaw, maxilla and teeth is needed to provide the mechanical support necessary for lip protrusion. We tested this hypothesis by simulating two conditions: lip protrusion with and without teeth support. Such conditions are straight-forward to simulate because contact constraints in the model can be turned off, in which case there is no resistance to the lips from interpenetrating the teeth and vice versa.

Simulations are shown in Fig. 11.12 and were found to support our hypothesis of the importance of skeletal support. The lack of skeletal and teeth support resulted in reduced protrusion of the lips and was generally disruptive of the rounding gesture.

11.4.4 Jaw Opening and Lip Closure

We believe that coupling of the jaw and face is a functionally important aspect of speech movements. We expected that jaw opening would affect the lips, e.g. by reducing the capacity to produce lip closure due to this coupling. Lip closure is known to be possible even at low jaw positions during speech movements such as bilabial consonants /b/ or /p/ [35]. Through simulation, we wanted to assess which

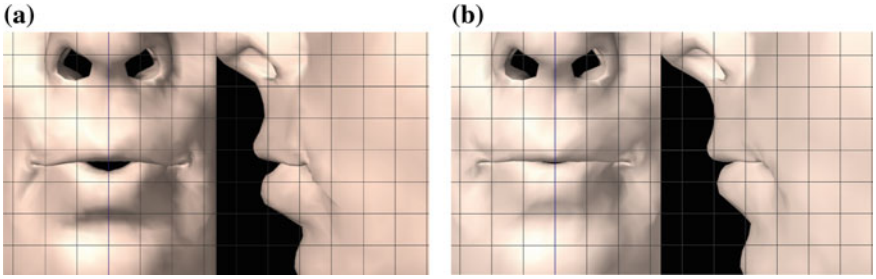

Fig. 11.12 **a** Lip protrusion is achieved with skeletal support, **b** lip protrusion is reduced without mechanical support of the underlying bone structures of the jaw, maxilla, and teeth

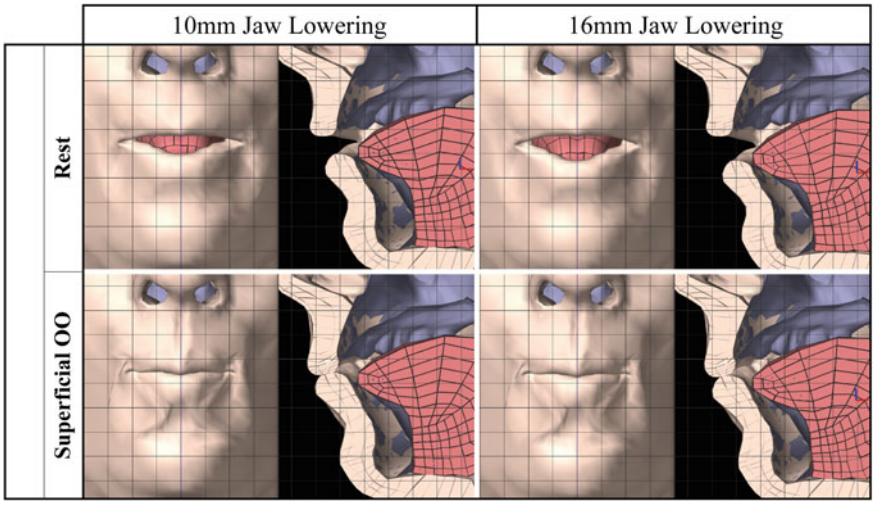

Fig. 11.13 Lip closure is achieved for an open jaw posture with activation of the superficial region of the orbicularis oris muscle. From Ref. [10]. Copyright 2013 by American Speech-Language-Hearing Association. Adapted with permission

parts of the OO muscle would be activated to best achieve a closure for low jaw postures [10].

Our simulations showed that activating the superficial layer of the OO muscle was best suited for achieving lip closure for a low jaw posture. The results are plotted in Fig. 11.13. The additional recruitment of middle, marginal portion achieved a lip closure with a very low jaw posture. The peripheral OO activation provided the required closure of the lips by downward movement of the upper lip and upward movement of the lower lip. Notably, we also observed coupling effects between the face and jaw: activation of OO to achieve lip closure induced a slight jaw closure. These simulations demonstrated that lip closure is compatible with variable jaw heights [10].

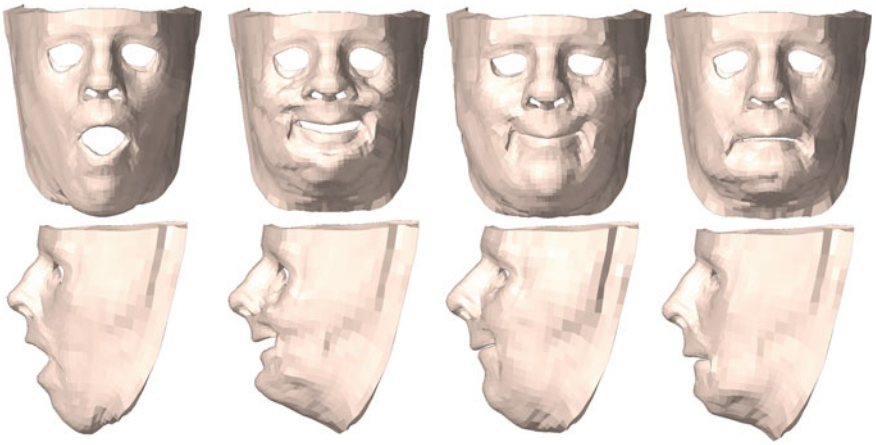

Fig. 11.14 Muscle-driven simulations of different facial expressions. From Ref. [11]. Copyright 2013 by Taylor & Francis. Adapted with permission

11.4.5 Facial Expression Simulations

We also used our face-jaw-tongue-hyoid model to simulate a series of facial expressions and compared the displacement of landmarks with experimental measurements in the literature [11]. For these simulations, the hypodermis, represented by the inner and middle layer of elements in the face model, was simulated using a Mooney-Rivlin material. The outer layer of elements representing the epidermis and dermis was modeled using an anisotropic material with parameters based on in vivo tests as described above.

For these simulations, a novel aspect of the face model was the imposition of a pre-stress corresponding to the tension inherent in living skin. The inner nodes of the facial elements were scaled prior to the finite element analysis. During the first step of the analysis, they were displaced back to their reference positions. This resulted in a tension field similar to the RSTLs observed by Borges [33].

The simulated facial expressions included a closed-mouth smile, an open-mouth smile, pursing of the lips, and lips turned downwards (Fig. 11.14). These were achieved by activating appropriate sets of orofacial muscles. For all facial expressions, the mouth corner experienced the largest displacement, which was in agreement with experimental observations. The simulated landmark displacements were within a standard deviation of the measured displacements (Fig. 11.15). For open and closed-mouth smiles, increasing the stiffness of the skin layer resulted in smaller landmark displacements (Fig. 11.15). Increasing the in vivo skin tension had a variable effect on landmark displacements.

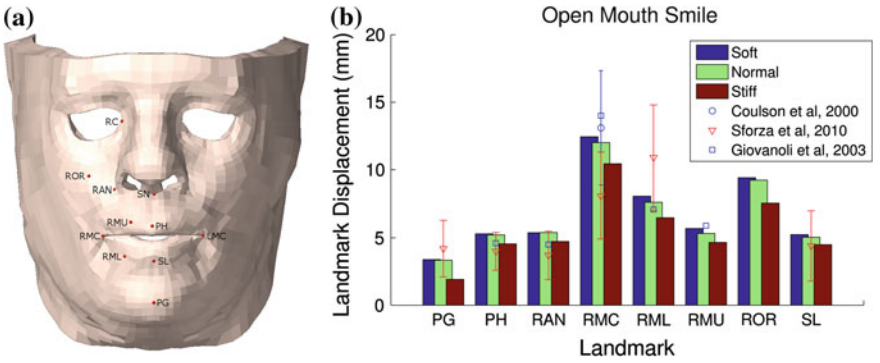

Fig. 11.15 **a** Facial landmarks, **b** landmark displacements for an open-mouth smile with different skin-types. From Ref. [11]. Copyright 2013 by Taylor & Francis. Adapted with permission

11.5 Summary

In summary, tissue-scale modeling of musculoskeletal systems involves a number of engineering challenges and presents a number of high impact applications in biomechanics and computer animation. In this chapter we have presented an approach to simulating coupled hard and soft tissue biomechanical systems at the tissue scale through combined finite-element analysis with multi-body dynamics. We have demonstrated our approach for simulating face-jaw-tongue movements. Our approach is generally applicable to modeling musculoskeletal systems other than the head and neck, and we are currently pursuing simulations studies with tissue-scale models of the upper extremity [36].

Future directions for this work include new computational techniques to improve simulation speed as well as additional experimental work to refine the model and validate simulations. Measuring muscle activations for facial expressions and lip articulations would provide additional information to evaluate our predicted muscle forces. Further characterization of material parameters specific to the different regions of facial skin would improve the model's prediction of tissue strains. We are currently extending the model to include food bolus models for simulations of mastication and swallowing. We are also pursuing simulations to study motor control of speech production as well as the design of maxillofacial reconstructions that predict post-operative orofacial function in addition to post-operative aesthetics.

Acknowledgments We gratefully thank Pierre Badin at Gipsa-Lab Grenoble for providing the CT data used for subject specific morphology. We also thank Poul Nielson and collaborators at the Auckland Bioengineering Institute for their assistance with the subject-specific material properties experiments. We also thank ANSYS for making licenses available. Funding for this work has been provided by the Natural Science and Engineering Research Council of Canada and the Michael Smith Foundation for Health Research.

References

1. Delp, S. L., Anderson, F. C., Arnold, A. S., Loan, P., Habib, A., John, C. T., et al. (2007). Opensim: Open-source software to create and analyze dynamic simulations of movement. *IEEE Transactions on Biomedical Engineering*, *54*(11), 1940–1950.
2. Blemker, S. S., Asakawa, D. S., Gold, G. E., & Delp, S. L. (2007). Image-based musculoskeletal modeling: Applications, advances, and future opportunities. *Journal of Magnetic Resonance Imaging*, *25*(2), 441–451.
3. Terzopoulos, D., & Waters, K. (1990). Physically-based facial modelling, analysis, and animation. *The Journal of Visualization and Computer Animation*, *1*(2), 73–80.
4. Sifakis, E., Neverov, I., & Fedkiw, R. (2005). Automatic determination of facial muscle activations from sparse motion capture marker data. In *ACM Transactions on Graphics (TOG), ACM* (Vol. 24, pp. 417–425).
5. Hung, A. P. L., Wu, T., Hunter, P., & Mithraratne, K. (2011). Simulating facial expressions using anatomically accurate biomechanical model. In *SIGGRAPH Asia 2011 Posters, ACM*, p. 29.
6. Gerard, J. M., Perrier, P., & Payan, Y. (2006). 3d biomechanical tongue modeling to study speech production. In *Speech production: Models, phonetic processes, and techniques* (pp. 85–102). New York: Psychology Press.
7. Buchaillard, S., Perrier, P., & Payan, Y. (2009). A biomechanical model of cardinal vowel production: Muscle activations and the impact of gravity on tongue positioning. *The Journal of the Acoustical Society of America*, *126*(4), 2033–2051.
8. Stavness, I., Lloyd, J. E., Payan, Y., & Fels, S. (2011). Coupled hard-soft tissue simulation with contact and constraints applied to jaw-tongue-hyoid dynamics. *International Journal for Numerical Methods in Biomedical Engineering*, *27*(3), 367–390.
9. Nazari, M. A., Perrier, P., Chabanas, M., & Payan, Y. (2011). Shaping by stiffening: A modeling study for lips. *Motor Control*, *15*(1), 141–168.
10. Stavness, I., Nazari, M. A., Perrier, P., Demolin, D., & Payan, Y. (2013). A biomechanical modeling study of the effects of the orbicularis oris muscle and jaw posture. *Journal of Speech, Language, and Hearing Research*, *56*, 878–890.
11. Flynn, C., Stavness, I., Lloyd, J. E., & Fels, S. (2013a). A finite element model of the face including an orthotropic skin model under in vivo tension. *Computer Methods in Biomechanics and Biomedical Engineering* (in press).
12. Zhang, Q., Liu, Z., Quo, G., Terzopoulos, D., & Shum, H. Y. (2006). Geometry-driven photorealistic facial expression synthesis. *IEEE Transactions on Visualization and Computer Graphics*, *12*(1), 48–60.
13. Mori, M., MacDorman, K., & Kageki, N. (2012). The uncanny valley (from the field). *IEEE Robotics & Automation Magazine*, *19*(2), 98–100.
14. Beeler, T., Hahn, F., Bradley, D., Bickel, B., Beardsley, P., Gotsman, C., Sumner, R. W., & Gross, M. (2011). High-quality passive facial performance capture using anchor frames. In: *ACM Transactions on Graphics (TOG), ACM* (Vol. 30, p. 75).
15. Hannam, A. (2011). Current computational modelling trends in craniomandibular biomechanics and their clinical implications. *Journal of Oral Rehabilitation*, *38*(3), 217–234.
16. Chabanas, M., Luboz, V., & Payan, Y. (2003). Patient specific finite element model of the face soft tissues for computer-assisted maxillofacial surgery. *Medical Image Analysis*, *7*(2), 131–151.
17. Mollemans, W., Schutyser, F., Nadjmi, N., Maes, F., Suetens, P., et al. (2007). Predicting soft tissue deformations for a maxillofacial surgery planning system: from computational strategies to a complete clinical validation. *Medical Image Analysis*, *11*(3), 282–301.
18. Claes, P., Vandermeulen, D., De Greef, S., Willems, G., Clement, J. G., & Suetens, P. (2010). Computerized craniofacial reconstruction: conceptual framework and review. *Forensic science international*, *201*(1), 138–145.

19. Rohner, D., Guijarro-Martinez, R., Bucher, P., & Hammer, B. (2013). Importance of patient specific intraoperative guides in complex maxillofacial reconstruction. *Journal of Cranio-Maxillofacial Surgery*, *41*(5), 382–390.
20. Nazari, M. A., Perrier, P., Chabanas, M., & Payan, Y. (2010). Simulation of dynamic orofacial movements using a constitutive law varying with muscle activation. *Computer Methods in Biomechanics and Biomedical Engineering*, *13*(4), 469–482.
21. Hannam, A. G., Stavness, I., Lloyd, J. E., & Fels, S. (2008). A dynamic model of jaw and hyoid biomechanics during chewing. *Journal of Biomechanics*, *41*(5), 1069–1076.
22. Peck, C., Langenbach, G., Hannam, A., et al. (2000). Dynamic simulation of muscle and articular properties during human wide jaw opening. *Archives of Oral Biology*, *45*(11), 963–982.
23. Bucki, M., Lobos, C., & Payan, Y. (2010a). A fast and robust patient specific finite element mesh registration technique: Application to 60 clinical cases. *Medical Image Analysis*, *14*(3), 303–317.
24. Bucki, M., Nazari, M. A., & Payan, Y. (2010b). Finite element speaker-specific face model generation for the study of speech production. *Computer Methods in Biomechanics and Biomedical Engineering*, *13*(4), 459–467.
25. Flynn, C., Taberner, A., Nielsen, P., & Fels, S. (2013). Simulating the three-dimensional deformation of in vivo facial skin. *Journal of the Mechanical Behavior of Biomedical Materials, 28*, 484–494.
26. Schiavone, P., Promayon, E., & Payan, Y. (2010). Lastic: A light aspiration device for in vivo soft tissue characterization. *Lecture Notes in Computer Science, 5958,* 1–10.
27. Blemker, S. S., Pinsky, P. M., & Delp, S. L. (2005). A 3d model of muscle reveals the causes of nonuniform strains in the biceps brachii. *Journal of Biomechanics*, *38*(4), 657–665.
28. Weiss, J. A., Maker, B. N., & Govindjee, S. (1996). Finite element implementation of incompressible, transversely isotropic hyperelasticity. *Computer Methods in Applied Mechanics and Engineering*, *135*(1), 107–128.
29. Gerard, J. M., Ohayon, J., Luboz, V., Perrier, P., & Payan, Y. (2005). Non-linear elastic properties of the lingual and facial tissues assessed by indentation technique: Application to the biomechanics of speech production. *Medical Engineering & Physics*, *27*(10), 884–892.
30. Mooney, M. (1940). A theory of large elastic deformation. *Journal of applied physics*, *11*(9), 582–592.
31. Rivlin R (1948) Large elastic deformations of isotropic materials. iv. Further developments of the general theory. *Philosophical Transactions of the Royal Society of London Series A, Mathematical and Physical Sciences*, *241*(835), 379–397.
32. Fung, Y. C. (1993). *Biomechanics: Mechanical Properties of Living Tissues*. New York: Springer.
33. Borges, A. F. (1984). Relaxed skin tension lines (rstl) versus other skin lines. *Plastic and Reconstructive Surgery*, *73*(1), 144–150.
34. Lloyd, J. E., Stavness, I., Fels, S. (2012). ArtiSynth: A fast interactive biomechanical modeling toolkit combining multibody and finite element simulation. In Y. Payan (Ed.), *Soft tissue biomechanical modeling for computer assisted surgery* (Vol. 11, pp. 355–394). New York: Springer.
35. MacNeilage, P. F., & Davis, B. L. (2000). On the origin of internal structure of word forms. *Science*, *288*(5465), 527–531.
36. Stavness, I., & Kim, S. (2013). Towards a multi-compartment finite-element model of the supraspintus muscle (pp. 115–116). In *Computer Methods in Biomechanics and Biomedical Engineering*.

Part V
Medical Analysis

Chapter 12
Computer Aided Diagnosis: State-of-the-Art and Application to Musculoskeletal Diseases

Patrizia Parascandolo, Lorenzo Cesario, Loris Vosilla and Gianni Viano

12.1 Introduction

With the rapid advances in computing and electronic imaging technology, there has been an increasing interest in developing *Computer Aided Diagnosis* (CAD) systems to improve the medical service. CAD is emerging as an advanced interdisciplinary technology which combines fundamental elements of different areas such as digital image processing, image analysis, pattern recognition, medical information processing and management. This technology can be applied to all imaging modalities, including projection radiography, computed tomography (CT), magnetic resonance imaging (MRI), ultrasound (US) and nuclear medicine imaging (PET, SPECT), used for all body parts such as the skull, thorax, heart, abdomen and extremities, and for all kinds of examinations including skeletal imaging, soft tissue imaging, functional imaging and angiography.

Although current CAD systems cannot fully replace human doctors for medical detection/diagnosis in clinical practice, the analytical results will assist doctors in providing functionalities for diagnosis, treatment, adequate follow-up, and timely monitoring of disease indicators [1–9]. Therefore, for the development of a successful CAD, it is necessary not only to develop computer algorithms, but also to investigate how useful the computer output would be for physicians in their diagnosis, how to quantify the benefits of the computer output for physicians, and how to

P. Parascandolo (✉) · L. Cesario · L. Vosilla · G. Viano
Softeco Sismat S.r.l, Via De Marini 1, Genova, Italy
e-mail: patrizia.parascandolo@softeco.it

L. Cesario
e-mail: lorenzo.cesario@softeco.it

L. Vosilla
e-mail: loris.vosilla@softeco.it

G. Viano
e-mail: gianni.viano@softeco.it

N. Magnenat-Thalmann et al. (eds.), *3D Multiscale Physiological Human*,
DOI: 10.1007/978-1-4471-6275-9_12,

maximize the effect of the computer output on their diagnosis. Thus, the research and development of CAD has involved a team effort by investigators with different backgrounds such as physicists, radiologists, computer scientists, engineers, psychologists and statisticians.

CAD has become one of the major research subjects in medical imaging and diagnostic radiology. In fact, a large number of CAD systems has been employed for assisting physicians in the early detection of cancer (breast tumors in mammograms [10, 11], lung nodules in chest radiographs/CT [12, 13], colorectal polyps in CT colonography [14]), intracranial aneurysms in magnetic resonance angiography (MRA) [15, 16] or musculoskeletal diseases (vertebral fracture or deformity due to osteoporosis in radiographs/MRI [17], bone erosions due to rheumatoid arthritis in MRI [18, 19]).

This chapter provides an overview of the main functionalities of CAD systems, with particular attention to musculoskeletal diseases (MSD). MSD and related disorders are often considered as an inevitable consequence of aging [20]. Many MSD lead to joint pain, stiffness and limited motion, affecting all human body articulations. As the population ages and physical capabilities decline, the aspiration to maintain a normal and active lifestyle will unfortunately increase the development of MSD yielding a staggering economical burden [21] and significant challenges in healthcare. As recognized by the new EU strategic programme [22], the strong synergy of ICT and medicine that includes the CAD systems paves the way for predictive medicine to better prevent and treat illnesses [23].

The chapter is organized as follows. In Sect. 12.2, the state of the art of CAD systems will be presented and some hints will be given on historical review and current research status. In Sect. 12.3, the main functionalities of CAD systems will be described. In Sect. 12.4, a CAD case study related to musculoskeletal diseases will be presented: the Rheumatoid Arthritis (RA) scenario will be described in the framework of the RheumaSCORE system [18] and some clinical trials will be discussed. In Sect. 12.5, the chapter will be concluded by a summary and future prospects.

12.2 CAD Systems: State of the Art

Early studies on quantitative analysis of medical images by computers [24–29] were reported in the 1960s. At that time, it was generally assumed that computers could replace radiologists in detecting abnormalities, because computers and machines are better at performing certain tasks than human beings. Although interesting results have been reported, these early attempts were not successful, because computers were not sufficiently powerful, advanced image-processing techniques were not available, and digital images were not easily accessible. However, a serious flaw was an excessively high expectation from computers. In fact, many different approaches to automated computer diagnosis have been attempted as aids in decision-making in many fields of medicine since the 1950s.

In 1963, Lodwick et al. [24] investigated the use of a computer in diagnosing and grading of bone tumor. In 1964, Meyers et al. [25] proposed a system to automatically distinguish normal from abnormal chest radiographs by measuring the cardio-thoracic ratio. In 1967, Winsberg et al. [26] described their study on computer analysis and detection of radiographic abnormalities in mammograms by means of optical scanning. The system automatically analyzes mammograms for abnormalities based on bilateral comparison. Another early computer system for breast cancer detection was reported by Ackerman and Gose [30] in 1972. The computer system was designed to classify breast lesions on xeroradiographs.

In the medical subspecialty of hematology, R. L. Engle [31] stated in the conclusion of his review article on 30 years' experience in using computers as diagnostic aids in medical decision making, that the computers cannot replace the physicians, but only support them during the diagnostic process. This awareness was already confirmed in the 1980s, when another approach emerged which assumed that the computer output could be utilized by radiologists, but not replace them. This concept is currently known as computer aided diagnosis, which has spread widely and quickly.

The year 1998 is one of the most important years in the history of CAD. It marked the transition of CAD technologies from the research phase to industrial practice with the success of the ImageChecker^{TM} (R2 Technology, Inc., Sunnyvale, CA; later acquired by Hologic, Inc. in 2006) in obtaining a Food and Drug Administration (FDA) approval. The ImageChecker^{TM} is a computer system intended to mark regions of interest on routine screening mammograms. The system was based on a prototype developed earlier at the University of Chicago [32]. Following the success of ImageChecker^{TM}, iCAD, Inc. (Nashua, NH) and the Eastman Kodak's Health Group (Carestream Health Inc. since 2007) also obtained FDA approval for their CAD system for mammography in 2002 and 2004, respectively. In 2002, R2 Technology, Inc. further obtained a FDA approval for its CAD system used in full-field digital mammography. The CAD system CADstream^{TM} was developed for the analysis and interpretation of breast MRI by Confirma, Inc. (Bellevue, WA). In breast US, Medipattern Corporation (Toronto, ON) first obtained a FDA approval for their B-CAD^{TM} Software in 2005. The initial software product was designed to analyze breast US images by automatically segmenting and analyzing shape and orientation characteristics of suspicious lesions in user-selected regions-of-interest (ROIs). The B-CAD^{TM} software is now available through Cedara Software Corp. (Mississauga, ON), a Merge Healthcare company. It should be mentioned that the approval of Medicare CAD reimbursement in the U.S. in 2001 has boosted the sales of CAD systems significantly. Today, it is estimated that more than 5000 mammography CAD systems are in current use in hospitals, clinics and screening centers in the U.S.

The success of CAD in mammography was quickly repeated in chest radiography. In 2001, the RapidScreen^{TM}, a CAD system for chest radiography developed by Deus Technologies (acquired by Riverain Medical in 2004) for the detection of early-stage lung cancer in association with solitary pulmonary nodules from 9 to 30 mm in size, obtained a FDA approval. In Japan, Mitsubishi Space Software has developed a

CAD system with temporal subtraction of sequential chest radiographs and also for detection of lung nodules in chest images. A number of prototype systems for detection of pulmonary nodules in thoracic CT have been developed by manufacturers and are being evaluated at medical centers around the world. In 2004, a CAD system for lung CT, the ImageChecker^{TM} CT, developed by R2 Technology, Inc., obtained FDA approval.

In other applications, the MeVis LiverAnalyser/LiverViewer Software^{TM}, a software product for liver surgery planning and lesions segmentation, developed by the Center for Medical Diagnostic Systems and Visualizations GmbH, Bremen, Germany, obtained FDA approval. MEDIAN Technologies of France also received a FDA approval in 2007 for its LMS-Liver, an image visualization and analysis software package for the evaluation of liver lesions in CT images.

CAD in colonoscopy has been receiving a lot of attention in the last few years. A number of visualization and image analysis software systems dedicated to colonoscopy have been developed and approved by FDA. For instance, the CT colonography/navigator two software package by GE Medical systems, Inc, was approved by FDA in 2001 and the Syngo Colonography software package by Siemens Medical Solutions USA, Inc., was approved in 2003. Both systems allow the user to examine the colon by examining the inside, wall, and outside of the colon on CT images. Ongoing efforts are made by a number of commercial companies including R2 Technologies, Inc., in developing sophisticated colon CAD systems.

Recently, Arimura et al. [33, 34] have developed a computerized scheme for automated detection of unruptured intracranial aneurysms in MRA, based on the use of a 3D selective enhancement filter for dots (aneurysms). During the past decade, there has been considerable interest in the roles of "less invasive" imaging modalities such as computed tomographic angiography (CTA) and MRA in the detection of intracranial aneurysms [15, 16]. However, it is still difficult and time consuming for radiologists to find small aneurysms, and it may not be easy to detect even medium-sized aneurysms on maximum-intensity-projection (MIP) images, because of overlappings with adjacent vessels and because of unusual locations. Therefore, the system developed by Arimura is useful in assisting radiologists in the detection of intracranial aneurysms, especially those that are small, by means of MRA.

In the context of MSD, Kasai et al. [17, 35] developed a computerized method for detection of vertebral fractures on lateral chest radiographs in 2006, in order to assist radiologists' image interpretation and thus the early diagnosis of osteoporosis, a chronic musculoskeletal pathology. Vertebral fracture (or vertebral deformity) is a common outcome of osteoporosis, which is one of the major public health concerns in the world. Early detection of vertebral fractures is important because timely pharmacologic intervention can reduce the risk of subsequent additional fractures [36]. Because vertebral fractures can be detected by computers, radiologists can use the detection results as a "second opinion". This allows for the improvement of the detection accuracy of vertebral fractures on lateral chest radiographs by radiologists, resulting in an improvement of early diagnosis of osteoporosis. Although this non-commercial system is useful for the detection of vertebral fractures, it does not

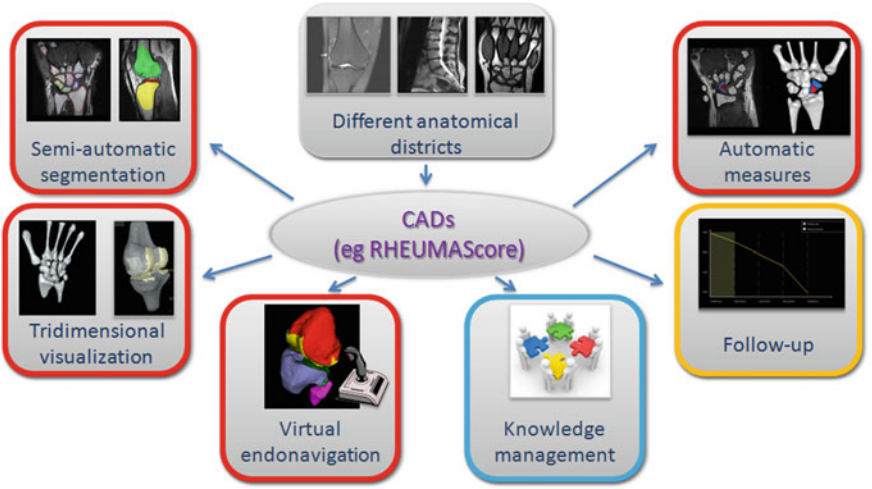

Fig. 12.1 CAD system main features. The pictures with *red contours* are related to investigation features, the pictures with *orange contours* are related to follow-up features, the pictures with *blue contours* are related to tracking feature

provide features related to follow-up or knowledge management that are key factors in the assistance of physicians during the diagnosis.

The current trend of the research in this field is the development of CAD systems assembled as packages, associated with some specific imaging modalities such as digital mammography, CT, and MRI, and implemented as a part of PACS (Picture Archiving and Communication Systems). For example, one of the potential advantages in packaging a CAD in the PACS environment is the comparison between images and related measured data acquired in different times (follow-up). Another potential advantage is the use of similar cases in practical clinical situations: a unique database that includes a large number of cases which can be used as a tool for finding cases similar to an unknown one (knowledge management). In that sense, a first result for MSD application is the RheumaSCORE software [18], a specific CAD for RA, a rheumatic disease.

12.3 Main Functionalities of a CAD System

CAD is a computerized analysis method to obtain quantitative measurements from medical images along with clinical information to give clinicians and radiologists support to more objectively assess the clinical state of a patient. The basic technologies involved in CAD systems are (Fig. 12.1):

1. imageprocessing/clinical data storage for detection, visualization and qualitative/quantitative evaluation of abnormalities (*Investigation features*, pictures with red contours in Fig. 12.1);
2. comparisons among images and clinical data of the same patient (*Follow-up features*, pictures with orange contours in Fig. 12.1);
3. quantitative evaluation and retrieval of clinical cases similar to those of unknown lesions (*Tracking feature*, pictures with blue contours in Fig. 12.1).

12.3.1 Investigation Features

These features are grouped in two main subjects: recognition and diagnostic. The first group is related to the exploitation of medical image data, the recognition of anatomical elements and their visualization. The second group offers all the features useful for the diagnosis process.

12.3.1.1 Recognition Features

This section describes all those features extracted in medical image analysis with a CAD system that provides a qualitative view of all anatomical structures (healthy and diseased) and their location and shape in the patient's body.

Medical image data

Medical image data are usually represented as a stack of individual images. Each image represents a thin slice of the scanned body part and is composed of individual *pixels* (picture elements). These pixels are arranged on a 2D grid, where the distance between two pixels is typically constant in each direction.

Volumetric data combine individual images into a 3D representation on a 3D grid. The data elements are now called *voxels* (volume elements), and they are located on the grid points.

In medical imaging, any of the various types of equipment or probes used to acquire images of the body, such as radiography, CT, US or MRI are called *modalities*. Each modality is based on different physical phenomena and thus captures different types of information. Independently from the image acquisition technique employed, medical image data are physically stored together with the information that is essential for the interpretation of the images, like patient's and investigator's data, image number, image position, image resolution, acquisition time and modality and scan parameters.

This information is highly standardized as a result of dedicated and long-term standardization activities. These have led to the Digital Imaging and Communications in Medicine standard (DICOM), which was established by the National Electrical Manufacturers Association (NEMA). The current version, 3.0, was established in 1993. DICOM is the industry standard for the transfer of radiological images and other medical information between computers and medical devices. DICOM enables digi-

tal communication between diagnostic and therapeutic equipment and CAD systems from various manufacturers.

2D visualization: browsing slices and evaluation in different orientations

An important interaction facility in a CAD is to browse through the slices of medical acquisitions. The layout may consist of one large slice display or several slices shown simultaneously. If one slice is shown, the user can scroll forward and backward. If several slices are shown, either all slices are replaced when the user scrolls forward or backward or only one new slice is presented while the other slices remain.

However, when images are displayed simultaneously in modern monitors, they are often too small to allow for the reliable recognition of small features. Therefore, layouts with several images serve primarily as an overview. A feature that is not commonly used in conventional diagnosis is the provision of an animated movement through all slices (referred to as *cine mode*). The cine mode is effective because the continuous movement smoothly blends one cross-sectional slice with the next, which considerably reduces the cognitive effort required to mentally integrate these images.

Another ability of CAD is reformatting the stack of slice data. With this facility, the three orthogonal views (axial, coronal, or sagittal), may be created. CAD systems must support the simultaneous display of the three orthogonal slicing directions.

Segmentation

For some advanced image analysis facilities, identification and delineation of certain structures (segmentation) are a prerequisite. Image segmentation usually represents the core of image analysis. This process assigns labels (unique identifiers) of anatomical or pathologic structures to parts of the image data, in order to determine important characteristics such as the size, shape or volume of an anatomical structure.

The goal of segmentation is to simplify and/or change the representation of an image into something that is more meaningful and easier to analyze. Image segmentation is often a sophisticated, time-consuming process that produces geometric descriptions of the relevant structures. Visualization benefits from image segmentation, because it allows for the selective emphasis of relevant objects. Moreover, image segmentation is the prerequisite for many interaction techniques to explore data and to carry out treatment planning.

CAD systems can have semi-automatic segmentation algorithms (e.g. Thresholding [37], Region Growing [38], Level set [39–42]). As a feedback, it is common to overlay the segmented region onto the slice data as a semitransparent colored region.

3D visualizations: techniques and user interaction

Volume visualization is concerned with the generation of a visual representation of volumetric data. Medical volumetric data can be considered as a stack of aligned images or slices of the same resolution and adjacent position in depth direction. The standard study mode in radiology is the examination of the individual images (slices), whereas the volume visualization aims at a visual representation of the full dataset,

hence of all images at the same time. Therefore, the individual voxels of the dataset must be selected, weighted, combined, and projected onto the image plane.

A frequently used technique for 3D visualization is the maximum intensity projection (MIP). With this technique, images are generated by tracing rays from the viewing plane to the 3D volume data in the direction of the virtual camera. For each pixel of the view plane, the voxel with maximum intensity is displayed. MIP images do not convey depth-relations reliably, but they allow assessment of contrast-enhanced vascular structures (these are often the voxels with highest intensity; other structures are therefore effectively suppressed). Diagnosis of vascular structures is therefore the most important application of MIP images.

Another visualization technique available in many CAD systems is surface rendering. Volumetric data are composed of a very large number of individual voxels. One approach to extract information from this large data set attempts to do so by focusing on a data subset. Structures of interest in volumetric data are typically differentiated from the surrounding image data by a boundary or a material interface. Typically, this boundary is on voxels that have the same or a similar intensity value. Hence, the resulting surface on these voxels is called an *isosurface*. An isosurface can be specified as an implicit surface, where the implicit function equals the isovalue (also called threshold) or where the difference of the implicit function and the isovalue is zero. The simplest example of an isosurface volumetric data is a binary segmented image, in which the isosurface value is equal to the foreground value of segmentation. Typically, images are generated using one of the segmentation algorithms provided by the CAD. A lot of digital techniques for surface-based visualization have been developed, such as Contour Tracing [43], the Cuberille Voxel Representation [44], and the Polygonal Isosurface Extraction [45]. Usually, some lighting is applied to produce shaded visualizations, which convey depth relations well.

In contrast to surface rendering, volume rendering produces semi-transparent renditions based on a transfer function. For volume rendering, two transfer functions are defined: one for mapping intensity values to gray or color values (as in 2D visualization), and one for mapping intensity values to transparency values. According to these transfer functions, voxels are overlaid from front to back. Opaque voxels block all voxels behind. If several semitransparent voxels are encountered that are projected to the same pixel, the gray value is determined as an interpolation of the gray values of these voxels. Volume rendering does not produce any intermediate representation, such as polygonal meshes. To emphasize this property, volume rendering is often referred to as direct volume rendering (DVR), whereas surface rendering is an indirect method of rendering volume data. The most important (i.e., the most frequently used) direct volume rendering approaches are ray casting [46] and shear warp [47].

All 3D visualization techniques are combined with interaction techniques that allow the adjustment of arbitrary viewing directions and zooming into relevant regions. To support depth perception, interactive rotation is essential. To convey the current viewing direction, some sort of orientation indication is important. Often, a so-called orientation cube is included in the 3D visualization and rotated together with the 3D scene. Its faces are labeled “A”nterior, “P”osterior, “L”eft, “R”ight, “H”ead, or “F”oot, which refer to the anatomical names of viewing directions.

12.3.1.2 Diagnostic Features

The quantitative analysis is crucial for many tasks in diagnosis and treatment planning and is a useful addition to the qualitative visual assessment. Furthermore, measurements are crucial for quality assurance and for documenting diagnostic or therapeutic decisions. Currently, it is common practice in radiology to use 2D measurement tools to define measures such as distances, diameters, areas, or angles by means of planar slices of radiological data. This, however, gives only a rough estimation for spatial measurements, such as the extent of a 3D object. To overcome the limitations of 2D measurements, 3D measurement tools are required to integrate them in 3D visualizations. CAD systems provide such 2D or/and 3D measurement functions.

The usability of measurement tools depends on a number of presentation parameters. The selection of presentation parameters is guided by the following requirements:

- *Clear relation between measurements and objects*. It should be clearly recognizable which object or region a measurement refers to.
- *Distinct assignment of measurement numbers to measurement tools.* If several measurements are included in a visualization, it is necessary that the affiliation between a measurement number and tool is shown unambiguously. The placement of numbers relative to a measurement tool and the choice of presentation parameters, such as color, are important for this goal.
- *Flexibility*. Due to the large variety of the spatial relations to be analyzed and due to personal preferences, it is important that the default values concerning font and line parameters as well as units of measurement tools are adjustable.

Distance measurement

Distance lines are employed to precisely determine Euclidean distances. Distance measures are crucial for surgery planning, for example to evaluate whether there is enough space to separate certain structures or whether vessel reconstruction is required. Similar tasks may be the estimation of the size of the neck of an aneurysm or the resection planning for lung tumors [48].

Rulers are well-known measurement facilities from daily life. A simple variant of a ruler can be found in radiological displays; usually, a vertical scale is attached to the right border of a viewer. Interactive rulers are useful for approximating the magnitude of structures and for estimating several distances along a straight line simultaneously.

Angular measurements

Angular measurements are defined between vectors or lines. In diagnosis and treatment planning, angular measurements are often used to evaluate the orientation of elongated structures with regard to some vector or midline. In these cases, the vectors that define an angle are the directions of the longest extent.

In general, angular measurements are carried out to define angles between anatomical or pathologic structures such as, for example, the lordosis or sacral angle to estimate spine pathologies and angles of blood vessel branches to perform a vascular

analysis. Angles that describe different orientations of objects are often important for the assessment of the severity of complex bone fractures (e.g., whether a surgical intervention after fractures of the arm is required depends on the angle between the bones).

Volume measurements

Volumetric measurements are essential to evaluate the success of a therapy [49]. Examples that illustrate this importance are the change of a malignant tumor's volume in the course of chemotherapy which determines the success of the treatment and wrist erosions' volume of a patient affected by RA, which determines the disease progression and the success of the treatment. However, the 3D nature decreases the reliability of traditional ruler-based in-slice measurements to an extreme level. Hence, volumetric measurements can benefit tremendously from computer-based methods.

In general, and particularly for volumetric measurements, the process of measurements can be organized into two stages: first, we need to select the relevant structure (volume selection), and second, we need to compute the respective volume of that structure (volume approximation). Typically, the volume selection corresponds to 3D segmented elements. Once we have selected all voxels of a target structure, the volume represented by these voxels can be approximated for volumetry.

A straightforward approach is to weight every voxel belonging to that selection with the size of a respective volume cell. This method achieves a reasonable approximation for interior core voxels. However, it does not reflect the boundary voxels properly, where the separating isosurface may be closer or farther away from the voxels, depending on the voxel values and the threshold. While this difference is almost negligible for compact selections, which have a relatively small boundary, it can be significant for small or elongated structures. Luft et al. [50] showed, for example, that up to 50 % of all volume cells of the cerebral ventricular system contain a boundary. In [51], it was shown that 40 % of all volume cells of such a ventricular system of a typical patient dataset contained a boundary representing more than 20 % of the total volume. These facts clearly show that the straightforward weighted counting of all voxels will compute a very inaccurate volume in too many cases.

Bartz et al. [51] describes a subdivision approach for these boundary voxels. First, the boundary voxels are examined in their volume cell context, where a boundary cell contains between one and seven selected voxels. Similar to the case table of the Marching Cubes approach [45], the boundary cells are classified into simple (one or seven voxels are selected) and complex cases (between two and six voxels are selected). Simple cases can be resolved immediately by weighting the respective volume with the interpolated isovalue parameter. The complex cases are recursively subdivided into eight subcells using trilinear interpolation until either only simple cases remain or the respective full voxel volume is below an error threshold.

Virtual endoscopy

Virtual endoscopy is a procedure inspired by real endoscopy, in which an endoscope is moved through air-filled or water-filled structures for diagnostic or therapeutic purposes [48]. Virtual endoscopy is based on CT or MRI data and simulates

the view through a real endoscope. The virtual camera is moved along a path in the center of the relevant structure. The calculation of this path requires segmentation and center-line extraction of the relevant structure. The relevant structure may be visualized by means of surface or volume rendering.

Virtual endoscopy can be applied with a variety of different goals. These goals depend largely on the clinical questions of the original real endoscopic procedure being mimicked by virtual endoscopy. Some of the goals are aimed at reducing costs in the clinical routine, a topic of almost permanent relevance in modern health care; others are aimed at improving the intervention quality by reducing the risks of complications. Another possible goal is the reduction of the training costs for medical specialists. Several technical issues need to be addressed for virtual endoscopy. The first issue concerns the rendering of the virtual endoscopy view, and the second issue relates to the navigation of the virtual camera through the visual representation of the respective body cavity. Furthermore, the CAD system user-interface and the functionality must be carefully integrated to provide a seamless workflow.

Hong et al. [52] pointed out that in the context of such a system, three different navigation options are available: automatic navigation, manual or free navigation, and guided navigation. *Automatic or planned navigation* relies on a predefined camera path through the representation of the respective body cavity. This camera path must specify positions and view directions (orientations) of the virtual camera. Afterwards, a fly-through is computed based on that path. While this option offers a good overview of the target area, it requires the refinement of the camera path, and the subsequent regeneration of the fly-through, to capture details that were previously not sufficiently visible. The second possibility is *manual or free navigation*, where the camera is transformed freely. This navigation paradigm is particularly popular for viewing computer graphics models from the outside. For virtual endoscopy applications, however, free navigation poses severe difficulties due to the high complexity of many body cavities. Furthermore, the lack of collision avoidance mechanisms and the difficulties of adding those to a free navigation system worsen this issue. The best option for virtual endoscopy combines navigation flexibility with guidance and is hence called *guided navigation* [53]. It combines a set of constraints that guide the user to a predefined target area.

The most important application is virtual colonoscopy, in which the virtual endoscope is moved through the colon to detect polyps (which are often a presage of colon cancer). Computer support for virtual colonoscopy (path planning and navigation support) is provided by a number of manufacturers and has matured over the last years.

12.3.2 Follow-Up Features

For some chronic illnesses, frequent monitoring provided by health care staff is an integral part of the treatment plan (e.g., blood pressures, MRI scan, …) [54, 55]. All

the patients' data examined in time can be recorded in a database linked to the CAD system for storage or retrieval.

One important aspect for guaranteeing the quality of follow-up results is the *reproducibility*. For instance, when a reconstruction that has been created some time ago is to be compared to a recent one, the same parameters for the visualization have to be used in order to guarantee that obvious changes to the symptoms are not due to the changed nature of the visualization. For the sake of reproducibility and other legal issues, a CAD should be able to save the entire "session", which represents all the actions a user took to generate all the patients' data (e.g. anatomical elements, clinical data, diagnostic parameters, annotations). This includes the current state of work along with the history of all changes, like the results of certain computed parameters. By saving this information in the patients' database, CAD systems provide features useful for quantitative and qualitative comparisons between exams acquired at different times.

12.3.2.1 Quantitative Evaluation

Follow-up studies during the treatment involve the acquisition of images at various stages, such as three, six, and twelve months after the beginning of the therapy. The evaluation of these images involves a comparison, for example, with respect to tumor growth or to other clinical indicators (e.g. erosion scoring for RA, blood sugar for diabetes).

For example, the difference between numerical results of clinical parameters obtained using one or more of the techniques described in the previous sections or using graphical elements, such as plots or charts, leads to the quantitative evaluation of the disease regression or progression. This helps the physician to eventually modify the treatment plan.

12.3.2.2 Qualitative Evaluation

The visualization of anatomical elements in 2D or 3D images through overlapping or side-by-side views leads to qualitative evaluation. For radiologists, some diseases have become easier to identify, grade and follow with the help of 3D visualization. For instance, typical 3D techniques include the synchronized rotation of the whole dataset, synchronized zooming towards relevant structures, synchronized movement of clipping planes, synchronized movement of the camera along a certain path (for example, through tubular structures), and synchronized gradual changes of the transparencies of objects.

12.3.3 Tracking Features

At present, the main usage of clinical images in PACS is the comparison of the current image with previous images of the same patient, but not of other patients with similar diseases. Therefore, it would not be an overstatement to say that the vast majority of images in PACS are currently "sleeping" and need to be awakened in the future for daily use in many clinical situations. The use of an appropriate CAD package, linked to a specific database integrating images from PACS and other data (measurements, user annotations, etc.), makes it possible to search for and retrieve cases with similar images or data from this database, using a reliable method developed for quantifying the similarity between a pair of exams.

12.3.3.1 Annotation

Annotation is the process of enhancing selected images with information to convey the findings of the radiologist. An annotation is the expression (e.g. drawn arrow, circle, text) of a medical opinion related to a specific case. For example, consider a MRI acquisition of a patient with degenerative disc disease. A radiologist, seeing a positive indication of degeneration will dictate a finding such as "Slight degenerative disc disease is identified in the L4/L5 and L5/S1 region". The radiologist might further annotate this in the MRI images with arrows or circles, highlighting the specific region.

It is useful to connect the annotation mechanism to the CAD system in order to link each of the selected parts with concepts and attributes expressed in a given domain ontology, thus easing the documentation accuracy and the retrieval performance.

12.3.3.2 Ontology-Based Retrieval

Ontology aims at modeling knowledge of general or specialized medicine, of health care networks and of their actors. The ontology will represent the conceptual vocabulary common to the actors of a health care network, and will be used for information retrieval [56].

This knowledge can be integrated in a semantic net, which is a flexible knowledge representation. This semantic net can enable a CAD system to find similar clinical cases from its patients' database.

12.4 RheumaSCORE: CAD for Rheumatoid Arthritis

The potential of CAD systems usage is well demonstrated in applied cases, for instance the early diagnosis and the follow-up of RA.

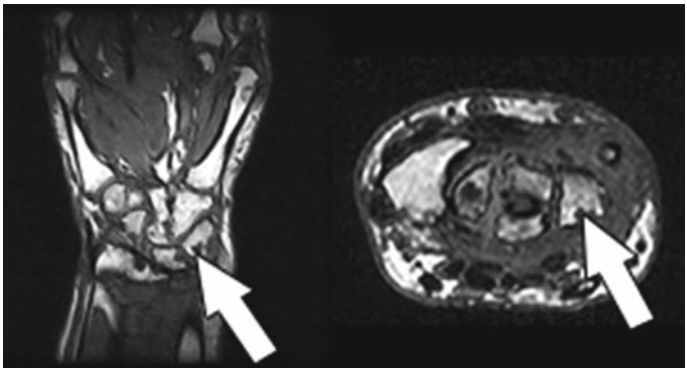

Fig. 12.2 MRI of a wrist affected by RA and with bone erosions. The *white arrows* indicate on the coronal plane (*left*) and on the axial plane (*right*), the erosion of the triquetral bone

Rheumatoid arthritis is one of the most common and serious forms of arthritis. It can lead to long-term joint damage, resulting in chronic pain, loss of function and disability. This chronic disease affects about 2.9 million people in Europe [57, 58]. An early diagnosis, the continuous monitoring of disease activity and the constant evaluation of therapy effects can improve patients' quality of life and may reduce related social costs. Several laboratory tests (e.g. rheumatoid factor, C-reactive protein) and instrumental exams (e.g. MRI) are available to evaluate RA progression and joint damage. MRI has been demonstrated to be two to ten times more sensitive than conventional radiography in detecting wrist erosions in RA (Fig. 12.2), especially in its early phases [59]. In general, erosions detectable on MRI may become visible in x-ray images only 2–6 years later [60–62]. This increased sensitivity is explained by the fact that MRI is a multi-planar technique. Moreover, it can display the soft tissues, including the synovial membrane, fluid and tendons, in addition to bones and cartilage. The quantification of synovial volume can be used to monitor the response to therapy and to predict which patients are more likely to develop erosions within one year [63].

The wide use of MRI in the assessment of joints in RA patients in the last years emphasizes the need for an objective and reproducible scoring system of RA lesions. An international working group developed a MRI scoring system to assess both inflammation (activity) and bone lesions (damage) in RA patients based on the Outcome Measures in Rheumatology Clinical Trials (OMERACT) [64].

The OMERACT Rheumatoid Arthritis Magnetic Resonance Image Scoring, or RAMRIS (RA-MRI) Scoring system was developed in order to measure the lesions observed in the wrist/hand of patients with RA. These lesions comprise *synovitis* (inflammation of the synovial membrane and other typical forms of arthritis), *bone marrow edema* (inflammation of the bone marrow), and *erosion* (the destructive bone erosion typical of RA). The erosion score is estimated visually by the user in the traditional RAMRIS: each eroded bone is considered individually and the ratio between the volume of the erosion and the hypothetically healthy bone is evaluated, analyzing

all the slices covering the bone. The global score of the erosion is evaluated considering the eroded bone volume compared to the intact bone, with 10 % increments. As a result, the rating of the erosion per single bone is comprised between 0 (healthy bone) and 10.

Manual evaluation of bone erosions volume is however tedious, time consuming and not fully repeatable (especially for inexperienced users). Considering the big amount of patients suffering from RA, this is a critical task. The *RheumaSCORE* software was developed by Softeco Sismat S.r.l. to face the RA problem [18, 19, 65].

12.4.1 RheumaSCORE

RheumaSCORE is a CAD system that supports the user (e.g. radiologist or rheumatologist) during the diagnostic process and the management of RA progression, by means of analysis, visualization, measurement and comparison of MRI acquisitions of different patients.

This application offers the physician most of the features described in the previous sections. For each patient, RheumaSCORE can load several DICOM files (study or series) simultaneously, which are used to evaluate the current disease status and monitor its progress over time. The physician is supported through several functional environments addressing:

- the *investigation*, through the recognition of wrist/hand bones and the automatic evaluation of the bone erosion scores;
- the *follow-up*, through the automatic comparison of parameters measured in image pairs acquired at different times;
- the *tracking,* through the management of clinical data, the insertion of free annotations and the retrieval of similar RA cases on the basis of historical clinical data, RA measurements or keywords specified in free notes.

The software has a modular architecture, which can be easily expanded with other segmentation techniques and 3D visualizations to deal with other anatomical districts and pathologies.

12.4.2 Evaluation of RA Status and Progression

RheumaSCORE allows for the analysis of the bones in the hand and the wrist to assess the RA status through erosion scoring and progression monitoring. The system supports the user during the 3D segmentation process of the bone structures, which is a necessary step to automatically evaluate the bone erosion scoring.

In the recognition environment, the system provides a custom segmentation procedure for each element of interest (carpal, metacarpal and forearm bones). A semi-automated method based on the level set technique using Geodesic Active Contour

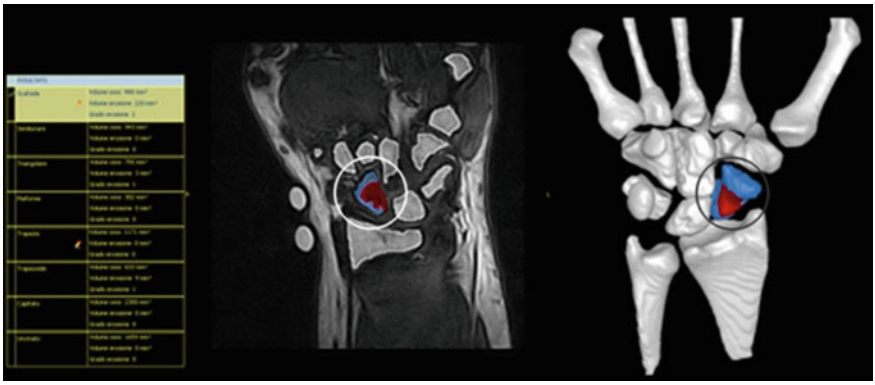

Fig. 12.3 Erosion scoring in the RheumaSCORE software

approach [41] has been applied, which does not rely on any prior knowledge of the shape of healthy bones. Segmentation results are reconstructed in 3D and displayed using the Marching Cube algorithm [45].

After segmentation, the system provides automatic scoring of the bone erosion, using the same method proposed by OMERACT RAMRIS (see Fig. 12.3). It identifies and measures bone erosions, defined as the missing volume of substance of the segmented bone with respect to an average statistical model, which is built on bones of healthy subjects. Processing takes a few minutes for all wrist bones (or hand bones), which leads to a substantial reduction of diagnosis time and costs.

A preliminary clinical test has been carried out at DIMI.[1] Twenty six patients (21 women and five men) diagnosed with early RA according to the 1987 ACR criteria were studied. The wrists were imaged in an extremity-dedicated MRI device (Artoscan C, Esaote, Genova, Italy) using a turbo T1-weighted sequence. Some experts evaluated the erosion scores using the manual RAMRIS method and the RheumaSCORE software. The results of this study showed a good correlation between the RheumaSCORE analysis and the RAMRIS erosion score [19].
Moreover, the framework permits the management and storage of clinical data (like C-reactive protein), useful for measurement and monitoring the disease activity of RA. Physicians can also add annotations, possibly using the system ontology, in order to highlight lessons learnt or critical issues linked to specific features of the current patient.

All the information related to the patient's examination (e.g. acquired DICOM images, anatomical 3D segmented elements, 3D features, user annotations) are stored in the system database and are available for retrieval. The patient disease follow-up is supported by storing, visualizing and comparing several sets of data acquired at different times. Differences among parameters and trends can be computed and visualized.

[1] *DIMI—Dipartimento di Medicina Interna, Clinica Reumatologica, Università degli Studi di Genova.*

12.5 Conclusions

Computer-aided diagnosis has become a part of clinical work in the detection of breast cancer by means of mammograms or lung nodules by means of CT, but is still in the infancy of its full potential for applications to many different types of lesions obtained with various modalities, for instance the bone erosion with MRI. In that sense, the RheumaSCORE software is a good starting point.

The current trend is the integration of CAD system into PACS, as a package for detection of lesions and also for differential diagnosis. CAD will be employed as a useful tool for diagnostic examinations in daily clinical work. The success of CAD-supported analysis processes depends on the capabilities of automated solutions to simulate and improve what physicians and radiologists do when they inspect digital data. The key challenges are:

- software applications should be able to *identify and measure* clinical practice parameters based on the same criteria used by physicians;
- retrieval of *similar* clinical cases should be based on ontology-based techniques in order to speed up the diagnosis process and to support comparative analysis among known cases;
- gathering information about specific patients in a database linked to the CAD system should ease the evaluation of the *follow-up* in order to highlight temporal trends of pathology markers, possibly depending on current therapy.

Acknowledgments This work is supported by the FP7 Marie Curie Initial Training Network "MultiScaleHuman": Multi-scale Biological Modalities for Physiological Human Articulation (2011–2015), contract MRTN-CT-2011-289897. Softeco wishes to thank Esaote Spa and DIMI (Dipartimento di Medicina Interna, Clinica Reumatologica, Università degli Studi di Genova) for their collaboration. The RheumaSCORE software has been developed within the P.O.R. Liguria FESR (2007–2013)—Asse 1 "Innovazione e competitività"—Bando Azione 1.2.2—Progetto SIDARMA.

References

1. Doi, K., Giger, M. L., MacMahon, H., et al. (1992). Computer-aided diagnosis: Development of automated schemes for quantitative analysis of radiographic images. *Sem Ultrasound CT MR, 13*(2), 140–152.
2. Doi, K., Giger, M. L., Nishikawa, R. M., Hoffmann, K. R., MacMahon, H., Schmidt, R. A., et al. (1993). Digital radiography: A useful clinical tool for computer-aided diagnosis by quantitative analysis of radiographic images. *Acta Radiologica*, *34*, 426–439.
3. Doi, K., MacMahon, H., Giger, M. L., & Hoffmann, K. R. (Eds.), (1999). *Computer aided diagnosis in medical imaging*. Amsterdam: Elsevier.
4. Doi, K., MacMahon, H., Katsuragawa, S., Nishikawa, R. M., & Jiang, Y. (1999). Computer-aided diagnosis in radiology: Potential and pitfalls. *European Journal of Radiology*, *31*, 97–109.
5. Doi, K. (2000). Present status and future horizons for computer aided diagnosis in radiology. In: P. E. Sharp & A. C. Perkins (Eds.), *Physics and engineering in medicine in the new millennium* (pp. 84–87). London: Institute of Physics and Engineering in Medicine.

6. Doi, K. (2000). Computer-aided diagnosis in radiology: Basic concept, current status and future potential. In: N. -Z. Xie (Ed.), *Medical imaging and precision radiotherapy* (pp. 125–138). Guangzhou: Foundation of International Scientific Exchange.
7. Giger, M. L., Huo, Z., Kupinski, M. A., & Vyborny, C. J. (2000). Computer aided diagnosis in mammography. In: J. M. Fitzpatrick & M. Sonka (Eds.), *The handbook of medical imaging*, vol. 2, *Medical imaging processing and analysis* (pp. 915–1004). Bellingham: SPIE.
8. Li, Q., Li, F., Armato, S. G., 3rd, Suzuki, K., Shiraishi, J., Abe, H., et al. (2005). Computer-aided diagnosis in thoracic CT. *Seminars in Ultrasound. CT MRI*, *26*, 357–363.
9. Yoshida, H., & Dachman, A. H. (2004). Computer-aided diagnosis for CT colonography. *Seminars in Ultrasound. CT MRI*, *25*, 404–410.
10. Chan, H. P., Doi, K., Vyborny, C. J., Schmidt, R. A., Metz, C. E., Lam, K. L., et al. (1990). Improvement in radiologists' detection of clustered microcalcifications on mammograms: The potential of computer-aided diagnosis. *Investigative Radiology*, *25*, 1102–1110.
11. Moberg, K., Bjurstam, N., Wilczek, B., Rostgard, L., Egge, E., & Muren, C. (2001). Computer assisted detection of interval breast cancers. *European Journal of Radiology*, *39*, 104–110.
12. Shiraishi, J., Abe, H., Engelmann, R., Aoyama, M., MacMahon, H., & Doi, K. (2003). Computer-aided diagnosis to distinguish benign from malignant solitary pulmonary nodules on radiographs: ROC analysis of radiologists' performance-initial experience. *Radiology*, *227*, 469–474.
13. Arimura, H., Katsuragawa, S., Suzuki, K., Li, F., Shiraishi, J., & Doi, K. (2004). Computerized scheme for automated detection of lung nodules in low-dose CT images for lung cancer screening. *Academic Radiology*, *11*, 617–629.
14. Summers, R. M., et al. (2001). Automated polyp detection at CT colonography: Feasibility assessment in the human population. *Radiology*, *219*, 51–59.
15. Wardlaw, J. M., & White, P. M. (2000). The detection and management of unruptured intracranial aneurysms. *Brain*, *123*, 205–221.
16. White, P. M., Teasdale, E. M., Wardlaw, J. M., & Easton, V. (2001). Intracranial aneurysms: CT angiography and MR angiography for detection-prospective blinded comparison in a large patient cohort. *Radiology*, *219*, 739–749.
17. Kasai, S., Li, F., Shiraishi, J., Li, Q., Nie, Y., Doi, K. (2006). *Development of computerized method for detection of vertebral fractures on lateral chest radiographs: Proceedings of SPIE 6144:61445D1-11*. Bellingham: SPIE Press.
18. RheumaSCORE, http://www.research.softeco.it/rheumascore.aspx
19. Barbieri, F., Parascandolo, P., Vosilla, L., Cesario, L., Viano, G., Cimmino, M. A. (2012). Assessing MRI erosions in the rheumatoid wrist: A comparison between RAMRIS and a semiautomated segmentation software. *Annals of the Rheumatic Diseases*, *71*(3), 296.
20. OSH in figures (2010). Work-related musculoskeletal disorders in the EU—Facts and figures. European Agency for Safety and Health at Work.
21. Managing musculoskeletal disorders. European foundation for the improvement of living and working conditions. www.eurofound.europa.eu
22. Green paper (2008). On the European workforce for health. Commission of the European Communities.
23. Giger, M. L. (2002). Computer-aided diagnosis in radiology. *Academic Radiology*, *9*(1), 1–3.
24. Lodwick, G. S., Haun, C. L., Smith, W. E., et al. (1963). Computer diagnosis of primary bone tumor. *Radiology*, *80*, 273–275.
25. Myers, P. H., Nice, C. M., Becker, H. C., et al. (1964). Automated computer analysis of radiographic images. *Radiology*, *83*, 1029–1033.
26. Winsberg, F., Elkin, M., May, J., et al. (1967). Detection of radiographic abnormalities in mammograms by means of optical scanning and computer analysis. *Radiology*, *89*, 211–215.
27. Kruger, R. P., Towns, J. R., Hall, D. L., et al. (1972). Automated radiographic diagnosis via feature extraction and classification of cardiac size and shape descriptors. *IEEE Transactions on Biomedical Engineering*, *19*, 174–186.
28. Kruger, R. P., Thompson, W. B., Turner, A. F. (1974). Computer diagnosis of pneumoconiosis. *IEEE Transactions on Systems, Man, and Cybernetics*, *4*(1), 40–49.

29. Toriwaki, J., Suenaga, Y., Negoro, T., et al. (1973). Pattern recognition of chest X-ray images. *Computer Graphics and Image Processing*, *2*, 252–271.
30. Ackerman, L. V., & Gose, E. E. (1972). Breast lesion classification by computer and xeroradiograph. *Cancer*, *30*(4), 1025–1035.
31. Engle, R. L. (1992). Attempt to use computers as diagnostic aids in medical decision making: A thirty-year experience. *Perspectives in Biology and Medicine*, *35*, 207–219.
32. Nishikawa, R., Haldemann, M., Papaioannou, R. C., Giger, J., Lu, M. L., Schmidt, P. et al. (1995). *Initial experience with a prototype clinical intelligent mammography workstation for computer-aided diagnosis: Proceedings of SPIE*, (vol. 2434, pp. 65–71). Medical Imaging 1995: Image Processing.
33. Arimura, H., & Li, Q. (2004). Automated computerized scheme for detection of unruptured intracranial aneurysms in three-dimensional MRA. *Academic Radiology*, *11*, 1093–1104.
34. Arimura, H., Li, Q., Korogi, Y., Hirai, T., Katsuragawa, S., Yamashita, Y., et al. (2006). Computerized detection of intracranial aneurysms for 3D MR angiography: Feature extraction of small protrusions based on a shape-based difference image technique. *Medical Physics*, *33*, 394–401.
35. Kasai, S., Li, F., Shiraishi, J., Li, Q., Doi, K. (2006). Computerized detection of vertebral compression fractures on lateral chest radiographs: Preliminary results of a tool for early detection of osteoporosis. *Medical Physics*, *33*, 4664–4676.
36. Chesnut, C. H., 3rd, Silverman, S., Andriano, K., Genant, H., Gimona, A., Harris, S., et al. (2000). A randomized trial of nasal spray salmon calcitonin in post-menopausal women with established osteoporosis. *American Journal of Medicine*, *109*, 267–276.
37. Huang, D., & Wang, C. (2009). Optimal multi-level thresholding using a two-stage Otsu optimization approach. *Pattern Recognition Letters*, *30*, 275–284.
38. Selle, D., Preim, B., Schenk, A., & Peitgen, H.-O. (2002). Analysis of vasculature for liver surgery planning. *IEEE Transactions on Medical Imaging*, *21*(11), 1344–1357.
39. Kass, M., Witkin, A., & Terzopoulos, D. (1988). Snakes: Active contour models. *International Journal of Computer Vision*, *1*(4), 321–331.
40. Osher, S., & Sethian, J. A. (1988). Fronts propagating with curvature dependent speed: Algorithms based on Hamilton-Jacobi formulation. *Journal of Computational Physics*, *79*, 12–49.
41. Caselles, V., Kimmel, R., & Sapiro, G. (1995). Geodesic active contours. *ICCV*, *69*, 4–699.
42. Chan, T., & Vese, L. (2001). Active contours without edges. *IEEE TIP*, *10*(2), 266–277.
43. Ghuneim, A. G. (2005). Contour tracing, tutorial in image processing place. www.imageprocess-ingplace.com/DIP/dip
44. Chen, L. S., Herman, G. T., Reynolds, R. A., & Udupa, J. K. (1985). Surface shading in the cuberille environment. *Computer Graphics and Applications*, *5*(12), 33–43.
45. Lorensen, W. E., & Cline H. E. (1987). Marching Cubes.*A high resolution 3D surface construction algorithm: Proceedings of ACM SIGGRAPH* (pp. 163–169).
46. Sobierajski, L., & Kaufman, A. (1994). Volumetric ray tracing. *Proceedings of IEEE/ACM Symposium on Volume Visualization* (pp. 11–18).
47. Schulze, J., Niemeier, R., & Lang, U. (2001). The perspective shear-warp algorithm in a virtual environment. *Proceedings of IEEE Visualization* (pp. 207–214).
48. Bartz, D., Fischer, J., del Rio, A. Hoffmann, J., & Freudenstein D. (2003a). VIRTUE: A navigated virtual endoscopy system for maxillo-facial and neurosurgery. *Proceedings of 3D Modelling*, Paris.
49. Preim, B., Tietjen, C., Spindler, W., Peitgen, H. O. (2002b). Integration of measurement tools in medical visualizations. *Proceedings of IEEE Visualization* (pp. 21–28).
50. Luft, A., Skalej, M., Welte, D., Kolb, R., Burk, K., Schulz, J., et al. (1998). A new semiautomated, three-dimensional technique allowing precise quantification of total and regional cerebellar volume using MRI. *Magnetic Resonance in Medicine*, *40*(1), 143–151.
51. Bartz, D., Orman, J., & Gurvit, O. (2004). Accurate volumetric measurements of anatomical cavities. *Methods of Information in Medicine*, *43*(4), 331–335.
52. Hong, L., Muraki, S., Kaufman, A., Bartz, D., & He, T. (1997). Virtual voyage: Interactive navigation in the human colon. *Proceedings of ACM SIGGRAPH* (pp. 27–34).

53. Galyean, T. (1995). Guided navigation of virtual environments. *Proceedings of ACM Symposium on Interactive 3D Graphics* (pp. 103–104).
54. van Hulst, L. T., Fransen, J., den Broeder, A. A., Grol, R., van Riel, P. L., & Hulscher, M. E. (2009). Development of quality indicators for monitoring of the disease course in rheumatoid arthritis. *Annals of the Rheumatic Diseases*, *68*, 1805–1810.
55. Grigor, C., Capell, H., Stirling, A., McMahon, A. D., Lock, P., Vallance, R., et al. (2004). Effect of a treatment strategy of tight control for rheumatoid arthritis (the TICORA study): A single-blind randomised controlled trial. *Lancet*, *364*, 263–269.
56. Kuntz, R. D., & Minier, D. (2006). Building and using a medical ontology for knowledge management and cooperative work in a health care network. *Computers in Biology and Medicine*, *36*, 871–892.
57. Markenson, J. A. (1991). Worldwide trends in the socio economic impact and long-term prognosis of rheumatoid arthritis. *Seminars in Arthritis and Rheumatism*, *21*, 4–12.
58. Weinblatt, M. E. (1996). Rheumatoid arthritis: Treat now, not later (editorial). *Annals of Internal Medicine*, *124*, 773–774.
59. Østergaard, M., Hansen, M., Stoltenberg, M., Jensen, K. E., Szkudlarek, M., Pedersen-Zbinden, B., et al. (2003). New radiographic bone erosions in the wrists of patients with rheumatoid arthritis are detectable with magnetic resonance imaging a median of two years earlier. *Arthritis and Rheumatism*, *48*, 2128–2131.
60. Benton, N., Stewart, N., Crabbe, J., Robinson, E., Yeoman, S., & McQueen, F. M. (2004). MRI of the wrist in early rheumatoid arthritis can be used to predict functional outcome at 6 years. *Annals of the Rheumatic Diseases*, *63*, 555–561.
61. McQueen, F. M., Benton, N., Perry, D., Crabbe, J., Robinson, E., Yeoman, S., et al. (2003). Bone edema scored on magnetic resonance imaging scans of the dominant carpus at presentation predicts radiologic joint damage of the hands and feet six years later in patients with rheumatoid arthritis. *Arthritis and Rheumatism*, *48*, 1814–1827.
62. Østergaard, M., Hansen, M., Stoltenberg, M., Jensen, K.E., Szkudlarek, M., Klarlund, M., et al. (2002). MRI bone erosions in radiographically non-eroded rheumatoid arthritis wrist joint bones give a 4-fold increased risk of radiographic erosions five years later. *Arthritis and Rheumatism*, *46*, S526–S527.
63. Savnik, A., Malmskov, H., Thomsen, H. S., et al. (2002). MRI of the wrist and finger joints in inflammatory joint diseases at 1-year interval: MRI features to predict bone erosions. *European Journal of Radiology*, *12*, 1203–1210.
64. Ejbjerg, B., McQueen, F., Lassere, M., Haavardsholm, E., Conaghan, P., O'Connor, P., et al. (2005). The EULAR-OMERACT rheumatoid arthritis MRI reference image atlas: The wrist joint. *Annals of the Rheumatic Diseases*, *64*(1), 23–47.
65. Catalano, C. E., Robbiano, F., Parascandolo, P., Cesario, L., Vosilla, L., Barbieri, F., et al. (2012). Exploiting 3D part-based analysis, description and indexing to support medical applications. *Proceedings of Workshop on Medical Content-Based Retrieval for Clinical Decision Support, in conjunction with MICCAI*. France: Nice.

Chapter 13
Accessing and Representing Knowledge in the Medical Field: Visual and Lexical Modalities

Imon Banerjee, Chiara Eva Catalano, Francesco Robbiano and Michela Spagnuolo

13.1 Introduction

One of the challenging directions of the research in modern medicine is modeling a ***digital patient***, i.e. a digital counterpart that should represent and abstract the real patient in all his/her medically relevant aspects. The digital patient is nowadays a realistic vision: we witness a huge flow of data every day, either born-digital or easy to digitize. This flow is constituted by numerical measurements (lab data, bedside measurements, home instrumentation), recorded information (family history, patient medical history, current complaints, symptoms), signals (ECG, EEG, EMG), images (X-ray, MRI, CT, Ultrasound), physical examinations, and narrative text (e.g. doctor's notes, discharge summaries) [1].

Given this variety of sources (see Fig. 13.1), digital healthcare needs a multimodal and combined access to interrelated heterogeneous information in addition to traditional sources: books, posters and 3D physical mock-ups are used to convey medical knowledge but their support is no longer suitable for the new technological challenges.

In the digital era such pieces of knowledge are even more valuable when integrated or at least interconnected so that doctors and professionals in the field are able to navigate data more easily and directly gather all the relevant information available.

I. Banerjee · C. E. Catalano (✉) · F. Robbiano · M. Spagnuolo
CNR IMATI-Genova, Via De Marini 6, 16149 Genova, Italy
e-mail: chiara.catalano@ge.imati.cnr.it

I. Banerjee
e-mail: imon.banerjee@ge.imati.cnr.it

F. Robbiano
e-mail: francesco.robbiano@ge.imati.cnr.it

M. Spagnuolo
e-mail: michela.spagnuolo@ge.imati.cnr.it

N. Magnenat-Thalmann et al. (eds.), *3D Multiscale Physiological Human*,
DOI: 10.1007/978-1-4471-6275-9_13,

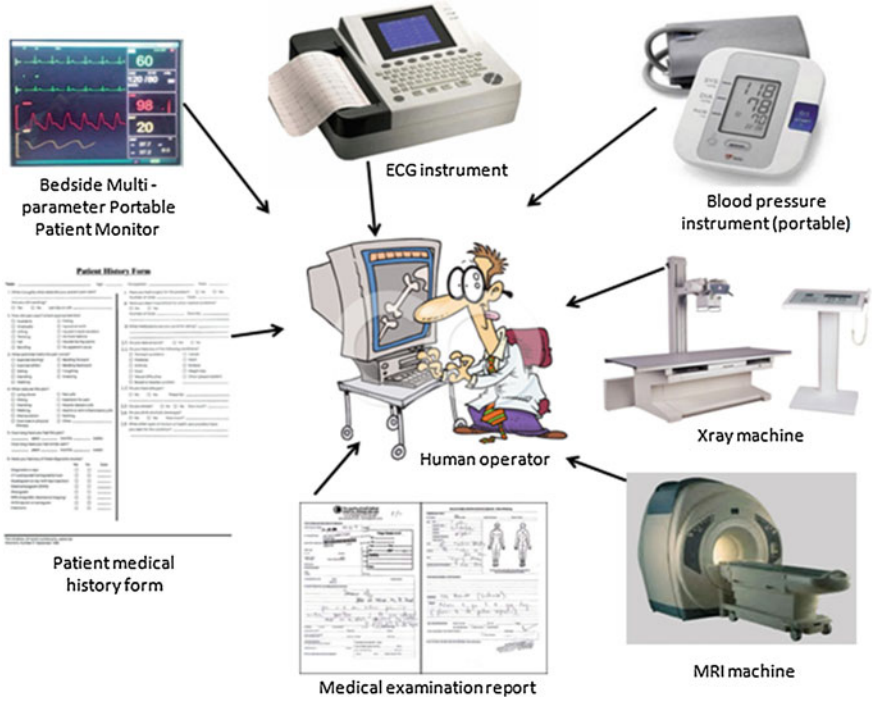

Fig. 13.1 Different knowledge acquisition sources in the medical domain

How to get access to such knowledge in the digital patient perspective? Two dominant modalities for information access emerge, which apply also to the traditional sources: the ***visual*** (i.e. based on images and 3D models) and the ***lexical*** (i.e. based on words, in a natural or formal language) modalities. In conventional cases, the two modalities are usually integrated, at least to some degree: for instance, body parts are usually labeled with their scientific names in an anatomy poster. Scientific illustrations of medical knowledge have been subject of research also in the computer graphics community as a way to enhance the communication of knowledge to students and professionals in the field [2].

Hence, the research questions are: to what extent can we use these two natural channels of communication in the modern digital medicine? How to combine them in such a way that we benefit from the strengths of both and improve the ability of conveying knowledge and supporting new data correlation?

At first we have to discuss on the type of information involved and how it is represented and accessed: is it about anatomy? Can it be localized within some anatomical district? Is it decoupled from anatomy and does it concern diagnosis, symptoms analysis, or forensic categorization of pathologies? In the following sections we will provide examples of different research efforts taking into account different information types. Most of the efforts are tailored just for one or few applications,

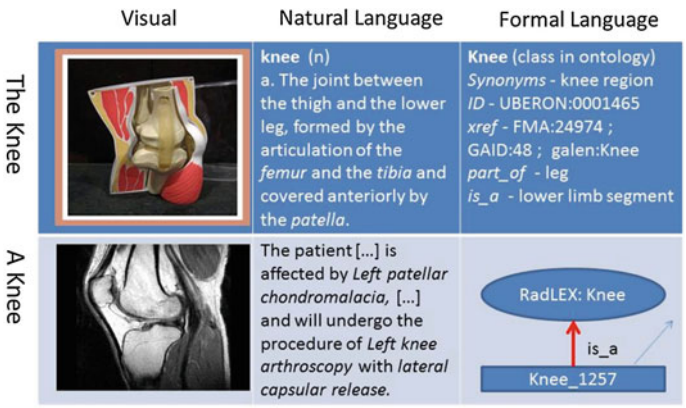

Fig. 13.2 Knowledge about the generic knee (*top*) versus knowledge about a specific knee (*bottom*): examples of how it can be conveyed by visual means (*left*), natural language (*middle*) and formal language (*right*)

whereas some of them either are general purpose or try to federate different initiatives. Obviously, the disciplinary vantage point is the most discriminative: radiologists and surgeons are likely to be interested in different characterizations of the same conceptual entity.

More general questions to assess the scope and the aim of digital knowledge representation efforts may arise. For instance: is just one scale addressed (e.g. organ, tissue) or is the same entity represented at different scales? If an entity is characterized by its shape (e.g. an organ), is there an explicit connection to the actual representation of the shape? When a vocabulary is involved, is it used in a natural language or in a formal language? To what extent is it expressive? Is it narrow (i.e. focused on a specific domain) or broad (i.e. general-purpose)? Is it shallow (e.g. not much detailed, considering only the most important terms) or deep?

In the following, we will comment on the "digital patient" by surveying state-of-the-art initiatives dealing with visualization and knowledge formalization of the human body, focusing on the peculiarities of these two different modalities to approach medical information management. Special attention will be given to the specificity of each solution (see Fig. 13.2): do they refer to generalized human prototypes, to patient-specific data or to hybrid models (e.g. a parameterized human model)?

When possible, the knee (or anything related to the knee) will be used as a common example in order to grasp better the difference between the numerous initiatives. How is the knee (or a knee, in case of patient-specific information) represented? Is it possible to visualize it? How is it connected to its subparts or to other related districts? How detailed is the expression of the concepts concerning it?

In particular, in Sect. 13.2 we will revise initiatives to handle knowledge in the medical domain primarily from the visual perspective. In Sect. 13.3 we will tackle the lexical modality. Finally, in Sect. 13.4, combination perspectives and their potential will be discussed.

13.2 Visual Modality

Data visualization is a common medical practice for different purposes. In particular, digital models of the human body may be used for training students in anatomy, surgery and other disciplines. Indeed, very sophisticated and interactive digital models are available to maximize immediacy and spatial feel and the visual components are often paired with textual tags. For diagnostic purposes, images (e.g. x-rays, MRI, CT) and 3D models are the main visual means to represent medical data for inspection, parameter measurement and simulation.

The distinction between patient-specific and canonical data depends on the object of interest: do we want to study 'a knee' of a specific patient (e.g. in a diagnostic effort) or 'the knee' as a generic concept (e.g. for training purposes)? Recent visualization tools try to integrate these two aspects, and one of their main goals is to compare and link the canonical case with the patient-specific information in order to have a personalized atlas of the human body. In the following, we will show state-of-the-art initiatives and tools that we consider interesting to visualize medical data.

13.2.1 Medical Image Processing Applications

Thanks to the wider adoption of medical images for diagnostic purposes in clinical practice, several open medical image processing platforms have been developed in the academic environment, for example, OsiriX [3], YadiV [4] and 3DSlicer [5]. These tools were initially developed as image visualization tools but have been enhanced to support doctors in diagnosis. In fact, some systems (e.g. OsiriX) not only visualize 2D data but also 3D and even 4D data (i.e. 3D series with a temporal dimension, such as cardiac CT) and 5D (i.e. 3D series with temporal and functional dimensions, such as cardiac PET-CT) images. These systems support also the automatic computation of multi-planar 3D reconstructions, visualization tools like surface and volume rendering, and dynamic visualization depending on the user defined parameters.

Beyond typical visualization functionalities, these tools provide specific modules for data processing: for example, it is possible to measure key parameters, to reconstruct full 3D models, to segment and annotate according to the context and finally to link such information with existing or new data (e.g. reports, segmented parts, annotated tags) through visual interfaces.

Segmentation is a crucial 2D/3D processing technique, which subdivides the global volume of images in meaningful regions of interest (ROIs) according to the specific clinical analysis tasks, and extracts useful information from the acquired data. YadiV and 3DSlicer, among others, give some automatic/semi-automatic segmentation facilities, while OsiriX supports segmentation only through specific plug-ins, which may be included also by the users. Here, visualization is still the preferred method to interact with data. Nevertheless, there is the possibility of manually annotating images for further reference.

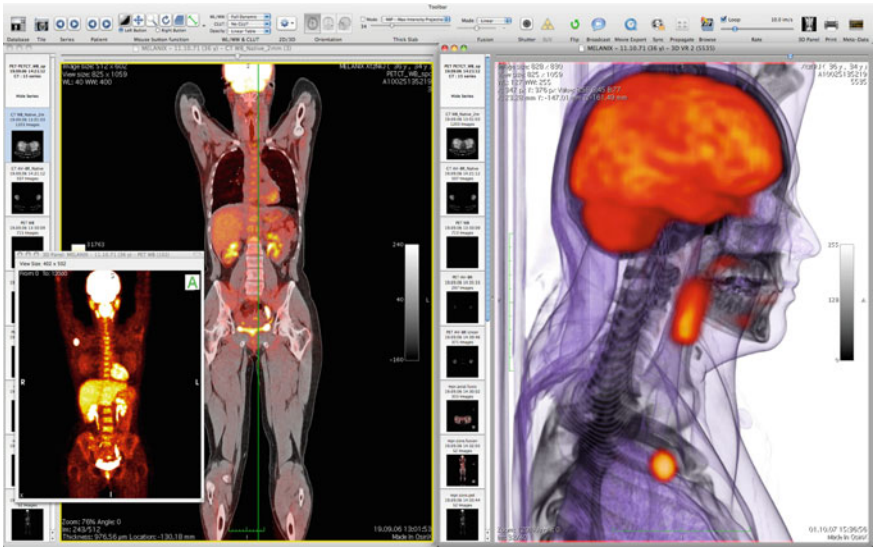

Fig. 13.3 Pet-CT (hybrid scanner) and 3D viewers in OsiriX

Among the platforms, OsiriX is specifically designed for display and processing of multi-modal radiological applications and is able to perform image fusion between different imaging modalities (for example, PET-CT or PET-MRI). Visualization of the images generated by the fusion process allows for the interpretation of multi-scale information related to both anatomy and metabolism outside the actual hybrid imaging devices (see Fig. 13.3).

Being a DICOM compliant software, OsiriX allows the host device to be identified as a node on the DICOM network which is the base for data query and communication purposes: simple queries and active interaction with the selected DICOM servers are allowed, based on standard metadata (e.g. the patient name, the acquisition date). From the collaborative perspective, OsiriX can extract the metadata stored in the header of DICOM files to sort images according to demographic, technical and acquisition protocol. Images and corresponding data are stored in its local databases and can be shared among different remote workstations that can even be located in different departments or different hospitals to access selected patients' records. In fact, it has been already adopted in many hospitals and radiology departments as well as other clinical departments such as surgery and cardiology for medical image analyses.

YaDiV ("Yet Another DIcom Viewer") is a program for interactive visualization of 3D medical volume data developed by Welfenlab. Its main goal is the visualization of 3D data, but it is also designed to support the semi-automatic data segmentation task: there are several segmentation algorithms which are popular in medical fields already implemented, like Region Growing, Snake, Energy snake (see Fig. 13.4).

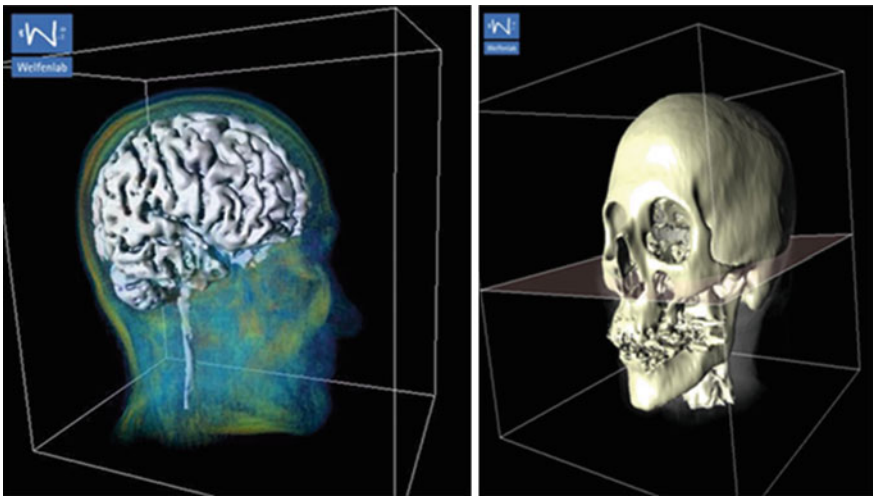

Fig. 13.4 3D segment visualization and isosurface rendering using marching cube in YaDiV

As OsiriX, it gives the user data freedom to approve or modify the segmentation according to his/her choice and attach annotation to each segmented part.

Finally, 3Dslicer is another open source application for medical image visualization and analysis. It is mainly used to visualize acquired patient's data but it includes also different algorithms for image segmentation and registration, developed by researchers around the world. Currently, this platform also gives some functionalities for supporting diagnosis, such as matching the acquired data with canonical shape models.

13.2.2 Multiscale Spatiotemporal Visualisation

The Multiscale Spatiotemporal Visualisation (MSV) project is an International cooperation between the European @neurIST and VPHOP integrated projects, the US National Alliance for Medical Imaging Computing (NA-MIC), and the New Zealand-based IUPS Physiome [6]. The aim of the MSV project is to develop an open source library for the visualization and interaction with multi-scale biomedical data (see Fig. 13.5). The main interesting feature of this project is that the medical visualization platform aims at incorporating knowledge. In fact, this project is working on the explicit use of knowledge to fill the gap between visualization across different scales of the same patient's data.

The main goals of this project for multi-scale visualization are: (i) the visualization across time and space (spatial and temporal data); (ii) the integration of large data sets from different levels and scales; (iii) the handling of gaps among different

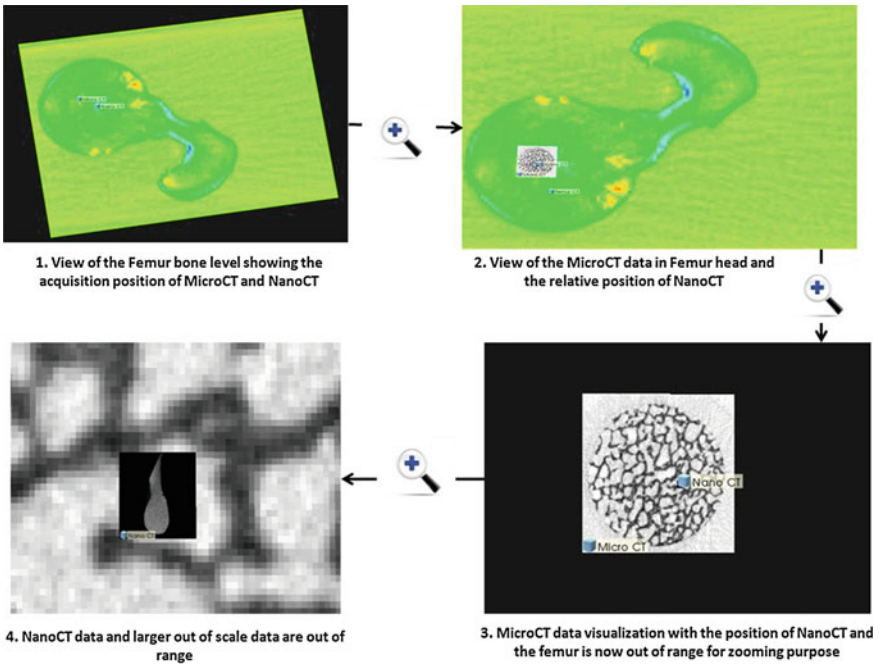

Fig. 13.5 Multiscale visualisation of a femur by using MicroCT and NanoCT data

scales, multivariate and heterogeneous data. The project is ongoing, but the expected outcome is a patient-specific visualization system enabling a smooth transition between different scales of patient's body from bones (CT, MRI) to tissues and cells (MicroCT). For this purpose it will link the data acquired with different imaging modalities representing structures on different scales, e.g. CT scan for representation of bones, MRI scan for soft-tissue representation, Micro-CT for cell and tissue representation.

13.2.3 Google: The Body Browser

The Google Body Browser [7] provides a human body atlas and allows accessing it in an interactive way, which is a very efficient approach for transferring the anatomical knowledge for an academic/training target. This browser visualizes a pre-processed model of a generic man and a generic woman and explores the body organs using a navigation widget with different level of transparencies. It was meant mainly as a demonstrator for the WebGL technology, but it has been recently acquired by a private company which develops 3D anatomical models.

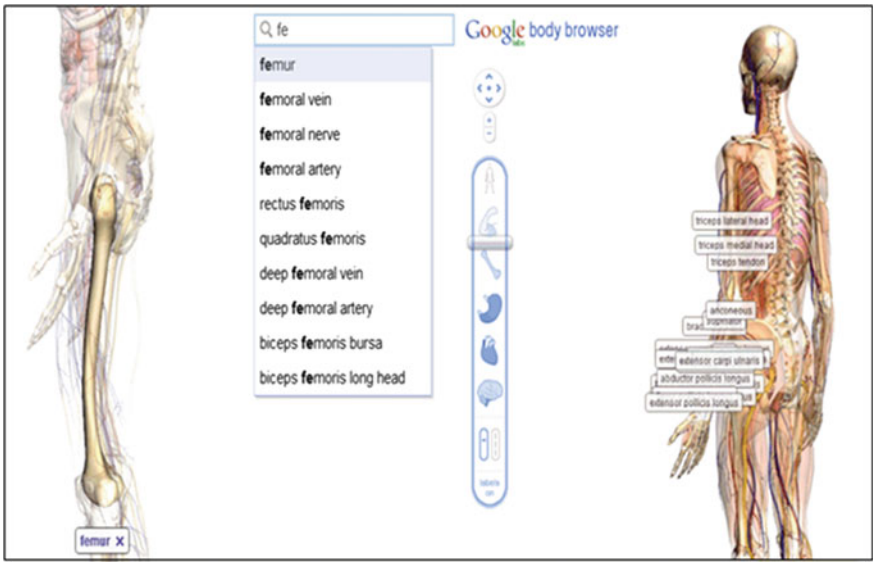

Fig. 13.6 The Google body browser

The human body anatomy is very complex and specific for different instances but in this case the user may visualize the general anatomical structure. The most interesting feature of this project is that each of the 3D body parts is segmented and tagged with knowledge at different scales.

If we consider the 'Knee', we can visualize the knee district from different perspectives, like the skin of the knee, the muscles involved in its articulation, the constituting bones and the blood vessels running through that particular district. Specific bones such as the femur can be searched by keyword and their position as well as their connection with other body parts are then visualized (see Fig. 13.6).

13.2.4 Bodyparts 3D

BodyParts 3D [8, 9] is a dictionary-type database for anatomy in which anatomical concepts are represented by 3D structured data that specify corresponding segments of a 3D whole-body model for an adult human male. It encompasses morphological and geometrical knowledge of anatomy and complements with ontological representations. Nowadays, 382 anatomical concepts have been specified; the expansion of the dictionary by adding further segments and details to the whole body model will continue in collaboration with clinical researchers until sufficient resolution and accuracy for most clinical applications are achieved.

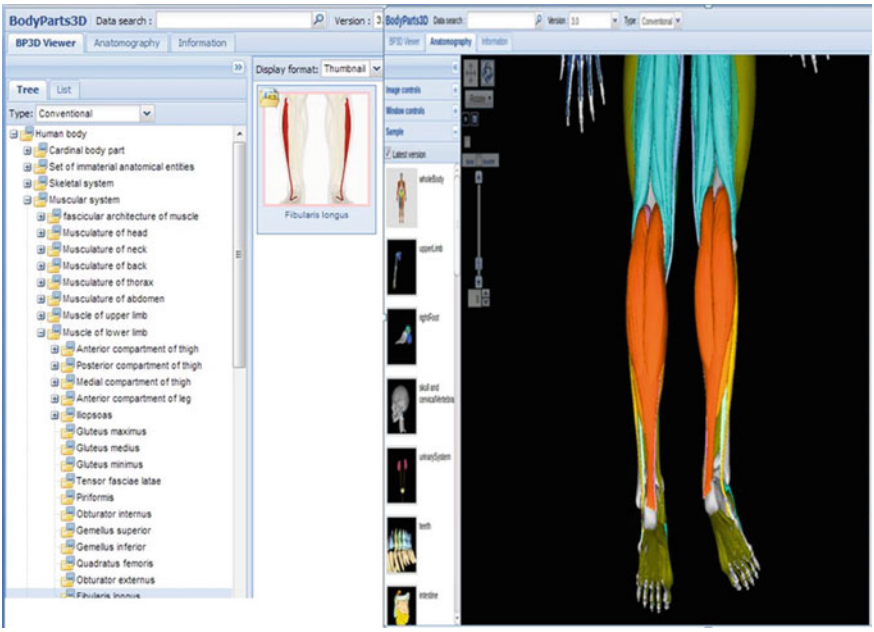

Fig. 13.7 Representation of the muscles of the lower limb in bodyparts3D [9]

It represents only generic information and can be used to gather knowledge about the canonical body parts in 3D with textual descriptions. The main interesting feature of this initiative is that it is able to populate the Foundation Model of Anatomy (FMA) ontology [10, 11] with 3D models of body parts of individuals (see Sect. 13.3) and it allows a hierarchical navigation through the FMA ontology.

As users have access to knowledge more efficiently with a 3D visualization tool, the Bodyparts3D initiative enriches the FMA ontology by adding a 3D canonical description of each body part. It also includes some geometrical attributes, such as volume and area for each of the concepts.

Considering the knee, some of the anatomical concepts in FMA, e.g. patella, have a specific 3D visual representation linked to a corresponding geometric model (see Fig. 13.7). Users are allowed to adjust their specific model (e.g. a specific knee) to the generic one included in BodyPart3D in order to create personalized 3D models and share them.

13.2.5 Voxel-Man

One prominent example of a biomedical tool supporting both visualization and annotation is 'Voxel-Man' [12] in which a 3D model of a human body was

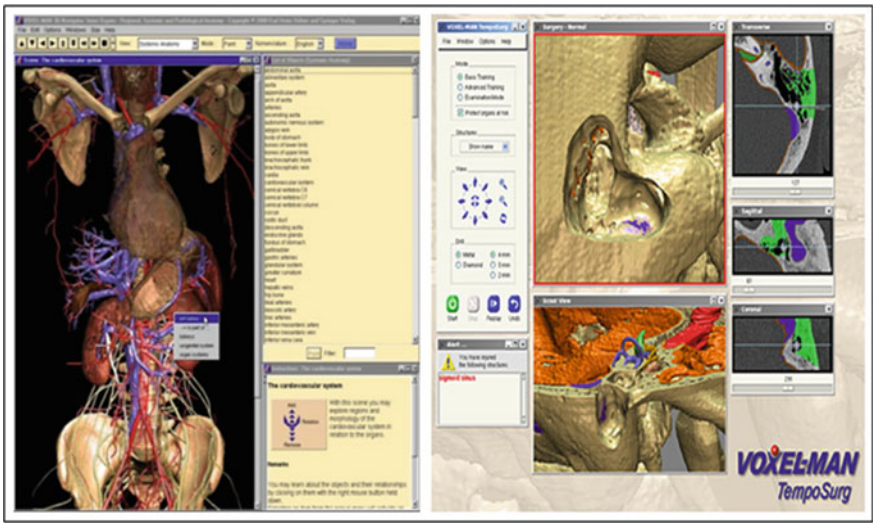

Fig. 13.8 Voxel-man viewer [12]

extensively segmented and mapped to a structured vocabulary (see Fig. 13.8) by using the Visible Human Data [13] set, which contains a high quality CT and MRI full body scan of a male and a female human body and also high resolution images. Unlike other digital atlases as Google body browser, it provides a detailed and annotated model of brain, skull and inner organs inside the torso. In this way, an interactive exploration of a 3D parameterized anatomical model with the possibility of querying is allowed at a very fine level of detail.

In particular, even if it is based on two fixed reference models, the VOXEL-MAN 3D-Navigator application is intended for studying the anatomy in 3D, improving the understanding of both X-ray and cross-sectional radiological images. This is specifically suitable for surgery simulators.

13.3 Emphasis on Lexical Modality

Knowledge technologies and, more in general, knowledge formalizations, are intended to exploit the expressive power of the language to describe in details the medical concepts to focus on. Since natural language is often affected by a certain degree of subjectivity, many efforts are made to provide a shared and formalized lexicalization. In this way, it is possible to address not only standardization, but also machine-readability (due to the formalized representation). Having a precisely formalized terminology, the medical domain looks as an ideal domain to be crystallized into a formal conceptualization. Yet, this field is so broad and heterogeneous that it is difficult to refer to one single conceptualization which is agreed upon. Different

fields are involved (e.g. medicine, biology, chemistry), different facets can be considered (e.g. anatomy, pathology, clinics) and different goals can be set (e.g. simulation, assisted surgery, assisted diagnosis, training). Moreover, some conceptualizations are bound to be compliant with widely adopted standards, such as the ones used for forensic categorization of pathologies.

In this section, we will survey knowledge representation and access efforts and we will analyze them while paying special attention to what they represent (e.g. bones, muscles, blood vessels, medical reports, lab exams), which perspective they originate from (e.g. radiology, anatomy), their expressivity, and their association to visual information. Moreover, we will discuss whether such initiatives are intended to represent general information or patient-specific information, as they can refer to a unique fixed prototype, to multiple prototypes, to parameterized models, or to patient-specific data.

Some comments on the language used to represent knowledge will be also given. Ontologies are the most complete approach to provide an expressive, structured and shared vocabulary because of their intrinsic power of encoding structural complexity; in fact, their use in the medical field started with a focus on the representation and (re-)organization of medical terminologies, e.g. FMA (Foundation Model of Anatomy), ICD (International Classification Diseases) and SNOMED (Systematized Nomenclature of Medicine).

Following the advancement of semantic web technologies, the scenario of medical ontologies is currently evolving: besides providing a common terminology, ontologies can also be used to provide connections among concepts, following the structural, functional and topological connections that exist within the medical information. The development of ontologies has therefore targeted also the support of computational frameworks for clinical decision (e.g. OntoQuest [14]) or the study of the human anatomy and the functional behavior of the organ in a more interactive way (e.g. My Corporis Fabrica).

In the following, we provide a brief summary of some examples of ontologies related to human anatomy that have been developed according to the aforementioned evolution trend, starting from the ontologies describing only terminology up to more structured ontologies.

13.3.1 Systematized Nomenclature of Medicine (SNOMED)

The Systematized Nomenclature of Medicine—Clinical Terms [15], SNOMED CTR, was originally created by the College of American Pathologists (CAP) and is now maintained and distributed by the International Health Terminology Standards Development Organization (IHTSDO). SNOMED CTR aims to provide comprehensive coverage of the health care domain such as diseases, findings, procedures, microorganisms and pharmaceuticals, and indeed is the most comprehensive clinical terminology available.

SNOMED CTR provides a complete conceptualization, and medical documentation can be added as instances to such concepts and consists of 19 independent hierarchies.

One of the interesting features of SNOMED is that it gives a detailed and linked structural description of anatomical entities as well as micro-level entities, and the chance to link instances of such structures to clinical procedures, reducing the variability in the way data are encoded and used for clinical care of patients and research. Examples of micro-level entities are 'Cell structure' and 'Tissue structure' while the relationships among these structures are subclasses of 'Anatomical organizational patterns' (e.g. 'Cell to cell relationship' characterized by 'focal cell contact' is a subclass of 'Cell to cell relationship, distinctive', which is a part of 'Cell structure').

In case of the example of the knee, it is described mainly based on its anatomy and structure: there is no specific concept for 'Knee' but there is a 'Knee region structure', which is a subclass of 'Lower extremity part' which is in turn a 'Body part structure'. The concept 'Knee region structure' is further subdivided into several constitutional parts, like 'Bone structure of knee', 'Knee joint structure', 'Muscle acting on knee joint' or 'Skin and subcutaneous tissue structure of knee'. Some interesting attributes are assigned to the subclass 'Knee region structure' that goes beyond pure anatomical and structural characteristics. For instance, the 'direct_procedure_site_of' attribute contains all the clinical operations which can be performed over 'Knee region structure' (e.g. Combination therapy to knee, CT of knee, Radiography of soft tissue of knee, MRI of knee, Arthroscopy and biopsy of knee); the 'finding_site_of' attribute describes different kind of abnormalities or diseases or injury of whole 'Knee region' (e.g. Acquired deformity of knee, Crushing injury of knee, Open wound of knee).

SNOMED has a rich description of pathologies and procedures, and each of them can be linked with instances of the specific 'Body Part'. In the case of 'Knee Region', we can take the example of 'Knee disarticulation' (semantic type: Therapeutic or Preventive Procedure) which is a subclass of 'Disarticulation'.

13.3.2 Foundational Model of Anatomy (FMA)

The Foundational Model of Anatomy [10] has been developed and is maintained by the Structural Informatics Group at the University of Washington. The FMA represents anatomical entities ranging from biological macromolecules to cells, tissues, organs, organ systems, and major body parts, including the entire body.

It is strictly constrained to pure anatomy, i.e. the structural organization of the body: the FMA is concerned with the representation of classes and relationships necessary for the symbolic modeling of the structure of the human body in a form that is both understandable by humans and navigable by machine-based systems. It can be considered as the reference domain ontology for the discipline of anatomy and provides a template for evolving biomedical domain ontologies (e.g. PRO, the Physiology Reference Ontology [16]).

In FMA the knee is represented by three different concepts, i.e. 'Knee', 'Knee joint' (which is a subclass of 'synovial joint of free limb'), and 'segment of knee', which is actually the structural description of knee. Oddly, these three representations of the same concept are not linked with each other explicitly. The focus of FMA is mainly to provide detailed terminology from the anatomic point of view and not to provide significant connections among the involved classes. In fact, only the two basic relations (i.e. 'is a' and 'part of') are considered. Many other initiatives such as Bodyparts3D and My Corporis Fabrica use and extend FMA because of the richness of its vocabulary.

13.3.3 RadLEX

Radlex^{TM} [17] is a controlled terminology project by the Radiological Society of North America (RSNA). Its aim is to provide a uniform or standard lexicon for indexing and retrieval of a variety of radiology data to be used for teaching, research and reporting procedures. It also unifies and supplements other lexicons and standards, such as SNOMED-CT and DICOM.

It describes all the important terminology in radiology related to anatomy, medical devices, radiology reports, imaging modalities and protocols. The pathology and imaging section describes in details the relationships between pathology and the affected anatomical entity. Also, it makes an explicit connection to the visual modality. In fact, it refences to a set of acquired images (MRI, MicroCT, CT etc.) corresponding to anatomical entities in order to provide a visual representation of canonical data that can be coupled with the radiologic terminology.

In RadLex, the most important concepts related to the knee are 'Knee' and 'Knee Joint'. It provides a detailed structural description of 'Knee joint', like 'articular surface of knee joint', 'ligament of knee joint', 'knee meniscus' (see Fig. 13.9).

13.3.4 GALEN

The Generalized Architecture for Languages, Encyclopedias and Nomenclatures (GALEN) in Medicine was produced during the 1990s by the University of Manchester within the OpenGALEN project, a European Union Project that sought to support reuse of information to integrate medical records, decision support and other clinical systems. The GALEN project established the GALEN Common Reference Model (CRM) [19], an ontology formulated in a specialized description logic, which uses the GALEN Representation and Integration Language (GRAIL) [20]. This ontology contains the building blocks for defining procedures (e.g. anatomy, surgery, and diseases) and their modifiers used in the definitions of surgical procedures. It does not give only the anatomical description but also the clinical act and pathology in details for the body parts.

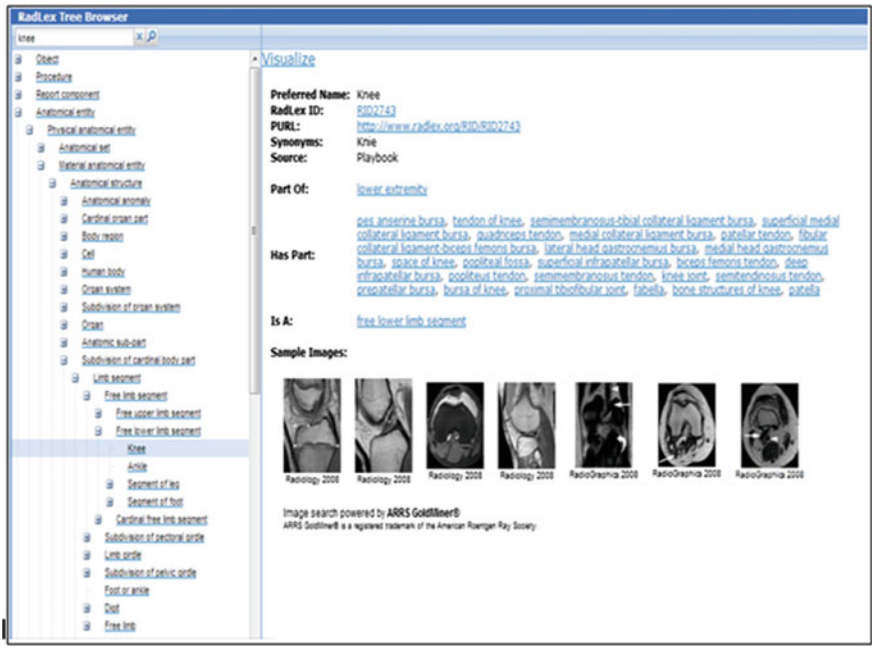

Fig. 13.9 Knee representation in RadLex^{TM} term browser [18]

Unlike traditional terminological resources whose terms are predefined and fixed, this model comprises rules to combine entities so that many descriptions can be composed from a manageable number of base concepts, resulting in the building blocks to define procedures. The main cores of the project are the Semantic Encyclopedia of Terminology (SET), which consists of a generative Master Notation, and a COding REference (CORE) Model for medical terminology.

13.3.5 Unified Medical Language System (UMLS)

The UMLS, or Unified Medical Language System [21], is a software designed to bring together many health and biomedical vocabularies and standards to enable interoperability among ontology systems (see Fig. 13.10). The purpose of the National Library of Medicine® Unified Medical Language System (UMLS) is to facilitate the development of computer systems that behave as if they "understand" the meaning of the language of biomedicine and health.

Three UMLS Knowledge Sources exist:

- The Metathesaurus®, which contains over one million biomedical concepts from over 100 source vocabularies, such as ICD-9-CM [22], NCI Thesaurus [23],

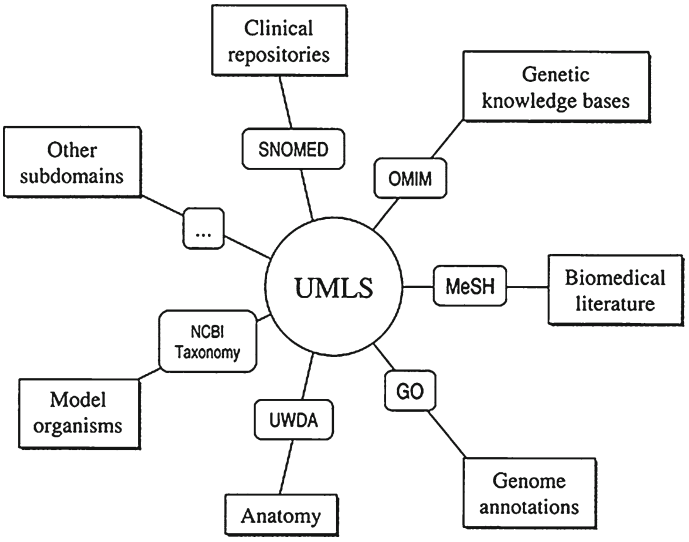

Fig. 13.10 The various subdomains integrated in the UMLS (Courtesy U.S. National Library of Medicine) [21]

MedDRA [24], and SNOMED Clinical Terms. It also contains Concept Unique Identifiers (CUIs), which are used to create a unique reference for resources represented in the different ontologies, treating them as a single resource.

- The Semantic Network, which defines 133 broad categories and 54 relationships between categories for labeling the biomedical domain.
- The SPECIALIST Lexicon and Lexical Tools, which provide lexical information and programs for language processing.

With such tools, UMLS permits to integrate and distribute key terminology [25], classification and coding standards in biomedicine, to manage resources in order to promote the creation of effective and interoperable biomedical information systems and services, and to coordinate patient care among several departments within a hospital.

13.3.6 My Corporis Fabrica

My Corporis Fabrica (MyCF) [26] focuses on the formalization of anatomical knowledge and suggests its computational representation for anatomy modeling. The main objective is to combine knowledge systems with 3D technologies. It provides a framework to manage the connections between abstract anatomic concepts and actual patients and to produce realistic physical models through virtual representations of the human body (see Fig. 13.11). Its main contribution is to create and store

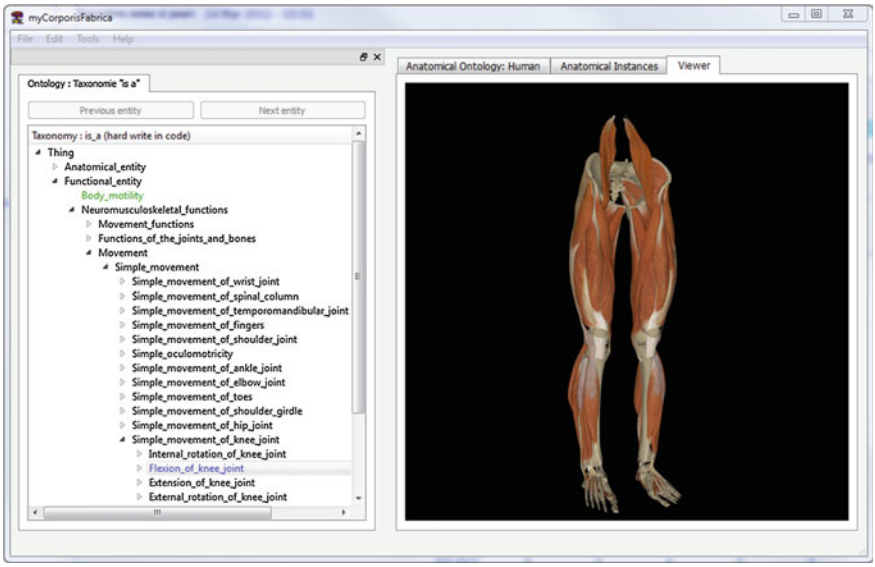

Fig. 13.11 MyCF browser screenshot on lower limbs

links between canonical descriptions of anatomical entities and reality-grounded instances of such descriptions. These instances are parameterized, i.e. characterized in terms of geometrical and physical attributes. A-priori anatomical knowledge can be used to complete patient-specific content. The MyCF browser provides facilities of searching and navigating through the database.

As an example, the Human Knee is modeled by two bones (femur and tibia) and a ligament. Suppose that a user needs to reconstruct a specific model, starting from the models of the femur and of the tibia. To do so, the user needs to know where to insert the extremities of the ligament on the bones. If the parameter corresponding to that position is stored in the database, the user just has to request that attribute, i.e. the position. If the value is unknown, it is possible to set manually a specific value or use a canonical one. In this way, bridging between canonical and specific knowledge is achieved: canonical knowledge is used to model the patient-specific information in absence of specific data.

13.4 Discussion and Future Perspectives

In each of the state-of-the-art solutions we presented it is possible to ask the following question: which of the two approaches (visual and linguistic) has priority over the other?

This question deserves a specific comment, as linguistic and visual approaches look complementary: pure visualization emphasizes immediacy and direct access to information, whereas natural language is targeted at expressivity and communicability. When machine-readability and automatic reasoning tasks have to be triggered, natural language is often not enough, and a formal conceptualization is required.

As we could see, some solutions such as Google body browser are already designed to exploit the power of both visual and linguistic technologies but only for generic models. Such double-sided connection is even more interesting and difficult to obtain when we want to address both general models (prototypes) and patient-specific data.

If we want to identify the possible paths to access the available knowledge, it is interesting to point out how it is possible to move from one piece of knowledge to another. In the visual modality, the user can follow the proximity or the similarity paths: an example of navigation by proximity in the human body may look like "liver → pancreas → stomach", while an example of navigation involving similarity estimation is "the liver of patient P1 → the liver of patient P2". In the linguistic modality, the structure of the language that is used directly influences the ability to navigate: when a lot of meaningful relations are available, it is possible to navigate according to them. For example, if equivalent terms in different languages are linked, it is possible to move from "ginocchio" (i.e. "knee" in Italian) to "knee" in the user navigation; if the structural components of the same district are linked then it is possible to move from "knee" to knee ligament; if a body part is linked to the pathologies that can affect it, then it is possible to move from the knee ligament to "pathology of the knee ligament", then to "chronic pathology" and so on. Actually, the goal of easing the navigation among related information is the basis of the recent hype on Linked Data. In fact, Linked Data [27] is about using the Web to connect related data that were not previously linked, or using the Web to lower the barriers to link data currently linked using other methods. It is possible to say that data recorded using formalisms which are expressive and rich in terms of relations with other data are good candidates to become a qualitative reference for the lexical modalities of the next generation. The capability of easily connecting the two modalities together would open up an effortless dynamic navigation in the available knowledge, as the aforementioned knowledge navigation paths would be potentially infinite, creating advanced pathways in the modern information society and stimulating new medical reasoning and correlations. In this perspective, the digital atlas of the human body may be used as an interface in its generic form and as a repository of all the clinical information of an individual if properly personalized with the patient's data, as prospected by the project DISCIPULUS [28], whose goal is to produce a roadmap for the digital version of the real patient to run the simulations of health and disease processes virtually. Some of the most feasible applications are *running medical simulations* or *surgery predictions*. For example, a digital template of the human leg could be personalized with the patient's data and used to create the 3D model of the prosthesis obtained after running the opportune simulation. MyCF is a first attempt into this direction even if a functional template model of organs is not available yet.

A first issue in need of extensive investigation to reach such an ambitious goal is *how to extract knowledge out of visual data* [29]. Whereas several solutions have been provided both from academia and industry to interpret medical images (e.g. segmentation algorithms), there is still no complete methodology for 3D shape understanding [30]. Thanks to state-of-the-art computational tools, the fully 3D models permit measurements and the extraction of meaningful features which are much richer than the ones derived by stacks of images, but the capabilities of such computational tools in the medical domain are not fully exploited yet. Such tools would help also to fit parametric models from scan data as well as motion capture data and create personalized models of the body part under observation including kinematics.

A second issue to be tackled is *how to enhance the visual model with such knowledge,* i.e. how to accomplish semantic media annotation. Again, while some solutions exist for 2D models, a stable mark up of 3D shapes is not available. In fact, a crucial aspect to take into account is that annotation may be related to either an entire object or its parts; if the target of the annotation is a part of the object, this part has to be selected with appropriate—manual or (semi)automatic—tools and associated with textual data. Such operations are not trivial in the 3D case. Another crucial open problem is how to couple and maintain consistently the annotations with respect to the many representations of the geometry, possibly at different levels of resolution.

Related to this, another key issue concerns a *comprehensive and formal way to document such knowledge* for sharing, search and retrieval purposes. There are a number of general open problems that should be addressed to realize an ideal cataloguing and documentation of the life cycle of 3D objects which apply also to the medical domain. Among those we can mention coding of the data provenance and version control, effective metadata structures and interoperability. In parallel, a standardization issue arises on how to create and manage very large digital repositories, which should involve many actors.

Another issue to tackle is related to the *semantic visualization of a 3D model*, for which multi-scale visualization is one of the possible options. The biggest challenge is how to optimize the rendered images of the 3D data and simplify their visual complexity while retaining the meaningful details visible. This should be done by taking into account the characteristics of the specific device which will display the 3D content and the portion of related knowledge to show to the user. Two important connected issues are involved in this challenge. The first one refers to the so-called *semantic zooming*: while under geometric (standard) zooming the view depends on the physical properties of what is being viewed, the effect of the semantic zoom is that of changing the representation of the object (or of some of its parts) for different spatial scales. When zooming away, instead of seeing a scaled down version of an object, the user may see a different representation which depends on the meaning to be imparted. This is clearly much more sophisticated than a Level-Of-Detail representation and calls for a semantic description of the shape and its parts. The second aspect, more technical yet meaningful in terms of outreach, concerns the adaptation of the content to the end device. In this case, compression and resizing algorithms are needed, which again should preserve the meaningful features according to the model

to be visualized, to the visualization purpose, to the type of insight to be achieved and to the type of decision to be taken after.

Finally, when considering *semantic interaction*, we may think of 3D search as a type of interaction with the user. Content-based and context-based search of 3D models call for new requirements for information representation, filtering, aggregation and networking, which are as intuitive as possible and effective in their capability of bringing the users to the 3D content they wish to access.

Acknowledgments This work is supported by the FP7 Marie Curie Initial Training Network "MultiScaleHuman": Multi-scale Biological Modalities for Physiological Human Articulation (2011–2015), contract MRTN-CT-2011-289897. We kindly acknowledge the partial support of the FP7 "VISIONAIR": Vision Advanced Infrastructure for Research (2011–2015), grant no. 262044, POLITECMED—Research and Innovation Pole of the Regional Centre for Research and Innovation of the Regione Liguria, and the Italian CNR Flagship project INTEROMICS, InterOmics PB05, research unit WP15. Finally, we kindly thank Osman Ratib for his comments on OsiriX.

References

1. Garber, A. M., Owens, D. K., Singer, S. J., & Enthoven, A. C. (2006). In E. H. Shortliffe & J. J. Cimino (Eds.), *Biomedical informatics: Computer applications in health care and biomedicine*. Newyork: Springer.
2. Andrews, B. (2006). Introduction to "perceptual principles in medical illustration". *ACM SIGGRAPH 2006 Courses, SIGGRAPH '06*. NY, USA: ACM. Retrieved July 30, 2006, from DOI=10.1145/1185657.1185691 http://doi.acm.org/10.1145/1185657.1185691
3. Rosset, A., Spadola, L., & Ratib, O. (2004). OsiriX: An open-source software for navigating in multidimensional. *Journal of Digital Imaging*, *17*(205–216).
4. Friese, K. I., Blanke, P., & Wolter, F. E. (2011). YaDiV–An open platform for 3D visualization and 3D. In *The visual computer 27*. Newyork: Springer.
5. 3D Slicer. http://www.slicer.org/
6. White paper on multiscale visualisation (2012). s. l.: http://www.msv-project.eu
7. Google. *Google body browser*. http://www.zygotebody.com/
8. Mitsuhashi, N., Fujieda, K., Tamura, T., Kawamoto, S., Takagi T., & Okubo, K. (2009). BodyParts3D: 3D structure database for anatomical concepts. *Nucleic Acids Research*, *37*, D782–D785.
9. BodyParts3D. The Creative Commons Attribution-Share Alike 2.1 Japan. http://lifesciencedb.jp/bp3d/
10. Rosse, C., & Mejino, J. L. V. (2003). A reference ontology for biomedical informatics: The foundational model of anatomy. *Journal of Biomedical Informatics*, *36*, 478–500.
11. FMA on Bioportal. http://bioportal.bioontology.org/ontologies/1053
12. Voxel-Man. http://www.voxel-man.de/3d-navigator/inner_organs/
13. Visible Human Dataset. http://www.nlm.nih.gov/research/visible/getting_data.html
14. Chen, L., Martone, M. E., Gupta, A., Fong, L., & Wong-barnum, M. (2006). OntoQuest: Exploring ontological data made easy. *Very Large Data Bases—VLDB* Conference, (pp. 1183–1186).
15. Spackman, K. (2000). Snomed rt and snomed ct. promise of an international clinical terminology. *Computer Molecular Dynamics*, *17*(6), 29.
16. Cook, D. L., Mejino, J. L. V., & Rosse, C. (2004). Evolution of a foundational model of hysiology: Symbolic representation for functional bioinformatics. *Medinfo*, *11*, 336–340.
17. RadLex. http://www.radlex.org/

18. Langlotz, C. P. (2006). RadLex: A new method for indexing online educational materials. *Radiographics, 26*, 7–1595. (Pubmed citation).
19. Zanstra. P. E., van der Haring, E. J., Flier, F., Rogers, J.E., & Solomon, W. D. (1997). Using the grail language for classification management. *Fifteenth International Congress of the European Federation for Medical Informatics* (Vol. 97, pp. 441–445). Thessaloniki, Greece: MIE.
20. Rector, A. L., Bechhofer, S., Goble, C. A., Horrocks, I., Nowlan, W.A., & Solomon W. D. (1997). The grail concept modelling language for medical terminology. *Artificial Intelligent Medicine*, *9*(2), 139–171.
21. U.S. National Library of Medicine. (2011, March) *Unified medical language system® (UMLS)®*. Retrieved March, 2011 from http://www.nlm.nih.gov/research/umls/quickstart.html
22. International Classification of Diseases, Ninth Revision, Clinical Modification (ICD-9-CM). http://www.cdc.gov/nchs/icd/icd9cm.htm
23. NCI Thesaurus (NCIt). https://wiki.nci.nih.gov/display/EVS/NCI+Thesaurus+(NCIt)
24. MedDRA. http://www.ich.org/products/meddra.html
25. Bodenreider, O. (2004). The unified medical language system (UMLS): Integrating biomedical terminology. *Nucleic Acids Research, 32*, 267–270.
26. Palombi, O., Bousquet, G., Jospin, D., Hassan, S., Revéret, L., & Faure, F. (2009). *My Corporis Fabrica: A unified ontological, geometrical and mechanical view of human anatomy*, (Vol. 5903, pp. 207–219). Lecture notes in computer science. In 2nd workshop on 3D Physiological Human, 3DPH2009, Zermatt: Springer.
27. Heath, T., & Bizer, C. (2011). Linked data: Evolving the web into a global data space. In *Synthesis lectures on the semantic web: Theory and technology* (Vol. 1, issue 1, pp.1–136). Florida: Morgan and Claypool
28. The Digital Patient. http://www.digital-patient.net/
29. Catalano, C. E., Mortara, M., Spagnuolo, M., & Falcidieno, B. (2011, August). Semantics and 3D media: Current issues and perspectives. *Computers and Graphics*, *35*(4), 869–877.
30. Catalano, C. E., Robbiano, F., Parascandolo, P., Cesario, L., Vosilla, L., Barbieri, F., Spagnuolo, M., Viano, G., & Cimmino, M. A. (2013). Exploiting 3D part-based analysis, description and indexing to support medical applications. In *Proceedings of MCBR-CDS 2012: Medical Content-based Retrieval for Clinical Decision Support, MICCAI workshop, LNCS 7723, (pp. 21–32)*, Newyork: Springer.